

6th INTERNATIONAL ENGINEERING SYMPOSIUM – IES2017

**Faculty of Engineering (Building No.2)
Kumamoto University**

March 1-3, 2017



Conveners
Shuichi TORII
Professor, Department of Mechanical System Engineering
Kumamoto University, Japan
&
Katta VENKATARAMANA
Professor, Department of Civil Engineering
NITK, Surathkal, India

Organized by
Graduate School of Science & Technology
Kumamoto University, Japan

In association with
National Institute of Technology Karnataka, India

PROCEEDINGS OF
**6th INTERNATIONAL ENGINEERING
SYMPOSIUM – IES2017**

Venue

Faculty of Engineering (Building No.2)
Kumamoto University

Date

March 1-3, 2017

Conveners

Shuichi TORII

Professor, Department of Mechanical System Engineering
Kumamoto University, Japan

&

Katta VENKATARAMANA

Professor, Department of Civil Engineering
NITK, Surathkal, India

Organized by

**Graduate School of Science & Technology
Kumamoto University
Kumamoto City, Japan**

In association with

**National Institute of Technology Karnataka
Surathkal, Mangalore, India**

PREFACE

The 1st International Engineering Symposium (IES2011), the 2nd International Engineering Symposium (IES2012), the 3rd International Engineering Symposium (IES2013), the 4th International Engineering Symposium (IES2015) and the 5th International Engineering Symposium (IES2016) were organized very successfully at Kumamoto University with more than 100 participants from India, Japan, Indonesia, Thailand, Taiwan, Vietnam and other countries. With the objective of continuing the interaction between the researchers during these symposia, the 6th International Engineering Symposium (IES2017) has been organized in the month of March, 2017. This symposium provides a common platform for bringing together researchers for expanding academic collaboration.

As part of this symposium, the researchers and the students from abroad have been invited to visit Kumamoto University and get exposed to its educational and research activities. The event focuses on the current R&D of the participating institutions on topics of mutual interest, with a special emphasis on "Science & Technology". The emerging technology and scientific advancements are discussed during the symposium. Presentations feature new and innovative technologies in the relevant fields.

This proceedings volume contains the technical papers presented at the symposium. The topics include a wide spectrum of themes covering major disciplines of science and engineering. The effort put in by the faculty, the staff and the students of Kumamoto University in organizing this event are greatly appreciated.

We sincerely hope that you will find the contents of this proceedings volume useful and productive. We look forward to more intense academic collaborations and research interactions in the coming days, to achieve the common goal of technological advancement for global peace and prosperity.

Shuichi Torii
Katta Venkataramana
Conveners

6th International Engineering Symposium - IES 2017

March 1-3, 2017, Kumamoto University, Japan

IES2017 Program Schedule

Venue: Faculty of Engineering, Building No.2

March 1, 2016 (Wednesday)

11:00 – 11:30	Registration
11:30 – 12:00	<i>Opening Address & Introduction of GSST</i>
12:00 – 12:20	Keynote Lecture (K1)
12:20 – 12:40	Keynote Lecture (K2)
12:40 – 13:10	Keynote Lecture (K3)
13:10 – 14:00	Lunch
14:00 – 17:00	Campus Tour & Laboratory Visits
17:00 – 17:30	Free Time
17:30 – 19:00	Welcome Reception

March 2, 2016 (Thursday)

10:00 – 11:30	Technical Sessions (C1, E1, M1, A1)
11:30 – 11:45	Tea Break
11:45 – 13:00	Technical Sessions (C2, E2, M2)
13:00 – 14:00	Lunch
14:00 – 15:30	Technical Sessions (C3, C4, M4)
15:30 – 16:00	Tea Break
16:00 – 17:30	Free Time
17:30 – 19:00	Symposium Dinner

March 3, 2017 (Friday)

9:00 – 18:00	Field visits
--------------	---------------------

Lunch & Dinner Venue - FORICO Cafeteria

Notations:

K Keynote Lectures

M Technical Sessions (Mechanical Engineering & Related Fields)

C Technical Sessions (Civil Engineering & Related Fields)

E Technical Sessions (Electrical, Electronics, Computer Engineering & Related Fields)

A Technical Sessions (Chemistry, Chemical Engineering & Related Fields)

Contents

Keynote Lectures

- K1 Finite Element Simulation for Input Shaping Design of Long Range Motion Systems: Analyses and Applications - *Weiju Chen, Kuo-Shen Chen and Yun-Hui Liu*
- K2 Mathematical modelling of removal of Xenobiotic Organic Chemicals (XOCs) on the basis of biodegradation kinetics - *Kshitija Kakade, and Arun Kumar Thalla*
- K3 Solids drying studies in a multiple draft tube spouted bed dryer
Yoshitaka Nakanishi

Civil Engineering & Related Fields

- C1-1 Failure - Manifestation & Manipulation
K.S. Babu Narayan
- C1-2 Stabilization of Expansive Clays using Granulated Blast Furnace Slag and Polypropylene Fibers - *Anjana M and B.M. Sunil*
- C1-3 Laboratory Evaluation of Cold Bituminous Mixtures
Chinju Chandran and Suresha S.N.
- C1-4 Vegetation Growth in Waste Rock Produced from Opencast Coal Mines with Different Additives - *K. Ram Chandar and G. Vikas Chitanya*
- C1-5 Mechanical and Durability Properties of Concrete with Precious Slag Balls (PS Balls) as Replacement for Fine Aggregates
Gayana B.C, Sharath S and K. Ram Chandar
- C1-6 Building Extraction from Quickbird-2 Imagery
A Arkal Vittal Hegde and Jagalingam P
- C2-1 Soil Arching Effect in Columnar Embankments
Riya Roy and Anjana Bhasi
- C2-2 Settlement Behaviour of Geocell Reinforced Embankments Supported by Stone Columns- *Vibhoosha M P, Anjana Bhasi and Sitaram Nayak*
- C2-3 Analysis of Stresses Around a Tunnel Opening
Ragini Nikumbh and K. Ram Chandar
- C2-4 Study of Interference of Strip Footing on Clay
Amrita and R Shivashankar

6th International Engineering Symposium - IES 2017

March 1-3, 2017, Kumamoto University, Japan

- C2-5 A Review on Probabilistic Methods in Seismic Hazard Analysis
Shreyasvi C and Katta Venkataramana
- C3-1 Numerical Simulation of Prefabricated Horizontal Drains (PHD) Induced Consolidation in Clayey Deposits – *Anjana R Menon and Anjana Bhasi*
- C3-2 The Influence of Angle of Internal Friction on Cantilever and Anchored Sheet Pile Walls in Cohesionless Soil- *Mahima R and Sitaram Nayak*
- C3-3 Effect of Surcharge on Slope Stability
Surya E V and Sitaram Nayak
- C3-4 Electrical Resistivity of Soil – Impacts and Applications in Geotechnical Engineering
Divya Nath, Nimi Ann Vincent, R. Shivashankar and K.N.Lokesh
- C3-5 Effect of Benching on the Stability of Slopes
Jolsna Narayan and Sitaram Nayak
- C3-6 Effect of pile aspect ratio on geogrid reinforced piled embankments
Sreelekshmy. S, Radhika. M. Patel, B. R. Jayalekshmi and R. Shivashankar
- C4-1 Development of decision support system for dewatering system selection for water supply projects- *Sooraj Balakrishnan P and M K Nagaraj*
- C4-2 Development of methodology for deactivation modeling of Citrobacter by UV radiation - *Priti Deshpande and C.P. Devatha*
- C4-3 Use of Ferrofluid for Contaminants Removal from Wastewater
Shwetha Sreekumar, Amandeep Narang and Dhanashree Sanket
- C4-4 Ferrofluid Synthesis and Its Use in Oil Removal from Water Surface
Amandeep Narang, Shwetha Sreekumar and Dhanasree Sanket
- C4-5 Seismic Response of Buildings with Confined Masonry Construction: A Review
Seethu K and Katta Venkataramana
- C4-6 A Study on FEMA P58: Next Generation Building Seismic Performance Assessment Methodology – *Bindhya K V and Katta venkataramana*
- C4-7 Recent Developments in the Performance-Based Seismic Design
Haseena M Mumthas and and Katta venkataramana

Mechanical Engineering & Related Fields

- M1-1 Enhancement of Boiling Heat Transfer on a Vibrating Heating Surface
Kohei Hamahata and Hiroyuki Shiraiwa

- M1-2 Reliability Analysis on Solid Rocked Engine Vessel
LIU Chong, TORII Shuichi and CHEN Yuting

- M1-3 Computational Study of mixed convection in a lid-driven cavity with square block subjected to constant heat flux
G Narendran, D Arumuga Perumal and N Gnanasekaran

- M1-4 Simulation of Solar ORC system for small scale power generation
Suhas Upadhyaya and Veershetty Gumtapure

- M1-5 Study on Molding Properties of Obsidian Perlite
Kota KAWAMURA, Shunta MORI, Yasuo MARUMO, Taekyung LEE, Yasuhiro IMAMURA, Takanori MASU and Akikazu ETO

- M1-6 Evaluation of physical properties of WC-CrC-Ni reinforced stainless steel composite prepared by Metal injection Molding
Veeresh Nayak C, Sudip Kumar Samanta, M R Ramesh and Vijay Desai

- M2-1 Development of New Apparatus to Evaluate Ultrasonic Reflection Characteristic for Wrinkling in Press Forming -*Yuji Segawa, Takuya Kuriyama, Yasuo Marumo, Taekyung Lee, Yasuhiro Imamura, Tomohiro Nonaka and Yutaka Sakata*

- M2-2 Performance Analysis of a Model Water-Wave Energy Harvesting System with a Paddling-Wall Wave Tank -*Po-Hsun Chen and Tian-Shiang Yang*

- M2-3 Microstructure, mechanical and corrosion properties of accumulative roll bonded Mg-2%Zn/anodized Al-7075 composite
Gajanan Anne, M R Ramesh, H Shivananda Nayaka and Shashi Bhushan Arya

- M2-4 Effect of Spark Timings on Combustion and Emissions Characteristics of 4 Stroke - 4 Cylinder S. I. Engine using Hydrogen at 1500 rpm
Parashuram R. Chitragar, Thirumoorthy and G.N.Kumar

- M2-5 High Temperature Erosion Behaviour of Plasma Sprayed NiCrAlY-25WC-Co/Cenospheres Composite Coating
Mahantappa Mathapati, Ramesh M R and Mrityunjay Doddamani

- M3-1 Small Scale Biomass Gasification Challenges for Power Generation in Rural Area, A Review
Priyambodo Nur Ardi Nugroho and Shuichi Torii

- M3-2 Heat Transfer Enhancement Using Graphene Oxide/Water Nanofluid in a Two-Phase Closed Thermosyphon
Mohamed Salem, Tarek A. Meachail, Magdy A. Bassily and Shuichi Torii

- M3-3 Biogas as an Entrusted Alternative for Fossil Fuels: A Review
Farhana Huqe and Shuichi Torii

6th International Engineering Symposium - IES 2017

March 1-3, 2017, Kumamoto University, Japan

- M3-4 Fundamental Study of Simple Prediction Method for Temperature Drop at Contact Portion of Solids with Thin Disk-Like Protrusion
Taewan Do, Toshio Tomimura and Yasushi Koito
- M3-5 Mechanical behavior of compression molded glass microballoon/HDPE syntactic foams - *Jayavardhana M L, Mrityunjay Doddamani*
- M3-6 Investigation of heat transfer coefficient and Bubble dynamics of ethanol during subcooled flow boiling - *Suhas B.G and Sathyabhama A*
- M3-7 Wear behavior of AM80 magnesium alloy processed by equal channel angular pressing - *Gopi K R and H Sivananda Nayaka*
- M3-8 Effect of Electro-Thermal Parameters on Lesion Formation during Radiofrequency Ablation in Different Tumor Tissues
Charanakumar E, Kamini Kaushal and Ajay Kumar Yadav
- M3-9 Semi Active Vibration Control of Partially Treated Magnetorheological Fluid Sandwich Composite Beams - *Vipin Allien J, Hemantha Kumar and Vijay Desai*

Electrical, Electronics, Computer Engineering & Related Fields

- E1-1 Wireless Monitoring of Water Resources in a Campus
N. Shekar V. Shet, Naveen Kumar Panguluri, Harsha M P and Abhishek MB
- E1-2 Wirelessly monitoring of water usage in smart campus: A CPS perspective
Abhishek M B and N. Shekar V. Shet
- E1-3 Hierarchical Clustering Algorithm for Green IOT
Spoorthi P. Shetty and Udaya Kumar K. Shenoy
- E1-4 Heuristics for Strong Minimum Energy Topology Problem in wireless sensor networks
Pushparaj Shetty D
- E1-5 Optimal Probabilistic Logical Key Hierarchy schema for secure group communication in Mobile Ad-hoc Networks - *N. Hemanth Kumar and Alwyn R. Pais*
- E1-6 Performance Comparison of Region Consistency Activation Algorithm on Pixel wise Scene Labeling - *Dinesh Naik and Jaidhar C D*
- E2-1 Design Of Fuzzy Logic Speed Controller For BLDC Motors Using MATLAB/SIMULINK
Sukanya.M. Sundaram
- E2-2 Predictive Data Analytics for Counterterrorism
Sahana Roy
- E2-3 Automation and Communication in Wildlife Monitoring & Management
Sukriti Singh

6th International Engineering Symposium - IES 2017

March 1-3, 2017, Kumamoto University, Japan

- E2-4 Big Data Analytics in Transportation Economics: Opportunities and Challenges
Savita Bhat
- E2-5 Face Classification using Convolution Neural Networks
Raghurama, Gururaja Rao P, Rajesh Poojary, Gajendra S Patagara, B. Neelima
- E2-6 Gesture Based Home Automation Using Internet-of-Things
Srinivasan.C.K, Subhin Antony and Sreekantha.D.K
- E2-7 Trust Aware Secure Service-Composition in Cloud Environment
Usha Divakarla and K.Chandrasekaran

Chemistry, Chemical Engineering & Related Fields

- A1-1 Aqueous Two-phase Extraction of anthocyanin from fruits of *Garcinia indica*
Basavaraj Nainegali, Regupathi I and Prasanna B. D
- A1-2 Simulation and Control of Continuous Crystallization Process
Yashas Mohankumar, Sai Dinesh B and C. Sankar Rao
- A1-3 Photoluminescence Quenching in Calcium Interacted Graphene Quantum Dots
Praveen Mishra and Badekai Ramchandra Bhat
- A1-4 Optimization of lipase mediated enrichment of n-3 PUFA glycerides in Indian Sardine Oil - *Charanya Sampath, Prasanna D Belur and Regupathi I*
- A1-5 Ultrasound assisted synthesis of γ -MPS modified HNTs-Polystyrene Nanocomposites by Miniemulsion Polymerization - *Kezia Buruga and Jagannathan. T. K*
- A1-6 Screening of Reverse micellar system for the extraction of Bovine Lactoferrin
Swapnali S. Pawar, Regupathi I and Prasanna B. D

KEYNOTE LECTURES

Finite Element Simulation for Input Shaping Design of Long Range Motion Systems: Analyses and Applications

Weiju Chen¹, Kuo-Shen Chen² and Yun-Hui Liu³

1 Department of Mechanical System, National Cheng-Kung University, Taiwan.

*2 Department of Mechanical Engineering, National Cheng-Kung University, Taiwan.
email:kschen@mail.ncku.edu.tw*

3 Department of Mechanical Engineering, Southern Taiwan University of Science and Technology, Tainan, 710, Taiwan, R.O.C. email:yhliu@mail.stust.edu.tw

ABSTRACT: Flexible long range motion systems have been widely used for objects transportation and precision positioning tasks. However, the motion-induced swing and residual vibration could result in extra time for settling and thus reduce the system performance. Input shaping is an effective method for vibration suppression. For counting the situation of insufficient actuator bandwidth, new shapers which have better robustness called HDZV shaper are proposed. Both simulation and experimental data exhibit highly correlated results. Finally, a real size simulation case have been investigated and the results indicate that input shaping can effectively enhance the transportation efficiency of these applications and the design of input shaper based on finite element dynamic analysis would be a viable approach for flexible systems with complicate dynamics and constrains such as non-holonomic systems.

Keywords: *Long Range System, Input Shaping, Robustness, Finite Element Method*

INTRODUCTION

Long range motion system have been widely used in many factory and cargo ship transportation applications [1,2,3]. For those purposes, it is desired that the transportation process being as rapid as possible for efficiency considerations. In general, a gantry crane with hoisting cables and an end payload can be modeled as a pendulum in linear translation and its effectiveness is often limited by both the transient swing and the residual oscillation of the payloads after reaching their destinations. Furthermore, any excess in swings and oscillations could also be dangerous to people working underneath. As a result, devising a method to rapidly transport the payloads with minimum swing during transportation and minimal residual vibration after reaching the destination is a non-trivial task. One possibility for solving the above-mentioned

problem is to utilize command shaping method for performing an efficient trajectory planning to minimize swing and suppress motion-induced residual vibrations after reaching the destination.

Previously, the problems are usually treated as a pendulum mounted with rigid links mounted on a trolley with controlled movements [4] and only the rigid body modes such as swing are considered. However, the compliance of the structures were not considered in those studies. This is not trivial since the structural vibration could also be excited due to the compliance existed in cable or structures.

As shown in Fig. 1, cranes can be modeled either as single or double pendulums. By utilizing time optimization schemes, it is possible to find commands for trajectory optimization. Such an open-loop based input shaping scheme has been

demonstrated to be effective for suppressing motion induced vibrations of flexible structures and swing of long range motion structures such as cranes [4]. For designing the corresponding command shapers, the system dynamics and responses must be modeled. However, there are two major problems faced when employing analytical modeling. First, the problem is essentially nonlinear. In order to be solvable analytically, the system dynamics requires extensive linearization, which could lead to the loss of important information and cause the designed shapers to have inferior performance. Second, for more realistic systems, it might be difficult to use a set of independent generalized coordinates to represent the system and the nonholonomic Lagrange's equation must be applied. This approach yields more differential equations than the number of degrees of freedom. Consequently, it could be more difficult to solve the equations and the shaper design becomes more challenging. In addition, it is expected that as the structure flexibility is considered, the dynamic equations would become more difficult to obtain and solve. From a practical perspective, in such a circumstance, the analytical modeling loses its advantages and becomes less attractive thus a numerical scheme is usually employed. In order to handle such systems, one may prefer to use a finite element (FE) dynamic analysis, which can handle both of the rigid body and extremely complicated structural modes with sufficient accuracy. It is also possible to characterize the necessary parameters for designing the associate input shapers such as natural frequencies and mode shapes. Furthermore, it is also possible to handle nonlinear dynamics due to geometric or material constitutive relations. By adapting the viewpoint of force balance and energy conservation, it should be able to expand the traditional linear superposition based shaper design into nonlinear systems. These are the major advantages of using FE for conducting input shaping design and this may eventually lead to a more efficient command shaper design and verification.

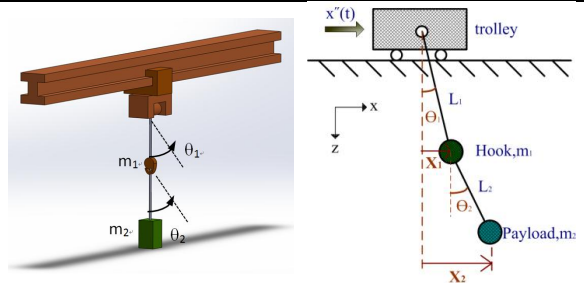


Fig. 1 Schmatic plot of a gantry crane with payload and its corresponding double pendulum model

Previously, Dai and Chen [5] investigated the swing control of cranes using input shaping method. The crane hoist was either modelled as a travelled single pendulum analytically or by a finite element beam model for evaluating the influence of the cable compliance. In this work, more general scenarios are considered. Namely, for suppressing both the bending and torsional vibration of flexible structures when they undergo high speed maneuver. A simplified slender elastic structure model is constructed for mimicking the behavior of a long compliant robot arm in high speed maneuver. The associated finite element simulations would then be performed to analyze the dynamic characteristics of the model for subsequent input shaping design. Finally, with input shaper ready, the dynamic behavior of the entire shaped system can then be simulated by finite element method again. By comparing the simulation and the experimental results, the effectiveness of the finite element-based input shaping design are examined first. After correlated with experimental data, the FE based input shaping design approach would then be used in systems with more complicated structural dynamics.

Input Shaping Schemes

As shown in Fig. 2, by properly convolving the original input commands with specific impulse trains, it is possible to optimize the original command to achieve a faster settling. In particular, as shown in Fig. 3, shapers resulting in 'zero vibration' (ZV)

and 'zero vibration and derivative' (ZVD) are developed based on linear discrete models [6]. In comparison with incorporating with active controls, the input shaping scheme is cheaper and more flexible, and has been applied to reduce the system settling time in various applications. In addition, it is also possible to integrate both input shaping and active control design for achieving a better performance. However, due to its open loop nature, the success of input shaping relies on accurate dynamic modelling and the robustness itself.

For long range motion 2-DOF applications, the motion command can be convolved the original bang-bang command with impulse trains and methods such as ZVZV and ZVZVD methods [6] have been developed and the motion command are shown in Fig. 4. Meanwhile, an input shaping scheme, called as half double zero vibration (HDZV) shaper is also used in this work for examining its effectiveness [7]. In comparison with ZVZV, the HDZV should provide better robustness [7].

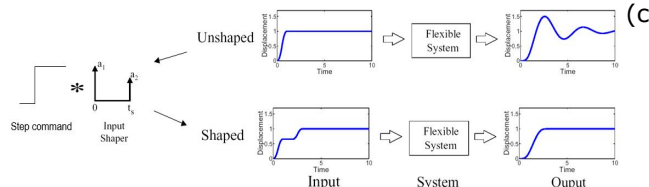


Fig. 2 Schematic plot of input shaping for suppression residual vibrations

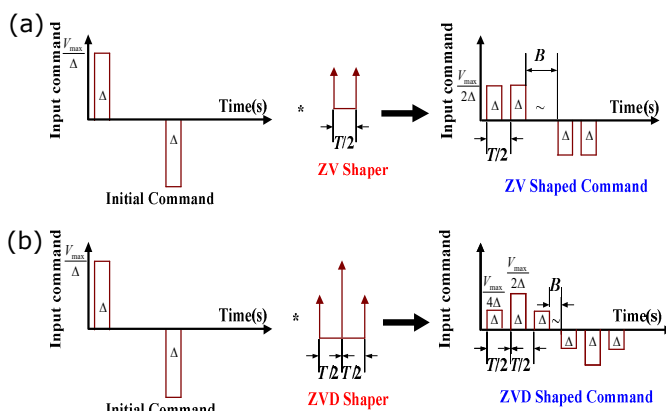


Fig. 3 Schematic plots of (a) ZV and (b) ZVD shaping schemes in long range point to point maneuver

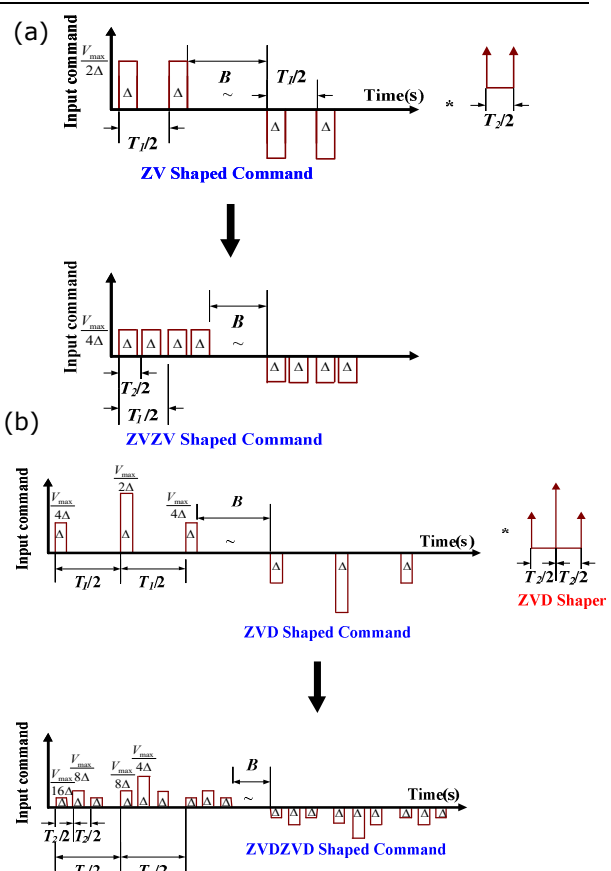


Fig. 4 Schematic plots of input shaping schemes in dual mode suppression. (a) ZVZV, (b) ZVDZVD, and (c) HDZV methods

Experimental System Setup

In this work, it is desired to suppress both the motion-induced bending and torsional vibrations, which could be excited for gantry-type robots during service shown in Fig. 5a. The corresponding experimental system is shown in Fig. 5b, which consist

of two flexible beams under an eccentric configuration. By both structural test and finite element analysis, the natural frequencies are 0.67 and 1.24 Hz for the torsional and the bending modes, respectively. Three ADXRS614 MEMS gyroscopes are hired as the vibration sensors for monitoring both vibration modes. The schematic flow of experiment is shown in Fig. 6. A Yokogawa two-axis linear motor controlled by a computer is used for driving this torsion-bending structure. In parallel, associated vibration data collected by the three gyroscopes are then processed and analysed by the other computer. The motor is commanded to perform a long range motion (e.g., 40cm) with speeds typically in the vicinity of 20 cm/s. Both ZVZV and HDZV are used for evaluating the performance of vibration suppression.

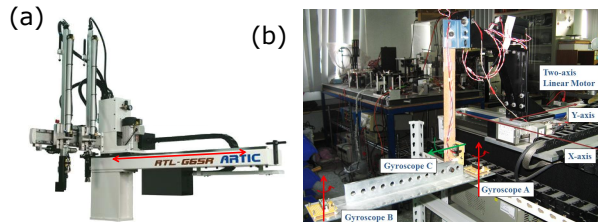


Fig. 5 (a) The gantry type robot arm and (b) the corresponding experimental system.

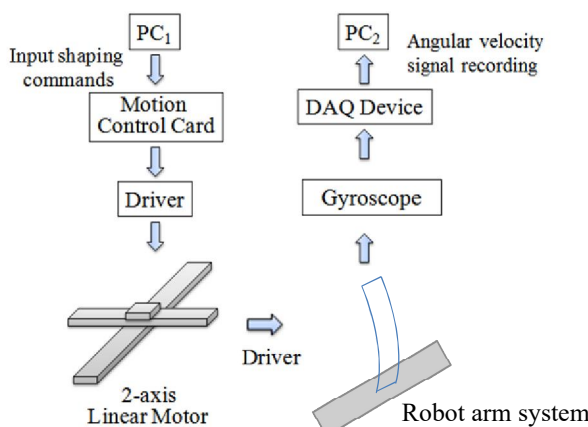


Fig. 6 The experimental flow

Experimental Results

Based on the natural frequencies characterized above, input shaping schemes are implemented. As shown in Fig. 7, it can be found that the vibration is severe under a simple bang-bang command. On the other hand, commands modified by ZVZV or HDZV can effectively suppress the motion-induced vibration. Meanwhile, both gyroscopes A and B indeed catch the torsional mode, on the other hand, the major vibration mode caught by the gyroscope C is the bending mode. This observation also agrees with prediction in our design.

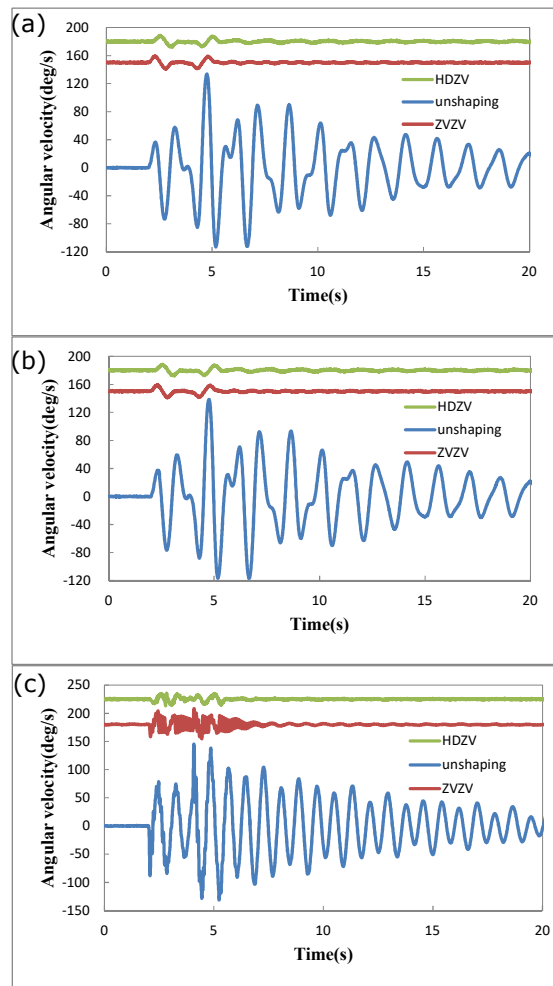


Fig. 7 The experimental results from (a)gyroscope A (b)gyroscope B and (c)gyroscope C

Finite Element Simulations

Next, the corresponding finite element dynamic simulation of the experimental

structure are performed by using Simulia Abaqus. Fig. 8a shows the mesh and the simulation results are shown in Fig. 8b-d based on the same input conditions. It can be seen that the FE simulation results agree with the experimental data very well. Both the vibration frequencies (0.7 Hz and 1.2 Hz) and the effectiveness of input shaping schemes have been revealed. Based on this validation, it is possible to use finite element dynamic simulation for design input shapers in real complex systems.

Now, consider an optical inspection system schematically shown in Fig. 9a, its cantilever nature implies that the vibration modes could possibly be excited during maneuver and the inspection yield would be degraded due to longer settling time. Here we would like to use finite element simulation to design the input shapers for overcoming this concern. The corresponding finite element model is shown in Fig. 9b. The first two natural frequencies are calculated as 20.78 and 23.26 Hz, respectively. Three shapers, ZVZV, HDZV, and ZVDZVD, are hired in this case.

A sharp turn trajectory is then used to illustrate the design. The model is command to travel with a speed of 1cm/s in x-direction for 10 mm and then in y-direction for another 10 mm after a sharp turn. From Fig. 10, it can be seen that a residual vibration with amplitude around $70\mu\text{m}$ are generated after the sharp turn with standard unshaped command. On the other hand, with input shapers, the vibration levels can be reduced significantly. For example, under a ZVZV command, the vibration amplitude can be reduced to $0.6\mu\text{m}$ and the amplitudes are even less for the other two shapers.

Finally, it is also interesting to examine the robustness of these shapers. By assuming a 10% mismatch in all shaper parameters in the FE model, the performance of these shapers are shown in Fig. 11. It can be seen that the degradation is within the tolerance limit. The robustness of ZVDZVD is better than that of ZVZV and HDZV. Nevertheless, the performances of

these shapers are all acceptable for real applications.

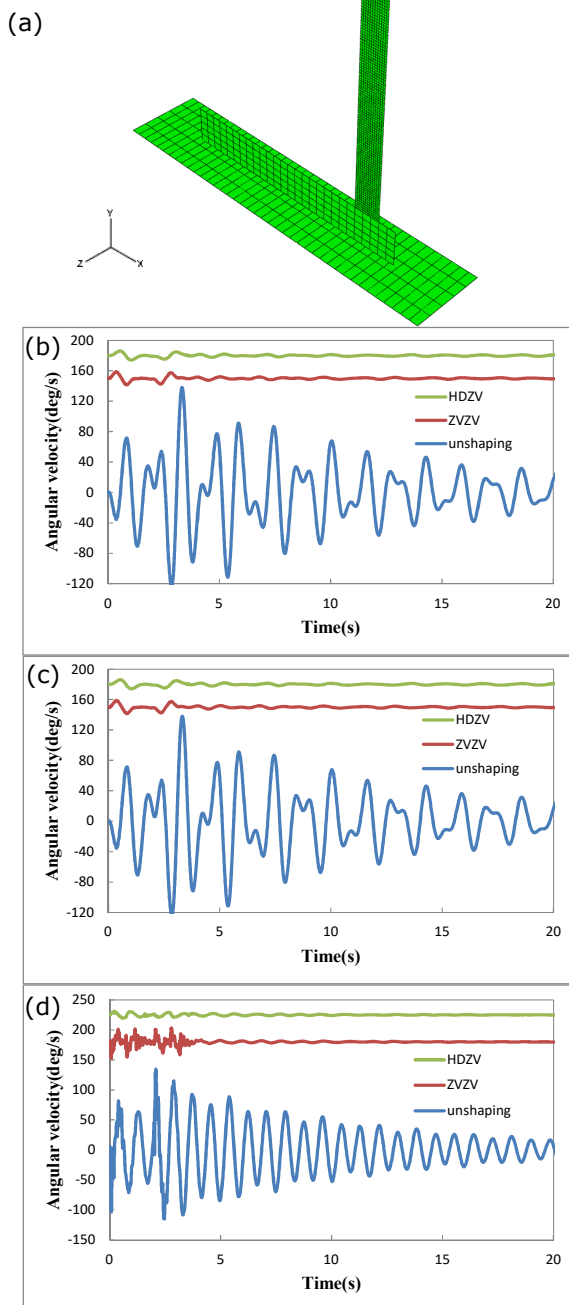


Fig. 8 (a) the finite element model and the simulation results from (b) gyroscope A (c) gyroscope B and (d) gyroscope C

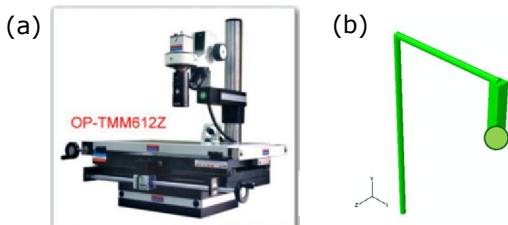


Fig. 9 (a) an optical inspection system and (b) its corresponding finite element model

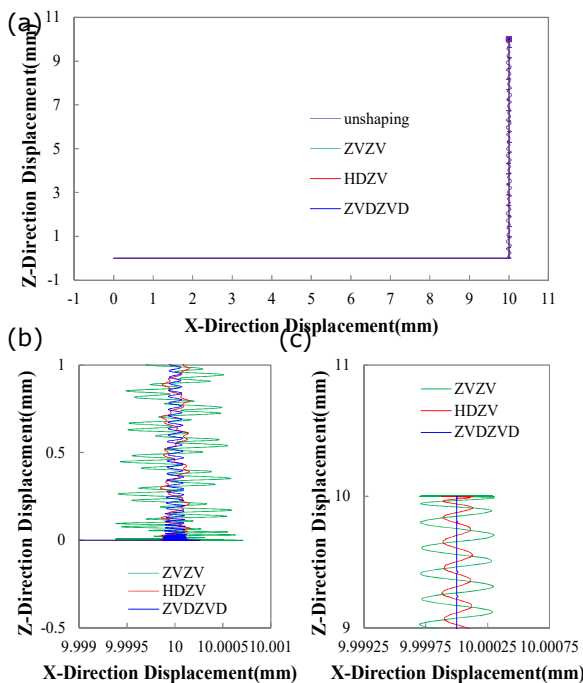


Figure 10 The moving trajectory of the optical inspection system with a sharp turn motion under various commands: (a) global view, and enlarged view at (b) corner, and (c) destination.

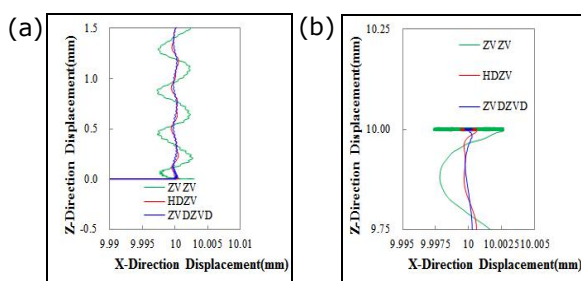


Figure 11. The motion trajectory of the system with intentional input shaping parameter shifting (a) enlarged view at (a) corner and (b) destination.

CONCLUSIONS

In this work, the suppression of motion swing in flexible long range motion systems is investigated using various input shaping techniques. Both experimental and finite element simulation are performed. Their results are highly correlated and the performances are well. An example on the operation of a precision inspection system is further simulated to elucidate the concept. The successful results indicate that it is possible to use finite element simulation for designing input shapers in complex mechanical systems such as systems with non-holonomic constraints

ACKNOWLEDGEMENTS

This work was supported by the Ministry of Science and Technology (MOST) of Taiwan under contact numbers MOST 105-2221-E-006-100-MY3, MOST 105-2221-E-006-074-MY3, and MOST 105-2221-E-218-016.

REFERENCES

- [1] Abdel-Rahman, E. et al (2003), Dynamics and Control of Cranes: A Review." *Journal of Vibration and Control*, vol. 9, pp. 863-908.
- [2] Singhoose, W. et al (1996), Improving Repeatability of Coordinate Measuring Machines with Shaped Command Signals," *Precision Engineering*, vol. 18, pp. 138-146.
- [3] Wang, W. C. et al (2014), Design and Vibration Control of a Notch-Based Compliant Stage for Display Panel Inspection Applications," *Journal of Sound and Vibration*, Vol. 333, pp. 2701-2718.
- [4] Singhoose, W. et al (2008), Input Shaping Control of Double-Pendulum Bridge Crane Oscillations." *ASME Journal of Dynamic Systems, Measurement, and Control*, vol. 130: 034504-1.
- [5] Dai, C. X. and Chen, K. S., (2013), Residual Vibration Suppression of Crane Movement by Input Shaping: Experimental Investigation and Finite Element Dynamics Simulations, *Journal of Chinese Society of Mechanical Engineers*, Vol. 34, pp. 497 - 506.
- [6] Singer, N. and Seering, W. (1990), Preshaping Command Inputs to Reduce System Vibration," *ASME J. of Dynamic Systems, Measurement, and Control*, Vol.112, pp. 76-82.
- [7] Chen, W. (2011), Finite Element Simulations for Input Shaping Design of Flexible Long Range Motion Systems: Analyses and Applications, MS Thesis, National Chen-Kung University, Taiwan.

Mathematical modelling of removal of Xenobiotic Organic Chemicals (XOCs) on the basis of biodegradation kinetics

Kshitija Kakade¹, Arun Kumar Thalla²

¹ Department of Civil Engineering, National Institute of Technology Karnataka, Surathkal, Mangalore 575025, India. email:kshitijakakade@gmail.com

² Department of Civil Engineering, National Institute of Technology Karnataka, Surathkal, Mangalore 575025, India. email:thallpce@gmail.com

ABSTRACT: Water and Wastewater treatment plants generally receive XOCs in very low concentration($\mu\text{g/lit}$) and Industrial Wastewater treatment plants receive them at higher concentrations (up to hundreds of mg/lit). Inspite of this large variation in concentration of XOCs, biological treatment systems have been found very robust in removal of such chemicals if designed considering their biodegradation kinetics. Biodegradation of XOCs is extremely fortuitous because of its physical and chemical properties. The perspective of this work is to hypothesize a growth linked ASM based process model including aerobic growth of a specific XOC degrading organism. Model parameters must be altered according to mechanisms by which XOCs inhibit microbial growth and substrate removal. To quantify the effects of XOC biodegradation, extant kinetic parameters μ (specific growth rate) and K_s (half saturation coefficient) are estimated in a model as they are better predictors of bioreactor performance. These developments in the model help to predict accurately concentration of XOCs in effluents of treatment plants.

Keywords: XOC, biodegradation kinetics, inhibition, growth linked, extant kinetic parameters.

INTRODUCTION

The term xenobiotic means "foreign to the biosphere" and xenobiotic organic chemicals(XOCs) are those that have been produced by mankind through our chemical industry. Modern chemical industry has had a large beneficial effect on society and there have also been negative effects associated with the release of XOCs to the environment. Sources of these XOCs are Petroleum industry, Plastic industry, Pesticides, paints, Electronics, Pharmaceuticals, Paper Pulp Industry and Cosmetics. More than 7 million chemicals are in existence and approximately 80000 of them are in common use worldwide (GAO, 1994b). New chemicals that are yet to enter into market undergo Premanufacture Notification Process (PMN).

More than half of all PMNs come in the door with no toxicity studies and environmental fate data. Less than 1 of 100 PMN submissions submit any biodegradation data-which is indicator of how persistent chemical is in environment. The question with any chemical is whether the benefits outweigh the risk of using it. Number of environmental issues due to such chemicals is ignored. It is accepted that constituents of concern cause severe impacts but is judged that cost of control does not outweigh the adverse impacts being created. Some hazardous moment triggers the acceptance of risk and then controls are implemented. For mitigation purposes, laboratory researches are conducted on pilot scale which produces some solution, often physico-chemical. The ongoing cost of such technologies is accounted when they are implemented on full scale, provide incentives to develop biological technologies which have lower

6th International Engineering Symposium - IES 2017

March 1-3, 2017, Kumamoto University, Japan

operating costs. Nutrient and odour control gives example of such evolution. Project costs and duration can be greatly influenced by the kinetics of the dominant biological reactions.

The influent of WWTP may contain several thousand XOCs which are removed by physical-chemical processes such as sorption, volatilization and biological degradation. The extent of biodegradation of a specific XOC will be function of operational conditions(hydraulic retention time(HRT), sludge retention time(SRT)), environmental parameters(temperature, Ph),compound specific parameters (sorption potential, degradability).XOC removal in activated sludge mainly depends upon understanding of these parameters and how they affect the removal process. Mathematical models are excellent tools for studying such interconnections. International Water Association(IWA) Task Group on Mathematical Modelling for Design and Operation of Biological Wastewater Treatment are well known, Henze et al.(2000). These models were developed for removal of COD, Nitrogen, and Phosphorous.

In order to establish fate and transport of XOCs various other models were formulated and published. The perspective is to develop an integrated model structure for designing and operating WWTPs removing XOCs in addition to other organic matter.

CLASSES OF BIODEGRADATION

Growth linked: Microorganisms performing the biodegradation receive their carbon and energy from XOC. Transformation products from reaction with XOC enter into normal metabolic pathways resulting into complete mineralization of XOC.

Cometabolic: Cometabolism is the transformation of organic compound by microbes where microbes derive no nutritional benefit from a substrate that they cometabolize. Cometabolism is easy to demonstrate in pure culture, Criddle et al. (1993).The modelling of cometabolic biodegradation is more complicated than growth linked biodegradation and involves lot of parameters. The cometabolic transformation is usually modelled as an

enzymatic reaction. Competition may occur between growth substrate and cometabolic substrate for the shared enzyme for which rate expressions must be considered while modelling. From literature review, procedures for the estimation of required kinetic parameters is given but the database from their application is small.

FACTORS INFLUENCING BIODEGRADATION

Physical and chemical properties: Recalcitrance of a xenobiotic molecule is due to xenophores. Xenophores are substituent on organic molecules that are physiologically uncommon or entirely non physiological and has major influence on biodegradability of XOCs. Halogens, nitro groups and cyanide groups are typical xenophores. Important chemical properties are solubility in water, vapour pressure, octanol-water partition coefficient, dissociation constant in water. Most xenobiotic materials have high molecular mass, low solubility in water. Thus, they have tendency to adsorb on soil and sediments. They mainly consists of condensed benzene and pyridine rings that is polycyclic structures, three fold substituted N atoms, quaternary carbon atoms, unphysiological bonds and substituent R-X where -X= -O-R, -N=N-, -Cl-, -F-, -Br-, -NO₂-, -CF₃-, -SO₃H. Some of the relationships between chemical structure and biodegradability are outlined below:

Table 1 Relative biodegradation

capabilities

Type of compound Or substituent	More degradable	Less degradable
Hydro carbons	Higher alkanes (-12C)	Lower alkanes
	Straight chain paraffinic	Branched paraffinic
Aromatic substitutes	-OH	-F
	-COOH	-Cl
	-NH ₂	-Br

6th International Engineering Symposium - IES 2017

March 1-3, Kumamoto University, Japan

	-OCH ₃	-NO ₂
Aliphatic chlorine	-Cl>6 carbon atoms from terminal C	-Cl<6 carbon atoms from terminal C

Solubility: The rate at which bacteria grow on a substrate is a function of its liquid phase concentration which means solubility has effect on the biodegradability of XOCs. Many xenophores reduce aqueous solubility and thereby reducing biodegradability.

Other factors are pH, temperature, availability of nutrients and electron acceptor that affects biodegradation.

INHIBITION KINETICS

In treatment of XOCs in industrial wastewaters, it is observed that specific growth rate of microorganisms reaches maximum and declines as substrate concentration increases. Monod equation cannot depict this situation. Andrews equation depicts this situation of inhibitory organic substrates on bacterial growth rate. Its form is:

$$\mu = \frac{\mu_{max} \cdot S_s}{K_s + S_s + \frac{S_s^2}{K_i}} \quad (1)$$

where K_i is inhibition coefficient, μ_{max} is maximum specific rate, S_s is substrate concentration. When K_i value is very large the Andrews equation simplifies to Monod equation. Few other inhibition models proposed are Yano and Koga(1969), Webb(Edwards 1970), Teisser(Edwards 1970), Aiba et al.(1968), Luong(1968), Han Levenspiel(1988).

Han Levenspiel Model

Sometimes organic chemicals inhibit the growth of heterotrophic bacteria on biogenic organic matter. Han Levenspiel equation depicts the effect of inhibitor concentration (S_i) on a relationship between μ and K_s .

It is given as:

$$\mu = \mu_{max} \left(1 - \frac{S_i}{S_c} \right)^n \frac{S_s}{S_s + K_s \cdot \left(1 - \frac{S_i}{S_c} \right)^m} \quad (2)$$

where S_i is inhibitor concentration, S_c is critical concentration at which all microbial

activity ceases, m and n are exponents that reflect the impact of increasing inhibitor concentration on μ and K_s . Santiago I.et al(1990) studied the response of activated sludge to inhibitory shock loads. While modelling growth linked biodegradation, effect of inhibitor concentration on μ and K_s is neglected and process is generally modelled considering Monod equation. Major drawback of such process design is such biological systems cannot sustain shock loads of XOCs and are unsound. Inhibition studies must be carried out in labs to know critical inhibitor concentration (S_c), which inhibition model is best fitted for the process which in turn helps to know effect on μ and K_s .

Following table gives idea about type of inhibition and its effect on kinetic parameters:

Table 2 Types of inhibition

Type	Effect on μ	Value of n	Effect on K_s	Value of m
Competitive	None	0	Increase	<0
Non-competitive	Decrease	>0	None	0
Un-competitive	Decrease	>0	Decrease	>0
Mixed	Decrease	>0	Increase	<0

EXTANT KINETIC PARAMETERS

There are two types of kinetic parameter estimates intrinsic and extant. Intrinsic parameters are those unaffected by the growth history of biomass and useful for determining relative biodegradability of organic compounds. Extant kinetic parameters reflect physiological state of biomass in reactor, useful in predicting process performance. Extant parameter estimates are characterized by lower μ and K_s values than intrinsic parameters. As it reflects state of biomass, these kinetic parameters must be used while modelling biodegradation of XOCs.

Two respirometrically based procedures are available for determining extant kinetic parameter values developed by Lamb et al. and refined by Chudoba and colleagues.

Substrate is injected into respirometer at number of concentrations. The net oxygen

6th International Engineering Symposium - IES 2017

March 1-3, 2017, Kumamoto University, Japan

uptake rate(OUR) in response to an injection is proportional to the substrate utilization rate. Dividing OUR by active biomass gives specific oxygen uptake rate(SOUR) which can be used to calculate the specific growth rate associated with the concentration of substrate supplied by injection:

$$\mu_e = \left(\frac{Y}{1-Y} \right) SOUR \quad (3)$$

where μ_e is extant specific growth rate. Other parameters can be determined by linearization technique given by Hanes.

Nomenclature

HRT- hydraulic retention time(d)
b_{xoc} - decay rate(d^{-1})
K_{sor} - sorption rate(1 mg / VSS d)
K_{des} - desorption rate(d^{-1})
K_d - solid/liquid partition coefficient(l g /SS)
K_{xoc} - half saturation coefficient for XOC(mg/lit)
Q_{in} - influent flow rate(m^3/d)
Q_w - wastage sludge flow rate(m^3/d)
S_{xoc} -soluble concentration of XOC(mg/lit)
SRT – sludge retention time (d)
SS – suspended solids(mg/lit)
V – total reactor volume(m^3)
VSS – volatile suspended solids(mg/lit)
$X_{b,xoc}$ – concentration of specific XOC degrading bacteria (mg/lit)
P_{xoc} – particulate concentration of XOC (mg/lit)
μ_{xoc} – specific growth rate(d^{-1})
Y_{xoc} – yield coefficient
in – index denoting influent

considered while formulating equations. The specific growth rate(μ) is related to Monod equation if XOCs are not inhibitory to its biodegradation or to other inhibitory models described in the literature. The mechanism by which specific XOC inhibit the growth of microbes and substrate removal is not well defined and has become topic of interest. Inhibition studies must be carried out to know correct values of (μ) which is important parameter in removal of XOCs .At higher concentration of inhibitory XOCs, increase in SRT does not encourage XOC removal because the critical concentration eliminates the capable biomass and system fails to remove XOCs from influent. Beyond such critical concentration of XOCs, biological treatments cannot be used for their removal.

The proposed model is however general and can be integrated with other ASMs as well. It consists of four processes that are aerobic growth of specific organism of XOC, Decay of specific organisms, Sorption of XOC, Desorption of XOC. It includes three model components as soluble concentration of XOC(S_{xoc}), the particulate concentration of XOC(P_{xoc}) and a third component describing the concentration of specific XOC degrading bacteria($X_{b,xoc}$). Many of XOCs are hydrophobic which tend to adsorb rather than biodegrade, hence adsorption is considered. Sorption to inorganic particulate matter is not considered. Desorption is assumed to be proportional to the concentration of particulate XOC in a first order manner with desorption rate K_{des} .

Model formulation

The proposed model is one of the several hypotheses and other biological models are possible. At low concentration of XOCs, model based on cometabolic biodegradation might be closer to reality. There can be formation of non-biodegradable or slowly biodegradable metabolic intermediates of XOCs which is not considered in this model, instead complete mineralization of XOCs is proposed. The model employed is for natural microbial communities rather than pure microbial culture. Extant kinetic parameter values (μ and K_s) are

Removal by biodegradation:

Degradation is assumed to be performed by a specific population of microbial community $X_{b,xoc}$ which possesses the genetic capability to metabolize XOC under aerobic conditions and utilize it for growth. The decay follows the first order kinetics with decay rate b_{xoc} .

MODEL EQUATIONS

By considering the above processes mentioned, following equations are obtained:

6th International Engineering Symposium - IES 2017

March 1-3, 2017, Kumamoto University, Japan

$$\frac{dSxoc}{dt} = \frac{Qin}{V} (Sxin - Sxoc) - \frac{\mu xoc}{Yxoc} (Xb,xoc) - Ksor \cdot Sxoc \cdot VSS + Kdes \cdot Pxoc \quad (4)$$

$$\frac{dPxoc}{dt} = Ksor \cdot Sxoc \cdot VSS - \frac{Qw}{V} (Pxoc) - Kdes \cdot Pxoc \quad (5)$$

$$\frac{dXb,xoc}{dt} = \left(\mu xoc - bxoc - \frac{Qw}{V} \right) Xb,xoc \quad (6)$$

where μxoc can be calculated as extant kinetic parameter or by Han Levenspiel equation with prior inhibition studies carried out on a specific XOC. Using these parameters one can predict how system behaves under shock loads and what measures are to be taken to make it robust.

PARAMETER ESTIMATION

In order to determine biological process parameters, immediate sorption equilibrium is assumed. With $dPxoc/dt=0$ Eq.(5) is used to express $Pxoc$ as a function of $Sxoc$ and Qw

$$Pxoc = \frac{Ksor \cdot VSS \cdot Sxoc}{Kdes + \frac{Qw}{V}} \quad (7)$$

which if inserted in Eq.(4) gives:

$$\frac{dSxoc}{dt} = \frac{Qin}{V} \cdot Sxin - A \cdot Sxoc - \frac{\mu xoc}{Yxoc} \cdot Xb,xoc \quad (8)$$

Where

$$A = \frac{Qin}{V} + \frac{\frac{Ksor \cdot VSS \cdot Qw}{V}}{Kdes + \frac{Qw}{V}} \quad (9)$$

With the above assumptions, parameters like μxoc , $bxoc$, $Yxoc$ can be determined experimentally. The steady state specific biomass concentration(Xb,xoc) can be found from Eq.(8)

$$Xb,xoc = \frac{Yxoc}{\mu xoc \cdot Sxoc} \left(\frac{Qin}{V} \cdot Sxin - A \cdot Sxoc \right) \quad (10)$$

By solving these equations effluent concentration of XOC can be determined. Suitable changes are to be done in this model considering physical, chemical properties of a specific XOC for calibration and validation.

CONCLUSION

Following conclusions can be drawn from this hypothesized model:

- This model when calibrated to particular wastewater, it allows engineer to predict XOCs concentration in the effluent accurately. By simulating such models to various biological systems, it's easy to set operational strategies.
- Inhibition studies for a specific XOC are to be carried out to determine kinetic parameters correctly.
- More complex models can be formulated for mixed substrate considering cometabolic biodegradation and enzyme kinetics.
- Model once calibrated helps to understand removal of XOCs and should be considered as objective of process design.

REFERENCES

- [1] Chang H.L and Alvarez Cohen,(1995), Model for the cometabolic biodegradation of chlorinated organics. Environmental Science and Technology 29:2357-2367.
- [2] Criddle,C.S., The kinetics of cometabolism. Biotechnology and Bioengineering 41:1048-1056,1993
- [3] Environmental Protection Agency (EPA).1997 Chemistry Assistance Manual for Premanufacture Notification Submitters. Office of Pollution Prevention and Toxics. EPA 744-R-97-003.
- [4] Erik Lindblom,Peter A Vanrolleghem,Peter Mikkelsen,Mogens Henze(2009), Dynamic experiments with high bisphenol-A concentrations modelled with an ASM model extended to include a separate XOC degrading micro-organism,Water Research 43(3169-3176)
- [5] Henze, M., Grady, C.P.L., Gujer, W., Marais, G.V.R., Matsuo, T.,A general model for single-sludge wastewater treatment systems. Water Research 21 (5), 505-515,1987.
- [6] Henze, M., Grady, C.P.L.,et al(1987), A general model for single-sludge wastewater treatment systems. Water Research 21 (5), 505-515.
- [7] Keehyun Han , Octave Levenspiel(1987),Extended Monod Kinetics for Substrate, Product and cell inhibition.Biotechnology and Bioengineering,Vol.32,Pp.430-437.
- [8] Sanitago I. And C.P.L. Grady Jr.,Simulation studies of transient response of activated sludge systems to biodegradable inhibitory shock loads.44th Industrial Waste Conference,pp.191-198,1990.

Surface Engineering for Tribology

Yoshitaka Nakanishi

*Graduate School of Science & Technology, Kumamoto University, Japan
Email: y-naka@mech.kumamoto-u.ac.jp*

ABSTRACT: According to the glossary of the OECD, "Tribology" is defined as "the science and technology of interacting surfaces in relative motion and of related subjects and practices." Controlling of friction and wear in each and every product contributes to improve its reliability, as well as saving energy and resources. Friction and wear can be seen between two surfaces, because the two surfaces sometimes contact each other at microscopic levels.

"Surface Engineering" is one of the key word for improving the tribological issues. In the research field, new materials, their appropriate surface profiles, and their innovative precision machining methods, have been developed.

This talk will give a clear exposition of "Tribology" and "Surface Engineering" from various practical applications.



Assistive Technology



Orthopedic Implant



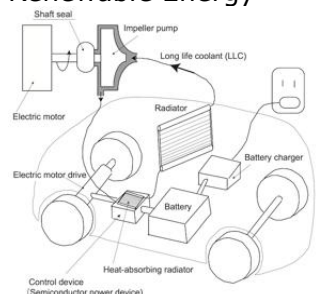
Training System for Surgery



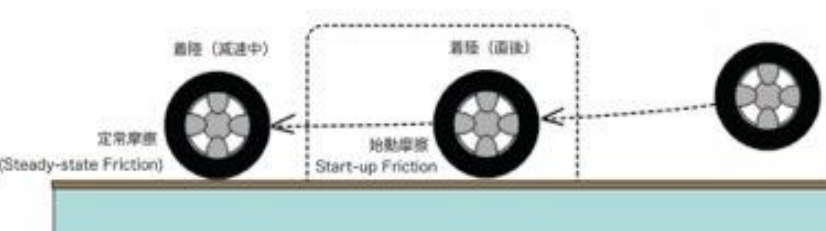
Renewable Energy



Airplane



Next-generation Vehicle



Airplane

6th International Engineering Symposium - IES 2017

March 1-3, 2017, Kumamoto University, Japan

CIVIL ENGINEERING & RELATED FIELDS

Failure - Manifestation & Manipulation

K.S.Babu Narayan ¹

¹ Department of Civil Engineering, National Institute of Technology Karnataka, Surathkal, PO: Srinivasnagara- 575 025, India. E-mail: shrilalisuta@gmail.com

ABSTRACT: Concept of failure and its avoidance is the central idea of all engineering designs. An engineering design's success heavily depends on how well failure has been anticipated, understood and addressed. Prefixed norms are essential to judge satisfactory performance. Quantification of performance levels helps in selection, comparison, discrimination, validation and adoption of design strategies. Ability to calculate gives the ability to predict performance and make appraisals. A brief account of importance of failure, its manifestation and manipulation in engineering system's design is presented.

Keywords: Failure, Performance, Safety, Reliability.

FAILURE - THE CONCEPT

Non-performance and performance below prefixed norms are deemed as failure. Engineering analysis and design are keys to understand why and how things can fail and to suggest methods of elimination and mitigation of unacceptable behaviour of systems.

MATH MODELS – TOOLS FOR PREDICTION OF ENGINEERING SYSTEM'S BEHAVIOR

Mathematical models represent engineering system's behaviour in quantitative terms. They are powerful and valid decision making tools in understanding system's behaviour and accomplishing the goals of performance based design.

Following are the logical sequential steps in math modelling.

- Setting out well defined end objectives (Expected output from the model)
- Conceptualization (Ideas and valid assumptions on basis of which the model is to be built)
- Selection of model type (Statistical, Causal, Hybrid etc.)

- Mathematical representation (Formulation of equations connecting variables)
- Calibration (Fine tuning / System noise reduction)
- Verification (Check on performance of model output with field observations)
- Sensitivity analysis (Check on robustness)
- Validation (Fixation of operational range)
- Application (Utilization for the purpose for which the model is built)

Mathematical models greatly reduce time, money and effort necessary for monitoring and managing engineering system.

FAILURE – MANIFESTATION

Failure manifests in different ways in different situations. Functional failure is incapability to satisfy the end use.

Satisfaction of stability, strength, safety, serviceability and durability are structural requirements, which when violated lead to structural failure. Non-technical failures like unacceptability due to social, aesthetic, ethical, environmental and economic considerations are also issues of concern to the designer.

FAILURE – MANIPULATION

Working stress design with linear elastic theory as basis was the first traditional method that still survives and finds application where serviceability is the prime concern. Ultimate load method based on plastic theory of structures followed working stress design and greatly helps in assessment of structural strength and associated safety. Limit state design embraces both working stress and ultimate load methods by checking performances both under service conditions and at ultimate states of collapse.

General principles for checking performance and associated safety define methods for quantifying strength and serviceability aspects of behaviour. Recognition of the fact that loads and material properties are random variables have led to the advent of probabilistic approaches like reliability based designs. As the very definition of reliability is, Reliability = 1-Probability of failure, high reliance can be placed on designs where failure probabilities are very low.

Accomplishment of absolute safety is impossible hence high levels of reliability are targeted.

Full scale reliability based designs need tremendous amount of data and computational efforts. Hence analysis and design of this kind classified as level III, is practiced only for sensitive and very important structures.

Level II analysis, settles for evaluation of reliability indices and achievement of targets. Though is simple than Level III, calls for optimization techniques and makes it less attractive for routine designs.

Level I reliability analysis is the most popular and widely used method by designers. In this method multiple safety factor approach is adopted.

Codes of practice provide necessary recommendations and guidelines for accomplishment of minimum levels of safety and reliability. Codes also take cognizance of the need to address transient and non-transient loads and their combinations by recommending manipulations of load factors. Also expected material behaviour for accommodation of transient and extreme

loads are presented to help the designers to take advantage of material behaviour aspects.

For instance, in quake resistant design it is suggested that there should be no damage due to minor quakes, repairable minimal damage due to moderate quakes and collapse prevention should be targeted due to major quakes though the structural damage is extensive.

The aforesaid provisions in material behaviour parlance, translate to expectation of elastic, elasto-plastic and plastic ranges in minor, moderate and major earthquake events respectively.

Deflection is the end product of the loading process and can never be eliminated. Hence excessive deflections need control. Cracking is inherent to concrete, and the very theory of design of RC sections is the cracked section theory. Here again it should be borne in mind that the phenomenon of cracking needs mitigation as elimination is impossible. Perceptible motion of tall buildings, undue and excessive vibration of bridges and building floors need control. The distribution of mass, stiffness and damping characteristics in the structure determines how well the structure responds.

Fundamental equation of equilibrium is

$$m\ddot{x} + c\dot{x} + kx = P(t) \quad (1)$$

$$\ddot{x} = \frac{P(t) - c\dot{x} - kx}{m} \quad (2)$$

Equation 2 very clearly suggests acceleration response can be reduced by modifying mass, stiffness and damping characteristics. Addition, deletion, substitution of elements, modification of configuration, employment of passive, semi-active, active, hybrid, tuned, sloshing, viscous, visco-elastic, friction, metallic yield, variable stiffness, magneto and photo rheological damping techniques and devices are being employed to exercise real time aggressive control to suppress undesirable vibratory motions and effects. Pushover analysis techniques are being refined and re-defined to trace the behavioural aspects of structures in the linear and non-linear ranges of

6th International Engineering Symposium - IES 2017

March 1-3, Kumamoto University, Japan

material behaviour to understand modes of failures and check performance levels and acceptability.

As absolute safety can never be guaranteed or accomplished, desired modes of failure are being seriously considered to direct and guide failure modes when it is inevitable.

CONCLUSION

Understanding the concept of failure is the first and foremost step to good engineering. The one who has the clearest view of qualitative and quantitative aspects of failure mechanism will be in a position to understand the manifestation of failure and will be able to strategize manipulations. Mathematical models as valid decision making tools are of immense help in prediction of failures and quantification of performance levels. Their usage also helps to reduce time, resources and monitoring efforts.

REFERENCES

- [1] Henry Petroski., (1996), "Invention by design" *Harvard University Press*, Cambridge, Massachusetts, London, England.
- [2] Rise & Fall of the American icons, *Ambuja technical literature series*, 69, Gujarat, Ambuja cements, Tech. services division, Nov 2001.
- [3] Ahsan Kareem, Tracy Kijewski, Yukio Tamura, (1999), "Mitigation of motion of tall buildings with specific examples of recent applications", *Wind & Structures an International Journal*, Vol 2, No. 3.
- [4] Mark Sarkisian, (2016), Designing tall buildings, 2nd Ed., Routledge, Taylor and Francis group, NY& London.

Stabilization of Expansive Clays using Granulated Blast Furnace Slag and Polypropylene Fibers

Anjana M¹, and B.M. Sunil²

¹ Department of Civil Engineering, National Institute of Technology Karnataka, Surathkal, PO: Srinivasnagara- 575 025, India. Email: anjanavengat@gmail.com

² Department of Civil Engineering, National Institute of Technology Karnataka, Surathkal, PO: Srinivasnagara- 575 025, India. Tel.: (0824) 2474000 Extn. 3345, Fax: (0824) 2474030, E-mail: sunilm@nitk.edu.in, bmsunil@gmail.com

ABSTRACT: Poor subgrade soil conditions can result in inadequate pavement support and reduce pavement life. Several ground improvement methods are adopted to stabilize problematic soils. In the present study usage potential of granulated blast furnace slag, polypropylene fiber and polyvinyl acetate were utilized to modify the properties of expansive clay. Compaction characteristics of blended clay soil were determined. Laboratory CBR tests were also conducted on dry and saturated samples. From the experimental investigation it is found that black cotton soil blended with the combination of polypropylene (PP) fiber, granulated blast furnace slag and polyvinyl acetate in the ratio of 3%, 10% and 15% respectively improved the strength of both dry and saturated samples.

Keywords: Expansive clay, granulated blast furnace slag, polypropylene fibres, soil stabilization.

INTRODUCTION

With the reduction of available land resources, more and more construction of civil engineering structures is carried out over weak or soft soil, which leads to the establishment and development of various ground improvement techniques such as soil stabilization and reinforcement (Tang et al 2006). When stabilizing agents are added to soil, a series of reactions take place. These processes cause stronger bonds between grains, fill up voids, and consequently cause higher load bearing capacity in soil (Abtahi et al 2013).

Recently, the use of fiber reinforced soil has been developed which has many advantages over other methods. Tang et al (2006) studied the effects of discrete short polypropylene fiber (PP-fiber) on the strength and mechanical behaviour of unstabilized and lime stabilized clayey soil. The test results indicated that the inclusion of fiber reinforcement within unstabilized and lime stabilized soil resulted in an increase in the unconfined compressive

strength (UCS), shear strength and axial strain at failure, a decrease in the stiffness, the loss of post-peak strength and changed the lime stabilized soil's brittle behaviour to more ductile. The shear strength of short, randomly distributed fiber-reinforced soil is a function of fiber weight fraction, aspect ratio, and surface friction, soil characteristics (Ranjan et al 1996). Kumar et al (2007) studied influence of fly ash, lime, and polyester fibers on compaction and strength properties of expansive soil. And found that fibers had no significant effect on maximum dry density and optimum moisture content of fly ash-soil-lime-fiber mixtures. However the ratio of split tensile strength and unconfined compressive strength increases with increase in fiber content. Akbulut et al (2007) investigated the use of waste fiber materials such as scrap tire rubber, polyethylene, and polypropylene fiber for the modification of clayey soils. It mainly focused on the strength and dynamic behaviour of the

6th International Engineering Symposium - IES 2017

March 1-3, 2017, Kumamoto University, Japan

reinforced soils with randomly included waste fiber materials. The study found that with the addition of these materials there is significant increase in UCS value up to a certain limit after that it decreased. Maher et al (1994) did an investigation on the effect of polypropylene fibers, glass fibers and soft wood pulp fibers on kaolinite clay. The authors found that, inclusion of fibers increased the peak compressive strength splitting tensile strength and ductility of kaolinite clay, with the increase being more pronounced at lower-composite water contents. Increase in fiber length reduced the contribution of fibers to peak compressive strength, while increasing the contribution to energy absorption or ductility.

CBR value and UCS of expansive soil is found to be improving with the addition of blast furnace slag (Nagakumar et al 2014 and Sharma et al 2012). This improvement is achieved through the formation of cementitious compounds due to the pozzolanic reactions takes place between soil and slag (Salimi et al 2015).

Since it is easy to use and rapid to perform, poly vinyl acetate is used to improve soft soil properties. But low water resistance is the main drawback of these resins (Abtahi et al 2012). Yasrobi et al 2011 and Zandieh et al 2010 did an investigation on the effect of polyvinyl acetate on stabilization of dune sands. And it is found that strength development increases with curing period. It was observed that in the stabilized samples in saturated environmental conditions, there was little decrease in the CBR strength with respect to the dry state, indicating the stiffness and stability of the compounds against moisture (Yasrobi et al 2011).

Researchers have investigated the effect of granulated blast furnace slag (GBFS) in stabilization of soil. GBFS is reactive or pozzolanic in nature, and it was proposed to use in this study for the stabilization of problematic clayey soil (black cotton soil).

EXPERIMENTAL METHODOLOGY

Materials

Black cotton soil was procured from Northern part of Karnataka District, in India. After transportation to the laboratory the soil was sieved and stored

for further analysis in accordance with relevant Indian Standard Codes. The study soil was classified as CH, based on the Indian Soil Classification System. Its properties are listed in Table 1. The maximum dry density, optimum moisture and unconfined compressive strength were 15.8 kN/m³, 21% and 34 kN/m³ respectively.

Other material chosen for the present investigation are granulated blast furnace slag (GBFS), polypropylene fibres (PP) and a resin, polyvinyl acetate (PVA). The granulated blast-furnace slag is sand-type by-product obtained during the manufacture of pig iron in the blast furnace. Thick strands of polypropylene, used in this study is a thermoplastic polymer (Fig.1). Polyvinyl acetate is a polymeric material which is obtained from polymerization of free vinyl radicals based on Vinyl monomers.

Table 1 Geotechnical properties of black cotton soil

Properties	Value
Specific gravity	2.65
Sand size fraction (%)	14
Silt and clay size fraction (%)	86
IS classification	CH
Liquid limit (%)	62
Plasticity index (%)	27
Shrinkage limit (%)	11
γ_{dmax} (kN/m ³)	15.8
OMC (%)	21
Unconfined compressive strength (kN/m ²)	34
CBR (soaked)	2
CBR (unsoaked)	4



Fig 1 Polypropylene fiber

Some properties of additives used in the present study are presented in Tables 2,3 and Table 4 respectively.

6th International Engineering Symposium - IES 2017

March 1-3, 2017, Kumamoto University, Japan

Table 2 Chemical properties of GBFS

Parameter	Result
pH	9.2
Specific gravity	1.4-1.6
Calcium oxide (CaO)	41
Silica	35
Iron oxide	0.18
Alumina	18

Table 3 Properties of PP fiber

Property	Value
Width (mm)	4
Length (mm)	12
Shape	Rounded strip
Fiber type	Stiff single fiber
Unit weight	<1
Aspect ratio	3
Colour	Transparent
Resistance to acid/alkalies	Stable
Water absorbency	Nil

Table 4 Properties of PVA

Parameter	Result
Chemical formula	
Colour	
Appearance	
Average molecular weight	
Density	
Solubility in water	
Soluble in	

PREPARATION OF SOIL SPECIMENS

To study the behavior of stabilized black cotton soil; compaction and CBR tests (in dry and saturated condition) were carried out. All tests were conducted as per the relevant Indian Standard Codes. The following mix proportion was adopted to mix different additives.

- BC soil blended with different PP fibers in the range 0.5 to 5%
- BC soil blended with 10 % GBFS and PP fiber in the range 0.5 to 5%
- BC soil blended PVA in the range 1%, 1.5% and 2%.
- BC soil blended with optimized PP fiber, PVA and 10% GBFS

During this study Standard Proctor compaction characteristics of soil

(unblended and blended specimens) were determined in accordance with ASTM D 698 (1995). The compaction curves were plotted and the values of optimum water content and maximum dry unit weight were determined from the compaction curves.

The California bearing ratio (CBR) is a penetration test for evaluation of the mechanical strength of road subgrades and base courses. During this investigation the test is performed (in dry and saturated condition) by measuring the pressure required to penetrate a soil sample with a plunger of standard area.

Before the tests the soil mixed with stabilizers and water, was kept in closed polyethylene bags for 2 days in laboratory at room temperature to get uniform mixture. And the mixture thus obtained is used for the preparation for test specimens.

RESULTS AND DISCUSSIONS

Effect of stabilizers on compaction characteristics

To study the effect of polypropylene fiber on the compaction characteristics of the black cotton soil, was mixed with 0.5%, 1%, 2%, 3%, 4 % and 5% synthetic fiber (on dry basis). A reduction in maximum dry density (see Fig.2) is observed with the PP fiber addition. For unstabilized soil maximum dry density is 15.8 kN/m³ and for black cotton soil blended with 5% polypropylene fiber maximum dry density reduces to 13.4 kN/m³. This behaviour can be attributed to the reduction of average unit weight of solids in the mixture of soil and fiber. However in most cases the optimum moisture content almost remained constant (see Fig.3). It's because polypropylene fiber does not react or absorb moisture.

With the addition of GBFS, there is a decrease in maximum dry density and a slight increase in optimum moisture content. The presence of GBFS having a relatively low specific gravity is the cause for this reduction in dry density. The increase in optimum moisture content can be attributed to the increasing amount of

fines which require more water content because of their larger surface area.

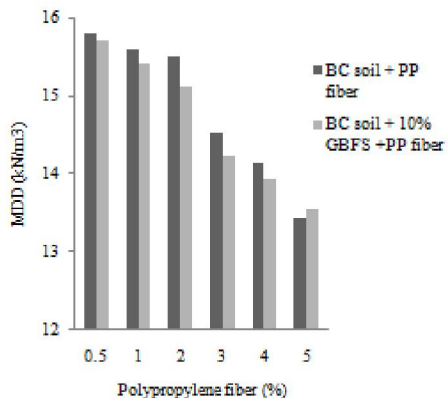


Fig 2 Variation of MDD on addition of stabilizers

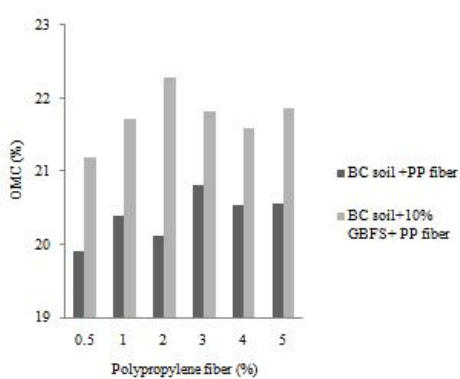


Fig 3 Variation of OMC on addition of stabilizers

Effect of additives on CBR

CBR tests were conducted in both dry and saturated conditions. Fig. 5 shows the effect of different additives on black cotton soil. It is observed that CBR of soil increases up to 3% addition of PP fibres (optimum value) and then decreases with further addition of PP fibers. With the increase in fiber content (up to 3%) the strength of stabilized soil increases. This can be explained on the basis that the total contact area between fibers and soil particles increases while increasing the fiber content and consequently the friction between them increases, which contributes to the increase in resistance to the force

applied. However, too much fiber added could reduce the effectiveness of improvement in the strength. Because the fibers adhere to each other and form lumps and cannot contact with soil particles fully.

When 10 % GBFS and optimal value of PP fibres (3%) is added to the black cotton soil the strength increases in both the cases (i.e. in dry and saturated conditions) The increment in the CBR in dry and saturated states can be attributed to the gradual formation of the cementitious compounds from CaO present in the granulated blast furnace slag. And it was observed that saturated CBR value is more as compared to the dry state. This trend shows that the presence of water (moisture) helps to further formation of the cementitious compound between soil and the pozzolanic reactions between soil and GBFS.

Effect of Resin on CBR

During the investigation black cotton soil is treated with 1%, 1.5% and 2% polyvinyl acetate (dry basis) to optimize the dosage. CBR tests were then conducted in dry and saturated conditions. It was found that black cotton soil treated with 1.5% polyvinyl acetate (dry state) yielded higher CBR value. And beyond 1.5% addition reduces the effectiveness. Polyvinyl acetate increases the interfacial friction between soil grains and thus it shows an improvement. If more quantity is added it fill almost completely all the voids and since it having lower strength as compared to soil grains it reduces the CBR value for more addition of PVA.

Effect of GBFS, PP and PVA

Combined effect of polypropylene fibers, granulated blast furnace slag and polyvinyl acetate on CBR of study is shown in Fig. 4. At the optimum contents of polypropylene fiber (PP), granulated blast furnace slag (GBFS) and polyvinyl acetate (PVA) i.e. with 3 % PP, 10 % GBFS and 1.5 % PVA the CBR value enhanced from 3.57 to 9.38, about 163 % increase in dry states; and

from 2.23 to 9.82, about 341 % in saturated states. As it is clear from the results, fiber-slag-resin composite has a very good workability in both saturated and dry states.

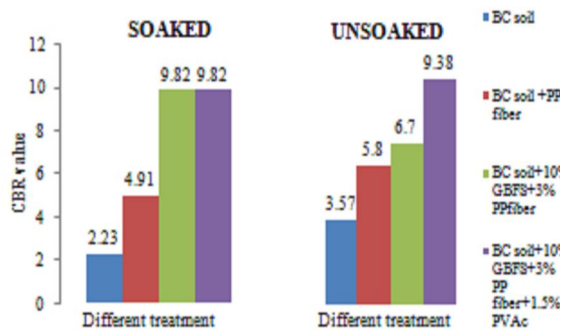


Fig 4 CBR value for different treatment

CONCLUSIONS

Compaction and CBR tests were conducted to study the effect of polypropylene fibers, GBFS and PVA to study the behavior of soil composite. Maximum dry density decreased from an initial value of 15.8 kN/m³ to 13.4 kN/m³ by addition of 10% granulated blast furnace slag in soil-fiber composite. CBR tests were conducted in both dry and saturated states. The results show that 3% PP fibres, 10% GBFS and 1.5% PVA contents is more effective on compaction and CBR values of treated black cotton soil. The optimum contents of additives i.e. 3% PP fibres, 10% GBFS and 1.5% PVA enhanced CBR of treated soil from an initial value of 3.57 to 9.38 (in dry state) and from 2.23 to 9.82 (in saturated state).

ACKNOWLEDGEMENTS

The authors would like to thank the Kirloskar Ferrous Industries, Koppal for providing the granulated blast furnace slag for conducting this research work.

REFERENCES

- [1] Abtahi SM, Esmaeil Masoumi, Farzad Abdi Nian(2012) "problematic soft soil improvement with both polypropylene fiber and polyvinyl acetate resin" Geotech Geol Eng (2013) 31:143-149
- [2] Akbulut Suat ,Seracettin Arasan, Ekrem Kalkan (2007), "Modification of clayey soils using scrap tire rubber and synthetic fibers" Science direct, Applied Clay Science 38 (2007) 23-32
- [3] IRC: 37, "Guidelines for the Design of Flexible Pavements (Third Revision)", Indian Road Congress, New Delhi, 2012.
- [4] Maher M. H., Y. C. Ho (1994) "Mechanical properties of kaolinite / fiber soil composite" ASCE, J. Geotech. Engrg., 1994, 120(8): 1381-1393
- [5] Pradhan, Rabindra Kumar Kar, Ashutosh Naik (2011) "Effect of Random Inclusion of Polypropylene Fibers on Strength Characteristics of Cohesive Soil" Geotech Geol Eng (2012) 30:15-25
- [6] Gopal Ranjan, R. M. Vasan and H. D. Charan (1996), "Probabilistic analysis of randomly distributed fiber-reinforced soil" ASCE, Vol. 122, No.6, June, 1996.
- [7] Salimi, A.R. Goodarzi (2015) "Stabilization treatment of a dispersive clayey soil using granulated blast furnace slag and basic oxygen furnace slag" ScienceDirect, Applied Clay Science 108 (2015) 61-69
- [8] SharmaA.K. and Sivapullaiah P.V.(2012) "Improvement of Strength of Expansive Soil with Waste Granulated Blast Furnace Slag" Geo Congress 2012.
- [9] Tang Chao-Sheng, Yi Cai, Bin Shi, Charles WW Ng (2006) "Effect of polypropylene fiber and lime admixture on engineering properties of clayey soil" Science direct, Engineering Geology 87(2006), 230-240
- [10] Yasrobi Shahaboddin, Zandieh Reza (2010) "Study of Factors Affecting the Compressive Strength of Sandy Soil Stabilized with Polymer" Geotech Geol Eng (2010) 28:139-145
- [11] Yasrobi Shahaboddin, Ziba J. Homauoni (2011) "Stabilization of Dune Sand with Poly(Methyl Methacrylate) and Polyvinyl Acetate Using Dry and Wet Processing" Geotech Geol Eng (2011) 29:571-579.

Laboratory Evaluation of Cold Bituminous Mixtures

Chinju Chandran¹ and Suresha S.N.²

¹ Formerly Department of Civil Engineering, National Institute of Technology Karnataka, Surathkal, Mangalore 575025, India. email: krishna.chandran57@gmail.com

² Department of Civil Engineering, National Institute of Technology Karnataka, Surathkal, Mangalore 575025, India. email: sureshasn@nitk.ac.in

ABSTRACT: This paper presents the research findings of experimental studies carried out on cold bituminous mixtures (CBM). The study was aimed at investigating the role of fly ash (FA) and ordinary Portland cement (OPC) as mineral fillers for the CBM. Slow-setting and cationic type bituminous emulsion was used as a binder and crushed granite stones were used as coarse and fine aggregates. Coating test, determination of optimum moisture content, volumetric properties, Marshall stability and flow, indirect tensile strength test, and rutting tests were performed on various CBM. Findings suggest that the CBM with OPC as filler performed better than the mixtures with FA as a filler. The entire study was carried out as per the guidelines laid down in the special publication of Indian Roads Congress (IRC: SP: 100-2014).

Keywords: Cold bituminous mixtures, Emulsion, Fly ash, Cement, Marshall stability, Indirect Tensile Strength, and Rutting Test.

INTRODUCTION

Cold Bituminous Mixes (CBMs) are normally produced with unheated aggregates and bitumen emulsion. In India, CBMs are mainly recommended for pavement maintenance works including periodic treatments such as patching, pothole repair, cold recycling, bituminous macadam, premix carpet, mix seal surfacing, and semi-dense bituminous concrete. According to International Bitumen Emulsion Federation (IBEF), India is one of the top ten countries consuming bitumen emulsion for the above-mentioned purposes (Azeem, 2012).

Several factors that have led to the increasing use of bitumen emulsion in road construction and maintenance i) the energy scarcity and crisis, ii) bitumen emulsions do not require petroleum solvent to make it liquid, iii) bitumen emulsions can generally be used without additional heating, iv) concerns about reducing atmospheric pollution, v) the ability of certain types of bitumen emulsions to coat damp

aggregate surface, which eventually reduces the fuel requirements for heating and drying aggregates, vi) availability of a variety of emulsion types which have led to development of new formulations and improved laboratory procedures in order to satisfy the design and construction requirements, vii) the ability to use cold bituminous materials at remote sites, viii) the applicability of emulsions for use in preventative maintenance so as to increase the service life of existing distressed pavements, ix) success stories of the use of warm and cold mix technologies in construction and maintenance of rural roads, and x) health of construction worker.

In view of these, Indian Roads Congress (IRC), very recently, brought out a special publication (IRC: SP: 100, 2014) on the use of cold mix technology in construction and maintenance of roads using bituminous emulsion.

This paper presents the findings of experimental study carried out on CBM for pavement wearing course

6th International Engineering Symposium - IES 2017

March 1-3, 2017, Kumamoto University, Japan

corresponding to nominal maximum aggregate size (NMAS) of 19 mm. The primary objective of this study was to compare the influence of two different types of filler materials, fly ash (FA) and ordinary Portland cement (OPC) on the properties of CBM. Coating test, Marshall stability and flow test, indirect tensile strength test, and rutting test were performed on different CBM.

LITERATURE REVIEW

In any type of bituminous mixture i.e hot bituminous mix (HBM) or non-HBM, mineral filler (particles finer than 0.075 mm) occupies up to 10 per cent of total weight of aggregate. These may be used in the form of crusher fines, lime, OPC, FA. Two primary purpose of using mineral fillers are i) to fill the voids between the aggregate and, ii) stiffness asphalt binder at higher service temperatures. A typical specification requires filler to binder ratio from 0.6 to 1.2 by weight. Research findings show that the properties of mineral fillers have a significant effect on the performance of the asphalt mixtures (Kandhal, 2016). Chen et al. (2016) studied the performance characteristics of patching materials based on the four aspects relate to initial stability, in-service durability, water resistance, and workability. Wendling et al. (2014) suggest that the use of gyratory compactor it is possible to assess the onsite behaviour of CBM. Findings of Modarres and Ayar (2014) suggests that the use of coal waste and coal waste ash up to 7% in cold recycled mixture can result in significant increase in the Marshall stability, tensile strength and resilient modulus. Use of recycled asphalt pavement (RAP) in CBM contributes to resistances to rutting, plastic deformation, and fatigue cracking (Arimilli et al., 2015). Properties of dense graded CBM can be improved by adopting aggregate gradation based on the packing theory (Dash and Panda, 2015). In such CBM, it may be required to maintain the mineral filler in the range of 2 to 8% by weight of total aggregate. Nassar et al. (2016) studied the role of binary and ternary blended

fillers on mechanical, durability and microstructure properties of cold asphalt emulsion mixtures. Findings suggest that the fillers contributed in higher creep stiffness modulus and thus there was a significant amount of reduction in the susceptibility to permanent deformation.

PRESENT STUDY

As per the IRC: SP: 100-2014, the three major steps involved in design of CBM are (i) testing of bitumen emulsion, (ii) testing of aggregate, (iii) determination of premixing water content, and (iv) determination of optimum binder content.

Cationic bitumen emulsion of slow setting-2 (SS-2) conforming to the requirements of IS 8887:2004 was used as a binder. The crushed granite aggregate available from the local quarry was used in the present investigation.

Aggregate impact value, water absorption, combined flakiness and elongation index were found to be 22.5%, 0.45%, and 27%, respectively and conforms to the requirements of Specifications for Roads and Bridge Works, Ministry Road Transport and Highways, Government of India. FA and OPC that are having minimum specific surface area of 225 m²/kg were used as mineral fillers. Blend of aggregates conforming to the gradation requirements of Asphalt Institute's Manual Series-14 were used, as shown in Table 1.

In order to determine the premixing water content, it is required to determine the quantity of bitumen emulsion using the equation (1).

$$P = 0.05A + 0.1B + 0.5C \quad (1)$$

where, P = quantity of bitumen emulsion (%); A = % aggregate retained on 2.36 mm sieve; B = % aggregate passing on 2.36 mm sieve and retained on 0.090 mm sieve; C = % aggregate passing on 0.090 mm sieve.

Different samples of aggregate and emulsion mixes were prepared keeping the quantity of bitumen emulsion constant, as determined from Eq.(1) and varying the water content. Binder

6th International Engineering Symposium - IES 2017

March 1-3, 2017, Kumamoto University, Japan

coating on the aggregate surface was visually observed. The minimum water content at which maximum coating of aggregate surface was considered as the optimum water content (OWC) required for premixing of aggregate to be used for CBM. Fig. 1 shows the loose CBM sample for visual inspection of surface area coating.

Optimum binder content (OBC) was determined by the Marshall compaction method. To prepare each cylindrical specimen of diameter 101.15 mm, loose dry aggregate blend of 1100 g was mixed with OWC for pre-wetting. Such aggregate blend was added with a known quantity of binder for preparing specimen in triplicates. Then each loose mixture was dried for about 1-2 hours using a electric fan. Each of the cold mix is then kept in over at 40°C for 2 hours. Further, each mixture was transferred into the Marshall mould and compacted with 50 blows of Marshall hammer on both the faces. Similarly, the Marshall specimens are then prepared for binder contents of 5, 6, 7, 8, and 9 per cent by weight of aggregates. The compacted specimens were extracted from the mould after 24 hours and cured in air oven at 40°C for 72 hours before subjecting to different Marshall stability tests. Volumetric properties such as bulk density, air voids content, voids in mineral aggregate, and voids filled with bitumen were determined for each compacted CBM specimen.

Resistance to moisture-induced damage of CBM with OBC, were assessed by tensile strength ratio (TSR), which is the ratio of indirect tensile strength (ITS) of conditioned specimen to unconditioned specimen. Fig. 2 shows the loading frame that can be used for Marshall stability and ITS tests. Immersion wheel-tracking device was used to assess the rutting resistance of CBM.

RESULTS, ANALYSIS AND DISCUSSION

Bitumen emulsion required for coating test was computed using Eq. (1) and it was found to be 7.19%. OWC required for CBM with OPC as filler found

to be 4.5% and in the case of FA as filler found to be 3.5%.

To determine the OBC, CBM with bitumen emulsion content varying from 5.0% to 9.0% were prepared and tested for volumetric properties and Marshall stability and flow values. The bulk density values of CBM with OPC and FA as filler were found to be in the ranges of 2.12 - 2.16 g/cc and 2.03 - 2.10 g/cc, respectively. The total air voids content in the compacted CBM with OPC and FA as filler were found to be in the ranges of 10 - 15% and 12 - 16%, respectively. Marshall stability for soaked and unsoaked samples were found to be ranges of 4.654 - 8.131 kN and 3.428 - 5.498 kN for CBM with OPC and FA as fillers, respectively. Marshall flow values these mixtures were found to be in the ranges of 3.23 - 5.33 mm and 3.50 - 6.20 mm, respectively. On the basis of these results, the OBC for CBM with OPC and FA as filler were arrived as 7.19% and 8.00% by weight of total mix, respectively.

TSR values were determined based on the ITS test, which was conducted on CBM at the OBC for unconditioned and conditioned specimens, at curing period of 3-days. In addition, ITS tests were conducted on specimen (unconfined) for a curing periods of 1-day and 3-days and specimen (confined) cured for 7-days. In all these conditions, ITS was limited to a maximum value of 70 kPa, which very low compared to dense graded HMA mixture. Both the CBM, i.e. for two different fillers, exhibited a minimum TSR of 80%. These values cannot be considered as evidence of resistance to moisture damage. Consequence of poor ITS, CBM mixtures exhibited a very poor resistance to rutting. Rut depth of 13.8 mm was reached within the 700 number of wheel passes, with a contact pressure 0.5 MPa.

Conclusions and Recommendation

Based on results of the experiments conducted on CBM with OPC and FA as filler materials, it can be concluded that the variations in the results are not significant. Thus, FA can be used as potential filler by replacing OPC in CBM.

6th International Engineering Symposium - IES 2017

March 1-3, 2017, Kumamoto University, Japan

This can contribute to the marginal reduction in the cost of pavement repair and maintenance work without compromising the quality of CBM. Results of ITS test and wheel-tracking test indicate that the CBM developed in this study is inferior in quality than that of developed by the other researchers (Arimilli et al., 2015; Chen et al., 2016).

References

1. Arimilli S., Jain P.K., and Nagabhushana M.N., 2015, Optimization of Recycled Asphalt Pavement in cold Emulsified Mixtures by Mechanistic Characterization. *Journal of Materials in Civil Engineering*, (28)2.
2. Azeem, R., 2012, Bituminous emulsion and road maintenance. Ali, A., 7th Australian Road Engineering & Maintenance Conference, Melbourne.
3. Chen J-S., Ho H-C., Liao M-C., and Wang T-Y., 2016, Engineering Properties of Asphalt Concrete Patching Mixtures. *Journal of Testing and Evaluation*, 44(1), pp. 534-542.
4. Dash S., S., and Panda M., 2015, Effect of Aggregate Gradation on Cold Bituminous Mix Performance. *Advances in Civil Engineering Materials*, 4(1) pp. 154-174.
5. IRC:SP:100, 2014. Use of Cold Mix Technology in Construction and Maintenance of Roads Using Bitumen Emulsion. *Indian Roads Congress*, New Delhi.
6. Kandhal P.S., 2016, Bituminous Road Construction in India. PHI Learning Private Limited, Delhi.
7. Modarres A., and Ayar P., 2014, Coal waste application in recycled asphalt mixtures with bitumen emulsion. *Journal of Cleaner Production*, 83, pp. 263-272.
8. Nassar A.I., Mohammed, M.K., Thom, N., and Parry T., 2016, Mechanical, durability and microstructure properties of cold asphalt emulsion mixtures with different types of filler. *Construction and Building Materials*, 114, pp. 352-363.
9. Wendling L., GaudefroyV., Gaschet J., Ollier S., and Gallier S., 2014, Evaluation of the compactability of bituminous emulsion mixes: experimental device and methodology. *International Journal of Pavement Engineering*, 17(1), pp. 71-80.

Table 1 Aggregate Gradation

Sieve Size (mm)	Adopted Gradation	MS-14 Requirement
19	100	100
12.5	95	90 – 100
9.5	-	-
4.75	57.5	45 – 70
2.36	40	25 – 55
0.300	12.5	5 – 20
0.075	5.5	2 – 9



Fig.1. Loose CBM samples



Fig. 2. Marshall Loading Frame with ITS Breaking-Head

Vegetation Growth in Waste Rock Produced from Opencast Coal Mines with Different Additives

K. Ram Chandar *¹, G. Vikas Chitanya ²

1 Department of Mining Engineering, National Institute of Technology Karnataka, Surathkal, Mangalore- 575025, INDIA. e-mail: krc_karra@yahoo.com

2 Formerly Department of Civil Engineering (Env. Engg.), National Institute of Technology Karnataka, Surathkal, Mangalore 575025, India.

*Corresponding author

ABSTRACT: Mining causes disturbance in landscape and soil properties. Reclamation can restore soil quality to certain extent over a period of time. A systematic scientific study is taken up with an aim to increase the fertile characteristics of coal mine overburden (OB) so that some useful plantation is possible causing faster reclamation on the dump sites or the waste rock produced from mining activity can be used at some other place for vegetation with some additives. The additives chosen for the study are also waste products like fly ash, bottom ash and secondary sludge from sewage treatment plant. These are added to the mine overburden waste rock in the proportion of 25% and 50% by volume. The macro and micro nutrients required for the plant growth and other parameters are analyzed before and after addition of additives. Soil texture, pH, electrical conductivity and moisture content of waste rock are determined through different laboratory methods. Cassia Siamea, Dendrocalamus strictus, Gliricidia Sepium, Phyllanthus emblica, Peltophorum are the plant species used for the study of growth of plants. From this study, sewage sludge and bottom ash gave better results. The waste rock was found to be slightly alkaline in nature and no liming was required. On addition of sewage sludge considerable increase in the properties was observed. Healthy growth of plants was observed in additives of sewage sludge and bottom ash.

Keywords: mine waste, fertile characteristics, coal mine over burden, sewage sludge, vegetation.

INTRODUCTION

Open cast coal mining involves the extraction of coal deposits and the removal of overlying soil & other rock and their storage in the form of overburden dumps. The damage due to mining activity has been reflected on decrease in green cover or water resource or both. The measures commonly employed in the mined out areas are: Compensatory afforestation, reclamation, rehabilitation based on mine closure guidelines. Successful and long term mine soil reclamation of overburden dumps requires the establishment of stable nutrient cycles from plant growth and microbial processes (Singh et al., 1996, Kavamura and Esposito, 2010, Sheoran et al., 2010) and the selection of appropriate species for vegetation. For

reclamation, studies addressing the soil fertility, structure, microbial populations, top soil management and nutrient cycling have to be done in order to retain the land to useful and as self-sustaining ecosystem. Fertility of mine waste rock can be increased by adding various natural materials like saw dust, wood residues, sewage sludge, animal manures, as these stimulate the microbial activity which provides the nutrients (N, P) and organic carbon to the waste material (Sheoran V et al., 2010). Compost provides organic matter; decreases bulk density & erosion and increases aggregate stability, aeration, water infiltration and retention (Tester, 1990; Serra et al., 1996; Ros et al., 2001). It also increases concentrations and availability of micro and macro nutrients (Guerrero et al., 2001; Martinez et al., 2003), providing a wider range of nutrients

6th International Engineering Symposium - IES 2017

March 1-3, 2017, Kumamoto University, Japan

than inorganic fertilizers, with less nitrate leaching and water contamination (Gagnon et al., 1997; Mamo et al., 1999). Bio solids also serve many purposes, including pH control, metal control and fertilization. Establishment of revegetation on mine overburden dumps renders biologically productive, contribute towards physical stabilization, pollution control, visual improvement and removal of threats to surrounding population.

On the other hand, dumping of waste from opencast mines needs a large quantity of land and maintaining it in a stable condition is very crucial. Every year millions of tons of waste rock is being dumped on thousands of hectares of land. So attempts can be made to use the waste dump material for other purposes like using coarse and fine particles in construction industry to some extent. Some material of fine size can be used for vegetation purpose. But this material may lack in nutrients. Some additives are to be added to improve the fertile characteristics. So, an attempt is made through this study to assess the coal mine waste rock characteristics and to find its suitability for vegetation. Some additives are added which are basically waste materials to improve fertile characteristics of mine waste.

METHODOLOGY

Initially, waste rock samples were collected from four different places of an opencast coal mine dump site at different horizons using spade and trowel. From each site, 50cm x 50cm dimension pits were dug with 50cm deep using spade and trowel and about 10kg of sample was scraped from each of the 4 pits randomly chosen. As the samples are similar in nature in terms of physical properties, they were mixed thoroughly. Later 8 more samples were collected following the same procedure and were mixed. Soil pH, Electrical Conductivity (EC) and Moisture Content are determined by standard methods (IS: 2720 and Page 1982). The details of laboratory results were discussed by the authors elsewhere (Ram Chandar & Chaitanya, 2014). Seeds belonging to 5 different species were chosen and are

sowed individually in all the samples with additives and in native soil and were watered daily. The species are:

- Cassia Siamea - common name is kassod tree. It's a fast growing tree it can withstand strong wind and grow well in exposed areas (Plant- 1).
- Dendrocalamus strictus also known as Male Bamboo is a tropical clumping species native to Southeast Asia. It is extensively used as a raw material for paper pulp and has edible shoots (Plant- 2).
- Gliricidia Sepium, often simply referred to as Gliricidia: is a medium size leguminous tree belonging to the family Fabaceae. It is considered as the second most important multi-purpose legume tree (Plant- 3).
- Phyllanthus emblica (syn. Emblica officinalis), the Indian gooseberry (Amla), is a deciduous tree of the family Phyllanthaceae. It is known for its edible fruit of the same name (Plant- 4).
- Peltophorum is a genus of between 5–15 species of flowering plants in the family Fabaceae, subfamily Caesalpinoideae. The genus is native to certain tropical regions across the world. The species are medium-sized to large trees growing up to 15–25 m (rarely 50 m) tall (Plant- 5).

The seeds of these plant species are sowed individually in all the samples and were watered daily. The growth of the plants was studied every day and height was measured once in a week.

RESULTS AND DISCUSSION

The comparative study of growth of the plants in different additives is discussed below.

Fly Ash as Additive

Fig. 1 shows growth comparisons of different plant species in OB sample with fly ash 25% volume/volume (V/V). Of the 5 species only 2 species have grown in this mix proportion. Plant 2 started growing after 3rd week whereas plant 5 started

growing after 4th week. Fig. 2 shows the growth comparison of different plant species in OB sample with fly ash 50% V/V. It is clear that only 2 species of plants have grown out of 5. Plant 2 started growing after 3rd week and plant 4 has started growing after 4th week.

Sewage Sludge as Additive

Fig. 3 shows growth comparison of different plant species in OB sample with sewage sludge 25 % V/V. All species have grown in this sample. Plant 3 had shown substantial growth compared to other species, 36cm by 8th week. Plant 2 and plant 5 have started growing from 3rd week onwards. Fig. 4 shows growth comparisons of different plant species in OB sample with sewage sludge 50% V/V. All the species have shown good results and plants 1, 2 and 3 have shown extremely good results. Plant 3 grown to 34 cm in 8 weeks, which is the maximum height during this study. This is the only sample in which all the plant species have grown more than 15 cm. Similarly, plant 5 grown only 16cm in 8weeks, which is the lowest. 3 out of 5 species have started growing from week 1 whereas other two started growing from week 2. This may be due to the high nutrient content present in sewage sludge. Sewage sludge has highest % of organic carbon, organic matter and clay content which are supporting the growth of plants.

Bottom Ash as Additive

Fig. 5 shows growth comparison of different plant species in OB sample with bottom ash 25% V/V. Out of 5 species all species have grown except plant 1. The rate of growth has increased for all plants, but growth rate is very high in plant 2 compared to the others. Fig. 6 shows growth comparisons of different plant species in sample with bottom ash 50% V/V. Out of 5 species all species have grown except plant 1. Plant 2 and plant 3 have shown significant growth. There is a little growth during week 5 and week 6 for plant 5. Among all, plant 3 grown tallest to 33cm in 8 weeks.

Plant Growth in Native Soil

Fig. 7 shows the growth comparison of all five plant species in native soil. The soil was collected from our academic camps, where lot of trees / species grow naturally. This was done to compare the fertility of native soil with waste burden consists of different additives. All the species have shown healthy results showing growth from very 1st week. Plant 2 and plant 3 have grown more than 25cm in 6 weeks and all the other species have grown more than 15cm in 6 weeks.

Cassia Siamea and Dendrocalamus strictus has shown better growth (23.8cm and 29.5cm respectively) in sewage sludge mixed with OB sample in 50% V/V proportion than native soil (22.5cm and 25.8cm respectively). All the remaining species have shown better growth results in native soil. Though bottom ash didn't show good experimental results as sewage sludge, the growth of plants is almost same as sewage sludge mixed with OB sample. Peltophorum has grown a little more height (12.7cm) in 6 weeks in bottom ash mixed with OB sample in 25% V/V proportion than sewage sludge mixed with OB sample in 25% V/V and 50% V/V proportion (8.8cm and 12 cm respectively). Except for Cassia Siamea remaining all the species have grown in both the proportions of bottom ash additive whereas only 3 species have grown in sewage sludge mixed with OB sample in 25% V/V and 4 species have grown in sewage sludge mixed with OB sample in 50% V/V. But overall growth rate is high in sewage sludge than in bottom ash additive when height is taken into consideration. Though a total of 3 species have grown in both proportions of fly ash, they are weak and growth is very less compared to other additives. A few pictures showing the growth of plants in different combinations of materials is shown in Figure. 8. Summary of growth of all the plants with different additives is given in Table-1.

CONCLUSIONS

The field samples (overburden waste rock) collected from an opencast coal mine were analysed in the laboratory and found that they are sandy in nature and they contain

6th International Engineering Symposium - IES 2017

March 1-3, 2017, Kumamoto University, Japan

very less percentage of clay and also very poor in fertile characteristics that plays a major role in the growth of plants. No heavy metal contamination was found in OB sample or in any additive when analysed using SEM (EDAX method). Different additives like fly ash, bottom ash, sewage sludge are added to waste rock (sand stone) of coal mines by 25% and 50% by volume. Five different types of species were planted in waste rock with different additives and the growth rate was monitored weekly for 8 weeks. No species of plant is able to grow in OB sample, whereas all the species have grown in sewage sludge mixed with OB sample in 50% V/V showing the improvement in fertile characteristics of OB sample. One plant species started growing from week 3 in fly ash mixed with OB sample and two more species started growing from 4th week. 3 out of 5 species in sewage sludge mixed with OB sample in 50% V/V started growing from week 1. The other two species have started growing from week 2 and a maximum height reached was 11.8cms among all the species. Gliricidia Sepium has grown 36cms in 8 weeks which is the highest growth that was observed during the study in sewage sludge mixed with OB in 25% V/V proportion. This has shown better result than native soil. 3 of species have grown more than 30cms in 8 weeks and other 2 species have grown more than 16cms in same time period. Except for Cassia Siamea, all the other species have grown well in both the proportions of bottom ash additive. A maximum height of 33cms was observed for Gliricidia Sepium and remaining species showed healthy growth. Sewage sludge has given better results both experimentally and supported growth of plants compared to other additives. Bottom ash also showed promising results in plant growth. Instead of using chemical fertilizers, these additives can be added, which are improving the properties of OB sample and supporting the growth of plants.

REFERENCES

- [1] Gagnon, B et al (1997), Effect of Composts and Inorganic Fertilizers on Spring Wheat Growth and N uptake, *Can. Jl. Soil Sci*, 77, 487-495.
- [2] Guerrero, C et al (2001), Reclamation of a Burned Forest Soil with Municipal Waste Compost: Macronutrient Dynamic and Improved Vegetation Cover Recovery, *Bioresour Technol*, 76, 221-226.
- [3] IS: 2720 (1976), Indian Standard Methods of Test for Soils (PART XXIV).
- [4] Kavamura, V N and Espostio, E, (2010), Biotechnological Strategies Applied to the Decontamination of Soil Polluted with Heavy Metals, *Biotechnology Advances*, 28, 61-69.
- [5] Mamo, M et al (1999), Nitrogen and Carbon Mineralization in Soil Amended with Municipal Solid Waste Compost, *Can. J. Soil Sci*, 79, 535-542.
- [6] Martínez, F et al (2003), Bio Waste Effects on Soil and Native Plants in a Semiarid Ecosystem, *Jl. Environ. Qual*, 32, 472-479.
- [7] Ram Chandar, K et al (2015), Experimental Study for the Assessment of Suitability for Vegetation Growth on Coal over Burden, *Int. Jl. Mining And Mineral Engineering*, Vol-6, No. 3, 218-233.
- [8] Ros, M et al (2001), The Use of Urban Organic Wastes in the Control of Erosion in a Semiarid Mediterranean Soil, *Soil Use Manage*, 17, 292-293.
- [9] Serra-Wittling, C (1996), Modification of Soil Water Retention and Biological Properties by Municipal Solid Waste Compost, *Compost Sci. Util*, 4, 44-52 (1996).
- [10] Sheoran, V et al (2010), Soil Reclamation of Abandoned Mine Land by Revegetation: A Review, *International Journal of Soil, Sediment and Water Documenting the Cutting Edge of Environmental Stewardship*.
- [11] Singh, R S (1996), Restoration of Coal-Mine Overburden Dump- a Case Study. *Coal International*.
- [12] Tester, C F (1990), Organic Amendments Effects on Physical and Chemical Properties of a Sandy Soil, *Soil Sci. Soc. Am. J*, 54, 827-831.

6th International Engineering Symposium - IES 2017
March 1-3, 2017, Kumamoto University, Japan

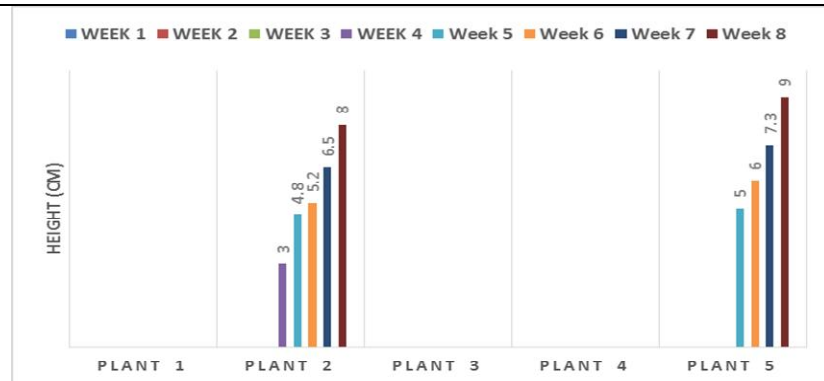


Fig.1 Growth comparison of different plant species in fly ash 25% V/V

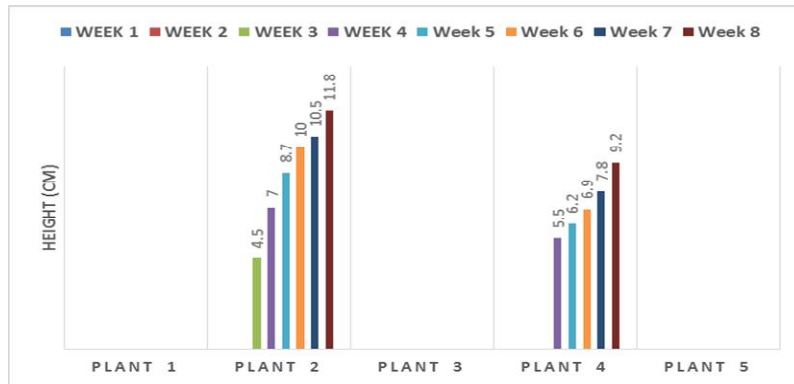


Fig. 2 Growth comparisons of different plant species in fly ash 50% V/V

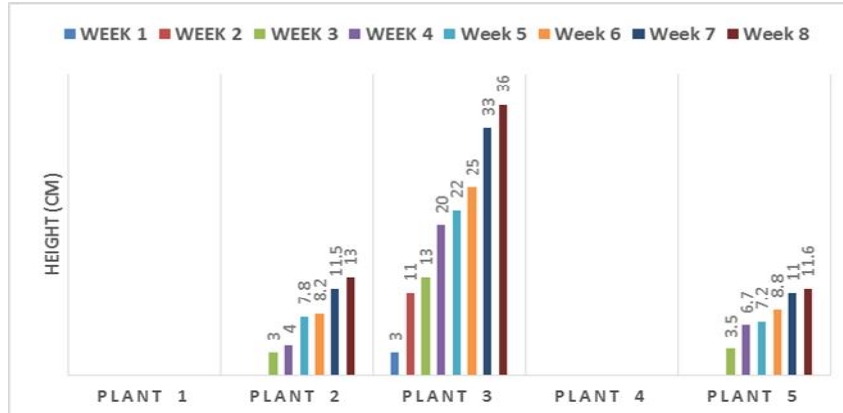


Fig. 3 Growth comparisons of different plant species in sewage sludge 25% V/V

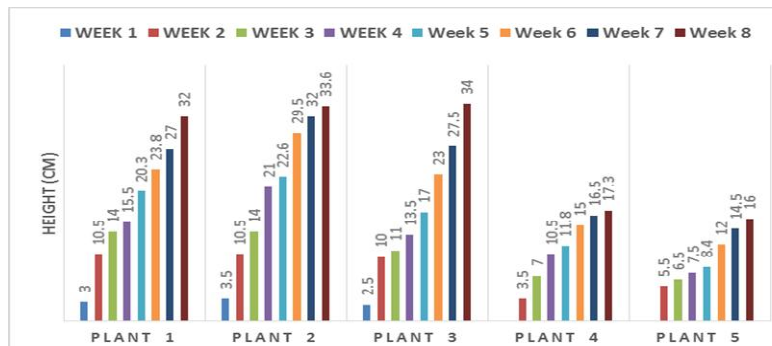


Fig. 4 Growth comparisons of different plant species in sewage sludge 50% V/V

6th International Engineering Symposium - IES 2017
March 1-3, 2017, Kumamoto University, Japan

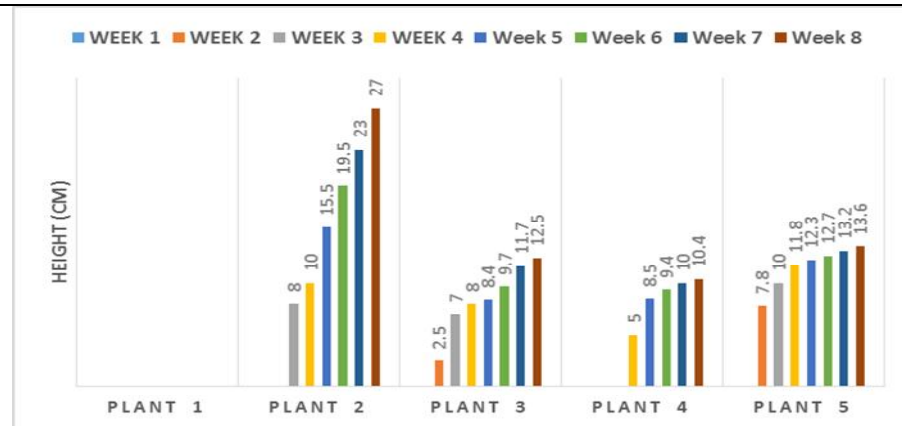


Fig. 5 Growth comparisons of different plant species in bottom ash 25% V/V

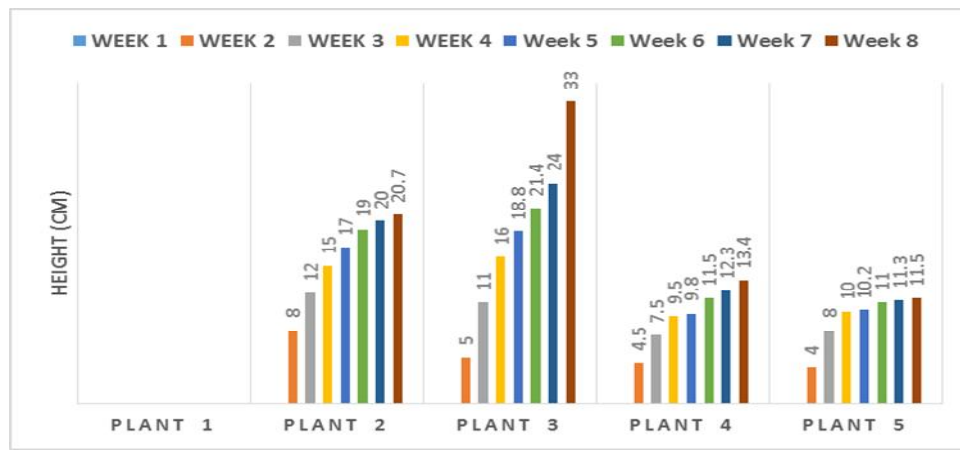


Fig. 6 Growth comparisons of different plant species in bottom ash 50% V/V

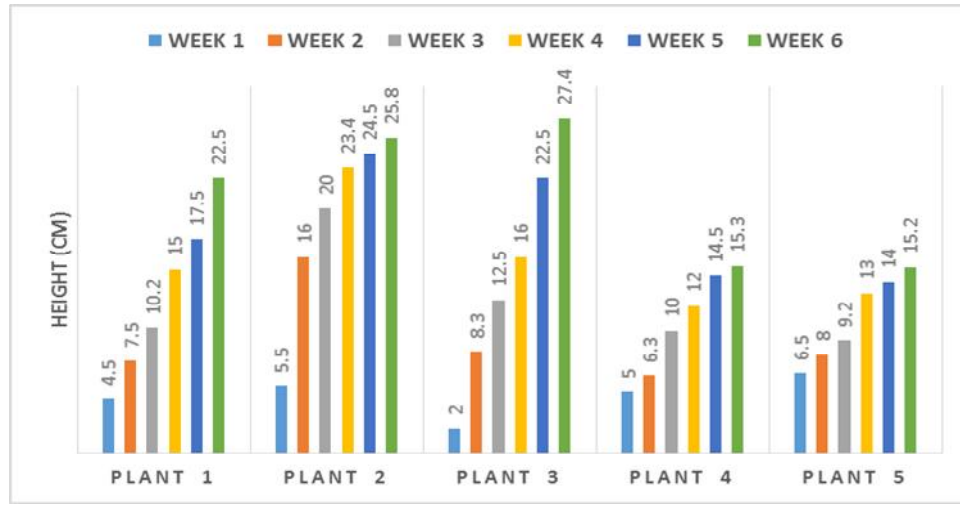


Fig. 7 Growth comparisons of different plant species in native soil

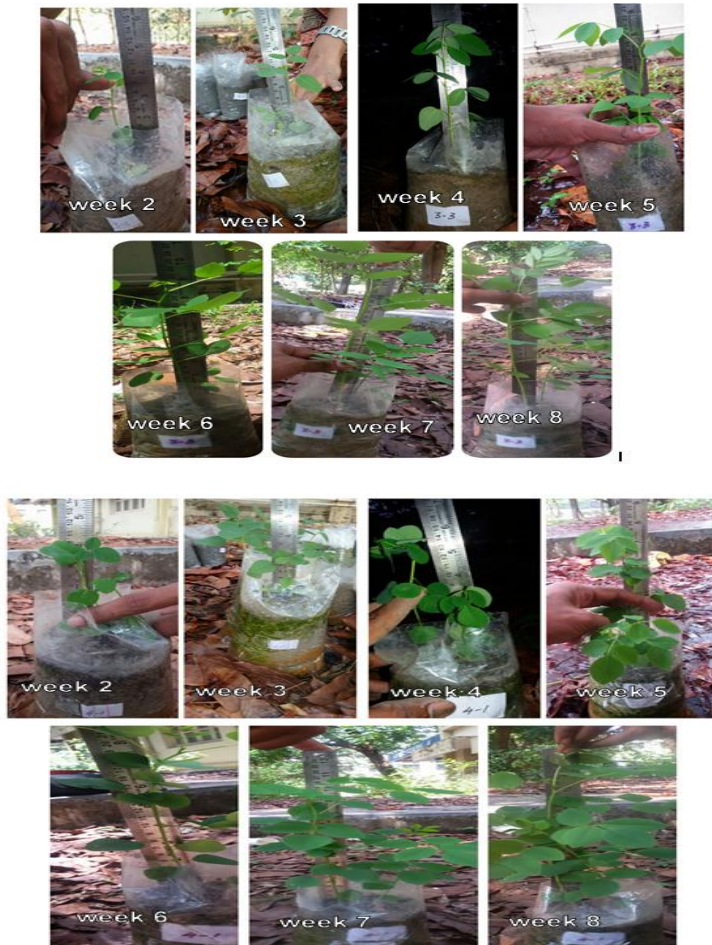


Fig. 8 Sample pictures showing growth of different plants

Table 1 Summary of growth of all the plants with different additives

Sl. No.	Additive	Growth height of plants (cm)				
		Plant-1 Cassia Siamea	Plant-2 Dendrocalamus strictus	Plant-3 Gliricidia Sepium	Plant-4 Phyllanthus emblica	Plant-5 Peltophorum
1	Fly ash- 25%	-	8.0	-	-	9.0
2	Fly ash-50%	-	11.8	-	9.2	-
3	Sewage Sludge- 25%	-	13.0	36.0	-	11.6
4	Sewage Sludge- 50%	32	33.6	34.0	17.3	16.0
5	Bottom ash- 25%	-	27.0	12.5	10.4	13.6
6	Bottom ash- 50%	-	20.7	33.0	13.4	11.5
7	Native soil	22.5	25.8	27.4	15.3	15.2

Mechanical and Durability Properties of Concrete with Precious Slag Balls (PS Balls) as Replacement for Fine Aggregates

Gayana B.C ^{*1}, Sharath S ² and Dr. K. Ram Chandar³

- 1 *Department of Mining Engineering, National Institute of Technology Karnataka, Surathkal, Mangalore 575025, India. Email: bkgayana@gmail.com*
 - 2 *Formerly National Institute of Technology Karnataka, Surathkal, Mangalore 575025, India. Email: sharath.s1993@gmail.com*
 - 3 *Department of Mining Engineering, National Institute of Technology Karnataka, Surathkal, Mangalore 575025, India. Email: krc_karra@yahoo.com*
-

ABSTRACT: The construction industry is the one that stand out in the use of industrial by-products, replacing aggregates with waste or by-products of different industries. A systematic experimental investigation is taken up to study the feasibility and sustainability for the use of precious slag (PS) balls as replacement of fine aggregates in concrete from the technological and economic point of view. The effect of PS balls at various percentages (20%, 40%, 60%, 80% and 100%) on their mechanical properties such as compressive strength, splitting tensile strength and flexural strength were carried out. Also, to determine the durability properties, permeability test was done. Results indicated that compressive strength increased with concrete mix containing 40% of PS balls as replacement for fine aggregates, i.e., 1.1 times that of the reference mix. Durability tests indicate that concrete containing higher content of PS balls resulted in lower permeability, leading to durable concrete. Wide range of application of PS balls in civil works were found to be in pre-stressed concrete piles, pavements, floor material, bricks and other concrete works.

Keywords: Precious Slag Balls, Concrete, Sustainability, Replacement of Fine aggregates

INTRODUCTION

Concrete is a reliable, universal, durable and versatile construction material that can endure for centuries. It is a compacted mixture of cement, aggregates and admixtures which in the presence of water hardens and gains strength due to hydration. With rapid progress in infrastructure development, demand for concrete has been increasing exponentially. This has led to a lot of stress on mining of aggregates and other raw materials. Unauthorized and unscientific methods have been resorted to, for catering the increasing demand for fine and coarse aggregates. A lot of problems are being faced for the

procurement of good quality fine aggregates. Therefore, efforts have been continued to find a substitute for conventional fine aggregates.

The use of by-products of various origins in the production of concrete has become an increasingly widespread practice in recent times. The main advantages are the elimination of scraps and a reduction in over-exploitation of quarries. The use of these industrial by-products in concrete has paved the way for safe disposal of waste, leading to recycling of materials, reducing adverse impacts on the environment along with reducing the stress for new mining activities.

6th International Engineering Symposium - IES 2017

March 1-3, 2017, Kumamoto University, Japan

The replacement of cement or aggregate by recycled materials in concrete improves material greenness. It is also necessary to ensure material durability in the use to attain true sustainability of concrete infrastructure (Keoleian et al. 2005). To promote the sustainability of concrete, extensive efforts have been put into screening suitable industrial by-products to partially replace cement or aggregate in concrete, thereby reducing the need for natural resources (Badur et al. 2008).

Singh et al. (2015) conducted experiments on concrete by replacing fine aggregates with GBFS. Maximum compressive strength was obtained for 50% replacement of sand by GGBS and the mixes containing GBFS showed higher compressive strength than the reference mix.

Zhao et al. (2014) conducted experimental study for the replacement of sand with iron ore tailings to prepare UPHC (Ultra High Performance Concrete). When the replacement level was not more than 40% for 90 days standard cured specimen, the mechanical behavior of the tailings were comparable to that of the control mix and the compressive strength decreased by 11% and flexural strength increased by 8% in comparison to control mix for specimens that were steam cured for 2 days.

Huang et al. (2013) used iron ore tailings powder as cement replacement for developing green ECC (Engineered Cementitious Composite) and concluded that the replacement of cement by less reactive IOTs in ECC reduces the matrix fracture toughness. Increasing the replacement of cement beyond 40% replacement ratio reduces the compressive strength of ECC.

Matwally (2007) reported that the use of finely milled waste glass in concrete mixtures improved the mechanical properties of concrete at later stages. Batayneh et al. (2007) reported a gradually increase in compressive strength, splitting tensile strength and flexural strength of concrete containing crushed

waste glass as fine aggregate at levels of 5%, 10%, 15% and 20% by weight.

Wu et al. (2010) investigated the mechanical properties of high strength concrete incorporating copper slag as a fine aggregate and concluded that less than 40% copper slag replacement was higher than that of the control specimen and the workability was also higher.

The research studies were conducted to investigate the feasibility of using PS Balls as a replacement for sand, with focus on the performance of concrete containing PS Balls in fresh state and hardened state and its durability.

METHODOLOGY AND MATERIALS:

Methodology: The materials required for the study were collected from different sources and tests were carried out to determine their physical properties. The mix proportion of M40 grade concrete mix was arrived as per IS 10262-2009 guidelines. The mixing and casting of these mixes were carried out and the behaviour of the resulting concrete mixes in their fresh and hardened state was evaluated.

Cement: Ordinary Portland cement of 53 grade conforming to IS 12269:2013 was used for the laboratory investigations. The required tests for assessing the properties of cement were carried out according to IS 4031. The test results are shown in Table 1.

Fly Ash: Class F Fly Ash conforming to IS 3812 was used for the experiment. The specific gravity of Fly Ash was found out to be 2.2. Amount of Fly Ash retained in 45µm sieve was measured equal to 30%, which is within the prescribed limit. Fly Ash was utilised for the experiment in order to make the mix cohesive and improve workability.

Coarse aggregate: Locally available crushed stone coarse aggregates of size 20 mm down were used. The aggregates were composed of a mixture of rounded and angular aggregates. The various properties of aggregates are determined as per IS

6th International Engineering Symposium - IES 2017

March 1-3, 2017, Kumamoto University, Japan

2386 (Part III, IV): 1963 and the specifications are checked as per IS 383: 1970 requirements. The physical properties of coarse aggregates are shown in Table 2.

Fine aggregate: Two types of fine aggregates were used in the present study namely River sand and precious slag balls.

River sand: Locally available river sand conforming to zone II as per IS 383:1970, passing through 4.75 mm sieve was used. The physical properties of sand are as shown in Table 3 and the grading curve is shown in Fig 1.

PS Balls: PS balls were collected from a steel plant in Bellary District of Karnataka State in India. Sampling was done according to IS 2430:1986. The physical properties of PS Balls are shown in the Table 4. Fig 2 shows the grading curve of PS balls. PS Balls conforms to zone I as per IS 383:1970. PS Balls of size smaller than 600µm were added in concrete to comply with grading Zone II as sand.

Water: The amount of water in a concrete mix has a direct effect on the strength development of the mixture. Sufficient water must be added to lubricate the solids in the mixture. Tap water was used for concreting.

Superplasticizer: Sulphonated naphthalene polymer based Conplast SP430 superplasticizer was used in the present study to improve the workability of concrete.

RESULTS AND DISCUSSIONS:

Workability: Concrete was designed for 75-100 mm range of slump. Water cement ratio and super-plasticizer content was kept constant for all mixes (Fig 3).

Compressive strength: Cubes of 150*150*150mm were casted and tested for different curing days (Fig 4). The test results are given in Table 5. It was observed that the concrete mix in which 40% of sand was replaced with PS Balls showed the highest increase in

compressive strength. Fig. 5 shows increase in compressive strength of concrete mixes from 7 days to 28 days and to 90 days.

Flexural and Split tensile strength: Both flexural strength and splitting tensile strength showed similar behaviour to that of compressive strength with increasing trend till 40% replacement of sand by PS balls and decreasing trend afterwards (Table 6). The decrease in strength is attributed to smooth surface of PS Balls (Fig 6). The splitting tensile strength for all the mixes containing PS Balls was higher than that of control mix as shown in Fig 7. The concrete specimens containing PS Balls exhibited brittle failure similar to that of the reference concrete.

Durability of concrete: In this study, permit ion permeability test was carried out to study the permeability characteristics of concrete with slab size 500*500*50mm. The rate of conductivity in the present study for reference concrete with water cement ratio of 0.4 is 3.33 micro Siemens per minute (Table 7). Lower the rate of conductivity, lower will be the permeability of concrete i.e., concrete will be denser with lesser voids and better durability. Fig. 8 & 9 shows that, the rate of conductivity decreases with the addition of PS balls as fine aggregates in concrete. Hence, with the addition of PS balls the permeability of concrete decreases leading to concrete which is more durable.

CONCLUSIONS:

PS Balls are modified form of slag processed using slag atomizing technology. The following are the main conclusions drawn based on the test results obtained in this study:

- This study indicates that, it is possible to use PS Balls as fine aggregate in concrete in the condition as it is produced in the industry without any modification.
- The slump values increased with increase in PS Ball content. Concrete with PS Balls as 100% of fine aggregate yielded 40mm more slump than reference mix for same water-cement

6th International Engineering Symposium - IES 2017

March 1-3, 2017, Kumamoto University, Japan

- ratio. This shows that PS Balls can be used to produce better workable concrete at lower water content.
- In concrete incorporating PS Balls as fine aggregate, the quantity of superplasticizer to be used for obtaining a specific range of slump can be reduced.
- The study showed that the concrete incorporating PS Balls withstood higher compressive loads than reference concrete, with SP 40 mix giving highest increase in compressive strength of 10.7% and 10.1% than that of reference mix at the age of 7 days and 28 days respectively. SP 100 mix containing only PS Balls as fine aggregates yielded 2.1% and 4.4% increase in compressive strength than that of reference mix at the age of 7 days and 28 days respectively.
- The concrete containing PS Balls up to 60% yielded higher flexural strength than that of reference mix which is favorable for concrete pavements.
- All the mixes containing PS Balls yielded higher splitting tensile strength than that of reference mix.
- The durability indicated that, the concrete containing higher amount of PS Balls results in denser concrete with compact structure and lesser voids, leading to concrete which is more durable.

REFERENCES

- [1] Badur, S and Rubina, B (2008), Utilization of hazardous wastes and by-products as a green concrete material through s/s process: A review. *Reviews on Advance Material Science*, Vol.17, No. 1-2, pp. 42-61.
- [2] Batayneh Malek, Marie Iqbal and Asi Ibrahim (2007), Use of selected waste materials in concrete mixes. *Waste Management*, Vol. 27, pp. 1870-6.
- [3] Gaurav Singh, Souvik Das, AbdulazizAbdullahi Ahmed, Showmen Saha, Somnath Karmakar (2015), Study of Granulated Blast Furnace Slag As Fine Aggregate In Concrete For Sustainable Infrastructure. *Procedia – Social and Behavioural Sciences*, Vol. 195, pp. 2272-2279.
- [4] IS 383-1970, Specification for coarse and fine aggregates from natural sources for concrete, Bureau of Indian standards (BIS), New Delhi, India.
- [5] IS: 10262-2009, Concrete mix proportioning – guidelines, Bureau of Indian Standards (BIS), New Delhi, India.
- [6] IS: 12269-2013, Specification for 53 grade ordinary Portland cement, Bureau of Indian standards (BIS), New Delhi, India.
- [7] IS: 2386-1963, Methods of tests for aggregates for concrete, Bureau of Indian standards (BIS), New Delhi, India.
- [8] Keoleian, G A et al (2005), Life cycle modeling of concrete bridge design: Comparison of ECC link slabs and conventional steel expansion joints, *Journal of Infrastructure system*, Vol. 11, No.1, pp. 51-60.
- [9] Metwally, I M (2007), Investigations on the performance of concrete made with blended finely milled waste glass. *Advances in Structural Engineering*, Vol. 10, No.1, pp. 47-53.
- [10] Permit ion permeability test, Operating manual, Amphora NDT.
- [11] Sujing Zhao, Junjiang Fan and Wei Sun (2010), Utilization of iron ore tailings as fine aggregate in ultra-high Performance concrete. *Construction and Building Materials*, pp. 540-548.
- [12] Wei Wu, Weide Zhang and Guowei Ma (2010), Optimum content of copper slag as a fine aggregate in high strength concrete. Elsevier, *Materials and Design*, Vol. 31, pp. 2878-2883.
- [13] Xiaoyan Huang, Ravi Ranade and Victor C Li (2013), Feasibility Study of Developing Green ECC Using Iron Ore Tailings Powder as Cement Replacement. *Journal of Material of Civil Engineering*, Vol. 25, No.7, pp. 923-931.

6th International Engineering Symposium - IES 2017
March 1-3, 2017, Kumamoto University, Japan

Table 1 Physical properties of cement

Sl. No	Properties	Values Obtained	Requirement as per IS 12269:2013	Remarks
1	Specific Gravity	3.15	----	The cement satisfies the requirement for 53 grade OPC stipulated by IS 12269:2013. Tests are conducted as per guidelines of IS 4031.
2	Standard Consistency	29%	----	
3	Fineness	300 m ² /kg	Should not be less than 225 m ² /kg	
4	Initial Setting Time	60 minutes	Should not be less than 30 minutes	
5	Final Setting Time	450 minutes	Should not be more than 600 minutes	
6	Soundness (By Le Chatelier Mould)	2 mm	Should not exceed 10 mm	

Table 2 Physical properties of coarse aggregates

Sl. No	Property	Value
1	Specific Gravity	2.8
2	Bulk Density	1370 kg/m ³
		1670 kg/m ³
3	% Of Voids	40%
4	Moisture Content	Nil
5	Water Absorption	0.5%

Table 3 Physical properties of river sand

Sl. No	Property	Value
1	Specific Gravity	2.70
2	Bulk Density	1440 kg/m ³
		1700 kg/m ³
3	% Of Voids	38%
4	Moisture Content	Nil
5	Water Absorption	1%

Table 4 Physical properties of PS Balls

Sl. No	Property	Value
1	Specific Gravity	3.58
2	Bulk Density	2300 kg/m ³
	Loose Compacted	2550 kg/m ³
3	% Of Voids	28.8%
4	Moisture Content	Nil
5	Water Absorption	0.2%

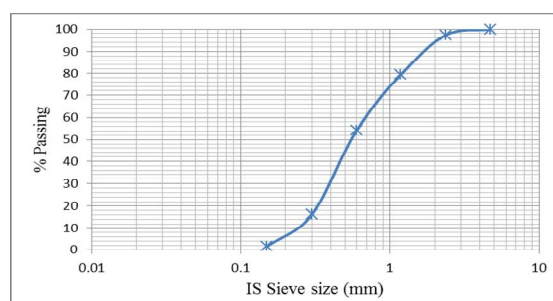


Fig. 1 Grading curve of River sand

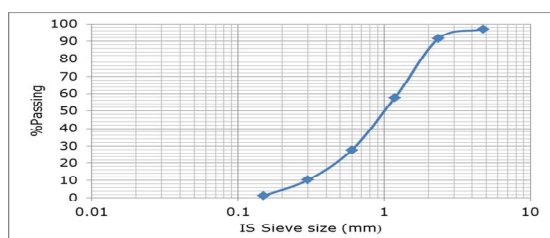


Fig. 2 Grading curve of PS Balls



Fig. 3 Slump test



Fig. 4 Compression test

6th International Engineering Symposium - IES 2017

March 1-3, 2017, Kumamoto University, Japan

Table 5 Compressive strength at 7 days, 28 days and 90 days

Age	7-day	28-day	90-day
Mix	Compressive strength (MPa)		
Control mix	36.33	57.11	59.22
SP 20	39.11	61.11	62.78
SP 40	40.22	62.89	64.00
SP 60	39.22	60.44	62.00
SP 80	38.33	59.56	61.22
SP 100	37.11	59.66	60.67

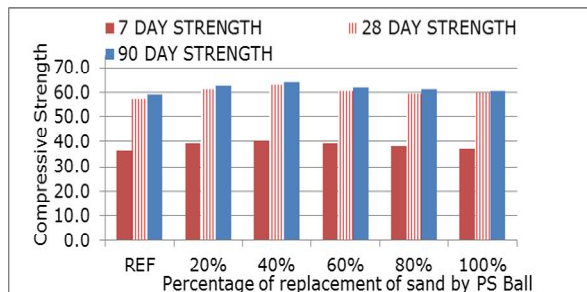


Fig. 5 Increase in compressive strength of concrete mixes from 7 days to 28 days and to 90 days

Table 6. Compressive strength of concrete mixes at 7, 28 and 90 days

Age	28 day	
Mix	Flexural strength (MPa)	
Control mix	6.90	3.11
SP 20	7.05	3.75
SP 40	7.50	3.82
SP 60	7.33	3.67
SP 80	6.40	3.67
SP 100	6.26	3.40

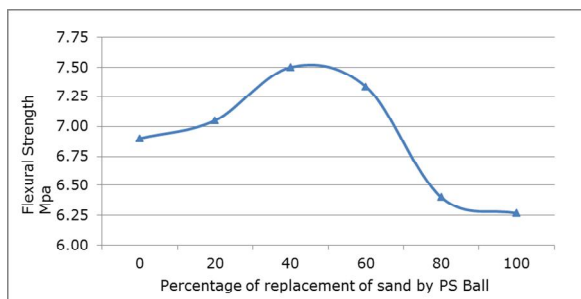


Fig. 6 Variation of flexural strength for different percentage of replacement of sand by PS balls

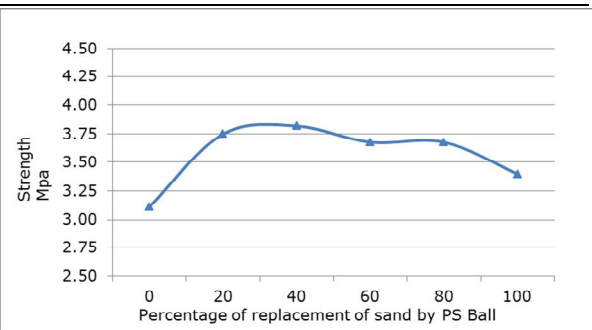


Fig. 7 Variation of splitting tensile strength for different percentage of replacement of sand by PS Balls.

Table 7 Rate of conductivity of different concrete mixes

Concrete mix	Rate of conductivity ($\mu\text{s}/\text{min}$) (28 Day)
Control mix (100:0)	3.33
SP 40 (60:40)	3.06
SP 100 (0:100)	2.47

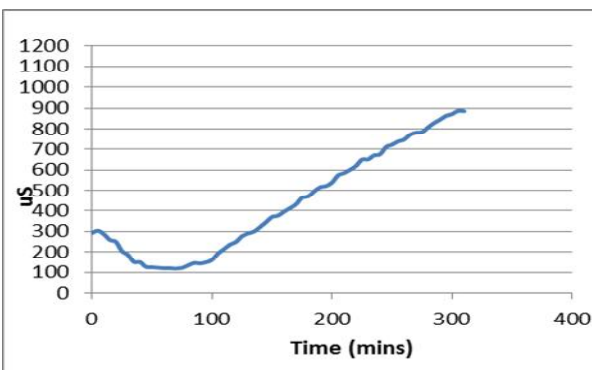


Fig. 8 Conductivity Time plot for control mix at age of 28 day

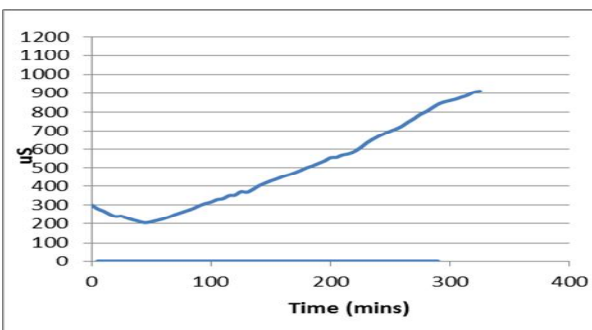


Fig. 9 Conductivity Time plot for SP 40 mix at age of 28 day

Building Extraction from Quickbird-2 Imagery

Arkal Vittal Hegde¹ and Jagalingam P²

- 1 *Department of Applied Mechanics and Hydraulics, National Institute of Technology Karnataka, Surathkal, Mangaluru, Karnataka- 575025, India.
email: arkalvittal@gmail.com*
- 2 *Department of Applied Mechanics and Hydraulics, National Institute of Technology Karnataka, Surathkal, Mangaluru, Karnataka- 575025, India.
email: lingam.jai10@gmail.com*

ABSTRACT: Extraction of buildings from very high resolution satellite imageries is a challenging problem and many automatic algorithms have been proposed in the literature to extract this information from various satellite imageries. Detection of buildings from the satellite imageries has many significant applications in the domain of urban mapping, urban planning, urban change detection analysis, target detection and Geographic Information System (GIS). In the present paper, an automatic algorithm, based on the adaptive k-means clustering, followed by morphological fill and open operators, are used to extract the buildings from the Quickbird-2 imagery. The performance of this automatic algorithm for the extraction of buildings is evaluated using qualitative (visual) analysis. The experimental results obtained show that the algorithm extracted the buildings reasonably well, even though the buildings in the imagery analysed, were in different shapes, sizes and colours.

Keywords: Building extraction, adaptive k-means clustering, Morphological operators, Quickbird-2

INTRODUCTION

Extraction of buildings from the remote sensing satellite imageries is one of the most challenging problems. The availability of high spatial and spectral resolution images, camera sensors, quality of image, seasonal and weather circumstances and the appearance of buildings is extremely challenging to develop a commonly applicable algorithm for the extraction of building.

Detection of buildings is important for urban mapping, urban planning, urban change detection analysis, target detection, geographic information system (GIS) (Shorter & Kasparis, 2009). Further, detection of buildings is very much important to assess the extent of destruction caused after the natural disasters such as floods, earthquake and military operation (Chaudhuri et.al, 2016).

The previous studies found in the literature extracted the buildings which were

homogenous either in shape or texture (Muller & Zaum, 2004), and also buildings with unique roof colour are distinguished from the background colour (Sirmacek & Unsalan, 2008). Contour based detection based technique is adopted when the high contrast image is available (Katartzis & Sahli, 2008).

(Liasis & Stavrou, 2016) In this work, the framework based on the active contour segmentation is processed by analysing the properties of red, green and blue (i.e. RGB) representation and the holdings of hue, saturation and value (HSV) were used to extract the buildings from the satellite image. Initially, the vegetation and shadow features are removed by using the clustering technique. A new active contour model was developed, based on the HSV representation of the image. To attain superior segmentation, a new energy span is encoded for biasing the contour. Finally, the morphological operator is adopted to remove misleading information. Both,

6th International Engineering Symposium - IES 2017

March 1-3, 2017, Kumamoto University, Japan

qualitative and quantitative analyses are performed to estimate the performance of proposed method.

(Wang & Pan, 2013) proposed a novel approach by using corner detection, segmentation and adaptive windowed Hough transform for detecting buildings from Quickbird satellite imagery. Firstly, the input image was segmented into a number of classes by adopting a mean shift segmentation algorithm. Secondly, the corners of the buildings were extracted by using the scale invariant feature transform (SIFT). Finally, extraction of building roof boundary was achieved by using adaptive windowed Hough transform. It was concluded that the proposed method can only detect buildings with rectangular shape.

Majority of algorithms work efficiently for detecting buildings with the same shape (i.e. rectangular, square), colour and size. Only a few algorithms are available for detecting buildings using very high resolution satellite imageries (i.e. less or equal than 1 m spatial resolution).

In the present work, the main objective is to extract the buildings from the original multispectral (MS) imagery of Quickbird-2 in which, the buildings are in different shapes, sizes and colours. The automatic approach is adopted to extract the buildings. In this approach: firstly, the vegetation portion is removed from the input image. Secondly, adaptive k-means clustering algorithm is adopted to cluster the pixels into different classes. Finally, the morphological operator fill and open is implemented to extract the buildings.

DATA USED

The high-resolution imaging satellite Quickbird-2 was launched on October 18, 2001. Quickbird-2 acquires five bands covering panchromatic, blue, green, red and near-infrared (NIR). The satellite sensor captures the Pan image with a high spatial resolution of 0.60 m and the MS image with high spectral resolution but a low spatial resolution of 2.4 m. The data location is the opera house in Sydney,

Australia ($33^{\circ} 51' 25''$ S, $151^{\circ} 12' 55''$ E) provided by Digital Globe.

METHODOLOGY

The methodology for extracting the buildings using automatic approach from the Quickbird-2 satellite imagery is shown in the Figure 2.

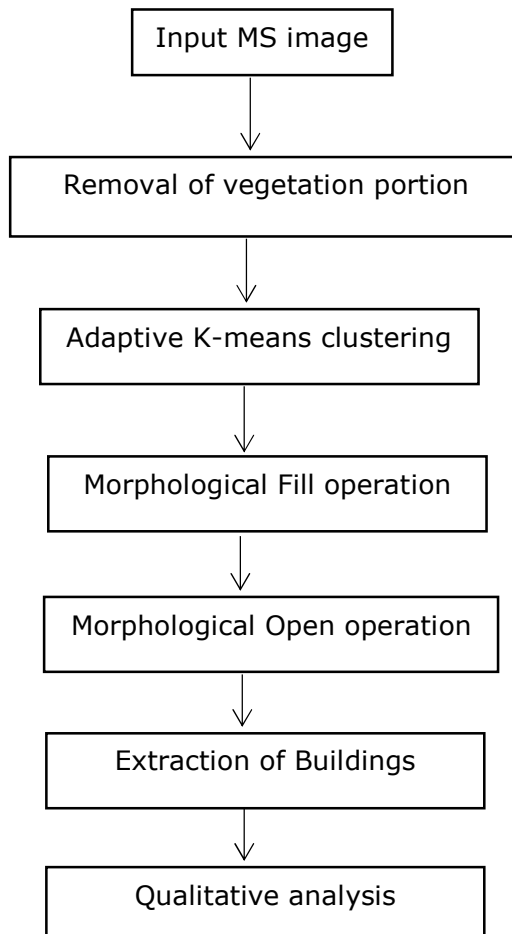


Fig. 1 Methodology for extracting the building automatically

Removal of Vegetation portion

From the multispectral imagery of Quickbird-2, it is visualised that the vegetation is dominant when compared to the other features. Therefore the portion of vegetation is removed based on the representation of intensity value.

Adaptive K-means clustering

The Adaptive K-means clustering algorithm functions by automatically choosing the appropriate K elements from the input image (Bhatia, 2004). The algorithm

6th International Engineering Symposium - IES 2017

March 1-3, 2017, Kumamoto University, Japan

automatically determines the K elements and generates the group of clusters (i.e. the feature with the same intensity value are grouped together). More information about adaptive clustering can be found in (Pappas, 1992; Chen et.al, 1998). The algorithm automatically determines the K elements and generates the group of clusters (i.e. the feature with the same intensity value are grouped together). Generally, the algorithm classifies each pixel into the clusters, based on their intensity values. Firstly, the algorithm computes the distance between the selected element and the number of clusters. This process also helps to determine the distance between the two elements. In order to compute the distance, it is important to normalize the distance properties, so that the domination of distance from one property (or) certain properties are not omitted from the computation of distance. The method, Euclidean distance is adequate for determining the distance between two elements.

Morphological fill and open operation

Fill operation: The following syntax is used to fill the holes in the image

$$I2 = imfill(I) \quad (1)$$

Where, I is the binary image. The advantage of the fill operation is to fill the holes in the image by describing it as an area of dark pixels bounded by light pixels and to produce another binary image I2.

Open operation: The following syntax is used to extract the objects from the input image.

$$IM = bwareaopen(I, P) \quad (2)$$

The open operation eliminates all the associated components (i.e. objects) that have less than P pixels from the binary image I and produced another binary IM image.

Finally, the building is extracted from the multispectral imagery of Quickbird-2 and evaluated qualitatively.

RESULTS AND DISCUSSION

The MS image of Quickbird-2 is shown in Figure 2. The MS image contains different features such as buildings, roads, vehicles and vegetation, etc. It is important to note that the patterns, shapes, sizes and spectral reflectance of the buildings are vary from each other. And also it is visualized that the color reflectance of roads and color reflectance of buildings are similar. Therefore, the attempt is made to extract the buildings with different sizes, shapes, colors and patterns.

The automatic approach for extracting the buildings from the original MS image is shown in the Figures 3 to 8. Firstly, the vegetative portion of the image is removed and shown in the Figure 3. Secondly, the adaptive k-means clustering algorithm automatically classifies the different pixels based on the intensity values into five different classes (Figure 4). From the classified image, it is notable that the buildings with the same intensity value are clustered into one class. Further, it is also notable that the intensity value corresponding to some buildings is close to the intensity value of roads and hence it is segregated in the same class. In order to differentiate the buildings from the features such as roads, vehicle, etc., the classified image is then converted into a binary image and is shown in the Figure 5.

It clearly indicates that some portion of the road is identified as building due to the similarity in intensity value and spectral reflectance. Moreover, since some buildings roof top is void, in order to reduce the potential error, further filling of voids using morphological fill operator was done (i.e. the void presented in the buildings, after the classification process is identified with the reference to the original pan image) which is shown in the Figure 6. To extract the buildings from the image, the morphological open operator is adopted and the result is shown in the Figure 7. The extracted buildings in the RGB color mode are shown in the Figure 8.

6th International Engineering Symposium - IES 2017

March 1-3, 2017, Kumamoto University, Japan

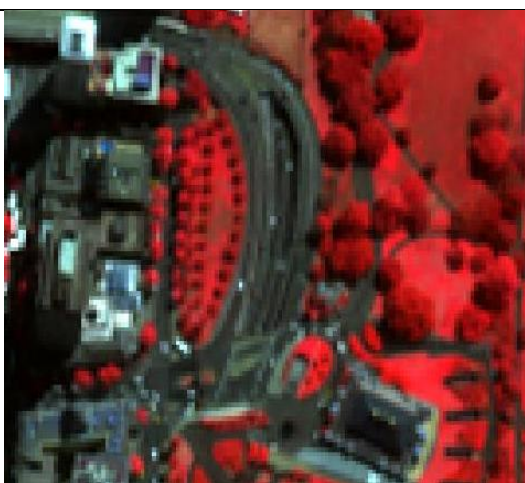


Fig. 2 Original MS image of Quickbird-2



Fig. 5 Conversion of classified image into binary image



Fig. 3 Removal of vegetation



Fig. 6 Morphological fill operation



Fig. 4 Adaptive k-means



Fig. 7 Morphological open operation



**Fig. 8 Conversion of binary mage
(area open) to RGB**

CONCLUSIONS

In the present paper, the automatic approach for extraction of buildings is presented for the Quickbird-2 imagery. From the results of the automatic approach, it is visualized that the major buildings are detected correctly for the original MS imagery of Quickbird-2. It is to be noted that the performance of automatic algorithm is very effective when all the buildings are in the rectangular shape. In the present work, the building shapes in the imagery are different. Nevertheless, the performance of the automatic approach used in the work for the extraction of buildings with the different shape, size and color is quite reasonable.

REFERENCES

- [1] Shorter N, Kasparis T (2009), Automatic vegetation identification and building detection from a single nadir aerial image, *Remote Sensing*, 1(4), 731–757. <http://doi.org/10.3390/rs1040731>.
- [2] Chaudhuri D, Kushwaha N K, Samal A, Agarwal R C (2016), Automatic Building Detection From High-Resolution Satellite Images Based on Morphology and Internal Gray Variance, *IEEE Journal of Selected Topics in Applied Earth Observations and Remote Sensing*, 9(5), 1767–1779. <http://doi.org/10.1109/JSTARS.2015.2425655>
- [3] Muller S and Zaum D (2005), Robust building detection in aerial images, In CMRT, pages 143–148, Vienna, Austria.
- [4] Sirmacek B and Unsalan C (2008), Building detection from aerial imagery using invariant color features and shadow information, In ISCIS, Istanbul, Turkey.
- [5] Katartzis A and Sahli H (2008), A stochastic framework for the identification of building rooftops using a single remote sensing image. *IEEE Trans. GRS*, 46(1):259–271.
- [6] Bhatia K S (2004), Adaptive K-means clustering algorithm. In Proceedings of Florida Artificial Intelligence Research Symposium, 2004. <http://dx.doi.org/10.1117/12.750002>.
- [7] Pappas T N (1992), An adaptive clustering algorithm for image segmentation, *Signal Processing, IEEE Transactions on*, 10(4), 901–914. <http://doi.org/doi: 10.1109/78.127962>
- [8] Chen, C., Luo, J., & Parker K J (1998). Image segmentation via adaptive K-mean clustering and knowledge-based morphological operations with biomedical applications. *IEEE Transactions on Image Processing*, 7(12), 1673–1683. <http://doi.org/10.1109/83.730379>.
- [9] Liasis G & Stavrou S (2016). Building extraction in satellite images using active contours and colour features. *International Journal of Remote Sensing*, 37(5), 1127–1153.
- [10] Wang, J., Qin, Q., Chen, L., Ye, X., Qin, X., Wang, J., & Chen, C. (2013). Automatic building extraction from very high resolution satellite imagery using line segment detector. In 2013 IEEE International Geoscience and Remote Sensing Symposium - IGARSS (pp. 212–215). IEEE. <http://doi.org/10.1109/IGARSS.2013.6721129>.

SOIL ARCHING EFFECT IN COLUMNAR EMBANKMENTS

Riya Roy¹ and Anjana Bhasi²

1. Department of Civil Engineering, National Institute of Technology Karnataka, Surathkal, Mangalore, India. Email:riyaanna.roy207@gmail.com
2. Department of Civil Engineering, National Institute of Technology Karnataka, Surathkal, Mangalore, India. Email: anjanabhasi@yahoo.com

ABSTRACT: Column supported embankments provide a practical and efficient solution for construction on soft soil due to the low cost and short construction times. In the recent years, geosynthetic have been used in combination with column systems to support embankments. The load transfer mechanism in these systems is a combination of soil arching and membrane effect of the geosynthetic. The effect of soil arching on columnar embankments has been studied by various design methods such as Hewlett & Randolph (1988), BS 8006:1995, Guido method. However the assumptions involved vary from method to method and the results obtained are not consistent. Therefore choosing the right solution is a major problem. This paper aims at analysing the soil arching effect by numerical methods and also studying the effect of various design parameters.

Keywords: numerical analysis, geogrid, soft soils

INTRODUCTION

Before the advancement of geotechnical engineering, the only choice of foundation engineers was to design the foundation which matches to the existing subsoil conditions at the site. But nowadays, due to the advancement in geotechnical techniques and with the help of latest technology, it is possible to improve insitu soil characteristics to suit the foundation of our choice. Such method of improving insitu soil properties to our desired quality is known as ground improvement techniques. The changes made through these techniques are permanent and are not affected with the passage of time or due to change in the weathering condition. Four groups of ground improvement techniques are distinguished- mechanical modification, hydraulic modification, chemical and physical modification, and modification by inclusion and confinement. Designing structures such as buildings, embankments, slopes etc on soft foundation soils faces a lot of challenges regarding instability, settlement problems and lateral movement. Techniques including preloading, geosynthetic reinforcement, soil improvement

techniques, column supported earth platforms can be used for addressing above problems. The main advantage of the column supported earth platform includes reduction of total and differential settlements, construction of superstructure in a single stage, and reduction of earth pressures.

The columns in columnar earth platforms can be of stone columns, piles etc. Piled (stone columns) embankments provide an economic and effective solution to the problem of constructing embankments over soft soils. This method can reduce settlements, construction time and cost. Columnar earth platforms have been used either with reinforcement or without reinforcement. A system with reinforcement is advisable since it can carry more loads and can reduces settlement when compared with a system without reinforcement.

In the case of piled embankments with geosynthetic reinforcement, the interactions among the pile, foundation soil and geosynthetic are schematically represented in fig 1. The embankment fill mass between the piles has a tendency to move downwards under the influence of fill weight, W_1 . This downward movement is

partially restrained by shear resistance, τ , from the fill above the pile. This shear resistance increases the load on piles and reduces the pressure acting on geosynthetic. This load transfer mechanism is termed as "soil arching effect" by Terzaghi(1936). This soil arching will take place when the columns are located very close to each other. If geosynthetic reinforcement is provided along with the columns, the number of piles required can be reduced and it also improves the overall design efficiency. Due to soil arching, the embankment load gets shifted to the columns and eventually transferred to the competent soil or rock layer below the soft foundation soil.

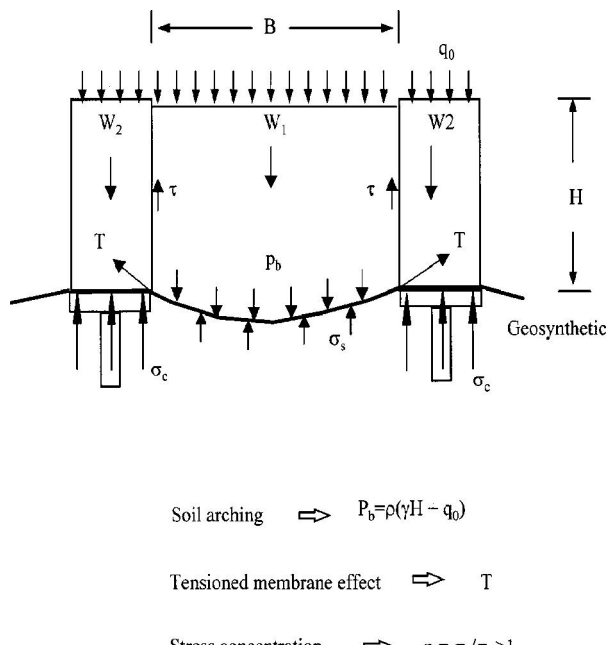


Fig 1. Load transfer mechanisms of geosynthetic reinforced pile supported earth platforms(Han et al (2002))

In this paper, the effect of soil arching in columnar embankment is studied by various design methods such as Hewlett & Randolph (1988), BS 8006:2010, Guido method. A numerical model is developed using ABAQUS software and the effects of design parameters like height of embankment, elastic pile modulus are also studied.

CURRENT DESIGN METHODS

1. Hewlett & Randolph (1988)

Hewlett et al (1988) developed this method based on three dimensional model tests conducted on sand at Cambridge University in the early 1980s and from plasticity theory based on the observed hemispherical dome geometry seen to develop in the model tests. The analysis was based on the arching effect in granular free draining soil. This effect was analysed by considering the limiting equilibrium of stresses in a curved region of sand between adjacent pile caps. In this method, arches were positioned in a semi-circular format, without overlapping, within a two-dimensional plane with the column width being double to the arches, which is shown in fig 2. The soil stresses are assumed to be redistributed in the arching shell alone because of the soil arching. It was also assumed that the arching fails either at the crown of the arch or at the pile cap. This method is better than the BS 8006 technique as it considers the embankment fill's strength.

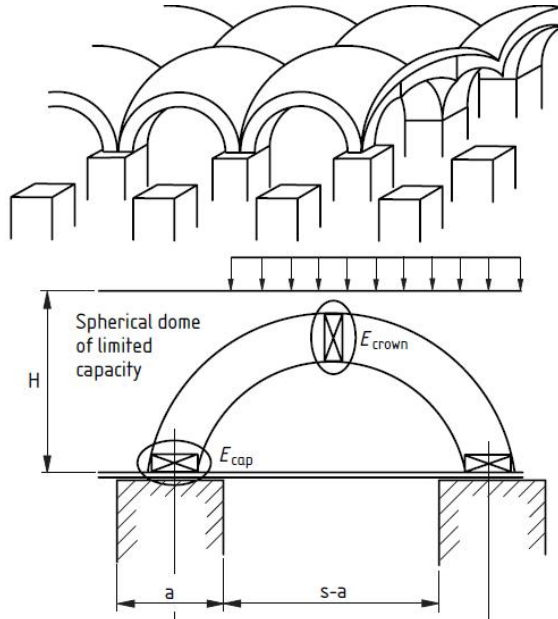


Fig 2. Arching theory according to Hewlett and Randolph (Hewlett et al (1988))

2. BS 8006-1:2010

The BS 8006 method is based on 2D pipeline theory, not the actual 3D situation which exists at the base of a piled

6th International Engineering Symposium - IES 2017

March 1-3, Kumamoto University, Japan

embankment. And also the method doesn't satisfy simple vertical equilibrium and also doesn't consider the condition at the crown of the arch. The soil arching between adjacent pile caps induces greater vertical stresses on pile caps, then on surrounding foundation soils. The recommended embankment height in order to avoid localized differential deformations as per BS code is given by

$$H \geq 0.7(s-a) \quad (1)$$

Where 'H' is the embankment height, 's' is the center to center spacing between piles and 'a' is the size of pile caps. The calculations of distributed loads on reinforcement are based on Marston's formula and the equations are designed for 3D analysis of piled embankments. The equation for the distributed load on reinforcement using Marston's formula is given by

$$P_c' / \sigma_v' = [(C_c * a) / H]^2 \quad (2)$$

Where

P_c' is the vertical pressure on the piles, σ_v' is the mean vertical pressure at the embankment base, C_c is the arching coefficient.

The distributed load W_T carried by the reinforcement between adjacent pile caps may be determined from:

when $H > 1.4(s-a)$

$$W_T = [1.4 s f_{fs} \gamma (s-a) / (s^2 - a^2)] (s^2 - a^2) (P_c' / \sigma_v') \quad (3)$$

and when $0.7(s-a) \leq H \leq 1.4(s-a)$

$$W_T = [s (f_{fs} \gamma H + f_q w_s) / (s^2 - a^2)] [s^2 - a^2] (P_c' / \sigma_v') \quad (4)$$

Where

γ is the unit weight of embankment fill.

w_s is the uniformly distributed surcharge loading.

$\sigma_v' = (f_{fs} \gamma H + f_q w_s)$ and is the factored average vertical stress at the base of the embankment.

3. Guido method

This method derives from laboratory plate loading tests carried out by Guido et al (1987) on samples of geogrid reinforced sand in a confined, rigid box. This design method is fundamentally different from the other two methods. If reinforcement layer is placed in embankments, then it will enhance the arching capability of the soil, rather than by membrane action. This

method considers arches in a triangular formation are placed with 45° internal angles.

This method relies on support from the underlying soil to prevent the fill beneath the developed arch from falling out. However, in the situations where there is no support from underlying soil, or having very little support, the method may not give reliable results as it may underestimate the quantity of reinforcement required.

NUMERICAL MODELLING

Site conditions

The site is located in a northern suburb of Shanghai, China (Liu et al (2007)). The soil profile is shown in fig 3. There is a 1.5m thick coarse grained fill of unit weight 20 kN/m³ overlying a 2.3m thick deposit of silty clay having a unit weight of 20kN/m³; this deposit overlies a 10.2m thick soft silty clay of unit weight 18 KN/m³. Underneath the soft silty clay, there is a 2m thick medium silty clay which is followed by 9m thick sandy silt. The ground water table is at a depth of 1.5m.

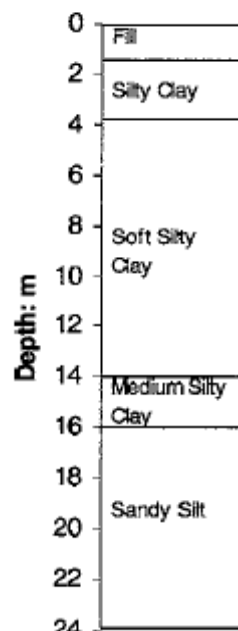


Fig 3. Soil profile(Liu et al (2007)) GRPS embankment

The embankment was 5.6 m high with side slope 1V: 1.5H. The fill material consisted of pulverized fuel ash with a cohesion value of 10 kPa and angle of internal

friction of 30° and an average unit weight of 18.5kN/m³. The embankment was supported by a cast in place concrete piles of diameter 1m and 16m length. The concrete piles were arranged in square pattern at a distance of 3m from the center to center of the adjacent piles. One layer of a biaxial polypropylene geogrid of thickness 1m was sandwiched between two 0.25m thick gravel layers to form a 0.5m thick composite reinforced bearing layer. The embankment was constructed in 9 layers to a height of 5.6m over a period of 55 days.

Modelling

The numerical analyses for an axisymmetric unit cell of the given piled embankment were performed by using a finite element software called ABAQUS. Numerical analyses had been done in 2D axisymmetric conditions. Fig 3 represents the finite element meshes for this 2D analysis. The pile was modelled as a linear isotropic elastic material with a Young's modulus of 20 GPa and a Poisson's ratio of 0.2. The embankment fill, gravel and the surface coarse grained fill were modeled in a drained manner using a linear elastic-perfectly plastic model with Mohr-Coulomb failure criterion. The parameters required for the Mohr-Coulomb model are effective cohesion, c' , friction angle, ϕ' , dilatancy angle, Ψ , effective Young's modulus, E , and Poisson's ratio, ν . The four foundation soils were modeled as modified cam clay materials. The modified cam clay model requires five material parameters for each type of soil- slope of virgin consolidation line, λ , slope of swelling line, κ , the void ratio at unit pressure, e_1 , slope of critical state line, M and Poisson's ratio, ν . The geogrid was modelled as an isotropic linear elastic material with a tensile stiffness of 1180 kN/m and a Poisson's ratio of 0.3. The element used for the pile was 20 noded quadratic brick with reduced integration elements without pore pressure whereas for foundation soils, 20 noded quadratic displacement, linear pore pressure and reduced integration elements were used. For geogrid, 8 noded biquadratic axisymmetric membrane elements were used. The finite element meshing done for the unit cell is given in fig 4.

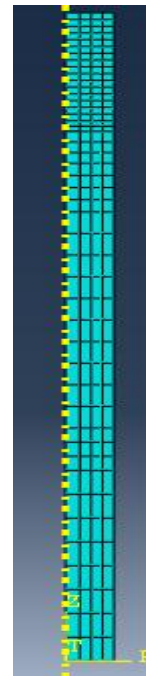


Fig 4. Finite element meshes for axisymmetric model

ANALYSIS OF RESULTS

Maximum settlement

The effect of height of embankment and elastic modulus of pile on the maximum settlement observed at an elevation is shown in fig 5 and fig 6. Fig 5 shows the maximum settlement computed from the numerical analysis results at the pile head elevation. From the graph, it is evident that the maximum settlement increases with the height of embankment fill. When the embankment height is small, the maximum settlement observed is less. As embankment height increases, settlement also increases.

The maximum settlement also depends on the elastic modulus of pile material. The variation of maximum settlement with the elastic modulus of pile at ground surface and pile head elevations is shown in fig 6. The increase of pile modulus can reduce the maximum settlements and the inclusion of geosynthetic can further enhance the reduction in settlements.

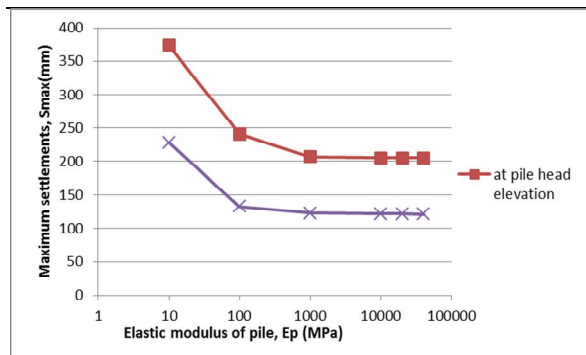


Fig 5. Influence of pile modulus on maximum settlements

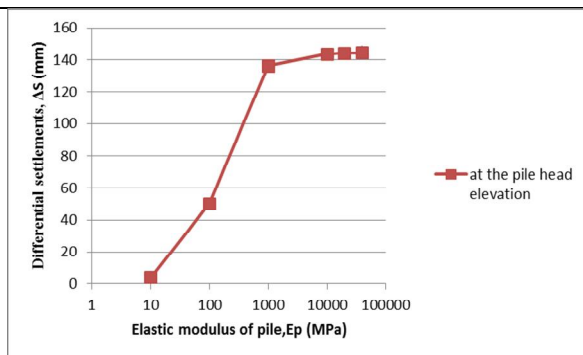


Fig 7. Influence of pile modulus on differential settlements

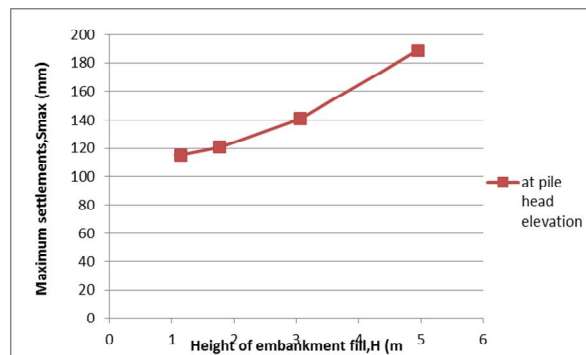


Fig 6. Influence of height of embankment fill on maximum settlements

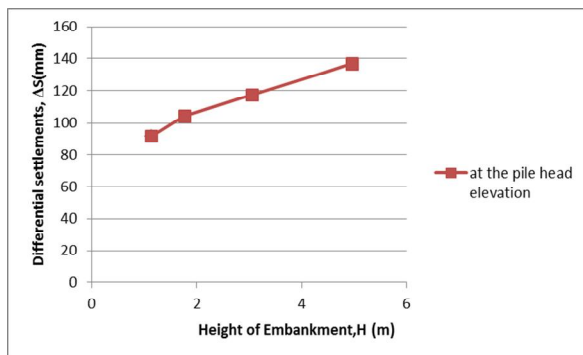


Fig 8. Influence of height of embankment on differential settlements

Differential settlement

In fig 7, the differential settlement at the pile head elevation, defined as the settlement difference between center of pile and midspan of the pile spacing, is computed. As the height of the embankment fill increases, the differential settlements at the elevation of the pile head also increase.

The variation of differential settlement at the pile head elevation with the pile elastic modulus is shown in fig 8. As the elastic modulus increases, differential settlement is also increased. This increasing trend is due to the modulus difference between the pile and soil materials. The differential settlement at the ground surface is almost zero, which is due to the development of soil arching above the pile heads.

CONCLUSIONS

The results of the numerical study has given the following conclusions

- The maximum settlement at the pile head elevation shows an increasing trend as height of the embankment increases
- The maximum settlement at both ground surface and pile head elevation decreases with increase in pile modulus of pile
- The differential settlement at the pile head elevation increases with increase in height of embankment.
- As the elastic modulus of pile increases, the differential settlement at the pile head elevation also increases.

6th International Engineering Symposium - IES 2017

March 1-3, 2017, Kumamoto University, Japan

REFERENCES

- [1] British Standard BS 8006-1 (2010).
*Code of Practice for Strengthened/
Reinforced Soils and Other Fills*, British
Standard Institution, London,
162.
- [2] Han, J., and Gabr, M. A. 2002.
"Numerical analysis of geosynthetic
reinforced and pile-supported earth
platforms over soft soil." *J. Geotech.
Geoenviron. Eng.*, 128(1), 44-53.
- [3] Hewlett, W. J., and Randolph, M. F.
(1988). "Analysis of piled embankments."
Ground Eng., 21(3), 12-18.
- [4] Liu, H. L., Charles, W. W. 2007.
"Performance of a geogrid- reinforced and
pile-supported highway embankment over
soft clay: Case Study." *J. Geotech.
Geoenviron. Eng.*, 133(12), 1483-1493.

SETTLEMENT BEHAVIOUR OF GEOCELL REINFORCED EMBANKMENTS SUPPORTED BY STONE COLUMNS

Vibhoosha M P¹, Anjana Bhasi² and Sitaram Nayak³

¹ Department of Civil Engineering, National Institute of Technology Karnataka, Surathkal, Mangalore 575025, India. email:vibhoosha@gmail.com

² Department of Civil Engineering, National Institute of Technology Karnataka, Surathkal, Mangalore 575025, India. email: anjanabhasi@yahoo.com

³ Department of Civil Engineering, National Institute of Technology Karnataka, Surathkal, Mangalore 575025, India. email: Snayak65@yahoo.co.in

ABSTRACT: Use of stone columns is an ideal technique for flexible structures such as embankments and storage tanks due to their higher strength and stiffness compared to the surrounding soft soil by means of which columns sustain larger proportion of the applied load. Moreover, being highly permeable, they also provide good drainage for pore water dissipation which accelerates the consolidation settlement in the clay soil.

The three dimensional polymeric geocells are the latest adaptation in the avenues of geosynthetic reinforcements. The reinforcement mechanism in the geocells is by all-round confinement of soil within its pockets. The individual application of both these techniques has been studied well. However, combined application of both stone column and geocell has remained least explored. This paper aims to study the settlement behaviour of geocell reinforced embankment supported by ordinary stone column as well as encased stone column - using Plaxis-2D with axisymmetric models.

Keywords: stone column, geocell, embankment, geosynthetic encasement, settlement

INTRODUCTION

Among various methods of ground improvement, stone column technique is considered as one of the most versatile and cost effective method mainly because of its higher permeability and material stiffness which helps in bearing capacity improvement and settlement reduction in soft soils. This ground improvement technique has been successfully applied for foundation of structures like liquid storage tanks, earthen embankments, raft foundations, etc., where a relatively large settlement can be tolerated by the structure.

In order to improve the performance of the stone columns when treating weak deposits, it is imperative that the tendency of the columns to bulge should be resisted or prevented effectively. Such a condition can be achieved through encasement of stone columns through geosynthetics over the full or partial height of the column

Raihel et al. (2002), Alexiew et al. (2005).

The latest technique to improve the stability of embankments is the use of three dimensional cellular forms of geosynthetic materials known as Geocells. Geocell membrane increases the load carrying capacity of soil by means of three dimensional confinements. Manish Yadav et al. studied about various applications of geocell in reinforcement soil. They concluded that the use of geocell is suitable from the stability as well economical point of view. The lateral restraint offered by the geocell material that prevents the material from spreading and hence reduces the stresses coming onto the soft sub grade. Use of geocell mattress over the soft soil can reduce the settlement and increase the load carrying capacity Zang et al. (2010).

Use of geocell mattress over the soft soil can reduce the settlement and increase

6th International Engineering Symposium - IES 2017

March 1-3, 2017, Kumamoto University, Japan

the load carrying capacity Zhang et al. (2010).

Geocell act as rigid mattress and it distribute the applied load over larger area due to which pressure intensity on the soft soil decreases Dash et al. (2007).

Numerical simulations of the geocells are not so easy due to its complex 3D honeycomb structure. Generally, the equivalent composite approach is used to model the geocells and in which the geocell-soil composite is treated as the soil layer with improved strength and stiffness values.

In this paper, a trial is made to analyze settlement of embankments constructed on clayey soils reinforced with stone columns and geocell using Plaxis 2D software.

LITERATURE REVIEW

Analytical methods for estimating the settlement of stone column treated ground generally assume an infinitely wide loaded area reinforced with stone columns having a constant diameter and spacing. For this condition of loading and geometry, the unit cell concept by Barron (1948) is theoretically valid and has been used by many authors to develop theoretical solutions for predicting the settlements.

Ambily and Gandhi (2006) determined the actual stress intensity on the stone column and soil using Finite Element Analysis (PLAXIS). Sand pad is provided at the surface for drainage and the effect of sand pad thickness on load sharing between column and soil is studied by the analysis for both flexible and rigid loading condition.

Murugesan and Rajagopal (2010) performed tests on the qualitative and quantitative improvement of individual load carrying capacity of encased stone column. Load tests are performed on single and group of stone columns with and without encasement. It is found that load carrying capacity of the stone column increases due to encasement. The increase in load capacity depends on the modulus of encasement and the diameter of the stone column.

Rong-Her Chen studied about the confinement effect of geocells under triaxial compression. They found out that the apparent cohesion of reinforced

samples vary with the shape, size and number of cells, of which the cell size is the most significant factor. Among the cells of all shapes, the circular cells induce the highest apparent cohesion. In addition, the effectiveness of the reinforcement is more significant at low confining pressure. From model tests on laboratory, [14, 29] Sitharam T.G et al. (2013) found that the Geocells increased the load carrying capacity and reduced the settlement significantly.

NUMERICAL ANALYSES

All the analyses were performed using the finite element software PLAXIS 2D 2015 version. Stone column is modelled as Mohr-Coulomb material; surrounding soil as Soft Soil model, encasement as linear elastic continuum and equivalent composite approach is used to model the geocells.

The finite element model of an ordinary stone column is simulated as an axisymmetric model based on unit cell idealization where only half of the stone column and the surrounding influence area are modelled with radial symmetry around the vertical axis passing through the centre of the stone column. A 15 node triangular element is used to generate the FE mesh. A single end bearing stone column of 0.8m diameter and 10m length is assumed to be installed in square pattern with a centre to centre spacing of $2d$, where d is the diameter of the stone column. The thickness of the soft clay used is 10m.

A 1 m thick sand mat for column drainage is placed over that a layer of geocells laid prior to embankment fill. The 6m embankment construction is assumed to be undertaken in 2 m stages, each of which is constructed in 20 days and consolidated for further 30 days before application of the following stage.

The finite element model for GESC is generated in a similar way to that of OSC except that a geogrid element is introduced at the soil-column interfaces and modelled as a linear elastic material.

The material models used for different soil layers and their properties adopted from are given in Table 1. The water table is set at the top surface of the soft soil. Installation effects are not considered.

6th International Engineering Symposium - IES 2017

March 1-3, 2017, Kumamoto University, Japan

RESULTS AND DISCUSSIONS

Finite element models used in Plaxis were shown in Fig 1 and Fig 2. From the consolidation analysis the settlements were calculated in each time interval. Fig. 3 represents the comparison of the settlement-time curves for different cases, (a) Ordinary Stone column (b) Encased Stone column (c) Stone column with Geocell (d) Encased Stone column with geocell.

The permeable geocell enhances consolidation and required settlement can be achieved faster. Thus in case of encased stone column with geocell the embankment settles faster. Also the tensile strength of the geocell is mostly responsible for imparting the strength to the embankment.

From the Numerical study it can be proved that a layer of geocells at the interface of the encased stone column and embankment fastens settlement by 45% during construction period.

CONCLUSIONS

The following conclusions are deduced from this study:

- Improvement of the soft clay with stone columns and geocell leads to significant effect in the behaviour of the soft clay.

- Geosynthetic encased stone column along with geocell can be effectively used for the construction of embankment since it reduces consolidation time of clay beneath the embankment.
- 45% increment in settlement can be achieved by geocell reinforced encased stone column supported embankments during construction time.

REFERENCES

- [1] Ambily, A.P., and S.R.Gandhi (2007) Behaviour of stone columns based on experimental and FEM analysis. *Journal of Geotechnical and Geo environmental Engineering*, ASCE, 133 (4), 405-515.
- [2] Manish Yadav, Arvind Kumar Agnihotri, Akash Priyadarshee, Gaurav Dhane (2014) *Journal of Civil Engineering and Environmental Technology* Print ISSN: 2349-8404; Online ISSN: 2349-879X; Volume 1, Number 5; August, 2014 pp. 60 – 64
- [3] Thakur, J.K., Han, Jie., Pokharel, S.K., and Parsons, R.L.(2012) Performance of geocell reinforced recycled asphalt pavement (RAP) bases over weak subgrade under cyclic plate loading. *Geotextiles and Geomembranes*. 35, 14-24
- [4] Sitharam, T.G and A. Hegde (2013) Design and construction of geocell foundation to support the embankment on settled red mud. *Geotextiles and Geomembranes*, 41 pp, 55-63.
- [5] S. Murugesan, K. Rajagopal (2006) Geosynthetic-encased stone columns: Numerical evaluation. *Geotextiles and Geomembranes*, 24, 349–358
- [6] Yoo, C. (2010) Performance of geosynthetic-encased stone columns in embankment construction: Numerical investigation. *Journal of Geotechnical and Geoenvironmental Engineering*, 136(8), 1148-1160.

Table 1: Constitutive Model Parameters used

Parameter	Notation	Clay	Stone column	Sand	Unit
Material model		Soft Soil	Mohr-Coulomb	Mohr-Coulomb	
Type of material behaviour		Undrained	Drained	Drained	
Soil unit weight above phreatic level	γ_{unsat}	16	22	17	kN/m ³
Soil unit weight below phreatic level	γ_{sat}	17	23	18	kN/m ³
Permeability in ver. Direction	K_v	2.3×10^{-9}	1.2×10^{-4}	1.2×10^{-5}	m/s
Young's modulus	E_{ref}	-	40000	2000	kN/m ²
Poisson's ratio	ν	0.3	0.3	0.3	-
Cohesion	C_{ref}	5	4	3	kN/m ²
Friction angle	ϕ	24	40	28	°
Dialtancy angle	ψ	0	10	10	°

Table 2: Properties of Geocell

Parameter	Quantity
Geocell	
Polymer	
Cell Size (mm)	250 x 210
No of cells/m ²	40
Cell Depth (mm)	150
Strip thickness (mm)	1.53
Cell Seam Strength (N)	2150
Density (g/cm ³)	0.95

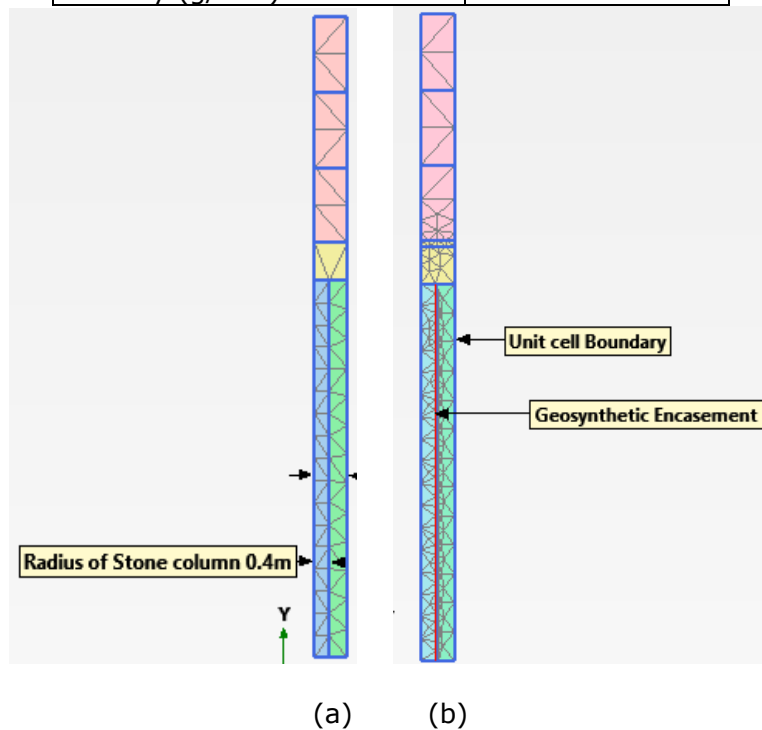


Fig 1: Finite-element discretization of embankment reinforced by (a) Stone column alone (b) Encased Stone column and Geocell

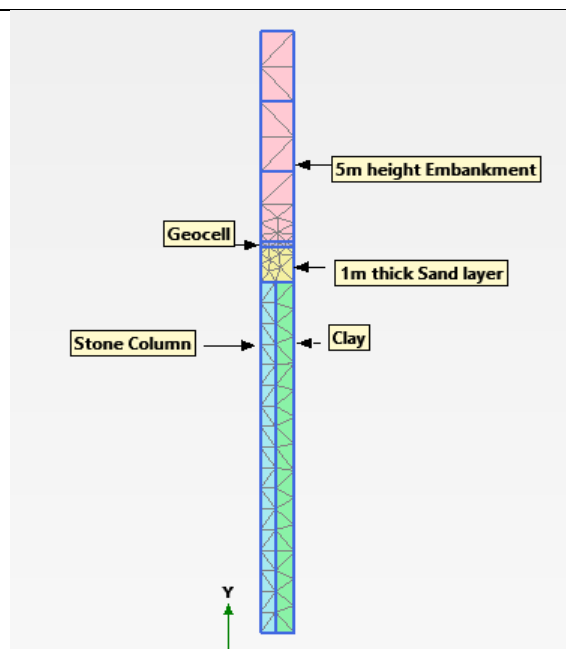


Fig 2: Finite-element discretization of embankment reinforced by stone column and geocell

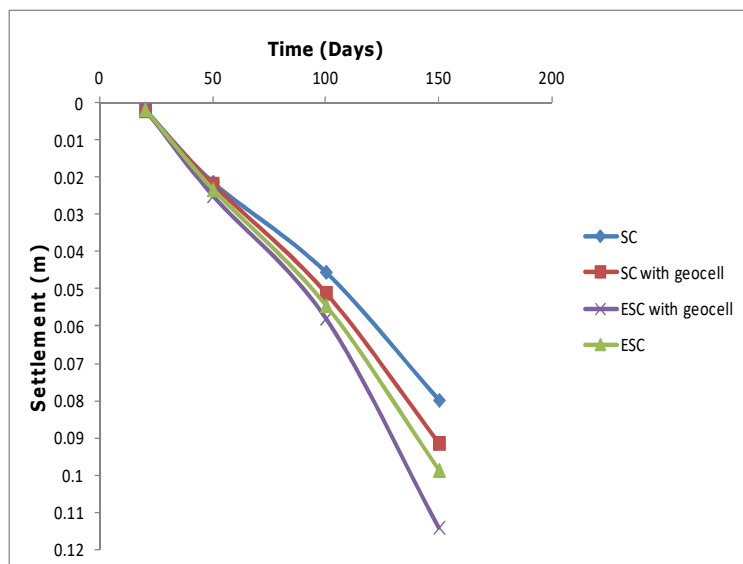


Fig 3: Time Settlement Graph for different cases

ANALYSIS OF STRESSES AROUND A TUNNEL OPENING

Ragini Nikumbh¹ and **K. Ram Chandar²**

¹ Department of Civil Engineering, National Institute of Technology Karnataka, Surathkal, Mangalore 575025, India. Email: ragininikumbh@gmail.com

² Department of Mining Engineering, National Institute of Technology Karnataka, Surathkal, Mangalore 575025, India. Email: krc_karra@yahoo.com

ABSTRACT: Tunnels are underground passages used for a variety of purposes i.e., to carry traffic, water, power cables, sewage, gas etc. During excavation, a tunnel passes through various types of rocks and soils. The most important aspects of tunnel construction are, the factor of safety and the cost of tunnelling, these are primarily related to geological features of the excavated area, progress of tunnelling work, safety factors and type of tunnel construction. Thus, it's important to identify and assess the stability of the tunnel of a given size in the proposed working conditions well in advance to the commencement of the tunnelling operation. Hence, Simulation of tunnels for studying the stresses around the opening is significant. By carrying out such studies, it is possible to predict the stress on the tunnel and therefore support requirements can be made effectively.

An attempt has been made in this paper to analyse the stress distribution around tunnel openings of diameter of 6m. Further analysis is carried out to assess the influence of tunnel on the surrounding slope. The distance between the tunnel and slope is maintained at 4m with slope angle of 70° and the berm width is varied from 5m to 8m at an interval of 1m. Thus, it has been observed that maximum displacement and maximum stress occurs on the rock mass between the tunnel and slope for a berm width of 6m.

Keywords: Tunnel, Stress distribution, ANSYS, Displacement

INTRODUCTION

A tunnel is a long, narrow, essentially an underground opening, the length of which greatly exceeds its width or height (Walhstrom, 1973). Tunneling is increasingly been seen as an environmentally preferable means of providing infrastructure such as transportation and utilities to densely populated urban areas. It is often cost effective as an alternative to over-ground solutions, when the risk and cost of disruption during construction is taken into account. During excavation, a tunnel passes through various types of rock and soils. Depending upon the type of strata encountered, the condition of tunnel may vary from self-sustaining to highly weak, requiring special drilling technique and intensive support system. The most

important aspects of tunnel construction are the Factor of Safety (FOS) and the cost of tunneling. There is an increasing need for realistic calculations of stability of the tunnel of a given size in proposed working condition. The fundamental requirement for the design of a stable tunnel is the determination of distribution of stresses around it. The design problem often gets complicated when tunnels are driven at a considerable depth or shallow depth or when wide tunnels re-driven, for example in mining operations and power projects. The problem of designing an opening in rock is more difficult as the rock may fail less than one set of conditions as a brittle material by fracturing and under another set of conditions by deforming excessively. The closed form solutions are of limited value in calculating the stresses, displacements and failure of the rock mass

6th International Engineering Symposium - IES 2017

March 1-3, 2017, Kumamoto University, Japan

surrounding underground excavations. A number of numerical methods which are computer-based have been developed over the past few decades and these methods are used for obtaining approximate solutions to these problems. The powerful capacity of numerical methods of stress analysis allows the possibility of simulating stress condition around a tunnel opening.

NUMERICAL MODELLING

Numerical modeling is extensively used in mining to predict stresses in various difficult conditions. Of the existing numerical methods, followings are used most frequently:

- Boundary Element Method
- Finite Difference Method
- Finite Element Method

Finite Element Method (FEM)

The basis of FEM is discretization of the object under analysis into a number of elements of finite size. Finite element analysis is a reliable tool which can help in assessing expected stress distribution around the tunnel opening. This method is highly computer dependent and development of high speed and large memory computers have encouraged the extensive use of FEM. With an approximate idea of the strata behavior provided by the FEM we can choose the design parameters of the tunnel like size, supports, depth best suited for the given geological conditions. Different softwares are available like NISA, ANSYS, etc.

ANSYS

ANSYS is a finite element design and analysis software that helps a user to model problems in structures, thermal or fluid flow and electromagnetics. ANSYS includes a graphical user interface based on pre-processor and post-processor with modeling, simulation, and results evaluation capabilities. It is important to remember that ANSYS does not assume a system of units for intended analysis. The amount of Details required will depend on the dimensionality of the analysis type (1D, 2D, axi-symmetric, 3D).

MODEL GENERATION

The ultimate purpose of the finite element analysis is to re-create mathematically the behaviour of an actual engineering system. The model comprises of all the nodes, elements, material properties, constants, boundary conditions and other features that are used to represent the physical system. Thus, model generation means the process of defining the material properties i.e. Soil/Rock properties and the geometry configuration of the models nodes and elements.

CASE STUDY

In order to assess the stability of a tunnel alongside a slope a systematic approach is used using numerical modelling. Modelling has been carried out for a tunnel diameter of 6m, while, the berm width is varied from 5m, 6m, 7m and 8m. Also, the bottom end is kept fixed while the sides and faces are provided with roller support.

Soil/Rock properties of model

In the given numerical model, concentration has been given on adopting elastic and non-linear properties to study various static and live loads only. The properties such as young's modulus, Poisson's ratio and density, for the different layers of the soil along with their depths are tabulated as shown in Fig.1 and Table 1 below. A model is created in ANSYS as shown in Fig.1 with the soil properties mentioned in the Table.1. (Sarika K , 2013).

STATIC ANALYSIS MODEL

In general, a finite element solution may be broken into the following three stages:

- Pre-processing: Defining the problem
- Solution: Assigning loads, constraints and solving.
- Post-processing: Further processing and viewing of the results.

The major steps involved in pre-processing are defining key points/lines/areas/volumes, element type and material/geometric properties, followed by meshing of lines/areas/volumes as required. In areas of significance the mesh refinement can be made much finer, so that better results can be achieved.

6th International Engineering Symposium - IES 2017

March 1-3, 2017, Kumamoto University, Japan

In this model we have incorporated the basic Drucker-Prager model to incorporate the values of cohesion, angle of friction and dilatancy angle.

The basic Drucker-Prager material model has the following features:

- Available for LINK1, LINK8, PIPE20, BEAM23, BEAM24, PLANE42, SHELL43, SOLID45, PIPE60, SOLID62, SOLID65, PLANE82, SHELL91, SOLID92, SHELL93, SOLID95
- Assumes perfectly plastic behavior (no strain hardening)
- It is used for pressure-dependent inelastic behaviour of materials such as soils, rock, concrete, and powder.

For the given model, the Element considered is SOLID 65. Gravity (9.81m/s^2) is applied globally on the model, while 0.8MPa of pressure is applied on the berm width which is because of the live load of the moving vehicles coming on the highway. The stresses induced due to such pressures are prominent and its consideration becomes vital in analysing the tunnel system.

In the post processing stage the lists of nodal displacements, element forces and moments, deflection plots and stress contour diagrams are obtained.

RESULTS

The values for the displacement, maximum stress and minimum stress are tabulated in Table 2.

- A maximum displacement of 0.80mm takes place in the Y-direction, a maximum stress of 622.01N/m^2 is observed in the Y-direction and a minimum stress of -83.60 N/m^2 is observed in the Z-direction for a berm width of 5m.
- A maximum displacement of 1.42mm takes place in the Y-direction as shown in Fig.4, a maximum stress of 367.52 N/m^2 is observed in the Y-direction as shown in Fig.5 and a minimum stress of -456.02 N/m^2 is observed in the Z-direction as shown in Fig.3 for a berm width of 6m. Fig.2 shows a displacement of 0.39mm in X-direction, Fig.6 shows a displacement of 0.03mm in Z-direction which is negligible and

Fig.7 shows maximum stress of 308.73N/m^2 and a minimum stress of -456.02N/m^2 in X-direction for a berm width of 6m.

- A maximum displacement of 0.728mm takes place in the Y-direction, maximum stress of 639.80N/m^2 is observed in the Y-direction and a minimum stress of -370.54N/m^2 is observed in the X-direction for a berm width of 7m.
- A maximum displacement of 0.66mm takes place in the Y-direction, maximum stress of 650.03N/m^2 is observed in the Y-direction and a minimum stress of -73.749N/m^2 is observed in the Z direction for a berm width of 8m.

Thus, it is observed that the maximum displacement observed is 1.42mm which is for a berm width of 6m. For the maximum stress in Y direction the minimum value of 367.52N/m^2 is observed for a berm width of 6m. Also, for the minimum stress in X direction the maximum value of -467.02N/m^2 is observed for a berm width of 6m.

Fig. 8 shows the graph between displacement and distance between tunnel and slope for the berm width of 5m, 6m, 7m and 8m. Fig.9 shows the graph between stress and distance between tunnel and slope for the berm width of 5m, 6m, 7m and 8m.

CONCLUSIONS

ANSYS provides simple as well as sophisticated Drucker-Prager models to suit different users' needs. The *ANSYS Theory Reference* is the best source to understand the assumptions related to each Drucker-Prager variant.

The following conclusions are deduced from this study:

- The maximum displacement observed is 1.42mm which is for a berm width of 6m.
- For the maximum stress in Y direction the minimum value of 367.52N/m^2 is observed for a berm width of 6m.
- Also, for the minimum stress in X direction the maximum value of -

6th International Engineering Symposium - IES 2017

March 1-3, 2017, Kumamoto University, Japan

467.02N/m² is observed for a berm width of 6m

Thus it can be concluded that the berm width of 6m is the critical berm width with maximum displacement and maximum stress occurring over it.

REFERENCES

- [1] Classic Drucker Prager Model (2013), ANSYS Mechanical APDL Material Reference, Release 15.0, Drive Canonsburg, PA, Page no. 47.
- [2] Classic Drucker Prager Model (2013), ANSYS Mechanical APDL Theory Reference, Release 15.0, Drive Canonsburg, PA, Page no. 87.
- [3] G. G. Boldyrev and A. J. Muyzemnek (2008), The Modeling of Deformation Process in Soils With Use of Ansys and Ls-Dyna Programs, International Conference on Case Histories in Geotechnical Engineering. Paper 37.
- [4]https://www.researchgate.net/post/What_is_the_best_element_for_modeling_soil_in_finite_element_analysis_software_ANSYS
- [5] Lakshmi Sreedharan M. (2013), Prediction and Assessment of Surface and Sub-Surface Settlement due to Tunneling, M.Tech Thesis, NITK, Surathkal.
- [6] Sarika K (2013), Numerical Predictions Of Vibrations Generated By The Passage Of Metro Trains In Underground Tunnels, M.Tech Thesis, NITK, Surathkal.
- [7] Sheldon Imaoka, Sheldon's ANSYS.NET Tips and Tricks: Drucker-Prager Model (2008), Memo Number STI:08/02
- [8] Shubhajit Saha, Manjunath B. Reddy (2007), Analysis of Stresses around Tunnel openings at Shallow Depth, M.Tech Thesis, NITK, Surathkal.
- [9] Raghavendra V, Stanley Jose, G.H Arjun Shounak, Dr. T.G Sitharam (2015), Finite Element Analysis Of Underground Metro Tunnels, International Journal of Civil Engineering and Technology (IJCIET), ISSN 0976 – 6308 (Print),ISSN 0976 – 6316(Online), Volume 6, Issue 2, pp. 06-15 © IAEME.

**Table 1 Soil profile of supervising training center of Bangalore metro tunnel
(Sarika K, 2013)**

Layers and its depth (m)	γ_{UNSAT} (kg/m ³)	γ_{SAT} (kg/m ³)	Young's Modulus (N/m ²)	Poisson's Ratio	Cohesion (N/m ²)	Angle of Friction (deg)	Dilatancy Angle (deg)
Clayey Silt (0-3m)	15	19	5e+6	0.35	1e+3	40	10
Silty Sand (3-8m)	16	21	7e+6	0.30	1e+3	37	15
Highly Weathered Rock (8-11.50m)	0	24	3e+7	0.35	2e+6	50	0
Hard Rock (11.50m onwards)	27	27	7e+7	0.35	0	0	0

Table 2 Results of ANSYS Model

Distance between Tunnel and Slope	5 m	6 m	7 m	8 m
Displacement in X Direction(mm)	0.26	0.39	0.23	0.23
Displacement in Y Direction(mm)	0.80	1.42	0.73	0.66
Displacement in Z Direction(mm)	-0.01	0.025	0.06	0.02
Maximum stress in X Direction (N/m ²)	263.61	172.02	295.23	317.68
Maximum stress in Y Direction (N/m ²)	622.01	367.52	639.80	650.03
Maximum stress in Z Direction (N/m ²)	427.02	308.73	369.98	428.76
Minimum stress in X Direction (N/m ²)	-79.29	-456.02	-370.54	-63.62
Minimum stress in Y Direction (N/m ²)	-42.49	-128.68	-90.29	-36.71
Minimum stress in Z Direction (N/m ²)	-83.60	-177.78	-176.97	-73.75

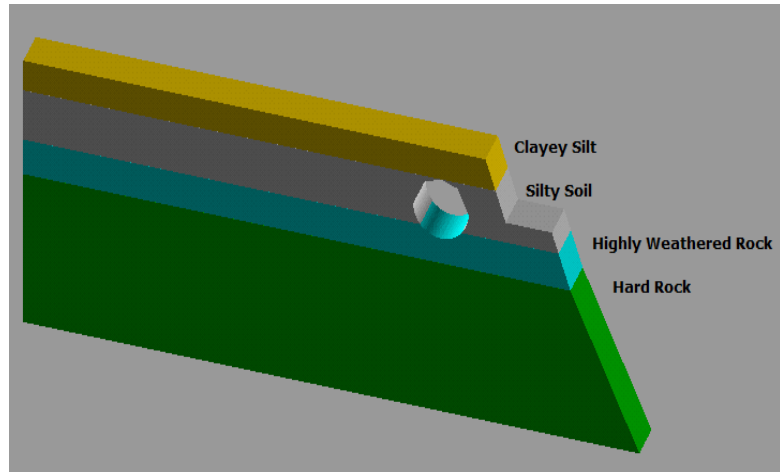
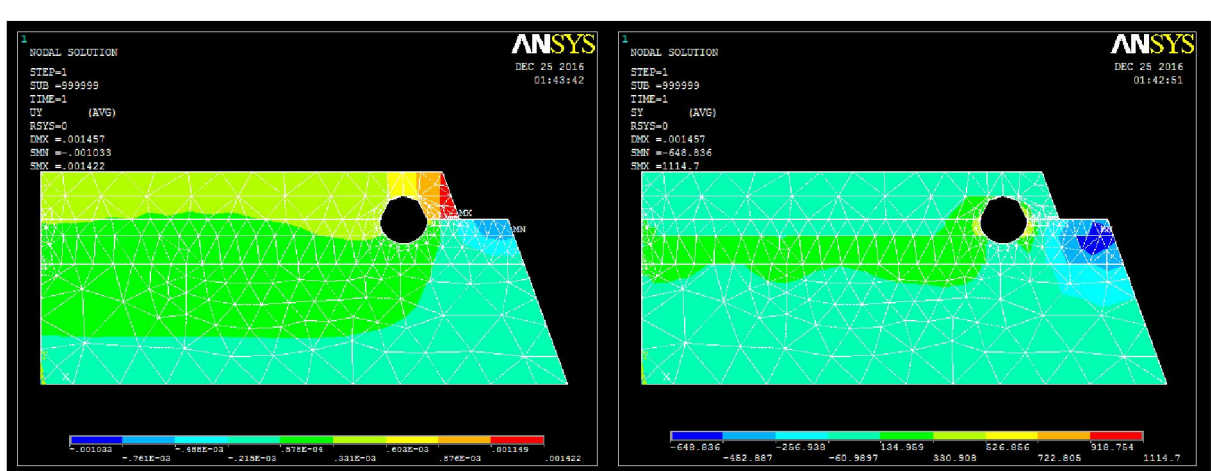
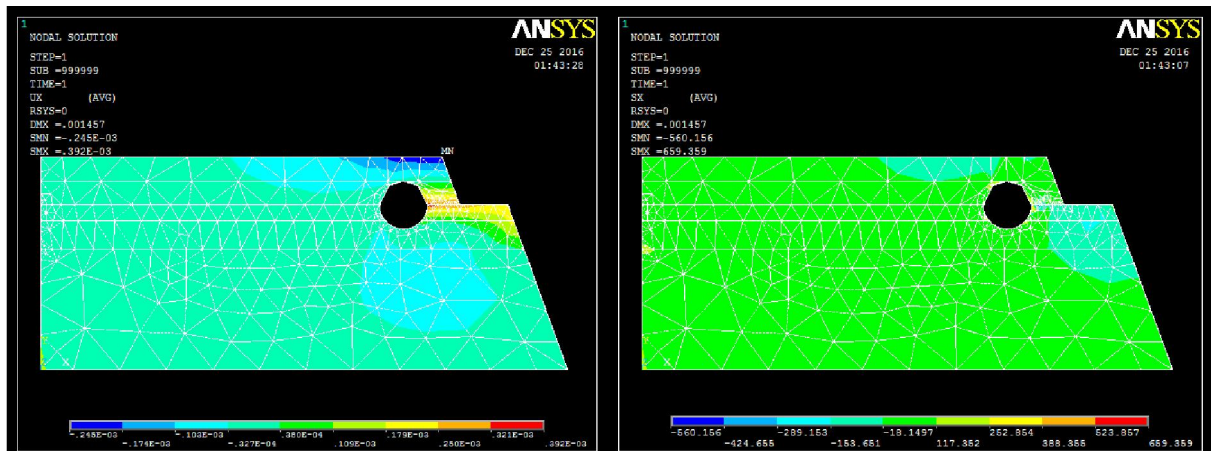


Fig.1 Model indicating material layers



6th International Engineering Symposium - IES 2017

March 1-3, 2017, Kumamoto University, Japan

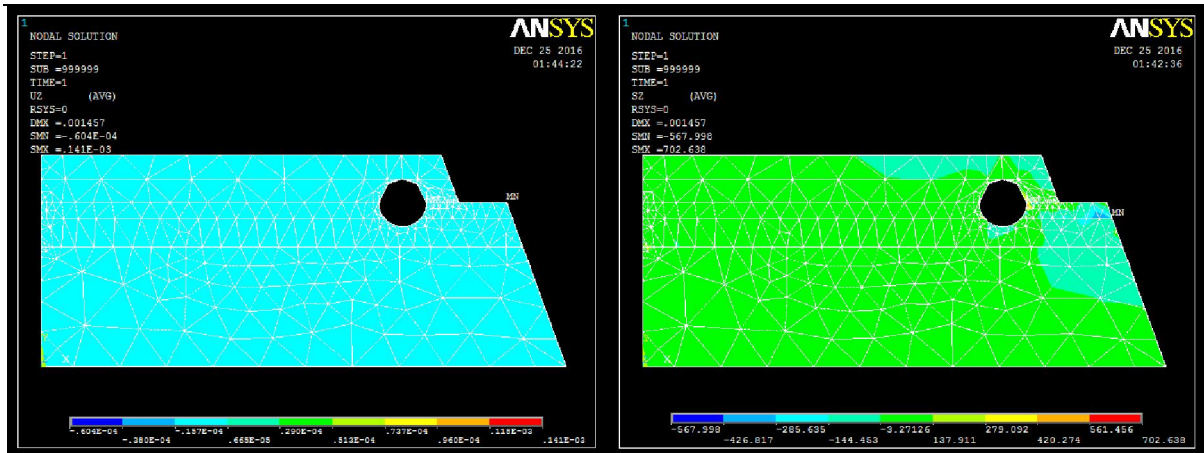


Fig.6 Displacement in Z direction for a berm width of 6m.

Fig.7 Stress in Z direction for a berm width of 6m.

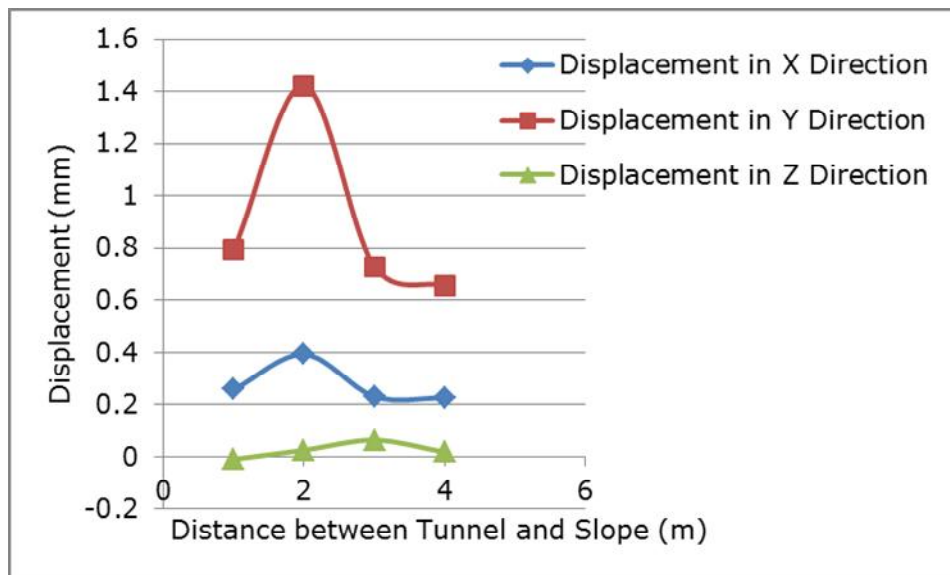


Fig.7 Graph of displacement v/s distance between the tunnel and slope

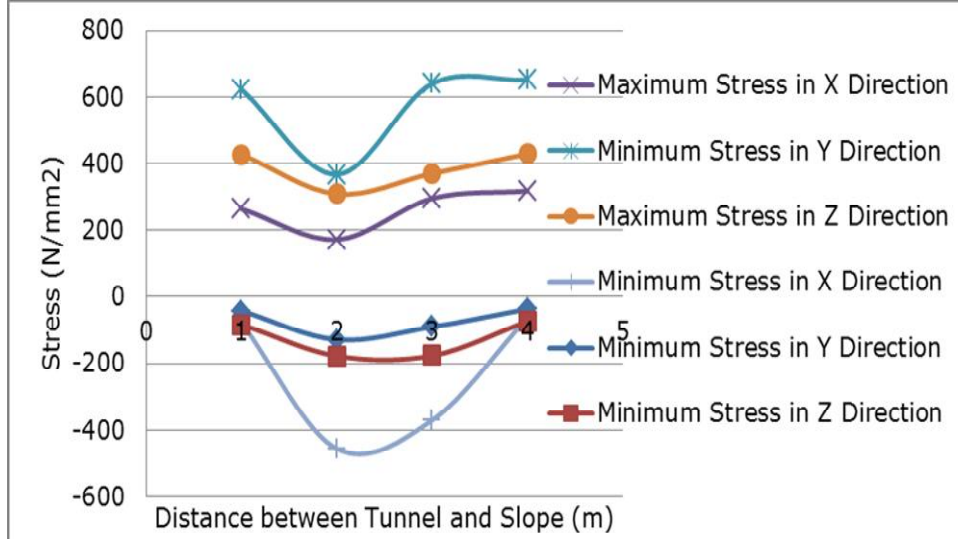


Fig.8 Graph of stress variation with distance between the tunnel and slope

STUDY OF INTERFERENCE OF STRIP FOOTING ON CLAY

Amrita¹ and R Shivashankar²

¹ Department of Civil Engineering, National Institute of Technology Karnataka, Surathkal, Mangalore 575025, India. email:23amritar@gmail.com

² Department of Civil Engineering, National Institute of Technology Karnataka, Surathkal, Mangalore 575025, India. email: shivashankar.surathkal@gmail.com

ABSTRACT: In the present study, the interference of two strip footings is investigated. The footing resting on soft clay and very soft clay is considered. In this study the effect of interference on the behaviour of footings which occurs when two rigid strip footings are placed at various distances from each other has been studied using Plaxis 2D. The perfectly rough strip footings are considered to be resting on the surface of clay layer, and the soil is assumed to behave as linear elastic material under the foundation load. The effect of clear spacing between the footings has been determined. Results obtained from analysis indicate that settlement decreases as the spacing between the increases.

Keywords: interference, strip footing, finite element method

INTRODUCTION

Foundations are important components of the structure which are basically designed based on two criterion namely Bearing Capacity and Settlement criterion. In general as per the Terzaghi (1943), when an isolated shallow foundation is loaded, the stress or the failure zone in the foundation soil extends in horizontal direction on either side of the footing to about twice the width of the footing and in vertical downward direction to about three times the width of the footing. Unless until the stress or failure zone of individual footings do not interfere, the individual footings behave as an isolated footing. However, in many situations such as lack of construction space, the foundations or group of foundations may be placed close to each other. In such cases the stress isobars or the failure zone of closely spaced isolated footings may interfere with each other leading to the phenomenon called Interference. Owing to the phenomenon of footing interference, the failure mechanism, load-settlement, bearing capacity, settlement, rotational characteristics etc. of an isolated footing may be altered. The presence of clayey

soil deposits in the construction site adds further uncertainty to this problem because there is no consensus among the researchers regarding interfering footing behaviour on clay. Therefore, the study of interference of closely spaced footings is one of the significant practical importances.

METHODOLOGY AND MODELING

The finite element program Plaxis software package was used to model strip interfering footings on soft clay and very soft clay. In analyses conducted in the present study, we assume that footings are located on the ground surface, and the soil is cohesive and dry. In general, the initial conditions comprise the initial ground water conditions, the initial geometry configuration, and the initial effective stress state. The soft clay in this study was dry, so there was no need to enter ground water condition.

The problem is modeled in PLAXIS-2D as plane strain problem since the length of the footing is more compared to its width. The 15 noded triangular plane strain elements were used to model the soil with elastic behaviour. The Mohr- Coulomb failure criteria which is an elastic, perfectly

6th International Engineering Symposium - IES 2017

March 1-3, 2017, Kumamoto University, Japan

plastic model was selected for its simplicity, practical importance and the availability of the parameters needed.

The concrete footings were modeled using plate elements with linear elastic behaviour. Footing is modeled as rough footing having width $B=1\text{m}$ laid at the surface. Clear spacing between two interacting footings is represented as S .

The 2D soil model geometry of 30 m width and 15m depth is adopted. Soil model is fixed at the bottom and roller supported at the side boundaries and uniformly distributed load was applied on the strip footing.

Load settlement behaviour of two strip footings, loaded simultaneously and spaced at S/B ratio of 0.5 to 5.0 are analyzed. The load 80kN/m^2 and 160kN/m^2 are applied on the two footings and deformations are noted.

The properties soil medium and footing characteristics are enumerated in Table 1, Table 2 and Table 3. Typical soil model with deformed mesh and the vertical displacement contours are shown in Fig.1 and Fig. 2 respectively.

RESULTS AND DISCUSSIONS

Typical soil model with deformed mesh and the vertical displacement contours are shown in Fig.1 and Fig. 2 respectively.

The variation of settlement with depth is also represented in Fig.3, Fig.4, Fig.5, Fig.6 and Fig.7

It can be inferred that for footings on soft clays the interference is observed upto S/B=2 beyond which the interference of the nearby strip footing is negligible. The settlement reduces as the spacing between the footing increases.

CONCLUSIONS

In the present study, a numerical finite difference analysis is performed to determine the settlement characteristics of two rough strip footings which are placed at different spacing on very soft and soft clay layer. And the following conclusions can be inferred:

- The proximity of footings founded on clay enhances the responses of foundations in terms of settlement.
- The settlement of closely spaced footings reduces continuously as the spacing between the footings increases.
- The interference effect is negligible when the spacing between the footings is greater than five times the footings size.

REFERENCES

- [1] Ghosh P and Pawan Kumar,(2009) "Interference effect of two nearby strip footings on reinforced sand". Contemporary Engineering Sciences, Vol. 2, no. 12, 577 – 592.
- [2] Khalida Daud (2012), "Interference of shallow multiple strip footings on sand". The iraqi journal for mechanical and material engineering, vol.12, no.3, 2012.
- [3] Priyanka Ghosh and Anirudh Sharma(2010),"Interference effect of two nearby strip footings on layered soil: theory of elasticity approach" Acta Geotechnica (2010) 5:189–198
- [4] Dr. V. G. Mutualik Desai, Vidyasagar .V. Moogi,(2016)" Study of Interference of Strip Footing using PLAXIS-2D" International Advanced Research Journal in Science, Engineering and Technology Vol. 3, Issue 9, September 2016.
- [5] Reza Noorzad & Ebrahim Manavirad,(2014)" Bearing capacity of two close strip footings on soft clay reinforced with geotextile" Arab J Geosci (2014) 7:623–639.
- [6] Plaxis-2D Tutorial manual.

Table 1 Material properties of very soft clay

PARAMETER	VALUE
Material model	Mohr Coulomb
Material type	Drained
Unsaturated unit weight(kN/m^3)	16
Saturated unit weight(kN/m^3)	19
Young's modulus(E) in kN/m^2	2000
Poisson's ratio(μ)	0.4
Cohesion(C) in kN/m^2	100
Angle of internal friction(ϕ)	10

6th International Engineering Symposium - IES 2017

March 1-3, 2017, Kumamoto University, Japan

Table 2 Material properties of soft clay

PARAMETER	VALUE
Material model	Mohr Coulomb
Material type	Drained
Unsaturated unit weight(kN/m ³)	16
Saturated unit weight(kN/m ³)	19
Young's modulus(E) in kN/m ²	25000
Poisson's ratio(μ)	0.4
Cohesion(C) in kN/m ²	300
Angle of internal friction(ϕ)	15

Table 3 Characteristics of footing

PARAMETER	VALUE
Width of footing (B) in mm	1000
Axial stiffness (EA) in kN/m	18.75×10^6
Flexural stiffness (EI) in kN/m ² -m	878.9×10^3
Equivalent thickness of plate (d) in mm	75
Weight of footing (w) in kN/m/m	18.75
Poisson's ratio(μ)	0.2

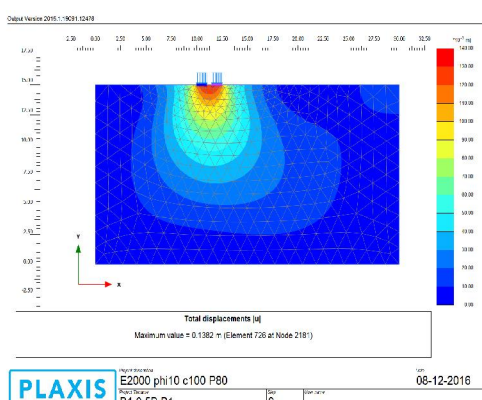


Fig.1 Vertical displacement under the load

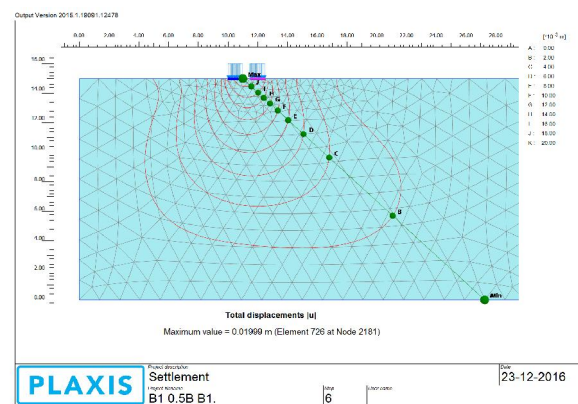


Fig.2 Vertical displacement contour

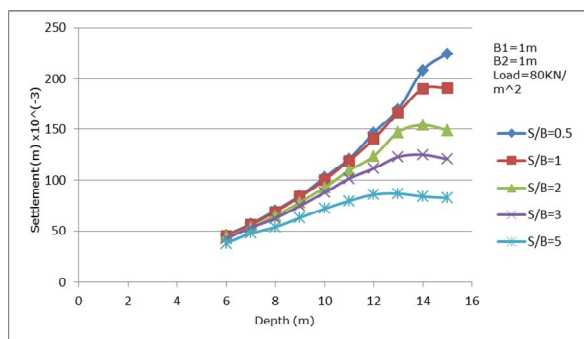


Fig.3 Variation of settlement with distance in very soft clay

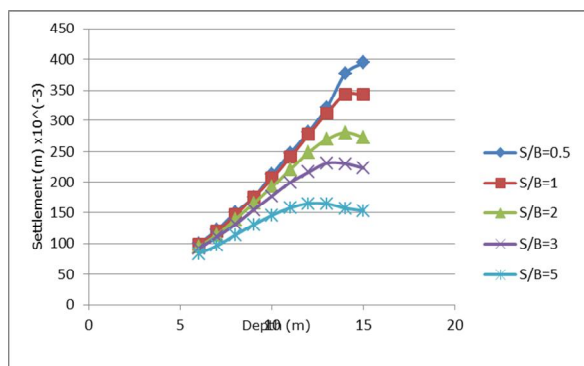


Fig.4 Variation of settlement with distance in very soft clay

6th International Engineering Symposium - IES 2017
March 1-3, 2017, Kumamoto University, Japan

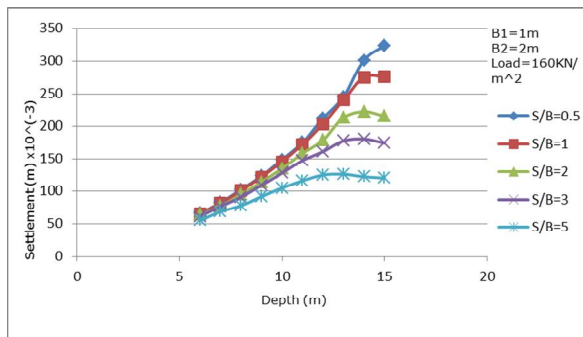


Fig.5 Variation of settlement with distance in soft clay

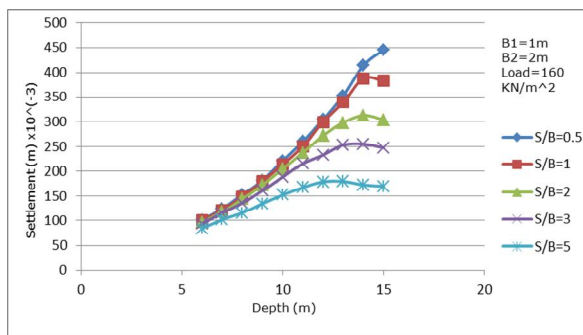


Fig.6 Variation of settlement with distance in soft clay

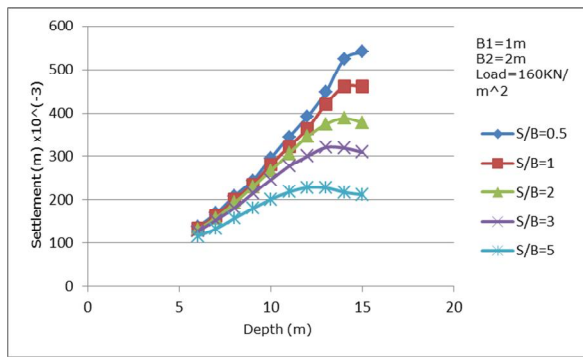


Fig.7 Variation of settlement with distance in soft clay

A Review on Probabilistic Methods in Seismic Hazard Analysis

Shreyasvi C ¹, Katta Venkataramana ²

¹ Department of Civil Engineering, National Institute of Technology Karnataka, Surathkal, Mangalore 575025, India. email:shreyasvic@gmail.com

² Department of Civil Engineering, National Institute of Technology Karnataka, Surathkal, Mangalore 575025, India.
e-mail:ven.nitk@gmail.com

ABSTRACT: Probabilistic Seismic Hazard Analysis (PSHA) considers uncertainty in magnitude, location and recurrence rate of earthquakes with respect to the existing geological conditions at the chosen site of interest. These uncertainties are explicitly considered and evaluated for quantification in a step by step manner and combined together to obtain the final output. The output of PSHA is expressed in terms of hazard curve, which is a plot of probability of exceedance of a selected ground motion parameter during a specified time interval. Uniform Hazard Spectrum (UHS) is a site specific response spectrum constructed from the hazard curves for different return periods. This paper outlines various methodologies that are available for the quantification of the uncertainties that constitutes the final output of PSHA and also the limitation of this technique.

Keywords: Seismicity, earthquake catalogue, G-R recurrence law, Attenuation relationship, logic tree approach.

INTRODUCTION

The goal of any structural analysis taking earthquake into consideration is to ensure that the structure can resist a certain level of ground shaking while performing according to the predefined performance objective. To ascertain the extent of ground shaking to which the structure will be subjected to is quite challenging. Seismic hazard analysis deals with the quantification of the hazard due to ground motion that can be expected at a particular site. This site specific hazard quantification can be performed deterministically and probabilistically. This paper explains the probabilistic approach for seismic hazard analysis.

Probabilistic seismic hazard analysis (PSHA) reports the probability of experiencing a ground motion of certain intensity at a particular site in a given time of reference. The seismic hazard or the potential of a site to experience ground

motion due to an earthquake cannot be altered. (Iyengar R N et al, 2010)

There is a great deal of uncertainty about the location, size, and resulting shaking intensity of future earthquakes. PSHA aims to quantify these uncertainties, and combine them to produce an explicit description of the distribution of future ground motion that may occur at a site.

The methodology for administering PSHA was developed by Cornell C A (1968). Cornell's method consists of identification of seismogenic zones in the chosen study area and magnitude recurrence relation is developed for each of these zones. To account for the uncertainty in the location of earthquakes uniform distribution is considered over the entire zone. A suitable attenuation relationship is adopted to match the regional geological condition and seismotectonics of the study area. All the quantified uncertainties are combined using a total probability theorem to develop a hazard curve predicting the

6th International Engineering Symposium - IES 2017

March 1-3, 2017, Kumamoto University, Japan

ground motion at a particular site with a desired confidence level. The various steps involved in determining seismic hazard are shown in Fig 1.

PSHA deals with two types of uncertainties such as epistemic uncertainty and aleatory uncertainty. Epistemic uncertainty mainly arises due to inadequacy of data and lack of exact scientific understanding of the physical phenomena involved in the generation of earthquakes and ground motion at a site (Gupta I D, 2005) The second type, aleatory uncertainty is inherent to the natural process under observation. This cannot be reduced with more data or knowledge. PSHA can address both types of uncertainties by adopting different source model and attenuation relations following the logic tree approach.

Early history of PSHA:

The seeds of PSHA were sown in the early 1960s in the form of two efforts that came together in 1966. One was the 1964 doctoral dissertation of Allin Cornell which studied probability distributions of factors affecting engineering decisions. Cornell proposed that the probability distribution of a complicated, dependent variable can be derived given its relationship with other independent variables whose probability distributions are known or can be assumed. The second effort consisted of studies at the Universidad Nacional Autonoma de Mexico (UNAM) by Luis Esteva, Prof. Emilio Rosenblueth, and co-workers, who were studying earthquake ground motions, their dependence on magnitude and distance, and the relationship between the frequency of occurrence of earthquakes and the frequency of occurrence of ground motions at a site (McGuire R K, 2008)

The PSHA formulation by Cornell failed to showcase the importance of attenuation relationship. However, this was accounted by Anderson and Trifunac (1978) and they also extended PSHA to spectral amplitudes at different natural periods of vibration. The present methodologies are in principle, similar to this theory and the

general formulation has been summarised in the subsequent section.

Need for PSHA:

It is important to understand the seismicity and the extent to which the given site is prone to earthquakes. Past earthquakes have demonstrated that buildings should be resilient and robust. In order to design earthquake resistant buildings estimation of the seismic forces at a given site plays a major role. In this regard, seismic hazard has to be evaluated accurately. Also, the outcome of PSHA will be of immense use to local authorities and policy makers in developing risk mitigation strategies during earthquake events.

Methodology:

The PSHA formulation is a step by step procedure which has been presented in the form of a flowchart in Fig 2.

Identification of seismogenic zones:

The first step is the delineation of seismogenic zones in the study area. This involves identifying the active and dormant faults, shear zones and lineaments in the region. In a considered region, not all sites have same seismic potential and it is due to this reason zoning is performed in order to maintain homogeneity within the zone. The seismic source can be a point, line or areal source.

An attempt in this direction was made by National Disaster Management Agency (NDMA), India. It has been reported that the entire country can be divided into thirty two seismogenic zones on the basis of seismotectonics and historical seismicity. Seismicity is often misunderstood with seismic zonation. Seismicity represents the location and characteristics of the previous earthquakes whereas seismic zonation deals with extent of ground motion or force for earthquake resistant design.

Seismic activity of a region is correlated with the presence of faults and lineaments and also the number of past earthquakes. Few earthquake events cannot be uniquely

6th International Engineering Symposium - IES 2017

March 1-3, 2017, Kumamoto University, Japan

related to a particular fault. In such cases, diffuse aerial zones are considered in the hazard estimation. In seismic zonation, it is assumed that the site with a historical background of earthquakes is more likely to be subjected to earthquakes in near future.

Earthquake catalogue and recurrence relation:

A comprehensive database of location, date and magnitude of past earthquakes is required in compiling the earthquake catalogue for any region. In earthquake data, there are three types. One is non instrumental data and the other is instrumental data while the third is paleo earthquake data. Non instrumental or historic data refers to the period when instrumental recording of the data was not available and the only source of information is ancient scriptures and various articles. Though minor earthquakes may go unnoticed, major earthquakes would have been reported in newspapers or recorded by historians.

Instrumental data is the most accurate data and gives complete information about earthquakes as the ground motion will be captured in the seismogram. It has been available for last few decades since instruments have been set up at various places. Paleo earthquake data is obtained from interpretation of geological evidence such as surface faulting, earthquake induced liquefaction and deformation features to identify the location, time and size of prehistoric events (McCalpin, 2009). However, this type of data covers only major earthquakes.

One of the common problems faced while assembling the earthquake data collected from various sources for compilation of earthquake catalogue is different sources have a record of magnitude in different scales. Usually all the reported values are converted to moment magnitude (M_w) numbers in order to maintain the homogeneity. Scordilis, E. M. (2006) derived empirical relation between body wave magnitudes (M_b); surface magnitude (M_s) and moment magnitude (M_w) which is

commonly used for inter conversion. Idriss, I. M. (1985) introduced an empirical formula to convert M_L to M_w . All the magnitude scales have certain drawbacks and only M_w scale can represent earthquakes of magnitude more than 8.2. Hence, M_w is the common scale used to represent earthquake magnitudes in catalogue.

Occurrence of earthquakes is considered as a poisson process i.e. time independent, size independent and location independent in the estimation of recurrence parameters. Hence, it is important to remove the dependent events such as fore shocks and aftershocks of the main event. The most widely used declustering techniques is the one developed by Gardner and Knopoff (1974) which was later modified by Urhammer (1986). The compiled catalogue comprises of paleo seismic, historic and instrumental data implying temporal variation of seismic activity at the considered site. This fact demands verification of completeness of magnitude in time and the procedure for this was proposed by Stepp J C (1972). In this method, the time interval in which a magnitude class is complete is determined.

The seismic activity of a source zone is characterised by recurrence rates of earthquakes of different magnitudes. Recurrence relations are the means of defining the relative distribution of large and small earthquakes and incorporating the seismic history. On the basis of worldwide seismicity data, Gutenberg and Richter established log-linear relation (Gutenberg and Richter, 1954) given by

$$\text{Log } N(M) = a - bM \quad (1)$$

Here $N(M)$ is the number of earthquakes per year with a magnitude equal to or greater than M , a & b are constants for the seismic zone. The value of N is associated with a given area and time period. The constant 'a' is the logarithm of the number of earthquakes with magnitudes equal to or greater than zero. The constant 'b' is the slope of the distribution and controls the relative proportion of large to small earthquakes. It is to be noted that the

6th International Engineering Symposium - IES 2017

March 1-3, 2017, Kumamoto University, Japan

earthquake recurrence rate models are only approximate.

The methodology proposed by Kijko and Graham (1999) to combine prehistoric, historic and instrumental data is being widely used to estimate the maximum magnitude and (a, b) values in recurrence relation.

Selection of attenuation relationship based on regional factors

After quantifying the distribution of potential earthquake magnitudes and locations, the next step is to employ a ground motion prediction model. These models predict the probability distribution of ground motion intensity, as a function of many predictor variables such as the earthquake's magnitude, distance, faulting mechanism, the near-surface site conditions, the potential presence of directivity effects, etc. It is current practice to select an appropriate attenuation relationship that relates the median value of the seismic motion parameter to be mapped to the magnitude of the earthquake and distance from the source. Attenuation relationships are empirical descriptions providing the median and standard deviation of various intensity measures of the strong ground motion, assumed to be log-normally distributed, in terms of earthquake size, distance, source mechanism and site conditions. When using a predictive relationship, it is important to know how parameters such as magnitude and site-to-source distance are defined and use them in a consistent manner. Ground motion prediction models are generally developed using statistical regression on observations from large libraries of observed ground motion intensities.

Various researchers have developed ground motion prediction equation (GMPE) for different regions. Raghukanth S T G & Iyengar, R. N. (2007) gave GMPE for Peninsular India by considering the seismic catalogue of the region along with its associated seismotectonics.

Computation of seismic Hazard

The epistemic uncertainties associated with the definition of source zones,

distribution of seismicity in a source zone, the recurrence relations for various sources, and the ground motion prediction equations used can be analysed using logic tree approach (Kulkarni et al., 1984). In this approach, all possible inputs are represented in the form of a decision flow path consisting of nodes and branches as shown in Fig 4. Each branch depicts a discrete choice of a model or a parameter, and is assigned a weight for the likelihood of it being correct.

The information gathered from the previous steps will be combined together using total probability theorem.

$$\lambda_{y^*} = \sum_{i=1}^N \alpha_i \int_{M_{\min}}^{M_{\max}} \int_{R=0}^{R=\infty} f_i(M) f_i(R) P(Y > y|m, r) dr dm \quad (2)$$

where λ_{y^*} is the expected number of exceedance of ground motion level y^* , α_i is the mean rate of occurrence of earthquakes in the i^{th} source, $f_i(M)$ is the probability density distribution of magnitude within source i , $f_i(R)$ is the probability density distribution of epicentral distance between the various locations within source i and the site for which the hazard being estimated and $P(Y > y|m, r)$ is the probability that a given earthquake of magnitude m and epicentral distance r will exceed ground motion level y . This annual probability of exceedance can be obtained by simply adding the individual annual probabilities of exceedance corresponding to each of the considered seismic sources.

PSHA estimates the probability of exceedance of spectral acceleration S_a at a site due to all possible future earthquakes as visualised by previous hazard scenarios. (Iyengar R N et al, 2010). The probability that Y exceeds y^* in a time interval T years is given as

$$P(Y > y^* \text{ in } T \text{ years}) = 1 - \exp(-\mu_y * T) \quad (3)$$

The reciprocal of the probability of exceedance gives the return period for the corresponding ground motion value. There will be sites which get affected by events originating in different zones and waves

6th International Engineering Symposium - IES 2017

March 1-3, 2017, Kumamoto University, Japan

passing through regions with different quality factors. Suitable computer programs have been developed that incorporate all faults and regions around a site.

The effects of all the earthquakes of different sizes, occurring at different locations in different earthquake sources with different probability of exceedance are integrated into one curve that shows the probability of exceeding different levels of ground motion at the site during a specified period of time. The output of PSHA is expressed in the form of hazard curves and site specific response spectra.

Conclusion:

The paper has presented an overview on the various aspects of the currently used probabilistic seismic hazard analysis (PSHA) formulation to compute the probability of exceeding a specified level of a hazard parameter at a site due to any of the earthquakes expected to occur during a given life-period of the structure. The limitations of PSHA are as listed below.

- It is difficult to explain the physical meaning of the ground motion obtained from PSHA
- Statistical characteristics of ground motion are not clear or lost in PSHA
- PSHA provides ground motion corresponding to any mean annual rate of exceedance and so it does not provide a unique choice for users and decision makers.

REFERENCES

- [1] Anderson, J. G., & Trifunac, M. D. (1978). "Uniform risk functionals for characterization of strong earthquake ground motion". *Bulletin of the Seismological Society of America*, 68(1), 205-218.
- [2] Baker, J. W. (2008). "An introduction to probabilistic seismic hazard analysis". *Report for the US Nuclear Regulatory Commission, page Version, 1.*
- [3] Cornell, C. A. (1968). "Engineering seismic risk analysis". *Bulletin of the Seismological Society of America*, 58(5), 1583-1606.
- [4] Gardner, J. K., & Knopoff, L. (1974). "Is the sequence of earthquakes in Southern California, with aftershocks removed, Poissonian?" *Bulletin of the Seismological Society of America*, 64(5), 1363-1367.
- [5] Gupta, I. D. (2005). "Probabilistic seismic hazard analysis with uncertainties". *Proceedings of the Symposium on Seismic Hazard Analysis and Microzonation, Roorkee*.
- [6] Gutenberg, B. U., & Richter, C. F. (1954). "Seismicity of the earth and related phenomena". *Princeton (NJ)*.
- [7] Idriss, I. M. (1985). "Evaluating Seismic Risk In Engineering Practice". *Proceedings of the Eleventh International Conference on Soil Mechanics and Foundation Engineering, San Francisco, 12-16 AUGUST 1985. Publication of: Balkema (AA)*.
- [8] Iyengar, R. N., Chadha, R. K., Balaji Rao, K., & Raghukanth, S. T. G. (2010). "Development of probabilistic seismic hazard map of India". *Report on the National Disaster Management Authority, Government of India, India*.
- [9] Kalyan Kumar G (2010]. "Probabilistic Seismic Hazard Analysis for Ground Motion Studies At Chennai And Kanchipuram" (*Unpublished doctoral dissertation*). Indian Institute of Technology Madras, Chennai, India.
- [10] Kijko, A. N. & Graham, G. E. (1999). "Parametric-historic Procedure for Probabilistic Seismic Hazard Analysis Part II: Assessment of Seismic Hazard at Specified Site". *Pure and applied geophysics*, 154(1), 1-22.
- [11] Kulkarni, R. B., Youngs, R. R., & Coppersmith, K. J. (1984, July). "Assessment of confidence intervals for results of seismic hazard analysis". *Proceedings of the Eighth World Conference on Earthquake Engineering*(Vol. 1, pp. 263-270).
- [12] McCalpin, J. P. (Ed.). (2009). "Paleoseismology" (Vol. 95). Academic press.2nd edition, P-613
- [13] McGuire, R. K. (2008). "Probabilistic seismic hazard analysis: Early history". *Earthquake Engineering & Structural Dynamics*, 37(3), 329-338.
- [14] Raghukanth S T G., & Iyengar, R. N. (2007). "Estimation of seismic spectral acceleration in peninsular India". *Journal of Earth System Science*, 116(3), 199-214.
- [15] Scordilis, E. M. (2006). "Empirical global relations converting M S and m b to moment magnitude". *Journal of Seismology*, 10(2), 225-236
- [16] Stepp, J. C. (1972). "Analysis of completeness of the earthquake sample in the Puget Sound area and its effect on statistical estimates of earthquake hazard". *Proceedings of the 1st Int. Conf. on Microzonazion, Seattle*, Vol. 2, pp. 897-910.
- [17] Uhrhammer, R. A. (1986). "Characteristics of northern and central California seismicity". *Earthquake Notes*, 57(1), 21.

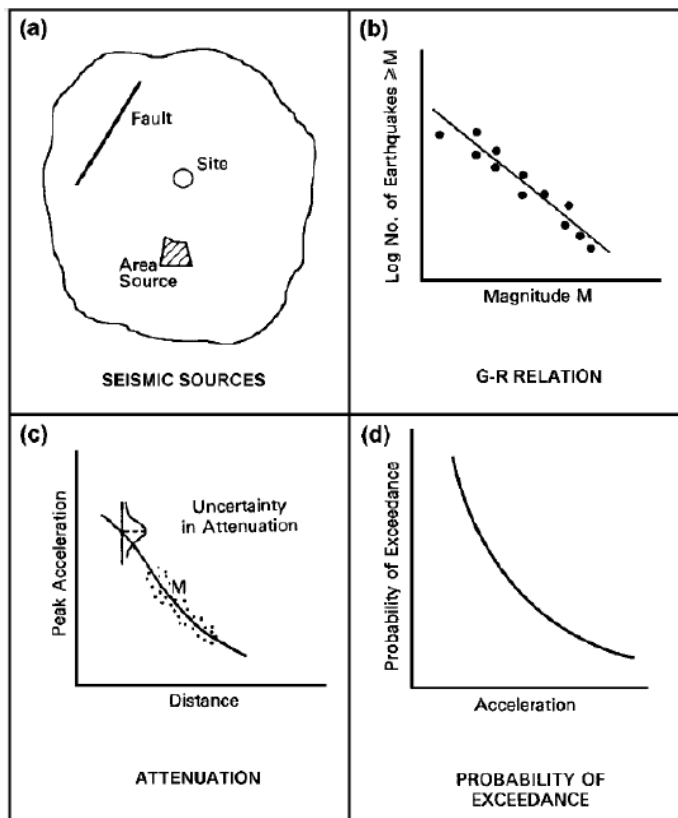


Fig 1: Steps in Seismic Hazard Analysis (Kalyan, 2010)

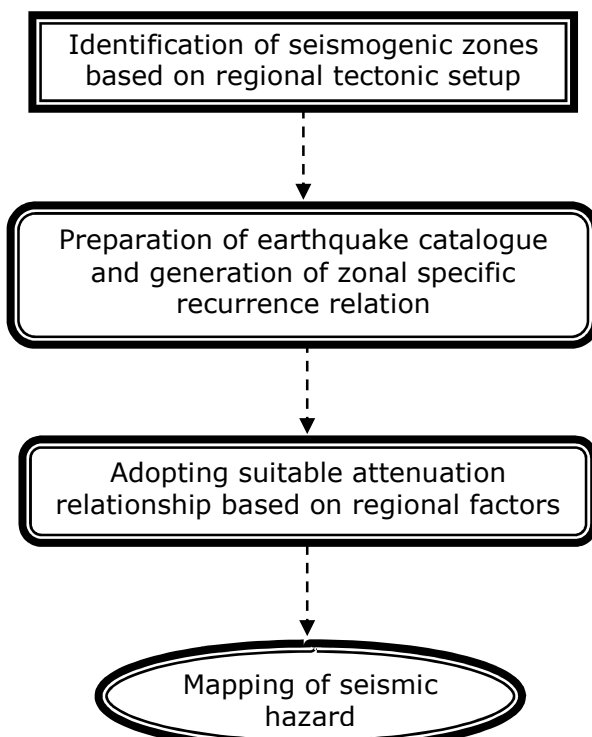


Fig 2: flowchart of PSHA formulation.

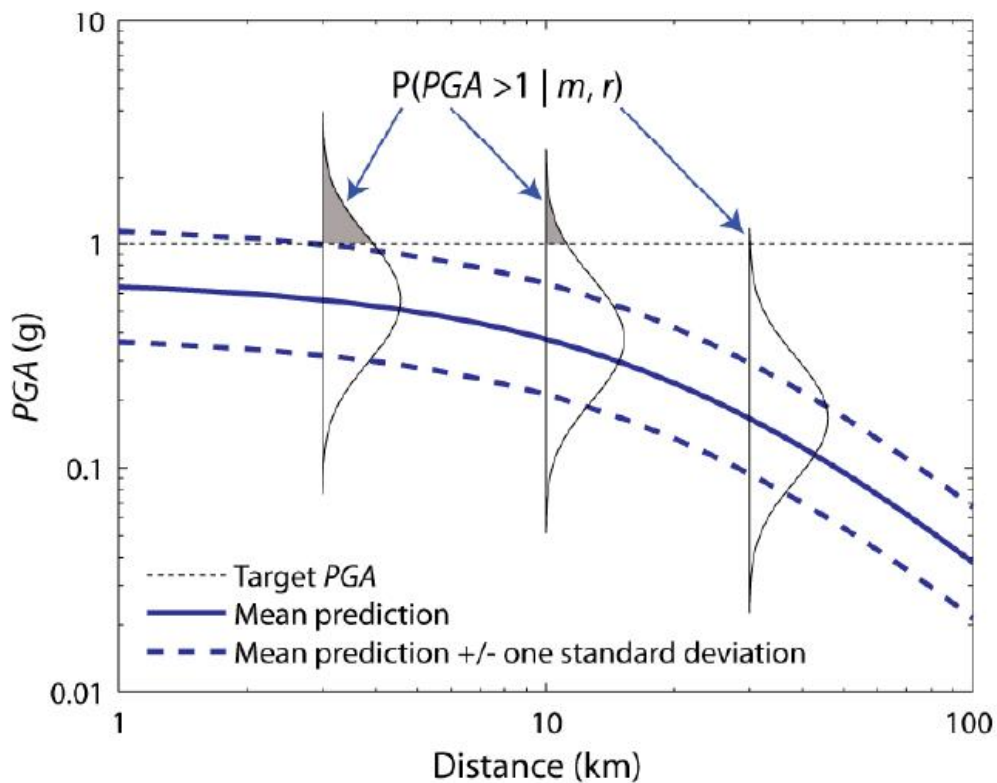


Fig 3: Graphical depiction of the example ground motion prediction model for a magnitude 6.5 earthquake, and the probability of $PGA > 1g$ at several source-to-site distances. (Baker, 2008)

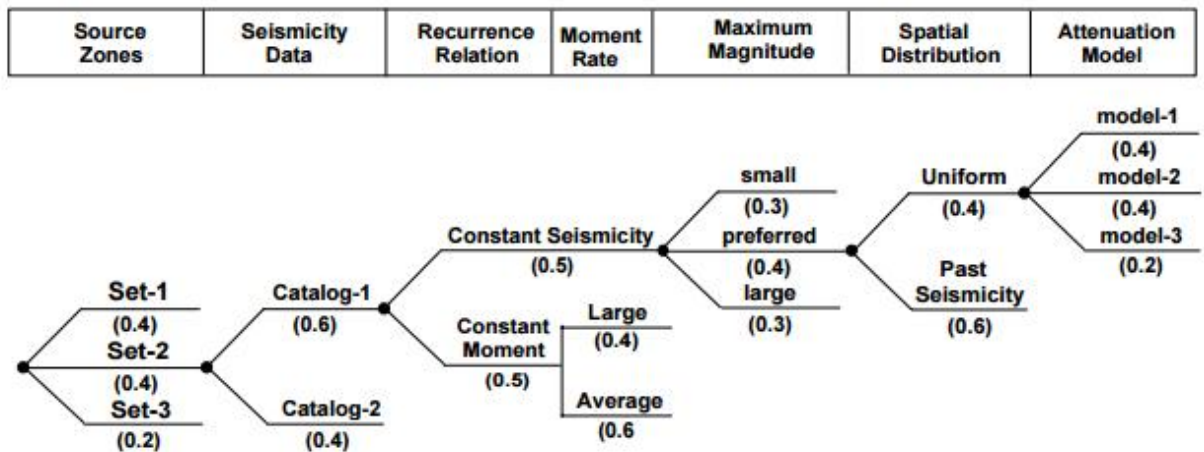


Fig 4: A typical logic tree to account for the epistemic type of uncertainties in the PSHA formulation (Gupta I D, 2005)

Numerical Simulation of Prefabricated Horizontal Drains (PHD) Induced Consolidation in Clayey Deposits

Anjana R.Menon¹ and Anjana Bhasi²

¹ Department of Civil Engineering, National Institute of Technology Karnataka, Surathkal, Mangalore 575025, India. email:anjanam5193@gmail.com

² Department of Civil Engineering, National Institute of Technology Karnataka, Surathkal, Mangalore 575025, India. e-mail:anjanabhasi@yahoo.com

ABSTRACT: PVD induced consolidation is a widely established ground improvement method. In recent years, a new idea of installing the drains horizontally in strip form i.e., Prefabricated Horizontal Drains (PHD), has come up. This helps in accelerating consolidation in embankments with clayey backfills, and dredged mud deposits. Horizontal drains offer many advantages like less space, easy installation and monitoring, etc. Analytical studies and approximate theories have been recently developed in this regard .This paper aims at investigating the process by numerical approach using ABAQUS. The paper briefs the applications and advantages of PHDs and the analytical models and theories developed so far in the area. The suitability of the FEM code ABAQUS to analyse consolidation, is checked by comparing the results with that of Terzaghi's one dimensional consolidation theory. The results are found to be in concordance, which validates the numerical method. Further, the effect of PHD is analysed using ABAQUS, in terms of pore pressure dissipation, and settlement.

Keywords: PHD, consolidation, ABAQUS, pore pressure, settlement

INTRODUCTION

Consolidation of clayey deposits has been an ever haunting problem for civil engineers. Many ground improvement techniques have been developed to address this issue, the most relevant one being the installation of Prefabricated Vertical Drains (PVD), with or without vacuum for accelerated consolidation of clayey deposits. Extensive research has been done in this area, including the theoretical solutions, numerical and analytical approach, factors affecting the performance of PVDs, and so on. Meanwhile, horizontal drains using pipes or aggregates have been in use for slope stabilization since decades. However, in the recent years, a novel idea was developed, namely Prefabricated Horizontal Drains (PHD), which is much like a PVD installed horizontally. The drain is a much cheaper high-flow drainage

system which allows better drawdown of water than aggregate drains. PHD essentially consists of an outer geotextile filter fabric which permits water flow through it, restraining the soil particles, towards an inner polymeric core, which then drains the water to designated drainage exits (Fig 1). This paper brings a brief discussion about the applications and advantages of PHDs and the different approaches developed for the analysis of PHD induced consolidation. The numerical modeling of PHDs using FEM code ABAQUS is also presented with an example.

APPLICATION OF PREFABRICATED HORIZONTAL DRAINS

PHDs are used mainly for two applications. The first and major application is the consolidation of embankments with clayey backfills. Usually, clayey soils are not used for embankment fill, owing to its delayed consolidation and settlement problems.

6th International Engineering Symposium - IES 2017

March 1-3, 2017, Kumamoto University, Japan

However, by installing a system of PHDs at proper spacing in the fill, the consolidation of the fill can be accelerated, and unpredicted settlements can be avoided. This enhances the scope of using clayey soil for backfills, thus reducing the alarming demand for coarse grained soils for fills and drainage purposes (Fig 2). The other important application of PHD is in the consolidation of dredged mud deposits. PHDs help in depositing the dredged soft clayey soil with a small deposition thickness. Since consolidation is accelerated, more can be deposited in a reduced space within a shorter period. The consolidation can be further enhanced by coupling the PHD with vacuum pressure.

ADVANTAGES OF PREFABRICATED HORIZONTAL DRAINS

- **Low installation cost:**

The combined material and installation cost of PHDs is usually less than half of that of aggregate drains.

- **Reduced space requirements:**

Compared to aggregate drains or pipe drains, the PHDs are very thin, and thus can be installed in a much reduced space. This reduces the excavation work and turf damage.

- **Easy to handle, install and inspect:**

PHDs are lightweight and can be easily placed manually, without using any heavy equipment or skilled labour. It is inexpensive and can be easily stored and transported. Moreover, the material and installation can be visually inspected.

- **High flow capacity, no clogging:**

The core of the PHD provides multiple channels for drainage, whereas the filter fabric helps prevent clogging, by restraining solid particles into the core.

- **Strong and durable:**

The high crushing strength of the drain core ensures safe installation, while the high tear and puncture resistance of the filter fabric helps to prevent damage during backfilling or use.

- **Predictable performance:**

The PHDs are industrially manufactured under controlled conditions, thus ensuring uniform properties and predictable

performance, unlike aggregate drains which may vary in thickness and properties.

- **Chemically resistant**

Both the core and filter fabric material are resistant to all naturally occurring soil chemicals. It can even be specially designed for unusual chemical exposure conditions.

SMEAR EFFECT AND WELL RESISTANCE EFFECT

The performance of drain is significantly influenced by the installation process and the inbuilt properties of soil and drain. When drains are driven statically by a mandrel, the soil around the mandrel gets disturbed and forms a less permeable zone, which is called the smear zone. The reduced permeability in smear zone affects the overall rate of consolidation, and must be considered in the design and analysis. However, in case of mixed or remoulded soil, and where PHDs are placed manually in layers within the soil, smear effect need not be considered.

Another aspect to be considered is the long term clogging of drain, called the well resistance effect. The discharge capacity must be properly fractioned to consider this effect. However when the discharge capacity is quite high, well resistance can be ignored.

ANALYSIS OF PHD INDUCED CONSOLIDATION

Ever since the process of consolidation was studied, numerous theories were developed to analyse the process. One of the oldest and simplest theories was Terzaghi's theory of one dimensional consolidation under constant load. This theory still holds importance in many practical situations, due to its simplicity.

(Biot 1941) However, whenever drains are installed in soil, the major part of consolidation occurs due to the radial flow of pore water towards the drain. Hence theories involving three dimensional consolidation have to be used for the analysis of such situations. Moreover, the analysis of drain induced consolidation essentially involves the study of various theories have been developed in this

6th International Engineering Symposium - IES 2017

March 1-3, 2017, Kumamoto University, Japan

regard, which vary in their degree of rigor and complexity.

One of the oldest, and most rigorous, but complicated solution is based on Biot's (1941) consolidation theory, and were derived for equal strain boundary conditions by Yoshikuni and Nakanodo (1974), and Onoue (1988). Less rigorous solutions, considering both well resistance and smear effect, but neglecting vertical flow, have been developed by Barron(1948), Hansbo (1981), and Zeng and Xie(1989).All of these assume equal strain conditions .Hansbo's solution and that of Zeng a Xie 91989) are relatively simple in computation, compared to Barron's solution. (**J Chai 2011**). Thus, in general, for clayey subsoils improved by PVDs installed in square or triangular pattern, there are several consolidation theories available. e.g., Barron, 1948; Hansbo, 1981; Ong et al., 2012; Deng et al., 2013; Tang et al., 2013; Liu et al., 2014. (**J.Chai et al., 2014**) But of all these, the most common and accepted theories for PVD induced consolidation are the Barron(1948) and Hansbo(1981) solutions. (**J Chai 2011**).

However, in case of Prefabricated Horizontal Drains, the vertical and horizontal spacing between the PHDs may not be equal, and hence the influence zone for a single PHD will be rectangular in vertical cross section. Thus, none of the available theories are directly applicable for the analysis of PHDs. (**J Chai et al., 2014**)

ANALYTICAL SOLUTION

J.chai et al. (2014) developed a matching method for the PHD induced consolidation of clayey deposits, based on the established axisymmetric (Hird et al. (1992)) or plane strain (Hansbo et al. (1981)) unit cell theories. Since the PHDs can neither be modeled under pure plane strain or axisymmetric conditions, these solutions were not directly applicable to the situations. Hence equivalent models were developed using matching functions. For this, two main parameters were defined.

$$SR = S_v/S_h \text{ and } WS = w/S_h \quad (1)$$

Where, S_v , s_h and w are the vertical spacing, horizontal spacing, and width of PHD respectively.

They proposed two functions for permeability coefficient, K and coefficient of consolidation, c , by comparing the time require for 50% consolidation, from FEM analysis (using CRISP program) and theoretical solutions. For this, they defined two parameters f_a and f_b to be the ratio of time required for 50% consolidation by FEM and theoretical solutions for axisymmetric and plane strain conditions respectively.

Functions f_a and f_b were then defined as functions of SR and WS . By plotting the variation of f_a and f_b with varying SR and WS , the researchers plotted suitability zones for axisymmetric and plane strain conditions. They observed that, when $f_a < f_b$, it was more of an axisymmetric condition, and vice versa.

By modeling the soil with relevant parameters, they obtained a value of c , and thus, for any value of SR and WS , the modified value of c can be obtained as $c^* = c/f_a$ or c/f_b , as per the zones of suitability.

J.Chai et al. (2014) also proposed solution for consolidation analysis of a surface layer subjected to vacuum pressure at a depth, and installed with PHDs. They defined parameters that can consider the effect of smear and well resistance together, in the analysis, to get degree of consolidation U and pore pressure u

The applicability of this method was proved by analyzing a case history of consolidation of dredged mud deposit assisted by vacuum pressure and PHD.

NUMERICAL MODELLING OF DRAIN INDUCED CONSOLIDATION

J.Chai et al. (2011) has mentioned the methods of modeling the behaviour of prefabricated drain induced consolidation of clayey deposits. Four different approaches are described. The first one, proposed by **Shinsha et al. 1982; Indraratna and Redana 1997**, uses solid elements to represent individual drains, and simulate the axisymmetric and

6th International Engineering Symposium - IES 2017

March 1-3, 2017, Kumamoto University, Japan

plane strain models by matching the time for 50% consolidation, by finding equivalent coefficient of permeability in horizontal direction under plane strain conditions. The second method (Sekiguchi et al. 1986) adopts a macro element in the FEM program to represent the hydraulic behaviour of the drain. The third approach, the most used one, presented by Hird et al. 1992; Chai et al. 1995, involves using one dimensional drainage element to represent the drain. The fourth and last approach is also popular due to its simplicity with reasonable accuracy. In this approach, developed by **Chai et al. (2001)**, an equivalent hydraulic conductivity in the vertical direction is defined, to consider the combined effect of drainage effect of drain, and the natural soil permeability in vertical direction.

The equivalent diameter of the drain has to be evaluated, to model it in axisymmetric conditions. Several equations have been developed for this. One of the well accepted relation is based on equal drainage parameter, suggested by **Rixener et al.(1986)**, verified by **Chai and Miura (1999)** and is given by,

$$\text{Equivalent diameter } D_e = (w+t)/2 \quad (2)$$

Where, w and t are width and thickness of the drain.

NUMERICAL MODELLING OF PHD USING ABAQUS

A numerical investigation into the process of PHD induced consolidation, using finite element code ABAQUS, is briefly presented in this paper.

Initially the suitability of the FEM to analyse consolidation process is studied with an example, by comparing the results of a standard example with Terzaghi's one dimensional consolidation theory (**Sam Helwany 2007**).

A cylindrical clay sample 4cm in diameter and 3.5cm height, with open and permeable top surface, is considered. Soil is modeled as linear elastic, with a permeability 6×10^{-6} cm/mt. Young's Modulus $E = 18.15\text{Kg/cm}^2$, coefficient of consolidation $C_v = 0.16135 \text{ cm}^2/\text{min}$, initial void ratio 1, and Poisson's ratio 0.33. The specimen is confined by impermeable, smooth, rigid cylindrical container, and

subjected to a surcharge of 4Kg/cm^2 . The element chosen was CAX8RP. The displacement boundary conditions were given such that bottom was fixed, and sides were restrained from horizontal movement. Regarding the hydraulic boundary conditions, no flow was allowed across the walls of the container-this is the natural boundary condition in ABAQUS, hence it was not specified. However, after sudden application of surcharge, the top surface was made pervious, so that consolidation occurs, and excess pore pressure at this level was set to zero. The problem is run in four steps. The first step is of single increment, applying a sudden load, without providing drainage. The consolidation is formulated in three steps with equal sub steps. At this stage, the top boundary is made pervious. From the results of the FEA, average degree of consolidation (U) is plotted with dimensionless time factor (T_v). U is calculated as

$$U = 1 - u_{ave}/u_0, \quad (3)$$

where u_{ave} is the average excess pore pressure in the center of the model and u_0 is the initial excess pore pressure($=4 \text{ kg/cm}^2$). The results are then compared with the exact solution obtained using Terzaghi's one dimensional theory. It is found that the numerical solution agrees well with the theoretical solution.

The variation in effective stress and pore pressure with respect to time, is also compared. This also shows reasonable agreement with the theoretical values.

As suggested by **J.Chai et al (2014)**, the PHD can be either modeled as plane strain or axisymmetric conditions, depending on the parameters WS and SR, which further depends on the spacing and width of the drain.

The effect of PHD is analysed by modeling a drain of width 100mm and thickness 10mm, placed at horizontal spacing 0.2m and vertical spacing 1.2m. From the zone of suitability suggested by **J.Chai et al (2014)**, the situation comes under plane strain condition. Hence, plane strain modeling is done using ABAQUS.

6th International Engineering Symposium - IES 2017

March 1-3, 2017, Kumamoto University, Japan

The soil is modeled as linear elastic, with $E=5000\text{ kPa}$, density 18 Kg/m^3 , $\mu=0.3$ and coefficient of permeability $k=3.5\text{e-}5 \text{ m/hr}$. The drain is modeled as one dimensional drainage element. The PHD induced consolidation process is evaluated and compared with the unimproved soil, in terms of degree of consolidation, and settlement.

RESULTS

Fig 4 shows that the FEM code ABAQUS analyses the consolidation process, with reasonable accuracy. The study on effect of PHDs in consolidation shows that (Fig 5, Fig 6) the pore pressure dissipation is considerably accelerated by the presence of PHDs, and final settlement is reached within a shorter period, compared to the unimproved soil.

CONCLUSION

A brief review of the applications and advantages of Prefabricated Horizontal Drains (PHD) was done, along with a review of the existing theories and analytical approaches developed in this regard. The study lead to the following conclusions.

- The consolidation results using ABAQUS and theoretical solutions are in good agreement, which proves the usefulness of the FEM code for consolidation analysis.
- The study on effect of PHD in accelerating the consolidation show that PHDs accelerate the consolidation of clay significantly, and reduces post construction settlement. Hence, PHDs are very useful in improving soft clay embankments and dredged mud deposits.

REFERENCES

- [1] ABAQUS/CAE User's Manual, Hibbit, Karlsson & Sorensen, Inc.
- [2] ABAQUS version 6.14, documentation, Dassault Systèmes SIMULIA, Providence, <http://www.simulia.com/>
- [3] Biot,M.A(1941) , General Theory of Three-Dimensional Consolidation ,Journal of Applied Physics 12, 155
- [4] Chai, J and Carter, J.P. (2011), Deformation Analysis in Soft Ground Improvement, Geotechnical, Geological and Earthquake Engineering 18
- [5] Chai.J.C, and Miura,N,(1999), Investigation Of Factors Affecting Vertical Drain Behavior, Journal of Geotechnical and Geoenvironmental Engineering, Vol. 125, No. 3,March1999
- [6] Chai J-C, Shen S-L, Miura N, Bergado DT (2001) Simple method of modeling PVD improved subsoil. J Geotech Geoenvir Eng ASCE 127(11):965-972
- [7] Chai,J , Horpibulsuk,S, Shen ,S, Carter,J.P. (2014), Consolidation analysis of clayey deposits under vacuum pressure with horizontal drains, Geotextiles and Geomembranes 42 ,pp 437-444
- [8] Hansbo S (1981) Consolidation of fine-grained soils by prefabricated drains. Proceedings of 10th international conference on soil mechanics and foundation engineering, vol 3, Stockholm, pp 677-682
- [9] Helwany, S, Applied Soil Mechanics: with ABAQUS Applications. © 2007 John Wiley & Sons, Inc. ISBN: 978-0-471-79107-2, pp 124-162
- [10]Hird, C. C., Pyrah, I. C. & Russell, D. (1992) ,Finite element modelling of vertical drains beneath embankments on soft ground, Geotechnique 42, No. 3,pp 499-511
- [11]http://www.americandrainagesystems.com/horizontal_strip_drain.htm
- [12]Indraratna B, Redana IW (1997) Plane train modeling of smear effects associated with vertical drains. J Geotech Geoenvir Eng ASCE 123(5):474-478
- [13].Long,R.P, and Covo,A (1994), Equivalent Diameter Of Vertical Drains With An Oblong Cross Section, Journal of Geotechnical Engineering, Vol. 120, No. 9, September, 1994.
- [14]Nagaharaa,H, Fujiyamab,T, Ishigurob,T, Ohtac,H,(2004), FEM analysis of high airport embankment with horizontal drains, Geotextiles and Geomembranes 22 ,pp: 49-62
- [15]Tajudin,S.A.A, et al. (2015), Numerical Modelling of Prefabricated Vertical Drain for Soft Clay using ABAQUS , Applied Mechanics and Materials Vols. 773-774 pp 1502-1507

6th International Engineering Symposium - IES 2017
March 1-3, 2017, Kumamoto University, Japan



Fig.1 Close view of PHD

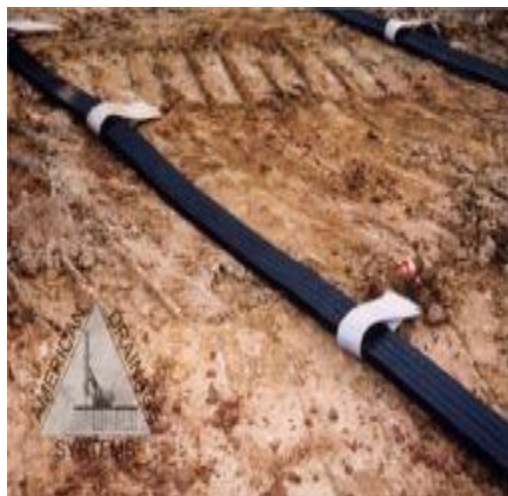


Fig.2 PHD laid in field

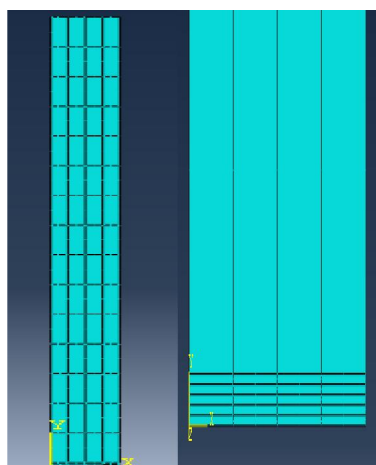


Fig 3: FEM mesh with PHD(PHD in close view)

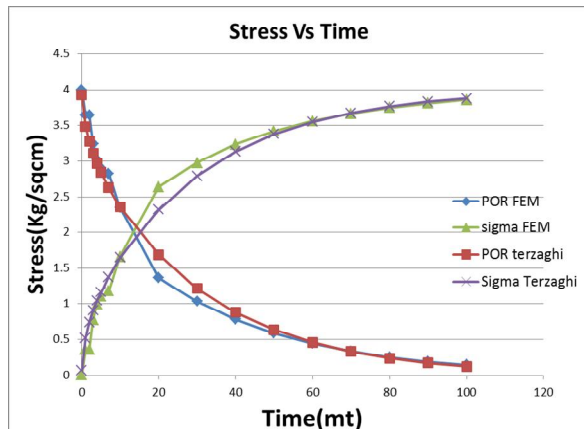


Fig.4 Comparison of ABAQUS and Terzaghi's results

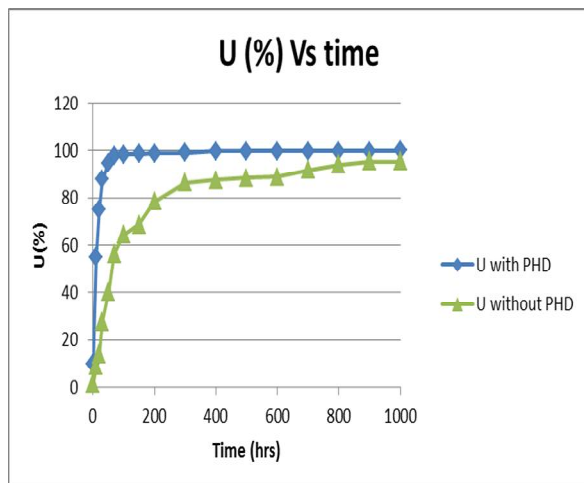


Fig.5 Effect of PHD on degree of consolidation

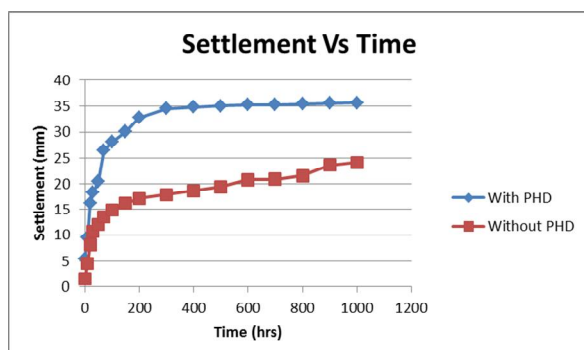


Fig.6 Effect of PHD on settlement

THE INFLUENCE OF ANGLE OF INTERNAL FRICTION ON CANTILEVER AND ANCHORED SHEET PILE WALLS IN COHESIONLESS SOIL

Mahima R ¹ and Sitaram Nayak²

¹ Department of Civil Engineering, National Institute of Technology Karnataka, Surathkal, Mangalore 575025, India. email: mahima.r2009@gmail.com

² Department of Civil Engineering, National Institute of Technology Karnataka, Surathkal, Mangalore 575025, India. email: snayak65@yahoo.co.in

ABSTRACT: This paper aims the study of the influence of angle of internal friction on embedment depth in cantilever sheet pile walls and embedment depth and anchor forces in case of anchored sheet pile walls. Using the conventional design approach ,for a fixed retaining height ,by changing the angle of internal friction the embedment depth was calculated. It was obtained that the depth of embedment decreases with increase in angle of internal friction in both cantilever and anchored sheet pile wall. And in case of anchored sheet pile wall the anchor forces reduces with increase in angle of internal friction.

Keywords: anchored pile, embedment depth, cohesionless

INTRODUCTION

The use of sheet piles has grown in popularity over the past six decades or more due to the great technological strides that have taken place coupled with the ever increasing economic, social, urban and developmental needs that have arisen. Cantilever sheet piles are generally used as temporary structures in civil engineering construction, and are employed for moderate heights only. Anchored sheet piles on the other hand are extensively used in water- front or marine construction, where the water table is high or the soils encountered are soft. The stability of such walls is catered for by the passive resistance developed in front of the wall as well as the anchor rod forces. The latter assists in reducing the embedment depth, lateral deflection and bending moments in the wall. cantilever sheet piles depend very largely for their stability on the passive resistance mobilized in front of the wall. It has long been recognized that the selection of an appropriate value of the angle of shearing resistance ϕ is of primary importance in assessing the passive resistance . In dense sands the adoption of the peak value of ϕ may result in the passive resistance being

over-estimated. In loose sands the wall deformation necessary to produce the maximum value of ϕ is very likely to be larger than what should be acceptable in practice. As a consequence for cohesionless soils, conservative values of ϕ may be necessary for design.

METHODOLOGY

Cantilever sheet pile wall in cohesionless soil :

The pressure distribution diagram for a cantilever sheet pile wall in cohesionless soil using the conventional design approach is given in figure 1. It is assumed here that the soil below the dredge line possesses the same angle of friction ϕ as the backfill above the dredge line. Considering the safety and stability the following equation from Bowles is adopted.

$$Y^4 + Y^3 P_p^- / C - Y^2 8R_a / C - \\ Y(6R_a / C^2 (2YC + P_p^-)) - (6R_a Y^- P_p^-) + 4R_a^2 / C^2 = 0 \quad (1)$$

where Y is the distance from the centre of rotation O or point of zero pressure of the pile to its base, R_a is the resultant force of all forces acting above O, C is the difference between the coefficients of

passive and active pressures multiplied by the unit weight of the soil, and Figure 1 identifies all the other terms. Equation (1) is used in calculating the required embedment depth D, given by

$$D = Y + a$$

where 'a' is the depth of point O below the dredge line where the active and passive pressures are equal. The total required length of the sheet pile is (H + D), and to guarantee stability using the conventional method, the computed embedment depth is increased by 20%.

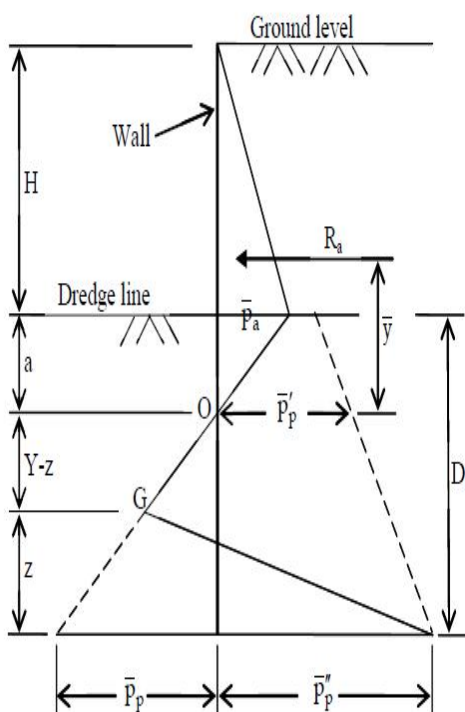


Figure 1 : Pressure distribution diagram for cantilever sheet pile walls in cohesionless soil.

$$\begin{aligned}
 C &= (K_p - K_a)Y' \\
 a &= P_a / (K_p - K_a)Y' \\
 P_p^- &= CY \\
 P_p^-' &= K_a Y H + (K_p - K_a)Y'a \\
 P_p^-'' &= P_p^-' + CY
 \end{aligned}$$

Anchored sheet pile wall in cohesionless soil :

In figure 2, at 'O' net earth pressure is zero which gives

$$P_a' + K_a Y' a - K_p Y' a = 0$$

$$a = P_a' / ((K_p - K_a)Y')$$

R_a be the resultant active earth pressure acting at y_1 below the anchor level

R_p = resultant passive earth pressure acting at y_2 below the anchor rod level

The stability of anchored sheet pile depends upon the anchor force in addition to that upon the passive earth pressure. Considering the safety and stability the following equation is formed

$$Y^3 * C/3 + Y^2 * C(h+a)/2 - R_a y_1 = 0 \dots \dots (2)$$

$$C = (K_p - K_a)Y'$$

$$D = Y + a ;$$

$$F_a = R_a - R_p$$

The total required length of the sheet pile is (H + D), and to guarantee stability using the conventional method, the computed embedment depth is increased by 20%.

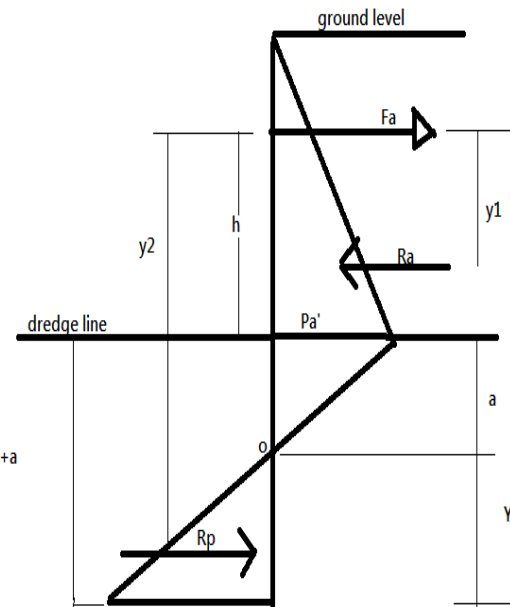


Figure 2 : Pressure distribution diagram for anchored sheet pile wall in cohesionless soil.

The above analysis has been carried out on cantilever sheet pile wall and anchored sheet pile wall in cohesionless soil whose respective angle of internal friction varies from 25 to 45 degree. The retained height of soil in the backfill has been kept constant at 6m. The water table level is assumed as 3m from the ground level. In

6th International Engineering Symposium - IES 2017

March 1-3, Kumamoto University, Japan

case of anchored sheet pile wall, the anchor depth for the analysis is considered as 1m and 2m respectively. The values of the remaining soil design parameters, though generally assumed, have been selected as being quite representative of those obtained in local practice.

RESULTS AND DISCUSSIONS

In order to ensure representative soil design parameters the unit weight of the soil has been varied somewhat from 15 KN/m³ to 21 KN/m³. However this is not considered to have any significant influence on the results of the study.

The result of table 1 demonstrate conclusively that for cantilever sheet piles in cohesionless soil the embedment depth decreases with increase in angle of internal friction. This trend is shown in fig 3. From table 2, it is evident that for anchored sheet piles in cohesionless soil, the embedment depth decreases with increase in angle of internal friction. And also, when the depth of anchor rod is more, the embedment depth is less. It is clearly evident from fig 4. From table 3, it is clear that the anchor force also decreases with increase in angle of internal friction but the anchor force is more, when anchor rod depth is more. The trend is evident from figure 5.

Table 1 Variation of embedment depth in cantilever sheet pile wall for different angle of internal friction

Angle of internal friction	Unit weight (KN/m ³)	Embedment depth (m)
25	15	12.684
30	15	9.708
35	18	6.768
40	20	5.124
45	21	4.008

Table 2 Variation of embedment depth in anchored sheet pile wall for different angle of internal friction

Angle of internal friction	Unit weight (KN/m ³)	Embedment depth(m)	
		Anchor depth 1m	Anchor depth 2m
25	15	6.264	5.928
30	15	4.5	4.224
35	18	2.88	2.676
40	20	2.028	1.872
45	21	1.476	1.356

Table 3 Variation of anchor forces in anchored sheet pile wall for different angle of internal friction

Angle of internal friction	Unit weight (KN/m ³)	Anchor force(KN)	
		Anchor depth 1m	Anchor depth 2m
25	15	74.51	82.71
30	15	53.41	60.39
35	18	46.28	53.60
40	20	38.1	44.83
45	21	29.8	35.50

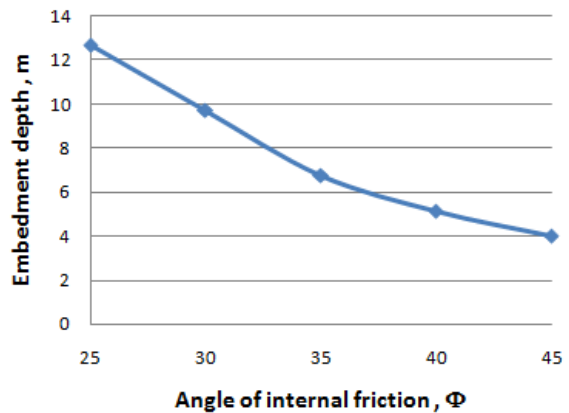


Figure.3 variation of embedment depth with angle of internal friction in cantilever sheet pile wall

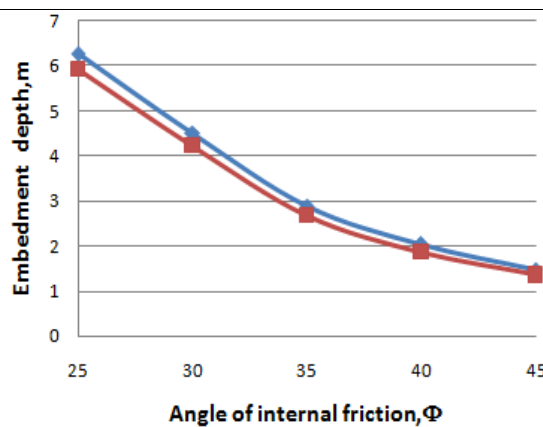


Figure.4 variation of embedment depth with angle of internal friction in anchored sheet pile wall

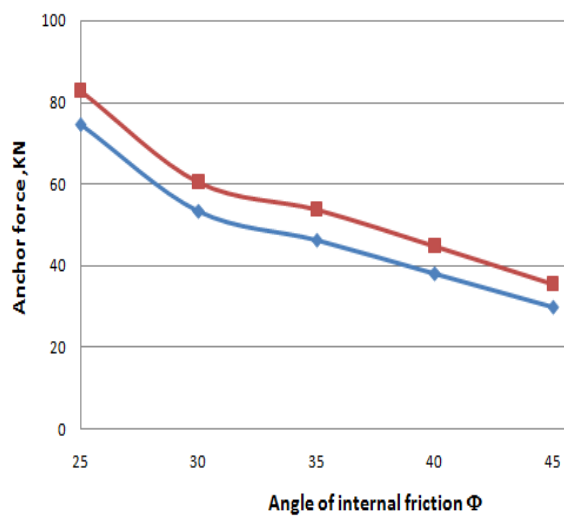


Figure.5 variation of anchor forces with angle of internal friction in anchored sheet pile wall

anchor depth 1m
 anchor depth 2m

CONCLUSIONS

The primary aim of the present study has been to assess the influence of angle of internal friction on embedment depth in cantilever and anchored sheet piles in cohesionless soil. Then following are the conclusions reached :

- For cantilever sheet piles in cohesionless soil the embedment depth decreases with increase in angle of internal friction.
- For anchored sheet piles in cohesionless soil, the embedment depth decreases with increase in angle of internal friction.
- In anchored sheet pile walls in cohesionless soil, as the depth of anchor rod is more, the embedment depth is less but the anchor force increases with increase in anchor rod depth.

REFERENCES

- [1] Bowles, J.E., (1988) Foundation Analysis and Design, 4th Edition, McGraw-Hill, New York, pp. 580–643.
- [2] Hagerty,D.J., and Nofal,M. M. (1992). "Design Aids: Anchored Bulkheads in Sand," Canadian Geotechnical Journal, Vol. 29, No.5, pp. 789-795.
- [3] King, G. J. W. (1995). Analysis of cantilever sheet-pile walls in cohesionless soil. J. Geotech. Engng Div., ASCE 121, No. 9, 629-635.
- [4] Nataraj, M. S., and Hoadley, P. G. (1984). "Design of Anchored Bulkheads in Sand," Journal of Geotechnical Engineering, ASCE, Vol. 110, No. GT4, pp. 505-515.
- [5] Rowe, P. W. (1951). Cantilever sheet piling in cohesionless soil. Engineering September 7, 316-319.

EFFECT OF SURCHARGE ON SLOPE STABILITY

Surya E V¹ and Sitaram Nayak 2

1 Department of Civil Engineering, National Institute of Technology Karnataka, Surathkal, Mangalore 575025, India. email:suryaevkal@gmail.com

2 Department of Civil Engineering, National Institute of Technology Karnataka, Surathkal, Mangalore 575025, India. email:snayak65@yahoo.co.in

ABSTRACT: Slope stability analysis is an important area in geotechnical engineering. This paper deals with the study of slope stability using computer based geotechnical software Oasys slope19.1 with different slope angles, angle of internal friction and cohesion under increasing surcharge load. The factor of safety has been determined using the Bishop's method of limit equilibrium analysis.

From the study it has been obtained that the factor of safety increases when the distance of surcharge increases from the crest of the slope up to a certain level and beyond that, the effect of surcharge remains constant. The factor of safety decreases with an increase in surcharge load intensity.

Keywords: slope stability, surcharge, factor of safety, slope angle, limit equilibrium

INTRODUCTION

Slopes are required in the construction of railway and road embankments, earth dams, levees and canals. Slopes can be natural or manmade. Every slope has forces acting on it that tend to disturb its stability. The main force is the self-weight of soil mass forming the slope, but seepage, seismic activity and external loads are also disturbing forces. Failure of natural and manmade slopes has been resulted into much death and destruction. Civil engineers are expected to check the stability of natural and slopes of excavation.

The slope stability analyses are performed to assess the safe and economic design of human-made or natural slopes. In the assessment of slopes, engineers primarily use factor of safety values to determine how close or far slopes are from failure. When this ratio is greater than 1, resistive shear strength is greater than driving shear stress and the slope is considered stable. When this ratio is close to 1, shear strength is nearly equal to shear stress and the slope is close to failure, if factor of safety (FS) is less than 1 the slope should have already failed.

The two main approaches in slope stability analysis are the limit equilibrium analysis and the finite element method.

The objectives of the present study are to assess the effect of intensity and position of surcharge on slope stability. This paper uses the Limit equilibrium method of slope stability analysis using Oasys slope 19.1 software based on Bishop's method on a homogeneous soil slope.

LIMIT EQUILIBRIUM METHODS

Limit equilibrium types of analysis for assessing the stability of earth slopes have been in use in geotechnical engineering for many decades.

Limit equilibrium method first define a proposed slip surface and analyse the stability of soil body within the surface. Shear stresses induced on the assumed failure surface by the body and the external forces are compared with the available shear strength of the material, to obtain the corresponding factor of safety of the slip surface. Likewise different trial slip, surfaces are selected and corresponding factors of safety are found out. The factor of safety with the minimum value is taken as the factor of safety of

slope and the corresponding slip surface is taken as the critical slip surface.

Some of the well-known and widely used LEM methods are Bishop Method (1955), Fellenius method (1936) and Spencer method (1967).

Bishop's method

Bishop's simplified method is very common in practice for circular shear surface. This method considers the inter slice normal forces but neglects the inter slice shear forces. It further satisfies the vertical force equilibrium to determine the effective base normal force P, which is given by,

$$P = \frac{[W - \frac{1}{F}(c'l \sin \alpha - ul \tan \phi' \sin \alpha)]}{m_\alpha} \quad (1)$$

Where,

$$m_\alpha = \cos \alpha + \frac{(\sin \alpha \tan \phi')}{F} \quad (2)$$

Taking moments about the center of the circle,

$$F = \frac{\sum \left[\frac{c'l \cos \alpha + (W - ul \cos \alpha) \tan \phi'}{\cos \alpha + (\sin \alpha \tan \phi')/F} \right]}{\sum W \sin \alpha} \quad (3)$$

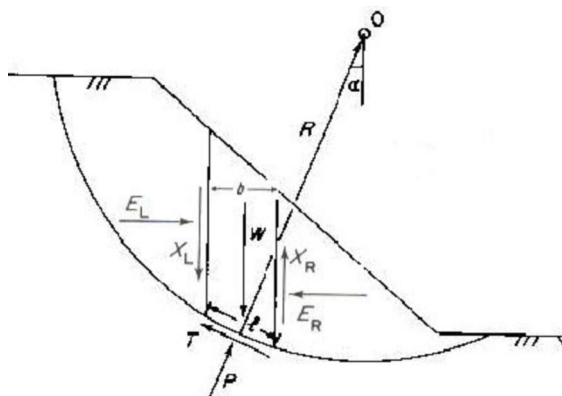


Fig.1 Bishop's simplified method of slices

As this equation contains F on both sides, it has to be solved iteratively.

Convergence is usually quick and so the method is suitable for hand calculation.

SLOPE STABILITY ANALYSIS BY OASYS SOFTWARE

The software code Oasys Slope 19.1 allows geotechnical engineers to carry out limit equilibrium slope stability analysis of existing natural slopes, unreinforced man-made slopes, or slopes with soil reinforcement. The program uses Swedish circle (Fellenius) method, Bishop's method, Janbu's method.

The use of these methods allows analysis of both circular and non-circular slip surfaces to be carried out. The location of circular surfaces is defined using a rectangular grid of centers and then a number of different radii, a common point through which all circles must pass or a tangential surface which the circle almost touches. The ground section is built up by specifying each layer of material, from the surface downwards, as a series of x and y coordinates. The strength of the materials is represented by specifying cohesion and an angle of shearing resistance. External forces can be applied to the ground surface to represent building loads or strut forces in excavations.

Soil properties used

The properties of soil used in the present study are presented in Table 1. Two types of soils are considered for the analysis.

Table 1 soil properties

Material	Unit weight (kN/m ³)	Friction angle (degree)	Cohesion (kN/m ³)
Soil 1	20	15	50
Soil 2	20	25	20

The analysis is carried out for a slope of homogeneous soil having a slope height of 4m. The intensity of surcharge q/yh varies as 0.25, 0.5, 0.75 and 1. Slope angles of 2H:1V, 1.5H:1V, 1H:1V are selected for the analysis. The graphical input for the problem is as shown in Fig.2.

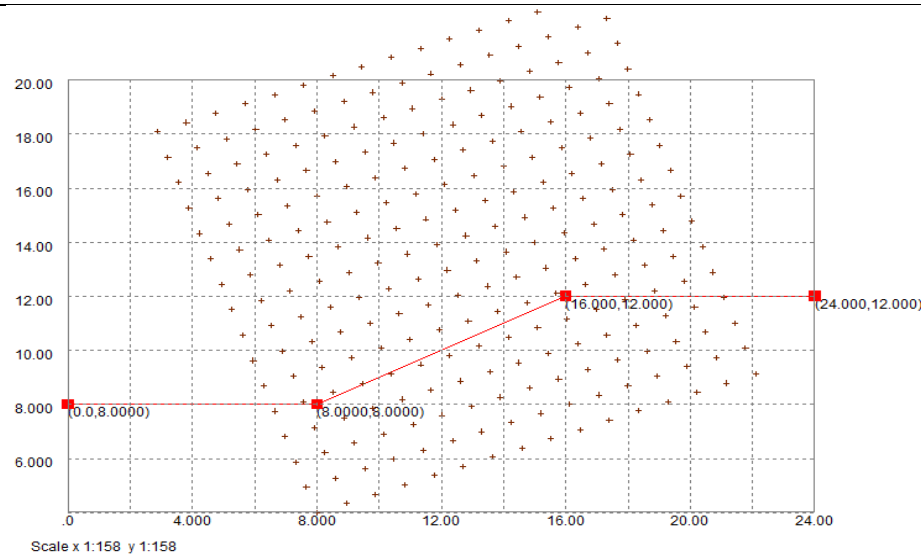


Fig.2 Graphical Input

STABILITY ANALYSIS AND RESULTS

Fig.3 shows the graphical output of the analysis.

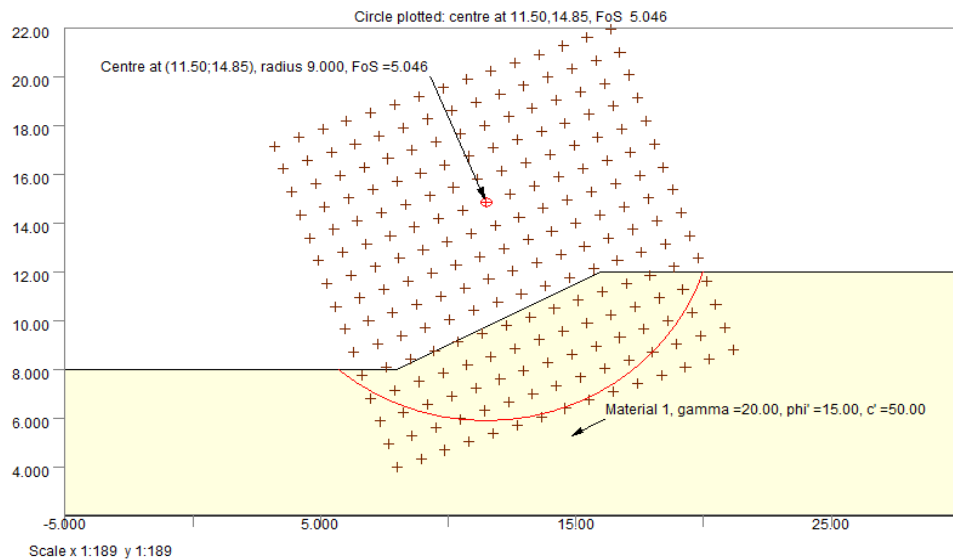


Fig.3 Graphical Output

6th International Engineering Symposium - IES 2017

March 1-3, 2017, Kumamoto University, Japan

The factor of safety is calculated by increasing the load on the slope crest. Fig:4 and 5 shows the variation of FS with surcharge for different slope angles. It indicates a gradual decrease in FS with surcharge.

Effect of variation of surcharge intensity on FS

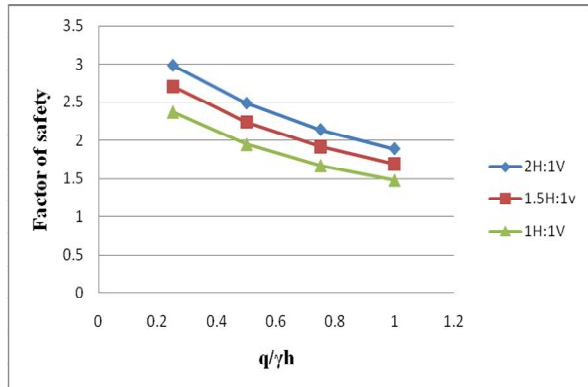


Fig.4 Variation of factor of safety with $q/\gamma h$ for gamma=20, phi=15, c=50, $x/h=0$

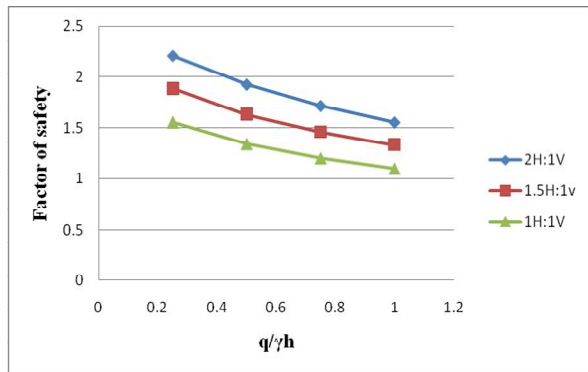


Fig.5 Variation of factor of safety with $q/\gamma h$ for gamma=20, phi=25, c=20, $x/h=0$

Effect of variation of x/h on FS

Fig.6, 7, 8, 9 depicts the variation of FS with the distance of surcharge from the crest of the slope. The result shows that the FS first increases with the distance up to a certain level and beyond that it remains constant irrespective of the type of soil and slope angle.

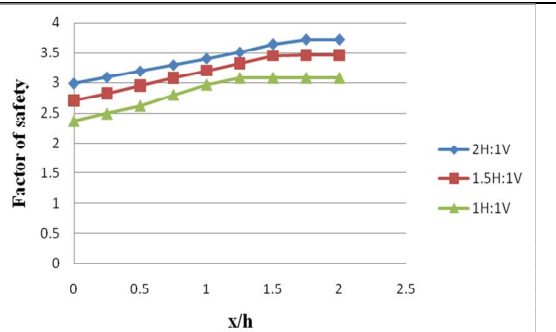


Fig.6 Variation of factor of safety with x/h for gamma=20, phi=15, c=50, $q/\gamma h=0.25$

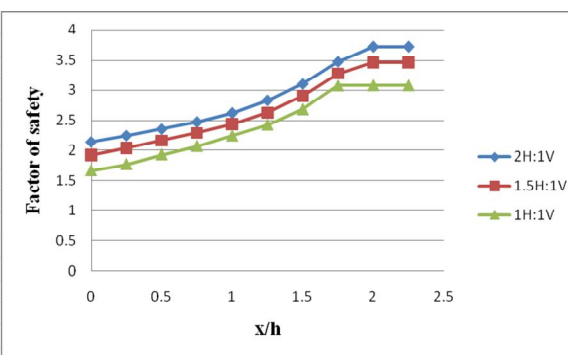


Fig.7 Variation of factor of safety with x/h for gamma=20, phi=15, c=50, $q/\gamma h=0.75$

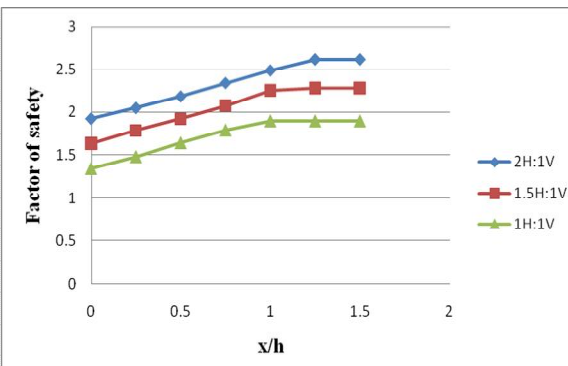


Fig.8 Variation of factor of safety with x/h for gamma=20, phi=25, c=20, $q/\gamma h=0.5$

6th International Engineering Symposium - IES 2017

March 1-3, 2017, Kumamoto University, Japan

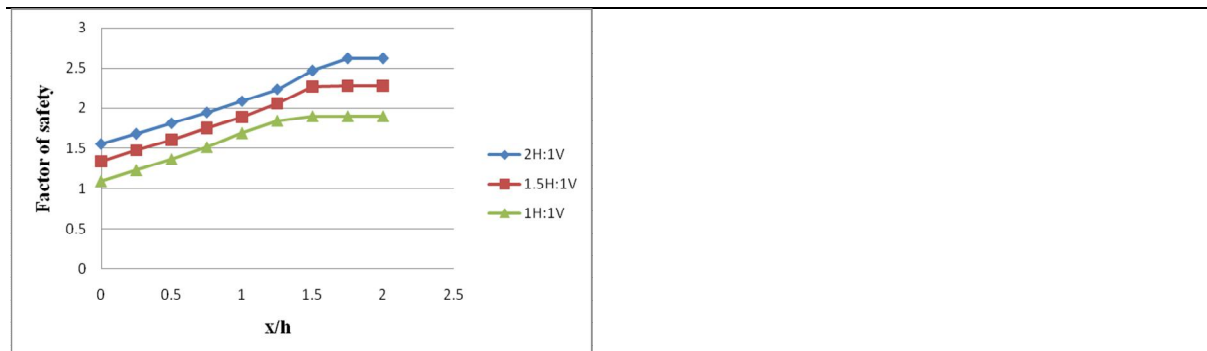


Fig.9 Variation of factor of safety with x/h for $\gamma=20$, $\phi=25$, $c=20$, $q/\gamma h=1$

CONCLUSIONS

The following conclusions have been drawn from this study:

- Factor of safety decreases with increase in surcharge load intensity irrespective of the type of soil and slope angles.
- Factor of safety is a function of the position of surcharge from the crest of slope .FS increases with increase in distance from crest of slope up to a certain level and beyond that level it has no influence on the FS.

REFERENCES

- [1] Ammar Rouaiguia, and Mohammed A. Dahim, (2013), Numerical Modeling of Slope Stability Analysis, International Journal of Engineering Science and Innovative Technology, Vol.2, pp 533-542.
- [2] Arora K R, (2003), Soil Mechanics and Foundation Engineering, 6th ed., Standard Publishers and Distributors, New Delhi.
- [3] Bishop A W, (1955), The Use of Slip Circle in the Stability Analysis of Slope, Geotechnique, Vol.5, pp 7-17.
- [4] Moniruzzaman moni, and Mahmud sazzad (2015), Stability Analysis of Slopes with Surcharge by LEM and FEM, International Journal of Advanced Structures and Geotechnical Engineering, Vol.4, No. 4, pp 216-225.
- [5] Pengpeng Ni, and Shuhong Wang (2016), Response of Heterogeneous Slopes to Increased Surcharge Load, Computers and Geotechnics, Vol. 78, pp 99-109.
- [6] Slope Tutorial Manual <http://www.oasys-software.com>.

ELECTRICAL RESISTIVITY OF SOIL – IMPACTS AND APPLICATIONS IN GEOTECHNICAL ENGINEERING

Divya Nath¹, Nimi Ann Vincent², R. Shivashankar³ and K.N.Lokesh⁴

- 1 Department of Civil Engineering, National Institute of Technology Karnataka, Surathkal, Mangalore 575025, e mail:divyanath92@gmail.com
 - 2 Department of Civil Engineering, National Institute of Technology Karnataka, Surathkal, Mangalore 575025, e mail:imin.nna.15@gmail.com
 - 3 Department of Civil Engineering, National Institute of Technology Karnataka, Surathkal, Mangalore 575025, e mail:shivashankar.surathkal@gmail.com
 - 4 Department of Civil Engineering, National Institute of Technology Karnataka, Surathkal, Mangalore 575025, e mail: lokesh @ nitk.ac.in
-

ABSTRACT: Prefoundation analysis on soils is necessary to avoid failure of important structures such as bridges, dams, buildings etc. Electrical resistivity tomography (ERT) is an attractive tool, which can be applied in field as an economical, non destructive & sensitive method. Electrical resistivity (ER) of soil shows clear correlation with geotechnical parameters. This paper reviews the relationship between soil ER and geotechnical parameters, and also various field conditions in which ERT can be applied. Emerging innovations in ERT, advantages and disadvantages of this method and the future scope of study are also reviewed.

Keywords: Electrical resistivity, Wenner configuration, pH, Ion Content and Resistivity

INTRODUCTION

All important engineering structures such as airport, runways, bridges etc are reside directly or indirectly on ground. Hence well examination on the underlying soil is of prime importance in civil engineering. Testing can be either laboratory testing of soil samples collected through boreholes or by geophysical methods. Various laboratory investigations are generally time-consuming and expensive. Geophysical methods include electrical resistivity, seismic, gravity, ground penetrating radar, magnetic, etc. Geophysical method has been able to produce good efficiency due to the cost, time, data coverage and the obtained data's can be processed in a very short time. Hence these methods are widely using in various field conditions.

Electrical resistivity method is non-destructive and very sensitive; it offers a very attractive tool for describing the

subsurface properties without digging. It can determine heterogeneity and high moisture zone easily. It has been already applied in various contexts like: groundwater exploration, landfill and solute transfer delineation, agronomical management by identifying areas of excessive compaction or soil horizon thickness and bedrock depth, and at least assessing the soil hydrological properties. (Samouelian .A. et al., 2005) Soil derives its spontaneous electrical resistivity properties because of its soil solid and liquid phase structure. Soil air can be considered as a dielectric. Soil electrical properties are the parameters of natural and artificially created electrical fields in soils and influenced by distribution of mobile electrical charges, mostly inorganic ions, in soils. For measuring soil electrical properties geophysical methods of vertical electrical sounding can be used. Using Resistivity

6th International Engineering Symposium - IES 2017

March 1-3, Kumamoto University, Japan

surveys we can measure the capacity of ground to pass an electrical current. This property can be utilised for designing earthing systems for substations or specialist plant, and for measuring the corrosion susceptibility of buried pipelines and other steel structures.

THEORY AND BASIC PRINCIPLE

Electrical resistivity defines how well a material can retard electrical conduction. It relates electric potential and current to geometrical dimension of the specified area. The resistivity of soils depends on several factors such as porosity, permeability, ionic content of the pore fluids, and clay mineralization. Two types of electrode spacing arrangements are commonly adopted in field:

- (a) Wenner Arrangement
- (b) Schlumberger Arrangement

During resistivity surveys, four equidistant electrodes are set-out in a fixed configuration and then a low frequency current is applied across the two outer electrodes with the resultant voltage measured across the inner electrodes. The current and potential electrodes are generally arranged in a linear array. In a resistivity sounding, the distance between the current electrodes and the potential electrodes is systematically increased using which successively greater depths can be analyzed...

The resistivity ρ ($\Omega\text{-m}$) of a body is defined as follows: $\rho = R \times (A/L)$ where

R =electrical resistance (Ω),

L =length of the cylinder (m) and

A=cross sectional area (m^2). The electrical resistance of the cylindrical body R (Ω) is defined by the Ohm's law as follows: $R = V/I$ where V =potential (V) and I =current (A). (Samouelian .A. et al., 2005)

Typical values soil electrical resistivities are shown in fig 1.

- Usual values: from 10 up to 1000 ($\Omega\text{-m}$)
- Exceptional values: from 1000 up to 10000 ($\Omega\text{-m}$)

Range of resistivities among rocks and rock materials is enormous, extending from

10^{-5} to 10^{15} ohm-m. Rocks and minerals with resistivity from 10^{-5} to 10^{-1} ohm-m are

considered good conductors: those from 1 to 10^7 ohm-m, intermediate conductors, and those from 10^8 to 10^{15} ohm-m poor conductors.

The Wenner arrangement consists of four equally spaced (A) electrodes driven approximately 20 cm into the ground as shown in fig.2

In this method a dc current of known magnitude (I) is passed between the two outer (current) electrodes, which produces an electric field within the soil. By means of the inner electrodes the potential drop 'E' for the surface current flow lines is measured. The apparent resistivity 'R', is calculated using the following equation 1.

$$R = \frac{2\pi AE}{I} \quad (1)$$

Where,
A in centimeters,
E in volts,
I in amperes, and
R in ohm-cm

The method known as electrical sounding is used when the variation of resistivity with depth is required. This enables rough estimates to be made of the types and depths of strata. A series of readings are taken, the (equal) spacing of the electrodes being increased for each successive reading. However, the center of the four electrodes remains at a fixed point. As the spacing is increased, the apparent resistivity is influenced by a greater depth of soil.

Relationship between soil ER and geotechnical parameters

1. Composition of solid
2. Moisture content
3. Temperature
4. Degree of saturation
5. Wetting and drying cycles
6. Specific surface area
7. Compaction
8. Porosity
9. Organic content

Relationship between soil water content & soil apparent electrical resistivity

Conduction of electrical current through soil only lies on phenomenon occurring in water. If moisture content present in soil increased from dry to full saturation level, adsorbed ions in the solid particles get released, thus

6th International Engineering Symposium - IES 2017

March 1-3, Kumamoto University, Japan

mobility of electrical charges increases and hence conduction increases.(Kibria golam(2011))

Conduction in soil occurs through water in pore spaces (Fig.3) or along the continuous films of water adsorbed on grain boundaries. Increasing the soil saturation level results in a decrease in the soil electrical resistivity, also there exists a critical soil saturation level, below which the resistivity will rapidly increase.

Change in the moisture level of the soil throughout the year during different seasons is the biggest reason for change in the ground electrode resistance. Voronin (1986) clearly described how moisture content variation changes electrical resistivity (Fig.4).

He obtained a non linear curve between In (w) & electrical resistivity(ER) (Ω) which is divided into several zones. Rapid decrease in ER observed in adsorption water zone. Initially immobile water molecules are present in this zone. However, dipolar water ions create a conductive path and hence electrical resistivity decreases sharply. In film water zone, van der Waal's force increases and hence decrease in resistivity is less sharpening. When water reaches fissures, relative portion of film water decreases and capillary water increases. In film capillary and capillary water zone molecular attraction is higher than the capillary force. Hence ER decreases less dramatically. In gravitational water zone there is not much relation between mobility of electric charges & movement of water molecules. Hence in this region ER is almost independent of water content.

Fahad Irfan Siddiqui and Syed Baharom Azhar Bin Syed Osman (2012) carried out experiments on 12 soil samples obtained from University Technology PETRONAS, Perak, Malaysia. Field investigations comprised of electrical resistivity survey (VES) and soil boring. They obtained good correlation between moisture content and resistivity values with regression coefficient.

Relationship between chemical composition of the soil solution &soil apparent electrical resistivity

The presence of soluble salts in the soil will significantly impact the resistivity of the

soil. Presence of soluble salts will enhance the conduction and thereby reduces electrical resistivity of soil considerably

Relationship between soil texture & soil apparent electrical resistivity

At the same soil saturation level, the electrical resistivity of sandy soil > silty sand > silt > silty loam > clay loam. The smaller the soil particle or the higher the clay contents of the soil, the lower the electrical resistivity

Relationship between soil porosity & soil apparent electrical resistivity

Soil Porosity, is inversely related to the bulk density. Porosity varies depending on particle size and is greater in clayey soils than in sandy soils. As the electrolytic conduction is partly carried out through interconnected pores of soil, the electrical resistivity of soil also depends on the porosity. At given water content, as the soil porosity decreases, the resistivity also decreases.

Relationship between soil temperature & soil apparent electrical resistivity

Above the freezing point of the water, temperature does not impact the soil resistivity significantly but the temperature below the freezing point of the water soil resistivity rises and will have significant impact. Sun-Young Seo et al. (2013), pointed out that for 40% and 60% degree of saturation, the electrical resistivity generally increases through the repeated freeze and thaw cycle

Relation between shear strength parameters and soil resistivity

Andy Anderson Bery and Rosli Saad (2012) reported that for the empirical correlation between resistivity and internal friction angle ϕ , for undisturbed clayey sand soils is given by eqn.2

$$\rho = 1378.0e^{-0.03(\phi)} \quad (2)$$

regression coefficient, R^2 for equation was approximately 0.647, they also pointed that internal friction angle is inversely proportional to the resistivity of samples. The empirical correlation between resistivity, ρ and undisturbed soil's effective cohesion, C' for clayey sand soils is given by eqn.3

6th International Engineering Symposium - IES 2017

March 1-3, Kumamoto University, Japan

$$\rho = 167.0e^{0.101(C)} \quad (3)$$

regression coefficient, R^2 was approximately 0.664.

Relation between compaction and soil electrical resistivity

As compaction increases soil resistivity decreases. This happens because compaction process expels void in the soil, which in turn reduces the electrical resistivity.

Organic content & ER

Usually organic contents include decayed materials which intermixed with soil minerals and formed a distinct texture in organic soil. Such soil has the capacity to retain higher proportion of water and electrolyte, which makes the soil conductive

Bulk density, degree of saturation & ER

Increase in bulk density implies reduction of pore air in soil. Hence the degree of saturation increases. Dissolved ions present in pore water have the tendency to form double layer in fine grained soil. Hence if degree of saturation increases, it will cause proportional decrease of resistivity, above a critical value of degree of saturation. Increase in bulk density increases contact between individual soil particles which allows easy conduction of current.

Applications of ER in various geotechnical fields

- swell shrinkage properties of compacted expansive soils can be evaluated using ER method
- Shrinkage, cracks, water sensitivity and uneven distribution etc. of lateritic soils can be studied using ER method.
- Can be used for subsurface investigation
- Groundwater exploration, landfill and solute transfer delineation, agronomical management(by identifying areas of excessive compaction)
- For assessing soil hydrological properties
- For detection of underground mine workings
- Mineral exploration and detection of cavities
- Waste site exploration.
- Oil exploration

Some advantages of electrical resistivity testing of soil over conventional soil testing procedures are summarized as follows:

- Useful in cases where conventional drilling, testing, and sampling are difficult (e.g., deposits of gravel, talus deposits) or where potentially contaminated soils may occur in the subsurface.
- Covers a relatively large area, and help to understand the soil strata in large extent with few tests Geophysical measurement assesses the characteristics of soil and rock at very small strains, typically on the order of 0.001 percent thus providing information on truly elastic properties.
- These methods are relatively inexpensive when considering cost relative to the relatively large areas over which information can be obtained.

LIMITATIONS OF GEOPHYSICAL TEST

Some of the general disadvantages of geophysical methods include:

- Large difference in stiffness between adjacent subsurface units is required for better interpolation.
- It is difficult to develop good stratigraphic profiling if hard material lies over soft material
- Useful results can only be analysed by an experienced engineer or geologist who is familiar with the particular testing method.
- Specialized equipment is required (compared to more conventional subsurface exploration tools)

CASE STUDY- corrosion susceptibility of buried pipelines

Electrical resistivity studies on site samples collected from different parts of Karnataka were carried out using 4 probe arrangement using soil resistivity box (Fig 5). 9 sites were selected with 10 km spacing in between and soil was tested for electrical resistivity, geotechnical properties and chemical properties. Tests were carried out for checking the suitability of soil for laying underground pipelines.

6th International Engineering Symposium - IES 2017

March 1-3, 2017, Kumamoto University, Japan

Instruments used:

Electrical Resistivity Box

A soil resistivity box of $7.4 \times 7.8 \times 3.55$ cm dimension was used. It consists of two stainless steel plates at both ends, which acts as current electrodes and two steel pins at one-third distance from both ends acting as voltage electrodes. (Fig.6)

Multimeters

2 high precise digital multimeters are used, one for voltage measurement. And the other one with mill ampere reading used for current measurement.

Standard solutions of NaCl and KCl, with different molarities and known electrical conductivity, are used for standardizing the test setup and the following calibration equation was derived.

$$pt = 1.373pc + 5.535 \quad (4)$$

where pt is true resistivity and pc measured resistivity.

DC power source

A 30 V DC power supply is used for external power supply

TEST PROCEDURE

Oven dried soil was filled inside the wooden box by hand compaction in 3 layer. Resistivity calculated at full compaction and 90% compaction. The circuit arrangement is shown in Fig.7. When current (I) is passed through the soil sample, the potential difference (ΔV) developed between the voltage electrodes for the one-third length between them is read by the multimeter which acts as the voltmeter. Measured resistivity (ohm-cm),

$$\rho = R \times (A/L) \quad (5)$$

Where A = cross sectional area of the sample, cm^2 , L = length between voltage electrodes, cm

The calculated resistivity values are substituted in the calibration equation (4) and the true resistivity is obtained. Results obtained were listed in table 1.

Soil resistivity is one of the driving factors determining the corrosiveness of soil. The soil corrosiveness is classified based on soil electrical resistivity by the British Standard BS-1377 as follow:

- $\rho_E > 100 \Omega\text{m}$: slightly corrosive
- $50 < \rho_E < 100 \Omega\text{m}$: moderately corrosive
- $10 < \rho_E < 50 \Omega\text{m}$: corrosive
- $\rho_E < 10 \Omega\text{m}$: severe

Soil samples were subjected to visual identification and Chemical analysis Two curves (a) between ER v/s pH was plotted with regression coefficient, R^2 is 0.497 (Fig.8), and (b) curve between ion concentration and ER (Fig.9)

Conclusions:

- Soil resistivity decreases when compaction increases
- KM-162 and Hassan IP are moderately corrosive plots whereas all other plots are slightly or non-corrosive hence buried pipelines can be installed in these plots
- Soil with high pH value with more coarser particles (gravel, sand etc.) and less clay particles have more electrical resistivity
- All the samples with $\rho_E > 100 \Omega\text{m}$ have lesser concentration of ions. Whereas samples with $50 < \rho_E < 100 \Omega\text{m}$ (KM-162 and Hassan IP) have comparatively more ion content in their soil lattice

ACKNOWLEDGEMENT

We would like to express our sincere gratitude to Department of Civil Engineering, NITK for the support in doing the research work.

REFERENCES

- [1] Abu-Hassanein, Z.S., Benson, C.H. and Blotz, L.R. (1996). "Electrical resistivity of compacted clays." *Journal of Geotechnical Engineering, ASCE*, 122, 397-406.
- [2] Andy Anderson Bery and Rosli Saad(2012)."Clayey Sand Soil's Behaviour Analysis and Imaging Subsurface Structure via Engineering Characterizations and Integrated Geophysical Tomography Modeling Methods" *International Journal of Geosciences*, 3, 93-104
- [3] Bhatt, S. and Jain, P.K. (2014). "Correlation between electrical resistivity and water content of sand - a statistical approach." *American International Journal of Research in Science*,

6th International Engineering Symposium - IES 2017

March 1-3, 2017, Kumamoto University, Japan

Technology, Engineering & Mathematics, 6(2), 115-121.

[4] Fahad Irfan Siddiqui and Syed Baharom Azhar Bin Syed Osman(2012). "Comparing Electrical Resistivity Values of Sub-Surface Soil Obtained from Field and Laboratory Investigation"

[5] Kibria Golam (2011)."Determination of Geotechnical Properties of Clayey Soil from Resistivity Imaging (RI)" M.S. thesis, Univ. Texase Arlington, Arlington, TX.

[6] Samouelian, A., Cousin, I., Richard, G., Tabbagh,A. and Bruand, A. (2003). "Electrical Resistivity Imaging for Detecting Soil Cracking at the Centimetric Scale." Soil Science Society of America Journal, 67, 1319-1326.

[7] Sun-Young S.,Seung-Seo, H., and Jong-Sub, L.(2013),"Electrical Resistivity Of Soils Due To Cyclic Freezing And Thawing" ISCORD 2013: Planning for Sustainable cold Regions. ASCE,149-154

[8] Voronin, A.D.(1986), "The base of soil physics."Mosk. Gos. Univ., Moscow.

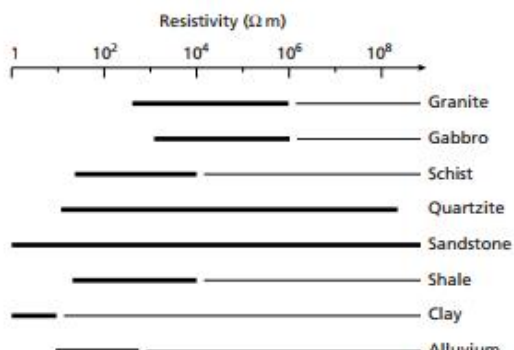


Fig. 1 Electrical resistivity value range

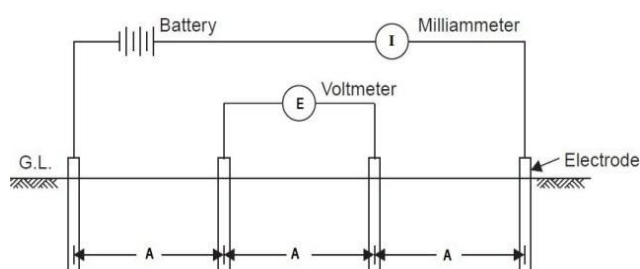


Fig.2 Wenner's Arrangement for Electrical Resistivity Test of Soil

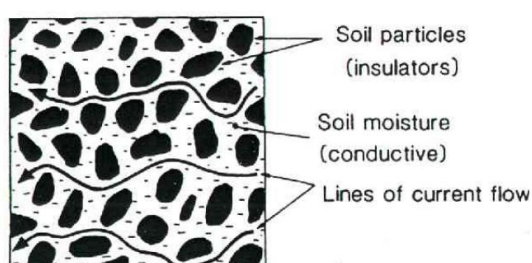


Fig.3 Soil structure showing electric conduction

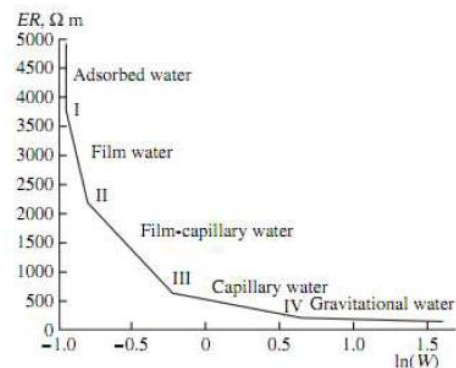


Fig.4 Relationship between soil moisture & ER (Voronin (1986))



Fig.5 Electrical resistivity laboratory testing arrangement



Fig.6 Soil filled inside resistivity box

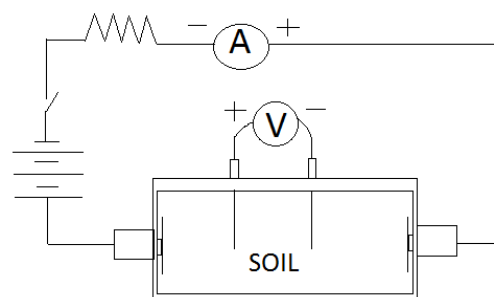


Fig.7 Resistivity box - schematic diagram

6th International Engineering Symposium - IES 2017

March 1-3, 2017, Kumamoto University, Japan

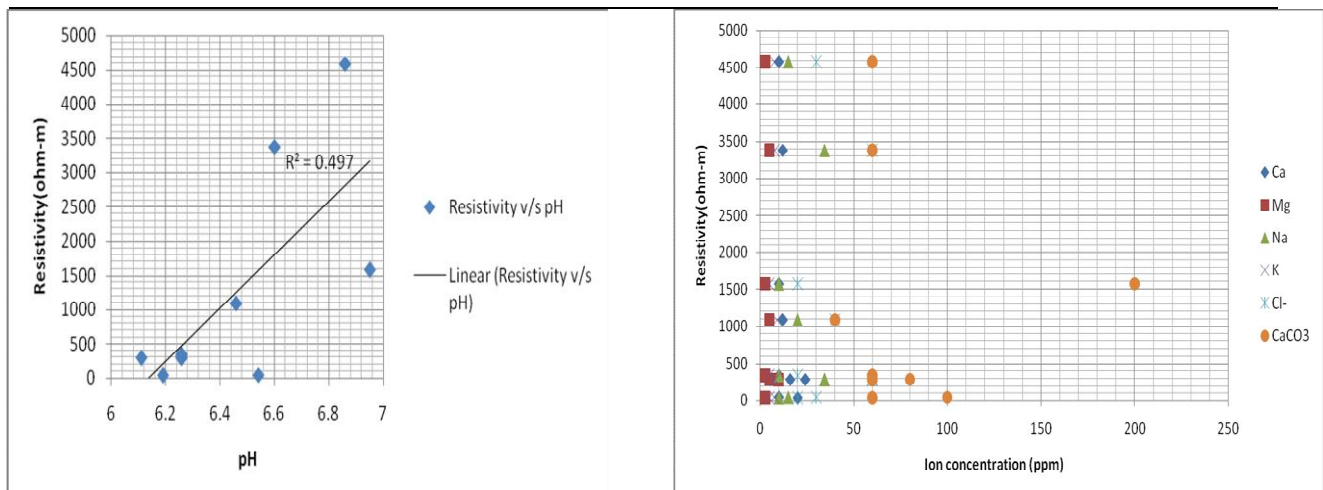


Fig.8 Resistivity v/s pH graph

Fig. 9 Resistivity v/s ion concentration graph

Table 1.Soil sample test results

DETAILS OF SOIL SAMPLE	SOIL TYPE	LAB ELECTRICAL RESISTIVITY (OHM-M)		pH	Ca ppm	Mg ppm	Na ppm	K ppm	Cl ⁻ ppm	Bicarbonate as CaCO ₃ ppm	Specific gravity G
		AT MAX. COMPACTION	AT 90% OF MAX. COMPACTION								
SV-03	Gravelly silty sand	4586	13310	6.86	10	2.45	15	7.5	30	60	2.62
KM- 52	Gravelly silty sand	1092.9	1789.8	6.46	12	4.85	20	9	40	40	2.65
KM-60	Gravelly silty sand	290.74	326.4	6.26	24	4.85	34.5	7.65	60	80	2.65
KM-179	Silty gravelly sand	344.28	499.76	6.26	10	2.45	10	4.6	20	60	2.66
Neriya IP	Silty sand	290.33	452.95	6.11	16	9.7	34.5	7.65	60	60	2.51
KM - 54	Silty sand	3381.6	4546.7	6.60	12	4.85	34.5	7.65	60	60	2.56
KM- 117	Silty sand	1574.4	2306.6	6.95	10	2.45	10	4.6	20	200	2.60
KM-162	Sandy clayey silt	37.4	40.11	6.19	20	2.45	10	4.6	20	60	2.57
Hassan IP	Sandy clayey silt	45.3	67.4	6.54	10	2.45	15	7.5	30	100	2.50

EFFECT OF BENCHING ON THE STABILITY OF SLOPES

Jolsna Narayan¹ and Sitaram Nayak²

- ¹ Department of Civil Engineering, National Institute of Technology Karnataka, Surathkal, Mangalore 575025, India. email:jolsna100@gmail.com Professor, Department of Civil Engineering, National Institute of Technology Karnataka, Surathkal, Mangalore 575025, India. email:snayak65@yahoo.co.in
- ² Department of Civil Engineering, National Institute of Technology Karnataka, Surathkal, Mangalore 575025, India. email:snayak65@yahoo.co.in
-

ABSTRACT:

The limit equilibrium methods for the analysis of slope stability has been in use in geo technical engineering for many decades. In this paper, the effect of benching on the stability of slopes is analysed by using the computer based geo technical software Oasys SLOPE 19.1. The factor of safety (FOS) has been determined using Bishop method. It is found that factor of safety increases with increase in bench width and increase in number of benches.

Keywords:

Slope stability, limit equilibrium, factor of safety,benching

1. INTRODUCTION

Slope is an exposed ground surface that stands at an angle with the horizontal. Slopes are required in the construction of highway and railway embankments, earth dams, levees, canals etc. Instability related issues in engineered as well as natural slopes are common challenges to both researchers and professionals. The evaluation of slope stability conditions becomes a primary concern. In the assessment of slopes, engineers primarily use factor of safety values to determine how close or far slopes are from failure. When factor of safety(FOS) is greater than 1, resistive shear strength is greater than driving shear stress and the slope is considered stable. When this is close to 1, shear strength is nearly equal to shear stress and the slope is close to failure, if factor of safety is less than 1 the slope should have already failed.

SLOPE 19.1 software allows the user to effectively perform the analysis and asses the stability of slopes.

2. ANALYSIS OF SLOPE STABILITY BY USING OASYS SLOPE 19.1 SOFTWARE

SLOPE19.1 is a leading software for analysing the stability of slopes. This program allows the users to choose various methods of analysis like Fellinius, Swedish slip circle analysis, Bishop method. For non-circular slip surface, Janbu's method can be used. Water pressure, material shear strength, surface loads and horizontal acceleration can be specified in this program. Robust numerical methods are used for the computation of results. Users can set up and run the program easily as the calculation is simple.

6th International Engineering Symposium - IES 2017

March 1-3, 2017, Kumamoto University, Japan

2.1. Theoretical framework of the proposed method

The slope is modelled in SLOPE19.1 Software. Material properties are initially assigned as : $\Gamma=17.5\text{KN/m}^3$, $\Phi=25^\circ$, $C=50\text{KN/m}^2$. inclination of slope, $i=45^\circ(1\text{H}:1\text{V})$. Then stratum is defined by giving the stratum coordinates. Slip surface is then defined. This generates a graphical input. User can choose among analysis methods like Swedish, Bishop and Janbu's methods. Once the analysis is complete, graphical and tabular outputs are generated.

For slope height, $H=3\text{m}, 6\text{m}$ and 9m , various cases of bench width ($0.2H, 0.3H, 0.4H$ and $0.5H$) are considered

Also cases of no bench, single bench, 2 bench and 3benches are analysed.

The material properties are same for all the above cases. Only the coordinates are varied accordingly.

2.2. Results and discussions

Figures shows a schematic diagram of 2D slope stability problem with slope height, $H=9\text{m}$. Input geometry for no bench, single, 2 and 3benches are shown.

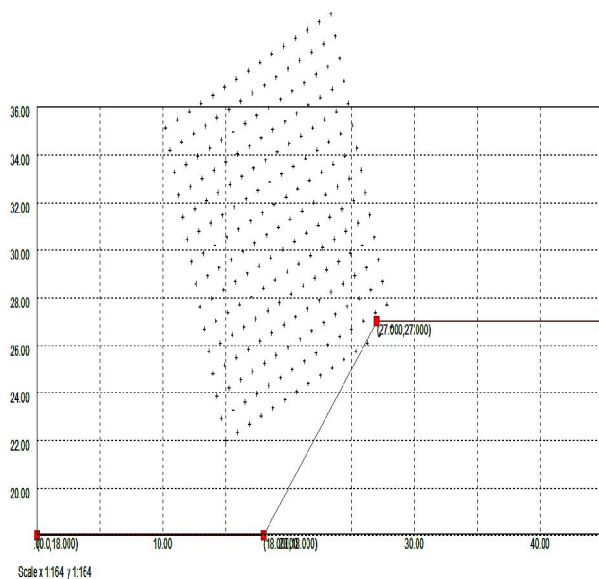


Fig.1 Graphical input for slope with no bench

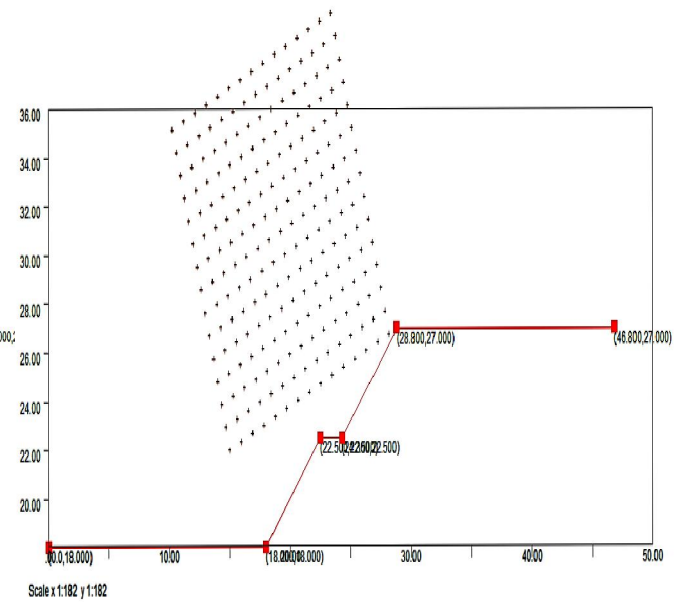


Fig.2 Graphical input for slope with single bench

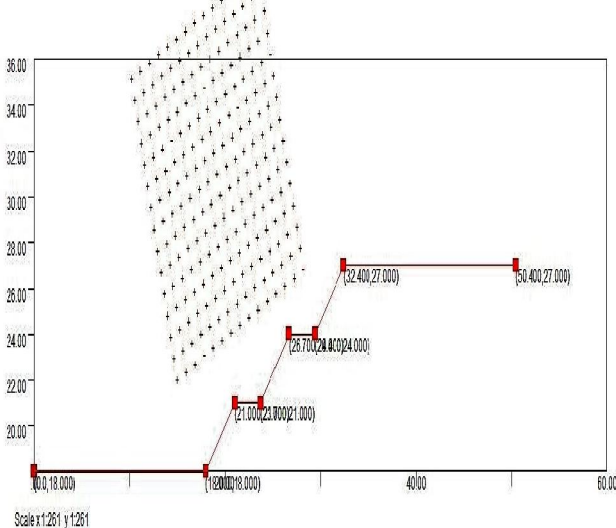


Fig.3 Graphical input for slope with two benches

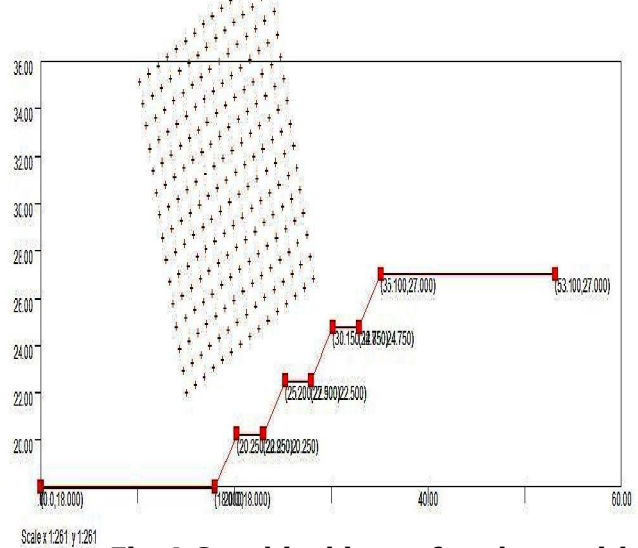


Fig.4 Graphical input for slope with three benches

6th International Engineering Symposium - IES 2017

March 1-3, 2017, Kumamoto University, Japan

Graphical output for no bench, single, two and three benches are shown below. The critical slip circle with coordinates of centre along with the factor of safety is labelled in the output.

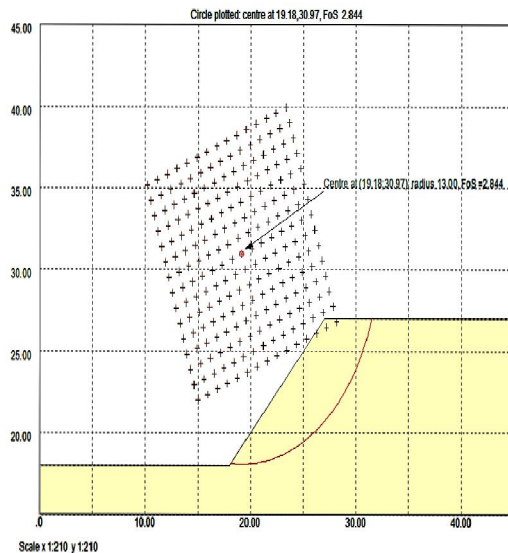


Fig.5 Graphical output for slope with no bench



Fig.6 Graphical output for slope with single bench

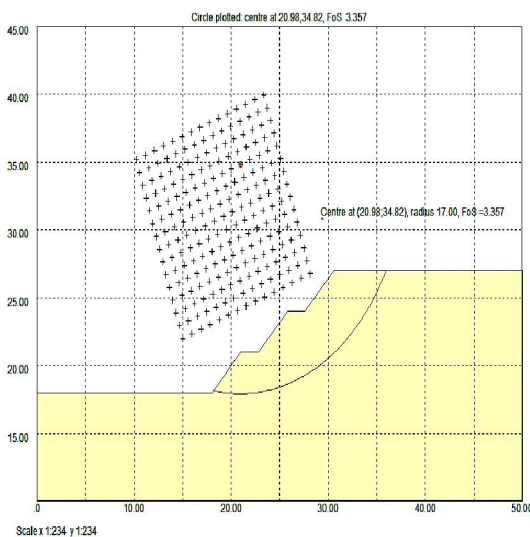


Fig.7 Graphical output for slope with two benches

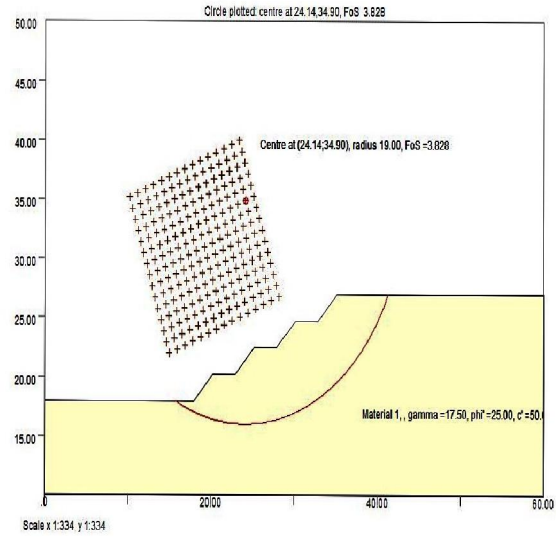


Fig.8 Graphical output for slope with three benches

6th International Engineering Symposium - IES 2017

March 1-3, 2017, Kumamoto University, Japan

From the analysis, factor of safety is obtained for all the cases. The results are tabulated and graphs are obtained as follows.

Table 1 FOS FOR SLOPE OF HEIGHT, H=3m				
BENCH WIDTH	NO BENCH	SINGLE BENCH	2 BENCH	3 BENCH
0.2H	6.787	7.262	7.575	7.757
0.3H		7.447	7.799	8.114
0.4H		7.686	8.042	8.418
0.5H		7.793	8.334	8.777

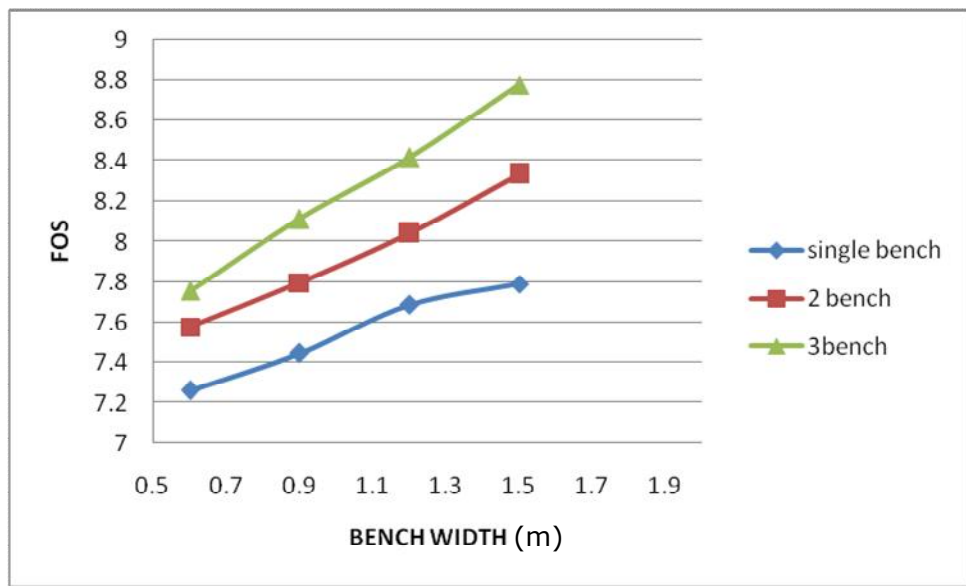


Fig. 9 variation of factor of safety with bench width for H=3m

Table 2 FOS FOR SLOPE OF HEIGHT, H=6m				
BENCH WIDTH	NO BENCH	SINGLE BENCH	2 BENCH	3 BENCH
0.2H	3.862	4.159	4.425	4.639
0.3H		4.353	4.688	4.948
0.4H		4.504	4.918	5.243
0.5H		4.676	5.123	5.534

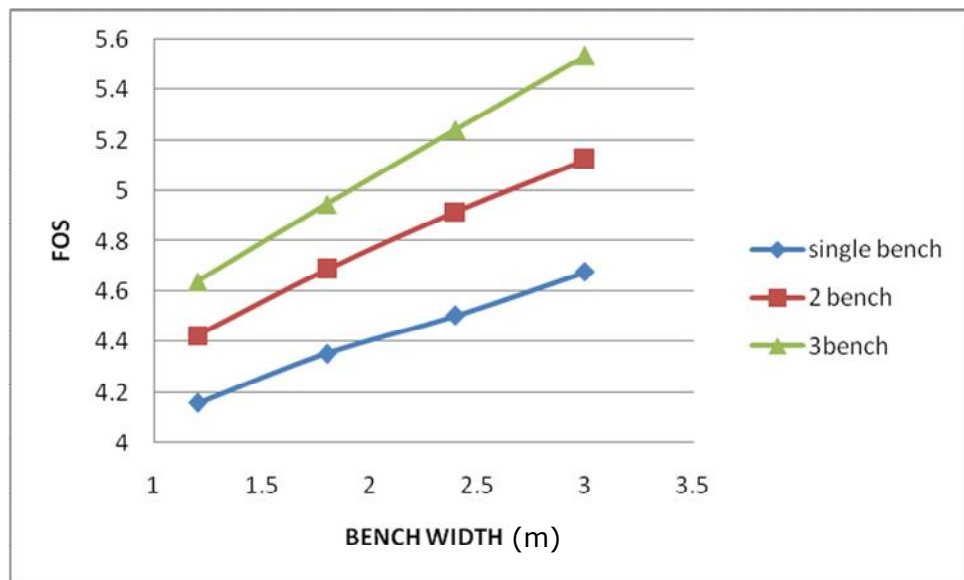


Fig.10 variation of factor of safety with bench width for H=6m

Table 3 FOS FOR SLOPE OF HEIGHT, H=9m				
BENCH WIDTH	NO BENCH	SINGLE BENCH	2 BENCH	3 BENCH
0.2H	2.844	3.12	3.357	3.531
0.3H		3.257	3.572	3.83
0.4H		3.426	3.799	4.109
0.5H		3.549	4.002	4.375

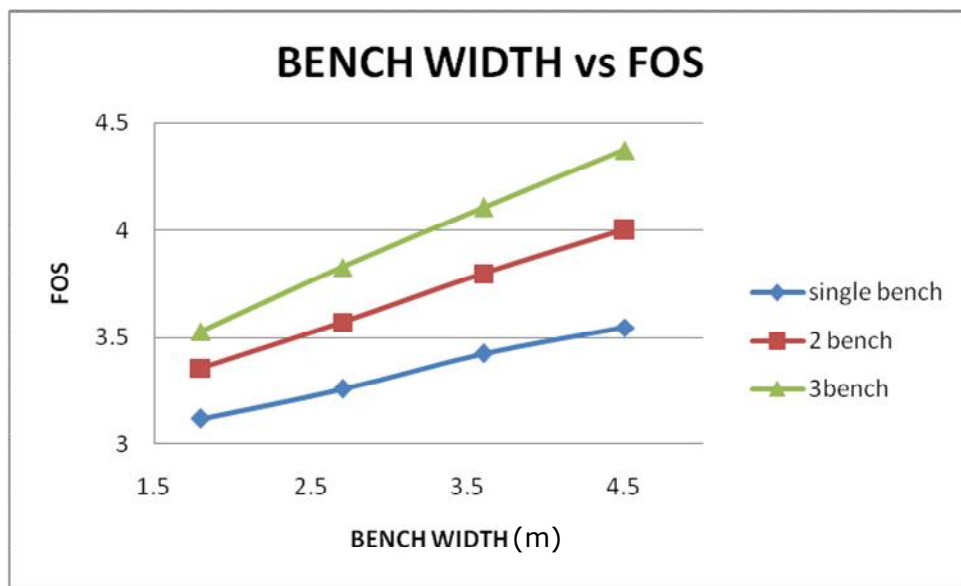


Fig. 11 variation of factor of safety with bench width for H=3m

It is found that factor of safety increases with increase in bench width and number of benches.

CONCLUSIONS

The following conclusions are deduced from this study:

- The study of slope stability problem by SLOPE19.1 provides more understanding considering failure mechanism and factor of safety for various cases.
- Factor of safety increases with the increase in bench width.
- Factor of safety increases with the increase in number of benches.

REFERENCES

- [1] Slope Tutorial Manual
<http://www.oasyssoftware.com>
- [2]Arora K R, (2003), Soil Mechanics and Foundation Engineering, 6th ed., Standard Publishers and Distributors, New Delhi.
- [3]Ammar Rouaiguia, and Mohammed A. Dahim, (2013), Numerical Modeling of Slope Stability Analysis, International Journal of Engineering Science and Innovative Technology, Vol.2, pp 533-542.
- [4]Prof. R. K. Sharma, Vishal Kumar, Nandika Sharma, Ajender Rathore,Slope Stability Analysis Using Software GEO5 and C Programming,International Conference on Chemical, Ecology and Environmental Sciences (ICEES'2012) march 17-18, 2012 Bangkok
- [5]Bishop A W, (1955), The Use of Slip Circle in the Stability Analysis of Slope, Geotechnique, Vol.5, pp 7-17.

Effect of pile aspect ratio on geogrid reinforced piled embankments

Sreelekshmy. S¹, Radhika. M. Patel², B. R. Jayalekshmi³ and R. Shivashankar⁴

- 1 Department of Civil Engineering, National Institute of Technology Karnataka, Surathkal, Mangalore 575025, India. email:lechusree93@gmail.com
 - 2 Department of Civil Engineering, National Institute of Technology Karnataka, Surathkal, Mangalore 575025, India. email:radikagmpatel@gmail.com
 - 3 Department of Civil Engineering, National Institute of Technology Karnataka, Surathkal, Mangalore 575025, India. email:br.jaya@gmail.com
 - 4 Department of Civil Engineering, National Institute of Technology Karnataka, Surathkal, Mangalore 575025, India. email:shivashankar.surathkal@gmail.com
-

ABSTRACT: Population explosion demands an increasing need for infrastructure development which forces engineers to construct roads on loose sands and soft clayey deposits which cannot sustain external loads without undergoing large deformations. In the case of bridge embankments built on these soils, maintaining the surface level between the bridge and the embankment has always been a cumbersome task. Among all the available ground improvement techniques, geogrid reinforced piled embankment system (GRPES) is preferred nowadays due to its reliability. A 4m high embankment having 20m crest width with side slope of 1V:1.5H supported over a 25m soil stratum has been considered with two types of foundation soil namely, soft clay and loose sand. 2D finite element analysis is carried out to study the effect of pile aspect ratio (in the range of 6 to 18) on settlement behavior of GRPES. It has been identified from the results that the pile aspect ratio is a significant parameter in settlement reduction of GRPES.

Keywords: Aspect ratio, pile foundation, geogrid reinforcement, finite element analysis.

INTRODUCTION

The boom in industrial developments over the past few decades have resulted in a change in the infrastructural façade of the world. This has also lead to the modification of transportation facilities all over the world. Roads and bridges are being built over every desirable or undesirable soil type. However, the construction of bridge embankments under problematic soils is a cumbersome task for engineers due to poor soil quality. Post-construction settlements at foundation level becomes an unavoidable issue due to low bearing capacity, insufficient shear strength and high compressibility of soft soil. The settlements further lead to instability of embankment also. Many techniques have been used in the past to tackle this crisis.

One of the most widely known technique is geogrid reinforced piled embankment system (GRPES). It consists of piled embankments which is reinforced with geogrid and thereby eliminating pile cap which makes GRPES economic as well as efficient. The main advantage of this construction is that it enables the embankment to be built in a single stage without prolonged waiting periods and also gives significant reduction in total and differential settlements. This has been used in many cases along with bridge construction. Although many studies has been conducted on this, the contribution of the pile aspect ratio in improving the efficiency of the system has not been looked into. Also, the behavior of the system in different types of soil need also be assessed. Hence, the main objective of the study is to analyse the effect of pile

aspect ratio on improving the efficiency of GRPES. Also, to study the change in behaviour of the pile system in GRPES for two different soil conditions.

METHODOLOGY

A gravelly embankment of height 4 m with 20 m crest width constructed over 25 m stratum is considered for the study. Two types of problematic strata are considered for the study namely, soft clay and loose sand. A hard stratum is assumed to exist below the clay layer. A slope of 1H:1.5V is considered. A geogrid layer is placed above the pile heads extending throughout the width of the embankment. Fixing the diameter of the piles as 1m with 3m spacing, the length is varied for analysing the effect of pile aspect ratios of 6, 9, 12, 15 and 18. Also, a fixed pile is also considered wherein the hard stratum is assumed to be limestone and a seating depth of 50mm is also provided into the stratum. The embankment geometry is shown in Figure 1.

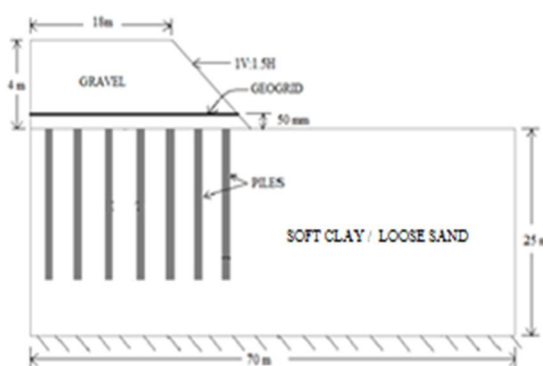


Figure 1. Embankment Geometry

Material properties

Detailed material parameters and the constitutive models used have been listed in Table 1. The geogrid was modelled as an isotropic elastic material with a tensile modulus of 1,500kN/m. The pile was modelled with an isotropic non-porous material with a Young's modulus of 25GPa and a Poisson's ratio of 0.15 with unit weight of 24kN/m³. The properties of the hard stratum is brought into analysis only in the case of fixed piles. The Poisson's ratio of limestone is taken as 0.25 and uniaxial compressive strength is 50 MPa.

Table 1. Soil Parameters

Property	Gravel	Soft Clay	Loose Sand	Lime-stone
Material model	Hardening soil	Soft soil	Hardening Soil	Hoek-Brown
Drained	Yes	No	Yes	Yes
Unit weight (kN/m ³)	19	17	17	24
Initial void ratio	0.5	1.0	0.5	0.5
Modulus of elasticity (MPa)	200	10	350	2500
Modified compression index	-	0.05	-	-
Modified swelling index	-	0.01	-	-
Cohesion (kN/m ²)	1.0	1.0	0	-
Friction angle	30	25	33	-
Dilatancy angle	0	0	3	35
Change in permeability	1.10^{15}	0.2	1.10^{15}	-

Boundary conditions

Symmetry of the model enabled performing the analysis only for one half of the geometry. For the model, the left boundary was fixed (or closed) as it was the line of symmetry. All the remaining boundaries were kept open for the dissipation of excess pore water pressure. The interface elements of were provided at a width of 250mm on one side of the pile for pile-soil interaction.

Finite Element Modeling

Finite element analyses were performed using PLAXIS 2D software. Due to the symmetry, only one half of the embankment geometry was considered for the analysis. The whole system was modelled using plane strain 15 noded

element. Fine meshing was used for the analysis. Vertical drains were provided to induce consolidation to a minimum excess pore water pressure of 1 kN/m^2 . The geogrid layer was horizontally placed at 500 mm above the pile head. Ground water table was assumed to exist beneath the clay layer. The geogrid layer extended to the full length of the embankment. The negative interface was provided for pile-soil interaction. The embankment was modelled as two layers of 3 m each. The total analysis consisted of 4 phases and an initial phase. The clay layer was allowed to consolidate while the embankment was being constructed upon it. Consolidation was carried out till a minimum excess pore water pressure of 1 kN/m^2 . The lengths of the pile were varied to see the changes in the settlement developed in the soil. The same analysis was carried out by substituting loose sand in place of clay. Finite element model of embankment in PLAXIS 2D after meshing is shown in Fig.2.

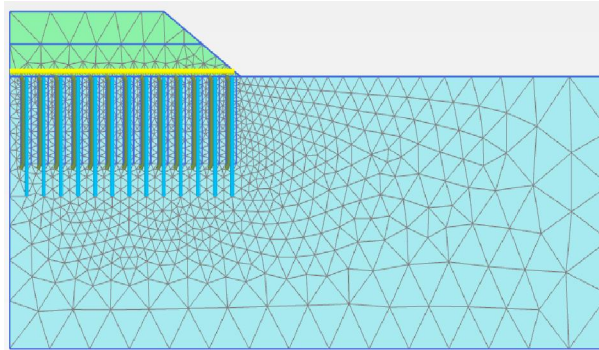


Figure 2. Finite element model of the embankment in PLAXIS 2D.

RESULTS AND DISCUSSION

Settlement of embankment surface after consolidation to minimum excess pore water pressure was analysed for different pile aspect ratio and soil condition. The analysis showed considerable settlement of the embankment. The total settlement of the embankment has been analysed and discussed. Figure 3 shows the deformed embankment after consolidation to minimum excess pore water pressure dissipation, with pile aspect ratio of 9.

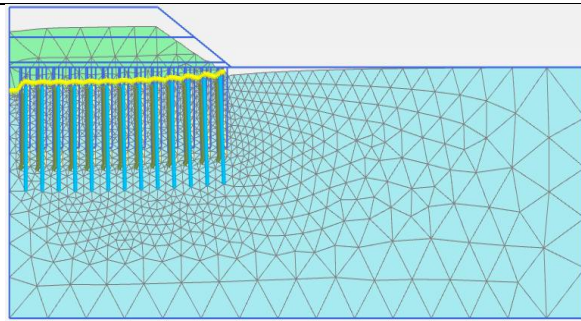


Figure 3. Settlement of embankment after consolidation

The settlements of the embankment for the two soil conditions have been represented in figure 4.

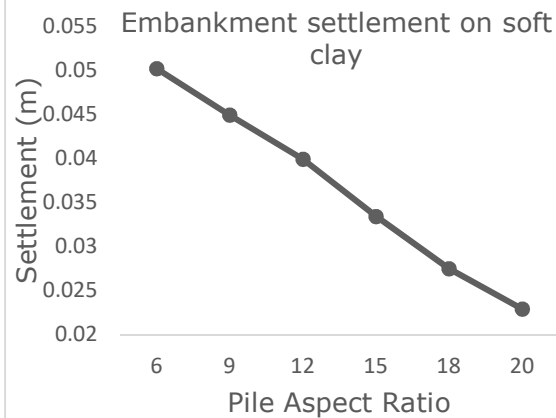


Figure 4(a). Embankment settlement on soft clay

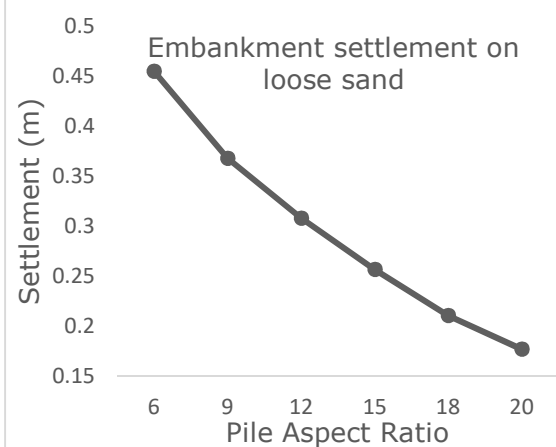


Figure 4(b). Embankment settlement on loose sand

From the graphs, it can be easily noticed that the as the pile aspect ratio increases, the settlement decreases. Settlement in GRPES followed the same trend in both the soil conditions. It was also clear that long piles reduce settlement more effectively.

6th International Engineering Symposium - IES 2017

March 1-3, 2017, Kumamoto University, Japan

The fixed pile condition had a pile aspect ratio of 20. From the graphs, it was clear that the fixed pile is most effective in reducing overall settlement than the rest of the floating piles. While comparing the behaviour of GRPES with different soil conditions, it was seen that the settlements in sand is 8 times more than the settlements in clay. This value can vary slightly with respect to the density of sand used for the analysis. However, during analysis it was found that piles with aspect ratio 20 which did not have a seating into the limestone tend to move up towards the embankment. This might be associated to the development of positive skin friction in the piles. So, it should be made a practise to give seating of at least 500mm or more for better functioning of fixed or end bearing piles. According to IS 2911 (Part 1), it can be seen that the piles with aspect ratio 6 and 9 belong to the category of short piles while, those with aspect ratio of 15 and 18 belong to long pile and aspect ratio of 12 belongs in intermediate pile. Hence, it can also be inferred that long piles are more efficient in reducing settlement. On a comparison with long floating and end bearing piles, the settlement reduction is more given by end bearing piles. The end bearing piles were able to reduce 16% more settlement than the long piles with aspect ratio 18. Thus, we can say that pile aspect ratio has a direct relation with settlement reduction in GRPES.

CONCLUSIONS

The GRPES system was analysed for the effect of pile aspect ratio as well as its behaviour in two types of soil conditions. It can be inferred that the pile aspect ratio plays an important role in improving the efficiency of GRPES.

- The larger the pile aspect ratio, the settlement will be lesser, while also implies that the system will be more efficient. As the pile enters into the end bearing condition, the efficiency seems to become even more.
- Considering the two soil conditions, the maximum settlements of the embankment in loose sand is 8 times larger than the settlements in soft clay. By ensuring achievement of pre-calculated density at different stages of

construction over loose sand, the embankment settlement may be controlled to a large extent in practical cases.

REFERENCES

- [1] Ariyaranthe, P., Liyanapathirana. (2015). Review of existing design methods for geosynthetic-reinforced pile-supported embankments. The Japanese geotechnical society. 55 (1), 17-34.
- [2] Bhasi, A., Rajagopal, K., (2013). Study of the effect of pile type for supporting basal reinforced embankments constructed on soft clay soil. Indian Geotech. J. 43 (4), 344-353.
- [3] Bhasi, A., Rajagopal, K.. (2014). Geosynthetic-reinforced piled embankments: comparison of numerical and analytical methods. Int. J. Geomech. ASCE. 15(5):04014074.
- [4] Bhasi, A., Rajagopal, K.. (2015). Numerical study of basal reinforced embankments supported on floating/end bearing piles considering pile-soil interaction. Geotextiles and geomembranes 43 (2015). 524-536.
- [5] IRC: 113-2013. Guidelines for the design and construction of geosynthetic reinforced embankments on soft subsoils.
- [6] IS 2911 (Part 1/Sec 1): 2010. Design and construction of pile foundations – Code of practice.
- [7] Joseph E. Bowles (1996). Foundation analysis and design. McGraw-Hill International editions.
- [8] Liu. H. L, Charles. W. W and K. Fei (2007). Performance of geogrid reinforced and pile-supported embankment over soft clay: Case study. ASCE Journal of Geotechnical and Geoenvironmental Engineering, Vol. 133, No. 12, ASCE, New York.
- [9] Syawal Satibi. (2009). Numerical analysis and design criteria of embankments on floating piles. (A PhD thesis submitted to the Universitat of Stuttgart, Stuttgart, Germany).

Development of decision support system for dewatering system selection for water supply projects

Sooraj Balakrishnan P ¹, M K Nagaraj²

- 1. Department of Civil Engineering, NITK, Surathkal, Mangalore, India, Pin:575025,
email: soorajbalakrishnan@gmail.com, sbp@Intecc.com*
 - 2. Dept. of Applied Mechanics and Hydraulics, NITK, India*
-

Abstract This paper will be describing the formulation of a decision support system for the selection of dewatering system for water supply projects which is developed on a software based platform so that the user will describe his/her requirements and the system will help in identifying the best dewatering method. It uses Simple Multi Attribute Rating Technique (SMART) for decision making and the attributes taken are efficacy and efficiency. The main parameters which govern the selection of dewatering system are identified as depth of water table, depth of excavation, soil condition, permeability of ground, excavation size, proximity to adjacent structures and project characteristics. The developed system will be validated on some water supply projects in India which have used a dewatering system. The method is quite encouraging and results can be applicable to varied site conditions. The success rate of the above sited method is quite high. In depth study helps a construction manager to take an appropriate decision for dewatering at site which will contribute in early completion of the project and also aim towards green technology.

Keywords: dewatering, decision support system, SMART

1. Introduction

1.1 Background of the paper

The impact of ground water on any construction work can be enormous. Water affects the design of the structure, construction procedure as well as to the overall cost of the project. We have seen water problems of unexpected severity cause major delays, often requiring drastic re-design. Study of water table and its effects have become a major concern thereafter. Removal of water or preventing the entry of water into the site could be done mainly by four different ways. Sump pumping is a method in which we will do the dewatering by allowing the water to enter into the site and then it will be removed by using a pump. In exclusion methods, we will construct structures which are permanent or temporary such as diaphragm walls,

sheet piles etc. to avoid the entry of water into the site. Grouted cut off method is another way which is similar to that of exclusion methods. Here we will inject chemicals such as cement or bentonite so as to form a barrier for the entry of water. Pre drainage method is the one having most significance because of its applicability in most of the practical cases.

A lot of measures are available to prevent the entry of water into the construction site as well as to remove out the entered water. The applicability of these methods is varying and depends upon a lot of factors. One method may fetch excellent results in a set of condition where as other methods may not. So it is necessary to find out the criteria required for each dewatering system.

1.2 Objectives

The main objective of the paper is to create a Decision Support System (DSS) for the selection of dewatering system for water supply projects. The paper explains the importance of DSS, various factors that affect the development of DSS, and how DSS could be developed. It also explains the limitations of this method. The developed system will be validated in a real world scenario.

1.3 Solution methodology

Required data is collected from various journals, text books, Indian Standard Codes and from experienced professionals. Multi Attribute Rating Technique will be used for decision making. All the factors that affect the selection of dewatering system will be tabulated and their relative importance will be found out. This is assessed by surveying professionals. Of course this cannot be found out accurately, and will be varying from person to person. But taking the sample size large, the chances of error can be reduced. The information gathered is fed into the system. A programming language will be used to create a user friendly platform so that for the site conditions and requirements given by the user, the DSS tool will give the best possible way. The developed system will be validated on live projects.

2. Literature Review

2.1 Development of dewatering system

An early application of pre-drainage was for the construction of Kilsby tunnel. Robert Stephenson encountered quick sand, and after some false starts he succeeded in stabilizing the sand with a

series of 13, engine driven well pumping 6800L/min. It was an early application of wellpoint system. The conclusions made by the Engineer are quite in agreement with modern hydrologic concepts. From that point, a number of engineers were started the investigation of ground water control by means of pre-drainage.

Pre-drainage with wells continued to be applied in the nineteenth century, especially in Europe. But wells are normally successful only in favorable aquifer situations and no doubt there were many failures. At the end of the century, well points began to appear. They were used successfully in clean, fine to medium sand in Gary, Indiana in 1901, and in similar soils in Atlantic City, New Jersey in succeeding years.

In 1925, Thomas Moore, encountered difficult water condition on a sewer project in New Jersey. The soil was very fine silty sand to sandy silt and driven well points clogged up immediately. Moore introduced several innovative concepts; he used well points with high infiltration area, he jetted the well points into position, thus providing a large hole with clean sides, and he backfilled the hole around the well points with selected filter sand. The fine grained soils were efficiently stabilized.

Moore's success demonstrated that pre drainage under very difficult condition were practical and dewatering techniques began to develop rapidly. The ejector system for dewatering was adapted from the domestic jet pump in the late 1950s. It is a most effective tool in certain job situations.

With appropriate theory and practical judgment, effective dewatering can be accomplished under almost any field condition. However, because of the uncertainties of the underground, any proposed dewatering program must be flexible, with provisions for modification if unexpected conditions are encountered.

2.2 Controlling ground water

At present, there are four basic methods for dealing with groundwater in a construction excavation: exclusion, grouted cut-offs, pumping, and pre-drainage. Each has its own advantages and disadvantages with respect to specific projects and site conditions. To make a proper selection of a dewatering system, the designer should usually consider the following parameters:

- (a) Proposed methods of excavation and ground support.
- (b) Type of soil.
- (c) Excavation depth.
- (d) Excavation size.
- (e) Depth of water below ground level.
- (f) Duration of excavation.
- (g) Proximity of the nearest structure.
- (h) Required depth of dewatering
- (i) Available equipments

Various methods that are currently in practice for dewatering in India are listed below.

2.2.1 Pumping method

Pumping is the process of removing water that has entered an excavation. It is usually the least expensive method from the standpoint of direct dewatering cost. It could be sumps, drains or open pumping. Under favorable conditions, it is a satisfactory method. One of the popular methods is sump pumping, by which sumps are usually sited at the corners of excavations below the general excavation level, and made big enough to hold sufficient water for pumping. This keeps the excavation floor relatively dry. A pump is provided for each sump and connected to a discharge pipe.

2.2.2 Exclusion method

The methods include

- (a) Sump pumping outside the excavation
- (b) Well point system
- (c) Staged well point system
- (d) Deep well system
- (e) Ejector system
- (f) Electro osmotic dewatering

In exclusion methods of dewatering, the requisite control is achieved by forming a membrane, temporary or permanent, around the area of excavation and down to a suitable cut-off stratum for the purpose of excluding water. The following are some of the exclusion methods:

- (a) Steel sheet piling.
- (b) Diaphragm wall.
- (c) Piles.
- (d) Slurry walls and trenches.
- (e) Ground freezing.

2.2.3 Grouted cut-off method/ Grout curtains

Grouting is defined as the injection of materials into soil or rock to accomplish a change in properties. Compared with exclusion method, it will make permanent changes in the soil properties which may make the soil strata impermeable permanently. Grouting cuts off water flow, rendering the soil or rock impermeable. It can also reduce soil or rock permeability by introducing grout into more pervious zones. So in the design stage itself, he expected after effects should be taken care of. The Grouted cut-off methods include:

- (a) Cement grout.
- (b) Bentonite-cement grouts.
- (c) Chemical grouts.

2.2.4 Pre-drainage methods

Here the aim is to lower the water table level so that it will not affect the excavation process. As long as the pre drainage stops, ground will be recharged again.

3. Development of DSS

A decision support system has been developed by some researchers in Singapore for dewatering system selection. The parameters taken were according to the conditions of the country. The procedure for this study also follows similar pattern. The main limitation of which is the absence of cost and equipment database. The same does not cover the feasibility of combination methods. Electro osmotic dewatering is a new advancement in the construction industry which will be mandatory for clayey soils. That method was also not incorporated by the researchers. So this study will be overcoming the above limitations as well as will be applicable exclusively for water supply projects in India.

3.1 Data from the user

The following details are mandatory from the user

- (a) Soil permeability.
- (b) Extent of the area to be dewatered.
- (c) Depth of the water table and the amount by which it has to be lowered.
- (d) Proposed methods of excavation and ground support.
- (e) Proximity of existing structures.
- (f) Available equipments.
- (g) Approximate cost of dewatering.
- (h) Duration of construction.

The following are the factors that primarily governs the selection of dewatering system

- (a) Soil type.
- (b) Excavation depth, depth to which water is to be lowered
- (c) Proximity of the nearest structure.
- (d) Level of water table
- (e) Permeability of the ground.
- (f) Extend of dewatering

3.2 Decision making

There are 15 alternatives for any given 6 set of conditions. The suitability of each method for different field condition will be analyzed. For decision making factors ranking values will be given which varies from zero to one. The value zero for any method means, the particular dewatering system is highly unsuitable for that particular set of conditions. For example, when the excavation depth is very less construction of diaphragm walls will not be feasible. So its ranking value for that condition will be near to zero. The ranking values may be classified as

- 0 – highly unsuitable
- 0.25- Unsuitable
- 0.50- Moderately suitable
- 0.75- Suitable
- 1.0- Highly suitable

In the above case the ranking value of diaphragm walls for low excavation depth will be anywhere from 0 to 0.25. The exact value will be calculated from the survey taken from experts who are working in the field of dewatering.

In the same way for all the site conditions, ranking value for each method will be calculated. From the practical experience, it could be concluded that if the depth of water table to be lowered is greater than 6m, deep well dewatering system is the best available followed by staged well points. So in that case deep well dewatering system will be having a ranking value in the range 0.75-1.0. For sandy soils sump pumping method will fetch excellent result. So its value will also lies between 0.75 to 1. In this regard for a set of conditions, the utility value of a particular dewatering system will be calculated by summing up the ranking value of that system for each individual parameter. Another drawback while adding directly is we didn't give weightage to each parameter. Of course soil characteristics will be having maximum weightage. For a total weightage of 100, each of this individual parameter will be given certain weightage and utility value

will be sum of (ranking value x weightage of parameter).

Time constraints and financial constraints have not been used in the present study. These also need to be incorporated. For that the maximum possible duration available for dewatering in terms of total project duration will be considered. In the same way the dewatering cost permitted in terms of total project cost will be considered. The weightage will be calculated by considering these factors and based on perception and experience of expert professionals.

4. Conclusions

It is possible to identify the most apt dewatering system by using the decision support system. By summing up all the three individual ranks as explained above will show the best dewatering system possible for that set of data. So it is possible to generalize the above method to develop a user friendly decision support system on a software based platform. Finally the system will be validated on live projects. The outcome of the study will help PMC and site engineers to plan any dewatering system based on site condition

and this will minimize cost and time over run of the project. This will also help in effective planning which will ensure safety of the construction and move a step ahead towards green construction.

References

- [1] Shou Qing Wang, Yong Ping Wee, George Ofori. DSSDSS: a decision support system for dewatering systems selection
- [2] J. Patrick Powers, Christine J. Herridge. Construction Dewatering and Groundwater Control: New Methods and Applications
- [3] Toll DG. Do geotechnical engineers need expert systems? Journal of Ground Engineering 1990
- [4] Prof. dr. ir. F. De Smedt . GROUNDWATER HYDROLOGY
- [5] Tony Starfield. Simple Multi-Attribute Ranking Technique SMART, recorded: 2005
- [6] Barry S. Chen, Roy E. Jensen, LHG. case studies of dewatering and foundation design: retail warehouses in Taiwan

Development of methodology for deactivation modeling of *Citrobacter* by UV radiation

Priti Deshpande¹ and C.P. Devatha²

¹ Department of Civil Engineering, National Institute of Technology Karnataka, Surathkal, Mangalore 575025, India. email: pritidd93@gmail.com

² Department of Civil Engineering, National Institute of Technology Karnataka, Surathkal, Mangalore 575025, India. email: devathafce@nitk.ac.in

ABSTRACT: The effluent from conventional wastewater treatment plant contains pathogenic bacteria which cannot be removed in the secondary treatment only and hence the disinfection is carried out. The disinfection by UV radiations overcomes the ill effects of chlorination. The paper aims at modeling of deactivation of *Citrobacter*, a gram negative coliform bacteria by ultraviolet disinfection technique. The model concept is based on hypothesis that specific bacterial population possesses its individual resistance power. The parametric model will be based on Chick's-Watson's equation for decay with the variable intensity of UV radiation and the time of exposure. The optimum UV dose and the time of exposure can be found out using this methodology for effective deactivation of *citrobacter*.

Keywords: *citrobacter*, disinfection, Chick's-Watson's equation

INTRODUCTION

The whole world is facing water crisis since past few decades. Unsafe drinking water causes water born diseases and serious health issues and many times it leads to death of the victim. The constraints on resource availability lead to reuse and recycle of wastewater effluents after proper treatment. The areas with little or almost zero access to safe drinking water, recycling of the used water with the treatment achieving the safe drinking water quality standards can be the best option. Of course, it depends on consumer's tendencies towards drinking the recycled water. The wastewater effluents can also be reused for agricultural, urban and industrial purpose.

The domestic waste water treatment with only secondary treatment cannot match with microbiological quality criteria for the reuse of wastewater. To achieve microbiological quality, disinfection is necessary. Various types of disinfections are in practice such as chlorination, ozonation, and with UV radiation. As the

chlorination leads to formation of carcinogenic compounds in water, it is being ruled out in most of the countries. The advance oxidation processes like UV give the best results overcoming the ill effects of chlorination.

The wastewater treatment plant effluent still contains pathogenic bacteria which can be removed by UV radiation. The resistivity powers of different bacterial groups are different.

Bacteria can be differentiated according to their cell wall properties by the means of gram straining technique. The coliforms which indicate the presence of faecal contamination are gram negative bacteria with cytoplasmic membrane, a thin peptidoglycan layer and an outer membrane containing lipopolysaccharide. *E coli* is the most used and studied indicator of fecal contamination. *Citrobacter* is another member of coliform group can be found out in wastewater.

Citrobacter can be found out in animal and human intestine and also in soil, water and wastewater. According to Joao P.S. Cabral (2010) *citrobacter* is present in low

6th International Engineering Symposium - IES 2017

March 1-3, 2017, Kumamoto University, Japan

numbers in the human intestine and its presence in natural waters makes it less effective indicator of faecal pollution. *Citrobacter* normally cause urinary tract infections, blood stream infections, intra abdominal sepsis, and pneumonia and other neonatal infection as stated by Public health agency of Canada. Though *E coli* is predominantly found in feces, it makes up only one third portion of coliforms found in raw wastewater while other two third belong to genera *Citrobacter* along with *Klebsiella* and *Enterobacter*. Nearly about 40 to 50 percent of total coliforms are *Enterobacter-Citrobacter* obtained in secondary treatment effluent according to study by A. W. Halley (1977). As wastewater effluents are released in water resources, *Citrobacter* concentration increases in it.

This particular study is based on deactivation of *Citrobacter* with help of UV radiation technique.

Nowadays UV-C radiation is accepted as effective disinfection technique. The reasons are less contact time, no ill effects after application, no chemical consumption and high reliability. It is studied by Brahmi and Hassen (2012) that the cell destruction occurs by rearrangement in DNA and hence inhibiting the growth. The efficiency of the disinfection depends on cell structure, intensity of radiation and the time of exposure.

MATERIALS AND METHOD

A low pressure mercury lamp generally emits UV-C radiation with wavelength of 254 nm. This wavelength possesses properties for effective deactivation of microorganisms but will not affect on chlorine, heavy metals and other organic compounds (Brahmi and Hassen, 2014). For the experimental procedure, a laboratory based UV chamber with variable intensity source of UV-C radiation can be arranged. UV intensity meter can be used for measuring intensities of radiation emitted from the source.

This particular study is dealing with *Citrobacter* and hence to obtain its population, either pure cultures can be

used to seed the water or the strains can be isolated from the effluent of secondary wastewater treatment. The cultures can be prepared in nutrient medium and can be incubated at 35°C for 18 to 20 hours. Then the growth can be collected with centrifugation and after washing twice with distilled water, the cultured organisms can be seeded into sterilised wastewater so as to obtain the count of *Citrobacter* about 10^4 to 10^6 CFU/100ml.

Then seeded wastewater sample is to be exposed to UV radiation in laboratory UV chamber. The convenient and suitable intensity of UV radiation can be chosen and kept constant while the time of exposure can be varied as 5, 10, 15, 30 seconds and then 1, 5, 10 and 15 minutes for a particular intensity of UV radiation. This is to be repeated for two more intensities. Then for a certain time of exposure, intensities are to be varied from 50 to $300\mu\text{W}/\text{cm}^2$ and similarly for two more constant time of exposure procedure is to be repeated. Intensities can be measured by intensity measuring device. Considering the minimum and maximum log survival and convenience, ranges can be modified. *Citrobacter* count before exposure (N_0) and after exposure (N_t) is to be measured.

For bacterial count the procedure can be as described follows. The samples (before and after exposure) are placed on Petri dishes of 90 mm diameter containing MacConkey agar and incubated for 24 hours at 37°C. The pink colonies will form on MacConkey agar as *Citrobacter* is lactose fermenting bacteria. The pink colonies will give the count and can be presented as CFU/100ml (Fig.1). There are very less chances that *E coli* will also form colony on plate and the colony will be of pink colour. So just for confirmation sake organism from a colony can be streaked on Simon's Citrate Agar and incubated for 24 hours at 37°C. The deep blue colour on the streaked part will show positive result and hence the confirmation of *Citrobacter*.

6th International Engineering Symposium - IES 2017

March 1-3, 2017, Kumamoto University, Japan

MODELING

The disinfection process follows first order kinetics representing mortality versus time data with straight line or semi logarithmic graph. This is Chick's law of disinfection. The modified Chick's law, known as Chick-Watson's law tells about the concentration of the disinfectant (eq.1).

$$\frac{N_t}{N_0} = e^{-kC^n t} \quad (1)$$

Where,

N_t = Number or concentration of organisms at time t .

N_0 = Number or concentration of organisms at initial time.

C = concentration of disinfectant

t = time of exposure

k =decay constant

The microbial exposure to UV radiations results in similar way of disinfections by heating or ozonation. (Mitscherlich, E. and E.H. Marth 1984) The first order equation for microbial decay with UV radiation is given as eq.2

$$\frac{N_t}{N_0} = e^{-kt} \quad (2)$$

K = rate constant ($\text{cm}^2/\mu\text{J}$)

I =UV intensity ($\mu\text{W}/\text{cm}^2$)

t =time of exposure (seconds)

Where, $1 \mu\text{J}=1 \mu\text{W}\cdot\text{s}$.

Here, varying one of the two parameters i.e. intensity and the time of exposure while keeping another parameter constant, the change in the rate constant can be studied. According to that, one can get information about how the log survival is changed with only change in either intensity or time of exposure.

We can have two equations here.

When intensity is constant,

$$\ln \frac{N_t}{N_0} = -k_1 It \quad (3)$$

Where k_1 =time dependent rate constant ($\text{cm}^2/\mu\text{J}$)

When time of exposure is constant,

$$\ln \frac{N_t}{N_0} = -k_2 It \quad (4)$$

Where k_2 = intensity dependent rate constant ($\text{cm}^2/\mu\text{J}$)

Considering eq.3, sets of observation are to be formed with constant intensities, while time of exposure is to be varied. Plotting the graph with time of exposure on X axis and log survival on Y axis for a constant intensity, one can get an equation of the trend line in the form of $y=m*x$. Here, slope $m=k_1*I$ as intensity I is constant, k_1 value can be found out. Similarly, sets with constant time of exposure and with variable intensities are to be obtained. Plotting the graph with intensities on X axis and log survival on Y axis for a constant time of exposure, k_2 value can be found out.

Hence the time dependent rate constant and intensity dependent rate constant can be found out.

Plot the dual Y axis graph with intensities on one y axis and times of exposures on other y axis while the values of respective k_1 and k_2 on x axis.

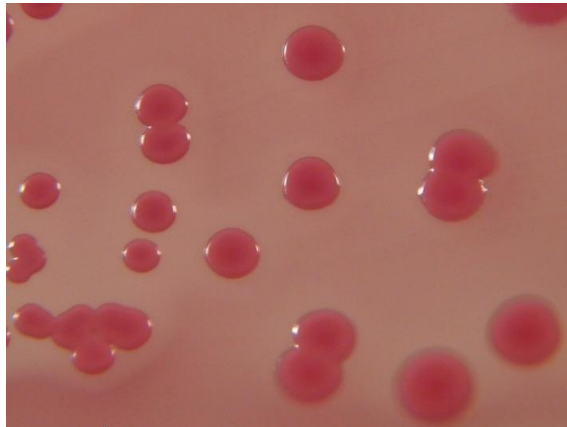
The intersection of the two lines will give the values of intensity and time of exposure where time dependent and intensity dependent rate constants are equal i.e. $k_1 = k_2 = k$.

6th International Engineering Symposium - IES 2017

March 1-3, 2017, Kumamoto University, Japan

The slope of the graph with time of exposure VS log survival is nothing but the first order kinetic rate constant. The graph plotted with first set of observations will give kinetic rate constant of *citrobacter*.

For *E coli*, the value of kinetic rate constant obtained with linear model is 0.07 per minute according to J. Rodríguez-Chueca et al. (2015). Both kinetic rate constants can be comparable as both the bacteria are gram negative.



CONCLUSION

The methodology using Chick's-Watson's equation is developed in the present study to analyze the time dependent and intensity dependent rate constants for deactivation of *citrobacter* and equally influencing rate constant is also established. The first order kinetic rate constant of *citrobacter* can be found out using Chick's law of disinfection.

REFERENCES

1. A. W. Halley (1977), Bacterial indicators / Health hazards associated with water.
2. Brahma M and Hassen A (2012), Ultraviolet radiation for inactivation of microorganisms in water, *J. Environ. Protect* 3:194-202. doi:10.4236/jep.2012.32024
3. Brahma M and Hassen A (2013), Modeling of ultraviolet (UV) radiation under a large pilot scale designed for wastewater disinfection and inactivation of selected bacteria *Pseudomonas Aeruginosa* in laboratory UV device, *African journal of Microbiology research*. Doi:10.5897/AJMR2013.6116
4. Joao P.S. Cabral (2010), Water Microbiology. Bacterial Pathogens and Water, Environment Research and public health. Doi:10.3390/ijerph7103657
5. J. Rodríguez-Chueca, M.P.Ormad, R.Mosteo, J.L.Ovellaero (2015), Kinetic modelling of *Escherichia coli* and *Enterococcus sp.* Inactivation in wastewater treatment by photo-Fenton and $H_2O_2/UV-vis$ processes, *Chemical Engineering Science*.
6. Mitscherlich, E. and Marth, E.H. (1984), *Microbial Survival in the Environment*.
7. Public Health agency of Canada. www.publichealth.gc.ca

Figure 1- *Citrobacter* colonies on MacConkey agar.

USE OF FERROFLUID FOR CONTAMINANTS REMOVAL FROM WASTEWATER

Shwetha Sreekumar¹, Amandeep Narang² and Dhanashree Sanket³

1. Department of Civil Engineering, National Institute of Technology Karnataka, Surathkal, Mangalore, India. Email: shwetha2192@gmail.com
2. Department of Civil Engineering, National Institute of Technology Karnataka, Surathkal, Mangalore, India. Email: ad.narang777@nitk.edu.in
3. Enviro Analyst and Engineers Pvt. Ltd, Mumbai.
Email: dhanashree.talekar@eaepi.com

ABSTRACT: In the past decade, ferrofluids have emerged as a new category of 'smart nanofluids', whose properties can be controlled by an external magnetic field and surface modification strategy. Ferrofluids are stable colloidal suspension of subdomain magnetic particles, in their aqueous or non aqueous liquid. These magnetic nanoparticles (MNPs) have the unique property of having both liquid and magnetic characteristics. In the absence of magnet field, the ferrofluid magnetite particles act like normal metal particles in suspension and in the presence of magnetic field, they get temporarily magnetized. Coating of the particles with surfactant prevents clumping, enabling them to remain stable and act predictably. Ferrofluids have a great potential and broad application in wastewater treatment. Due to its physicochemical characteristics, economic method and easy regeneration makes them an effective water purification method. Surface modification strategy of the nanoparticles increases its efficiency and enhances targeted removal of contaminant. In this paper, use of ferrofluids in treatment of wastewater has been discussed.

Keywords: Ferrofluids, magnetic, surface modification, contaminants

INTRODUCTION

Magnetic fluids are specific subset of smart materials which can adaptively change their physical properties in the presence of an external magnetic field. Magnetic control of the behaviour and properties of liquids are promising fields for advanced applications and a challenge for basic research. There are two main types of magnetic fluids that are known since 20th century, which are magnetorheological (MR) fluids and ferrofluids. The magnetorheological fluids are suspensions of micrometer-sized particles of magnetisable materials dispersed in a carrier liquid. The later, ideal ferrofluids are colloidal suspensions of ultrafine (5-10 nm) single domain magnetic nano-particles such as iron oxide, MnZn ferrites, and Fe and Co in either polar or non-polar carrier liquid. If

the solid particles in these fluids are between 15 and 40 nm, is still considered as ferrofluids. Above this, the fluid goes into the limits of the MR fluids. The carrier liquid used can be polar or nonpolar such as water or organic solvents. The magnetic particles have to be coated with an appropriate surfactant to avoid nanoparticles agglomeration, causing the material to act predictably. This coating makes them stable even under intense magnetic fields. Ferro fluids response to an external magnetic field enables the fluid's location to be controlled through the application of a magnetic field. The particles are so small in ferrofluids that they will not settle over time, but remain in place as long as a magnetic field is present. It has been known that ferrofluid viscosity increases with the intensity of

magnetic field, known as the magneto viscous effect.

When preparation is carried out in air Fe^{2+} gets oxidized to Fe^{3+} , therefore the synthesis is carried out under neutral atmosphere. There are some reports about the synthesis of ferrofluids in oxidative conditions. The synthesis of the iron oxide nanoparticles is intensively developed not just for their fundamental scientific interest but their important application in various fields. Utilization of iron oxide nanomaterials with novel property and functionality is widely studied due to their small size, magnetic property and high surface area. Modified magnetic nanoparticles have numerous applications in biomedical field such as magnetic resonance imaging, drug delivery, cellular labeling, hyperthermia, protein separation and remediation of environment.

Water pollution is increasing worldwide due to increasing human population, rapid growth of industrial, domestic and agricultural activities which leads to the threatening effects on human beings, aquatic life and wildlife. Nowadays, treatment of polluted water, both efficiently and economically, has become an important issue. In the area of environmental remediation, nanomaterials offer the potential for the efficient removal of pollutants. With the rapid development of nanotechnology, magnetic fluids are currently being widely studied in the field of water treatment.

SYNTHESIS OF FERROFLUID

The magnetic particle content, suspension viscosity, saturation magnetization and surfactants for stabilizing the ferrofluids are important factors that affect the stability, rheological properties and redispersibility of the ferrofluids. Based on the method of colloidal stabilization two main types of ferrofluids are synthesized, that are water-based ionic fluids and surfacted organic media based ferrofluids. For different applications, several chemical methods can be used to synthesize magnetic nanoparticles: co-precipitation, sol-gel syntheses, sonochemical reactions, hydrothermal reactions,

hydrolysis and thermolysis of precursors, reverse micelles and micro-emulsion technology, flow injection syntheses, and electrospray synthesis. The chemical coprecipitation method which is widely used involves the stoichiometric mixture of ferrous and ferric salts in ratio 2 : 1 ($\text{Fe}^{3+}/\text{Fe}^{2+}$) in aqueous medium in the presence of base. In the presence of oxygen, acid magnetite nanoparticles are converted into magnetite nanoparticles. The main advantage of this is that it produces a large amount of material, with control over particle size (2–20 nm) and shape afforded by adjusting pH, ionic strength, and the concentration of solution. Surface modification of iron oxide nanoparticles is done for different purposes.

Carrier liquid

The function of the carrier liquid is providing a medium in which the magnetic powder is suspended. Choice of carrier liquid depends on the type of the application. Ferrofluids used in different technology fields have been synthesized in carrier liquids such as water, silicone oil, mineral oil, synthetic or semi-synthetic oil, lubricating oil, kerosene and combinations of these and many other polar liquids. Boiling temperature, vapor pressure at elevated, freezing point are important parameters to be considered while choosing the carrier liquid. The carrier liquid should also be non-reactive with the magnetic phase and also with the material used in the device. Citric acid, oleic acid, and humic acid are used as additives to provide the stability. Oleate double layer gives rise to a true stable ferrofluid, whereas no or short term stability are achieved with the other additives. Steric repulsion was needed to ensure long term stability and the best way to achieve this is to use surfactants adsorbed on the surface of the particles with tails compatible with the liquid carrier. Ionic fluids are considered to be environmentally friendly, stable and due to low flammability, negligible vapor pressure, they are good candidate for colloidal media for nanoparticles.

Additives

In the synthesis of the ferrofluids, dispersants must be added to minimize the agglomeration of the particles and to increase colloidal stability which is very important in the applications of the ferrofluids. The additives must also match the dielectric properties of the carrier liquid. Various surfactants such as silica, polyvinyl alcohol (PVA), chitosan and ethylene glycol, are usually used to coat the nanoparticles to enhance dispersibility in aqueous medium. Oleic acid is a commonly used surfactant to stabilize magnetic nanoparticles synthesized by co-precipitation method. Besides oleic acid, tartaric and citric acids are also used to obtain stable ferrofluids over a large pH range (pH 3–11). Anti-oxidation additives can also be added to prevent oxidation. In water based MR fluids also pH control additives can be used.

Stability of the ferrofluids

Ferrofluid nanoparticles tend to aggregate due to strong magnetic dipole-dipole attraction between particles. The two basic attractive interactions between the magnetic particles are van der Waals – London interactions and dipole-dipole. Stability of the magnetic colloid depends on the thermal energy contribution and on the balance between attractive (van der Waals and dipole-dipole) interactions and repulsive (steric and electrostatic) interactions.

Removal of heavy metals

In the section recent literature results related to the application of magnetite nanomaterials for the removal of heavy metals and metalloids is described.

- Superparamagnetic iron oxide nanoparticles with a surface functionalization of dimercaptosuccinic acid (DMSA) can be employed as an effective sorbent material for toxic soft metals such as Hg(II), Ag(I), Pb(II), Cd(II) ions which effectively bind to the DMSA ligands and for As(III) which binds to the iron oxide lattices.
- Magnetite particles functionalized with carboxyl (succinic acid), amine (ethylenediamine) and thiol

(2,3-dimercaptosuccinic acid) groups were used for removal of toxic metal ions Cd(II), Pb(II) Co(II), Cr(III), Ni(II), Cu(II) and As(III)) and Escherichia coli (bacterial pathogens) from water.

- Fe_3O_4 nanoparticles coated with humic acid (HA) ($\text{Fe}_3\text{O}_4/\text{HA}$) used for the removal of toxic cations such as Hg(II), Pb(II), Cd(II), and Cu(II) from water. These were prepared by the co-precipitation method.
- Carboxymethyl- β -cyclodextrin modified Fe_3O_4 nanoparticles (CM β CD-MNPs) is proved to be used for removal of copper ions from aqueous solution by grafting CM β CD onto the magnetite surface via carbodiimide method. The grafted CM- β -CD on the nanoparticles contributes to an enhancement of the adsorption capacity because of the strong abilities of the multiple hydroxyl and carboxyl groups in CM- β -CD to adsorb metal ions. The adsorption of Cu(II) onto nanoparticles was found to be dependent on pH and temperature.
- Controlled adsorption of polyethylenimine (PEI) can be done onto 50 nm crystalline magnetite nanoparticles and these PEI-coated Fe_3O_4 NPs can be used for the magnetic capture and quantification of ultratrace levels of free cupric ions.
- Dendrimer-conjugated magnetic nanoparticles combining the superior adsorbent of dendrimers with magnetic nanoparticles (MNPs) for effective removal and recovery of Zn(II). The adsorption efficiency increases with increasing pH.
- The sorption of Cu(II), Cd(II), Ni(II) and Cr(III) ions with salicylic acid as chelate on silica-coated magnetite nanoparticles. The adsorbent can be characterized by XRD, SEM, BET and FT-IR measurements. The method is successfully applied to the evaluation of these trace and

- toxic metals in various waters, foods and other samples.
- Starch can be applied as a stabilizer in preparation of the Fe₃O₄ particles which will efficiently be able to reduce particle aggregation, thus, effective particle size, resulting in much greater specific surface area and adsorption sites. The presence of starch leads to the formation of more effective adsorbing sites on magnetite particle surfaces.
 - Silica coated magnetic nanoadsorbents provide stability and increase adsorption efficiency. Silica-modified magnetite nanoparticles functionalized with cetylpyridinium bromide complexation with 8-hydroxy quinolone is used for detection of heavy metal ions such as Cd(II), Co(II), Cu(II), Mn(II), Ni(II), and Pb(II) from the water samples.

Removal of organic pollutant

The ferrofluid can very rapidly absorb the oil, and repel the water. The oil absorbed nanoparticles can be easily removed with a magnetic field for collecting. The morphologies are different in ferrofluid synthesized in different alkali like NH₃.H₂O and NaOH. Ferrofluid prepared using NH₃.H₂O and NaOH, both have good performance in the oil removal. The oil can be removed from the ferrofluid surface by ultrasonically washing in ethanol for several minutes. The nanoparticles could be reused again after being dried in an oven to separate the water and oil mixture. Ferrofluid modified with sodium oleate or oleic acid or tetramethylammonium hydroxide are found to be both hydrophobic and lipophilic. Hence, ferrofluids have potential applications in the cleanup of large-area oil spills or organic contaminants on a water surface. Surface modification can also be used to absorb lubricating oil from an oil-water mixture. It is seen that as time proceeds, the oil film breaks and becomes lighter which indicates the continuous oil absorption by the nanoparticles. The oil adsorption capacity

is related to the wetting property of the adsorbent.

CONCLUSION

Application of ferrofluid nanoparticles for removal of heavy metals and organic pollutants from the aqueous systems developed as highly efficient and cost-effective nanoadsorbent. Surface modification of ferrofluid approach enhanced their stability and efficiency in the water. Magnetic nanoparticles possess magnetic property which helps it to be removed easily in the presence of magnetic field. The reuse of ferrofluid will decrease economic burden.

REFERENCES

- [1] Amir Hatamie, et al. (2016), Evaluating magnetic nano-ferrofluid as a novel coagulant for surface water treatment, *Journal of Molecular Liquids*, Vol 219, pp. 694–702.
- [2] C, Scherer and A, M, Figueiredo Neto, (2015), *Ferrofluids: Properties and Applications*, *Brazilian Journal of Physics*, Vol. 35, No. 3A, pp. 718-727.
- [3] E, Ghasemi, et al. (2008), Synthesis and rheological properties of an iron oxide ferrofluid, *Journal of Magnetism and Magnetic Materials*, Vol 320, No. 21, pp. 2635– 2639.
- [4] Kakoli Bhattacharya, et al. (2015), Molecular design of one dimensional magnetic FeNi₃ nanochains and their application in oil removal, *DAE Solid State Physics Symposium 2015*, AIP Conf. Proc. 1731, pp. 050105-1–050105-3
- [5] Ling Zhua, et al. (2012), A simple method to synthesize modified Fe₃O₄ for the removal of organic pollutants on water surface, *Applied Surface Science*, Vol 258, pp. 6326– 6330
- [6] Luciano Carlos, et al. (2013), Applications of Magnetite Nanoparticles for Heavy Metal Removal from Wastewater, *Waste Water - Treatment Technologies and Recent Analytical Developments*, pp. 63-77.
- [7] Pragnesh N, Dave and Lakhan V, Chopda (2014), Application of Iron Oxide Nanomaterials for the removal of Heavy Metals, *Journal of Nanotechnology*, Vol 2014, No. 398569, 14 pages
- [8] Satish B, et al. (2011), Characteristics of ferro fluid, *Indian Journal of Science and Technology*, Vol 4, No. 11, pp. 1505-1509.
- [9] S, Masoud Hosseini, et al. (2010), Rheological properties of g-Fe₂O₃ paraffin-based ferrofluid, *Journal of Magnetism and Magnetic Materials*, Vol 322, No. 23, pp. 3792–3796.

FERROFLUID SYNTHESIS AND ITS USE IN OIL REMOVAL FROM WATER SURFACE

Amandeep Narang¹, Shwetha Sreekumar² and Dhanasree Sanket³

¹ Department of Civil Engineering, National Institute of Technology Karnataka, Surathkal, Mangalore, India. Email: ad.narang777@gmail.com

² Department of Civil Engineering, National Institute of Technology Karnataka, Surathkal, Mangalore, India. Email: shwetha2192@gmail.com

*³ Enviro Analyst and Engineers Pvt Lim, Mumbai, India.
Email: dhanashree.talekar@eaepi*

ABSTRACT: Ferrofluids are colloidal suspension of magnetic nanoparticles (MNPs), based on Fe_3O_4 . These MNPs have high surface area, adsorption capacity and are thermally stable, hence can be used as a super adsorbent to remove oil from waste water effluents. The MNPs were finally separated by applying external magnetic field. This technique is economic, efficient and environmental friendly. These Fe_3O_4 MNPs were coated with surfactants such as TMAH (Tetra methylene ammonium hydroxide) or oleic acid to avoid clumping of nanoparticles. These particles have floating ability and remain suspended in the carrier liquid such as oil or water, they can adsorb the floating oil more than the particles weight. MNPs can be prepared in liquid or powdered form. The solution of Fe_3O_4 was air dried at 70°C. The obtained Ferrofluid was tested on water surface containing mineral oil and percentage removal was studied.

Keywords: Ferrofluid, Surfactant, Nanoparticle, Carrier fluid

INTRODUCTION

Water is the most vital component on earth for the activities of living beings. The studies done in recent years shows that the occurrence of water pollution caused by oil spillage is very much frequent. The demand of development of facile methods for fast and selective removal of oils from water surface is growing. Many conventional methods used to solve this problem include mechanical extraction, chemical dispersants, membranes, bioremediation, absorbent material and so forth. These methods were widely applied but all have their certain limitations like chemical dispersants will absorb the oil film but they will cause secondary pollution and the absorbents material such as activated carbon, zeolite, wool fibre, straw, fly ash etc have some limitations like low absorption capacity for the thin oil film, poor recyclability etc. These methods may remove not only oil but water too, which

leads to the reduction of separation efficiency.

Considering the leakage of oil in water can cause large area water pollution in a very short period of time so, for the efficient removal of oil from water surface the application of magnetic material has become a new hotspot. The material with Hydrophobic and superoleophilic properties will remove the oil and organic chemicals from water efficiently. This technique will allow the proper disposal of oil and does not cause any secondary pollution.

In the past decade the study of ferrofluid properties its application has been marked. Fe_3O_4 magnetic nanoparticle (MNPs), has both academic as well as industrial interests for many application fields, such as catalysis, magnetic storage, magnetic separation, so on. Fe_3O_4 nanoparticles have proven to be beneficial in practical

6th International Engineering Symposium - IES 2017

March 1-3, 2017, Kumamoto University, Japan

applications and it shows hydrophobic and superoleophilic characteristics so, they were able to selectively absorb a broad range of oils and organic solvents while completely repelling water. The oil absorbed nanoparticles could be quickly collected by a magnet bar. Ferrofluid shows an important application in the clean up of oil spills on the water surface. However, little attention was paid while preparing the nanoparticle with strong magnetic response, hydrophobicity and floating ability used in dealing with the thin layer of oil.

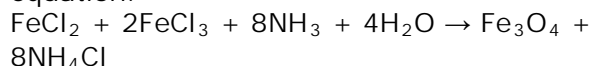
EXPERIMENTAL

MATERIALS

All the chemicals which are used in experiment were of analytical grade and can be used without further purification. Fe(II) chloride (FeCl_2), Fe(III) chloride hexahydrate ($\text{FeCl}_3 \cdot 6\text{H}_2\text{O}$), ammonium hydroxide (25% NH_3 in water, w/w) and oleic acid ($\text{C}_{18}\text{H}_{34}\text{O}_2$) were purchased from science house, mumbai and used as supplied. Distilled water was used throughout the experiment.

PREPARATION OF FERROFLUID

Co-precipitation of Fe(II) and Fe(III) salts was done to prepare the stable Fe_3O_4 ferrofluid. Formation of magnetite, Fe_3O_4 was based on reacting FeCl_2 and $\text{FeCl}_3 \cdot 6\text{H}_2\text{O}$ ions in an aqueous ammonia solution as shown in the following equation:



A typical experiment was conducted as follows:

1.0ml of 2M FeCl_2 solution and 4.0 ml of 1M $\text{FeCl}_3 \cdot 6\text{H}_2\text{O}$ were mixed in a beaker, and the mixture was stirred continuously using a magnetic stirrer. 50 ml burette was used for the dropwise addition of 50 ml of 0.7 M aqueous NH_3 solution. The formation of black precipitate of magnetite, Fe_3O_4 was observed. Ammonia solution was added slowly with continuous stirring for a period of 5 minutes. After the complete addition of ammonia solution, the stirrer was removed using a strong magnet and with gloved hands. The supernatant clear liquid was discarded after a complete settling of magnetite

without losing a substantial amount of solid. The content was transferred to a weighing boat and strong magnet was used to attract the ferrofluid to the bottom of the weighing boat. The ferrofluid was rinsed with water 3 times and the clear liquid was discarded. After rinsing of ferrofluid 2.0 ml of oleic acid was added (which works as a surfactant and avoid clumping of particles). The content was stirred with the glass rod to suspend the solids in the liquid. Ferrofluid was attracted at the bottom of a weighing boat using strong magnet and remaining oleic acid was poured off. As shown in Fig 1.

PROCEDURE FOR OIL REMOVAL

In a laboratory experiment, about 3.6 gm of mineral oil was taken in the beaker filled with water. Ferrofluid was dispersed over the oil. After 2-3 minutes, the ferrofluid appeared to absorb the oil (no mixing). The magnet was dipped in the oil/iron mixture. The magnet with attached oil/iron mixture was removed and was wiped clean with a paper towel. The process was repeated until there was no ferrofluid remaining. Increased weight of ferrofluid was added to the beaker for same quantity of oil and above process was repeated. The weight of the container was monitored throughout the process. The measured weights indicated the amount of ferrofluid which was needed for maximum removal of oil. Even after complete removal of oil small oil droplets could still be seen at the surface. Atleast 90% of oil removal can be done by this process.

ANALYSIS OF OIL REMOVAL

5 beakers were taken and each was filled with 20 ml water and 4.0 ml oil. Increasing amount of ferrofluid was added to the beakers. Once the ferrofluid forms layer on the surface of the oil. After the ferrofluid was completely wetted by oil. Its hydrophobic and superoleophilic characteristics helps in the removal of oil along with the fluid. Hence, after dipping the magnet in the beaker the ferrofluid along with the oil was removed. The beaker was again weighed to determine the amount of oil removed. The oil

6th International Engineering Symposium - IES 2017

March 1-3, 2017, Kumamoto University, Japan

removal capacity of the ferrofluid was calculated by the formula:

$$K = \frac{M_1 - M_2}{M_1}$$

where K is the removal capacity (g/g), M₁ is the weight of the material before oil removal, M₂ is the weight after oil removal. Powdered form of magnetite can also be used for removal of oil. The fluid form of magnetite was dried in oven at 65°C to obtain it in the powdered form.

RESULTS AND DISCUSSION

The removal of oil from the water surface using ferrofluid was seen in the experiment conducted in laboratory. By increasing the amount of ferrofluid in the beaker, increase in the percentage removal of oil was observed. Same quantity of oil (i.e 4ml which is equal to 3.68 grams) and increasing quantity of ferrofluid was added in all the beakers. Weight of oil removed (in grams) was calculated, then the percentage removal of the oil was determined.

CALCULATION

Weight of Beaker+Water = 52.73 gm

Weight of Beaker+Water+Oil = 56.41 gm

One drop of ferrofluid was added which was equal to 0.07 grams.

Then, Weight of B+W+O+ferrofluid

= 56.48 gm

After dipping magnet in the beaker for the removal of oil and ferrofluid

Weight of B+W-(O+F) = 56.30 gm

Total removal of oil and ferrofluid is:

56.48-56.30 = 0.18 gm

In which ferrofluid weight = 0.07 gm

So, Removal of oil = 0.18 gm -0.07 gm

=0.11 gm

Removal of oil in percent = 2.9 %

Similarly, percentage removal of oil is determined for different amount of ferrofluid using five trials shown in Table 1 and the plot for the table is also shown in Fig.2.

Surfactant play a vital role in the preparation of ferrofluid. It is of great interest to find that the Fe₃O₄ nanoparticles when coated with TMAH surfactant the nanoparticles quickly sank beneath the water surface when came in contact with water on the other hand Fe₃O₄ prepared with oleic acid could float

on the water surface. The unsinkability property of nanoparticles might be related to highly hydrophobic nature.

These results show practical importance for the application of Fe₃O₄ nanoparticles under oceanic conditions where oil spills are spread so fast on the surface of water.

CONCLUSION

In recent years, more studies have been done on the magnetic nanoparticle for higher performance. In this study, the beneficial application of magnetic fluid as a coagulant for oil removal from the water surface were investigated.

- Magnetic fluid have unique physico-chemical characteristics facile and fast separation by applying external magnetic field, Biological safety, Biocompatibility etc.
- These nanoparticles also have advantages of low cost, unsinkability, thermal stability, easy operation, good corrosion resistance and environmental friendliness.
- The oil were quickly and selectively absorbed by spreading the ferrofluid on the polluted water surface
- The oil absorption capacity was calculated is more than the weight of the nanoparticle.

In the experiment it was seen that while adding ferrofluid in the beaker optimum point was achieved after which the addition of more ferrofluid was resulting in the settling of the fluid due to the increase in the weight of the fluid with respect to the oil present in the beaker. Like, after adding 1 gram of ferrofluid for 3.68 grams of oil, the more addition of the fluid was resulting in the settling of the fluid at the bottom of the beaker.

And, the experiment was also carried out on the dairy sample (Vasudhara dairy, Mumbai) but ferrofluid was unable to remove oil from that sample due to the presence of high quantity of lipids, proteins, fat etc. Therefore, this kind of magnetic polymer nanocomposite are not suitable for this dairy waste but might be a good substitute for the absorbent materials in the easy and fast removal of oil spills from the water surface.

6th International Engineering Symposium - IES 2017

March 1-3, 2017, Kumamoto University, Japan

REFERENCES

- [1] Amir Hatamie, Hooshang Parham, Behrooz Zargar, Zahra Heidari (2016), Evaluating magnetic nano-ferrofluid as a novel coagulant for surface water treatment, Vol 219, pp. 694-702
- [2] Bo Ge, ZhaoZhu Zhang, Xiaotao Zhu, Guina Ren, Xuechu Men, Xiaoyan Zhao (2013), A magnetically superhydrophobic bulk material for oil removal, Vol 429, pp. 129-133.
- [3] G.A. Van Ewijk, G.J Vroege, A.P Philipse (1999), Convenient preparation methods for magnetic colloids, Vol 201, No. 1-3, pp. 31-33.
- [4] H. Shokrollahi (2013), Structure, synthetic methods, magnetic properties and biomedical applications of ferrofluids, Vol 33, No. 5, pp. 2476-2487.
- [5] John C Ulicny, Mark A Golden (2007), Oil spill recovery method using surface-treated iron powder, publication No. US7303679B2.
- [6] Junjun Gu, Wei Jiang, Fenghe Wang, Mudan Chen, jianyu Mao, Tan Xie (2014), Facile removal of oils from water surfaces through highly hydrophobic and magnetic polymer nanocomposites, Vol 301, pp. 492-499.
- [7] Ling Zhu, Chuanhao Li, Juan Wang, Hui Zhang, Yuhua Shen, Cun Li, Cuiping Wang, Anjian Xie (2012) A simple method to synthesize modified Fe₃O₄ for the removal of organic pollutant from surface water, Vol 258, pp. 6326-6330.
- [8] Robert, Kaiser (1972), Process for cleaning up oil spills, Publication No. US3635819A.



Fig. 1 preparation of ferrofluid using oleic acid

Table 1 Analysis of removal of oil from water surface by ferrofluid.

Weight of oil (gm)	Weight of ferrofluid (gm)	Oil removal(gm)	% of oil removal
3.68	0.07	0.11	2.9 %
3.68	0.36	0.32	8.79 %
3.68	0.56	0.41	11.37 %
3.68	0.80	0.88	22.79 %
3.68	1.0	1.34	36.57 %

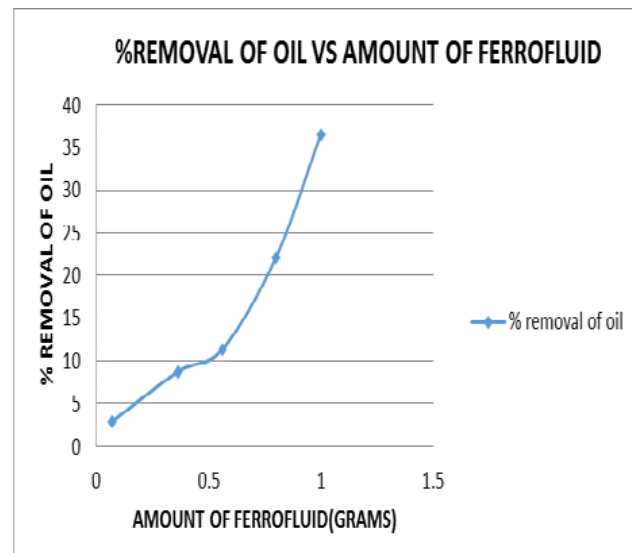


Fig.2 Removal of oil versus amount of ferrofluid used.

SEISMIC RESPONSE OF BUILDINGS WITH CONFINED MASONRY CONSTRUCTION: A REVIEW

Seethu K¹ Katta Venkataramana²

¹ Department of Civil Engineering, National Institute of Technology Karnataka, Surathkal, Mangalore 575025, India. email:seethuk01@gmail.com

² Department of Civil Engineering, National Institute of Technology Karnataka, Surathkal, Mangalore 575025, India. email:ven.nitk@gmail.com

ABSTRACT: Confined masonry construction has generally shown satisfactory behaviour during past earthquakes across the world. This paper is mainly concerned with the study on the seismic performance of confined masonry under quasi-static cyclic lateral loading and also the influences of masonry-tie connection. Confined masonry are intended to carry both vertical and seismic loads. Studies shows that confined masonry wall provides fair in-plane shear capacity and ductility and its behaviour can be significantly affected by tie-column to wall interface and presence of openings.

Keywords: Confined masonry, Masonry-tie connection, Seismic behaviour

INTRODUCTION

Most of the countries primarily make use of traditional masonry construction for residential purposes. Masonry has records of good performance and lasting qualities, however, due to relatively low capacity in tension and shear, it performs poorly in seismic events. The future of masonry is limited unless improvements in its seismic resistant features are made. Prediction of the seismic behaviour of masonry buildings is a wide-ranging and basic topic of earthquake engineering. The investigation of the response of a masonry building under earthquake loads involves many different questions, which need to be properly assessed. The consistent development in masonry construction evolved various types namely unreinforced masonry (URM), reinforced masonry (RM) and confined masonry (CM). The poor performance of masonry buildings in recent Nepal earthquake (2015) clearly shows that confining masonry buildings is more important.

Confined masonry (CM) is considered one of the popular forms of low-cost, low-rise constructions throughout the world; including the Middle East, South and

Central America, Mexico, South-East Asia, and South-Eastern Europe. The system relies on a load-bearing wall encased by small cast-in-place reinforced concrete tie columns and tie beams. The system consists of masonry panel, confined with horizontal and vertical RC elements with light reinforcement ratio.

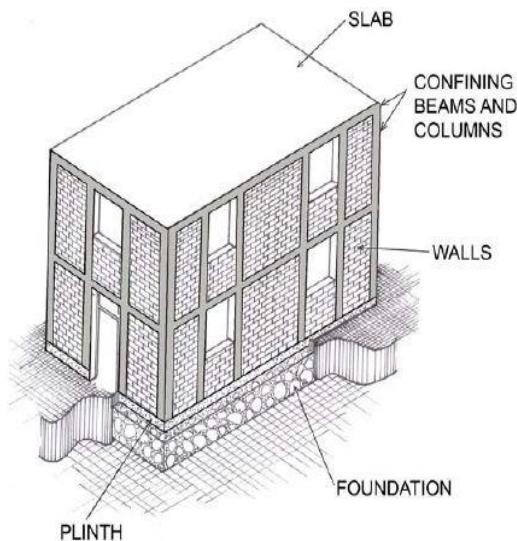


Fig.1 Typical confined masonry building (Schacher T, 2009)

COMPARISON BETWEEN MASONRY-INFILLED FRAMES AND CONFINED MASONRY

Brzev (2008) has compared the masonry-infilled frames against confined masonry, considering various factors as below.

1. Different Construction Sequence (Fig.2)

- In confined masonry construction, masonry walls are constructed first, followed by the cast in-place RC tie-columns, tie-beams & floor/roof slab construction.
- In RC frame construction infilled with masonry wall panels, the frame is constructed first, followed by the masonry wall construction.

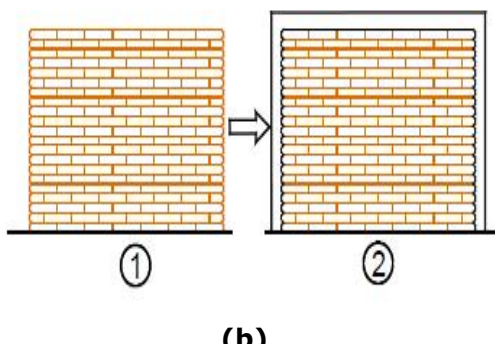
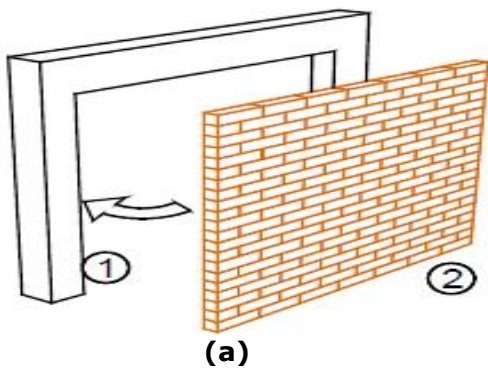
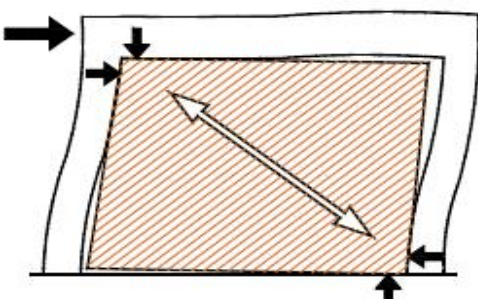


Fig.2 Construction sequence a) RC frames with masonry infill walls b) confined masonry (Schacher T, 2009)

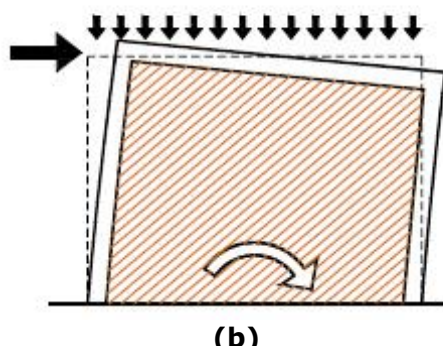
2. Different Behaviour (Fig.3)

- Gravity loads in confined masonry construction are mostly supported by the masonry walls, while infill in RC frames bear mostly self-weight.
- When subjected to lateral seismic loads, walls in confined masonry buildings act as shearwalls. On the other hand, infill wall panels in RC

frame buildings act as diagonal struts.



(a)



(b)

Fig.3 Seismic response a) RC frames with masonry infill walls b) confined masonry (Schacher T, 2009)

3. Different Design Complexity

- In confined masonry, RC elements act primarily in compression and tension and the connections between these elements are pinned hence, RC tie-beams and tie-columns are smaller in size and require less reinforcement.
- In Masonry-infilled frames, RC members largely undergo bending and shearing, and therefore they need to be larger in terms of size and amount of reinforcement.

KEY FACTORS INFLUENCING THE SEISMIC RESPONSE OF CONFINED MASONRY

- Wall density
- Masonry units and mortars
- Tie-Column
- Tie-beam
- Opening

6th International Engineering Symposium - IES 2017

March 1-3, 2017, Kumamoto University, Japan

LITERATURE REVIEW

Chourasia *et al* (2016) compared the seismic behaviour of full-scale single-room masonry buildings of different typology under quasi-static cyclic lateral loading. Among six tests, three tests were on original undamaged masonry construction system having similar material, geometry, construction practices and test procedure, employing URM, RM, and CM. The other three tests encompass URM-repaired, URM-retrofitted, and RM-retrofitted, with the same initial features. The seismic performance was studied in terms of crack pattern, lateral strength, drift, behavior factor, and energy dissipation ratio.

The tested masonry building viz. URM, RM, and CM exhibited distinct behavior in terms of crack pattern and deformation characteristics. The closely space lateral ties at end regions of tie-column of CM controlled the crushing of core concrete and improved the performance.

Table 1 Comparison of Drift, Ductility and Seismic Behavior Factors for Different model (Chourasia *et al*, 2016)

Building	Max Drift (%)	Ductility (μ_u)	Seismic behavior factor(q)
URM	0.12	1.29	1.26
URM-REP	0.51	4.72	2.63
URM-RET	0.54	4.06	2.27
RM	0.79	4.96	2.49
RM-RET	1.39	4.78	2.80
CM	1.80	5.76	3.34

The full-scale test of CM was terminated just before reaching the collapse stage of the building (1.8% drift) to avoid damage to instruments/equipments, although the building had further displacement/ductility capacity (Table 1).

The seismic behavior factor (q) may be represented in terms of global ductility factor (μ_u), and is expressed as

$$q = (2\mu_u - 1)^{1/2} \quad \dots \quad (1)$$

Among all the tested building, CM exhibited substantial increase in lateral strength. (Fig. 4)

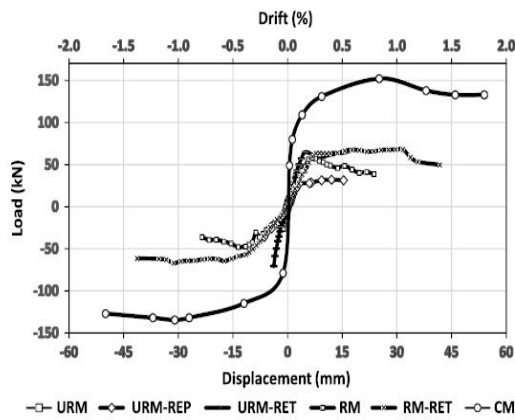


Fig.4 Average lateral load-deformation envelope for different masonry buildings (Chourasia *et al*, 2016)

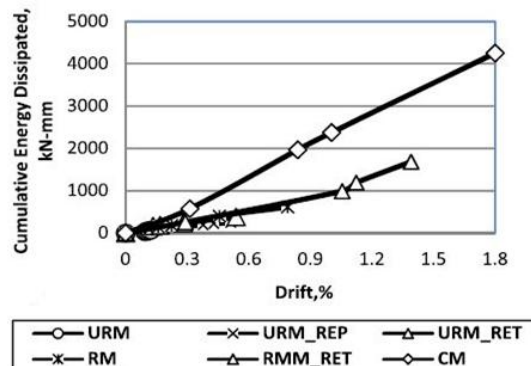


Fig.5 Cumulative energy dissipated in relation to drift(Chourasia *et al*, 2016)

CM building exhibited highest cumulative input and dissipation energy and its ratio among all masonry systems. (Fig. 5)

Wijaya *et al* (2011) studied the behaviour of four confined reinforced masonry walls with variations of wall-frame connection details in resisting in-plane lateral cyclic loads. In this study one specimen, with no anchorage between the wall and the reinforced concrete frame was chosen as a bench mark model. The other specimens were varied in the details of wall-frame connection, i.e. zigzag (toothing) connection, short anchor between column and wall, and continuous anchorage from column to column. (Table 2)

6th International Engineering Symposium - IES 2017

March 1-3, 2017, Kumamoto University, Japan

Table 2 Models (Wijaya et al, 2011)

Model	Type
A	Common practice
B	Short anchorage
C	Zigzag connection
D	Continuous anchorage

The models were then subjected to cyclic in-plane lateral loads, which represents earthquake loads, with increasing amplitude until collapsed. The behavior of these specimens was then evaluated and compared. (Table 3 and Table 4)

Table 3 Lateral load capacity (Wijaya et al, 2011)

Model	Lateral load capacity (kN)
A	49.88
B	53.31
C	41.75
D	65.66

Table 4 Input energy and dissipated energy (Wijaya et al, 2011)

Model	Input energy (kN-m)	Dissipated energy (kN-m)
A	196.29	142.27
B	231.39	172.39
C	178.41	128.68
D	283.19	211.17

Their study revealed that zigzag connection and short anchor did not improve the performance of the confined masonry wall; instead it is more likely to reduce the performance of the wall. Continuous anchorage strengthened the confinement of the wall and allowed the development of diagonal crack patterns.

As a result, the strut and tie mechanism between the wall and the confining column was able to develop as lateral load resistance mechanism. Therefore, better structural performance was observed for this specimen.

CONCLUDING REMARKS

The important conclusions from this review study are:

- Among all the tested building, CM exhibited substantial increase in lateral strength.
- The maximum drift and ductility up to 1.8% and 5.75, respectively, was achieved for CM buildings.
- CM buildings showed the highest energy dissipation capacity among all the tested masonry building systems.
- Installing proper wall-frame connection strategies is crucial in improving the structural performance of the confined masonry wall.
- The specimen having continuous anchorage shows more ductile behaviour as well as ability to withstand higher lateral load.

REFERENCES

- [1] Chourasia et al(2016), Seismic Performance of Different Masonry Buildings: Full-Scale Experimental Study, Journal of performance of construction facilities, 040160006, ASCE, pp 1-12.
- [2] Schacher.T (2009), Confined Masonry for one and two storey buildings in low-tech environments, A guidebook for technicians and artisans, National Information Center of Earthquake Engineering, IIT Kanpur, www.nicee.org.
- [3] Wijaya et al (2011), Experimental Study on Wall-Frame Connection of Confined Masonry Wall, *Procedia Engineering*, vol.14, pp 2094-2102
- [4] Brzez S N(2008), Earthquake-Resistant Confined Masonry Construction, National Information Center of Earthquake Engineering, IIT Kanpur, www.nicee.org.

A STUDY ON FEMA P58: NEXT GENERATION BUILDING SEISMIC PERFORMANCE ASSESSMENT METHODOLOGY

Bindhya K V¹ and Katta Venkataramana²

¹ Department of Civil Engineering, National Institute of Technology Karnataka, Surathkal, Mangalore 575025, India. email:bindhyabalankv@gmail.com

² Department of Civil Engineering, National Institute of Technology Karnataka, Surathkal, Mangalore 575025, India. email:ven.nitk@gmail.com

ABSTRACT: Performance based seismic design (PBSD) is a tool that can be used to reduce the damage and losses resulting from an earthquake or similar disaster. PBSD is based on the performance assessment of the building design. In present generation procedures performance is expressed in terms of a series of discrete performance levels identified as Operational, Immediate Occupancy, Life Safety and collapse prevention. Although a vocabulary is established and the engineers could quantify and communicate seismic performance to clients, implementation of these procedures uncovered certain limitations and some enhancements were needed. To overcome these limitations FEMA introduced next generation procedures. This paper presents a study on FEMA P58: Next Generation Building Seismic Performance Assessment Methodology.

Keywords: performance based seismic design, performance assessment

INTRODUCTION

Performance Based Seismic Design (PBSD) is a revolutionary development in seismic engineering. It can be done for an existing building or for a new building. PBSD is a generalised design philosophy in which design criteria are expressed in terms of achieving stated performance objectives when the structure is subjected to the stated level of seismic hazard. In PBSD identifying and assessing the performance capability of a building is an integral part of the design process, through which determining the probability of experiencing different types of losses, considering the range of potential earthquakes that may affect the structure. Fig 1 shows the flow chart that presents the key steps in the PBSD. It is iterative in nature. The primary step is the selection of performance objectives. Preliminary design is the following step. Then an assessment is done to whether or not the design meets the performance objectives. If not, the design must be revised or the objectives altered, until the assessed performance and the desired objectives meet.

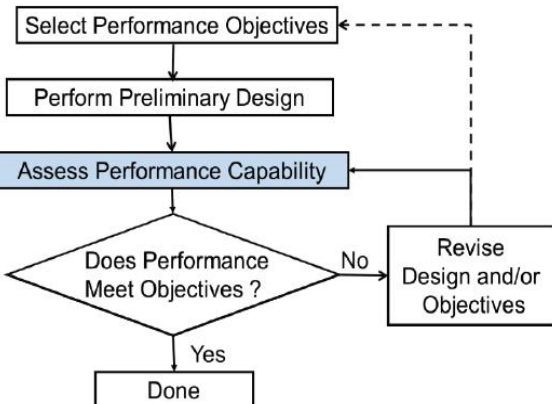


Fig. 1. PBSD Flow chart (Ref.2)

First generation performance-based procedures (Ref.1)

First generation procedure introduced the concept of performance in terms of discretely defined performance levels and also the concept of performance related to damage of both structural and non-structural components. Analytical procedures to simulate the seismic response of structures and set of guidelines on analysis techniques and acceptance criteria are provided. FEMA 273 Report, NEHRP Guidelines for Seismic Rehabilitation of Buildings (ATC 1997a)

6th International Engineering Symposium - IES 2017

March 1-3, 2017, Kumamoto University, Japan

and SEAOC vision2000 report outlined the initial concept of PBSD.

Present Second generation performance-based procedure

At present, PBSD practise is mainly based on FEMA 356 Prestandard and Commentary for the Seismic Rehabilitation of Buildings. With the development of second generation performance-based procedures the use of advanced nonlinear analysis techniques become more popular.

Need for Next generation performance-based procedures

Some limitations are identified for the current performance based procedures. These include: (i) questions about the accuracy of analytical procedure in predicting the actual building response. (ii) regarding the conservatism level in the acceptance criteria. (iii) inability in reliable and economical application of procedures to the design of new building and (iv) alternative ways of communication about the performance to stakeholders for decision making purpose is needed.

PERFORMANCE ASSESSMENT METHODOLOGY (Ref.2)

Technical basis of the methodology is the framework for Performance-based Earthquake Engineering developed by Pacific Earthquake Engineering Research Centre (PEER).

Types of performance assessment

This methodology can be used to develop three types of performance assessment:

(i) Intensity based: evaluate the probable performance of a building assuming that it is subjected to a specified earthquake shaking intensity.

(ii) Scenario based: in this type evaluating the probable performance of a building assuming that it is subjected to an earthquake scenario consisting of a specific magnitude occurring at a specific location relative to the building site.

(iii) Time based assessment: evaluate performance over time, considering all possible earthquake and their probability of occurrence.

Assessment methodology

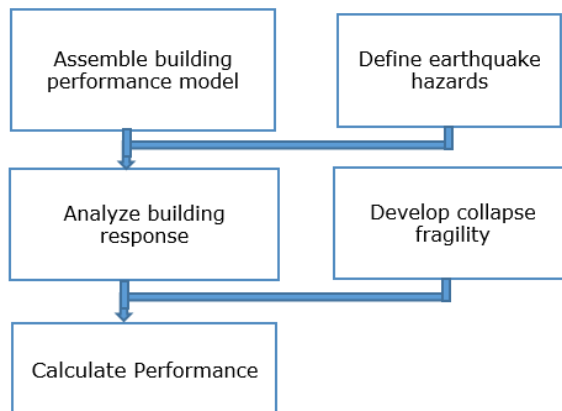


Fig.2 Flowchart of performance assessment methodology (Ref.2)

Assemble building performance model

The performance model of a building is an organized collection of data that are necessary to define building assets that are at risk and vulnerable to the effects of earthquake shaking. It includes: (i) basic data about the building such as its size, replacement cost and replacement time, (ii) occupancy, (iii) details of vulnerable structural components and (iv) details of vulnerable non-structural components.

The building performance model includes population models, fragility groups and performance groups. Elements and components that are vulnerable to damage are assigned a fragility specification in the building performance model and that are not vulnerable to damage are not included in the model even though they are considered in the repair cost estimation. A summary list of fragility groups available for identifying and defining the vulnerable components and contents in the buildings is presented in Appendix D of FEMA P58. Population model of a building defines the number of people present per 1000 square feet of floor area and characterized by time of the day, day of the week (weekday or weekend) and month of the year. Default values for peak population are provided along with the time of day during which peak populations are expected.

Earthquake hazards

Earthquake hazards are defined in terms of shaking and characterised by target

6th International Engineering Symposium - IES 2017

March 1-3, 2017, Kumamoto University, Japan

acceleration response spectra. It will vary according to the type of assessment. Ground shaking intensity can be represented by any user-defined acceleration response spectra for intensity based assessment. For scenario based assessment, acceleration spectra is derived for specific magnitude-distance pairs, using ground motion prediction equations, also called attenuation relationships. Ground shaking intensity is represented by a series of hazard curves which are used to derive the acceleration response spectra for time based assessment procedures.

Ground motion prediction equations are used for deriving the acceleration response spectra for scenario based assessments. Most of them provide geometric mean spectral response acceleration represented by

$$S_{gm}(T) = [S_x(T) \times S_y(T)]^{0.5} \dots\dots\dots(1)$$

where $S_x(T)$ and $S_y(T)$ are orthogonal components of spectral response acceleration at period T.

Because of the difference in functional form of the relationships we will get different estimates of the probable values of spectral response acceleration for the same scenario and site. It is important to ensure that the selected equation is appropriate to the building site and earthquake source mechanism.

Structural analysis

Analysis is done in the performance assessment process for two basic needs:
(i) to predict the structural response quantities

(ii) to find the floor response acceleration and interstorey drift for the non-structural response

Two alternative types of analysis can be used to predict the responses: nonlinear response history analysis and simplified analysis based on the equivalent lateral force method.

Nonlinear response history method is useful for any structure at any ground shaking intensity. The nonlinear component behaviour is characterised by initial stiffness, yield strength, peak strength, plastic deformation capacity and residual strength. The component modelling parameters should be verified

against test data or appropriate idealised backbone curves. The choice of backbone curve (monotonic or cyclic) is depending on the capabilities of analytical model, ie, whether it is capable of explicitly simulating cyclic degradation or not.

Simplified analysis uses linear models and lateral yield strength of the structure to estimate median values of response parameters. Pseudo lateral force is used to compute the storey drift ratios, velocities and accelerations. Steps and equations are provided. Also the steps to median estimates of demand such as storey drift ratios, floor accelerations and floor velocities are described.

Collapse fragility

Building collapse fragility is a relationship which defines the probability of collapse incurring as a function of ground motion intensity. Fragilities are expressed as probability distributions in order to account for the uncertainty and variability. To form fragility functions, first it is to establish measure of damage. Earlier the concept of damage indices are used as a measure of damage. Damage indices are non-dimensional parameters and it is difficult to relate them to repair cost and other measure of losses. So in this methodology damage is parameterized through the direct tracking of the condition of individual elements and components coupled with the global damage measures. An example for fragility curves for structural and non-structural components are shown in Fig.3 and Fig.4. These curves do not directly indicate the probability but it will be equal to greater than that correspond to specific state.

Performance calculation

Building performance calculation include generation of simulated demands, assessments process, collapse assessment and loss computation in the form of casualties, repair cost and time and unsafe placarding. A flow chart showing the performance calculation is given in Fig.5.

Decision making

Decision making is the following stage of performance calculation. Performance

6th International Engineering Symposium - IES 2017

March 1-3, 2017, Kumamoto University, Japan

assessment can provide useful information for many decisions associated with real property.

CONCLUDING REMARKS

From the study of FEMA P58, following are the conclusions reached:

- A practical procedure for prediction of building performance assessment is developed.
- The procedure is somewhat complex and time consuming but accurate compared to the presently available methodologies.
- Development of rapid strategies are needed.
- Makes the communication with the stakeholders easier.

REFERENCES

- [1] FEMA 440, Next – Generation Performance Based Seismic Design Guidelines, (2006)
- [2] FEMA P-58, Seismic Performance Assessment of Buildings, Volume1- Methodology, (2012)
- [3] Humberger, R et al (2004), The ATC-58 Project: Development of Next- Generation Performance – Based Earthquake Engineering Design Criteria for Buildings, 13th World Conference on Earthquake Engineering, Vancouver, Canada, August 1-6, Paper no.1819

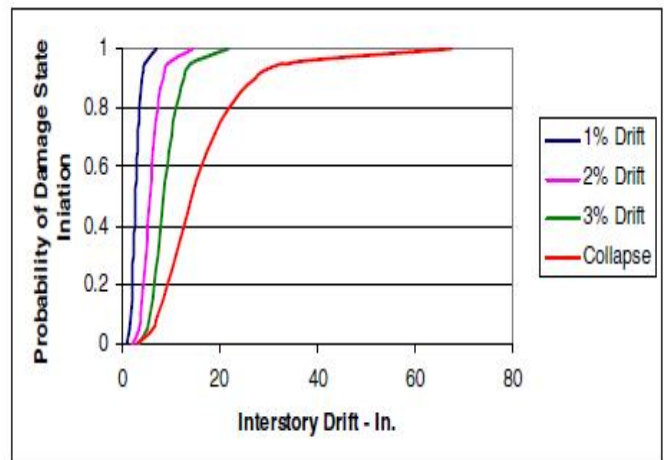


Fig.3 Example fragility function for Global structural behaviour (Ref.3)

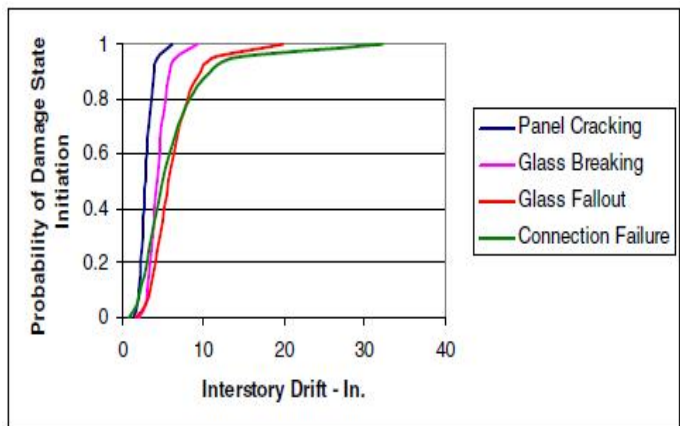


Fig.4 Example fragility curve for non-structural components (Ref.3)

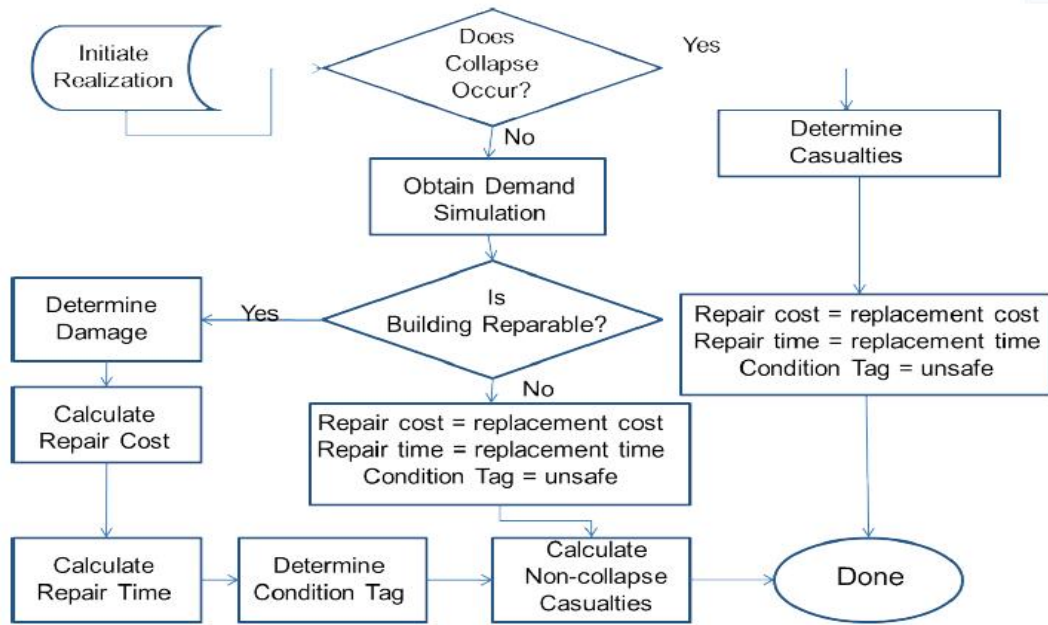


Fig.5 Flowchart of Performance Calculation (Ref.2)

Recent Developments in the Performance-Based Seismic Design

Haseena Mumthas M ¹, Katta Venkataramana ²

1 Department of Civil Engineering, National Institute of Technology Karnataka, Surathkal, Mangalore 575025, India.

e-mail:haseenamumthas1704@gmail.com

2 Department of Civil Engineering, National Institute of Technology Karnataka, Surathkal, Mangalore 575025, India. e-mail:ven.nitk@gmail.com

ABSTRACT: An important advancement in structural engineering in recent years has been the development of performance-based seismic design. Performance-based Seismic Design is an elastic design methodology done on the probable performance of the buildings under different ground motions. This paper reviews recent developments in performance-based seismic design by defining the performance objectives (levels), evaluation techniques, and assessment procedures.

Keywords: performance-based seismic design, performance objectives

INTRODUCTION

The purpose of any structural design is to ensure safety, serviceability, durability and considering effects of earthquakes, other effects to allow some damage or without damage to structure. Hence, performance of the structure is the aim of structural design. Performance cannot be automatically guaranteed by code conformance. Performance for a structure can be ensured without code conformance also. A Typical example is Pyramid. Pyramids were built before the codes were developed or even all the seven wonders were built before the code even existed. But all these were standing till today without much of structural repair or damages. Hence the performance of these structures is achieved designing without codes. Hence good performance is not ensured by codes compliance.

Performance based design is not new to engineering. The purpose of Performance-Based Seismic Design (PBSD) is to give a realistic assessment of how a structure will perform when subjected to either particular or generalized earthquake ground motion. While the code design provides a pseudo-capacity to resist a prescribed lateral force, this force level is

substantially less than that to which a building may be subjected during a postulated major earthquake. It is assumed that the structure will be able to withstand the major earthquake ground motion by components yielding into the inelastic range, absorbing energy, and acting in a ductile manner as well as by a multitude of other actions and effects not explicitly considered in code applications [7]. Although the code requires special ductile detailing, it does not provide a means to determine how the structure will actually perform under severe earthquake conditions. This is the role of PBSD [7].

STATE OF DEVELOPMENT

Since early twenty-century performance based seismic design is being practices and especially in countries like New Zealand and Australia. The International Code Council (ICC) has prepared code for performance based seismic design for voluntary design apart from Code prescribed design. In 1989, Federal Emergency Management Agency (FEMA) had made a first code for seismic rehabilitation of existing buildings (Applied Technology Council (ATC)-1989). Later in FEMA 273, NEHRP Guidelines for the Seismic Rehabilitation of Existing

6th International Engineering Symposium - IES 2017

March 1-3, 2017, Kumamoto University, Japan

Buildings, has incorporated for the first time different performance levels that are related to specific levels of seismic shaking. They have introduced four performance levels, namely Operational, Immediate Occupancy, Life Safety and collapse prevention. Later Structural Engineers Association of California (SEAOC, 1995) have developed a more rational approach for performance based seismic design called Vision 2000.

Over the years FEMA 273 had been reviewed and in 2006 American Society of Civil Engineers (ASCE) have published ASCE 41-Seismic rehabilitation of Existing Buildings, but it is generalized that it can be applied to New buildings also.

PERFORMANCE-BASED SEISMIC DESIGN

Performance based seismic design can be done for an existing building (evaluation and retrofitting of the building) or for a new building. In this method, the overall performance of the building is controlled as a function of design process.

Figure 1 shows a flow chart that represents the key steps in the performance-based design process. Each key Performance Indicator is a set of acceptable damage to the structure in the event of a natural hazard acted upon the structure like cost of repair, downtime of the building due to the repair time etc., accepted by all the stakeholders of the building. Stakeholders for the building generally include the Owners, Engineers, Designer, Public and a technical group of person who have technical expertise in this field.

Once the performance objectives are set (Key Performance Indicators as agreed by all the stakeholders), a series of simulations analyses of building response to loading are performed to estimate the probable performance of the building under various design events. If the simulated performance meets or exceeds the performance objectives, the design is complete. If not, the design is revised in an iterative process until the performance objectives are met. In some cases, it may not be possible to meet the stated objectives at reasonable cost, in which

case some relaxation of the original objectives may be appropriate.

After the conceptual design phase is completed, the numerical design phase is proceeded to determine the structural detailing, which satisfy the pre-quantified performance objectives. Preliminary design can be conducted through two different approaches [1].

1. Traditional force based design method followed by the check of performance objectives and
2. Direct design method starting from the pre-quantified performance objectives.

Preliminary design carried out by direct design method yields closer results to the performance objectives or the final performance based seismic design of the building it would take lesser iterations to achieve performance based design. From the results of the preliminary design, acceptance and evaluation of the performance objectives is done by performing non-linear pushover or non-linear time history analysis.

PERFORMANCE-BASED SEISMIC EVALUATION

Performance-based seismic engineering evokes the need for high-level analysis procedures. Next-generation PBSD guidelines have introduced a comprehensive framework for linear and nonlinear procedures. Nonlinear analysis procedures provide better perception of inelastic behavior and failure modes of structure during a severe seismic event [15]. Despite the accuracy and efficiency of nonlinear dynamic analysis (NRHA), engineers are attracted to nonlinear static procedures because of NRHA's time consuming computational process. Various nonlinear static procedures are used to estimate seismic performance of the buildings. N2 method and modal pushover analysis method are included in this paper.

N2 method

This method was first proposed by Fajfar and Fischinger (1989) as an alternative to Capacity Spectrum Method. This method has roots in Q-model developed by Saiidi and Sozen (1981), which is based on the work of Gulkan and Sozen (1974). The main difference between capacity

6th International Engineering Symposium - IES 2017

March 1-3, 2017, Kumamoto University, Japan

spectrum method and this method is that usage of different type of demand spectra for estimation of the target displacement. Detail procedure is hereby elaborated,

- i. Determination of equivalent Single Degree of Freedom model, generation of capacity spectrum is similar to that of Capacity Spectrum Method. Except that the Fajfar used the following formulae for generating capacity spectrum but the end capacity spectrum generated are identical. Bilinear idealize the capacity spectrum curve to determine yield strength F_y and yield displacement u_y .

$$S_a = V_h / \Gamma_j M^* \quad (1)$$

$$S_d = u / \Gamma_j \phi_n \quad (2)$$

Where,

$M^* = \sum M_i \phi_{ij}$ is the effective mass of the building

ϕ_n - roof element mode shape vector

Γ_j - participation factor for mode j

Damped elastic acceleration spectrum was converted to Acceleration Displacement Response Spectrum. Inelastic spectra are computed in terms of Ductility Reduction Factor R_μ is defined as

$$R_\mu = S_{ae} / a_y \quad (3)$$

Where,

S_{ae} - Pseudo acceleration ordinate from response spectrum

a_y - yield acceleration from capacity spectrum

Acceleration ordinate,
Spectral Displacement,

$$S_d = \mu S_{de} / R_\mu \quad (4)$$

As per vidic et.al (1994),

$$R_\mu = (\mu-1)T/T_c + 1 \quad T < T_c \\ = \mu \quad T \geq T_c \quad (5)$$

Where,

T_c is the characteristic period of the site and ground motion. It is defined as the transition period from constant acceleration region to constant velocity region of spectrum.

- ii. S_d , displacement demand of Equivalent Single degree of Freedom system is obtained by substituting eq.5 in eq.3. Thus,

$$S_d = S_{de} / R_\mu (1 + T/T_c (R_\mu - 1)) \quad T < T_c$$

$$= S_{de} \quad T \geq T_c \quad (6)$$

Displacement estimate will always be greater than the initial elastic displacement for short period structures, or structures that have fundamental period lower than the characteristic period.

- iii. Global seismic demand, roof displacement can be determined as

$$U_t = \Gamma_j S_d \quad (7)$$

Modal Pushover Analysis

Chopra and Goel (2002), proposed an improved pushover analysis procedure named modal pushover analysis to include the effects of higher modes on the structural response and redistribution of inertial forces during progressive yielding. The procedure is conceptually simple and easy to implement like pushover analysis with invariant lateral load pattern. Firstly, the procedure is applied to linearly elastic buildings and it was shown that the procedure is equivalent to the well-known response spectrum analysis. Then, the procedure was extended to estimate the seismic demands of inelastic systems by identifying the assumptions and the approximations involved. The procedure consists of the following steps:

- i. Determine the natural frequencies ω_n , and modes ϕ_n , for linearly elastic vibration of the structure.
- ii. For the n^{th} mode, develop the 'modal' capacity curve (base shear versus roof displacement) of the overall structure for the lateral force pattern $S_n^* = m\phi_n$.
- iii. Obtain the force-displacement relationship of the n^{th} mode inelastic SDOF from the corresponding 'modal' capacity curve.
- iv. Perform a nonlinear dynamic analysis for the ground motion excitation by utilizing the force-displacement relationship of n^{th} mode inelastic SDOF system to obtain the peak deformation D_n , of n^{th} mode inelastic SDOF system using any software.
- v. Calculate the peak roof displacement u_{mo} , associated with the n^{th} mode inelastic SDOF system from

6th International Engineering Symposium - IES 2017

March 1-3, 2017, Kumamoto University, Japan

$$U_{mo} = \Gamma_n \phi_m D_n \quad (7)$$

Where,

Γ_n - Modal participation factor for n^{th} mode

ϕ_m - Amplitude of n^{th} mode at roof level

D_n - Peak Spectral roof displacement

- vi. Extract any response r_{no} , from the pushover results at roof displacement U_{mo} .
- vii. Repeat steps 2-6 for as many modes required for sufficient accuracy; usually the first two or three modes will suffice.
- viii. Determine the peak value of total response by combining the peak modal responses r_{no} , using any appropriate modal combination rule, usually Square Root of Sum of Squares (SRSS) is used.

The procedure involves certain approximation and assumptions that coupling among modal coordinate due to yielding of the structure is neglected while calculating the peak roof displacements; U_{mo} , and superposition of peak modal responses to obtain the total peak response is utilized although superposition is valid only for elastic systems. Also, the total response is approximated by using an appropriate modal combination rule to combine the peak modal responses.

PERFORMANCE PARAMETERS

The seismic performance of a building can be evaluated in terms of pushover curve, performance point, displacement ductility, plastic hinge formation etc.

(1) Pushover Curve

The base shear versus roof displacement curve is obtained from the pushover analysis from which the maximum base shear capacity of structure can be obtained. This capacity curve is transformed into capacity spectrum ATC40 and demand or response spectrum is also determined for the structure for the required building performance level. The intersection of demand and capacity spectrum gives the performance point of the structure analysed. At the performance point, the resulting responses of the building should then be checked using certain acceptability criteria. The inelastic

VERIFICATION

capacity of structure needs to be taken into account to achieve better performance of building.

(2) Inter-storey drift

Inter-storey drift is defined as the ratio of relative horizontal displacement of two adjacent floors and corresponding storey height (h).

(3) Ductility demands

Ductility demands of the structure for various levels of performance can be expressed in terms of Inelastic Displacement demand ratio (IDDR). IDDR represents the ratio of inelastic displacement demand over the ultimate inelastic displacement capacity.

(4) Pattern of hinge formation

The sequence of plastic hinge formation and state of hinge at various levels of building performance can be obtained from analysis output. This gives the information about the weakest member and so the one which is to be strengthened in case of a building need to be retrofitted. Accordingly the detailing of the member can be done in order to achieve the desired pattern of failure of members in case of severe earthquakes. If the predefined performance objective is not satisfied then redefine the objective, else enhance the structures capacity to withstand the seismic damage achieve the objective.

CONCLUSIONS

- The Performance based Seismic design (PBSD) is both efficient and effective to minimize future earthquake losses.
- PBSD is a useful tool for design and to estimate the performance characteristics of buildings subjected to strong earthquake ground motion. It takes a combination of analytical procedures, data evaluation, judgment, experience and peer review to get a credible approximation of how a building works in the inelastic range of lateral motion.
- Various nonlinear static procedures are used to estimate seismic performance of the buildings and checking their accuracy with nonlinear time history analysis.

6th International Engineering Symposium - IES 2017

March 1-3, 2017, Kumamoto University, Japan

REFERENCES

- [1] Anwar, N (2013), International Seminar and Wrkshop on Performance Based Design of Reinforced Concrete Buildings, Asian Institute of Technology, <http://www.consulting.ait.ac.th/newsdetails.aspx?id=185>.
- [2] Chopra, A K, Goel, R K, (2002), A Modal Pushover Analysis Procedure for Estimating Seismic Demands for Building, Earthquake Engineering and Structural Dynamics, Vol.31, pp 561-582.
- [3] Fajfar, P and Fischinger, M (1989), N2 – A Method for Non-linear Seismic Analysis of Regular Buildings, Proceedings of the 9th world Conference on earthquake Engineering, Tokyo, Kyoto 1988, Vol.5, pp 111-116.
- [4] Fajfar, P (1999), Capacity Spectrum Method Based on Inelastic Demand Spectra, Eartquake Engineering and Structural Dynamics, Vol.28, pp 979-993.
- [5] Fajfar, P (2000), A Nonlinear analysis Method for Performance Based Seismic Design, Earthquake Spectra, Vol. 16, No.3, pp 573-592.
- [6] FEMA 273, NEHRP guidelines for the Seismic Rehabilitation of Buildings.
- [7] Freeman, S A et al (1998), Multi-mode pushover procedure (MMP) – a method to identify the effects of higher modes in a pushover analysis, Proceedings of the Sixth U.S. National Conference on Earthquake Engineering, Earthquake Engineering Research Institute, Oakland, California.
- [8] Gulkan, P and Sozen, M (1974), Inelastic Response of Reinforced Concrete Structures to Earthquake Motions, American Concrete Institute.
- [9] Kalkan, E and Kunnath, S K (2007), Assessment of Current Nonlinear Static Procedures for Seismic Evaluation of buildings, Engineering Structures, Vol.29, pp 305-316.
- [10] Kreslin, M and Fajfar, P (2012), The Extended N2 Method Considering Higher Mode Effects in Both Plan and Elevation, Bull Earthquake Engineering, Vol.10, pp 695-715.
- [11] Saiddi, M and Sozen, M A (1981), Simple Nonlinear Seismic Analysis of RC Structures, Journal of Structural Division, Vol.107, No.5, pp 937-953
- [12] SEAOC Vision 2000 Committee (1995), Performance-Based Seismic Engineering, Report prepared by structural Engineers Association of California, Sacramento, California.
- [13] Vidic, T et al (1994), Consistent Inelastic Design Spectra: Strength and Displacement, Earthquake Engineering and Structural Dynamics, Vol.23, pp 502-521.
- [14] Zameeruddin, M and Sangle, K K (2016), A Review on Recent Developments in Performance-Based Seismic Design of Reinforced Concrete Structure, Structure, Vol.6, pp 119-133.
- [15] Zou, X K and Chan, C M (2005), Optimal seismic performance based design of reinforced concrete buildings using nonlinear pushover analysis, Engineering Structures, Vol.27, No.8, pp 1289-1302.

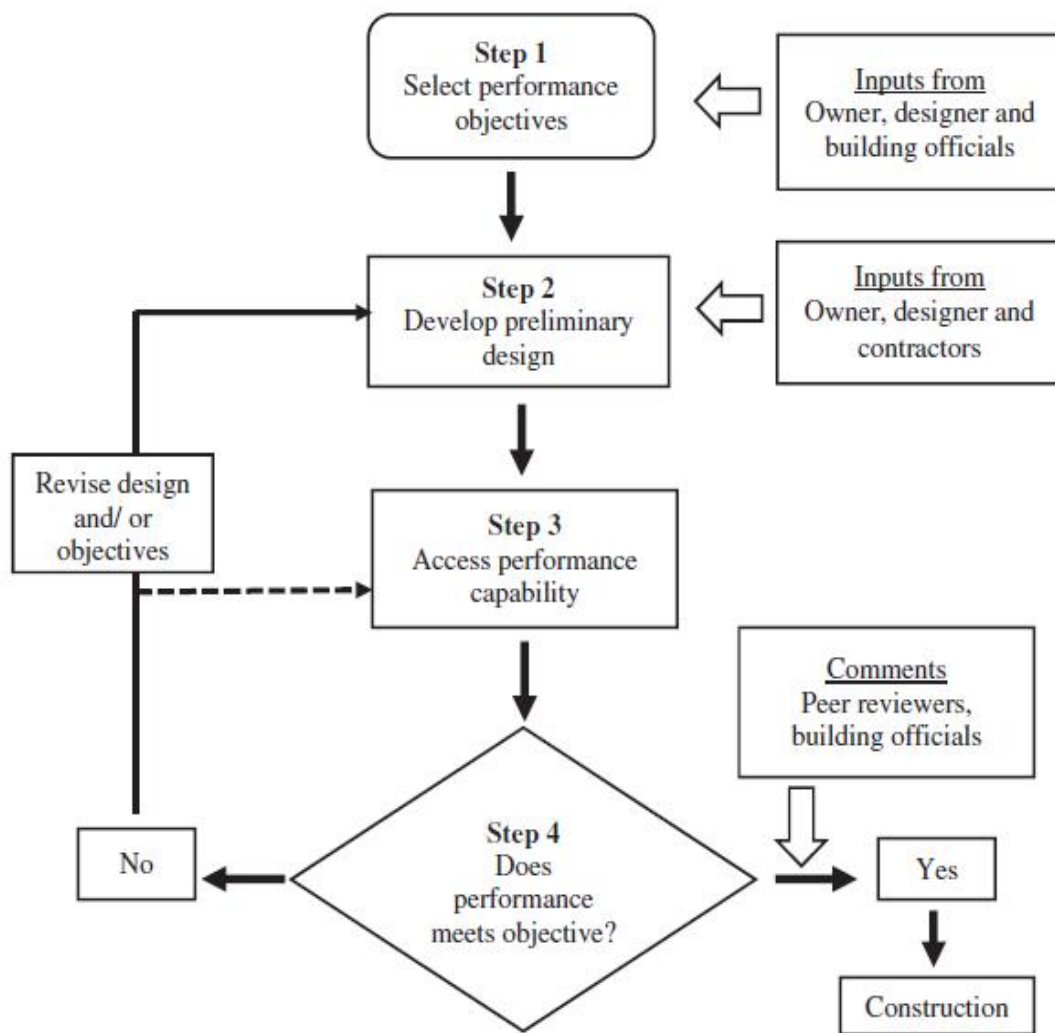


Fig.1 Performance Based Seismic Design flow diagram
(Zameeruddin and Sangle (2016))

6th International Engineering Symposium - IES 2017

March 1-3, 2017, Kumamoto University, Japan

**MECHANICAL ENGINEERING
&
RELATED FIELDS**

Enhancement of Boiling Heat Transfer on a Vibrating Heating Surface

Kohei Hamahata ¹ and **Hiroyuki Shiraiwa ²**

1 *Mechanical and Electrical Engineering Advanced Course, National Institute of Technology, Miyakonojo College, 473-1 Yoshio-cho, Miyakonojo, Miyazaki 885-8567, Japan. e-mail : m15hamahata@cc.miyakonojo-nct.ac.jp*

2 *Department of Mechanical Engineering, National Institute of Technology, Miyakonojo College, 473-1 Yoshio-cho, Miyakonojo, Miyazaki 885-8567, Japan.
e-mail: shiraiwa@cc.miyakonojo-nct.ac.jp*

Abstract: Many industrial products such as air-conditioner using boiling phenomenon have been frequently used for transportation equipment etc. with a vibration. However, the research about the influence on boiling of vibration, especially, the research on boiling heat transfer characteristics by vibration of the heating surface, has been hardly carried out. In this study, we consider influence on the boiling heat transfer characteristics of the inertial force and the shear force acting on bubbles. As a result, it was considered that the enhancement of the nucleate boiling heat transfer depended on the inertial force was much larger than the surface tension in the vertical direction, and depended on the shear force or the resultant force of the shear force and the inertia force when the inertial force was relatively small.

Keywords: Boiling bubbles, Vibration, Acceleration, Inertial force, Shear force

Introduction

Boiling phenomenon is composed of three regions of the nucleate boiling, the transition boiling and the film boiling. The heat transfer coefficient is larger than other heat transfer phenomena. Many industrial products such as air-conditioner using boiling phenomenon have been frequently used for transportation equipment etc. with a vibration. However, the research about the influence on boiling of vibration, especially, the research on boiling heat transfer characteristics by vibration of the heating surface, has been hardly carried out.

According to the previous our research, we confirmed that the boiling heat transfer was promoted with the increase in the amplitude and frequency of the vibration because boiling bubbles were efficiently removed by the vibration [Maeda, Y. (2014)]. In this study, to expand the boiling region and promote the boiling heat transfer, the heating surface is changed from the nickel wire to the platinum wire. In addition, the amplitude and the

frequency of experimental conditions and expanded more than that of previous research. And we consider influence on the boiling heat transfer characteristics of the acceleration and the resistance force acting on bubbles.

Bubble separation

Fig.1 shows the force that the bubbles receive under the vibration of the heating surface. Suppose that either the inertial force or the shear force reaches the maximum value and exceeds the surface tension of vertical direction when the bubbles disengages. Here, the applied vibration is a displacement sine wave in the vertical direction ($y=a\sin(2\pi ft)$, a : amplitude [m], f : frequency [Hz]). The maximum acceleration is $a=a(2\pi f)^2$, and the maximum velocity is $v=a(2\pi f)$ in vibration of vertically direction. The inertial force is a force acting in the direction opposite to the acceleration a . Assuming a bubble as a sphere, the maximum inertial force F_1 [N] acting on the boiling bubbles is given by Eq.(1).

$$F_1 = \rho_s \frac{4}{3} \pi \left(\frac{d_0}{2}\right)^3 A (2\pi f)^2 \quad (1)$$

where ρ_s is the density [kg/m³] of the bubble, and d_0 is the separation diameter [m] of the bubble.

In addition, the shear force is the resistance that a bubble receive from the viscosity of saturated water. The maximum shear force F_2 [N] acting on a boiling bubble is given by Eq.(2).

$$F_2 = C_D \frac{\pi d_0^2}{4} \frac{\rho v^2}{2} \quad (2)$$

where C_D is the resistance coefficient.

Also, the surface tension F_3 [N] in the vertical direction acting on a bubble is given by Eq.(3).

$$F_3 = \pi d_0 \sigma \sin \theta \times \sin \theta = \pi d_0 \sigma \sin^2 \theta \quad (3)$$

where σ is the surface tension [N/m], and θ is the separation contact angle [°] of the bubble.

Under the condition of roughly $F_1 < F_3 < F_2$, separation of bubbles due to inertial force is dominant. It is considered that the separation of bubbles due to the shearing force becomes dominant at $F_1 < F_3 < F_2$. This is considered to be an important factor that the vibration condition affects the boiling heat transfer characteristics.

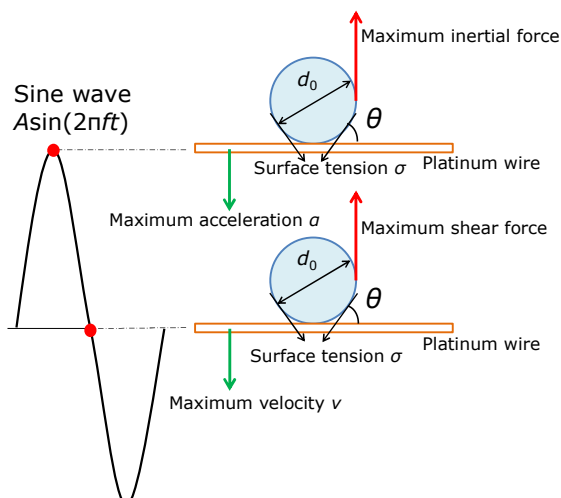


Fig.1 Force acting on bubbles

Experiment

In this experiment, since the boiling region is expanded to film boiling, the heating surface burns out or glows red-heat. The red-heat platinum wire can't be used again. For that reason, we changed the platinum wire every time and did the experiment. However, for reasons such as difficulty in making the same surface roughness and length, even with the same conditions, it was found that the reproducibility of the experiment was low such that the same result could not be obtained. This research divided into two experiments. Experiment No.1 is examined the effect of inertial force and shearing force on boiling heat transfer characteristics in the nucleate boiling region. Experiment No.2 is confirmed the effect of boiling heat transfer due to vibration in the film boiling region.

Experimental apparatus

Fig.2 shows the configuration of the experimental apparatus. The equipment of this experiment consists of the resistor ②, the platinum wire ③, the data logger ④, the vibrator ⑤, the DC stabilized power supply ⑧ and other measuring instruments. The platinum wire ③ is passed current and heated up with Joule heat. The platinum wire ③ is vibrated by the vibrator. The vibrator ⑤ is an electrodynamic vibration test device (512-A, EMIC Corporation) using electromagnetic force. This device can be set fine the frequency and the amplitude. Tachometer ⑪ is used to set the frequency. The amplitude is measured using the laser displacement sensor ⑩ (LGK050, KEYENCE Corporation) and the data logger ④ (GL800, GRAPTEC Corporation). At this time, the direction of vibration applied to the platinum wire ③ is the vertical direction. Also, because the resistance of the platinum wire ③ is very small, resistor ② was added between the

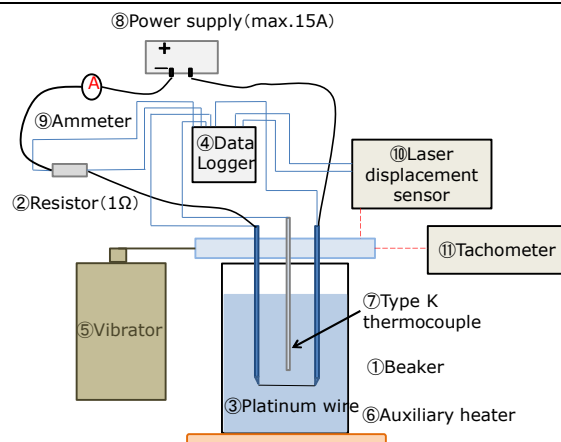


Fig.2 Experimental apparatus

DC stabilized power supply ⑧ and the platinum wire ③. The voltage and the current of the platinum wire ③ and the resistor ② and the temperature of the saturated water were recorded using the data logger ④. The K type thermocouple ⑦ was used for measuring the temperature inside the beaker ① is located 20mm above and 20mm below for the platinum wire ③.

Experimental methods

The series circuit was assembled as shown in Fig.2. Distilled water was boiled and well degassed for 40 minutes using the auxiliary heater ⑥. In the distilled water maintained at the saturation temperature, the platinum wire ③ was passed current and heated up. The platinum wire ③ was vibrated in the vertical direction using the vibrator ⑤. The value of the current was continuously increased by 1A in 10s using the DC stabilized power supply ⑧ and the ammeter ⑨. In experiment No.2, the current value was increased to the burnout point. After that, it was reduced to 0A. In experiment No.1, it was increased to 9A. The voltage and the current of the platinum wire ③ and the resistor ② and the temperature of the saturated water were recorded using the data logger at 0.5s intervals. The electric resistance of the platinum wire ③ was obtained from the current of the circuit and the voltage of platinum wire ③, and surface temperature of the platinum wire was calculated from these value.

Experimental conditions

Consider that the bubble receives the inertial force and the shear force of the vibration of the heating surface. From Eq.(1), the inertial force is proportional to the acceleration received by the bubble. From Eq.(2), the shear force is proportional to the square of the velocity of the bubble. Based on these, the experimental conditions were decided taking into consideration the maximum acceleration a and the square of maximum velocity v and the performance of the vibrator ⑤.

Table 1 shows the vibration condition which the maximum acceleration a received by the bubbles is approximately the same. Table 2 shows the vibration condition which the square of maximum velocity v received by the bubbles is approximately the same. Experiments are conducted under these two conditions, and the effect of inertial force and shear force on boiling heat transfer characteristics is studied.

Table 1 Experimental conditions of same the maximum acceleration a

Amplitude [mm]	Frequency [Hz]	Acceleration [mm/s ²]	Square of velocity [(mm/s) ²]
1	40	31583	15791
2	28	30951	30951
3	23	31326	46989
4	20	31582	63165

Table 2 Experimental conditions of same the square of maximum velocity v

Amplitude [mm]	Frequency [Hz]	Acceleration [mm/s ²]	Square of velocity [(mm/s) ²]
1	40	31583	15791
2	20	15791	15791
3	13	10008	15011

Calculation methods of evaluation value

The heat flux $q[W/m^2]$ in boiling heat transfer is given by Eq.(4).

$$q = \frac{V \cdot I}{A} \quad (4)$$

where V is the voltage [V] of the platinum wire, I is the current [A] of the platinum wire, and A is the surface area [m^2] of the platinum wire.

6th International Engineering Symposium - IES 2017

March 1-3, 2017, Kumamoto University, Japan

The surface temperature T_w [°C] of the platinum wire is given by the Eq.(5).

$$T_w = \left(\frac{V/I}{R_{100}} - 1 \right) \times \frac{1}{\alpha_{100}} + 100 \quad (5)$$

where α is the temperature coefficient [1/°C] of the platinum wire and R is the reference resistance [Ω].

The temperature coefficient α of the platinum wire and the reference resistance R are given by Eqs.(6) and (7).

$$R_{100} = \frac{\rho_{100} \cdot l}{S} \quad (6)$$

$$\alpha_{100} = \frac{\alpha_{20}}{1 + \alpha_{20}(100 - 20)} \quad (7)$$

where S is the cross-sectional area [m^2] of the platinum wire, and ρ is the electric low resistivity [Ωm]. The subscript 100 is for 100 [°C], and 20 is for 20 [°C].

The degree of superheat ΔT [K] is given by Eq.(8).

$$\Delta T = T_w - T_s \quad (8)$$

where T_w is the surface temperature [K] of the platinum wire, T_s is the saturation temperature [K] of water.

The heat transfer coefficient h [W/m²K] is given by Eq.(9).

$$h = \frac{q}{\Delta T} \quad (9)$$

Experimental results and discussion

Figs.3, 4 and 5 show the results of the experiment No.1. Figs.3 and 4 show the relationship between the degree of superheat ΔT and the heat flux q in the nucleate boiling region. According to Fig.3, the graphs $a=1mm_f=40Hz$, $a=2mm_f=28Hz$, $a=3mm_f=23Hz$ and $a=4mm_f=20Hz$ overlap. From Table 1, the maximum acceleration a received by the bubbles of these four conditions is approximately the same. Therefore, it can be considered that the increase of the heat flux q depends on the maximum acceleration a . And, according to Fig.4, the graphs $a=2mm_f=20Hz$ and $a=3mm_f=23Hz$ overlap. From Table 2, the square of maximum velocity v received by the bubbles of these two conditions is approximately the same. Therefore, under

these conditions, it can be considered that the increase of the heat flux q depends on the square of maximum velocity v . For the condition of $a=1mm_f=40Hz$, the square of the maximum velocity v is the same as these two conditions. Based on this result and the above result, it can be considered that the increase of the heat flux q depends on the maximum acceleration a when the maximum acceleration a is large, and depends on the square of the maximum velocity v when the maximum acceleration a is small.

Fig.5 shows the relationship between the degree of superheat ΔT and the heat transfer coefficient h in the nucleate boiling region. Because the results in Figs.5 and 3 are similar, it can be considered that the enhancement of the boiling heat transfer depends on the inertial force is much larger than the surface tension in the vertical direction, and depends on the shear force or the resultant force of the shear force and the inertia force when inertial force is relatively small.

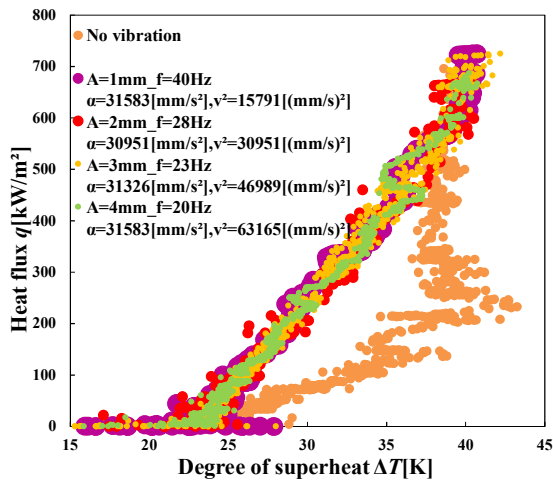
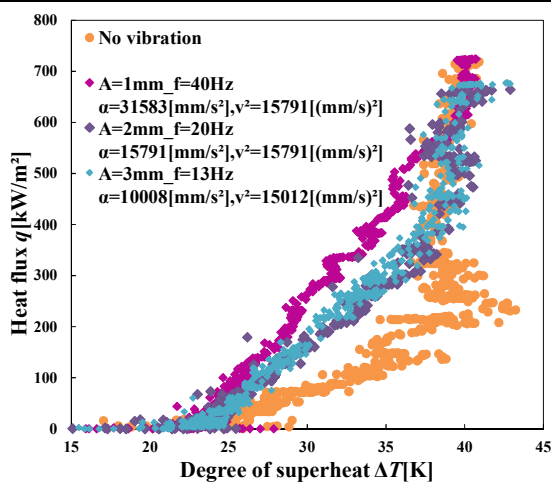


Fig.3 Relationship between the degree of superheat ΔT and the heat flux q in the nucleate boiling region (same acceleration)



**Fig.4 Relationship between the degree of superheat ΔT and the heat flux q in the nucleate boiling region
 (same the square of maximum velocity acceleration)**

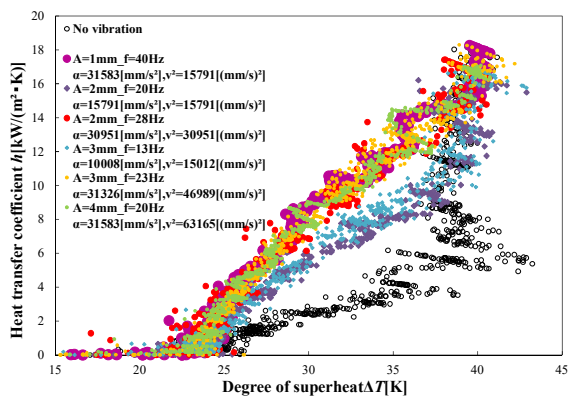


Fig.5 Relationship between the degree of superheat ΔT and the heat transfer coefficient h in the nucleate boiling region

Figs.6 and 7 show the results of experiment No.2. Fig.6 shows the relationship between the degree of superheat ΔT and the heat flux q in the nucleate boiling region and the film boiling region. According to Fig.6, it can be considered that the heat flux q and the degree of superheat ΔT suddenly increase after the heat flux q reaches the burnout point irrespective of the presence or absence of vibration, and film boiling is started. Actually, after the heat flux q reached the burnout point, the platinum wire glowed red-heat and covered with vapor film. In addition, red heat expands rapidly starting from notches etc. of platinum wire. Therefore, it can be

considered that the variation of the burnout point and the critical heat flux is affected by the condition of the platinum wire (tension, surface roughness, crease, etc.). Also, in the film boiling region, graphs overlap irrespective of the presence or absence of vibration. From this result, it is considered that the platinum wire is always covered with the vapor film in the film boiling region, and release of bubbles is hardly accelerated even when vibration is given.

Fig.7 shows the relationship between the degree of superheat ΔT and the heat transfer coefficient h in the nucleate boiling region and the film boiling region. According to Fig.7, in the nucleate boiling region, the same tendency as in Fig.6 is shown, but the heat transfer coefficient h rapidly decreases after reaching the burnout point. The reason for this is that the rate of increase of the degree of superheat ΔT is much larger than the rate of increase of the heat flux q . As in Fig.6, the relationship between the degree of superheat ΔT and the heat transfer coefficient h in the film boiling region is substantially the same irrespective of the presence or absence of vibration.

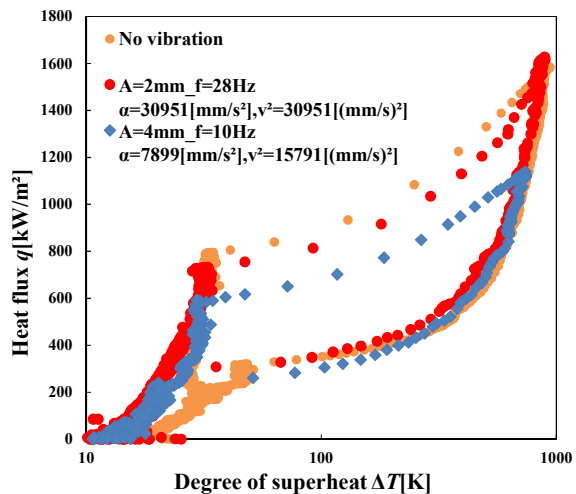


Fig.6 Relationship between the degree of superheat ΔT and the heat flux q in the nucleate boiling region and the film boiling region

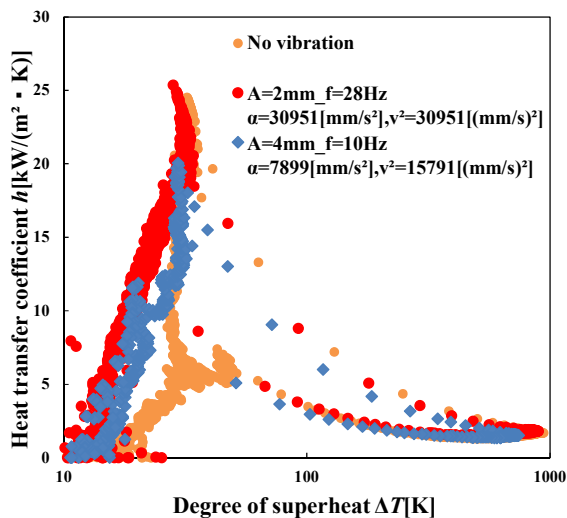


Fig.7 Relationship between the degree of superheat ΔT and the heat transfer coefficient h in the nucleate boiling region and the film boiling region

Conclusions

In this study, the following conclusions was obtained.

- (1) On the vibration heating surface, the enhancement of the nucleate boiling heat transfer depended on the inertial force was much larger than the surface tension in the vertical direction, and depended on the shear force or the resultant force of the shear force and the inertia force when inertial force was relatively small.
- (2) The variation of the burnout point and the critical heat flux were probably affected by the condition of the platinum wire (tension, surface roughness, crease, etc.).
- (3) In the film boiling region, because the heating surface was always covered with the vapor film, promotion of bubbles separation by vibration of the heating surface was small and boiling heat transfer was not enhanced.

References

- [1] Maeda, Y. (2014), Enhancement of Nucleate Boiling Heat Transfer on Vibrating Heating Surface, Graduation Thesis, National Institute of Technology, Miyakonojo College, pp.1-44.

Reliability Analysis on Solid Rocked Engine Vessel

LIU Chong ^{1,2}, TORII Shuichi ¹ and CHEN Yuting²

- 1 Department of Mechanical System Engineering, Kumamoto University, Kurokami, 2-39-1, Kumamoto 860-8555, Japan. e-mail: 162d9211@st.kumamoto-u.ac.jp
2 School of Chemical Equipment, Shenyang University of Technology, Hongwei, 111003, Liaoyang 0419-5319297, China. e-mail: 84316980@qq.com

ABSTRACT: The solid rocket engine is widely used in missile. In order to expand the scope of attack, both increase specific impulse and decrease weight are become the research goal. In this paper, we take the vessel of solid rocket engine as research object, simulate the pressure of hydrostatic test, establish the finite element model of solid rocket engine vessel, solve the stress for any element in solid rocket engine vessel and find the maximum stress point by ANASYS, and then we solve reliability by the method of random analysis. According to this reliability, change the pressure which load on the inside of solid rocket engine vessel while insure reliability higher than the criticality. In this analysis, we can increase the pressure which loads the solid rocket engine vessel and we achieve the sensitivity of all parameters.

Keywords: solid rocket engine, shell, ANSYS, reliability

1 INTRODUCTION

As the phase of fuel, rocket can be dividing into three types: solid rocket, liquid rocket and solid liquid hybrid rocket. Nowadays, most of missile employ solid rocket engine, because of the simple structure, easy maintain, quick response and so on, and this situation will still exist in the future. Reliability is the ability of a system or component to perform its required functions under sated conditions for a specified time. It was very difficult to solve the reliability in the past, with the development of computer technology, it is easier than before according to LIU P and ZHANG P, (2002).

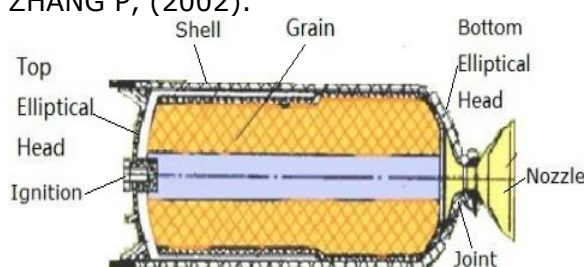


Fig.1 Structure of solid rocket engine

A typical solid rocket engine is shown in Figure1. Solid rocket engine has the following characteristics. Working time is

short, the longest working time are not more than 10 seconds according to ZHANG S and CAI H, (2003). The structure is simple, it is helpful to obtain high reliability. Solid rocket engine need to endure high temperature, high pressure, and another serious situation. After considering the characteristics of solid rocket engine, we counted and analyzed the solution, research the law of distribution from the viewpoint of probability theory. The reliability of vessel will influence the design of solid rocket engine, even influence the performance of solid rocket engine, in order to reach the reliability, we usually use the safety factor in the past according to LIU F and ZHANG W, (2002). But safety factor cannot measure the reliability, even bigger safety factor will lead to heavier weight, and then will result in lower specific impulse according to RUAN C (2002). Therefore, using the new method which is solving the reliability of solid rocket engine vessel base on the method of analysis design is significance. Particularly, we can obtain reliability by this method, verifying rationality of structure, and find the weak region. Moreover, the reliability is

considered as theoretical basis to optimal design and develop new product.

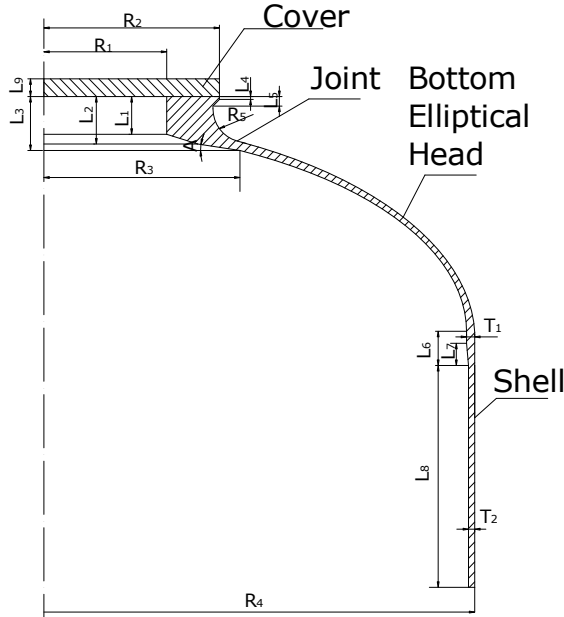


Fig.2 Simply structure of solid rocket engine vessel

Table 1 Mean and deviation of parameters

Symbol/Unit	Mean	Standard Deviation
R1/mm	57	0.1
R2/mm	81.5	0.117
R3/mm	91	0.117
R4/mm	200	0.153
R5/mm	12	0.06
L1/mm	17	0.06
L2/mm	21.4	0.07
L3/mm	24.3	0.083
L4/mm	1.3	0.033
L5/mm	4.3	0.04
L6/mm	15	0.06
L7/mm	10	0.06
L8/mm	100	0.116
L9/mm	8	0.05
T1/mm	3.8	0.04
T2/mm	2.9	0.033
A/°C	17	0.333
P/MPa	17	0.167
yies/ MPa	1750	72.6

2 Method

2.1 Structure and parameters

Vessel is a very important component of the solid rocket engine. Solid rocket engine vessel consists of top elliptical head, shell, bottom elliptical head and the joint.

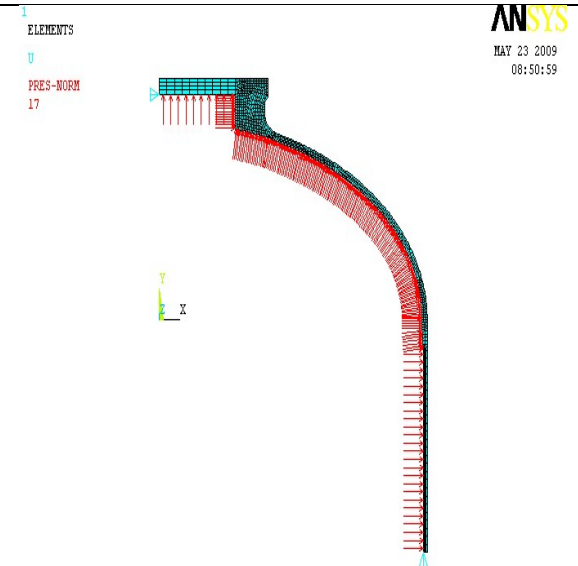


Fig.3 Finite element model include mesh, constrain and pressure

Though, we can establish the complete model, it is not only necessary but also make the work more complicated according to XIAO G (1999). The structure of shell is axisymmetric, the loading is also axisymmetric, and the top of elliptical head is stronger than the bottom of elliptical head, so the model of solid rocket engine vessel can be simplified, as shown in Figure2 according to LI F et al (2004), ZHAO H et al (2003) and ZHANG L et al (2003). Mean and standard deviation of parameters are shown in table 1. Material properties of vessel are shown in table 2.

Table 2 material property

Vessel	
Material code	30Si2MnCrMoVE
Elasticity modulus	2.1×10^5 MPa
Poisson ratio	0.3

2.2 Preprocessing

The model was treated as the following steps. Firstly, we set Solid 82 as element type, input all the value of parameters (Table 1) and material property (Table 2). Secondly, we mesh the simple model. Cover and shell are belong to regular shape, so cover is divided into 10×4 meshes and shell is divided into 3×25 . But elliptical head and the joint are not regular shape, so they are divided by free meshing. Thirdly, loading pressure on the inside of vessel and the pressure is 17 MPa. Finally, loading the constraint. One we loaded Y-direction constraint on the shell of cross-sectional area, because the shell is long enough, the

extension of shell is negligible. The other we loaded X-direction constraint on the cover of cross-sectional area, because we used cover just in the pressure of hydrostatic test, the cover is big enough, the extension of cover is negligible. The Finite element model as shown figure 3.

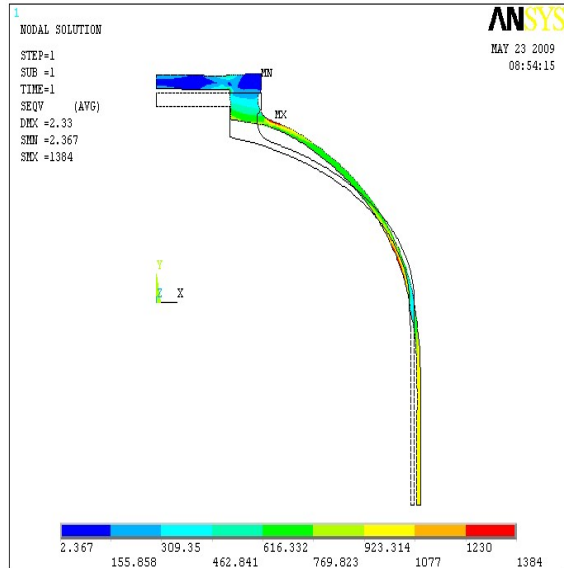


Fig.4 Stress contour plot under 17MPa

2.3 Solution

Solved and illustrated the solution by the figure 4. We can find two red regions. One red region arise on the outside of transition between joint and bottom elliptical head, here is the maximal stress region, the value of stress are reach 1384 MPa, so here it is the most dangerous region, the other weak point arise on the inside of transition between shell and bottom elliptical head, here is the second maximal stress region,

it is also dangerous region.

2.4 Random finite element analysis

As everyone knows, accurate size never exist in the world, all the size has a range. If we think any size is correct, the finish size just in the range of size according to XIAO G (1999). So random selected all the size in their range on the basis of Table 1. We took the sample base on the parameters and the number of samples is 50,000. The number we took the samples is too big, the work of calculation is too hard, the number we took the samples is too small, the solution maybe not accurate, so the number of sample is 50,000. Of course, the number of solutions is 50,000, in other words, the number of maximal stress is 50,000. Into the Equation 1 to calculate, when y_{ies} is greater than or equal to \maxstr , that is to say the value of Z is greater than or equal to zero, we think the solution is acceptable, otherwise is unacceptable. We can get the value of Z . Statistics used the method of Monte Carlo with Latin Hypercube and we can get the reliability according to ZHOU Z and ZHANG H (2003).

$$Z = y_{ies} - \maxstr \quad (1)$$

Where y_{ies} — admissible stress;

\maxstr — maximal stress.

Solution was shown as figure5, we can find the value of Z never lower than zero after 50000 times calculation. So the reliability is 100% with the confidence level of 95%. Distribution of Z value was shown as figure 6. Process of sampling was shown

Probability Result of Response Parameter Z

```

Solution Set Label      = YLRQ11
Simulation Method       = Monte Carlo with Latin Hypercube Sampling
Number of Samples        = 50000
Mean (Average) Value   = 3.8129122e+002
Standard Deviation     = 7.6981449e+001
Skewness Coefficient    = -1.#IND000e+000
Kurtosis Coefficient    = -1.#IND000e+000
Minimum Sample Value   = 7.0498154e+001
Maximum Sample Value   = 7.1640360e+002

```

The probability that Z is smaller than 0.0000000e+000 is:

Probability [Lower Bound, Upper Bound]
 0.00000e+000 [0.00000e+000, 0.00000e+000]

NOTE: The confidence bounds are evaluated with a confidence level of 95.000%.

Fig.5 Solution of reliability under 17MPa

as figure 7, we can see convergence has happened after calculating 12501 times, that means 50000 samples is enough.

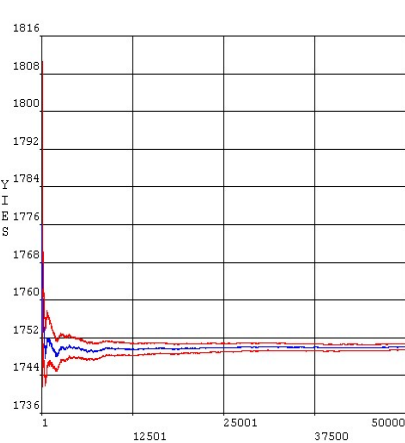


Fig.6 Distribution of Z value with confidence level of 95%

ANSYS

pressure of hydrostatic test is the second greatest influence on the value of Z, and the ratio of influence is about 8%. The third is parameter A and the fourth is parameter T1. The ratio of influence of other parameters is about 20%.

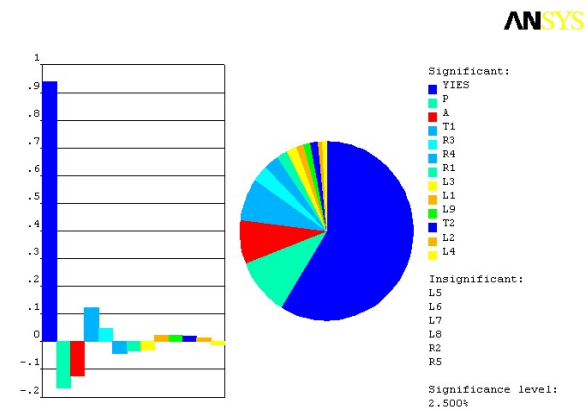


Fig.8 Distribution of parameters' sensitivity

ANSYS

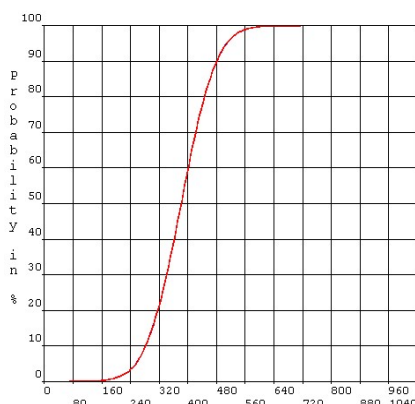


Fig.7 Process of sampling

The sensitivity Z value is shown in figure 8. The value of yies is the greatest influence on the value of Z, and the ratio of influence is about 55%. The second P which is the

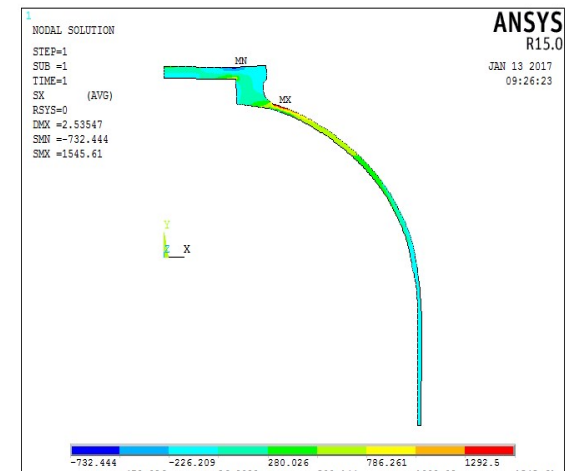


Fig.9 Stress contour plot under 18.5MPa

Probability Result of Response Parameter Z
=====

```
Solution Set Label = YLRQ11
Simulation Method = Monte Carlo with Latin Hypercube Sampling
Number of Samples = 50000
Mean (Average) Value = 2.6062051e+002
Standard Deviation = 7.7217177e+001
Skewness Coefficient = -1.#IND000e+000
Kurtosis Coefficient = -1.#IND000e+000
Minimum Sample Value = -5.9021971e+001
Maximum Sample Value = 5.8810819e+002
```

The probability that Z is smaller than 0.0000000e+000 is:

Probability [Lower Bound, Upper Bound]
3.89298e-004 [3.01086e-004, 4.77510e-004]

NOTE: The confidence bounds are evaluated with a confidence level of 95.000%.

The probability is interpolated between:
Z=-7.7279489e-001 which has rank 19 out of 50000 samples
Z= 8.8808561e-001 which has rank 20 out of 50000 samples

Fig.10 Solution of reliability under 18.5MPa

2.5 Optimal design

The reliability is 100% under 17 MPa with confidence level 95%, we can find the minimum value of Z is about 70 MPa by Figure 6. That means the vessel is reliable or safe but conservative. After trying numerous times, finally we raised the pressure of hydrostatic test and reach 18.5 MPa. Using the same method to solve, the solution is shown as Figure 9. We also fine two red regions, the location is the same to arise the two red regions under 17MPa. But the maximal stress is reach 1545.61 MPa.

$$Z = yies - maxstr \quad (2)$$

We use the equation (2) to estimate reliability in the conventional method. If Z is greater than or equal to zero, we think the vessel is reliability, otherwise it is not reliability. Notes, n is equate to 1.2, Z is not more than zero under 18.5 MPa. So this solution was unacceptable in the past, but it is shown as Figure 10, We can find the range of failure rate is from 3.01086 e-004 to 4.7751 e-004. So the range of reliability is from 99.952249% to 99.9698914% with confidence level 95%.The reliability is also can be accepted.

3 Conclusions

A. Solid rocket engine vessel is reliable or safe under 17MPa, but is conservative. Under the acceptable reliability, we can increase the pressure and reach 18.5 MPa. It is very important for the specific impulse of solid rocket, it is a base for expanding the scope of attack.

B. We can find which parameter is serious influence reliability of solid rocket engine vessel or not. It is theoretical base for optimal structure of solid rocket engine vessel.

C. By comparing the method of random analysis with conventional method, we can find the method of random analysis is significant for designing solid rocket engine vessel.

4 REFERENCES

- [1] LI F et al (2004), Application of Finite Element Analysis Software ANSYS to 3-D Modeling of Rocket Engine, *Applied Science and Technology*, Vol. 31, No.10, pp. 59-60.
- [2] LIU F and ZHANG W, (2002), Research and Realization of the Reliability Design System for Solid Rocket Motor, *Aeronautical Computer Technique*, Vol. 35, No.1, pp. 48-50.
- [3] LIU P and ZHANG P, (2002), The Technologies of Reliability Assessment of Solid Rocket Motors, *Journal of Solid Rocket Technology*, Vol. 25, No.1, pp. 1-4.
- [4] RUAN C (2002), Technical Problems for Tactical Missile Solid Rocket Motors, *Journal of Solid Rocket Technology*, Vol. 25, No.2, pp. 8-12.
- [5] XIAO G (1999), Reliability Assessment of Solid Rocket Engine Based on Converted Information, *Journal of Xi'an Jiao Tong University*, Vol. 33, No.7, pp. 33-36.
- [6] ZHANG L et al (2003), Establishment of Mechanical Model of High-speed and High-acceleration Solid Rocket Engine Case, *Journal of Air Force Engineering University (Natural Science Edition)*, Vol. 4, No.1, pp. 19-21.
- [7] ZHANG S and CAI H, (2003), Bayesian Approach of Performance Reliability Assessment of Solid Rocket Motors, *Journal of Solid Rocket Technology*, Vol. 26, No.4, pp. 9-11.
- [8] ZHAO H et al (2003), Numerical Simulation Computation of Plastic Flow of A Working Solid Rocket Motor Case, *Journal of Solid Rocket Technology*, Vol. 26, No.4, pp. 38-40.
- [9] ZHOU Z and ZHANG H (2003), Performance Deviation Calculation and Reliability Evaluation of Solid Rocket Motors, *Journal of Solid Rocket Technology*, Vol. 26, No.3, pp. 35-38.

Computational Study of mixed convection in a lid-driven cavity with square block subjected to constant heat flux

G Narendran ¹, D Arumuga Perumal ^{2,*} and N Gnanasekaran ³

- ¹ Department of Mechanical Engineering, National Institute of Technology Karnataka, Surathkal, Mangalore 575025, India. e-mail: narendranganesan24@gmail.com
² Department of Mechanical Engineering, National Institute of Technology Karnataka, Surathkal, Mangalore, India. email:Perumal.iit@gmail.com
³ Department of Mechanical Engineering, National Institute of Technology Karnataka, Surathkal, Mangalore, India. email:ngs.iitm@gmail.com
-

ABSTRACT: The present numerical study encounters the mixed convective flow and heat transfer characteristics in a lid-driven square cavity with square block subjected to constant heat flux condition. The fluid flow in the cavity is driven by top wall, while other three walls are stationary. The computation is solved by finite volume method (FVM) using SIMPLE scheme with examining parameters of Reynolds number ($Re = 10-1000$) and Prandtl number ($Pr = 1 -100$). The effect of fluid flow and heat transfer containing square blockage in the square cavity for different fluids is also studied. The results are presented in terms of Streamline plots and isotherms for all different parameters.

Keywords: Lid-driven cavity, mixed convection, Square block, Reynolds number, Prandtl number

INTRODUCTION

The influence of Prandtl number and Grashof number in lid driven cavity with triangular block of constant heat flux was investigated by Gangawane (2017). The numerical studies were carried by solving FVM (Finite Volume Method) for varying parameters ranging such as ($Pr=100$), ($Re=1000$) and ($Gr=0-10^5$) further the work on increasing the dimensions of the blockages was also performed. Khanafer and Aithal (2013) conducted numerical study on laminar mixed convection using lid driven cavity containing cylindrical obstruction. They observed addition of cylinder increases the average nusselt number with the increase in Richardson number. Increase in cylindrical radius also augments the Average Nusselt number predominately in mixed convection. Billah et al. (2013) presented numerical investigation for mixed convection flow with heated cylinder in lid driven cavity. The studies were performed by varying the

parameters such as Richardson number, diameter of the obstruction and thermal conductivity. Chamkha and Nada (2012) analysed the mixed convection effects of Water-Alumina nanofluids on single and double lid driven cavities using finite volume approach. They observed that increase in heat transfer was found for increased volume fraction on both single and double driven cavities. Kalteh et al. (2014) studied numerically the performance of nanofluid in a lid driven cavity with heated triangular source. Effects of parameters like volume fraction, particle diameter and different nanoparticles on their heat transfer enhancement are discussed. Mansour et al. (2010) performed numerical study on mixed convection for different nanofluid in a partially heated lid driven cavity. The heat transfer study on the influencing parameters such as Re , V_f , location of the heat source and its length. Sivasankaran et al. (2010) conducted studies on non-uniform heated walls on lid driven cavity

6th International Engineering Symposium - IES 2017

March 1-3, 2017, Kumamoto University, Japan

using finite volume method. Increase in Avg Nusselt number was observed for the provided Prandtl number and Reynolds number and maximum heat transfer was attained for Prandtl number of 6.5 at $Re=1000$. Laminar mixed convection study in a cavity containing square blockages with isothermal boundary solved with varied blockage ratios was presented by Islam et al (2012). Where the decrease in heat transfer was observed when Richardson number crosses 1 above which Nusselt number decreases significantly for the increase in block ratio. Mixed convection effects on cavity inclination studied were performed by Cheng and Liu (2014) for varying angles ranging from 0-90° with air as fluid. They reported that increase in inclination angle augments the heat transfer and maximum increment was at 75°. Amiri and Khanafer (2011) analysed the fluid structure interaction using flexible bottom wall in a square lid driven cavity. The finite element method is used to solve the transport equation in order to investigate the influence of flexible surface on increase in heat transfer. According to that flexible surface provided better energy and momentum transfer for natural convection in the cavity. Mixed convection on trapezoidal enclosures was performed by Bhattacharya et al. (2013) with Grashof number range varied from 10^3 to 10^5 . Further simulation were extended by inclining the side walls to 45°. It is observed that for higher Reynolds number ($Re=100$) flow is governed by lid movement but for lower ($Re=1-10$) which is accompanied by natural convection.

Problem description

The analysis involve in lid driven cavity with a constant heat flux square blockage at the centre of the cavity. The corresponding cavity width and height are A and B which is shown in Fig. 1. The blockage is positioned at a distance of C from the vertical wall with a blockage size of D . the cavity is filled with different fluids with Prandtl number varying from 1-100. Acceleration to the gravity is acting to the negative Y direction. This combined effect of the wall movement and gravity give

rise to the mixed convection in between the region of the blockage and the cavity.

Numerical Procedure

The study considers a two dimensional lid driven cavity with incompressible fluids under laminar condition. The effect of density variation has been included by implementing Boussinesq approximation. The respective governing equation for mass, momentum and energy equation are presented as such

$$\frac{\partial U}{\partial X} + \frac{\partial V}{\partial Y} = 0 \quad (1)$$

$$U \frac{\partial U}{\partial X} + V \frac{\partial V}{\partial Y} = - \frac{\partial P}{\partial X} + \frac{1}{Re} \left(\frac{\partial^2 U}{\partial X^2} + \frac{\partial^2 U}{\partial Y^2} \right) \quad (2)$$

$$U \frac{\partial U}{\partial X} + V \frac{\partial V}{\partial Y} = - \frac{\partial P}{\partial Y} + \frac{1}{Re} \left(\frac{\partial^2 \theta}{\partial X^2} + \frac{\partial^2 \theta}{\partial Y^2} \right) + \frac{Gr}{Re^2} \quad (3)$$

$$U \frac{\partial \theta}{\partial X} + V \frac{\partial \theta}{\partial Y} = \frac{1}{Pe} \left(\frac{\partial^2 \theta}{\partial X^2} + \frac{\partial^2 \theta}{\partial Y^2} \right) \quad (4)$$

Boundary conditions

The computations were carried out according to the boundary presented in the Fig. 1. The top and bottom walls of the cavity are provided with adiabatic boundary condition where as both the vertical walls are maintained at a low temperature of 300K. The blockage at the centre of the cavity is provided with constant heat flux at their walls. The numerical simulation is attributed to perform mixed convection by availing the gravity along the negative y direction. The lid movement is provided at the top of the cavity in positive x direction, further lid conditions were given in negative x direction to simulate anti parallel mixed convection.

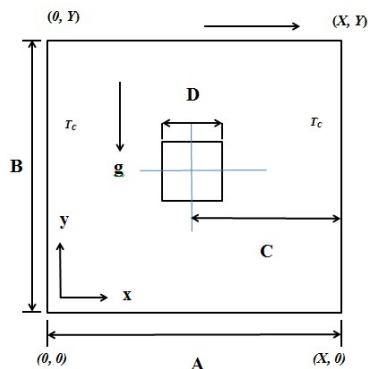


Fig 1. Schematics sketch of the problem
Numerical scheme

6th International Engineering Symposium - IES 2017

March 1-3, 2017, Kumamoto University, Japan

The analysis was conducted by discretizing the computational domain using finite volume method with commercial CFD software FLUENT 15. SIMPLE method has been used to couple velocity and pressure components. QUICK scheme for solving momentum equation accompanied with second order pressure correction. The above resulted algebraic equations were solved using Gauss-Seidel method of iteration. Under relaxation factors were taken care for pressure and energy correction for smooth convergence. The computations carried out till the residuals of continuity, momentum and energy settle lower than 1×10^{-6} .

The mixed convection nature of the current problem is validated for the results of Islam et al. (2012) with air as working fluid containing in the cavity. The verification were carried out for the boundary conditions and grid structures detailed by the authors. The grid system implemented in the numerical simulation has 100X100 nodes in respective X and Y directions. The resulting values sensitivity for the current system is checked with different grid systems. The analysed grid systems were 50X50, 100X100, 150X150, 200X200 and 250X250 nodes in X and Y directions. The results from 150X150, 200X200 grids were close to each other. Considering the computational time and resources needed for performing the analysis, second grid system 150X150 grid system is used in the current work.

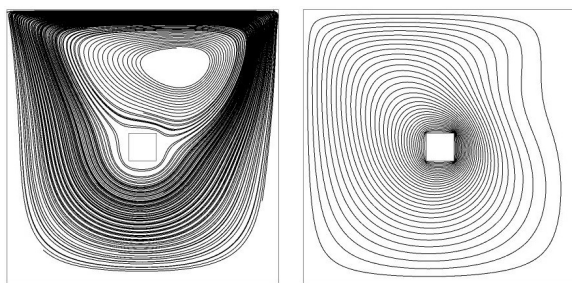


Fig 2. Streamline profiles and Isothermal of heated lid driven cavity for $Ri=0.1$.

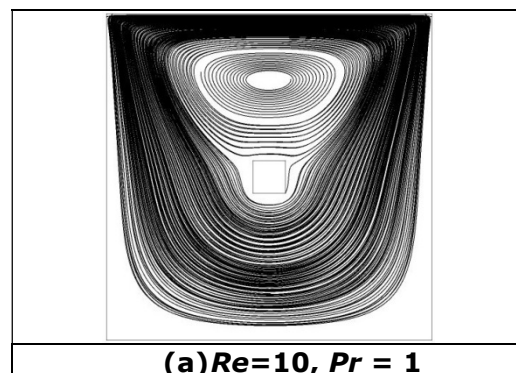
Results and Discussion

Mixed convection studies on lid driven cavity with central blockage for a heat flux of 500 W/m^2 is numerically studied and their performance characteristics are

presented with different fluids and Reynolds number. The effects of square blockage, Grashof number are discussed below.

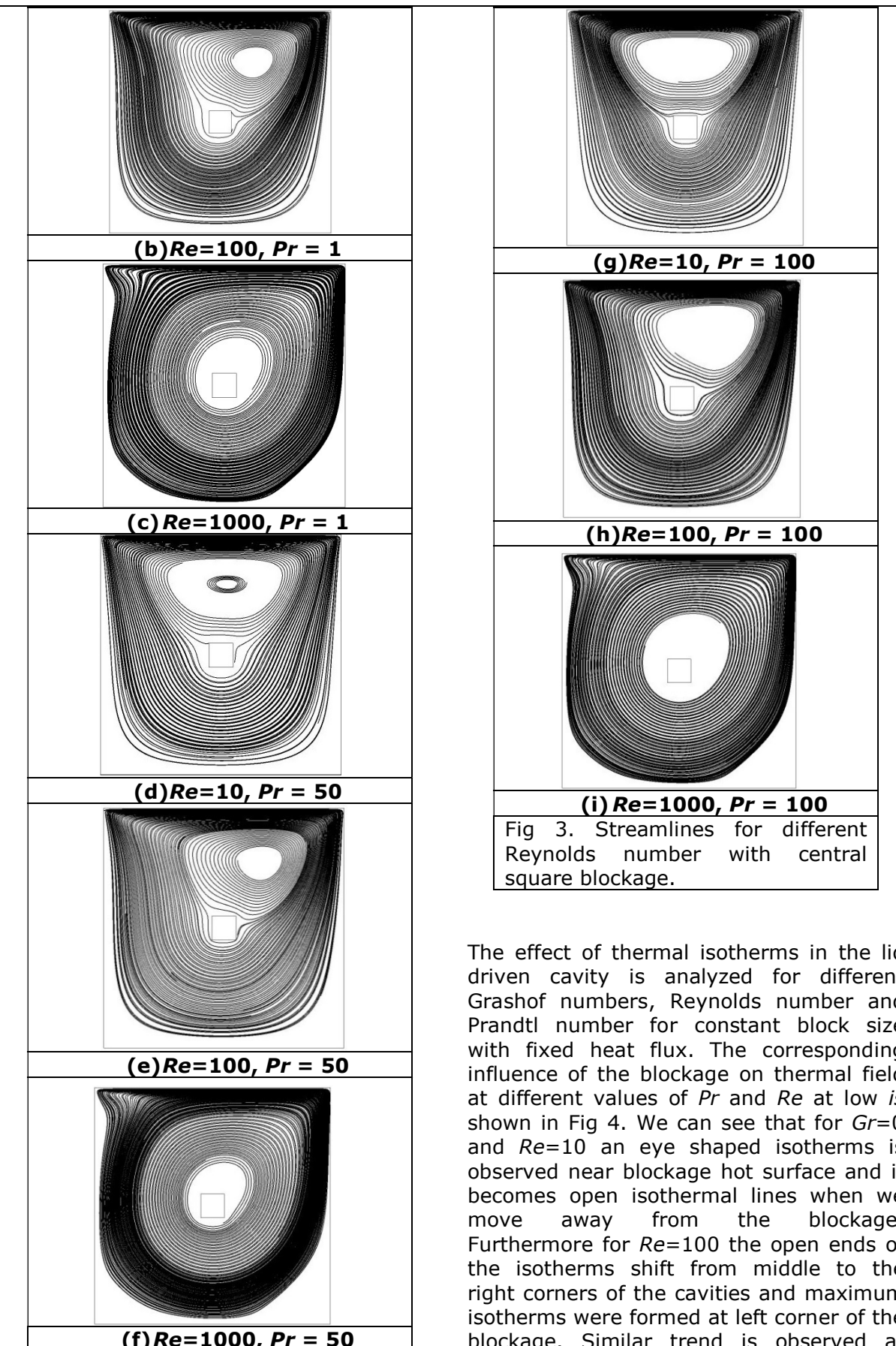
Flow study

Fluid flow inside the cavity is investigated by exploring the effects of Prandtl number (Pr), Grashof number (Gr) and Reynolds number (Re). The influence of the blockage at the centre of the cavity for the Grashof number $Gr=0$ is shown in Fig 3. The effect of the gravity was not involved and most of the fluid flows by the influence of velocity driven by the lid movement. At lower Reynolds number which attributes only at natural convection the interaction of the fluid and blockage is higher. The blockage attempts to split the streamline patterns and it again joins the primary streamline. This trend is seen in all the three different Prandtl numbers. The primary vortex is formed right above the blockage and the maximum velocity of the fluid is observed right below the top lid of the cavity. Increase in Reynolds number shifts the vortex away from the mid-section of the cavity. And the result shows the change in shape of the vortex centre from elliptic to oval shape due to higher velocity at right corner of the cavity. For $Re=100$ interaction of the fluid to the blockage is also seen higher. For $Re=1000$ the vortex was developed in the centre of the cavity which was seen in all the three different fluids. The very negligible effect of the blockage is felt due to the increased centrifugal force and it's more for higher density fluids ($Pr=100$). The core of the vortex expands gradually to form oval shape.



6th International Engineering Symposium - IES 2017

March 1-3, 2017, Kumamoto University, Japan



The effect of thermal isotherms in the lid driven cavity is analyzed for different Grashof numbers, Reynolds number and Prandtl number for constant block size with fixed heat flux. The corresponding influence of the blockage on thermal field at different values of Pr and Re at low is shown in Fig 4. We can see that for $Gr=0$ and $Re=10$ an eye shaped isotherms is observed near blockage hot surface and it becomes open isothermal lines when we move away from the blockage. Furthermore for $Re=100$ the open ends of the isotherms shift from middle to the right corners of the cavities and maximum isotherms were formed at left corner of the blockage. Similar trend is observed at

6th International Engineering Symposium - IES 2017

March 1-3, 2017, Kumamoto University, Japan

isotherms of different Re and Pr at $Gr=0$. When Re is increased to $Re=1000$ isotherms forms a circular pattern with the increased flat below the top lid.

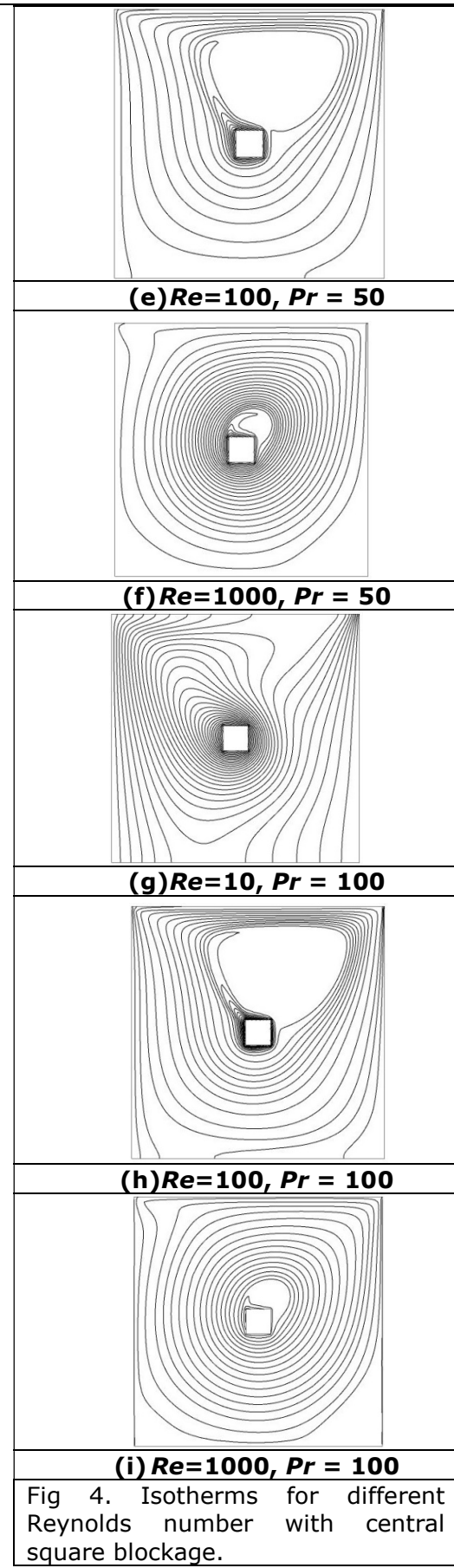
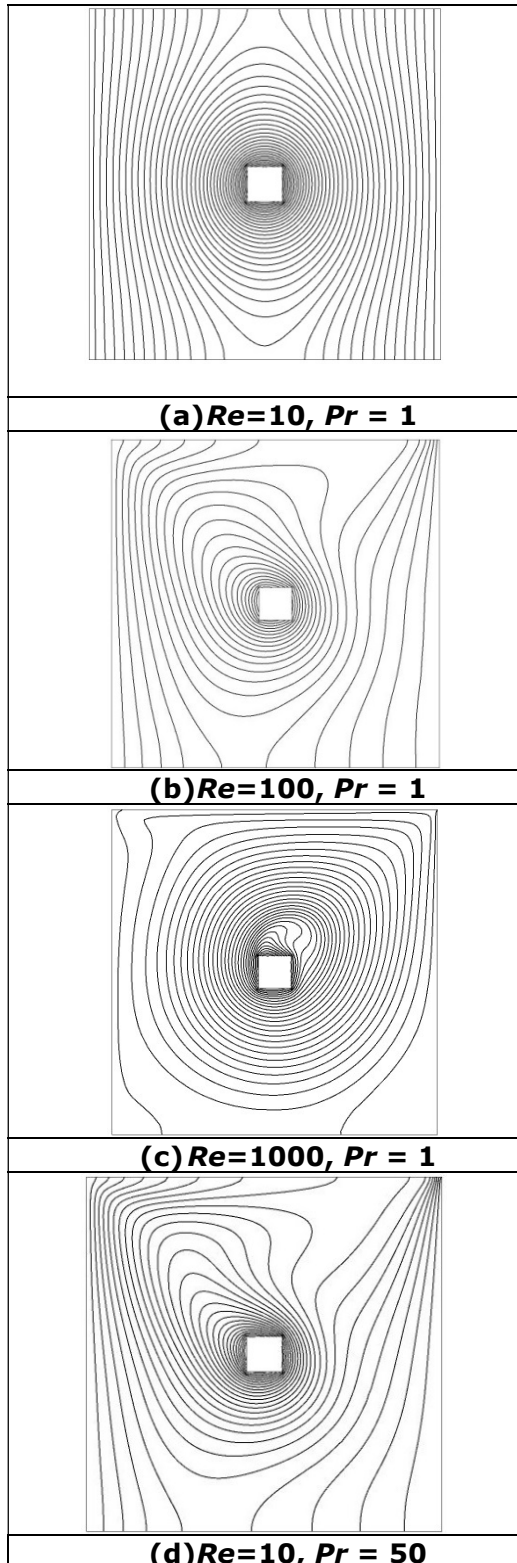
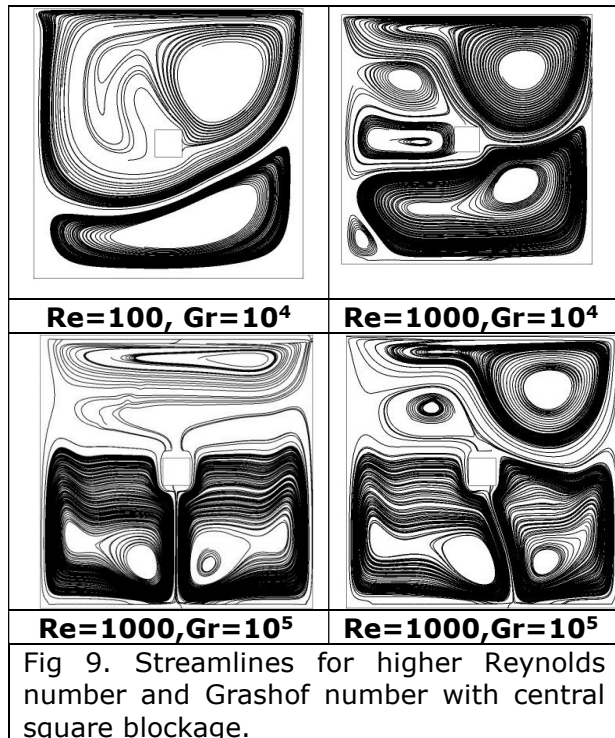


Fig 4. Isotherms for different Reynolds number with central square blockage.

6th International Engineering Symposium - IES 2017

March 1-3, 2017, Kumamoto University, Japan

Fig. 5 depicts the streamlines for the higher Reynolds number for $Gr=10^4$ and $Gr=10^5$. The inclusion of higher Grashof number two vortex is formed one which envelopes the blockage and another one in below. The formed vortex at right corner is big enough to be developed near the right side wall of the blockage. Remaining streamline fall below the blockage and continues to flow which was not seen at lower Gr . Further for $Re=100$ the above vortex becomes bigger and tend to push the bottom vortex in clockwise direction due to this another two new vortex are developed. For $Gr=10^5$ vortex is at the mid of the cavity and forms two vortexes for $Re=100$ and long vortexes are formed below the moving lid. Due to the gravity effect the influence of buoyancy accompanied natural convection did not affect much. But when the Reynolds number increases to $Re=1000$ the primary vortex near the lid pushes the outer two vortex above. And from above we can see increase in vortex for higher Grashof numbers.



Conclusions

A computational analysis is performed to study the mixed convection flow in a lid driven enclosure with a constant heat flux

square block which acts as a blockage. Results are obtained for three different Reynolds number. The following conclusion has been listed from the present investigations

- The square blockage size has a significant effect on the flow and thermal fields in the cavity. Higher interaction of the fluids are found at lower Reynolds number compared to that of higher Re where only edges are effected. The average temperature carried by the fluid is higher for the $Pr=100$.
- For higher Grashof number the effect of mixed convection is not effective at lower Reynolds number.

References

- Gangawane, K M, (2017) Computational analysis of mixed convection heat transfer characteristics in lid-driven cavity containing triangular block with constant heat: Effect of Prandtl and Grashof numbers, Int. J. of Heat & mass transfer Vol. 105, pp. 34-57.
- Khanafer, K, Aithal, S.M, (2013) Laminar mixed convection flow and heat transfer characteristics in a lid driven cavity with a circular cylinder, Int. J. of Heat and Mass Transfer Vol. 66, pp. 200–209.
- Billah, MM et al. (2011) Numerical analysis of fluid flow due to mixed convection in a lid-driven cavity having a heated circular hollow cylinder, Int. Com. in Heat and Mass Transfer Vol.38, pp. 1093–1103.
- Chamkha, AJ, Abu-Nada, E (2012) Mixed convection flow in single- and double-lid driven square cavities filled with water-Al2O3 nanofluid: Effect of viscosity models, Euro. J. of Mech. B/Fluids Vol. 36, pp. 82–96.
- Kalteh, M et al. (2014) Numerical solution of nanofluid mixed convection heat transfer in a lid-driven square cavity with a triangular heat source, Powder Technology Vol. 253, pp. 780-788.
- Mansour, MA, (2010) Numerical simulation of mixed convection flows in a square lid driven cavity partially heated from below using nanofluids. Int J. in Heat and Mass Transfer Vol. 37, pp. 1504-1512.
- Sivasankaran S et al. (2010) Numerical study on mixed convection in a lid-driven cavity with non-uniform heating on both sidewalls, Int. J. of Heat and Mass Transfer Vol. 53, pp. 4304-4315.
- A. W. Islam, M. A. R. Sharif, E. S. (2012) Carlson Mixed convection in a lid driven square cavity an isothermally heated square blockage inside Int. J. Heat and Mass Transfer, Vol. 55, pp. 5244-5255.
- Cheng, TS, Liu, WH, (2014) Effects of cavity inclination on mixed convection heat transfer in lid-driven cavity flows, Com.& Fluids Vol.100 pp. 108–122.
- Al-Amiri, A, Khanafer K, (2011) Fluid-structure interaction analysis of mixed convection heat transfer in a lid-driven cavity with a flexible bottom wall, Int. J of Heat & Mass Trfr Vol.54 pp.3826–3836.
- Bhattacharya M et al. (2013) Mixed convection and role of multiple solutions in lid-driven trapezoidal Enclosures, International Journal of Heat and Mass Transfer Vol. 63 pp. 366–388.

Simulation of Solar ORC system for small scale power generation

Suhas Upadhyaya ² Veershetty Gumtapure ^{1*},

- 1 Department of Mechanical Engineering, National Institute of technology, Karnataka, Surathkal, Srinivasnagar-575025, India.
e-mail:veersg@yahoo.co.in
2 Department of Mechanical Engineering, National Institute of Technology Karnataka, Surathkal, Srinivasnagar-575025, India. email:suhas.upa@gmail.com

ABSTRACT: Energy poverty refers to a lack of access to modern energy services, and the well-being of a large proportion of people in developing countries is affected by the very low consumption of clean energy. The photovoltaic module is a commercial technology to convert solar energy directly to electricity, but the low efficiency conversion and above all the need of batteries for storage purpose limits the application in developing countries. As a matter of fact, storage of electricity with batteries requires skilled maintenance and cost involved is also high. This is not easily achievable in remote locations. An off-grid Solar Organic Rankine Cycle (SORC) provides a sustainable and cost-effective alternative to conventional and expensive diesel generators for electricity generation. In the present study, a dynamic model of the SORC system is simulated using TRNSYS and EES. The system is designed for an evaporator inlet temperature of 90 °C and is intended to run steadily from 10 AM to 6 PM. Thermal efficiency of 12.9% was achieved. Evaporator pressure was fixed at 10 bars and the condenser pressure was set at 2 bars. The variation of thermal efficiency with evaporator pressure and work output with ORC working fluid flow rate are also studied. The findings of the study are expected to help rural practitioners, solar ORC developers and investors to consider a small-scale SORC system as economically feasible for producing electricity in unelectrified areas of developing countries.

Keywords: Photovoltaic, Organic, Rankine, TRNSYS, Evaporator and Efficiency

INTRODUCTION

According to a report by the International Energy Agency (IEA) in 2010, approximately 22% of the world's population, most of whom live in remote areas that are difficult to access and connect to national or regional grids, do not have access to electricity. The average household of four people uses approximately 300 kWh per year for lighting alone [1]. The photovoltaic module is a commercial technology to convert solar energy directly to electricity, but the low efficiency conversion and above all the need of batteries for storage purpose limits the application in developing countries. As a matter of fact, storage of electricity with batteries requires skilled maintenance and

it is not easily achievable in remote locations. An off-grid Solar Organic Rankine Cycle system provides a sustainable and cost-effective alternative to conventional and expensive diesel generators for electricity generation. An off-grid power supply can provide power for domestic uses, such as lighting, running televisions, radios, refrigerators, communications, and water pumping. Moreover, it can be used for public use, including electrification in rural schools and health clinics.

ORC Technology

Conceptually, the Organic Rankine Cycle is similar to a Steam Rankine Cycle in that it is based on the vaporization of a high pressure liquid which is in turn expanded

6th International Engineering Symposium - IES 2017

March 1-3, 2017, Kumamoto University, Japan

to a lower pressure thus releasing mechanical work. The cycle is closed by condensing the low pressure vapour and pumping it back to the high pressure. Therefore, the Organic Rankine Cycle involves the same components as a conventional steam power plant (a boiler, a work-producing expansion device, a condenser and a pump). However, the working fluid is an organic compound characterized by a lower ebullition temperature than water and allowing power generation from low heat source temperatures. Moreover, unlike conventional power cycles, this technology allows for decentralized and small scale power generation. These assets make the ORC technology more adapted than steam power to the conversion of renewable energy sources whose availability is generally more localized than that of fossil fuels [6].

ORC working fluid

The choice of the fluid depends on the following main factors:

- a) Thermodynamic performance and positive saturation vapour curve.
- b) High vapour density, low viscosity and high conductivity.
- c) Acceptable evaporating pressure and positive condensing gauge pressure.
- d) Low toxicity and flammability.
- e) zero ODP and low GWP.
- f) Good availability and low cost.

For low-power turbine applications, the fluid should have a high molecular weight to minimize the rotational speed or the number of turbine stages and to allow for reasonable mass flow rates and turbine nozzle areas. Theoretical analyses also show that R245fa is also an effective working fluid for low-temperature solar Rankine cycle. It shows high power-generating ability, high economic efficiency and acceptable environmental effect in the low-temperature range. Table 1 compares the characteristics and properties of some working fluids which have been used in experimental systems. It can be seen from Table 1 that R245fa possesses its own advantage in the operation of the low-temperature solar Rankine cycle system.

Comparing with CO₂ and R134a, R245fa has a lower pressure level, thus cheaper solar collectors and equipments could be used. Comparing with pentane and ammonia, R245fa's advantage is the non-flammability, thus the safety of the system is certifiable [7].

TRNSYS 16 Simulation

TRNSYS 16 is powerful software using FORTRAN subroutines which is able to simulate energy patterns with time dependent inputs. Therefore it is possible to include the fluctuating and variable sun irradiation as input and to monitor the energy fluxes linked to it. Each FORTRAN subroutine, linked together in the TRNSYS environment, represents a component of the system, and a mathematical model simulates its functions having inputs, outputs, variable with time, and parameters that is constant for all the duration of the simulation. The TRNSYS library has a wide set of already tested subroutines "type" for the simulation of solar collectors, thermal storage, and piping [3]. The subroutine for the simulation of the Organic Rankine Cycle has to be developed to include this component in the simulation. The simulation would be executed in a graphic environment called the 'Simulation Studio'. The collector loop which is highlighted in dark blue as shown in figure 1 consists of parabolic trough, Auxiliary heater, collector fluid (water) pump and a storage tank. A standard type 109 has been chosen to give the necessary irradiation values. The simulation reads the weather data from the chosen geographic location. In this case Mangalore is chosen as the location. This weather data type 109 is then connected to the solar collector array in the model.

ORC Mathematical Model

The ORC model will be developed within the EES software environment to compute the thermodynamic analysis of the vapour cycle. The EES commercial software contains the thermodynamic data for the organic fluid R245fa employed in the cycle [4]. The ORC mathematical model is

integrated with the TRNSYS software using the "type 66" component. 'Type 66' component will facilitate the integration of the ORC mathematical model with the TRNSYS software. The ORC system is simulated in Engineering Equation Solver (EES) by zero-dimensional energy and mass balances. Specific subprograms were developed for each component of the power block, each of them consisting in input and output variables and in a specific set of equations. The model allows one to calculate the output variables on the basis of the fixed input parameters. The organic fluid selected is R-245fa because of its advantages of being able to operate at low pressures and temperatures [2].

Thermodynamic assumptions

The following assumptions were made for the analysis of ORC performance, system and sub-systems:

1. All the thermodynamic processes and systems are in a steady state.
2. The simple ORC system has negligible pressure losses in the heat exchanger and piping system so it is neglected.

Calculation of system thermal efficiency [5]

a) Pump: Pump work is evaluated as

$$\dot{W}_p = \dot{m}_{wf} v_1 \times \frac{(p_2 - p_1)}{\eta_p} \quad (1)$$

b) Evaporator: The heat exchange in the evaporator can be expressed as

$$Q_h = \dot{m}_{wf} \times (h_3 - h_2) \quad (2)$$

c) Expander: The work extracted by the expander (turbine) is calculated as

$$\dot{W}_t = \dot{m}_{wf} \times (h_3 - h_4) \quad (3)$$

$$\eta_t = \frac{h_3 - h_4}{h_3 - h_{4s}} \quad (4)$$

$$\dot{W}_t = \dot{m}_{wf} \times (h_3 - h_{4s}) \times \eta_t \quad (5)$$

d) Condenser

Working fluid is condensed with heat exchange of cooling water. The heat transfer rate in the condenser is given by

$$Q_L = \dot{m}_{wf} \times (h_4 - h_1) \quad (6)$$

e) Thermal efficiency

The thermal efficiency is related to input power, output power and heat transfer rate.

$$\eta_{th} = \frac{\dot{W}_t - \dot{W}_p}{Q_h} \quad (7)$$

System Model

The Solar ORC system is dynamically simulated in TRNSYS, which is well-known software diffusely adopted for both commercial and academic purposes. The software includes a large library of built-in components, often validated by experimental data. The validation of the system as a whole is not yet possible, since this prototype has never been experimented in literature. Nevertheless, all the results returned by the simulations can be considered highly reliable, since all the component models are validated by experimental data, while the dynamic approach included in TRNSYS is widely adopted in literature for system simulation, particularly; the models taken from TRNSYS library (Solar Collector, Auxiliary heater, Storage tank, pump etc) are validated vs. experimental data. The model of the ORC is developed according to the best practices available in literature.

The graphic environment of Studio has been used to run the TRNSYS simulation. The system simulated is composed by the following components.

6th International Engineering Symposium - IES 2017

March 1-3, 2017, Kumamoto University, Japan

Irradiation (Solar Energy Source)

A standard type 109 has been chosen to give the necessary irradiation values. The simulation reads the weather data from the chosen geographic location. In this case Surathkal is the location where the prototype will be assembled and installed. Because TRNSYS dataset does not have the Surathkal data, Mangalore (Bajpe) data has been chosen. Surathkal is close to Bajpe, hence solar irradiation is similar.

Solar collector and Auxiliary heater

Compound parabolic solar collectors have been chosen to enhance the diffuse radiation absorption. Only one collector is used to test the simulation with the minimum module of the collector. Collector area is fixed at 50 m² and truncation ratio is 0.7. An auxiliary heater with a maximum heating rate of 40000 kJ/hr is connected in series with the collector in order to accommodate for the lesser solar radiation. The set point of the heater is fixed at 100 °C.

Storage tank and ORC unit

A suitable heat storage system is required to maximize the productivity of the solar plant and to provide solar heat at the desired rate regardless of the instantaneous solar radiation availability and the thermal needs. The overall aim of this basic component is the same for the high temperature concentrated solar power systems and for the small scale solar system with the difference that the second one has to directly face the user energy needs. In this case a plug flow type storage tank (Type 38) is used in the simulation since an auxiliary heater is used prior to the tank in order to maintain constant evaporator inlet temperature in ORC power block.

ORC power block (EES)

R245fa is selected as the working fluid. The condenser pressure is fixed at 2 bars. The pinch point temperature difference is kept constant at 10 K for both evaporator and condenser. Brazed plate heat

exchangers will be used while setting up the prototype as it enhances the rate of heat transfer and reduces pinch point difference for a given area and in turn reduces the size of the heat exchanger [8]. Evaporator pressure is varied to see how thermal efficiency changes with change in evaporator pressure. It can be observed from figure 2 that the thermal efficiency increases with increase in evaporator pressure. The pressure is varied from 6 bars to 14 bars with an increment of 2 bars. The simulation model is tested on 1st of January and May to check for seasonal fluctuations and whether this system is economically viable to be able to run throughout the year. The auxiliary heat that had to be supplied is tabulated for the month of January and May. This has been done to integrate a thermal storage system in the future with the present model. The auxiliary heat required gives an estimate of the storage tank design and the materials to be used. The results are tabulated in Table 2. The work output of 14.4 kW and thermal efficiency of 12.9% is achieved when evaporator pressure is fixed at 10 bars. Also the variation of work output with ORC working fluid flow rate is also presented in Figure 4. The trend clearly indicates that the work output increases with increasing flow rate. But there has to be a trade off between higher flow rate and expander size.

CONCLUSIONS

The following conclusions are deduced from this study:

- Thermal efficiency of 12.9% was achieved for evaporator pressure of 10 bars.
- Thermal efficiency increased with increase in evaporator pressure. Thermal efficiencies varies from 9.29% at evaporator pressure of 6 bars to 14.97% at pressure of 14 bars.
- Work output of 14.4 kW was achieved with evaporator inlet temperature of 90 °C and mass flow rate of 0.5 kg/s. This shows how work can be successfully extracted from low temperature sources using ORC technology.

6th International Engineering Symposium - IES 2017

March 1-3, 2017, Kumamoto University, Japan

- Auxiliary heat requirement on an average for 8 hour operation in January was about 43% of the generated power output and in May it was 37% of the generated power output.
- As evident from figure 3, not much variation is observed in auxiliary heat requirement from 2 PM to 4 PM for both the months. This data can be utilized as input for designing a thermal storage tank.
- Work output shows a linear increase with increasing mass flow rate.

ACKNOWLEDGEMENTS

This work was supported by National Institute of Technology, Karnataka, Surathkal. This project needed intensive literature review and latest research data which was provided by the institute.

REFERENCES

- [1] Alex Zahnd and Haddix McKay Kimber (2009), Benefits from a renewable energy village electrification system, *Renewable energy*, Vol. 34, pp 362-368.
- [2] Francesco et al (2015), Design and simulation of a prototype of a small scale solar CHP system based on evacuated flat plate solar collectors and Organic Rankine cycle, *Energy conversion and management*, Vol. 90, pp 347-363.
- [3] Klein S.A et al (2006), A Transient system simulation program, Madison: Solar Energy Laboratory, TRNSYS, University of Wisconsin.
- [4] Klein S.A et al (2010), Engineering Equation Solver; Middleton, WI: Solar Energy Laboratory, F-Chart Software.
- [5] Kuo et al (2011), Analysis of a 50 kW organic Rankine cycle system, *Energy*, Vol. 36, pp 5877-5885.
- [6] Liu et al (2011), A biomass-fired micro-scale CHP system with organic Rankine cycle (ORC) - Thermodynamic modelling studies, *Biomass and Bioenergy*, Vol. 35, pp 3985-3994.
- [7] Quoilin et al (2011), Performance and design optimization of a low-cost solar organic Rankine cycle for remote power generation, *Solar energy*, Vol. 85, pp 955-966.
- [8] Wang et al (2010), Performance evaluation of a low-temperature solar Rankine cycle system utilizing R245fa, *Solar energy*, Vol. 84, pp 353-364.

6th International Engineering Symposium - IES 2017

March 1-3, 2017, Kumamoto University, Japan

NOMENCLATURE

w	power (kW)
m	mass flow rate (kg/s)
v	specific volume (m ³ /kg)
P	pressure (kPa)
Q	heat transfer rate (kW)
h	specific enthalpy (kJ/kg)
T	Temperature

Subscripts

wf	working fluid
p	pump
t	turbine (expander)
1, 2, 3, 4	states in system

Table 1: Characteristics of some used working fluids

Working fluids	Molecular weight (g/mol)	T _{crit} (°C)	P _{crit} (MPa)	Std 34 Safety group	ODP	GWP (100 yr)
R-134a	102.03	101.1	4.06	A1	0	1300
R-245fa	134.05	154.1	4.43	B1	0	950
Ammonia	17.03	132.3	11.34	B2	0	<1
CO ₂	44.01	31.1	7.38	A1	0	1
Pentane	72.15	196.6	3.37	A3	0	20

Table 2: Auxiliary heat requirements for the Month of January and May

Time (hours)	Jan	May
10	7.71	4.55
11	4.06	3.16
12	2.83	2.27
13	3.17	2.57
14	3.96	3.98
15	4.77	4.97
16	5.98	6.02
17	8.36	6.66
18	8.72	7.93

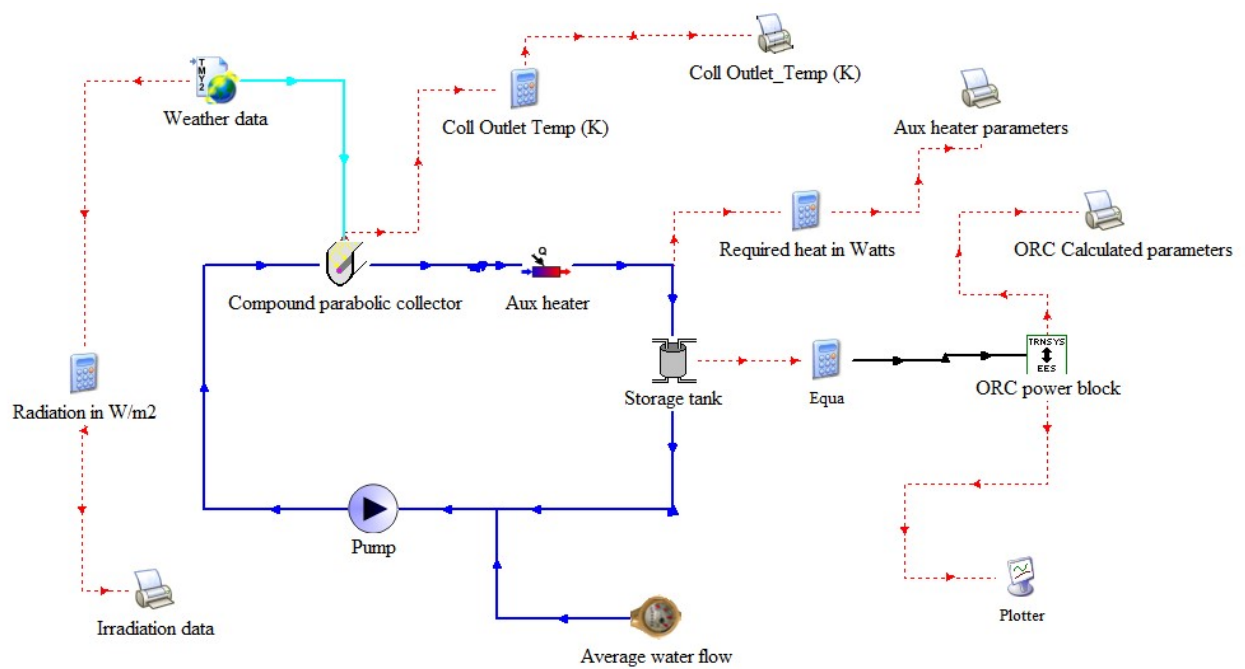


Figure 1 : Dynamic Simulation model using TRNSYS 16

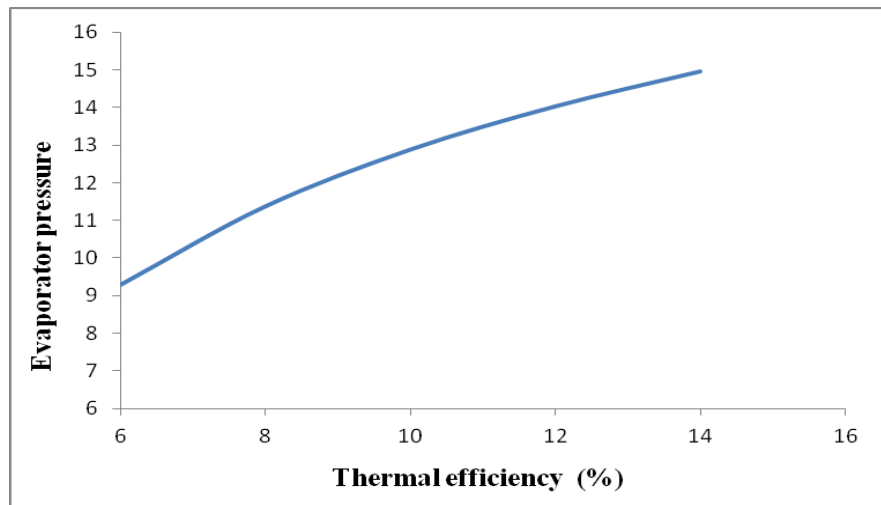


Figure 2: Variation of thermal efficiency with evaporator pressure

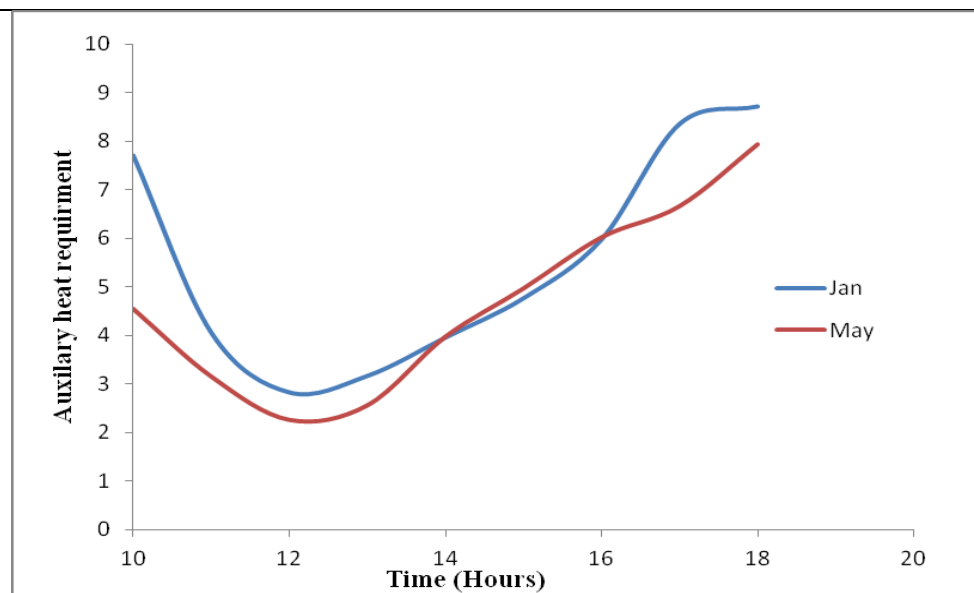


Figure 3: Comparison of Auxiliary heat requirements for the Month of January and May

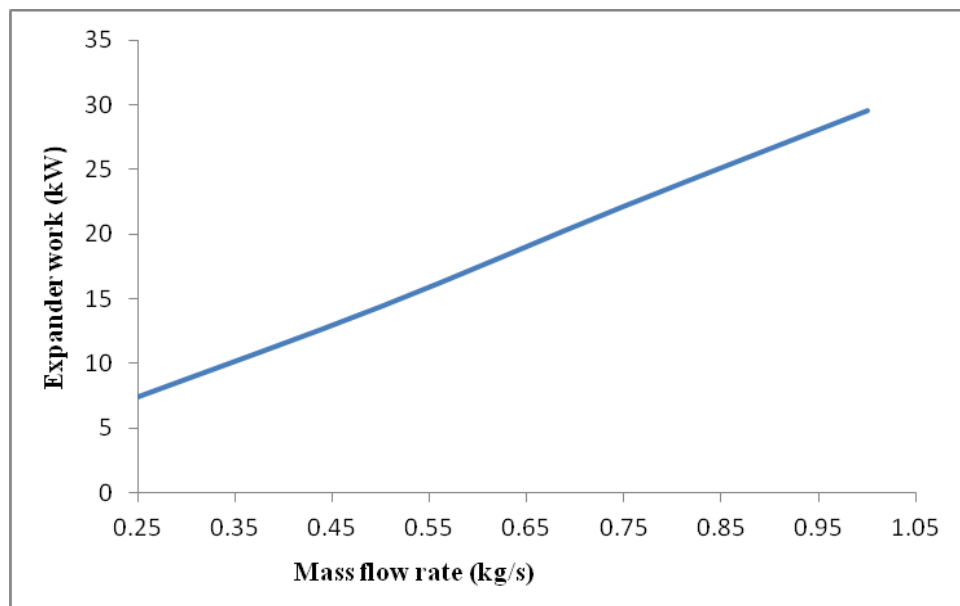


Figure 4: Variation of Expander work with ORC working fluid flow rate

Study on Molding Properties of Obsidian Perlite

**Kota KAWAMURA¹, Shunta MORI¹, Yasuo MARUMO^{2,*}, Taekyung LEE^{3,*},
Yasuhiro IMAMURA⁴, Takanori MASU⁵ and Akikazu ETO⁵**

¹ Graduate School of Science and Technology, Kumamoto University, Kumamoto 860-8555, Japan

² Faculty of Advanced Science and Technology, Kumamoto University, Kumamoto 860-8555, Japan

³ Magnesium Research Center, Kumamoto University, Kumamoto 860-8555, Japan

⁴ Technical Division, Faculty of Engineering, Kumamoto University, Kumamoto 860-8555, Japan

⁵ Ajimu Perlite Co. Ltd., Kitsuki, Oita 879-1313, Japan

*Corresponding authors:

Prof. Y. Marumo, Tel.: +81-96-342-3574, E-Mail: marumo@mech.kumamoto-u.ac.jp

Prof. T. Lee, Tel.: +81-96-342-3576, E-Mail: t-lee@mech.kumamoto-u.ac.jp

ABSTRACT: This study suggests a molding technology of obsidian perlite powder to improve mechanical properties. Molding experiment of obsidian perlite and characteristic test of molded body were carried out. By examining the characteristics and trends of the perlite product, we show the basic data on the experiment of the perlite product in the future.

INTRODUCTION

Powder can be effectively used in various ways, such as compounding and molding, and thus contrasted by a rigid material. A number of products have been fabricated using the advantages of powder in the industry (e.g., pharmaceuticals and machinery parts) in response to the demands for technological innovation¹⁾. A foamed material with the porous structure is one of those developed powder materials. It has attracted attentions due to the lightweight as well as the excellent thermal and sound insulation by confining the air in its pore structure. Obsidian perlite investigated in this work is a foamed material used for lightweight building material and soil improvement material. There have few studies related to this material in spite of its potential for the industry. Therefore, this study investigates a solidification molding technology of obsidian perlite powder to improve mechanical properties.

CHARACTERISTICS OF OBSIDIAN PERLITE

Obsidian perlite used in this study was produced by Ajimu Perlite Co. Ltd. from obsidian gemstone obtained in Ajimu district, Oita prefecture, Japan²⁾. This gemstone is characterized by rhyolite and few phenocryst in chemical composition, contrasted by continuous glass gob shown in a typical obsidian (Figure 1). The investigated obsidian perlite consists of 75-78% SiO₂, 12-16% Al₂O₃, 2-5% Na₂O, and 2-4.7% K₂O.

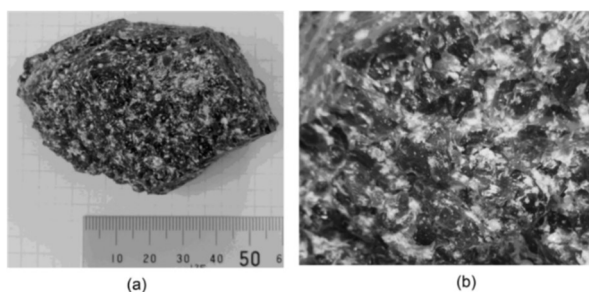


Figure 1. (a) Example of obsidian gemstones used in this work and (b) porphyritic texture

The thermal conductivity of obsidian perlite was measured to be $0.068 \text{ W}\cdot\text{mK}^{-1}$, suggestive of high thermal-insulation ability. The density was $0.1\text{-}0.3 \text{ kg}\cdot\text{L}^{-1}$ as a lightweight material. In addition, the obsidian perlite used in this study possessed a higher hardness than does a commercial perlite³⁾, making it difficult measure compressive strength by a conventional method. We instead measured the perlite strength using the compressive displacement (D_c) of material filled in a cylindrical container. The compression rate (R_c) was then determined as the ratio of the compressive displacement to the sample thickness (t), i.e., $R_c = D_c/t \times 100(\%)$. Figure 2 shows the schematic illustration of the compression machine used in this work. Figure 3 shows the compressive curve of the present obsidian perlite depending on the particle size.

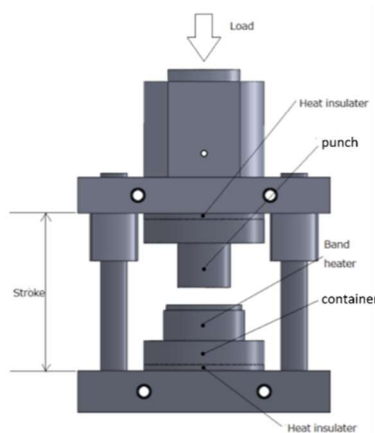


Figure 2. Compression overview

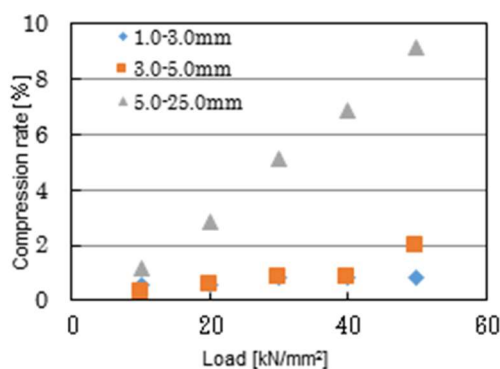


Figure 3. Variation in compression rate depending on the applied load

FABRICATION OF OBSIDIAN PERLITE MOLDED BODY

The perlite molded body was fabricated by blending two types of obsidian perlites with different ranges of particle size: 0.1-1.0 mm and 1.0-3.0 mm. Sodium silicate was employed to bind the obsidian perlite particles, due to a good binding capability between glass and ceramic as well as superior heat resistance. Aqueous solution of 40% sodium silicate and 60% perlite was mixed and then molded in a mold of 24 mm \times 18 mm \times 200 mm. Removing the mold, the molded sample was heated at 200°C and 400°C, respectively, for 2 h. Figure 4 summarizes the manufacturing procedures of obsidian perlite molded body.

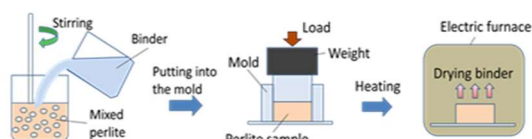


Figure 4. Overview of manufacturing procedures

Figure 5 shows the structure of the perlite molded body fabricated at a large perlite percentage of 33% and 200 degrees. Sodium silicate effectively joined perlite particles. However, large pores between particles were confirmed, which required strong force to avoid the fragmentation of the molded body. Figure 6 suggests an increase in the density of the molded as the fraction of large perlites was decreased. As the proportion of large grain perlite increases, the number of points of contact with each other decreases and the bending strength decreases

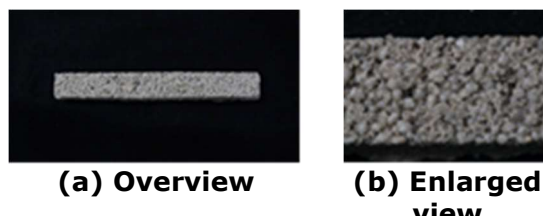


Figure 5. A perlite molded body formed at 200°C. The perlite fraction was 33%

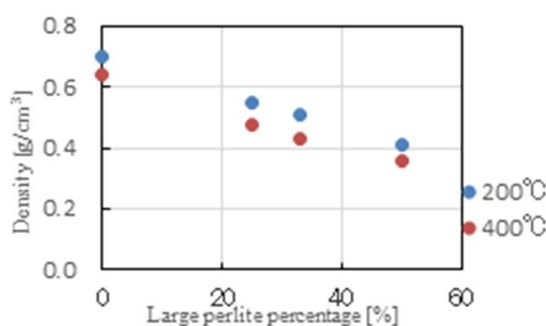


Figure 6. Variation in the density of the perlite molded body depending on the fraction of large perlite

BENDING STRENGTH OF OBSIDIAN PERLITE MOLDED BODY

Bending strength of the perlite molded body was evaluated at room temperature on the basis of JIS1664:2004 procedures⁴. Samples with a fraction of large perlite of 0%, 25%, 33%, and 50% were pressed up to a load of 600 N using a small hand press. This process is schematically shown in Figure 7.

Bending strength test was performed at room temperature, immediately before the experiment, the specimen was dried by heating at 200 °C for 30 minutes.g

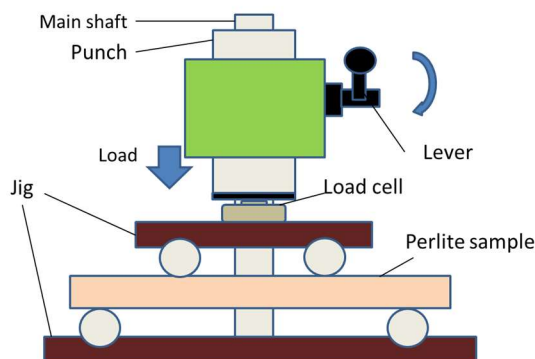


Figure 7. Scheme of the bending test

Figure 8 shows the perlite molded body after the bending test. Both samples were fractured near the center in the length direction. Fracture surfaces demonstrate the fracture of perlite particles in most cases, suggestive of stronger bonding strength of sodium silicate in comparison to that of perlite particles.



Figure 8. Fractured molded bodies after the bending test. Both samples were formed at 200°C: (a) 33% and (b) 25% in the perlite fraction

Figure 9 presents the influence of large perlite fraction upon the bending strength. Increasing fraction of large perlite gave rise to the deterioration in bending strength. Recalling Figure 6, such a reduction of bending strength resulted from the decrease in material density, i.e., increasing pore area. It is thus required to use small-sized perlite particles to obtain a strong molded body.

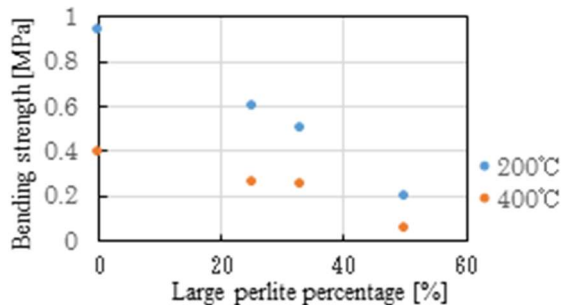


Figure 9. Relation between the bending strength and the fraction of large perlites

4. Conclusion

- Perlite molded body was successfully fabricated by molding an aqueous solution of obsidian perlite and sodium silicate.
- Increasing fraction of large perlite led to the formation of large pores between perlite particles, resulting in the decrease in material density.
- Bending strength of the perlite molded body was increased with decreasing fraction of large perlite.
- Using this material as a base material, it is expected to improve the performance of the perlite molded body by mixing materials that meet the requirements.

6th International Engineering Symposium - IES 2017

March 1-3, 2017, Kumamoto University, Japan

Reference

- 1) The society of powder technology: "Molding powder", NIKKAN KOGYO SHINBUN LTD
- 2) Patent application 2015-010940, "Foaming perlite", 0025-0040
- 3) Patent application 2015-010940, "Foaming perlite", 0041-0042
- 4) Testing method for bending strength of porous fine ceramics, JIS R 1664:2004

Acknowledgement

We would like to thank Prof. Kiyoshi Murakami and Mr. Yasuhiro Toda of Kumamoto University, Japan, for their advice and help regarding this research project.

Evaluation of physical properties of WC-CrC-Ni reinforced stainless steel composite prepared by Metal injection Molding

Veeresh Nayak C ¹, Sudip Kumar Samanta ², M R Ramesh ³, Vijay Desai ³

1. Department of Mechanical Engineering, National Institute of Technology, Karnataka, Surathkal 575025- India. Email:veru29@gmail.com
 2. Principal Scientist, Near Net-shape Manufacturing group, CSIR-Central Mechanical Engineering Research Institute Durgapur 713209-India Email: sudip@cmeri.res.in
 3. Department of Mechanical Engineering, National Institute of Technology, Karnataka, Surathkal 575025- India Email:rameshmr@nitk.edu.in, Email: desai@nitk.ac.in
-

ABSTRACT: Metal injection moulding (MIM) is an economical mass production technique, for the fabrication of complex shape and miniature parts with different material composition. Components are fabricated by combination of plastic injection moulding with the flexibility in sintering of metal particulates. In current investigation binder comprised of paraffin wax, polyethylene glycol, stearic acid and low density polyethylene are developed for moulding of composite powders of SS316L+WC-CrC-Ni. Green composites are subjected to thermal debinding at 500°C and sintering at 1200°C under hydrogen purged atmosphere. Composites are characterised with respect to microstructure by scanning electron microscopy, micro hardness and density. The effects of sintering temperature and heating rate on the above properties have been evaluated to obtain defect-free composite.

Keywords: Metal injection moulding (MIM), Microstructure, SS316L+WC-CrC-Ni

INTRODUCTION

In present trend the manufacturing process is developed for large amount of small and complex parts with increased production rate to full fill demands of verity products for modern day to day life. The manufacturing methods and processing of metal components have general limitations of traditional process for fabrication of metal components and it encouraging for finding alternative process. Hence alternative method for producing near net shape metal component is Metal injection moulding (MIM). The MIM is a mishmash of powder metallurgy and plastic injection moulding process. MIM can produce low cost products at large number, close tolerance and shape complexity, good mechanical properties, compare to conventional technologies since it eliminates secondary operations and also material losses while in case complex geometries for numerous applications in today's industry Jisa et al. (2016). Metal injection moulding (MIM) is

a near-net shaping method that is predominantly beneficial for the users where intricate shape with high density and precision and accuracy in dimensions are mandatory Torralba (2013).

In MIM process, binder acts like a temporary vehicle for evenly pack the metal powder in to mould cavity at desired profile and then holding the particle till sintering process begins. The selection of binder great influence on mixing rheology, agglomeration, particle packing, molding, debinding and dimensional correctness. The selected binder should be low viscosity at the initial moulding stage and sudden viscosity change through cooling. The binder essential free from toxic and it should be environmental friendly Liu et al.(2001).

In current work, the metal matrix composite(MMC) contain SS316L and WC-CrC-Ni powders. SS316L compromises good mechanical properties and corrosion resistance. WC-CrC-Ni has good hardness and offers good wear resistance. By using

6th International Engineering Symposium - IES 2017

March 1-3, 2017, Kumamoto University, Japan

the experimental trials for SS316L and WC-CrC-Ni powders, a set of suitable mixing technique, molding parameters and debinding schedule were established for the production of defect-free MMC parts. The effects of sintering factors on microhardness and density were then studied.

Experimental procedures

The composition of the metal powder was SS316L+WC-CrC-Ni. These powders (55 vol.%) and binders (45 vol.%) were warmed at 110°C and then mixed in a Sigma Z blade mixer at 135 °C for 3 h. Successively, the temperature was decreased and the mixture was removed and sliced using a granular machine to small granular size around 3-4 mm. The granular were prepared for filling into the feed hopper for injection molding machine. The green parts were debound at 47° C for 5 h in hexane and then sintered at 1100 and 1200 °C for 300 min. using a vacuum sintering furnace to achieve samples with higher density .

Analysis of Powder shape and particle size

Particle size of Metal powder and its distribution pattern have been investigated using a particle size analyzer at 36° C and the dispersion medium used is ethylene glycol 49%. The fig.1 shows mixer of SS316L and WC-CrC-Ni,has been analyzed through SEM. (Supplier:JSM6380LA, JEOL). The Distribution of particle size given in Table 1,

Preparation of Feedstock and MIM specimen

Feedstock has been framed with 56 vol.% SS316L (70%)+WC-CrC-Ni(30%), powder and 44 vol.% thermoplastic binder. The binder comprises of Paraffin Wax (PW), Polyethylene Glycol 600(PEG-600),Stearic Acid (SA) and Low Density Polyethylene (LDPE).Feedstock has been prepared in each batch according to the above composition in a sigma blade mixer (Make: Unique Mixers & Furnaces-Thane,India Capacity: 1 Lt) at 135°C for 90 minutes at

35 rpm. Once mixing thoroughly, the semi-solid tooth paste like viscous feedstock has been taken out from the mixer and permitted to cool at room temperature. It is then pelletized to supply feedstock to the injection moulding machine

The feedstock injecting in to injection moulding has been carried out in a tensile specimen mould using a 150 ton injection moulding machine In the first set, injection speed is set 5% of the maximum injection speed for 7.5 % of the total injection time (4s) and injection speed 15% of the maximum injection speed for rest of the injection time at injection temperature of feedstock 150° C ,155° C and 160°C.After several trials, the parameters selected for defect free tensile specimens are injection speed 38.4 cc/s ,injection time 2.9s and feedstock velocity 5.23m/s at injection machine barrel temperature 160 ,165 170 °C .

Debinding of the injection moulded samples has been carried out in steps. In the first stage solvent debinding has been carried out by submersing the moulded specimen in n-hexane (C6H14) bath and heating the bath below the melting temperature of PW, where most of PEG-600, PW and SA are removed by dissolving in n- hexane. In the second stage, thermal debindining has been carried out to remove almost all of the PEG-600,PW, SA and LDPE from the moulded sample. Solvent debinding have been carried out in a drying oven at different temperatures and time durations.Sintering of the debound tensile specimens are carried out in a tube type furnace (Make: Naskar & Co. Howrah) in hydrogen atmosphere.The specimens are heated to a temperature 1200°C.heating rate of 1-5°C/min and kept at that temp. for 30 minutes and then cooled to 200°C at a cooling rate of 5°C/min and then chilled down to room temperature through furnace cooling.

RESULTS AND DISCUSSION**Feedstock density Measurement**

The feedstock and binder density have been measured by applying Archimedes Principle. The density measured at room temperature. The results of density measurement of binder and feedstock have been given in table 2 and 3 respectively. The density of binder has been measured by submersing in Acetone (density 0.79 g/cc) and that for feedstock has been measured by submersing in water.

Debinding and sintering of MIM specimens

The debinding process is carried out. In the current investigation binder consists PEG- 600, PW, SA and LDPE. The binders are removed in steps because selected multi component binder system.. It is necessary to have one of the binder component at least 30 percentage or more Atre,et al.(2003),Abolhasani et al. (2010) to be removed first in the debinding to avoid insulated sample of pores . The moulded green samples are debinded in two stages: solvent debinding traced by thermal debinding. Since PEG- 600, PW and SA collectively constitute more than 30 percent and resolvable in n-hexane (C_6H_{14}) solvent, PEG 600, PW and SA have been removed from the compact by submerging the sample in n-hexane at different temperatures respectively. As the time increases, rate of PEG 600, PW and SA removal increases. This is in good promise with the published literature Yang et al.(2003). Due to amplified solubility and diffusivity at higher temperature, more PEG 600, PW and SA dissolve in n-hexane and come out from the sample thereby triggering more weight loss. Similarly, as time increases, more time is available to dissolve PEG 600, PW & SA in n-hexane and therefore, weight loss increases.

In solvent debinding above 50° C cracks are formed in the sample may be due to thermal expansion and contraction while debinding process,it is observed from

experimental. The swelling of sample occurred due to insoluble backbone binder stay long time in the n-hexane, and causes expansion Hwang et al.(2013),Guoxin et al.(2007). At the completion of the solvent debinding at greater temperatures when compacts are taken out of the solvent, solvent is drained out and evaporated from the surface of the specimen affecting a sharp temperature drop. Sharp drop in temperature roots contraction. This expansion and then sudden contraction encourages internal stresses in the sample and causes cracking also observed that solvent debinding above 60° C, sample sagging occurs may be owing to softening of binder component PEG 600, PW and SA. Since cracks and compact sagging occur above 50° C and few cracks also occurred in few specimens which are solvent debound at 50° C, fig.2 shows defect free solvent debinding compact temperature has been selected at 48° C where no crack or distortion has been observed in any sample.

Fig.3 and fig.4 show the micrograph of injection moulded green compact before debinding and after solvent debinding at 48° C for 5 hours respectively. It can be clearly seen in fig.3 that binder surrounds the powder particles. Due to removal of most of the major constituent of binder, PEG 600, PW and SA, in solvent debinding, powder particles are not fully surrounded by binders seen in fig.4. The binder LDPE and remains of PW and SA which have not been removed in solvent debinding.

In the thermal debound the major backbone binder LDPE and the rest of the PEG-600,PW and SA which remain after solvent debinding. are completely removed through previously created interconnected pores in solvent debinding. Normally, debinding time depends on the thickness of the green sample and it is proportional to the square of the green sample thickness Banhart (2001) . At temperature 500°C almost no binder is left after 5 hours of holding time. In this stage the compact is delicate to handle until sintered. Therefore, the samples those are sintered are all solvent debound at 48° C for 5 hrs in n-hexane followed by thermally

6th International Engineering Symposium - IES 2017

March 1-3, 2017, Kumamoto University, Japan

debound at 500° C for 5 hours under hydrogen atmosphere (fig.5).

In the present investigation, thermal debound tensile compacts have been sintered. It is seen that as the temperature increases, density increases but beyond formation of liquid phase, compact shape starts distorting Xiang-quan et al.(2007).

The MIM specimens of green compact , solvent debinded compact and sintered at 1200° C has been shown in fig.6 and the micrograph of the sintered tensile specimen shows fig.7 it is observed that SS316L+WC-CrC-Ni tensile specimen micrograph showing fishbone structure that powder particles are bound together and it is also observed that isolated pores are separated from the grain boundary .

Clear sign of the occurrence of liquid phase during sintering cycle appears in the samples, heated upto 1200 °C viewing herringbone morphologies. The average values of Micro harness and density of sintered specimens have been given in table 4. As the specimens are sintered, density increases by elimination of pores and substantial shrinkage occurs in the specimens Jamaludin et al.(2009). Shrinkage upon sintering of the specimens have been measured in length wise, width wise and thickness wise that is, in X, Y and Z direction (Table 5). Shrinkage variation is more in width wise direction compared to length and thickness wise direction, more segregation of powder and binder phase in width wise direction. The bigger the powders are the greater the green density and lower the linear shrinkage Onbattuvelli et al.(2013)

CONCLUSION

- Developed binders PW,LDPE and PEG-600 are successfully employed for defect free metal injection moulding component to selected powders.
- Injection parameters are optimized by several trials. Injection speed 38.4cc/s, injection time 2.9s and feedstock velocity 5.23m/s at injection temperatures 160, 165,170° C.
- The binder is removed in two stages: solvent debinding followed by thermal

debinding. In solvent debinding, as temperature of the solvent increases rate of PEG 600, PW and SA removal increases but it is found that 48°C is optimal temperature.

- Mechanical properties of sintered MIM specimens achieved best density and micro hardness of SS316L+WC-CrC-Ni shows 7.76 g/cc and micro hardness 457 Hv.
- The shrinkage of MIM specimens are achieved with in the 18 -20% for a selected powder loading.

REFERENCES

- [1] Abolhasani, H, et al (2010). Journal of Materials Processing Technology A New Starch-Based Binder for Metal Injection Molding." Journal of Materials Processing Tech. 210(6-7): 961-68.
- [2] Atre, Sundar V, et al(2003). Effect of Mixing on the Rheology and Particle Characteristics of Tungsten-Based Powder Injection Molding Feedstock. 356.
- [3] Banhart, John. (2001).Manufacture , Characterisation and Application of Cellular Metals and Metal Foams. 46: 559-632.
- [4] Guoxin, Hu, et al(2007). Fabrication of High Porous NiTi Shape Memory Alloy by Metal Injection Molding. 6: 395-99.
- [5]Hwang, Jihoon, et al (2013). Determination of the Flow Stress and Thermal Properties of Ceramic Powder Feedstock in Ceramic Injection Molding . 27(6): 1815-24.
- [6]Jamaludin, Khairur Rijal et al (2009).Moulding Parameter Optimisation for the Best Sintered Density. Engineering I: 1-5.
- [7]Jisa, R et al (2016).Tribological Properties of MIM Manufactured Copper Alloys Tribological Properties of MIM Manufactured Copper Alloys. 5831(August).
- [8]Liu, Z Y et al (2001). Binder System for Micropowder Injection Molding. (March).
- [9]Loh, N H, et al(2001). Production of Metal Matrix Composite Part by Powder Injection Molding. 108(September 2000): 398-407.
- [10]Onbattuvelli, et al (2013). The Effects of Nanoparticle Addition on SiC and AlN Powder-Polymer Mixtures: Packing and Flow Behavior. International Journal of Refractory Metals and Hard Materials 36: 183-90.
- [11]Torralba, José M. (2013). Powder Injection Moulding: Processing of Small Parts of Complex Shape. 8: 87-96.
- [12]Xiang-quan, et al(2007). Deformation Behavior and Strength Evolution of MIM Compacts during Thermal Debinding. (May).
- [13]Yang,et al (2003). Solvent Debinding Mechanism for Alumina Injection Molded Compacts with Water-Soluble Binders. Ceramics International 29(7): 745-56.

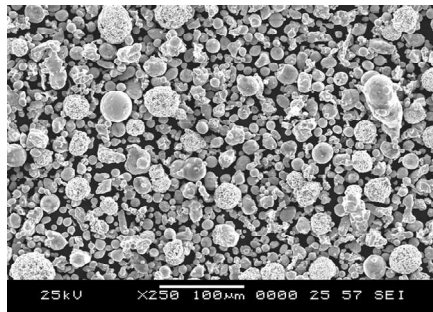


Fig.1 SEM micrograph of SS316L+WC-CrC-Ni powder

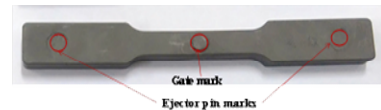


Fig. 2 Defect free solvent debinded compact at 48° C.

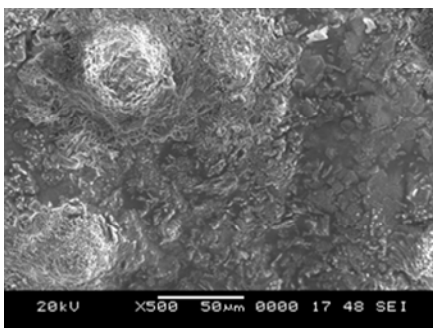


Fig.3 Micrograph of MIM green sample before debinding.

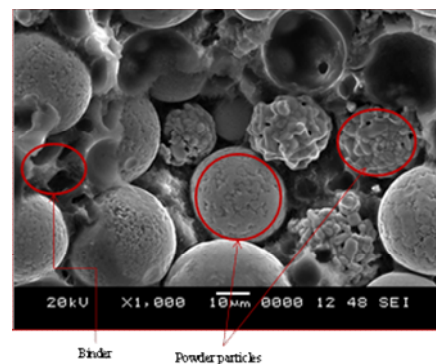


Fig.4 SEM Micrograph of MIM green sample after solvent debinding at 48 °C for 5 hours.

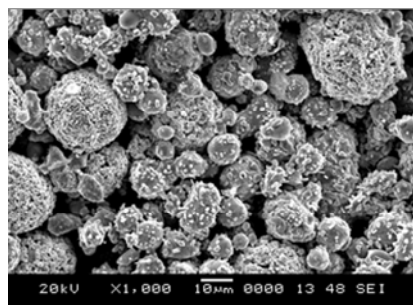


Fig. 5 Shows SEM Micrograph of a sample after thermal debinding a) SS316L+WC-CrC-Ni



Fig. 6 Tensile specimen sintered at 1200 °C

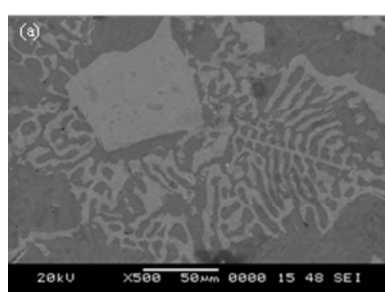


Fig. 7 Micrograph of the sintered tensile specimen a) SS316L+WC-CrC-Ni

6th International Engineering Symposium - IES 2017
March 1-3, 2017, Kumamoto University, Japan

Table 1 Distribution of particle size in (μm)

Metal powder	Property Distribution Particle size (μm)			
	D10(μm)	D50(μm)	D90(μm)	D97(μm)
SS316L	0.45	1.08	3.35	5.85
WC-CrC-Ni	0.42	1.07	17.68	31.56

Table:2 Binder density measurement

SL.No	Weight in air (g)	Weight in water (g)	Difference in weight.(g)	Density (g/cc)	Average density (g/cc)
1.	3.768	0.613	3.155	0.943	0.916
2.	5.451	0.68	4.771	0.902	
3.	12.78	1.603	11.177	0.903	

Table :3 feedstock density measurement

SL.No	Weight in air (g)	Weight in water (g)	Difference in weight.(g)	Density (g/cc)	Average density (g/cc)
1.	16.519	13.266	3.253	5.08	5.093
2.	13.304	10.7	2.604	5.11	
3.	15.417	12.391	3.026	5.09	

Table:4 Mechanical properties of tensile specimen

Material	Density (g/cc)	Micro hardness (Hv)
SS316L+WC-CrC-Ni	7.76	459

Table: 5 Linear shrinkage

Material	Length (Shrinkage %)	Width (Shrinkage %)	Thickness (Shrinkage %)
SS316L+WC-CrC-Ni	13.65 to 14.28	15.37 to 16.76	14.68 to 15.89

Development of New Apparatus to Evaluate Ultrasonic Reflection Characteristic for Wrinkling in Press Forming

**Yuji Segawa ¹, Takuya Kuriyama ², Yasuo Marumo ³, Taekyung Lee ⁴,
Yasuhiro Imamura ⁵, Tomohiro Nonaka ⁶ and Yutaka Sakata ⁷**

- ¹ Department of Mechanical Engineering, National Institute of Technology, Miyakonojo College, 473-1, Yoshio-cho, Miyakonojo, Miyazaki 885-8567, Japan.
e-mail: y_segawa@cc.miyakonojo-nct.ac.jp
- ² Graduate School of Science and Technology, Kumamoto University, 2-39-1, Kurokami, Chuo-ku, Kumamoto 860-8555, Japan.
- ³ Faculty of Advanced Science and Research, Kumamoto University
e-mail: marumo@mech.kumamoto-u.ac.jp
- ⁴ Magnesium Research Center, Kumamoto University
e-mail: t-lee@mech.kumamoto-u.ac.jp
- ⁵ Technical Division, Faculty of Engineering, Kumamoto University
- ⁶ Department of Integrated System Engineering, Nishinippon Institute of Technology, 1-11, Niitsu, Kanda-machi, Miyako-gun, Fukuoka 800-0344, Japan.
e-mail: nonaka@nishitech.ac.jp
- ⁷ Department of Integrated System Engineering, Nishinippon Institute of Technology, Japan. e-mail: ysakata@nishitech.ac.jp
-

ABSTRACT: It is difficult to completely prevent the formation of defects in metal press forming, unless inspecting the entire products. This study suggests an in-process inspection using an ultrasonic measurement in order to avoid such a problem. This method is effective for detecting wrinkles formed in a material during the process. A numerical analysis clarified the relationship between wrinkle shapes and the reflection behaviour of ultrasonic waves. In this study, we developed an experimental apparatus that provided quantitative data explaining the relationship between ultrasonic reflection intensity and the wrinkle shapes. The die of the developed apparatus was in sufficient contact with the specimen machined into the wrinkle shape. The ultrasonic reflection characteristics varied by the wrinkle characteristics.

Keywords: press forming, defect detect, wrinkle, in-process, ultrasonic measurement

INTRODUCTION

Press forming is a processing method for a mass production while maintaining a constant quality. The investigation of defects, such as wrinkles on the material surface, in press-formed products has been one of the most important issues for manufacturers. In general, the sampling inspection method is adopted considering the cost in the industry. However, this method often miss the outflow of defective products except for the investigation samples. Although there have been a

number of studies thus far (Katayama et al., 2004, Koga et al., 2007), it is still difficult to prevent the defects completely as various factors and complex relationship are related to the formation of defects.

To solve such a problem, researchers have suggested an in-process monitoring of defects using various types of sensors. For example, Traversin and Kergen (1995) controlled blank-holder force using various sensors embedded in the die. Siegert et al. (1997) embedded displacement transducers in the upper and lower binders in order to measure a wrinkle height

required for a closed-loop control of a press forming. Doege et al. (2002) performed a contactless online measurement of the material flow with an optical sensor in a die. Yang et al. (2003) utilized AE sensors to detect the position of friction sources during a press forming. Lo and Yang (2004) developed new embedded-type displacement sensors that enabled the closed-loop control of blank-holder force. Mahayotsanum et al. (2009) achieved the optimization of process management with a draw-in sensor. Nonaka et al. (2012a) successfully detected a scrap-jumping in a pierce processing using a fibre line-laser sensor.

Among a number of suggested approaches, the in-process measurement using the ultrasonic wave has been reported by Saiki et al. (1993, 1994), Stancu-Niederkorn et al. (1994) and Hagino et al. (2013) to be effective for monitoring the contact state between a tool and workpiece. According to the work of Nonaka et al. (2012b), the ultrasonic measurement using die-embedded probe successfully detected wrinkles generated during a press forming.

The relationship between the wrinkles and ultrasonic reflection characteristics must be clarified to introduce this method into the actual manufacturing process. Numerical analysis can be a good tool for resolving such problems. Finite difference time domain (FDTD) method (Yee, 1966) was developed to analyse the electromagnetic field. Recently, the FDTD method has been effectively used for the elastic wave analysis (Satyanayan et al., 2007, Hagino et al., 2014, Jinno et al., 2014). We visualized the propagation and reflection behaviour of ultrasonic waves in a sample containing periodic wrinkles using the FDTD method (Segawa et al., 2016).

This work developed an experimental apparatus to clarify the relationship between the wrinkles and ultrasonic reflection characteristics. The obtained data from this apparatus were compared to those calculated from a numerical analysis, providing the reliability of the apparatus. Then, operational checks and the ultrasonic measurement were performed using the developed experimental apparatus.

PRINCIPLE AND ESTIMATION

The wrinkles in the present samples were detected based on the ultrasonic reflection intensity I defined as the maximum amplitude of reflected wave. The ultrasonic reflection intensity is affected by the contact state of two media in contact with each other. Fig.1 shows the relationship between the reflection intensity and the contact state of die and workpiece. I_0 is the reflection intensity at the contact state between the upper die and air, which always shows the highest value. The reflection intensity decreases as the contact area with the workpiece is increased. In this experiment, the wrinkle is evaluated by a relative reflection intensity I/I_0 .

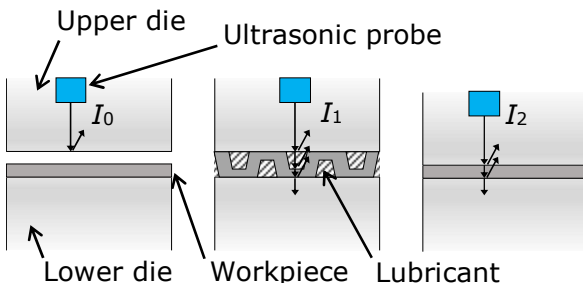


Fig.1 Variation in reflection intensity with the conditions of wrinkles ($I_0 > I_1 > I_2$)

EXPERIMENTAL APPARATUS

Fig.2 shows the structure of developed experimental apparatus. The apparatus is composed of three parts made of S50C steel: the ultrasonic probe storage box, the upper die and the lower die. These components were then assembled by bolting, as shown in Fig.2(a). Glycerine was used because it easily flowed into the narrow space formed by the wrinkled structure.

The ultrasonic probe storage box was manufactured to fix the position of the ultrasonic probe. A groove for setting the ultrasonic probe was provided on the lower surface of the box. A rubber plate was sandwiched between the groove and the upper surface of ultrasonic probe. The rubber plate was designed to be larger than the gap between the groove and ultrasonic probe in order to apply the elastic force, providing a sufficient contact between the probe and the upper die. Glycerine was also

applied to this area. The probe frequency was 2.25 MHz.

The upper die consisted of four components, *viz.*, A, B, C and D. The upper die A contained a punch with a height of 30 mm considering that the irradiation distance of ultrasonic wave was larger than the near field length for all frequencies used in the present study. Vertical and horizontal dimensions of punch were set to be 60 mm and 50 mm, respectively, in order to avoid affecting the ultrasonic propagation. The lower surface of the upper die was grinded to obtain the sufficient contact with the specimen. The grooves for bolting were provided to fix the upper and lower dies in the upper die A. These grooves were machined to respond the lateral movement of the lower die. Four screw holes in the

centre of the upper die A were provided for fixing the ultrasonic probe storage box. Four bolts in the corner of the upper die assembled the upper dies A-D.

The lower die was composed of two components of E and F integrated by bolting. The groove was also fabricated for fixing the specimen and receiving the glycerine lubricant in the lower die. As a result, the gap between the specimen and die could be filled with glycerine during the entire experimental process.

The O-ring was placed on the lower surface of lower die E to prevent glycerine from leaking out of the gap between the lower die E and F. Finally, we prepared three types of the lower die F with different heights considering the wrinkle height used in this work. The positioning bolt in Fig.2(e) is passed through the upper die B. The positioning bolt moves the lower die laterally. The moving direction of the lower die is constrained by the upper die C and D when the lower die is moved. Consequently, the movement of the ultrasonic irradiation position can be performed accurately by the positioning bolt, the upper die C and D. The gap between the upper and lower dies to place specimens, shown in Fig.2(e), was set to be 5% lower than the height of specimen to tightly bind the die and specimen.

Fig.3 shows peripheral equipment connected to the developed experimental apparatus. A pulsar receiver performed the transmission and reception of ultrasonic waves through the ultrasonic probe. The ultrasonic wave was then displayed on the oscilloscope, of which the data were recorded by the computer.

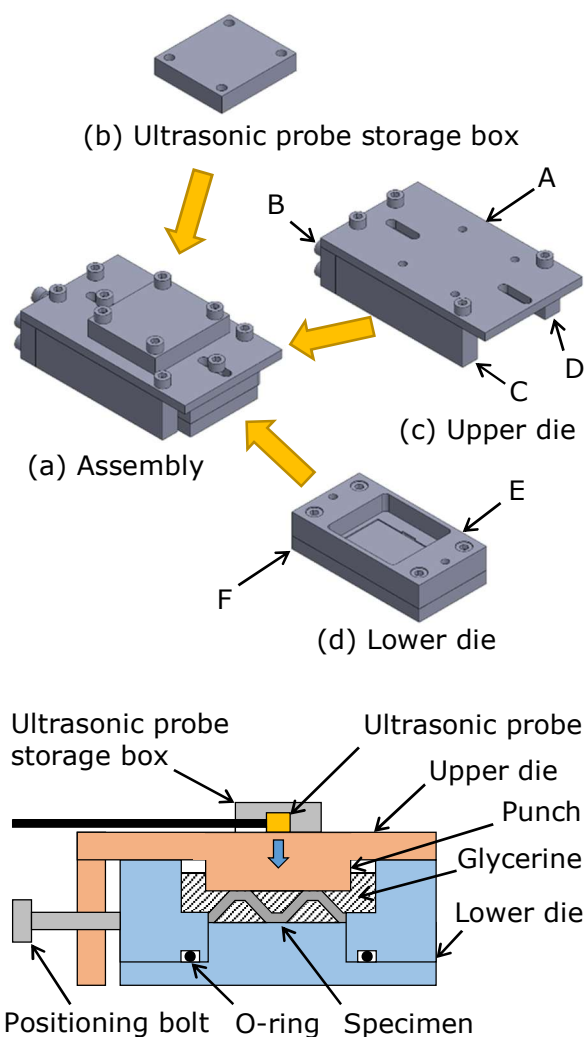


Fig.2 Experimental apparatus

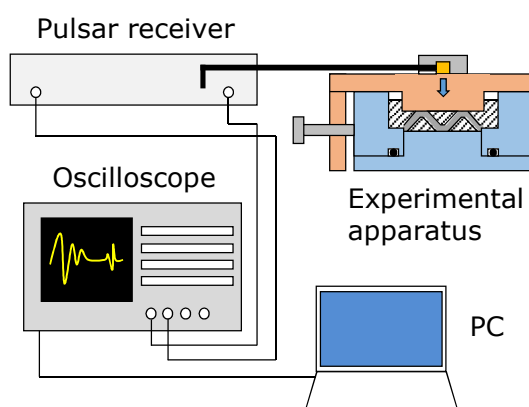


Fig.3 Experimental apparatus and peripheral equipment

SPECIMEN

Fig.4 shows the scheme of the specimen used in the present work. The specimen was made of A1050 pure aluminum. The wrinkles of specimen were produced in the trapezoidal shape by the electro-discharge machining. The surface roughness of the specimen was increased from $0.14 \mu\text{m}$ to $3.36 \mu\text{m}$ after this process.

Fig.5 describes the shape parameters for periodic wrinkle including a specimen thickness t_w , wrinkle height h , wrinkle slope angle a , contact width c_w and wrinkle wavelength λ_w . Thirteen different specimens were prepared with various shape parameters, of which the ranges are summarized in Table 1. The contact width c_w was fixed to be 1.0 mm for all cases.



Fig.4 Scheme of specimen

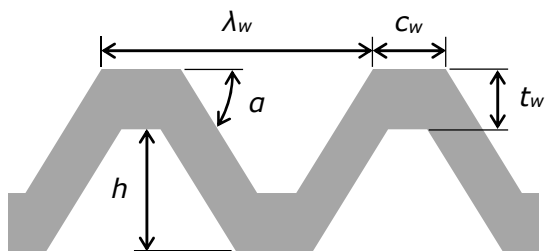


Fig.5 Shape parameters for periodic wrinkle

Table 1 Specimen dimensions

t_w [mm]	1.0-2.0
h [mm]	0.5-2.0
a [deg]	5.60-36.87
λ_w [mm]	4.0-12.0

CONTACT BETWEEN THE UPPER DIE AND SPECIMEN

The experiment was performed to confirm the contact between the upper die and the specimen using a pressure-sensitive paper made by ARUFUN. This paper was sandwiched between the upper die and the specimen. The contact area between the

upper die and the specimen was transferred to this paper when the experimental apparatus was assembled. Fig.6 shows the contact areas between the upper die and specimen transferred to the pressure-sensitive paper, suggesting that the upper die and the specimen were contacted sufficiently. Sufficient contacts were also obtained for the other specimens considering the clear pattern printed on the pressure-sensitive papers. These results demonstrated that the method of setting the gap between the upper die and lower die are effective to control the contact between the upper die and specimen.

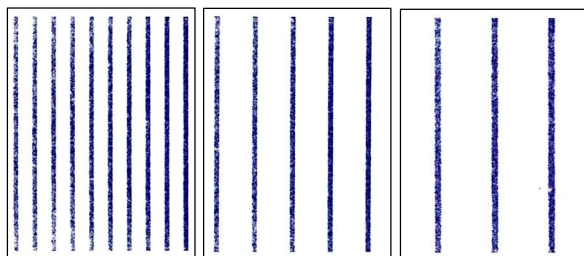


Fig.6 Contact areas between upper die and specimen transferred on pressure-sensitive paper, (a) $\lambda_w=4.0\text{mm}$, (b) $\lambda_w=8.0\text{mm}$ and (c) $\lambda_w=12.0\text{mm}$

ULTRASONIC MEASUREMENT

Fig.7 shows a reflected wave measured from the specimen, which varied by the contact state between the die and specimen. The amplitude of the reflected wave represented the magnitude of the reflection intensity. Fig.8 shows the results of ultrasonic measurement under different contact conditions on the bottom surface of upper die. The presented values were determined by averaging the maximum amplitudes obtained from hundred times of measurements. I/I_0 was 0.908 in contact with glycerine. The measured reflection rate (92%) was consistent with the theoretical value (90%). I/I_0 was slightly decreased to 0.810 in contact with the wrinkled specimen, while the value was more reduced to 0.738 with the flat plate produced by the electro-discharge machining. The acoustic impedance was decreased in the order of S50C steel, A1050 aluminium, glycerine and air. The reflection

of the ultrasonic wave was increased with increasing difference in the acoustic impedances, providing the validity of the trends shown in Fig.8. It is concluded from these results that the developed experimental apparatus could successfully measure the difference in reflection intensity caused by the presence or absence of wrinkles.

I_0 varied from 0.1 to 0.2 during repetitive experiments. Such scattered data would result from the change in the contact state between the ultrasonic probe and the upper die. The reflection intensity also varied. These results are likely attributed to the glycerine lubricant leaking out of the groove in the ultrasonic probe storage box when the upper die was tilted. Therefore, the experiment using the developed

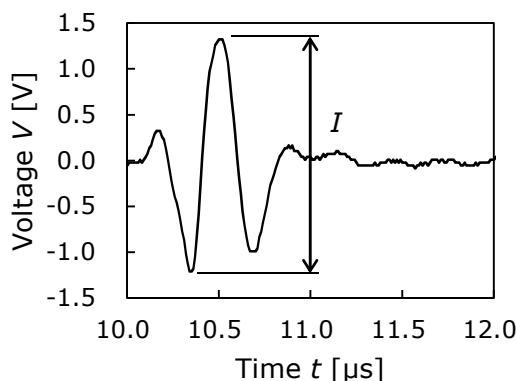


Fig.7 Reflected wave measured at $t_w = 2.0\text{mm}$, $h = 0.5\text{mm}$, $\alpha = 9.00\text{deg}$ and $\lambda_w = 8.0\text{mm}$

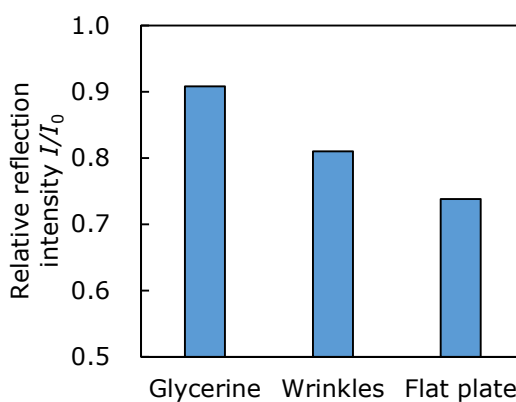


Fig.8 Comparison between contact states and relative reflection intensity (Parameters of wrinkles are $t_w = 2.0\text{mm}$, $h = 0.5\text{mm}$, $\alpha = 9.00\text{deg}$ and $\lambda_w = 8.0\text{mm}$)

0.5mm, $\alpha = 5.60\text{deg}$ and $\lambda_w = 12.0\text{mm}$)

apparatus should be performed under the condition that fixes the upper die horizontally.

Fig.9 shows the change in I_0 with time immediately after embedding the ultrasonic probe in the upper die and fixing this part horizontally. I_0 exhibited a suppressed scattering within a deviation of 0.02 after one minute from commencing the experiment; note that the deviation was 0.1 before applying the horizontal condition, suggestive of the importance of horizontal calibration of the upper die. However, it is noted that I_0 was radically increased in the initial stage (i.e., the first one minute) of the experiment. This could arise from the flow of glycerine between the ultrasonic probe and the upper die. It is thus strongly recommended to avoid the unreliable data obtained immediately after installing the ultrasonic probe.

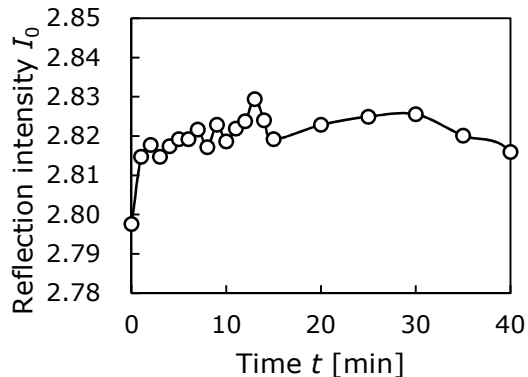


Fig.9 Relationship between reflection intensity I_0 and time after assembling ultrasonic probe

CONCLUSIONS

The experimental apparatus was developed to reproduce the FDTD analysis model, of which the operational checks were performed. The following conclusions were drawn from this work:

- The die and specimen showed a sufficient contact when assembled in the developed experimental apparatus.
- The developed apparatus successfully distinguished the difference in reflection intensity induced by the presence or absence

6th International Engineering Symposium - IES 2017

March 1-3, 2017, Kumamoto University, Japan

- of wrinkles, proving its ability of evaluating the relationship between the wrinkle shape and the ultrasonic reflection characteristic.
- The experiment should be performed at least one minute after embedding the ultrasonic probe in the upper die to obtain reliable data.

ACKNOWLEDGEMENTS

The authors are grateful to Mr. Ryunosuke Harada, undergraduate student, for his help in the experiment.

REFERENCES

- [1] Doege, E et al (2002), Contactless on-line measurement of material flow for closed loop control of deep drawing, *Journal of Materials Processing Technology* Vol.130-131, pp.95-99.
- [2] Hagino, N et al (2013), Reflection and Transmission Characteristics of Ultrasonic Waves in Flat Surface Die -Visualization of Contact Conditions between Die and Workpiece During Stamping 1-, *Journal of the Japan Society for Technology of Plasticity*, Vol.54, No.632, pp.826-830. (in Japanese).
- [3] Hagino, N et al (2014), Propagation behavior of ultrasonic wave around boundary surfaces of workpieces and dies, *Procedia Engineering*, Vol.81, pp.1073-1078.
- [4] Jinno, K et al (2014), Analysis on Nonlinear Ultrasonic Images of Vertical Closed Cracks by Damped Double Node Model, *Materials Transactions*, Vol.55, No.7, pp.1017-1023.
- [5] Katayama, T et al (2004), Development of process design system for press forming—multi-objective optimization of intermediate die shape in transfer forming, *Journal of Materials Processing Technology*, Vol.155-156, pp.1564-1570.
- [6] Koga, N et al (2007), Deep-drawing and ironing of 1050 aluminum sheets loaded with vibration using NC servo press machine, *Journal of Japan Institute of Light Metals*, Vol.57, No.6, pp.240-244. (in Japanese).
- [7] Lo, S W and Yang, T C (2004), Closed-loop control of the blank holding force in sheet metal forming with a new embedded-type displacement sensor, *The International Journal of Advanced Manufacturing Technology*, Vol.24, No.7-8, pp.553-559.
- [8] Nonaka, T et al (2012a), Development of Detection Technology of the Scrap-Jumping in Pierce Processing, *Applied Mechanics and Materials*, Vol.182-183, pp.472-476.
- [9] Nonaka, T et al (2012b), Application of Sensors to In-Process Defect Detection in Sheet Forming, *Steel Research International*, Special Edition, pp.387-390.
- [10] Mahayotsanun, N et al (2009), Tooling-integrated sensing systems for stamping process monitoring, *International Journal of Machine Tools & Manufacture*, Vol.49, No.1, pp.634-644.
- [11] Saiki, H et al (1993), Estimation of Contact Conditions of Frictional Interface in Forging Processes Using Ultrasonic Examination, *Transactions of the Japan Society of Mechanical Engineers, Series C*, Vol.59, No.562, pp.1934-1939. (in Japanese).
- [12] Saiki, H et al (1994), Estimation of frictional shearing stress under lubricated contact conditions in ring upsetting (application of ultrasonic examination), *Transactions of the Japan Society of Mechanical Engineers, Series C*, Vol.60, No.577, pp.279-284. (in Japanese).
- [13] Satyanarayan, L et al (2007), Simulation of ultrasonic phased array technique for imaging and sizing of defects using longitudinal waves, *International Journal of Pressure Vessels and Piping*, Vol.84, No.12, pp.716-729.
- [14] Segawa, Y et al (2016), Analysis of Ultrasonic Wave Reflection for Wrinkle Shapes of Press-formed Products Using FDTD Method, *The Proceedings of the 2016 Japanese Spring Conference for the Technology of Plasticity*, pp.53-54. (in Japanese).
- [15] Siegert, K et al (1997), Closed loop of the friction force. Deep drawing process, *Journal of Materials Processing Technology*, Vol.71, No.1, pp.126-133.
- [16] Stancu-Niederkorn, S et al (1994), Ultrasonic Investigation of Friction Mechanism in Metal Forming, *Journal of Materials Processing Technology*, Vol.45, No.1, pp.613-618.
- [17] Traversin, M and Kergen, R (1995), Closed-loop control of the blank-holder force in deep-drawing: finite-element modelling of its effects and advantages, *Journal of Materials Processing Technology*, Vol.50, No.1, pp.306-317.
- [18] Yang, M et al (2003), Data fusion of distributed AE sensors for the detection of friction sources during press forming, *Journal of Materials Processing Technology*, Vol.139, No.1, pp.368-372.
- [19] Yee, K S (1966), Numerical Solution of Initial Boundary Value Problems Involving Maxwell's Equations in Isotropic Media, *IEEE Transactions on Antennas and propagation*, Vol.14, No.3, pp.302-307.

Performance Analysis of a Model Water-Wave Energy Harvesting System with a Paddling-Wall Wave Tank

Po-Hsun Chen and Tian-Shiang Yang

*Department of Mechanical Engineering, National Cheng-Kung University, Taiwan.
email:tsyang@mail.ncku.edu.tw*

ABSTRACT: The oscillating water column (OWC) type wave energy converters are mostly installed on shorelines. And the Wells turbine is the most frequently utilized power take-off (PTO) component for OWC plants. However, such plants have a few aerodynamic problems remaining to be resolved so as to further improve plant performance. Here we thus explore the possibility of using a non-aerodynamic PTO device. In particular, a model system is analyzed in this study, which consists of a wave tank with two hinged side walls, which, in turn, are connected to two electric generators. The basic idea is to exploit a periodically varying pressure (say, supplied by OWC device) to excite surface waves in the water tank, which then drive the hinged side walls into periodic oscillation, and produce electric power through the connected generators. For the model system described above, a mathematical model is constructed and then solved analytically. For the natural response of the wave tank, both symmetric and antisymmetric linear-wave modes are found, and the corresponding natural frequencies are calculated. Moreover, for the forced response of the model system, both resonance and anti-resonance frequencies of the driving surface-pressure distribution are found, which produce maximum and zero output electric power, respectively. Optimization of system parameter setting to maximize the output electric power also is discussed.

Keywords: *Wave Energy Convertor, Oscillating Water Column, Paddling-Wall Wave Tank, Wave Modes, Resonance, System Optimization*

1. INTRODUCTION

The world energy consumption is expected to keep increasing considerably for a few decades into the future [1]. Meanwhile, environmental protection issues strongly demand more use of renewable energy. Although currently wave energy is not economically competitive with more mature technologies such as wind energy, it still attracts the interest of governments and industry because it has the highest energy density among all renewable energy sources. Specifically, one study estimates that the total wave energy resource for Europe is about 320 GW [1], while the total installed capacity of wind energy in the same region is about 106 GW [2]. It has also been estimated that, with an investment cost of EUR 820 billion,

a world-wide wave energy economic contribution in the electricity market on the order of 2,000 TWh/year, about 10% of the world electricity consumption, potentially can be achieved [3].

At present, there are a wide variety of wave energy technologies, not only varying in their ways to harvest wave energy, but also depending on the water depth and the location (e.g., shoreline, near-shore, or offshore). However, based on their working principles, most wave energy technologies can be categorized into three main types, namely the oscillating water column (OWC), the oscillating body, and the over spilling systems. (See [1,4] for a detailed description and review of the development of such technologies.)

In particular, the OWC devices comprise a partly submerged concrete or steel

structure, open below the water surface, inside which air is trapped above the water surface. The oscillating motion of the internal water surface produced by the incident waves makes the air to flow through a turbine that drives an electric generator. Such devices mostly are located on the shoreline or near shore; see [5] for a review on the development of OWC devices. For some examples of specific OWC system designs, the reader is referred to [6–8], where the modeling, analysis and optimization issues also are discussed.

Now, the present work is an investigation on the possibilities of improving the performance of OWC devices. At present, the Wells turbine is the most frequently used power takeoff component for OWC plants [4]. Generally speaking, they have the favorable features of (i) the enhanced possibility of energy storage by flywheel effect, (ii) a pretty good peak efficiency of about 0.7–0.8, and (iii) a relatively low cost to construct. However, they also have some weak points such as (i) a low or even negative torque at small flow rates, (ii) a possibly sharp drop in power output due to aerodynamic losses at flow rates exceeding the stall-free critical value, (iii) aerodynamic noise, and (iv) a relatively large diameter for its power [4].

As can be seen, most of the weak points summarized above have their aerodynamic causes. We thus wish to explore the possibility of exploiting a non-aerodynamic component for the power takeoff of OWC plants. Specifically, in the present study, a model system which consists of a wave tank with two hinged side-walls is considered; see Fig. 1. The basic idea behind such a system is to use the periodically varying pressure in an OWC plant to excite surface waves in a water tank, which, in turn, drive the hinged side walls into periodical oscillation. Through transmissions, the side-wall oscillations then can drive generators that deliver electric energy to the grid or a storage device. It is also interesting to note that the setup of this model system is somewhat similar to the oscillating-paddle WEC of Hazra et al. [9]. The difference here, however, is that in their system construction ocean waves drive the paddle

directly, while in the present model system the waves produce the pressure oscillations that excite the surface waves in the wave tank.

Admittedly, the model system is also constructed as such for its simplicity, so that a mathematical analysis can be carried out with some ease. In future work, we expect to remove some simplifications of the model system, and perhaps study more complicated model systems suitable for other types of WECs as well. We would also like to mention here that the pressure variation in OWC devices have been calculated analytically or numerically based on mathematical models by several authors; see [10–14] for example. But the present model system focuses on the power takeoff component of OWC devices instead, and therefore complements such works. Moreover, as will be detailed in the next section, our model also incorporates the electric components, and thus can be used to predict the overall efficiency of the whole plant.

In §2 we shall present the mathematical formulation. But due to space limitation, for analysis the reader is referred to the Master's thesis of Chen [15]. The results then will be discussed systematically in §3. And finally, in §4 a few remarks will be given to conclude this paper.

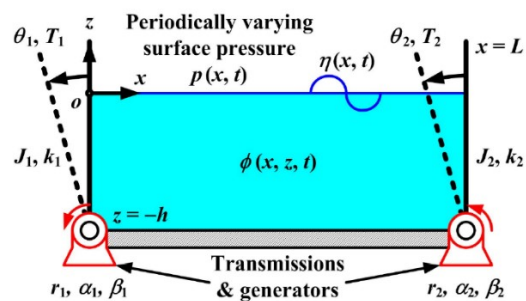


Fig. 1 Schematic of the model system for water-wave energy harvesting studied here.

2. Formulation

Here we present the mathematical formulation in dimensionless terms. For a dimensional formulation, the reader may consult [15]. Also, the definitions of

6th International Engineering Symposium - IES 2017

March 1-3, 2017, Kumamoto University, Japan

physical variables and parameters are shown in Fig. 1.

Note here, however, that the x and z coordinates of the system are normalized by L and h respectively. For the present linearized formulation, the displacement angles $\theta_{1,2}$ of the two rigid side walls implicitly are assumed to be small, and are normalized here by a small parameter $\mu = h/L$ to be identified immediately. Meanwhile, the water-surface elevation η is normalized by h , and the surface pressure p is normalized by the characteristic scale p_0 of its periodic temporal variation. Moreover, here we normalize time t by $\sqrt{h/g}$ (g being the gravitational acceleration), the velocity potential ϕ by $\varepsilon h \sqrt{gh}$, and define the small parameter ε by $\varepsilon = p_0 / \rho gh$. The electromotive potentials $V_{1,2}$, which the two generators produce, are normalized by

$$V_0 = (N_1 N_2)^{1/2} \cdot [k_1^{(e)} k_2^{(e)}]^{1/2} \cdot \varepsilon \sqrt{g/h},$$

Where $N_{1,2}$ are the gear ratios of the two transmissions, and $k_{1,2}^{(e)}$ are the electro-mechanical conversion coefficients of the generators; see [15]. The torques $T_{1,2}$ (acting on the side walls by the transmissions connecting them to generators) are normalized by

$$T_0 = (N_1 N_2)^{1/2} \cdot [k_1^{(e)} k_2^{(e)}]^{1/2} \cdot I_0,$$

where

$$I_0 = V_0 \cdot \left[\left[R_1^{(i)} + R_1^{(l)} \right] \cdot \left[R_2^{(i)} + R_2^{(l)} \right] \right]^{-1/2}$$

is a characteristic scale for the electric currents $I_{1,2}$. For a detailed discussion on how the above characteristic scales are determined, see [15].

In terms of dimensionless variables, we have the following dimensionless Laplace equation for the dimensionless velocity potential ϕ :

$$\frac{\partial^2 \phi}{\partial z^2} + \mu^2 \frac{\partial^2 \phi}{\partial x^2} = 0 \quad (0 \leq x \leq 1, -1 \leq z \leq 0), \quad (1)$$

subject to the tank-bottom kinematic boundary condition (KBC)

$$\frac{\partial \phi}{\partial z} = 0 \quad (z = -1), \quad (2)$$

and the water-surface KBC

$$\frac{\partial \phi}{\partial z} = \frac{\partial \eta}{\partial t} \quad (z = 0), \quad (3)$$

and dynamic boundary condition (DBC)

$$\frac{\partial \phi}{\partial t} + \eta = -p(x, t) \quad (z = 0). \quad (4)$$

In Eq. (1) the dimensionless parameter $\mu = h/L$. The linearized KBCs on the two side walls read

$$\frac{\partial \phi}{\partial x} = -\frac{1}{\mu}(z+1)\dot{\theta}_1 \quad (x = 0), \quad (5)$$

$$\frac{\partial \phi}{\partial x} = -\frac{1}{\mu}(z+1)\dot{\theta}_2 \quad (x = 1), \quad (6)$$

and the two KBCs there are given by

$$J_1 \ddot{\theta}_1 = -k_1 \theta_1 + K_\tau T_1 - \int_{-1}^0 \frac{\partial \phi}{\partial t} \Big|_{x=0} (z+1) dz, \quad (7)$$

$$J_2 \ddot{\theta}_2 = -k_2 \theta_2 + K_\tau T_2 + \int_{-1}^0 \frac{\partial \phi}{\partial t} \Big|_{x=1} (z+1) dz. \quad (8)$$

The dimensionless appearing in Eqs. (7) and (8) are defined by

$$J_{1,2} = \frac{\hat{J}_{1,2}}{\rho w h^4}, \quad k_{1,2} = \frac{\hat{k}_{1,2}}{\rho g w h^3}, \quad K_\tau = \frac{T_0}{\varepsilon \rho g w h^3},$$

Where ρ is fluid (water) density, w is the width of the wave tank, $\hat{J}_{1,2}$ are the dimensional moments of inertia of the two paddling walls, and $\hat{k}_{1,2}$ the dimensional rotational rigidity of the angular "springs" restraining the paddling walls. Note also that the electromotive potentials $V_{1,2}$ are related to the angular speeds $\dot{\theta}_{1,2}$ by

$$V_{1,2} = K_{1,2} \cdot \dot{\theta}_{1,2}, \quad (9)$$

where

$$K_{1,2} = \frac{N_{1,2} k_{1,2}^{(e)}}{(N_1 N_2)^{1/2} \cdot [k_1^{(e)} k_2^{(e)}]^{1/2}}.$$

The torques $T_{1,2}$ are assumed linearly related to the currents $I_{1,2}$ by

$$T_{1,2} = -K_{1,2} \cdot I_{1,2}. \quad (10)$$

And the equations for electric energy balance read

$$L_1 \dot{I}_1 + R_1 I_1 + \frac{1}{C_1} \int I_1 dt = V_1, \quad (11)$$

$$L_2 \dot{I}_2 + R_2 I_2 + \frac{1}{C_2} \int I_2 dt = V_2, \quad (12)$$

where

$$L_{1,2} = \frac{L_{1,2}^{(i)} I_0}{V_0 \sqrt{h/g}}, \quad C_{1,2} = \frac{C_{1,2}^{(l)} \cdot V_0}{I_0 \sqrt{h/g}},$$

and

$$R_{1,2} = \frac{R_{1,2}^{(i)} + R_{1,2}^{(l)}}{\left[R_1^{(i)} + R_1^{(l)} \right]^{1/2} \left[R_2^{(i)} + R_2^{(l)} \right]^{1/2}}.$$

Here $L_{1,2}^{(i)}$ are the inductances of the two

equivalent circuits for the generators, $C_{1,2}^{(l)}$ and $R_{1,2}^{(l)}$, respectively, are the capacitances and resistances of the circuits, and $R_{1,2}^{(l)}$ are the equivalent resistances representing the external loads of the circuits. All parameters defined above are dimensional; see [15] for detail.

3. Results and Discussion

As mentioned above, here we shall leave out the technical details of analysis (see [15]), and just discuss the major results and their implications. The values of the parameters also can be found in [15].

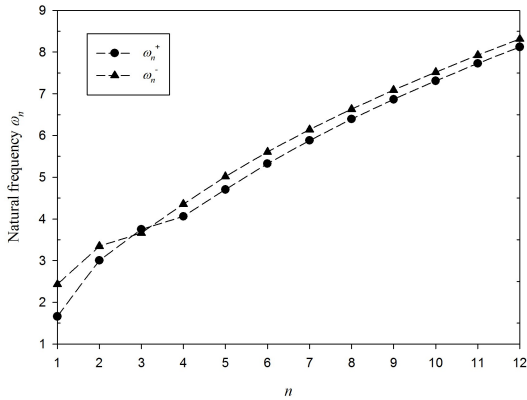


Fig. 2 The first few natural frequencies of wave tank. Here ω_n^+ are the natural frequencies for modes having the two paddles oscillating in phase, and ω_n^- are for those with the paddles oscillating out of phase by π .

3.1 Natural Response of the Wave Tank

First we detach the wave tank from the transmissions and generators, and study its free response. Technically, this amounts to setting the parameter K_r appearing in Eqs. (7) and (8) and the pressure distribution p in Eq. (4) to zero, and then look for steady-periodic solutions of the boundary-value problem formulated by Eqs. (1)–(8).

In particular, here the identical parameter values for the two sides of the system (including those for the paddling walls, transmissions, and generators) are set to be identical. The system itself therefore

has a left-right symmetry. As it turns out, two distinct sets of wave modes are found, and the corresponding natural frequencies, denoted by ω_n^+ and ω_n^- respectively, are plotted in Fig. 2. For the wave modes oscillating steady-periodically at angular frequencies ω_n^+ , the paddles on the two sides oscillate in phase, and the shape of the water surface thus appears to be anti-symmetric with respect to the center of the wave tank; see Fig. 3(a)–(c). By contrast, as shown in Fig. 3(d)–(f), for the wave modes oscillating at angular frequencies ω_n^- , the paddles oscillate out of phase by π , and the water surface appears to be symmetric.

Have a good knowledge about these wave modes is important, because it helps us understand the particular responses of the system under different types of excitations. For example, when the water-surface pressure distribution is symmetric (or anti-symmetric) with respect to the center of the wave tank, only the ω_n^- (ω_n^+)

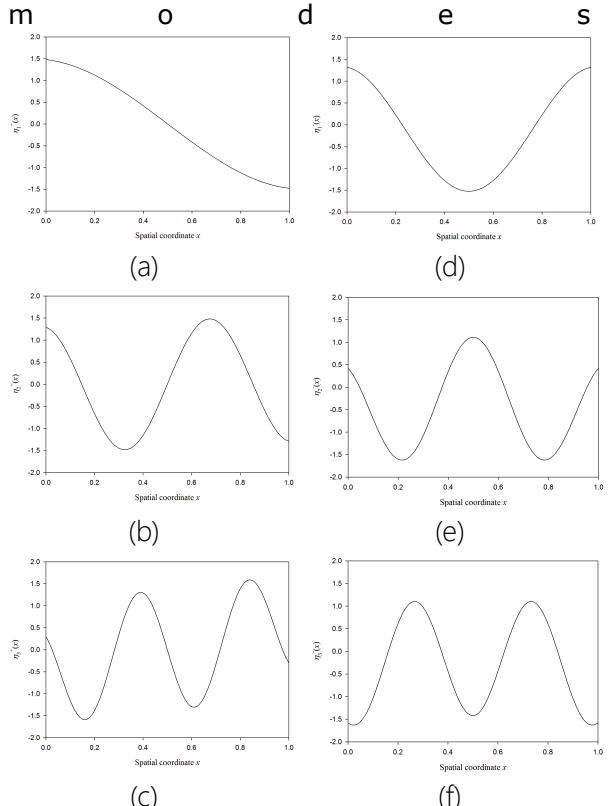


Fig. 3 The mode shapes of water-surface elevation corresponding to (a) ω_1^+ , (b) ω_2^+ , (c) ω_3^+ , (d) ω_1^- , (e) ω_2^- , and (f) ω_3^- . Here the water-surface elevations corresponding to ω_n^+ and ω_n^- are denoted by η_n^+ and

η_n^- respectively.

will be excited. And for an arbitrary pressure distribution that generally can be decomposed into an infinite number of symmetric and anti-symmetric components, resonance is expected when the frequency of pressure oscillation matches one of the natural frequencies, as we shall illustrate in §3.2.

3.2 Forced Response of the System

Here let us consider a symmetric surface pressure distribution having a spatial distribution given by $\hat{p}(x) = \cos(2\pi x)$. Note that $\hat{p}(x-1/2) = \hat{p}(1/2-x)$. As explained above, because of the left-right symmetry of the pressure distribution, only the ω_n^- wave modes are excited. Accordingly, the oscillation amplitude of the angular displacements of the paddling walls, and that of the currents in the circuits, are the same on the two sides, as expected. The phase angles of the paddling-wall oscillations on the two sides, however, differ by π .

In Fig. 4, the oscillating amplitude $R_1^{(\theta)}$ of the angular displacement (which is the same for the two walls) is plotted against the forcing frequency of the symmetric pressure distribution specified above. It is readily seen that $R_1^{(\theta)}$ not only increases tremendously as the forcing frequency ω approaches certain frequencies, but also plunges rapidly (to zero, as can be shown [15]) as ω approaches some other particular values. Of course, the former corresponds to resonance occurring when ω matches one of the natural frequencies, in this case one of ω_n^- ; see Fig. 5. Note also that, in the present case of symmetric pressure distribution, no resonance occurs when ω is close to any of the natural frequencies ω_n^+ . Meanwhile, the observation that the oscillation amplitude becomes zero at certain frequencies can be called "anti-resonance". It can be shown that at such frequencies no power is generated [15]. In practical design of such wave-energy harvesting system, such frequencies therefore should be avoided.

In Fig. 5, a comparison of the resonant frequency with the natural frequencies ω_n^+ also is made, for a case of anti-symmetric

surface pressure distribution. Briefly, resonance occurs when ω is close to one of the natural frequencies ω_n^+ , but none of the ω_n^- . Anti-resonance also occurs in such cases. See [15] for a detailed discussion. It should be warned here, however, that the oscillation amplitudes of the side walls plotted in Fig. 4 can be unphysical near resonance. Specifically, it can exceed the geometric limit of $\pi/2$. This shortcoming highlights the limitation of the present linear theory. Once a more realistic nonlinear mathematical model is constructed and analyzed, one can capture the resonant amplitude more accurately, and this will be pursued in a future work. Nevertheless, the results discussed above indicate that the model system design is promising.

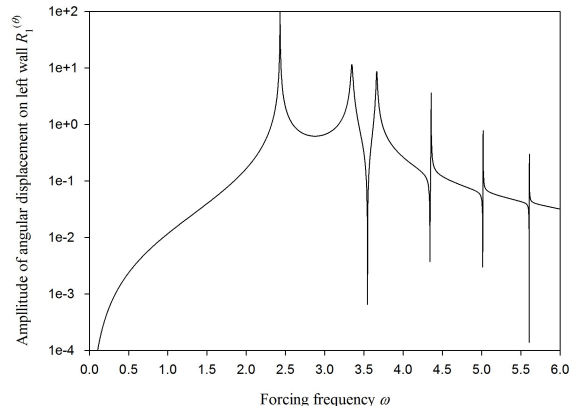


Fig. 4 The dependence of the oscillating amplitude of the left paddle on the forcing frequency of the water-surface pressure. Shown here is the particular case of symmetric pressure distribution.

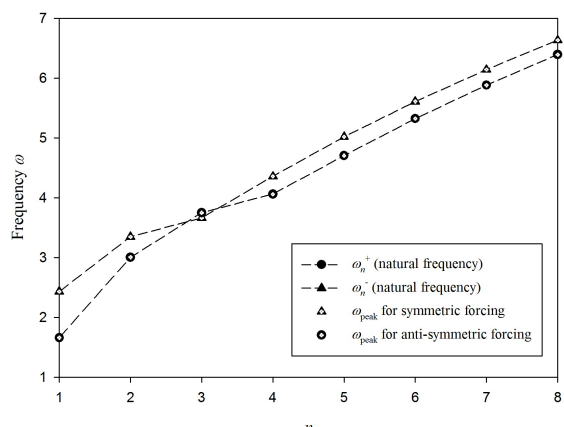


Fig. 5 Comparison of the resonant forcing frequencies with the two types of natural frequencies ω_n^+ and ω_n^- .

3.3 System Parameter Optimization

The possibilities of resonance and anti-resonance suggest that in actual applications the system parameters need to properly designed, so as to produce a high power output, but not to physically damage the system. The system optimization issue for a particular case is briefly discussed here. In that particular case, the dimensionless forcing frequency is fixed at 3.6 (which is about right in practical applications), the electric parameters are kept constant, but the rigidity and inertia parameters $k_{1,2}$ and $J_{1,2}$ are to be tuned to optimize the system performance. And again, the parameter values are detailed in [15].

Now, Fig. 6(a) shows the contour plot of the calculated output power of the system. In particular, the logarithmic value of the output power (in Watts) is indicated there, for a range of reasonable values of $k_{1,2}$ and $J_{1,2}$. It is seen that the output power obtains its maximum in a certain "optimal band" (which may not be exactly straight in the plot though). In fact, closer examination reveals that the maximum output power occurs when $k_{1,2} = 3.961$ and $J_{1,2} = 0.267$; see Fig. 6(b) for a close-up of the optimal band.

Although a system design in the optimal band would generate a high output power, as pointed out above this can be damaging. So we tentatively limit the oscillation amplitude to 10 degrees as a reasonable design. As shown in red dotted lines in Fig. 6(a), there still is a rather astonishing output power of about 3 MW, which is on the same order (and even exceeds) the output power of LIMPET (250 kW). Of course, a more careful nonlinear analysis may alter this estimate, but the order of magnitude should stay the same. So, the model system design studied here appears to be rather promising, and deserve further study, and even actual technology development, in future work.

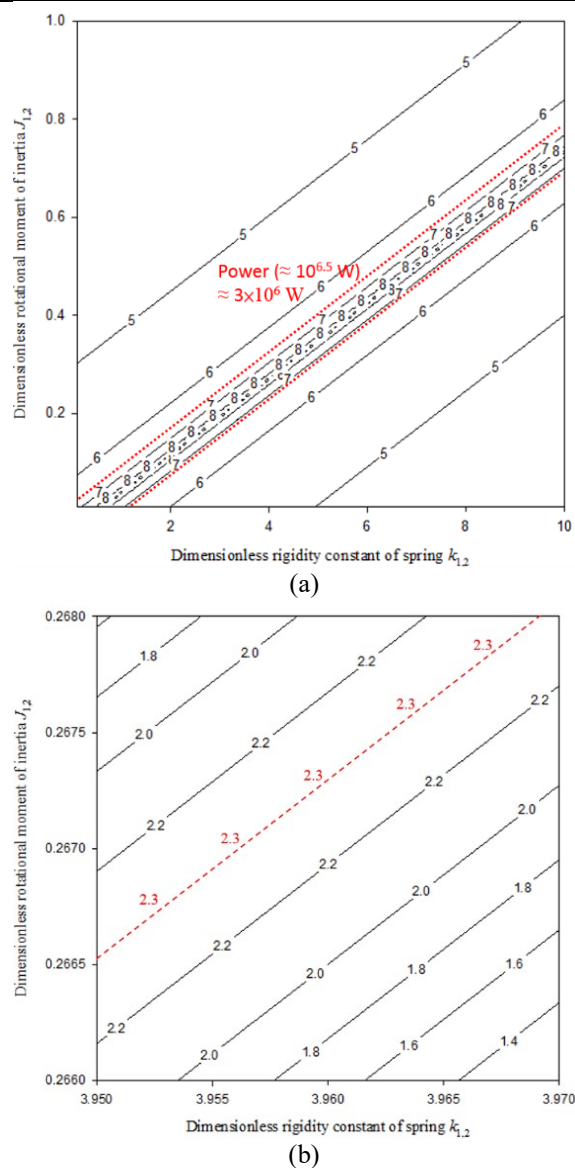


Fig. 6 (a) The contour plot of output power within reasonable ranges of $k_{1,2}$ and $J_{1,2}$. Indicated here is the logarithmic value of the output power in Watts. The red dotted lines correspond to the reasonably large 10-degree oscillation amplitude of the side walls, producing an output power of about 3 MW. (b) Close-up of the high-power-output region in (a). Indicated here is the output power in GWs.

6th International Engineering Symposium - IES 2017

March 1-3, 2017, Kumamoto University, Japan

4. CONCLUSION

In this work, we have analyzed the potential performance of a model wave-energy harvesting system. In particular, we have determined the wave modes of the model system and their natural frequencies, which help provide clear insights into the dynamic response of the model system. Moreover, we have identified the existence of resonant and anti-resonant regions of the system-parameter space, which would guide the system design in actual applications. Specifically, one may wish to construct a system whose forcing frequency falls in a resonant region for high power output, and away from the anti-resonant regions to avoid extremely low energy generation. In addition, we have also shown that an optimal band exist for the system parameter design. And more importantly, when the system is adequately designed, the output power appears to be compatible with existing wave energy converters. The model system design studied here therefore appears to be rather promising, and deserve further study, and even actual technology development, in future work.

ACKNOWLEDGEMENTS

This work was funded by Taiwan (R.O.C) Ministry of Science and Technology (formerly National Science Council) under grant NSC 101-2221-E-006-105-MY3.

REFERENCES

1. A. Clément, P. McCullen, A. Falcão, A. Fiorentino, F. Gardner, K. Hammarlund, G. Lemonis, T. Lewis, K. Nielsen, S. Petroncini, M. T. Pontes, P. Schild, B. O. Sjöström, H. C. Sørensen and T. Thorpe, "Wave Energy in Europe: Current Status and Perspectives", Renewable and Sustainable Energy Reviews, Vol. 6, No. 5, pp. 405–431, 2002.
2. C. M. Dent, "Wind Energy Development in East Asia and Europe", Asia Europe Journal, Vol. 11, No. 3, pp. 211–230, 2013.
3. T. W. Thorpe, "The Wave Energy Programme in the UK and the European Wave Energy Network", Proceedings of the 4th European Wave Energy Conference, Aalborg, Denmark, pp. 19–27, 2000.
4. A. F. de O. Falcão, "Wave Energy Utilization: A Review of the Technologies", Renewable and Sustainable Energy Reviews, Vol. 14, No. 3, pp. 899–918, 2010.
5. T. V. Heath, "A Review of Oscillating Water Columns", Philosophical Transactions of the Royal Society A, Vol. 370, No. 1959, pp. 235–245, 2012.
6. The Queen's University of Belfast Islay, LIMPET Wave Power Plant, report of a research funded in part by the European Commission in the framework of the Non Nuclear Energy Program Joule III, <http://cordis.europa.eu/documents/documentlibrary/66628981EN6.pdf>, 2002 (last retrieved on 22 April 2015).
7. M. Folley, R. Curran and T. Whittaker, "Comparison of LIMPET Contra-Rotating Wells Turbine with Theoretical and Model Test Predictions", Ocean Engineering, Vol. 33, No. 8–9, pp. 1056–1069, 2006.
8. B. M. Count and D. V. Evans, "The Influence of Projecting Sidewalls on the Hydrodynamic Performance of Wave-Energy Devices", Journal of Fluid Mechanics, Vol. 145, pp. 361–376, 1984.
9. S. Hazra, S. Bhattacharya, K. K. Uppalapati and J. Bird, "Ocean Energy Power Take-Off Using Oscillating Paddle", Proceedings of the 2012 IEEE Energy Conversion Congress and Exposition, Raleigh, NC, USA, pp. 407–413, 2012.
10. G. Malara and F. Arena, "Analytical Modelling of an U-Oscillating Water Column and Performance in Random Waves", Renewable Energy, Vol., 60, pp. 116–126, 2013.
11. K. Rezanejad, J. Bhattacharjee and C. G. Soares, "Stepped Sea Bottom Effects on the Efficiency of Nearshore Oscillating Water Column Device", Ocean Engineering, Vol. 70, pp. 25–38, 2013.
12. P. R. F. Teixeira, D. P. Davyt, E. Didier and R. Ramalhais, "Numerical Simulation of an Oscillating Water Column Device Using a Code Based on Navier–Stokes Equations", Energy, Vol. 61, pp. 513–530, 2013.
13. M. J. Ketabdar, F. Khorasani, S. Boreyri, V. Karami, "Numerical Performance Analysis of Oscillating Water Column Device Using Sea Waves", International Journal of Environmental Studies, Vol. 71, No. 6, pp. 840–849, 2014.
14. K. Rezanejad, J. Bhattacharjee and C. G. Soares, "Analytical and Numerical Study of Dual-Chamber Oscillating Water Columns on Stepped Bottom", Renewable Energy, Vol. 75, pp. 272–282, 2015.
15. P.-H. Chen, Performance Analysis of a Model Water-Wave Energy Harvesting System with a Paddling-Wall Wave Tank, Master's Thesis, Mechanical Engineering, National Cheng Kung University, Tainan, Taiwan, 2015.

Microstructure, mechanical and corrosion properties of accumulative roll bonded Mg-2%Zn/anodized Al-7075 composite

Gajanan Anne^{1a}, M R Ramesh^{1b}, H Shivananda Nayaka^{1c}, Shashi Bhushan Arya²

¹ Department of Mechanical Engineering, National Institute of Technology Karnataka, Surathkal, Mangalore 575025, India.

² Department of Metallurgical and Materials Engineering, National Institute of Technology Karnataka, Surathkal, Mangalore 575025, India.

^agajanan.anne25@gmail.com, ^brameshdmt@gmail.com, ^chsn_mech@nitk.ac.in,
^dsbhushanarya@gmail.com,

ABSTRACT: Multilayered composite of Mg-2%Zn/anodized Al-7075 was developed by accumulative roll bonding (ARB) of wrought Mg-2%Zn and anodized aluminium 7075 alloy. The Mg-2%Zn/anodized Al-7075 composite exhibited density of 2298 kg/m³ which is about 1.2 times lighter weight as compared to Al-7075 alloy. The transmission electron microscopy (TEM) showed an average grain size of 1 μm and 0.73 μm in Mg-2%Zn and anodized Al-7075 layers respectively, and with high angle grain boundaries. Mechanical properties were evaluated by microhardness and tensile tests and found significant improvement in strength and hardness values as compared with Mg-2%Zn alloy after four pass ARB process. The multilayered composite shows better corrosion resistance as compared to rolled Mg-2%Zn alloy evaluated using using potentiodynamic polarization test.

Keywords: ARB; UFG; Multilayered composites; EBSD; potentiodynamic polarization.

INTRODUCTION

Magnesium alloys are considered as the lightest structural metallic materials and have huge demand in industrial applications, especially in aviation and transportation industries [Kojima Y (2000), Luo A A (2003)]. However, wider spread applications are restricted due to some undesirable properties, such as comparative low strength, ductility and poor corrosion resistance. These limitations can be overcome by the grain refinement technique, which is proved to be improving both mechanical properties and corrosion resistance of Mg alloys, [Avedesian M M and Baker H (1999)]. In that aspect severe plastic deformation (SPD) is a suitable method for grain refinement for metals and alloys. Among all the SPD techniques, ARB is the most widely used because it enables cost-effective, continuous fabrication. The ARB process has been used to produce bulk ultrafine grained (UFG) materials [Tsuji N. et al. (2003), Hidalgo-Manrique P. et al.

(2016)]. Recently laminate composites are more popular than the monolithic alloys because laminate composites exhibits better corrosion resistance and improved mechanical properties [Wu K. et al. (2010)]. For Mg alloy laminated composite, Al alloys is the right material, because Al and its alloys have many advantages and excellent properties like low density, good ductility and formability, good strength, and corrosion resistance [Kaufman J G, and Rooy E L (2004)]. In this work efforts have been made to improve mechanical and corrosion behavior of the Mg-2%Zn alloy by bonding with anodized Al-7075 using ARB process. The Al-7075 alloys have good strength to weight ratio, it is extensively used in aviation industries mainly, plane structures, wings and fuselages [Starke E A, and Staley J T (1996)].

The aim of the present study is to develop Mg-2%Zn/ anodized Al-7075 multilayered composite by ARB using Mg-2%Zn alloy

6th International Engineering Symposium - IES 2017

March 1-3, 2017, Kumamoto University, Japan

and anodized Al-7075 alloy and investigate microstructure, mechanical and corrosion properties.

EXPERIMENTAL PROCEDURE

Materials

Mg-2%Zn was casted using permanent mould casting at temperature of temperature range of 750 °C to 800 °C in the inert atmosphere of 99% CO₂ using pure magnesium (99.9 wt. %) ingots as base metal and zinc (99.9 wt. %) granules as alloying element. The Mg-2%Zn alloy was homogenized at 400 °C for 24 h in the tubular furnace and then rolled into sheets with the thickness about 1 mm at 300 °C using laboratory rolling mill. Rolled sheet with a thickness of 1mm Al-7075 alloy was procured.

Anodization treatment

Al-7075 alloy sheets were anodized before ARB process. Clean the sample using NaOH solution and followed by immersion in HNO₃ solution. The anodizing treatment was done in an electrolyte bath containing 15 weight % H₂SO₄ solutions with operating potential of 16 V for 60 min at 18 °C with forced circulation in order to obtain uniform aluminium oxide film [Jamaati R. et al. (2010)].

Accumulative roll bonding

Rolled sheet of Mg-2%Zn alloy and anodized Al-7075 alloy were cut with the dimension of 100 mm × 30 mm × 1 mm. The sheets were degreased in acetone and wire brushed and stacked in such a way so as to obtain alternate layers of Mg-2%Zn and anodized Al-7075. The stacked sheets were heated in a tubular furnace at 350 °C for a period of 10 min and then roll bonded to a 50% reduction at 350 °C. The bonded was performed using laboratory rolling mill diameter 110 mm without using any lubrication done up to 4 ARB pass.

Microstructure evaluation

Microstructure analysis was done using scanning electron microscopy (SEM: JEOL JSM-6380LA). For SEM analysis, ARB processed samples (TD-RD plane) were fine polished using up to 2000 grit silica paper followed by 0.25 µm diamond paste polish and etched using acetic-

picral. TEM analysis was performed on 4-pass ARB samples (ND-RD plane) were mechanically polished and then final thinning was performed by dimpling machine followed by ion beam milling.

X-ray diffraction analysis and density test

X-ray diffraction (XRD) with Cu K_α radiation was used to identify the different phases multilayered composite. Density of the as rolled and multilayered composites was measured according to Archimedes principle.

Mechanical properties

Mechanical properties of the multilayered composite were evaluated using Vickers microhardness test and tensile test. Vickers microhardness test was performed at a load of 10 g for 11 s using Omni-tech microhardness tester. Tensile test was carried out using Tinius Olsen tensile tester. Tensile test samples were prepared according to ASTM E8M standards.

Electrochemical corrosion

Electrochemical corrosion measurements were carried out using an electrochemical workstation (EC lab-Biologic SP-150) with standard three-electrode system containing a saturated calomel electrode (SCE) as a reference electrode, a platinum electrode as a counter electrode, and the specimen surface as a working electrode. Potentiodynamic polarization was performed in 0.1 M NaCl solution having pH value of 7.5 at room temperature at a scan rate of 1 mV/s.

RESULTS AND DISCUSSION

Microstructure evolution

SEM micrographs (Fig. 1) reveal good bonding between the Mg-2%Zn and anodized Al-7075 layers because there are no cracks or delimitation between the interfaces. The average layer thickness was found to be in the range of 50-60 µm and slight waviness layer structure also observe the necking and some of the ruptured Mg-2%Zn layers because of high plastic deformation.

TEM analysis

TEM micrographs (Fig. 2) reveal the elongated grains with a high dislocation density in the rolling direction. It shows the fine grains and sub-grains in the microstructure of the multilayered composite. SAED pattern showed a net pattern, which indicated that the area had large misorientation.

XRD analysis and density test

According to the XRD results, the phase constituents of the multilayered composite were Al, αMg, Al₂O₃, Al₁₇Mg₁₂ and AlMg₄Zn₁₁ as shown in Fig. 3. It is due to interdiffusion between Mg-2%Zn and anodized Al-7075 layers. A small peak of Al₂O₃ found in the multilayered composite due to anodizing treatment before ARB process on Al-7075 alloy. The density of the rolled Mg-2%Zn, anodized Al-7075 alloy and Mg-2%Zn/anodized Al-7075 multilayered composite was found to be 1759 kg/m³, 2778 kg/m³, and 2298 kg/m³ respectively. It found that developed multilayered composite exhibited 1.2 times less weight as compared to Al-7075 alloy.

Mechanical properties

The microhardness of the multilayered composite was considerably improved by ARB processing such that the average microhardness increased to 97.6 HV and 256.2 HV from 74.9 HV and 170.5 for the respective as-rolled Mg-2%Zn and anodized Al-7075 sheets as shown in Fig. 4.

The yield strength, ultimate tensile strength and elongation to failure of Mg-2%Zn/anodized Al-7075 after 4-passes reached 233.6 MPa, 319.0 MPa and 6.4%, (Fig. 5) which are 2.11 times, 1.85 times and 1.52 times of the as-rolled Mg-2%Zn alloy. Enhanced strength and hardness was due to strain hardening and grain refinement during ARB process and presence of Al₂O₃ particles which constraint to localized deformation during indentation.

Fractography

The principal of fracture mechanism at every layer considered, found that Mg-2%Zn layers were fractured in the shear mode and free from dimples, it reveals

bright lines in the fracture surface which is the indication of cleavage fracture. However, anodized Al-7075 layer shows of elongated dimples on the fractured surface which evidently illustrate that the failure mode is shear ductile rupture as shown in Fig. 6.

Electrochemical corrosion

A shift of E_{corr} values was observed (Fig.7) in noble direction after ARB processing and E_{corr} values were found to be -1.63 V and -1.26 V for wrought Mg-2%Zn alloy and Mg-2%Zn/anodized Al-7075 respectively. The corrosion current density (i_{corr}), of the multilayered composite exhibited lower i_{corr} valves and which was 66.6% lower than that of the rolled Mg-2%Zn alloy. Corrosion rate decreases from 2.38 mm/y for the as-rolled Mg-2%Zn alloy to 0.69 mm/y for Mg-2%Zn/anodized Al-7075 multilayered composite, which demonstrates that the corrosion resistance of the multilayered composite can be significantly enhanced due to combination of ultra-fine grains, formation β phases (Al₁₂Mg₁₇ and AlMg₄Zn₁₁) along with alumina (Al₂O₃) [Argade G R et al (2012), Ralston K D and Birbilis N (2010)].

CONCLUSIONS

1. Mg-2%Zn/anodized Al-7075 multilayered composite was processed by ARB at 350 °C up to 4-passes successfully and exhibited 1.2 times lighter weight as compared to Al-7075 alloy.
2. TEM analysis showed an average grain size of 1 μm and 0.7 μm with high angle misorientation.
3. Microhardness and tensile strength of the multilayered composites increases significantly due to strain hardening and grain refinement during ARB process. Microhardness of the 4-pass ARB processed Mg-2%Zn layer and anodized Al-7075 layer increases ~56% and ~ 61%, in comparison with its counterpart rolled Mg-2%Zn alloy and anodized Al-7075 alloy respectively. The yield strength, ultimate tensile strength and elongation to failure found to be 233.6 MPa, 319.0 MPa and 6.4%, which is 2.11 times,

- 1.85 times and 1.52 times as compared to as-rolled Mg-2%Zn alloy.
4. Potentiodynamic polarization study showed that Mg-2%Zn/anodized Al-7075 multilayered composite exhibited better corrosion resistance as compared to wrought Mg-2%Zn alloy.

REFERENCES

- [1] Argade, G R et al (2012), Effects of grain size on the corrosion resistance of wrought magnesium alloys containing neodymium, *Corros. Sci.*, Vol.58, pp.145-151.
- [2] Avedesian, M M and Baker H (1999), *Mg and Mg Alloys ASM Speciality Handbook.*, ASM International, Ohio, pp. 38-40.
- [3] Hidalgo-Manrique, A et al (2016), Influence of the Accumulative Roll Bonding Process Severity on the Microstructure and Super plastic Behaviour of 7075 Al Alloy, *Journal of Materials Science & Technology*, Vol. 32, No.8, pp.774-782.
- [4] Jamaati, R et al (2010), High-strength and highly-uniform composite produced by anodizing and accumulative roll bonding processes, *Materials and Design*, Vol.31, pp.4816-4822.
- [5] Kaufman, J G, and Rooy, E L (2004), *Aluminum Alloy Castings Properties Processes, and Applications*, ASM International, USA.
- [6] Kojima, Y (2000) *Advanced Mg Technology Handbook*, Kallos Publishing Co, Ltd., Tokyo.
- [7] Luo, A A (2003), Recent magnesium alloy development for automotive power train application, *Mater. Sci. Forum*, Vol. 419-422, pp. 57-66.
- [8] Ralston, K D, and Birbilis, N (2010), Effect of grain size on corrosion, A Review, *Corrosion Sci.*, Vol. 66, pp. 075005-13.
- [9] Starke, E A, and Jr, Staley J T (1996) Application of modern aluminum alloys to aircraft, *Prog. Aerospace Sci.*, Vol. 32, pp. 131-72.
- [10] Tsuji, N et al (2003), Techniques to Produce Bulk Ultrafine Grained Materials, *Adv. Eng. Mater.*, Vol. 5, pp. 338-344.
- [11] Wu, K et al (2010), Microstructure and mechanical properties of the Mg/Al laminated composite fabricated by accumulative roll bonding (ARB), *Materials Science and Engineering A*, Vol. 527, pp. 3073-3078.

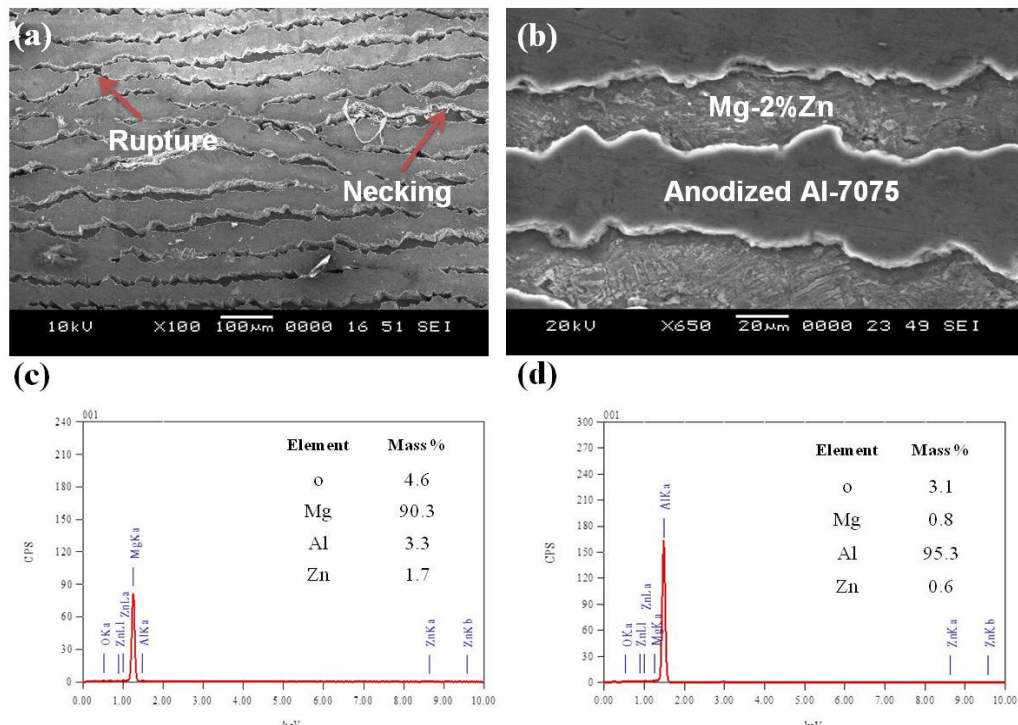


Fig. 1. SEM micrographs of the ARB processed Mg-2%Zn/anodized Al-7075 multilayered composite (a) four pass multilayered composite (b) magnified image of different layers (c) EDS of the Mg-2%Zn layer (d) anodized Al-7075 layer.

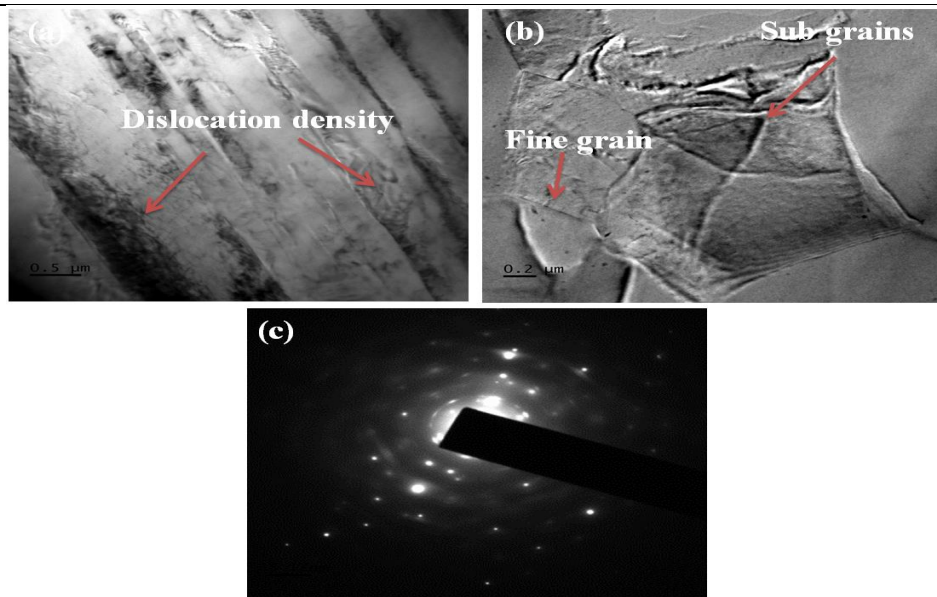


Fig. 2. TEM micrographs and SAED patterns of the four pass ARB Mg-2%Zn/anodized Al-7075 multilayered composite.

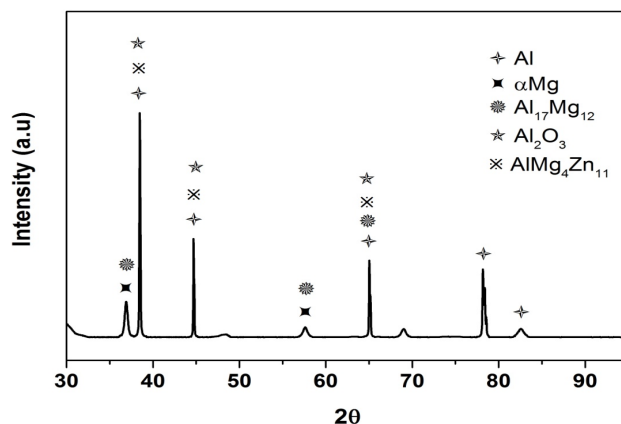


Fig. 3. XRD patterns along the cross section of accumulative roll bonded multilayered composite.

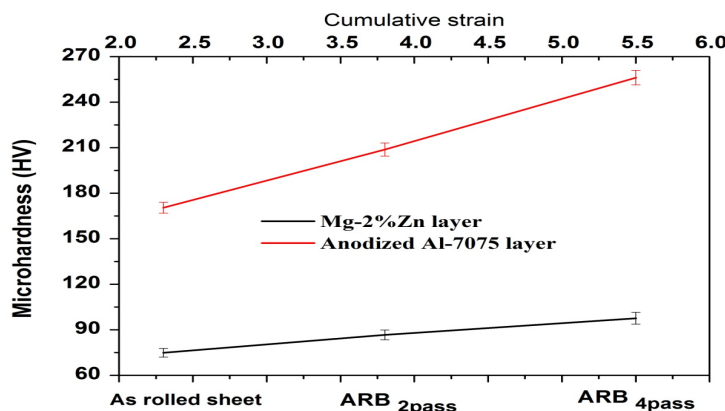


Fig. 4. Microhardness variation of Mg-2%Zn and Al-7075 layers during different passes of the ARB processed Mg-2%Zn/Al-7075 multilayered composite.

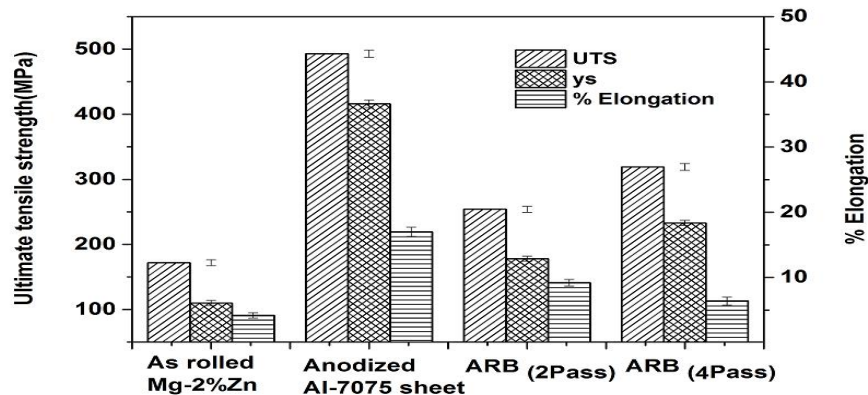


Fig. 5. UTS, YS and percentage elongation variations of as rolled Mg-2%Zn and Al-7075 alloy and different passes of the ARB process of Mg-2%Zn/Al-7075 multilayered composite.

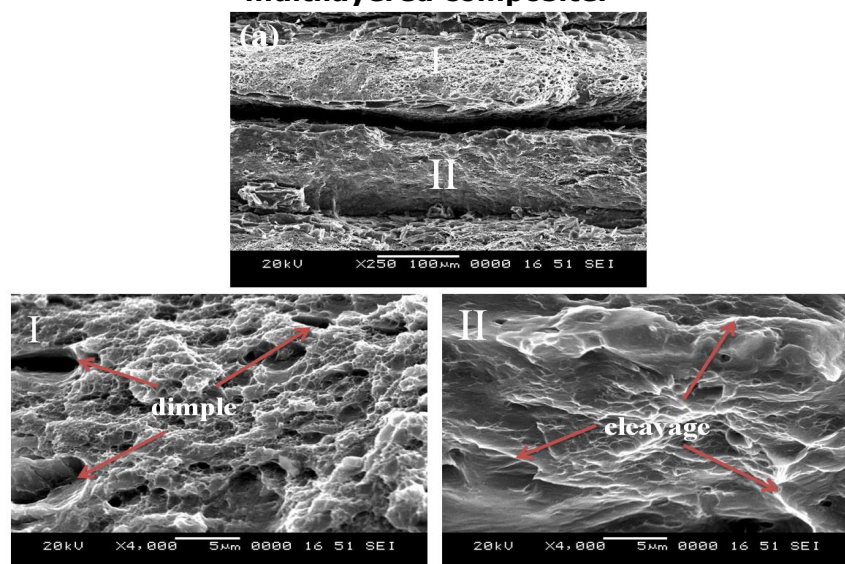


Fig. 6 (a). SEM micrographs of the fractured 4-pass ARB processed Mg-2%Zn/anodized Al-7075 multilayered composite (I) enlarged micrographs of the Mg-2%Zn layer (II) anodized Al-7075 layer.

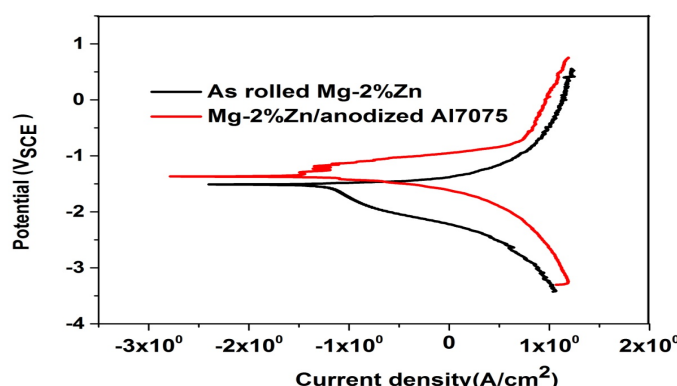


Fig. 7. Potentiodynamic polarization curves of the Mg-2%Zn and Mg-2% Zn/anodized Al-7075.

Effect of Spark Timings on Combustion and Emissions Characteristics of 4 Stroke - 4 Cylinder S. I. Engine using Hydrogen at 1500 rpm.

Parashuram R. Chitragar¹, Thirumoorthy² and G.N.Kumar³

¹ Department of Mechanical Engineering, National Institute of Technology Karnataka, Surathkal, Mangalore 575025, India. email:prchitragar@rediffmail.com

² Department of Mechanical Engineering, National Institute of Technology Karnataka, Surathkal, Mangalore 575025, India. email:thiru0593@gmail.com

³ Department of Mechanical Engineering, National Institute of Technology Karnataka, Surathkal, Mangalore 575025, India. email:gnkumar33@gmail.com

ABSTRACT: Use of automotive and limited resources of conventional fuel combined with alarming trend of environmental pollution and its control have led many researchers to look up alternative fuels for automobile use. Hydrogen found to be favourable substitute fuels due to its compatible properties and emissions.

This paper describes effect of 3 spark timings on performance parameters of four cylinder SI engine for 1500 rpm speed at wide open throttle condition (WOT) using neat hydrogen. Experiments were carried out adopting electronically controlled hydrogen induction system on existing MPFI engine. Experimental results revealed improvement in cylinder pressure, brake thermal efficiency as spark timings increased. Exhaust emissions like CO, HC were reduced and NO_x was increased for all spark timings.

Keywords: Alternative fuel, Hydrogen, Spark timing, Combustion, Emission.

INTRODUCTION

The uncontrollable conventional fuel prices and uncertain reserves along with their environmental pollution problems are strong motives for research of alternative fuel sources in case of transportations. In recent years, hydrogen (H₂) has gained much attention as a feasible future fuel for the transportation vehicles. Hydrogen has infinite source potential, noble combustion and clean burning characteristics. (Karim, 2003; Schefer et al, 2007; Heywood, 1988).

It has been demonstrated by several successful experiments that hydrogen in many respects is much better than existing automotive fuels. (Verhelst, 2014; Verhelst and Wallner, 2009; White et al. 2006; Guo et al. 1999, Tang et al. 2014). D.Andrea et al. (2004) examined the effect of equivalence ratios and various engine speeds on combustion of a hydrogen blended gasoline engine. They found that

the combustion duration decreases and the nitrogen emission increases with the increase of hydrogen blending fraction. Mariani et al. (2013) studied the combustion performances of hydrogen blended SI engine and found that the addition of hydrogen in the fuel-air mixtures resulted in the 16% reduction of CO₂ emission. Soberanis and Fernandez (2010) reported that the emissions of air-hydrogen mixture consist mainly of CO₂ and NO_x.

Kahraman et al. (2007) found that hydrogen blended gasoline engine emits lower amount of CO and HC emissions than the original gasoline engine. Ji et al. (2010) found that the indicated mean effective pressure (IMEP) first increased and then decreased with the increase of spark advance; maximum indicated thermal efficiency, and reduction in HC and NO_x emissions.

6th International Engineering Symposium - IES 2017

March 1-3, 2017, Kumamoto University, Japan

Huang et al. (2007) investigated combustion characteristics of spark-ignited engine fuelled with natural gas-hydrogen blends under various spark timings. The results showed that the spark timing has significant influence on engine performance, combustion and emissions. Brake mean effective pressure and the effective thermal efficiency increase and combustion durations decrease with the increase of hydrogen fraction in natural gas. Exhaust NO_x concentration increases with advancing the spark timing.

The exhaustive information is available in the area of utilisation of hydrogen as a fuel. However, only limited studies were related to hydrogen operated multi cylinder SI engines with different spark timings. On account of this, the experiments have been conducted to investigate the effect of spark timings on a modified four cylinder 4-stroke S.I. engine at wide open throttle condition (WOT) with 1500 engine speed.

II. EXPERIMENTAL PROCEDURE AND METHODOLOGY

A. Experimental Setup

The engine used for the experiment is four strokes, four cylinder Multi Point Fuel Injection (MPFI) SI engine. Detailed specification of the engine is shown in the Table 1 and schematic diagram of the experimental set up is shown in Fig. 1. The engine was modified to operate with bi-fuel (Hydrogen, and gasoline) by adopting ECU assisted port fuel injection system keeping its original gasoline line unchanged. Engine was equipped with instruments for measuring combustion and performance parameters which were interfaced to computer through NI based USB-6210 data acquisition system and "IC Engine Soft" for combustion analysis.

B. Experimental Procedure

All the trials were conducted at a speed of 1500 rpm and three spark timings (2, 5 & 8bTDC). At specified engine speed, experiments were conducted initially with

gasoline and thereafter, with hydrogen. For all testing conditions, 100 consecutive cycles were recorded and analysed through "IC engine soft", to obtain results. Exhaust emissions CO, HC and NO_x were recorded with the help of AVL digas 444 exhaust analyser. Photographic view of the experimental set up is shown in Fig. 2.

The compressed hydrogen gas is used for test. The flame trap was used as a safety measure and was situated between the hydrogen cylinder and engine.

Abnormal combustion such as knock, backfire and pre-ignition of hydrogen fuel were taken care by established engine control parameters and leak test was carried out by soap bubble method and precaution measures were taken to avoid any mishap out of hydrogen use in SI engine.

III. RESULTS AND DISCUSSION

A. Performance Characteristics:

1. Pressure-Crank angle: The pressure-crank angle diagram for gasoline and hydrogen is shown in Fig. 3. As depicted in figure, the cylinder pressure is drastically raised with pure hydrogen in comparison with gasoline. This is due to high adiabatic temperature and high flame speed of hydrogen [Ji. et al, 2010]. The maximum pressure of 38 bars is attained by hydrogen for 8 bTDC which is 22.5% higher than gasoline. Also peak pressure of hydrogen was shifted towards the TDC position in comparison with its counter fuel.

2. Brake Power and Brake Thermal Efficiency

The Fig. 4 shows the variations of brake power (BP) and brake thermal efficiency (BTE). From the graph it can be revealed that, as the spark timing increased BP and BTE is increased due to the fact that hydrogen has a much wider flammable range, a much faster flame propagation speed and a much higher adiabatic flame temperature than that of gasoline, which helps in accelerating the combustion process. But BP of hydrogen is reduced

6th International Engineering Symposium - IES 2017

March 1-3, 2017, Kumamoto University, Japan

compared to gasoline due to non-sufficient availability of air [Fontana and Galloni, 2010; Shiva Prasad et al., 2015]. The maximum value of brake thermal efficiency of 28% is achieved by the engine for hydrogen at 8 bTDC condition.

3. Brake Specific Fuel Consumption (BSFC)

Fig. 5 indicates the variation of BSFC for hydrogen and gasoline at 1500 rpm speed with three spark timings. Figure indicates that BSFC is much lower for hydrogen than gasoline at all spark timings and at WOT condition.

B. Emission characteristics

Fig. 6 depicts exhaust emissions for hydrogen and gasoline. It is well known fact that when hydrogen is used the emissions decreases. This was confirmed from the figure that toxic emissions CO, HC were decreased due to non-carbon content and incomplete combustion respectively whereas NO_x increased due to high temperature production by hydrogen than gasoline [Kahraman et al. 2007]. But CO, HC and NO_x emissions were increased as spark timing is increased. [K.V Shivaprasad et al. 2015, Subramanian et al., 2007]

CONCLUSIONS

- Cylinder pressure for hydrogen is improved as spark timing is increases and the maximum pressure of 38 bars is achieved for 8 bTDC condition. Peak pressure of hydrogen was shifted towards the TDC position.
- Brake power and brake thermal efficiency increased as the spark timing was increased; but brake power reduced for hydrogen operation.
- The brake specific fuel consumption is reduced as the spark timing is increased.
- CO and HC emission decreased and NO_x emission increased with hydrogen fuel but all emissions were increased with increase in spark timings.

REFERENCES

- [1] Ciniviz, Murat, and Hüseyin Köse, (2012), The use of hydrogen in internal combustion engine: a review. *International Journal of Automotive Engineering and Technologies*, 1(1), pp. 1-15.
- [2] D'Andrea, T P et al (2004), The addition of hydrogen to a gasoline-fuelled SI engine. *International Journal of Hydrogen Energy* 29, no. 14, pp. 1541-1552.
- [3] Guo, L S et al (1999), A hydrogen injection system with solenoid valves for a four-cylinder hydrogen-fuelled engine. *International Journal of Hydrogen Energy* 24, no. 4, pp. 377-382.
- [4] Heywood, John B. *Internal combustion engine fundamentals*. Vol. 930. New York: McGraw-hill, 1988.
- [5] Huang et al (2007), Combustion characteristics of a direct-injection engine fueled with natural gas-hydrogen blends under different ignition timings. *Fuel* 86, no. 3, pp. 381-387.
- [6] Ji, et al (2010), Effect of spark timing on the performance of a hybrid hydrogen-gasoline engine at lean conditions. *International Journal of Hydrogen Energy* 35, no. 5, pp. 2203-2212.
- [7] Ji, et al (2010), Combustion and emissions characteristics of a hybrid hydrogen-gasoline engine under various loads and lean conditions. *International journal of hydrogen energy* 35, no. 11, pp. 5714-5722.
- [8] K.V.Shivaprasad et al (2015), Experimental investigation of variations of spark timing on hydrogen blended gasoline operated SI engine. *Energy Technology*, 3(12), pp. 1174-1182.
- [9] Kahraman et al (2007), An experimental study on performance and emission characteristics of a hydrogen fuelled spark ignition engine. *International Journal of Hydrogen Energy* 32, no. 12, pp. 2066-2072.
- [10] Karim, Ghazi A (2003), Hydrogen as a spark ignition engine fuel. *International Journal of Hydrogen Energy* 28, no. 5, pp. 569-577.
- [11] Mariani, et al (2013), Combustion analysis of a spark ignition ic engine fuelled alternatively with natural gas and hydrogen-natural gas blends. *International Journal of Hydrogen Energy* 38, no. 3, pp. 1616-1623.
- [12] Porpatham E et al (2007), Effect of hydrogen addition on the performance of a biogas fuelled spark ignition engine. *International Journal of Hydrogen Energy* 2007; 32(12), pp. 2057-65.
- [13] Sandhu S S, (2013), Improvement in performance and emission characteristics of a single cylinder SI engine operated on blends of CNG and hydrogen. In *Proceedings of World Academy of Science, Engineering and Technology*, No. 79, pp. 698.
- [14] Schefer, et al (2008), Lean hydrogen combustion. *Lean Combustion Technology and Control*.
- [15] Shivaprasad, K V et al (2016), Influence of spark timing on the performance and emission characteristics of gasoline-hydrogen-blended high-speed spark-ignition engine. *International Journal of Ambient Energy*, pp. 1-8.
- [16] Soberanis, et al (2010), A review on the technical adaptations for internal combustion engines to operate with gas/hydrogen mixtures. *International journal of hydrogen energy* 35, no. 21, pp. 12134-12140.
- [17] Subramanian, V J et al (2007), Effect of water injection and spark timing on the nitric oxide emission and combustion parameters of a hydrogen

6th International Engineering Symposium - IES 2017

March 1-3, 2017, Kumamoto University, Japan

fuelled spark ignition engine. International Journal of Hydrogen Energy 32, no. 9, pp. 1159-1173.

[18] Tang, et al (2014), Progress in combustion investigations of hydrogen enriched hydrocarbons. Renewable and Sustainable Energy Reviews 30, pp. 195-216.

[19] Verhelst, Sebastian (2014), Recent progress in the use of hydrogen as a fuel for internal combustion engines. International Journal of Hydrogen Energy 39, no. 2, pp. 1071-1085.

[20] Verhelst, et al (2009), Hydrogen-fueled internal combustion engines. Progress in Energy and Combustion Science 35, no. 6, pp. 490-527.

[21] White, C M et al (2006), The hydrogen-fueled internal combustion engine: a technical review. International Journal of Hydrogen Energy 31, no. 10, pp. 1292-1305.



Table1. Engine specifications

Item	Value
Engine Make	Maruti Suzuki India Ltd.
Engine Type /Fuel	Zen (MPFI), Petrol
Cylinder and stroke	4
Compression ratio	9.4:1
Power and Torque	44.5kW @ 6000 rpm, 78.5Nm @ 4500 rpm
Stroke and Bore	61 and 72mm
Capacity	993 cc
Cooling	Water cooled

Fig.2 Photographic view of experimental set up.

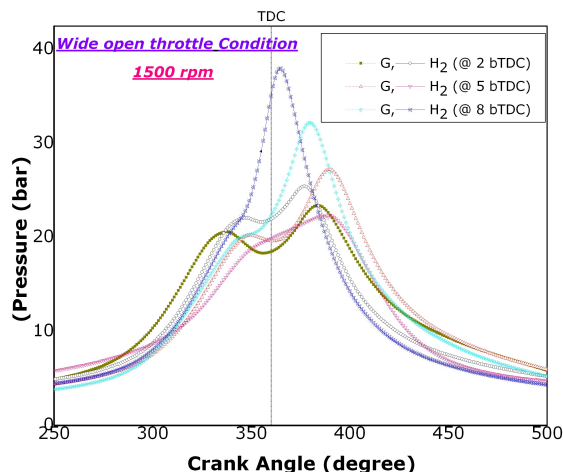


Fig.3 P-Theta for gasoline and hydrogen.

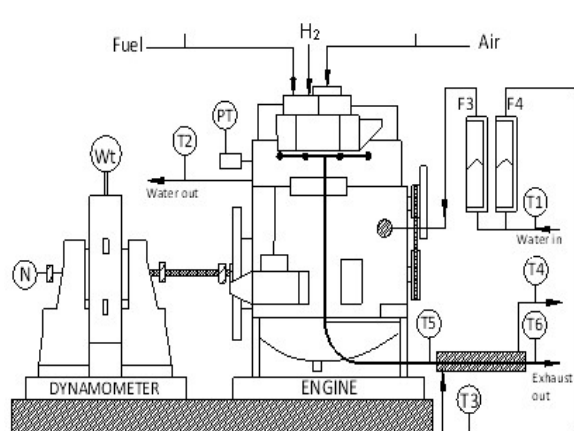


Fig.1 Schematic diagram of the experimental set up.

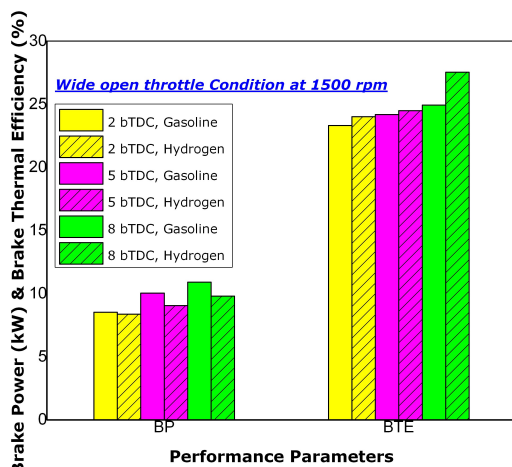


Fig.4 Brake power, brake thermal efficiency for gasoline and hydrogen.

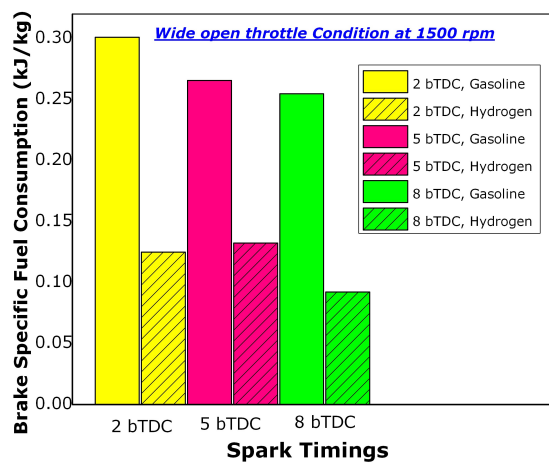


Fig.5 Brake Specific Fuel Consumption for gasoline and hydrogen.

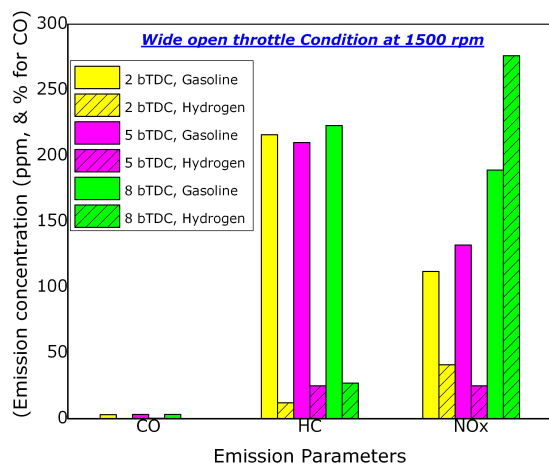


Fig.6 Exhaust emissions for gasoline and hydrogen

High Temperature Erosion Behaviour of Plasma Sprayed NiCrAlY-25WC-Co/Cenospheres Composite Coating

Mahantayya Mathapati¹, Ramesh M R² and Mrityunjay Doddamani²

- ¹ Department of Mechanical Engineering, National Institute of Technology Karnataka, Surathkal, Mangalore 575025, India. email:mahantkm.me14f09@nitk.edu.in
² Department of Mechanical Engineering, National Institute of Technology Karnataka, Surathkal, Mangalore 575025, India. email:rameshmr@nitk.edu.in, mrdoddamani@nitk.edu.in

ABSTRACT: Erosive behaviour of plasma sprayed NiCrAlY-25WC-Co (70%) + Cenospheres (30%) coating deposited on MDN 321 steel is dealt in the present work. Solid particle erosion tests are conducted on both substrate and coatings at 600°C. Angular alumina particles are used as erodent with velocity of 30 m/s impacting at an angle of 30 and 90°. Erosion volume loss is quantified using 3D optical non-contact profilometer. Eroded surface morphology of the coatings are analyzed using scanning electron microscope. Erosion volume loss is higher at 90° impact angle for both coating and substrate. Coating showed better erosion resistance than substrate at 30° impact angle. The developed coating can act as effective thermal barriers in turbine blade applications.

Keywords: Plasma spray, Cenospheres, Erosion, Turbine blade.

1 INTRODUCTION

Impingement of solid particles on a surface leading to the removal of a material is known as Erosion. It becomes trivial in components working at higher temperature like gas and steam turbines, jet engine parts, coal-fired power plant boiler tubes etc [Ramesh M. R. et al. (2010)]. Alloys used in these components provide good mechanical strength. Nevertheless, they lack better erosion, wear and corrosion resistance. [Mishra S. B. et al. (2013)]. Such degradation can be overcome by protective coatings using Thermal spray coating. Such techniques like high velocity oxy fuel (HVOF) and plasma spray are extensively used for better erosion, wear and corrosion resistive applications [Manjunatha M. et al. (2014), Rana N. et al. (2015), Somasundaram B. et al. (2014)] Like NiCrAlY coatings. [Chen S. F. et al. (2014), Mishra S. B. et al. (2006)]. However

NiCrAlY coatings exhibits poor wear resistance property and this can be overcome by incorporating carbides and oxides in the coating system [Bolelli G. et al. (2015)].

Thermal sprayed WC-Co and Cr₃C₂-NiCr coatings are widely used for high temperature wear application [Geng Z. et al. (2015), Yang G. J. et al. (2008)]. WC-Co possesses higher hardness, better elasticity, chemical inertness and lower frictional values. These properties improves the wear resistance capacity of WC-Co coatings [Jafari M. et al. (2013)]. Coating materials such as NiCrAlY and WC-Co are relatively expensive. Flyash, an industrial waste has great potential to be used as a coating material owing to presence of oxides such as SiO₂ and Al₂O₃, improving wear, erosion, corrosion and high temperature stability [Behera A. (2015), Muhammad M. M. et al. (2014), Sidhu B. S. et al. (2007)]. During last decade, various researchers developed the

6th International Engineering Symposium - IES 2017

March 1-3, 2017, Kumamoto University, Japan

plasma sprayed flyash composite coatings revealing superior bond strength, hardness and oxidation resistance [Mishra S. C. et al. (1999), Mishra S. C. et al. (2006)]. From the literature it is observed that systematic study of flyash composite coatings for high temperature wear applications are seldom available.

In the present work NiCrAlY+WC-Co+Flyash Cenospheres coating is deposited on MDN 321 steel substrate by using atmospheric plasma spray process. The erosion behavior of coating is studied at 600 °C under the impingement angles of 30° and 90°. Volume loss method was used to estimate erosion loss and scanning electron microscopy was used to elucidate erosion mechanism.

2 MATERIALS AND METHODS

2.1 Materials

MDN 321 steel procured from Mishra Dhatu Nigam Limited Hyderabad, India is used as a substrate. Chemical composition of the substrate is (wt. %): 0.10 C, 1.46 Mn, 0.55 Si, 0.005 S, 0.013 P, 18.13 Cr, 10.36 Ni, 0.62 Ti and balance Fe. Substrate was cut into the dimension of 25 × 25 × 4 mm before plasma spraying.

Commercial available flyash cenospheres (average particle size 60-65µm), agglomerated and sintered NiCrAlY and WC-Co (particle size 15-45 µm), available in powder form are used as a coating materials for plasma spraying. These powders are blended mechanically with mass fraction of 70% NiCrAlY-25WC-Co and 30% Flyash cenospheres. Blended powder morphology is presented in Fig. 1

2.2 Coating Deposition

Plasma spraying is carried out by METCO USA 3MB equipment at Spraymet Surface Technologies Private Limited, Bangalore, India. Before coating deposition substrates were degreased and roughened by grit blasting using alumina powder of having average particle diameter of 150 µm size. After grit blasting substrates are cleaned in acetone to remove the dust from the surface. Industrial optimized parameters were chosen as spray parameters (Table 1). Scanning electron microscope (SEM) is

used to examine the microstructure of the coating. Coating thickness was measured by the SEM images taken along the cross section.

2.3 Erosion Studies

Erosion test are carried out as per ASTM G76-13 standard using solid particle air jet erosion tester, TR-471-800 (Ducom instruments private limited, Bangalore, India) on substrate and coating using alumina particle erodent. Erodent is fed to the particle feeder with controlled rate to mix with dry high velocity air from the compressor. The mixture is then passed through the converging nozzle to impact the sample maintained at predefined temperature. The impact angle is varied by changing the orientation of the sample surface with reference to the particles stream. Erosion test conditions are presented in

Table 2. Samples are cleaned with acetone, dried and loaded in machine to reach the required test temperature. After every test the samples are cleaned in acetone to remove the erodent particles embedded on the surface and dried thereafter. 3D optical non-contact profilometer from Zeta instruments is used to quantify volume loss.

3 RESULTS AND DISCUSSION

3.1 Microstructural analysis of coating

The thickness of the coating measured from SEM image (Fig. 2) along the cross section (4 × 12 mm) of the sample is in the range of 400-450 µm. Lamellar dense

6th International Engineering Symposium - IES 2017

March 1-3, 2017, Kumamoto University, Japan

packed structure of NiCrAlY-WC-Co has been formed with even cenosphere particles uniformly distributed resembling dark grey colour. Some pores were also observed in the microstructure.

3.2 Erosion study

3D profile of eroded surface of substrate at 600 °C and impact angles of 30° and 90° are shown in Fig. 3.

Fig. 4 presents erosion volume loss of the substrate and coating. Erosion volume loss of the substrate is observed to be lower (4.16 mm³) at 30° impact angle and higher (4.73 mm³) at 90° impact angle. This difference being negligible substrate behaviour is neither ductile nor brittle.

3D profiles of eroded surface of substrate at 600 °C and impact angle 30° and 90° are shown in Fig. 5. Erosion volume loss of the coating at 30° impact angle was less (1.18 mm³) compared to 90° impact angle (6.27 mm³). Implying coating erosion in brittle mode. Coating showed better erosion resistance at 30° impact angle which is 3.5 times higher compared to substrate. Better erosion resistance of the coating might be due to the formation of oxide layers like SiO₂, Al₂O₃ and NiO at high temperature. As the erodent particles slides on the surface of the coating at 30° impact angle, the formed oxide layers resists the erosion loss. At normal impact angle substrate showed higher resistance than the coating due to the brittle nature of the coating.

3.3 Erosion Mechanism

Fig. 6 shows the morphology of the eroded surface of coating at 600°C with impact angle of 30°. Material is removed by the erodent particles by plastics deformation. Grooves and ploughs were formed from the plastic deformation suggesting the ductile behaviour of the coating. At 30° impact angle hard erodent particles slides on the surface and are in contact with the surface for longer time thus removing material by ploughing action.

Fig. 7 shows the morphology of the eroded surface of coating at 90° impact angle. Craters, lips and cracks formed by the deformation of coating. Initially cracks are generated at the interface of matrix and

hard particles such as carbides and oxides. One-third interface area is bonded together in plasma spray coatings while remaining area acts as interlamellar gaps which can be considered as pre-existing cracks. Ji G. C. et al. (2007). With progress of erosion by erodent particles cracks are developed and results craters.

4 CONCLUSIONS

The following conclusions are deduced from this study:

- NiCrAlY+WC-Co+Cenospheres powders are successfully coated on MDN 321 steel by plasma spray technique.
- Microstructure of the coating reveals that coating is uniform and WC-Co, cenosphere particles are dispersed well in NiCrAlY matrix.
- Both coating and substrate gives higher erosion volume loss at 90° impact angle and coating showed better erosion resistance at 30° compared to substrate.
- Coating exhibits brittle erosion mechanism where material was removed by crack formation and chipping.

ACKNOWLEDGEMENTS

The authors are grateful to Prof. Ramesh Singh, IIT Bombay, India, for providing the optical profile meter facility. The authors wish to thank Spraymet Surface technologies Pvt Ltd, Bangalore, India, for providing the facility of the plasma spray coating.

REFERENCES

- [1] Behera, A (2015), Air jet erosion test on plasma sprayed surface by varying erodent impingement pressure and impingement angle, In IOP Conference Series: Materials Science and Engineering, Vol. 75, No. 1, pp. 012004.
- [2] Bolelli, G et al (2015), Tribology of NiCrAlY+Al₂O₃ composite coatings by plasma spraying with hybrid feeding of dry powder+suspension, Wear, pp. 69-85.
- [3] Chen, S F et al (2014), Microstructure and Properties of HVOF-Sprayed NiCrAlY Coatings Modified by Rare Earth, Journal of Thermal Spray Technology, Vol. 23(5), pp. 809-817.
- [4] Geng, Z et al (2015), Wear behaviour of WC-Co HVOF coatings at different temperatures in air and argon, Wear, Vol. 330, pp. 348-353.
- [5] Jafari, M et al (2013), Microstructural and mechanical characterizations of a novel HVOF-sprayed WC-Co coating deposited from electroless

6th International Engineering Symposium - IES 2017

March 1-3, 2017, Kumamoto University, Japan

- Ni-P coated WC-12Co powders, Materials Science and Engineering: A, Vol. 578, pp. 46-53.
- [6] Ji, G C et al (2007), Erosion performance of HVOF-sprayed Cr₃C₂-NiCr coatings, Journal of Thermal Spray Technology, Vol. 16(4), pp. 557-565.
- [7] Manjunatha, M et al (2014), Investigation of HVOF Thermal Sprayed Cr₃C₂-NiCr cermet carbide Coatings on Erosive Performance of AISI 316 Molybdenum Steel, Procedia Material Science, Vol. 5, pp. 622-629
- [8] Mishra, S B et al (2006), Erosion performance of coatings produced by shrouded plasma spray process on a Co-based superalloy, Surface and Coatings Technology, Vol. 201(3), pp. 1477-1487.
- [9] Mishra, S B et al (2008), Characterisation and erosion behaviour of NiCrAlY coating produced by plasma spray method on two different Ni-based superalloys, Materials Letters, Vol. 62(12), pp. 1999-2002.
- [10] Mishra, S B et al (2013), Erosion-corrosion performance of NiCrAlY coating produced by plasma spray process in a coal-fired thermal power plant, Surface and Coatings Technology, Vol. 216, pp. 23-34.
- [11] Mishra, S C et al (1999), Fly ash as a coating material for plasma spray coatings.
- [12] Mishra, S C et al (2000), Plasma spray coating of fly ash pre-mixed with aluminium powder deposited on metal substrates, Journal of Materials Processing Technology, Vol. 102(1), pp. 9-13.
- [13] Mishra, S C et al (2006), Plasma Spray Coating of Fly Ash on Metals for Tribological Application.
- [14] Muhammad, M M et al (2014), Effect of plasma spray parameters on porosity of fly ash deposited coatings. In THE 2014 UKM FST POSTGRADUATE COLLOQUIUM: Proceedings of the Universiti Kebangsaan Malaysia, Vol. 1614, No. 1, pp. 116-121.
- [15] Ramesh, M R et al (2010), Solid particle erosion of HVOF sprayed WC-Co/NiCrFeSiB coatings, Wear, Vol. 269(3), pp. 197-205.
- [16] Rana, N et al (2015), High-Temperature Oxidation and Hot Corrosion Studies on NiCrAlY Coatings Deposited by Flame-Spray Technique, Journal of Thermal Spray Technology, Vol. 24(5), pp. 769-777.
- [17] Sidhu, B S et al (2007), Wear and oxidation behaviour of shrouded plasma sprayed fly ash coatings, Tribology international, vol. 40(5), and pp. 800-808.
- [18] Somasundaram, B et al (2014), Evaluation of Cyclic Oxidation and Hot Corrosion Behavior of HVOF-Sprayed WC-Co/NiCrAlY Coating, Journal of Thermal Spray Technology, Vol. 23(6), pp. 1000-1008.
- [19] Yang, G J et al (2008), High-temperature erosion of HVOF sprayed Cr₃C₂-NiCr coating and mild steel for boiler tubes, Journal of Thermal Spray Technology, Vol. 17(5-6), pp. 782-787.

Table 1 Plasma Spray Process Parameters

Argon	Pressure	7.5 bar
	Flow	150 lpm
Hydrogen	Pressure	3.5 bar
	flow	6 lpm

Current	1350 amps
Voltage	60-70 volts
Powder feed	120 g/min
Stand off distance	100-125 mm

Table 2 Air Jet Erosion Test Parameters

Erodent material	Alumina
Erodent average size	50 µm
Particle velocity	30 m/s
Erodent feed rate	2 g/min
Impact angle	30° and 90°
Temperature	600°C
Test time	15 min
Standoff distance	10 mm
Nozzle diameter	1.5 mm

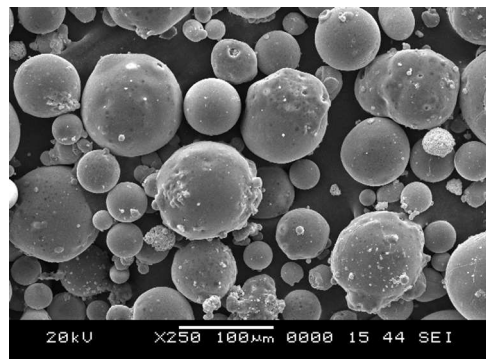


Fig. 1 Coating Powder Morphology

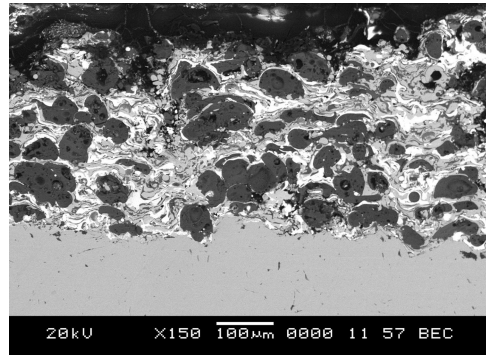
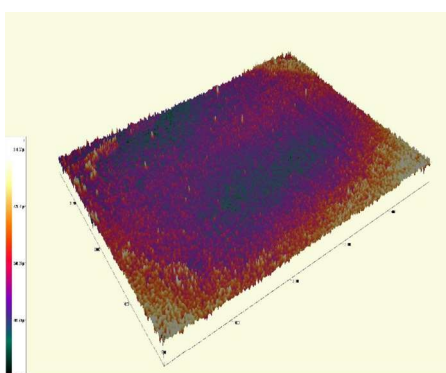
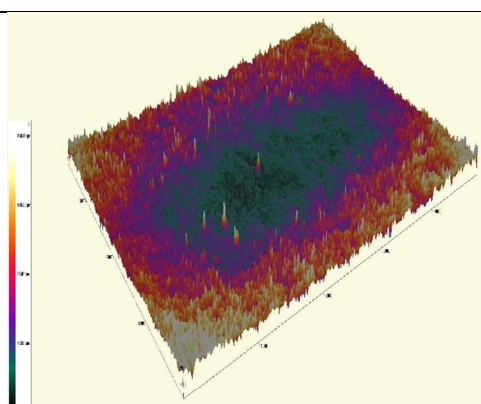


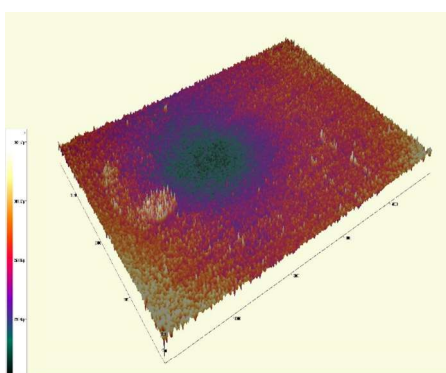
Fig. 2 Cross Sectional SEM Images of the Coating



(a)

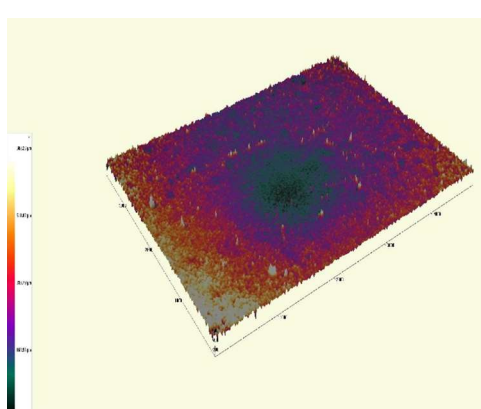


(a)



(b)

Fig. 3 3-D profile of eroded surface of substrate at 600°C and impact angle (a) 30° and (b) 90°



(b)

Fig. 5 3-D profile of eroded surface of coating at 600°C and impact angle (a) 30° and (b) 90°

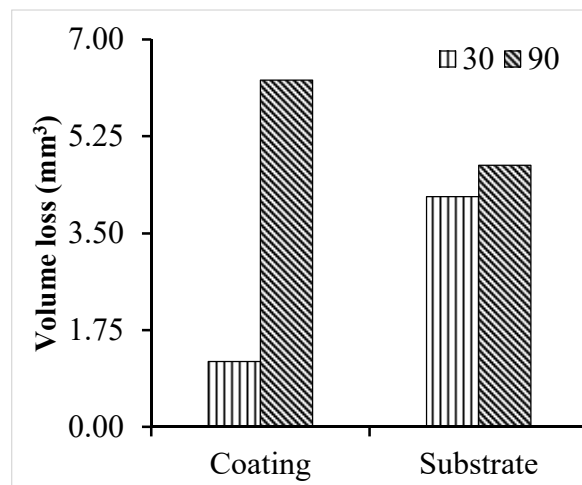


Fig. 4 Erosion volume loss of the coating and substrate at 30° and 90° impact angle

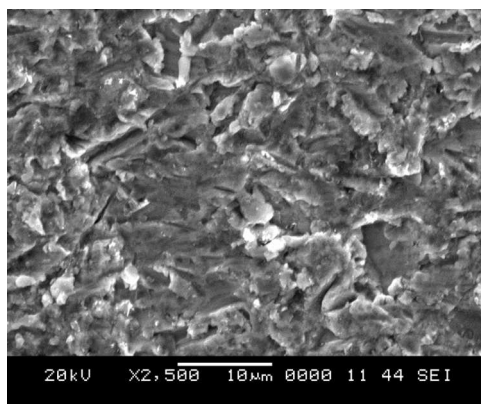


Fig. 6 SEM images of eroded surface of coating at 30° impact angle

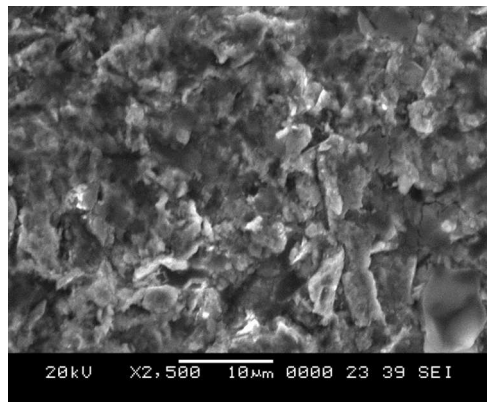


Fig. 7 SEM images of eroded surface of coating at 90° impact angle

SMALL SCALE BIOMASS GASIFICATION CHALLENGES FOR POWER GENERATION IN RURAL AREA, A REVIEW

Priyambodo Nur Ardi Nugroho^{1,2}, and Shuichi Torii¹

1 Department of Advanced Mechanical System Engineering, Kumamoto University, Kurokami, 2-39-1, Kumamoto 860-8555, Japan.

2 Politeknik Perkapalan Negeri Surabaya, Jl. Teknik Kimia, Kampus ITS Sukolilo, Surabaya 60111, Indonesia. Email : pr1y4mb0d0@gmail.com

ABSTRACT:

Nowadays, the world highly depends on the fossil fuels like coal, oil and natural gas for its energy source. Yet within the next decades, fossil fuels will be depleted. Furthermore, environmental issues such as greenhouse emission enforced the government to switch to renewable energy. Biomass is one of the promising renewable energy due to its unique characteristics and availability. The fact, however, utilization of biomass as a source of energy, particularly in small scale for a rural area, is very limited. Some challenges in converting biomass for power generation will be stressed in this review. As one of the most challenging steps, gasification of biomass will be highlighted for investigation. In accordance with the latest reports, an excellent gasification method could produce a specific gas composition suitable for power generation in the rural area.

Keywords: biomass, challenges, gasification, rural area, small scale.

INTRODUCTION

Energy has become one of the most fundamental needs for the human. Everyday energy is used for the industrial sector such as agriculture, mining, manufacturing, construction, transportation, housing like heating, cooling, lighting, and many other appliances. Based on IEA (2014), the world still relies on fossil fuel as its main energy source. Oil, coal, and natural gas remain on the top of energy source, followed by renewable energy like biomass, geothermal energy, hydropower, solar energy, tidal and wave power, and also wind power.

Fossil fuels need more than a million years to be formed. Once being used, it could not be filled anymore. It is estimated that the world will run out of fossil fuels within the next 50-120 years. Environmental issues caused by the used of fossil fuel such as carbon dioxide (CO_2) emission, that will form the layer in our atmosphere and prevent heat emitted by the earth. As a result, the temperature will

be increased and climate will be changed. Climate change could lead to flood, drought, famine, or spread of disease through the world. The need of renewable and sustainable energy is critical.

According to Basu (2013), human is very familiar with energy conversion from biomass, since it is as old as the history of civilization. Even some of its process already began from the early days of vegetation on the earth. Forest burnt because of the lightning is an illustration of flaming pyrolysis. Decomposition of biomass with methane gas formation and combustion could be seen in the blue flame in the swamp. While increasing soil fertility by burning trees is a model of biochar production.

Biomass is a natural energy source, coming mostly from agricultural crops and waste, forest waste, and animal waste. Biomass could also come from municipal waste produced by human. As one of the renewable energy, only biomass could be produced into solid, liquid or gas fuel. As a renewable energy source, biomass is

6th International Engineering Symposium - IES 2017

March 1-3, 2017, Kumamoto University, Japan

environment-friendly carbon neutral attribute as stated in McKendry (2002). It is a condition wherein net zero carbon emissions achieved due to balance amount of carbon released as a result of combustion, with an equivalent amount of carbon absorbed by the source of biomass, explained by Anderson (2009).

According to Asadullah, M (2014), Biomass gasification based power system made up of several steps including pretreatment of biomass, gasification of biomass, gas cleaning, and feeding the product gas into gas turbine or gas engine to produce electricity, or as a fuel for boiler to generate steam able to run the turbine.

BIOMASS PRETREATMENT

Moisture content in biomass gasification plays a critical role from technical point of view. During gasification process, heat added will generate steam derived from the moisture content and acts as gasifying agents, reacting with volatile matters and char to convert them to product gas, also enhance the hydrogen content in the reaction as explained by Yuan, L P et al (2007) and Yan, F et al (2010). For compost with moisture content less than 40%, self-combustion will be taken place investigated by Torii, S and Watanabe, S (2014). Higher moisture content above 40% however, reduces the thermal efficiency of the gasification system as investigated by Hosseini, M et al (2012).

The drying of biomass as a pretreatment has a crucial impact on the overall efficiency of the biomass-based power generation, as described by Asadullah, M (2014). Raw biomass, like palm empty fruit bunch in Malaysia and Indonesia usually content more than 50% of moisture, even though its plentifully available in these countries as reported by Ma, A N and Basiron, Y (2005). Biomass drying is one of the most challenging factors for maintaining the constant supply of biomass. There are several ways to lower the moisture content of biomass. Biomass could be dried by the sun at the source of origin where the biomass is produced. Sun drying is less expensive, but longer time is required, and also highly

depend on the weather. The longer the drying process, the more chance the biomass get mold and reduce its quality. While another way of drying is by using heat produced by the processing plant. This method, however, is more expensive due to additional equipment and constant heat needed. Acharjee, TC et al (2011) had already explored these methods.

Physical size of biomass often caused operational issue in the gasification process. Especially feeding the biomass into the gasifier. Biomass such as rice straw, wheat straw, grass, and empty fruit bunch are bulky and fibrous, hence usually get stuck in the feeding line. While some biomass like palm kernel shell and wood chips are easily fed into the gasification unit, though. The characteristics low bulk density of biomass could have a negative impact on the gasification process as mentioned by Chevanan, N et al (2010).

Even though additional process, energy consumption and cost needed, balling, briquetting and palletizing are the common techniques to overcome the low bulk density of biomass as investigated by Chen, L et al (2009) and Mani, S et al (2006). These techniques could make biomass more compact, thus avoid issue in regard to biomass feeding. Balling due to its size sometimes not applicable for constant feeding. Pallets are suitable for constant feeding instead, because of its size and shape, however, is difficult to break. Not to mention additional cost and energy to convert to pallets. Briquette comes as another option with balanced density, transported, stored and feed easily.

BIOMASS GASIFICATION

As reported by Dahlquist (2013), there are many methods to convert biomass to energy. Main biomass energy conversions are through combustion, gasification, pyrolysis, and torrefaction. Combustion is 100% oxidation of all organic contents of the fuel using air or oxygen. Gasification indicates partial combustion, where only 15-30% of the oxygen is being added in relation to what would be needed for 100% oxidation. Pyrolysis uses heat but without air, as a result, gaseous components of the organic material are

6th International Engineering Symposium - IES 2017

March 1-3, 2017, Kumamoto University, Japan

evaporated and later condensed as a liquid. And torrefaction is partial pyrolysis aim to remove some of the gaseous components, so that instead of liquid hydrocarbons produced, but a compact residue that could replace coal for coal power plants.

Compared to direct combustion, gasification technique produces lower NOx, CO and particulate emissions, and have more potential for efficient conversion process when generation power. On the other hand, gasification technology is currently still in the development phase and during the process need fuel with rather low size distribution and low moisture content. According to Knoef, H A M (2012), health, safety and environmental issues are found to be an important barrier for biomass gasification market. Hence risk assessment in biomass gasification is becoming increasingly important.

Biomass gasification is a promising, energy efficient technology for renewable energy generation and considered as a key technology for the use of biomass as described by Heidenreich and Foscolo (2014). Biomass gasification is a thermal conversion of biomass into useful combustible gas called producer gas or syn gas. Product gas produced by the gasification of biomass occurred at temperature ranging from 700 to 1000 °C could be burned in a boiler for heat production or in an internal gas combustion engine for combined heat and power generation.

Saidur, R et all (2012) within his exergy analysis research conclude that compared to other methods, gasification found to be the main thermochemical process and was the most effective method of converting biomass. Gasification also determined as one of the main sources of exergy losses. This means that exergy in gasification was the most transformed into anergy during its process.

Fluidized bed combustion, fixed bed combustion, and pulverized bed combustion are some of the available biomass combustion techniques as a fuel for boilers. According to Saidur, R et al (2011), fluidized bed combustion was

considered as the most excellent technology compared to other methods due to its ability to deal with low quality biomass, high ash content and low calorific value that often abundantly available in the rural area.

Due to the endothermic behaviour of the process, gasification require a significant amount of energy, hence the energy consumption is one of the most dominant restriction on the thermal efficiency and the design of the gasifier. In order to achieve optimal gasification process parameters, several modeling and simulation were needed in order to anticipate the actual process. Ahmad, A A et al (2016) conclude that reaction temperature, ER value and the presence of catalyst are the most important parameter in gasification that will determine the process performance and the quality of gas produced. While the biomass particle size was found to be the least significant parameter for process. Among the tools that could be used for modeling are Aspen Plus and Aspen Hysys, that able to apply the kinetic and equilibrium model.

BIOMASS GAS CLEANING

Product gas from gasification process could be used directly without further treatment for boiler application. In boiler application, product gas being used to generate steam, that will rotate the turbine to produce electricity. This method still, will reduce the overall efficiency of power generation through steam turbine to below 20% level, compared to about 50% in gas turbine and engine. One of the most challenging part is the cleaning of product gas in order to meet the gas turbine requirement and engine operation, especially for tar contaminant less than 100 mg N/m³ as reported by Asadullah, M (2014).

Raw syn gas produce by gasification of biomass contains essential gas like CO, CO₂, H₂ and CH₄, however raw syn gas also consist of small but significant amount of unwanted contaminants like tars, nitrogen compounds, sulfur compounds, hydrogen halides and other metals such as sodium and potassium. It is important to clean up the raw gas produced by gasification by employing cold, warm, and

6th International Engineering Symposium - IES 2017

March 1-3, 2017, Kumamoto University, Japan

hot gas clean up techniques. Abdoulmoumine, N et al (2015) found that cold gas cleanup was the most effective way to remove the contaminants at desirable lower concentration limit. This method posses some disadvantages because will reduce the overall efficiency caused by cooling, and increase cost as a result of complexity and additional steps needed for raw syn gas treatment.

Gas cleaning method could be done by physical gas cleaning. This method employs filter or wet scrubbing of the product gas so that tar and other particulate matter could be removed. This method may use gas/solid or gas/liquid interaction in high or ambient temperature. High temperature filter must utilize high tolerance material like ceramics, fiber glass, or sand. While ambient temperature may use other materials such as cotton fibers, charcoal and so on. Obstacle of these procedure are the fouling of particulate matter and sticky tar occurred in the passages. For greater application, filter may cause significant pressure drop. Water scrubbing could be one of the option to collect the particulate and tar, however it is difficult to handle a large amount of contaminated water and could be dangerous to the environment.

Tar could be cracked down into less dangerous molecules like methane, carbon dioxide and hydrogen by thermal process. As reported by Abuadala, A and Dincer, L (2010), tar thermal process could be done with very high temperature, it may reach 1000 °C. This will initial another issue like construction of high temperature and expensive alloys that need highly controllable and complex heating system. In addition, the ash melts in this temperature, and after the process, the product gas still need to be cooled with an intensive system.

Since physical filtration and thermal process found to be inefficient for gas cleaning process, utilization of effective catalyst may draw our attention because not only could reduce the concentration of tar and ammonia effectively, but also occurred in lesser temperature (600-800 °C). Another benefit for this techniques are due to same operation temperature, it does not need to be heat up or cool down.

In addition, catalyst could convert tar into CO and H₂, so will increase the burnable gas composition described by Asadullah, M (2014).

Absorption and adsorption process combination proven to be a feasible option for purification, because carbon grabbing, desulfurization, and moisture control occurred in the same period of time. As reported by Al Mamun, M R and Torii, S (2015), nanotechnology were applied for removal of H₂S and H₂O, while CO₂ could also removed by aqueous solution.

SMALL SCALE BIOMASS GASIFICATION POWER GENERATION

Spark ignition or compression ignition engines are the choice of technologies in gasification based power generation from biomass for the size range under 5 MW , as described by Larson (1998). While Williams (1998) said that fuel cell and micro gas turbines couples with biomass gasifier will offer considerably high efficiency at small scale compared to typical internal combustion engines, however this advanced technologies are still being developed. Product gas or syn gas from gasification process could be used for small scale Combined Heat and Power (CHP) units. Dong, L et al (2009) classify small scale CHP when produce less than 100 kW, and micro scale CHP for less than 15 kW. CHP or cogeneration has been considered as an alternative for energy saving as stated by Denntice (2003), and according to Bernotat (2004) heat will be produced along with power for environmental conservation.

Small scale gasification biomass power generation bring a better way to adapt biomass characteristic in rural area that very diverse and scattered. Bubbling fluidized bed gasification with steam, indirect heat supply and primary conditioning method with catalysts will improve product gas earning and quality. This system is more reliable, because of the better annual operation hours, more different types of biomass being used, greater load variation and other benefit. However due to the early development stages, global capital cost will be higher. As reported by Bocci, E et al (2014) for

6th International Engineering Symposium - IES 2017

March 1-3, 2017, Kumamoto University, Japan

high energy efficient heat and power generator like gas turbines or fuel cells, syngas quality still need to be refined, especially for syngas cleaning materials using catalyst.

Small scale CHP system are satisfactory for commercial building appliance, like hospitals, schools, industrial area, office building, and domestic houses. This system could supply adequate amount of energy required while keeping the positive social impacts. Environmental issues such as greenhouse emission effect, improved energy security, and also economical savings as a result of excessive electricity transmission omission distribution network and will lower the energy cost to the consumer. This already explained by Hawkes, A D and Leach, M A (2007). A small CHP also possess higher standard of dependability since this system operate independently, hence will not be affected by blackout from the grid.

Rural area has decentralized characteristic source of energy, hence biomass is consider as the fittest substitute of fossil fuel due to its intrinsic properties as mentioned by Fischer, IJ (2003). Transportation cost reduction will be a very good asset for small scale biomass plants, while it will be more tough to find an end user for the heat produced in larger power generation user, according to Eriksson, O et al (2007).

Larson (1998) stated that in rural areas, small scale gasification based biomass power generation is a promising strategy for maintain the sustainable electricity supply. Small scale gasification biomass power generation could contribute to rural development area in several manners. Biomass collection, delivery, power plant operation could employ people around the power plant. Economically competitive electricity produce by the power plant could attract even more employment, and benefit for income generative activities within the area, especially energy intensive industries. Surplus electricity power could be sent out to urban area that will lead to another advantages.

CONCLUSIONS

As an alternative source of energy, biomass have interesting characteristics suitable for rural area where limited electricity is to be expected. Plentiful point of supplies and historical background make biomass is familiar as a replacement of fossil fuels. Wood biomass remains the main energy source for widespread biomass powered CHP systems at small scale. Gasification of biomass using a gas engine (or gas turbine) presents interest possibility for small co-generation. Yet biomass gasification possess several aspects to be considered for the permanent replacement of fossil fuels. Pretreatment of biomass, syn gas contaminant are some of the barriers need to be solved. Researcher have done meaningful progress to overcome these obstructions. Briquetting techniques for pretreatment, modeling and simulation tools for biomass process flow prediction, the use of fluidized bed combustion, and syn gas cleaning process using catalyst or material selection are some of them. Integrating these most advanced techniques seem to be feasible and will promote the use of biomass and reduce fossil fuel in the near future.

ACKNOWLEDGEMENTS

The first author acknowledges support from the Indonesia Endowment Fund for Education (LPDP).

REFERENCES

- 2 Abdoulmoumine, N et al (2015), A Review on Biomass Gasification Syngas Cleanup, *Applied Energy*, Vol. 155, pp. 294-307.
- 3 Abuadala, A and Dincer, L (2010), Investigation of a Multi Generation System Using a Hybrid Steam Biomass Gasification for Hydrogen, Power and Heat, *International Journal of Hydrogen Energy*, Vol. 35, pp.13146-13157.
- 4 Acharjee, TC et al (2011), Effect of Thermal Pretreatment on Equilibrium Moisture Content of Lignocellulosic Biomass, *Bio resource Technology*, Vol. 102, pp. 4849-4854.
- 5 Ahmad, A A et al (2016), Assessing the Gasification Performance of Biomass : A Review on Biomass Gasification Process Conditions, Optimization and Economic Evaluation, *Renewable and Sustainable Energy Reviews*, Vol. 53, pp. 1333-1347.
- 6 Al Mamun, M R and Torii, S (2015), Removal of Contaminant Gases from Biogas by Chemical Purification Processes, *International Journal of Mechanical Engineering*, Vol. 3.

6th International Engineering Symposium - IES 2017

March 1-3, 2017, Kumamoto University, Japan

-
- 7 Anderson, D et al (2009), A Study for Carbon Neutrality : The Impact of Decision, Design and Energy, Perkins+Will Research Journal, Vol. 01.02.
- 8 Asadullah, M (2014), Barriers of Commercial Power Generation Using Biomass Gasification Gas : A Review, Renewable and Sustainable Energy Reviews, Vol. 29, pp. 201-215.
- 9 Basu, P. (2013), Biomass Gasification, Pyrolysis and Torrefaction, 2nd ed., Elsevier Inc, San Diego.
- 10 Bernotat, K and Sandberg, T (2004), Biomass Fired Small Scale CHP in Sweden and the Baltic States, a Case Study on the Potential of Clustered Dwellings, Biomass and Bioenergy, Vol. 27, pp. 521-530.
- 11 Bocci, E et al (2014), State of Art of Small Scale Biomass Gasification Power Systems : a Review of the Different Typologies, Energy Procedia, Vol. 45, pp. 247-256.
- 12 Chen, L (2009) et al, Renewable Energy from Agro Residues in China, Solid Biofuels and Biomass Briquetting Technology, Renewable and Sustainable Energy Reviews, Vol. 13, pp.2689-2695.
- 13 Chevanan, N et al (2010), Bulk Density and Compaction Behaviour of Knive Mill Chopped Switchgrass, Wheat Straw, and Corn Stover, Biomass and Bio energy, Vol. 101, pp 207-214.
- 14 Dahlquist, E. (2013), Technologies for Converting Biomass to Useful Energy, CRC Press, Taylor & Francis Group, Florida.
- 15 Denntice, M et al (2003), Micro Combined Heat and Power in Residential and Light Commercial Application, Application Thermal Engineering, Vol. 23, pp. 1247-1259.
- 16 Dong, L et al (2009), Development of Small-Scale and Micro-Scale Biomass Fueled CHP Systems - A literature review. Journal of Applied Thermal Engineering, Elsevier, Vol. 29, No 11-12, pp. 2119.
- 17 Eriksson, O et al (2007), Life Cycle Assessment of Fuels for District Heating : a Comparison of Waste Incineration, Biomass and Natural Gas Combustion, Energy Policy, Vol. 35, pp. 1346-1362.
- 18 Fischer, IJ (2003), Technologies for Small Scale Biomass CHP Plants - An Actual Survey.
- 19 Hawkes, A D and Leach, M A (2007), Cost Effective Operating Strategy for Residential Micro Combined Heat and Power, Energy, Vol. 32, pp. 711-723.
- 20 Heidenreich S, and Foscolo P U (2014), New concepts in biomass gasification, Progress in Energy and Combustion Science, Vol. 46, pp. 72-95.
- 21 Hosseini, M et al (2012), Steam and Air Fed Biomass Gasification : Comparisons Based on Energy and Exergy, International Journal of Hydrogen Energy, Vol. 37, pp. 16446-16452.
- 22 International Energy Agency (2014), 2014 Key World Energy Statistics, website: www.iea.org, pp. 6, 38.
- 23 Knoef, H A M (2012), Handbook Biomass Gasification, 2nd Ed, ISBN 978 □ 90 □ 819385 □ 0 □ 1, p. 374 □ 432.
- 24 Larson, E D (1998), Small Scale Gasification Based Biomass Power Generation, Biomass Workshop, Changchun, China.
- 25 Ma, AN and Basiron, Y (2005), Biomass Energy from the Palm Oil Industry in Malaysia and Indonesia, Ingenieur, Vol. 27, pp. 18-25.
- 26 Mani, S (2006) et al, Effect of Compressive Force, Particle Size and Moisture Content on Mechanical Properties of Biomass Pallets from Grasses, Biomass and Bio energy, Vol. 30, pp. 648-650.
- 27 McKendry P. (2002), Energy production from biomass. Part 1: Overview of biomass, Bioresour Technol, 83:37-46.
- 28 Saidur, R et al (2011), A Review on Biomass as a Fuel for Boilers, Renewable and Sustainable Energy Reviews, Vol. 15, pp. 2262-2289.
- 29 Saidur, R et all (2012), A Review on Exergy Analysis of Biomass Based Fuels, Renewable and Sustainable Energy Reviews, Vol. 16, pp. 1217-1222.
- 30 Torii, S and Watanabe, S (2014), Combustion Characteristics of Combustion Chamber Using Compost as a Fuel, Energy Procedia, International Conference on Applied Energy, Vol. 61, pp. 9-12.
- 31 Williams, R H (1998), Biomass Gasifier Fuel Cell Gas Turbine Power System, Biomass Workshop, Changchun, China.
- 32 Yan, F et al (2010), Hydrogen Rich Gas Production by Steam Gas Gasification of Char from Biomass Fast Pyrolysis in a Fixed bed Reactor : Influence of Temperature and Steam on Hydrogen yield and Syngas Composition, Bio resource Technology, Vol. 101, pp. 5633-5637.
- 33 Yuan, L P et al (2007), Hydrogen Rich Gas Production from Biomass Air and Oxygen Steam Gasification in a Downdraft Gasifier, Renewable Energy, Vol. 32, pp. 2173-2185.

Heat Transfer Enhancement Using Graphene Oxide/Water Nanofluid in a Two-Phase Closed Thermosyphon

Mohamed Salem^{1,2}, Tarek A. Meachail², Magdy A. Bassily³ and Shuichi Torii¹

- 1 Department of Mechanical System Engineering, Kumamoto University, Kurokami, 2-39-1, Kumamoto 860-8555, Japan. e-mail: Mohamed_salem@aswu.edu.eg
2 Department of Mechanical Power, Faculty of Energy Engineering, Aswan University, Aswan, Egypt.
3 Department of Mechanical Power, Faculty of Engineering, Minia University, Minia, Egypt.

ABSTRACT: A two-phase closed thermosyphon (TPCT) is a device for heat transmission. The TPCT is composed of three major parts: Lower evaporator, the adiabatic region in the central range and the condenser at the top. Fluids with nanoparticles (particles smaller than 100 nm) suspended in them are called nanofluids that they have a great potential in heat transfer enhancement. In the present study, Nanofluids of aqueous Graphene oxide (GO) nanoparticles suspensions are prepared in various volume concentration of 0.05–0.20% and used in a TPCT as working media. Experimental results showed that for different input powers, the heat transfer coefficient of the TPCT increases up to 33.04% when GO/water nanofluid is used instead of pure water. A decrease of 24.83% is achieved in thermal resistance at 0.20 vol.% for GO/water nanofluid.

Keywords: Thermosyphon, Nanofluid, Thermal resistance, Heat transfer coefficient

INTRODUCTION

Nanofluids, defined as fluids in which nanosized particles are suspended in a base liquid, are a novel types of working fluids used for heat transfer and coolings. Since Choi [1] first proposed the concept of using nanofluids to enhance thermal conductivity, these working fluids have shown great promise in heat transfer applications. The Two-phase closed thermosyphon heat pipes are one of the simplest and efficient types of heat pipes which can widely be employed in micro device cooling, computers, solar energy collectors, aeronautics sciences, missiles, spacecraft thermal control, micro-transportation systems, cooling loops, fuel cells and heat recovery systems.

Do et al. [2] experimentally investigated the effect of Al₂O₃/water nanofluids on the thermal performance of a heat pipe and

found that the thermal resistance was reduced by about 40% at the evaporator-adiabatic section of the heat pipe. They concluded that the Al₂O₃ nanoparticles formed a thin porous coating layer at the evaporator section, and the improved surface wettability and capillary wicking performance reduced the thermal resistance of the heat pipe. Tsai et al. [3] performed an experimental investigation for a circular meshed heat pipe using gold nanofluids. They presented that the thermal resistances of the heat pipe with solutions of various-sized gold nanoparticles ranged from 0.17 to 0.215 °C/W, which was 37% lower than the thermal resistance of the heat pipe using DI water. Solomon et al. [4] investigated the heat transfer characteristics of a copper heat pipe with nanoparticle deposition on the wick, at power levels of 100–200 W. They used a screen wire mesh wick and reported that a heat pipe coated

6th International Engineering Symposium - IES 2017

March 1-3, 2017, Kumamoto University, Japan

with copper oxide nanoparticles showed a maximum reduction in thermal resistance of 40%, as compared to the bare screen wire mesh, because the deposited nanoparticles provided more nucleation sites. Kang et al. [5] investigated the influence of silver nanofluids on grooved heat pipe with circular cross section and 200 mm length and 6 mm diameter. Results demonstrated that thermal resistance of the heat pipe was decreased by 10–80% in comparison with water. Rahimi et al. [6] studied the effect of resurfacing on the evaporator and the condenser of a closed two-phase thermosyphon. It was shown that the thermal performance of the surface modified thermosyphon was enhanced by 15% when compared to the plain surface. Huminic et al. [7] studied the heat transfer characteristics of two-phase closed thermosyphon with iron oxide-nanofluids as working media at different inclinations, operating temperatures and nano-particle concentrations. It was evident that the nanoparticles had a significant effect on the enhancement of heat transfer characteristics of thermosyphon.

In this research, the thermal performance of a two-phase closed thermosyphon (TPCT) was investigated experimentally under different constant heat fluxes (10 – 30W) and 100% fill charge ratio. Pure water and various volume concentrations of Graphene oxide (GO)/water nanofluid (0.05 – 0.2%) were employed as working fluid.

MATERIALS AND METHODS

Materials

Graphene oxide (GO)/water nanofluids were prepared by dispersing GO nanoparticles into pure water as a base fluid. GO nanoparticles were synthesized from natural graphite powder by a modified Hummers method [8, 9]. Graphite fine powders (45 µm) was purchased from Wako pure chemical industries (Japan), concentrated sulfuric acids (H_2SO_4), sodium nitrate ($NaNO_3$), potassium permanganate ($KMnO_4$), hydrogen peroxide (30% H_2O_2), hydrochloric acid (5% HCl) and de-ionized

water were used throughout Hummers method. GO/water nanofluids with four different volume concentrations at 0.05%, 0.1%, 0.15% and 0.2% were prepared for this experiment. The thermal conductivity and the viscosity of GO/water nanofluids were measured in our previous study [8].

EXPERIMENTAL SETUP

In this study, the results of the experimental determination of the thermal performance of a TPCT are reported. Fig. 1a shows a schematic diagram of the experimental apparatus that is used in this work. Fig. 1b shows the locations of the thermocouples. The apparatus consisted of a TPCT, data logger, variable transformer, vacuum pump, digital multi-meter, flow meter, pressure gauge and thermostatic bath.

In the experiment, a copper thermosyphon is used with a long of 200 mm, an outer diameter of 15 mm, and a thickness of 1 mm. The thermosyphon charged with the working fluids and tested with an evaporator length of 70 mm and a condenser length of 80 mm. The working fluids filled approximately 100% of the volume of the evaporator. The heat energy emitted to the evaporator section of TPCT by the electric heater was removed from the condenser by circulating cooling water. Eight K-type thermocouples were fixed at the outer surface of the TPCT to monitor the temperature distribution along the wall of the TPCT. Four thermocouples were embedded on the evaporator; three were placed on the condenser and one at adiabatic section. The temperature of the circulating cold water to the condenser section is maintained at 15°C with a flow rate 1.5 L/min for all test conditions. The heat input is varied from 10W to 30W for each concentration.

RESULTS AND DISCUSSION

Wall temperature distribution

Fig. 2 display the distribution of the wall temperature along the heat pipe, which was positioned vertically, with deionized water or the nanofluid as the working fluid using 10 W, 20 W and 30 W of power supplied into the heat pipe, respectively.

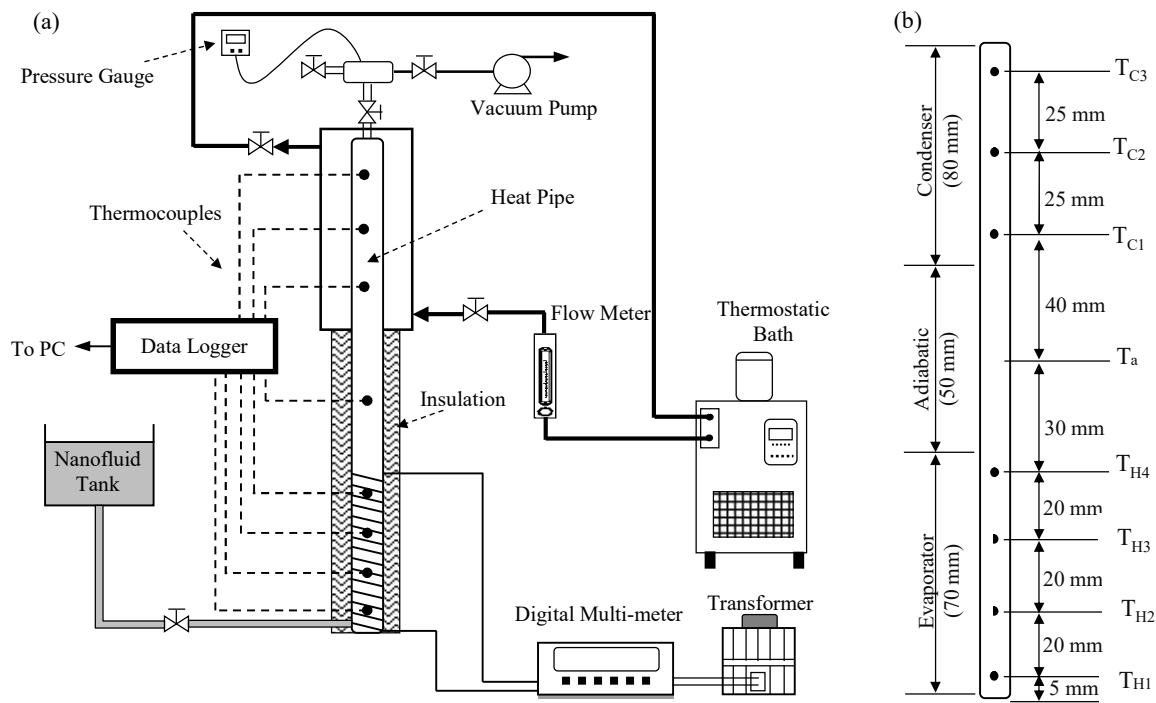


Fig. 1 (a) Schematic diagram of the experimental apparatus, (b) locations of the thermocouples

From Fig.2, a gradual decrease is observed in the temperature of the pipe wall in the direction from the evaporator to the condenser. The wall temperature distribution of the nanofluid containing heat pipes in the evaporator section is lower than that of the heat pipes containing distilled water at the same input power and increasing the volume fraction of nanoparticles caused the wall temperature to decrease significantly. However, the wall temperature rapidly increased to higher values as the applied input power is increased. Based on the experimental results, the maximum reduction in the mean evaporator temperature $((T_{H1}+T_{H2}+T_{H3}+T_{H4})/4)$ compared with pure water is registered for 0.20 vol.% at different input power (5.875 °C, 12.47 °C and 7.95 °C for input power of 10, 20 and 30 W, respectively).

Thermal resistance

The thermal resistance (R_{th}) of the TPCT is a measure of its thermal performance, defined as the ratio of the temperature difference to a given heat load:

$$R_{th} = \frac{T_H - T_C}{Q} \quad (1)$$

In this equation, the temperatures of the evaporator and the condenser are the respective average wall temperatures, and the heating power input Q could be evaluated by Eq. (2) as follows:

$$Q = V \times I \quad (2)$$

where V and I are the applied voltage and current, respectively.

Fig. 3 shows the effect of volume concentration and input power on the thermal resistance of the TPCT. According to Fig. 3, the thermal resistance decreased at the heat input power increased. Also, increasing the GO nanoparticles as the dispersed phase in water can significantly reduce the overall thermal resistance of the TPCT. The thermal resistance reached its minimum value at volume concentration of 0.20% for all heating loads. When compared with pure water, the maximum reduction in thermal resistance is 24.8% for volume concentration of 0.20% at input power of 20 W.

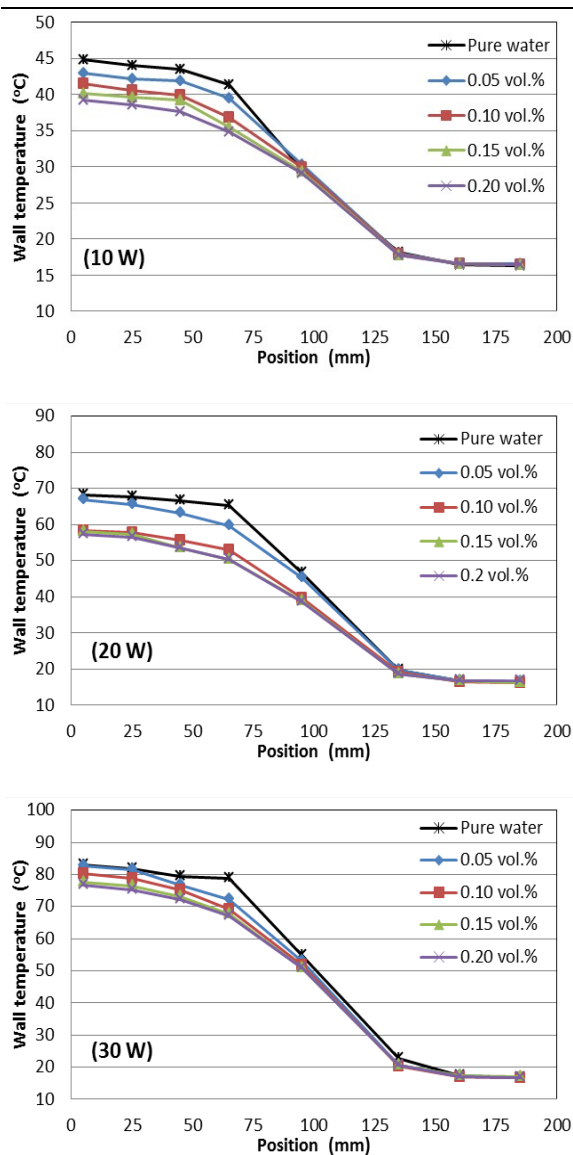


Fig. 2 Effect of GO concentration on the wall temperature distribution at input power levels of 10, 20 and 30 W

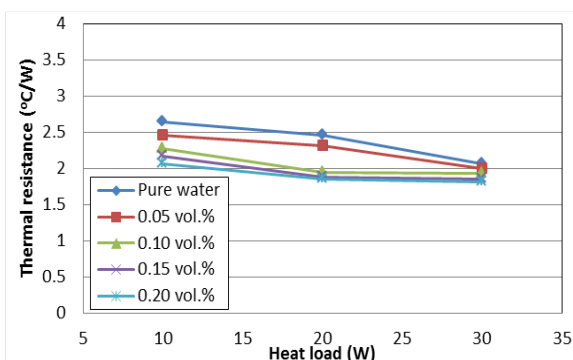


Fig. 3 Thermal resistance as a function of concentration and input power

Overall heat transfer coefficient

The overall heat transfer coefficient (h) is defined by the following equation:

$$h = \frac{Q}{\pi D L_e (T_H - T_C)} \quad (3)$$

where D is the outer diameter of the TPCT and L_e is the evaporator length.

Fig. 4 shows the effect of input heating power the overall heat transfer coefficient, when using pure water and GO/water nanofluids. Results showed that the overall heat transfer coefficient of the TPCT significantly increased with increasing the input heat power for all working fluids. For GO/water nanofluids, a higher heat transfer coefficient is registered for all volumetric concentrations of nanoparticles in comparison with those reported for pure water at a similar condition. Noticeably, with increasing the concentration of GO nanoparticles, the heat transfer coefficient of the TPCT dramatically increased. When compared with pure water, the maximum enhancement in the overall heat transfer coefficient is 33.04% for a volume concentration of 0.20% at input power of 20 W.

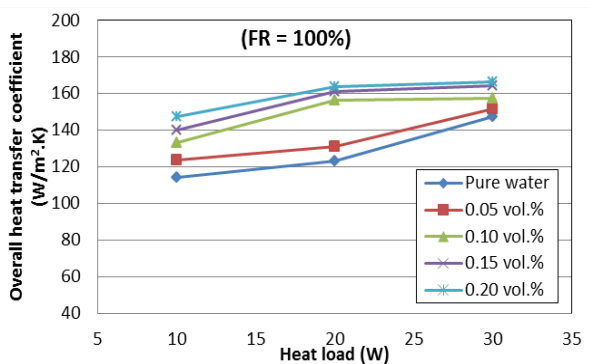


Fig. 4 Overall heat transfer coefficient as a function of concentration and input power

CONCLUSIONS

The objective of this study was to examine the effects of using graphene oxide nanofluids on the performance of a two-phase closed thermosyphon. Different concentrations (0.05%, 0.10%, 0.15%

6th International Engineering Symposium - IES 2017

March 1-3, 2017, Kumamoto University, Japan

and 0.20%) of GO nanoparticles were dispersed in distilled water as base fluid. The following conclusions are deduced from this study:

- Significant enhancement of heat transfer performance due to suspension of GO nanoparticles was observed in comparison with pure water as the working fluid.
- The enhancement depended on the GO concentration and the input heat power.
- The wall temperature of heat pipes declined significantly as concentration of GO nanoparticles increased. The maximum reduction in surface temperature was 12.47 °C for volume concentration of 0.20%.
- The thermal resistance was lowered by 24.8% for volume concentration of 0.20% at input power of 20 W.
- The overall heat transfer coefficient of the GO nanofluids was better than that of deionized water.

ACKNOWLEDGEMENTS

The first author would like to acknowledge the Cultural Affairs and Missions Sector, Ministry of Higher education, Egypt, for providing the financial support (PhD scholarship) for this research and the extended help of Thermal engineering laboratory under the Department of Mechanical System Engineering, Kumamoto University, Japan, for providing the facility for experimentation.

REFERENCES

- [1] S.U.S. Choi (1995), Enhancing thermal conductivity of fluids with nanoparticles, Developments and Applications of Nan-Newtonian Flows, FED-vol. 231/MD 66, pp. 99–105.
- [2] K. H. Do, H. J. Ha and S. P. Jang (2010), Thermal resistance of screen mesh wick heat pipes using the water-based Al₂O₃ nanofluids, International Journal of Heat and Mass Transfer, vol. 53, pp. 5888–5894.
- [3] Tsai, H.T. Chien, B. Chan, P.H. Chen, P.P. Ding and T.Y. Luh (2004), Effect of structural characteristics of gold nanoparticles in nanofluid on heat pipe thermal performance, Materials Letters, vol. 58, pp.1461–1465.
- [4] A.B. Solomon, K. Ramachandran and B.C. Pillai (2012), Thermal performance of a heat pipe with nanoparticles coated wick, Applied Thermal Engineering, vol. 36, pp. 106–112.
- [5] Kang, W.C. Wei, S.H. Tsai and S.U. Yang (2006), Experimental investigation of silver nanofluid on heat pipe thermal performance, Applied Thermal Engineering, vol. 26, pp. 2377–2382.
- [6] M. Rahimi, K. Asgary and S. Jesri (2010), Thermal characteristics of a resurfaced condenser and evaporator closed two-phase thermosyphon, International Communications in Heat and Mass Transfer, vol. 37, pp. 703–710.
- [7] G. Huminic and A. Huminic (2011), Heat transfer characteristics of a two-phase closed thermosyphons using nanofluids, Experimental Thermal and Fluid Science, vol. 35, pp. 550–557.
- [8] M. Salem, M. Bassily, T. Meakhail and S. Torii (2016), Experimental Investigation on Heat Transfer and Pressure Drop Characteristics of Graphene Oxide/Water Nanofluid in a Circular Tube, IPASJ International Journal of Mechanical Engineering, vol. 4, pp. 12–22.
- [9] Hummers W., JR., and Offeman R. (1958), Preparation of Graphitic Oxide, J.Am.Chem.Soc., vol. 80, pp. 1339.

Biogas as an Entrusted Alternative for Fossil Fuels: A Review

Farhana Huqe¹ and Shuichi Torii²

¹ Department of Mechanical System Engineering, Kumamoto University, Kurokami, 2-39-1, Kumamoto 860-8555, Japan. email: farhanahuqe@gmail.com

² Department of Mechanical System Engineering, Kumamoto University, Kurokami, 2-39-1, Kumamoto 860-8555, Japan. e-mail: torii@mech.kumamoto-u.ac.jp

ABSTRACT: Global warming has become the greatest challenge for the world today. Now, researchers are trying to find out an alternative energy source of traditional fossil fuels to evict green house effect. From recent studies it is observed that, biogas has the potential to become an entrusted energy source for the current world as it can be extracted from solid wastes and the extraction processes are not only ecologically sound but also cost effective and is also an hygienic process to dispose the solid wastes. Basically, biogas consists of methane (50-60%) and carbon dioxide (20-40%); with a small mixture of hydrogen sulfide and siloxanes as impurities. These impurities can damage the efficiency of biogas. But after successful removal of these impurities, the upgraded biogas can be used in different technologies which are effective to turn biogas into energy source. But, the matter of fact is that, the lacking of knowledge to select proper substrate, not having sufficient knowledge to apply appropriate pre and post treatments of the raw materials creating obstacles to explore the vast application field of biogas. In this paper, we would like to focus on some familiar technologies by which the utilization of biogas can be extended and help to optimize and control the energy crisis of the world.

Keywords: Anaerobic digestion, Biomethane, Upgradation

INTRODUCTION

At present, the limitation of fossil fuels and their effects on the environment have become the main reason for the world to search for a new and reliable energy source. There is no doubt that, within some decades we are going to face a severe scarcity of energy. Energy crisis throughout the world directed to the attention to the alternative sources of energy instead of underground fossil fuels as primary energy source has lead to global climate change, environmental degradation and human health problems [1]. Global climate change will inevitably lead to drought, flooding, increases the rate of hurricanes and cyclones and possibly widespread crop failure and global warming [19] [13]. Despite of rapid urbanization, Bangladesh, like other third

world agro based counties, among the total annual harvest, a significant portion of cultivable land is devoted for vegetable cultivation across the country. But due to the deficiency of efficient transportation and preservation process, a huge amount of these vegetables are wasted firstly in the land where it was grown and then in the vegetable markets as municipality wastes. Similar situation can be observed for other solid farm wastes. Due to their high moisture and organic contents and biodegradability, these wastes are the major contributors to the emission of greenhouse gases and volatile organic compounds. From the standpoint of pollution control, green and other solid wastes are not hazardous materials but their disposal in landfill poses serious environmental pollution [24]. Therefore the security of energy supply, especially development of sustainable energy and

6th International Engineering Symposium - IES 2017

March 1-3, 2017, Kumamoto University, Japan

reduction of carbon dioxide emission are the prior agenda worldwide. In this regards, biogas is a renewable energy source appear to be one of the most effective and efficient solutions [10]. It is carbon neutral, colorless, flammable gas produced from animal, plant, human, industrial and municipal wastes, to give mainly methane (50-60%), carbon dioxide (20-40%) and traces of other gases like hydrogen sulfide, nitrogen, water vapor etc. [11].

The main challenge for producing biogas is to select proper substrate and then the pre-treatment of these raw materials. The substrates used to extract biogas is organic compounds which can be obtained from numerous source of wastes from food industries, kitchen wastes, vegetable and fruit wastes, wastes from slaughterhouses and wastes from green markets. This feedstock undergoes anaerobic digestion and generates biogas (energy source) and digestate (organic manure). Biogas produced here needs to be cleaned or upgraded as it is mixed with some chemical compounds and they decrease the quality of biogas. The efficiency of biogas system can be upgraded by refining (pre-treatment) feedstock, optimizing operating parameters and improving the process. Some post-treatment may be required to clean the biogas and to enrich the methane composition in it.

CREDIBILITIES OF BIOGAS

The short storage of fossils fuels is creating a red alarm to the industrialized world. The high rate of carbon emission also made us to be concern about the environment. Global warming is causing the raise of the sea level, which becomes a threat to the lives of different species of flora and fauna. Besides, environmental pollution is also becoming a source of various diseases to the human life. Fossil fuel like coal and other petroleum oils are the major sources of air pollution. Usage of natural gas in the industries is also a major cause to decrease the amount of natural gas. But the modernized world can't run without industrialization. So, this is the high time that, we should introduce biogas as the alternative of fossil fuels. From the extraction to upgradation, the

biogas technologies are environment friendly. Besides, the wastes, which are being used as the raw materials for biogas production, can easily be drained without harming the surroundings. Not only this, but the biogas technologies are also cost effectives.

PRE-TREATMENT OF SUBSTRATE

The growing global demand with the limited storage of fossil fuels, high price of the fuels, threat for the environment necessitate the use of biogas. Though the stock of raw material for biogas production is huge, but it is important to choose proper substrates and it is more important to treat them before the extraction of biogas. The abundance and availability of lignocellulosic biomass worldwide as well as their high carbohydrate content present them as an attractive feedstock for biogas extraction. Lignocelluloses have been accounted for nearly 50% of biomass in the world and the production of lignocelluloses can count up to 200 billion tons in every year [3]. Recently, the lignocellulosic residues are being utilized as feedstock for methane production is not explored [8] because of their recalcitrant structure and it is also a big challenge [23].

At the first step of AD, i.e. during hydrolysis, the hydrolytic bacteria convert the insoluble complex organic matters into monomers and soluble oligomers such as fatty acids, amino acids and sugars. The enzymes involved in this process are celluloses, hemicelluloses, lipases, amylases and proteases [23]. For this reason, in biogas extraction process, almost all kinds of substrates can be hydrolyzed. The rate of hydrolysis step is highly dependent on the characteristics of the chosen substrates. Hydrolysis can proceed relatively faster if the required enzymes are produced by microorganisms and suitable surface area for physical content between the enzymes and the substrate is provided [4]. Otherwise, the substrates like celluloses needs more time to be degraded and sometimes the degradation remain incomplete [25]. Therefore, an initial pre-treatment process, which converts raw materials to a form that is amenable to microbial and

6th International Engineering Symposium - IES 2017

March 1-3, 2017, Kumamoto University, Japan

enzymatic degradation, is needed [30]. A suitable pre-treatment by disruption of secondary cell walls structure will reduce biomass recalcitrance and thus accelerate downstream process. Basically, a pre-treatment should also be cost effective and yields a polysaccharide rich substrate with limited amounts of by-products. There are three major types of pre-treatments. Such as,

1. PHYSICAL PRE-TREATMENT

This process involves mechanical size reduction method such as milling, shredding, cutting, chipping and so on. This method helps to enhance the availability of organic content, to increase the surface area of the biomass, reduce the mass and heat transfer restrictions and the degree of polymerization and crystallinity of cellulose and increase the biodegradability rate of lignocelluloses [20, 17]. Some process like milling produces huge amount of biogas but the process is energy intensive.

2. CHEMICAL PRE-TREATMENT

This process includes different types of chemical species, for example, iron liquids, organic solvents, alkali and acids to break the structure of lignin inside the substrates. Some alkali like potassium and sodium hydroxide, anhydrous ammonia, calcium hydroxide and hydrazine swells the substrate by increasing their internal surface area. This results the reduction of degree of crystallinity and polymerization of the substance. Dilute acid pre-treatment provides access to cellulose by hydrolyzing the hemicelluloses content to monomeric units [20].

3. BIOLOGICAL PRE-TREATMENT

In this process, the microorganisms are used to breakdown the biodegradable biomass containing polyphenols, lignin and hemicelluloses. Basically, fungal species are used for this purpose. The white rot and the soft rot fungal species are found to break the lignocelluloses content of the substrate. On the other hand, brown rot fungal species are good at degrading the cellulose part in the substrate. Since biological pre-treatment is a slow method,

for this reason it can't be suggested for biogas production procedure [20].

BIOGAS EXTRACTION

Biogas is extracted by anaerobic digestion (AD) process of biodegradable solid wastes which needs environmental factors like temperature, pH , contents of salts, available food etc. The waste excreted by a microorganism is consumed as food by the next stage microorganism [17]. The production of biogas is done by different biological reactions.

1. HYDROLYSIS

This is the first step in anaerobic digestion process. In this process, the organic matter is depolymerized. The complex insoluble and longer substrate units are hydrolyzed to smaller units. Many hydrolytic microorganisms are used to do this as they secret enzymes like cellulose, amylase, lipase, protease etc. The colonies of facultative and anaerobic microbes cover the substrate particles and break it down to monomeric units [17, 12].

2. ACIDOGENESIS

This reaction is the fastest reaction in the anaerobic digestion process to convert the complex substrates to liquid formulation. Here, long chained fatty acids, sugars and amino acids formed after the hydrolysis reactions, are being utilized by fermentative bacteria. Thus these substrates are converted into short-chained fatty acids, hydrogen, carbon dioxide, alcohols and other organic acids [12].

3. ACETOGENESIS

The rate of this reaction is slowed down by the acetogens, as they are slow growing microbes. They are extremely oxygen sensitive, can easily fluctuated during the loading of the organisms and their optimum pH is 6. After acetogenesis, electron sinks get developed because of the increment in hydrogen ion concentration, they are degraded by acetogens and hydrogen is produced which is used by the next step of microorganisms.

6th International Engineering Symposium - IES 2017

March 1-3, 2017, Kumamoto University, Japan

4. METHANOGENESIS

In this stage, methanogenic bacteria produce methane as metabolic by-product in their anoxic conditions. These organisms use methylated C1 compounds, acetate, hydrogen or carbon as energy source and for their growth [12]. The methane is produced in two ways, either by the cleavage of the acetic acid molecules that generates carbon dioxide and methane or through the reduction of carbon dioxide by producing hydrogen.

CHALLENGES OF ANAEROBIC DIGESTION

As it mentioned before that, in AD process the organic materials need combined activity of several different groups of microbes with different metabolic capacity [9]. For a stable biogas process, all the conversion steps involved in the degradation of organic matters and the microorganisms carrying out these steps should work in a synchronized pattern. Since methanogens are extremely sensitive bacteria as they have longer duplication duration, so it is important to prevent these groups of microorganisms from being washed away from the considered system. During the last decades, researchers have been developed some high rate systems to lower the effects of toxic compounds, by integrating the biological process with membrane separation techniques.

DESULPHURISATION OF RAW BIOGAS

The biogas produced by anaerobic process is mixed with several impurities like hydrogen sulfide, carbon dioxide and other gas. It is necessary to remove the impurities to upgrade the quality of biogas. Though carbon dioxide is the major contamination in the raw biogas, but the actual challenge is to demolish the presence of hydrogen sulfide from the biogas. As hydrogen sulfide is a hazardous gas and it is also a reason for the inefficiency of the biogas. For this reason, it is important to apply a proper method for hydrogen sulfide removal. There are several processes to remove sulfur contents, such as, in-situ desulphurization, biological desulphurization (biological scrubbing), chemical-oxidative scrubbing

etc. Among them, in-situ desulphurization is one of the most cheap and reliable processes to demolish sulfur content there. In this process, a little addition of liquid mixture of various iron salts like iron sulfate and iron chloride in the digester tank prior to the digester results precipitation of the sulfur content of the substrate by producing of nearly insoluble iron sulfide within the biogas fermenter. Then the precipitation can be removed from there with the digester. Not only this, ammonia can also be removed from there using this technology. This method is relatively cost effective rather than other methods like biological desulphurization and chemical-oxidative scrubbing. Though biological scrubbing is very clean and stable way to drain the sulfur content, but it is not an effective process. Because, this method is proper if the presence of sulfur content in the biogas is not high and pure oxygen is easily available during the oxidation process. Besides, the chemical-oxidative scrubbing can be advantageous if the amount of hydrogen sulfide is relatively moderate or high and substrates used for biogas extraction are changing frequently. After the successful removal of impurities, the biogas will taken for upgradation so that the amount of methane can be enriched and then the upgraded biogas is ready to be applied in different technologies [26].

CONVERSION OF BIOGAS INTO ENERGY SOURCE

The mostly adopted biogas technology is combined heat and power system (CHP) to convert the biogas into electricity and heat. In the public grid system and district heating networks are the two respective utilization of this technology. Without this technology, the upgraded biogas can be applied as a substitute of natural gas for cooking and electricity and fertilizer production. Other promising biogas technology is the alternative transport fuel of diesel and patrol in automobiles. These technologies are described briefly below.

1. ELECTRICITY

In this technology, the combustion of biogas is used to run the internal combustion engines, which can drive a

6th International Engineering Symposium - IES 2017

March 1-3, 2017, Kumamoto University, Japan

power generator [7, 21, 14]. This is the most popular technology where mostly cleaned biogas having 55% methane concentration is used for gas-to-energy conversion, and then it makes a fine contribution in national electricity grid [27]. Here, the heat is generated from the internal combustion is transferred via heat exchanging method and used in water heating, room heating, small heating networks etc. The energy produced in this process has a fair capability. From recent reports it is observed that, approximately 6.9% of total energy exerted from this process is utilized to fulfill the demand of energy such as energy for electrical components and computer support system in an agriculture anaerobic wet digestion plant [7]. Usually, this self-capable technology is independent from the import of external energy source to be run. In general, the electricity input for running CHP system varies dependent on the capacity of the system. Literature reveals that for a small scale biogas plant, 3% of total electricity is required for process requirement which may go up to 4.5% for a large scale biogas plant [15].

2. FUEL CELL TECHNOLOGY

This technology is performed by the conversion of chemical energy of the fuels through chemical reactions to electrical energy. This is very promising biogas technology as it has higher efficiency, lower emission and possible for the use of multiple fuels like biogas, natural gas, water and different fluids, which contain hydrogen [28]. This technology can be classified into two familiar groups.

A). High Temperature Fuel Cells (HTFC): The HTFC is consists of fuel cells that operate at temperature more than 873 K or 6000 C, such as Molten Carbonate Fuel Cell (MCFC) and Solid Oxide Fuel Cell (SOFC) [6].

B). Low Temperature Fuel Cells (LTFC): The LTFC is consists of fuel cells that work at temperature less than 473 K 2000 C, for example, Phosphoric Acid Fuel Cells (PAFC), Alkaline Fuel Cells (AFC), Direct Alcohol Fuel Cells (DAFC), Biological Fuel Cells (BFC) and Polymer Electrolyte Fuel Cells (PEFC) [6].

But the drawback of this technology is the cells can easily be damaged by the impurities present in the biogas. Low temperature fuel cells are higher sensitive towards CO, CO₂, CH₄, H₂S, NH₃, and high temperature fuel cells; the catalytic process is sensitive to H₂S as sulfur is a poison for the catalysts present in anode of the fuel cell [6].

3. MICRO GAS TURBINES

The gas turbines, which have the size less than 1 MW, are defined as micro gas turbines (MGT). This is very attractive technology as it has low impact on the environment and less operation and maintenance cost. It is very lightweight, small and compact system. It consists of very small components like high speed magnetic generator, radial turbine, and single stage centrifugal compressor.

In the MGT system the air is compressed using centrifugal compressor and sent to the regenerator. Here the compressed air is preheated by the exhaust gas from the micro gas turbine. The preheated compressed air is then used for combustion of fuel in the combustion chamber till inlet temperature requirement of turbine is achieved. The hot gases then expand in the turbine and conveyed to the regenerator for heating the compressed air.

The use of a high speed magnetic generator can be introduced in this technology to convert the gained energy up to 1600Hz alternative current. The power generated by modulator of this technique can be ranged from 30 KW to 200 KW. The thermal energy of this technology can also be increased greater than 70% by integrating with CHP [2].

4. HEAT FORM BIOGAS

The biogas can be served as a fuel for the technologies producing heat for several applications, for example, space heating or water heating. The heat generated by the biogas plant combined with combined heat and power generation technology or any other techniques can also be applied to the district heating networks is a centralized system to generate and distribute heat to the residential, institutional and commercial portions. A recent study has

6th International Engineering Symposium - IES 2017

March 1-3, 2017, Kumamoto University, Japan

reported that the heat required by the houses, commercial and industrial sector results 49% demand of energy and this demand exert 47% of carbon emission [16]. This growing demand varies with change in the season. Biogas powered heating networks are used for heating nearby greenhouse, horticulture houses, public amenities and public residential areas. The district heating networks can be applicable if two or more building connected to one heating source or if only one building having ten or more [5].

Without the above technique, biogas can also be used in the process of trigeneration of energy, which includes cooling, heating and electricity generation. This technology severally named as combined cooling, heating and power (CCHP). Trigeneration process is occurred through two ways, firstly the production of heat and power by CHP unit which is referred as cogeneration and secondly the utilization of the heat for cooling process in an absorber chiller. In this process, the after the power generation, the exhausted gas from the engine are conveyed to the chiller which generates chilled water for cooling purpose and the heat waste present in the exhausted gas passed to the heat exchanger to produce hot water. Therefore, the absorption chiller works to convert the heat generated from CHP to combine heat, power and cooling [18].

5. OTHER UTILIZATIONS

Purified biogas can also be used as substitution of transportation fuel. After taking the biomethane in the compression unit where it will be compressed to a pressure of 200 bar to make it suitable for the distribution systems and then it can be filled in the LPG cylinder [7, 21], then the compressed biogas can be used as transport fuel in the vehicles.

Another utilization of biogas is in the national grid system [7, 21]. This process of injecting biogas in the gas grid system can be an energy efficient solution. After compression of the biogas, its pressure increases and it becomes compatible for the pressurized lines of the gas grids. In many countries like Germany, USA, France, Austria and Ireland are using this process in their national gas grid system.

At last but not the least, the biogas technology has a huge probability of success in for cooking purpose. In many developing countries, which have small scale biogas plants are using this technology for cooking [29, 22]. In countries like India and Bangladesh, where the main consumption of natural gas is for cooking, biogas has made its importance as a sustainable alternative as it a heating capability and thermal efficiency.

CONCLUDING REMARKS

Biogas has created a new remark for the world with its versatile utilization and sufficient efficiency. Besides, the eco-friendly behavior of biogas production process and its application also have a great acceptance to the world. Thus the emerging energy demand for renewable energy compels us to explore new substrates and to develop new and sustainable technologies for biogas production and its utilization. New and stable techniques are also needs to be introduced for the removal of the impurities and upgradation of the biogas. Since AD is a complex microbial procedure of biogas production, a broad range of research is needed to find out the optimum conditions to get more production from less time period. Now the researchers are aimed to study the relationship between microbial community structure, operating conditions and processes to perform. Besides, it is now high time to broaden the field of gas to energy conversion technologies. The small and medium scale of utilization like utilization of biogas in the absorption chillers and cooking purposes needs more chance to be explored for the developing countries.

ACKNOWLEDGEMENT

Authors are thankful to the Graduate School of Science and Technology, Kumamoto University, Japan, for providing all necessary facilities to proceed this work.

6th International Engineering Symposium - IES 2017

March 1-3, 2017, Kumamoto University, Japan

REFERENCES

- [1] Budiyano, et al (2014), Increasing biogas production rate from cattle manure using rumen fluid as inoculums, *International Journal of Science and Engineering*, Vol. 6, No. 1 pp. 31-38.
- [2] Caresana, F et al (2010), Micro Gas Turbines. Gas Turbines, GurrappaInjeti (Ed.), ISBN: 978-953-307-146-6.
- [3] Claassen, P A M et al (1999), Utilization of biomass for the supply of energy carriers, *Applied Microbiology and Biotechnology*, Vol. 52, No. 6, pp. 741-755.
- [4] Deublien D and Steinhauser A (2011), Biogas from wastes and renewable resources: An Introduction, 2nd ed., Mörlenbach, Germany, Wiley-VCH Verlag GmbH & Co KGaA.
- [5] Ericsson, K (2009), Introduction and development of the Swedish district heating systems Critical factors and lessons learned. A report prepared as part of the IEE project "Policy development for improving RES-H/C penetration in European Member States (RES-H Policy).
- [6] Galvagno, A et al (2013), Biogas as hydrogen source for fuel cell applications, *International Journal of hydrogen energy*, Vol. 38, pp. 3913-3920.
- [7] Goulding D and Power N (2013), Which is the preferable biogas utilization technology for anaerobic digestion of agricultural crops in Ireland: Biogas to CHP or biomethane as a transport fuel? *Renewable Energy*, Vol. 53, pp. 121-131.
- [8] Hendriks A T W M and Zeeman G (2009), Pretreatments to enhance the digestibility of lignocellulosic biomass, *Bioresource Technology*, Vol. 100, No. 1, pp. 10-18.
- [9] Horvath, I S et al (2016), Recent Updates On Biomass Production-A Review, *Biofuel Research Journal*, Vol. 10, pp. 394-402.
- [10] Kaygusuz K and Kaygusuz A (2002), Renewable energy and sustainable development in Turkey, *Renewable Energy*, Vol. 25, pp. 431-453.
- [11] Maishanu, S M et al (1990), Biogas Technology: The output of the sokoto energy research center, *Nigerian Journal of Solar Energy*, Vol. 9, pp. 183-194.
- [12] Merlin, C P (2014), A review on anaerobic decomposition and enhancement of biogas production through enzymes and microorganisms. *Renewable and Sustainable Energy Reviews*, Vol. 34, pp. 167-173.
- [13] Mills, D M (2009), Climate change, extreme weather events, and us health impacts: what can we say?, *Journal of Occupational and Environmental Medicine*, Vol. 51, No. 1, pp. 26-32.
- [14] Murphya, J D et al (2004), Technical/economic/environmental analysis of biogas utilisation. *Applied Energy*, Vol. 77, pp. 407-427.
- [15] Poschl, M et al (2010), Evaluation of energy efficiency of various biogas production and utilization pathways, *Applied Energy*, Vol. 87, pp. 3305-3321.
- [16] Poyry and Faber Maunsell (2009), The potential and cost of district heating networks, A report to the Department of energy and climate change.
- [17] Schnurer A and Jarvis A (2010), Microbiological Handbook for Biogas Plants, Swedish Waste Management. Swedish Gas Centre Report, pp. 207.
- [18] Schuster, A (2009), Energetic and economic investigation of Organic Rankine Cycle applications. *Applied Thermal Engineering*, Vol. 29, pp. 1809-1817.
- [19] Sen, Z (2009), Global warming threat on water resources and environment: a review, *Environmental Geology*, Vol. 57, pp. 321-329.
- [20] Shah, F A (2015), Co-digestion, pretreatment and digester design for enhanced Methanogenesis. *Renewable and Sustainable Energy Reviews*, Vol. 42, pp. 627-642.
- [21] Shahnaz, A et al (2013), Simulation and introduction of a CHP plant in a Swedish biogas system. *Renewable Energy*, Vol. 49, pp. 242-249.
- [22] Surendra, K C et al (2014), Biogas as a sustainable energy source for developing countries: opportunities and challenges, *Renewable and Sustainable Energy Reviews*, Vol. 31, pp. 846-859.
- [23] Teghammar, A et al (2012), Enhanced biogas production from rice, straw, triticale straw and soft weed sprout by NMMO pretreatment, *Biomass and Bioenergy*, Vol. 36, pp. 116-120.
- [24] Thassitou P K and Arvanitoyannis I S (2001), Bioremediation: a novel approach to food waste management, *Trends in Food Science and Technology*, Vol. 12, pp. 185-196.
- [25] Vavilin, V A et al (1996), A description of hydrolysis kinetics in anaerobic degradation of particulate organic matter, *Bioresource Technology*, Vol. 56, No. 2, pp. 229-237.
- [26] Vienna University (2012), Promotion of biomethane and its market development through local and regional partnerships, Website: http://www.aile.asso.fr/wpcontent/uploads/2012/06/wp3-1-1_technologyreview_english.pdf.
- [27] Wellinger, A et al, The Biogas Handbook: Science, Production and Applications. Woodhead publishing series in energy, no. 52. ISBN: 978-0-85709-011-9.
- [28] Won Kang, D (2012), The effect of firing biogas on the performance and operating characteristics of simple and recuperative cycle gas turbine combined heat and power systems, *Applied Energy*, Vol. 93, pp. 215-228.
- [29] Yingjian, L et al, Operation proposal and efficiency analysis of direct-fired absorption chillers biogas produced in the brewer.
- [30] Zhang, Y H P (2008), reviving the carbohydrate economy via multiproduct lignocellulose biorefineries, *Journal of Industrial Microbiology and Biotechnology*, Vol. 35, No. 5, pp. 367-375.

Fundamental Study of Simple Prediction Method for Temperature Drop at Contact Portion of Solids with Thin Disk-Like Protrusion

Taewan Do ¹, Toshio Tomimura ² and Yasushi Koito ³

- 1 *Department of Advanced Mechanical Systems, Graduate School of Science and Technology, Kumamoto University, Kurokami, 2-39-1, Kumamoto 860-8555, Japan.
e-mail: taewan8933@naver.com*
 - 2 *Division of Energy Science, Faculty of Advanced Science and Technology, Kumamoto University, Kurokami, 2-39-1, Kumamoto 860-8555, Japan. e-mail: tomi@mech.kumamoto-u.ac.jp*
 - 3 *Division of Energy Science, Faculty of Advanced Science and Technology, Kumamoto University, Kurokami, 2-39-1, Kumamoto 860-8555, Japan. e-mail: koito@gpo.kumamoto-u.ac.jp*
-

ABSTRACT: Lots of experimental and theoretical studies have been done so far on the thermal contact resistance (TCR), that is, the temperature drop at the contact interface of solid materials. And, as is well known, the degree of TCR depends strongly on the surface conditions of the solid and the nominal contact pressure applied on the contact interface. Most of the fundamental studies have been conducted based on a flat surface with roughness. However, practically, solid surfaces have waviness with a height of tens to hundreds of microns, and it is strongly desired to develop a simple prediction method for TCR of a wavy surface with roughness. In this study, one-dimensional analysis has been carried to develop such a method. As the first stage, a contact surface with a thin disk-like protrusion having a height of 10 to 50 μm has been introduced as a basic model to simulate the surface waviness. Two kinds of one-dimensional models for estimating the temperature drop at the contact portion have been proposed. The one is a simple horizontal division case, and the other is a simple vertical division case. Furthermore, a series of TCR measurements have been performed by using test cylinders corresponding to the abovementioned contact surface. By comparing the estimated and measured results, the application limits of the simple horizontal and vertical division cases have been clarified. That is, the simple horizontal division case underestimates the temperature drop, whereas the simple vertical division case overestimates it. As a result, it has been shown that introducing the effect of contraction and expansion of heat flow to the present model is essential to estimate TCR correctly.

Keywords: Thermal contact resistance, Roughness, Waviness, One-dimensional analysis

INTRODUCTION

Concerning electronic equipment with high heat fluxes, it is well known that heat transfer modes of heat conduction, convection, and thermal radiation play an important role in heat removal from high-temperature regions in such equipment. In addition to those three modes, thermal contact resistance (TCR) can be cited as the forth important heat transfer mode.

And each mode rarely appears alone, and in actual equipment, some of them are complicatedly coupled, and appear at the same time.

A lot of theoretical and experimental studies have done so far on TCR or thermal contact conductance (TCC, which is defined as the reciprocal of TCR) mainly targeting flat rough surfaces made of copper, aluminium, stainless steel, brass

and so on. However, as pointed out in the past by Fletcher [1], Torii and Yanagihara [2], Torii [3], Okada and Matsumoto [4], and Madhusudana [5] et al., there are many differences in the predicted or measured TCRs. On the other hand, concerning to the wavy rough surfaces, the authors [6] have performed theoretical and experimental studies introducing a contact surface model approximated by a part of the spherical surface, which includes the unit cell model proposed by Tachibana [7] and Sanokawa [8]. And as a result, it is shown that (1) Sanokawa's equation can be successfully extrapolated to the lower mean nominal contact pressure of 0.1–1.0 MPa, and further, (2) Introduction of constriction resistance due to the macroscopic waviness seems to be necessary for a more accurate evaluation of the temperature drop.

In this study, based on a contact surface with a thin disk-like protrusion having a height of 10 to 50 μm , one-dimensional analysis has been carried to develop a simple prediction method for thermal contact resistance (TCR) or the temperature drop at contact portion of solids with waviness. In particular, two kinds of models for estimating the temperature drop have been proposed. The one is a simple horizontal division case, and the other is a simple vertical division case. Furthermore, a series of TCR measurements have been performed by using test cylinders corresponding to the abovementioned contact surface. And by comparing the estimated and measured results, the application limits of the simple horizontal and vertical division cases have been discussed.

ONE-DIMENSIONAL SIMPLE ANALYSIS OF THERMAL CONTACT RESISTANCE

Microscopic Roughness Model

Figure 1 shows the concept of the unit cell model [7]. In general, the surface-to-surface contact of solid "1" and solid "2" is made by protrusions due to roughness as shown in Fig. 1(a). And then, this contact state is modelled by lots of cylindrical protrusions distributed uniformly over the contact surface as shown in Fig. 1(b). As is easily understood from the figure, the

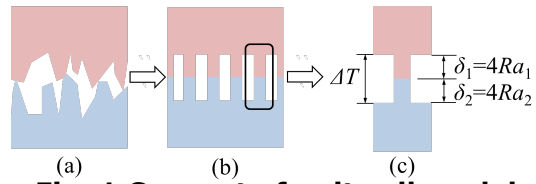


Fig. 1 Concept of unit cell model

temperature drop ΔT over the whole contact interface due to roughness can be estimated based on the unit cell model shown in Fig. 1(c). Here, δ_1 and δ_2 are the maximum height of roughness of each solid, and are given by four times the centreline average surface roughness Ra_1 and Ra_2 of each solid [9]. In this model, it is assumed that all the isothermal planes are parallel to the contact interface.

Based on this model, the following type of Eq. (1) for estimating the temperature drop ΔT at the contact interface of flat surfaces with roughness was given by Tachibana [7] and Sanokawa [8].

$$\Delta T = \frac{Q}{A} \cdot \frac{1}{k} \quad (k = k_s + k_{av}) \quad (1)$$

Where,

$$k_s = \frac{1}{\frac{\delta_1}{\lambda_1} + 2.3 \times 10^{-5} \left(\frac{1}{\lambda_1} + \frac{1}{\lambda_2} \right) + \frac{\delta_2}{\lambda_2}} \cdot \frac{p_m}{H_{\min}} \quad (2)$$

$$k_{av} = \frac{\lambda_a}{\delta_1 + \delta_2} \left(1 - \frac{p_m}{H_{\min}} \right) \quad (3)$$

Here, Q is the heat rate of flowing through the whole contact interface, A the whole heat transfer area, p_m the mean nominal contact pressure defined by dividing the load applied to the contact interface by the area A , H_{\min} the smaller value of the Brinell or Vickers hardness of solids 1 and 2, λ_1 , λ_2 and λ_a , the thermal conductivity of solid 1, solid 2 and air, respectively.

In the present study, this unit cell model and the resulting Eq. (1) are applied the circular protrusion region having a height of tens of microns at the contact surface.

Macroscopic Waviness Model

Figure 2 shows a simple horizontal division case of a macroscopic waviness model. The concept of the present horizontal division case is quite similar to that of the unit cell model. In this model, two cylinders "1" and "2" with the diameter $2r_o$, the length l , and the thermal conductivity λ , which have thin disk-like protrusions of

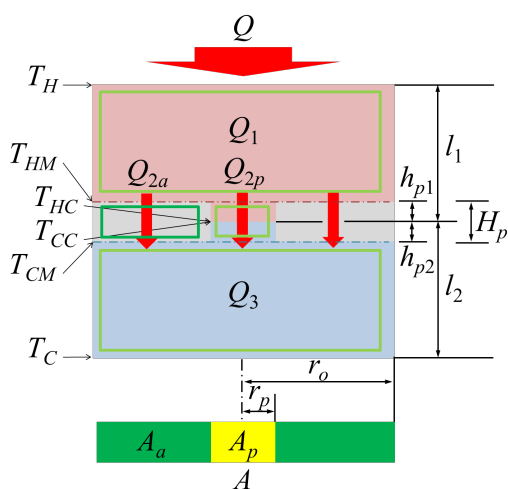


Fig. 2 Simple horizontal division case

the diameter $2r_p$ and the height h_p , are in contact with the axial load F . The top surface of the upper cylinder "1" is heated with the heat rate Q over its cross sectional area A . On the other hand, the bottom surface of the lower cylinder "2" is kept at the temperature T_c uniformly. The heat rate Q_1 flowing axially through the upper cylinder is given by the following equation.

$$Q_1 = \frac{T_H - T_{HM}}{l_1 - h_{p1}} \cdot A \cdot \lambda_1 \quad (4)$$

Here, T_H is the top surface temperature of the cylinder, and T_{HM} is the temperature at the root of the protrusion.

Next, the heat rate Q_2 at the contact portion by the upper and lower protrusions is composed of the following two components, that is the heat rate Q_{2a} flowing through the annular air layer with the heat transfer area A_a and the thickness $H_p (=h_{p1} + h_{p2})$, and the heat rate Q_{2p} flowing through the protrusions with the heat transfer area A_p and the thermal contact resistance given by Eq. (1). Accordingly, the following equation is obtained as the heat rate Q_2 .

$$Q_2 = A_p \frac{T_{HM} - T_{CM}}{\frac{h_{p1}}{\lambda_1} + \frac{1}{k} + \frac{h_{p2}}{\lambda_2}} + A_a \cdot \lambda_a \frac{T_{HM} - T_{CM}}{H_p} \quad (5)$$

Here, T_{CM} is the temperature at the root of the protrusion of the lower cylinder, and k is the thermal contact conductance at the contact interface of protrusions, and is composed of the sum of k_s and k_{av} given by Eqs. (2) and (3).

Concerning the heat rate Q_3 flowing axially through the lower cylinder is given by the following equation.

$$Q_3 = \frac{T_{CM} - T_C}{l_2 - h_{p2}} \cdot A \cdot \lambda_2 \quad (6)$$

In the present one-dimensional analysis, since all the heat rates Q_1 , Q_2 and Q_3 are the same with each other and are equal to the heat rate Q , the temperatures at each point can be given by the following equations under the conditions that Q and T_c are given.

$$T_H = T_C + Q \cdot (k_1 + k_2 + k_3) \quad (7)$$

$$T_{HM} = T_H - Q_1 \cdot \frac{l_1 - h_{p1}}{A \cdot \lambda_1} \quad (8)$$

$$T_{HC} = T_{HM} - Q_{2S} \cdot \frac{h_{p1}}{A_p \cdot \lambda_1} \quad (9)$$

$$T_{CC} = T_{HC} - Q_{2S} \cdot \frac{1}{A_p \cdot h} \quad (10)$$

$$T_{CM} = T_{HM} - Q_2 \frac{1}{A_p \cdot \frac{h_{p1}}{\lambda_1} + \frac{1}{k} + \frac{h_{p2}}{\lambda_2} + A_a \cdot \lambda_a \cdot \frac{1}{H_p}} \quad (11)$$

Here, T_{HC} and T_{CC} of Eqs. (9) and (10) are the surface temperatures at the upper and lower protrusions, respectively. In addition, k_1 , k_2 and k_3 included in Eq. (7) are given as follows;

$$k_1 = \frac{l_1 - h_{p1}}{A \cdot \lambda_1} \quad (12)$$

$$k_2 = \frac{1}{A_p \cdot \frac{1}{\frac{h_{p1}}{\lambda_1} + \frac{1}{k} + \frac{h_{p2}}{\lambda_2}} + A_a \cdot \lambda_a \cdot \frac{1}{H_p}} \quad (13)$$

$$k_3 = \frac{l_2 - h_{p2}}{A \cdot \lambda_2} \quad (14)$$

The temperature drop ΔT at the contact portion corresponding to the present measurements is evaluated by the temperature difference between T_{HM} and T_{CM} given by Eqs. (8) and (11).

Figure 3 shows a simple vertical division case of a macroscopic waviness model.

In this case, the heat rate Q is divided into two components Q_p and Q_a as shown in the figure. The former (Q_p) flows through the central part, that is, the upper cylinder → the upper protrusion → the contact interface → the lower protrusion → the lower cylinder.

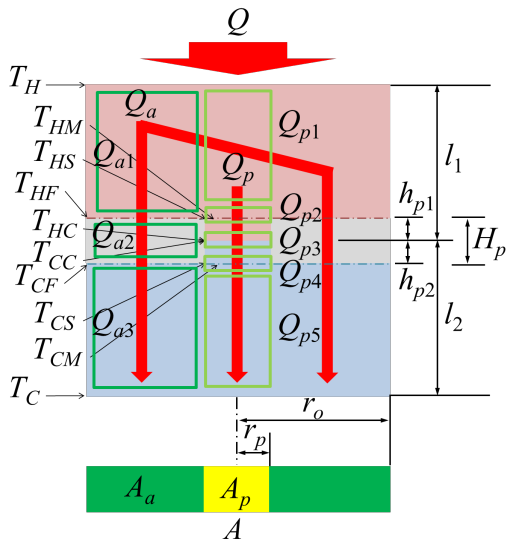


Fig. 3 Simple vertical division case

On the other hand, the latter (Q_a) flows through the peripheral part of the system in parallel, that is, the upper cylinder → the annular air layer → the lower cylinder. In the same way as the previous horizontal division case, by referring to the figure, and from the conservation conditions on the heat rates, that is, $Q = Q_p + Q_a$, $Q_p = Q_{p1} = Q_{p2} = Q_{p3} = Q_{p4} = Q_{p5}$, and $Q_a = Q_{a1} = Q_{a2} = Q_{a3}$, the temperatures at each point can be given by the following equations under the conditions that Q and T_C are given.

At the top of the upper cylinder,

$$T_H = T_C + Q \cdot \frac{1}{A_p \cdot k_4 + A_a \cdot k_5} \quad (15)$$

Here,

$$k_4 = \frac{1}{\frac{l_1 - h_{p1}}{\lambda_1} + \frac{h_{p1}}{\lambda_1} + \frac{1}{h} + \frac{h_{p2}}{\lambda_2} + \frac{l_2 - h_{p2}}{\lambda_2}} \quad (16)$$

$$k_5 = \frac{1}{\frac{l_1 - h_{p1}}{\lambda_1} + \frac{H}{\lambda_a} + \frac{l_2 - h_{p2}}{\lambda_2}} \quad (17)$$

In the central part of the cylinder,

$$T_{HS} = T_H - Q_{S1} \cdot \frac{l_1 - h_{p1}}{A_p \cdot \lambda_1} \quad (18)$$

$$T_{HC} = T_{HS} - Q_{S2} \cdot \frac{h_{p1}}{A_p \cdot \lambda_1} \quad (19)$$

$$T_{CC} = T_{HC} - Q_{S3} \cdot \frac{1}{A_p \cdot h} \quad (20)$$

$$T_{CS} = T_{CC} - Q_{S4} \cdot \frac{h_{p2}}{A_p \cdot \lambda_2} \quad (21)$$

In the peripheral part of the system,

$$T_{HF} = T_H - Q_{F1} \cdot \frac{l_1 - h_{p1}}{A_a \cdot \lambda_1} \quad (22)$$

$$T_{CF} = T_{HF} - Q_{F2} \cdot \frac{H}{A_a \cdot \lambda_a} \quad (23)$$

Here, T_{HS} given by Eq. (18) is the root temperature of the protrusion of the upper cylinder, and T_{HF} given by Eq. (22) is the bottom surface temperature of the upper cylinder. Similarly, T_{CS} given by Eq. (21) is the root temperature of the protrusion of the lower cylinder, and T_{CF} given by Eq. (23) is the top surface temperature of the lower cylinder, respectively.

The temperature drop ΔT at the contact portion corresponding to the present measurements is evaluated by the mean temperature difference between T_{HM} and T_{CM} obtained by the following equations.

$$T_{HM} = T_H - \frac{A_p \cdot (T_H - T_{HS}) + A_a \cdot (T_H - T_{HF})}{A} \quad (24)$$

$$T_{CM} = T_C + \frac{A_p \cdot (T_{CS} - T_C) + A_a \cdot (T_{CF} - T_C)}{A} \quad (25)$$

MEASUREMENT OF THERMAL CONTACT RESISTANCE

Figure 4 shows a schematic of the apparatus for TCR measurements. The top surface of the upper cylinder (2) is heated by a film heater (5). On the other hand, the bottom surface of the lower cylinder (1) is kept at low temperature using a cooling block (7). Both the upper and lower cylinders are covered with styrene foam insulation material with a thickness of 50 mm (4). On the film heater (5), an acrylic resin block with a thickness of 20

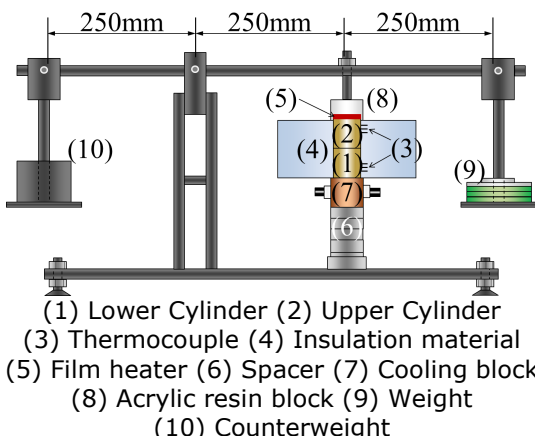


Fig. 4 Schematic of TCR measuring apparatus

mm thick (8) is placed for preventing heat dissipation from back side of the heater. To measure the axial temperature distribution of the cylinder and to obtain the temperature drop ΔT at the contact portion (that is, TCR), three sheathed thermocouples are inserted in the side surface of each cylinder.

The axial load F is applied to the cylinders by lever and hanging weight arrangement. And the present TCR measurements have been conducted under the mean nominal contact pressure $p_m = 0.1 - 1.0$ MPa, which is defined by F/A . Here, A is the cross sectional area of the cylinder.

As shown in the figure, a counterweight (10) is set at the opposite end of the lever to realise the no-load condition against the cylinders under the conditions that the weight (9) is not loaded.

Figure 5 shows a schematic of the tested cylinder with a thin disk-like protrusion.

The cylinder is made of an aluminium alloy (A5052), and the diameter $2r_o$ and the length l are 30 mm and 45 mm, respectively. There are three holes of 0.55 mm diameter and 10 mm depth on the side of the cylinder for axial temperature measurements, and are located at 22, 29, and 36 mm from the contact surface. In each hole, a copper-constantan sheathed thermocouple of 0.5 mm diameter is inserted by applying thermally conductive silver paste.

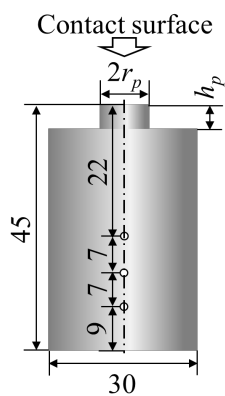


Fig. 5 Schematic of tested cylinder

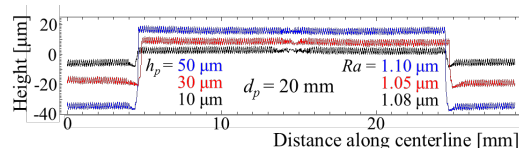


Fig. 6 Shape and roughness of contact surface with thin disk-like protrusion

Figure 6 shows the shape and roughness of contact surface with a thin disk-like protrusion measured by using a stylus profilometer. In the figure, each line shows the measured shape and roughness of contact surface for the diameter of the protrusion $d_p = 20$ mm, and the height $h_p = 10$ μm (black, $R_a = 1.08 \mu\text{m}$), 30 μm (red, $R_a = 1.05 \mu\text{m}$), and 50 μm (blue, $R_a = 1.10 \mu\text{m}$), respectively. Here, R_a is the centreline average surface roughness.

RESULTS AND DISCUSSION

Figures 7 and 8 show the relation between the temperature drop ΔT at the contact portion and the mean nominal contact pressure p_m , which are obtained by applying the one-dimensional analysis to the simple horizontal and vertical division cases, respectively. In these figures, the analysis results for the protrusion height $h_{p1} = h_{p2} = 10, 30$, and 50 μm are indicated by the solid, broken, and dash-dotted lines, respectively.

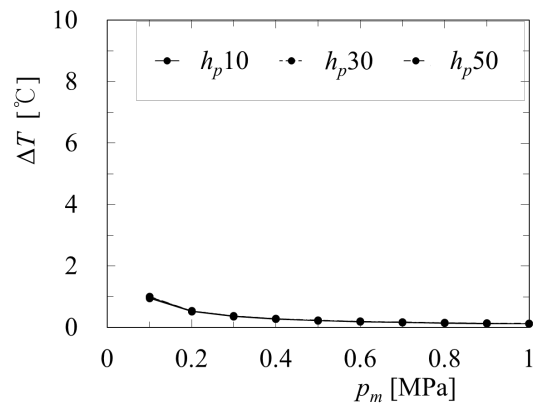


Fig. 7 Relation between ΔT and p_m (Horizontal division case)

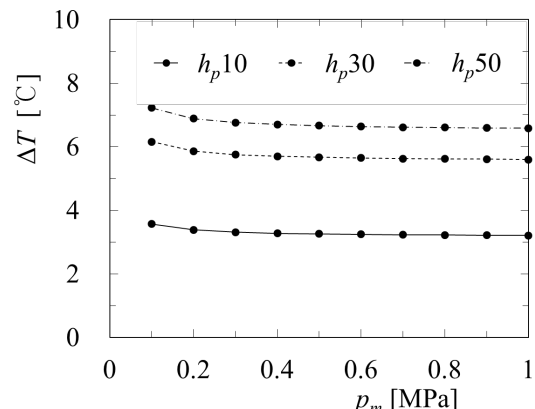


Fig. 8 Relation between ΔT and p_m (Vertical division case)

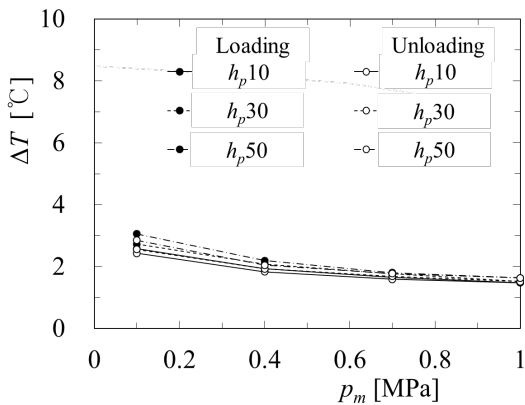


Fig. 9 Relation between ΔT and p_m (Measured results)

As seen from Fig. 7, when the cylinder is divided horizontally against its top or bottom surface, the height h_p has almost no effect on the temperature drop ΔT . On the other hand, as shown in Fig. 8, when the cylinder is divided vertically, that is parallel to its axis, ΔT increases with h_p mainly because of increase in the thermal resistance of the air layer existing in the outer peripheral portion of the protrusions. Figure 9 shows the measured results on the relation between ΔT and p_m . In the figure, the closed and open circles indicate the loading and unloading processes, respectively.

vertical division cases. From the above discussion, it is expected that more correct temperature drop ΔT could be estimated by introducing the effect of contraction and expansion of heat flow through the contact portion of the protrusions. -That is, the temperature drop ΔT would be increased in the simple horizontal case due to increase in TCR by the contraction and expansion effect of heat flow. Conversely, the ΔT would be decreased in the simple vertical case by relaxation of TCR.

CONCLUSIONS

For the purpose of developing a simple prediction method for thermal contact resistance (TCR) or the temperature drop at contact portion of solids with waviness, one-dimensional analysis and a series of measurements using a contact surface with a thin disk-like protrusion have been performed. And as a result, the following findings have been obtained.

- (1) In the case that the cylinder with a thin disk-like protrusion is divided horizontally against its top or bottom surface, the height h_p of the protrusion has almost no effect on the temperature drop ΔT at the contact portion (that is, TCR).
- (2) In the case that the cylinder is divided vertically, that is parallel to its axis, ΔT increases with h_p mainly because of increase in the thermal resistance of the air layer existing in the outer peripheral portion of the protrusions.
- (3) The measured temperature drop ΔT lies between those obtained by the simple horizontal and vertical division cases. That is, the simple horizontal division case underestimates the measured temperature drop, whereas the simple vertical division case overestimates it.
- (4) The introduction of the contraction and expansion effect of heat flow to the present model would be essential for predicting the temperature drop ΔT at the contact portion correctly.,

REFERENCES

- [1] L.S. Fletcher. (1988), Recent Developments in Contact Conductance Heat Transfer, Journal of Heat Transfer, Vol. 110, pp. 1059-1070.
- [2] K. Torii. J. Itizo. (1989), Thermal contact resistance in space environment, Journal of the Heat Transfer Society of Japan, Vol. 28, pp. 79-99.
- [3] K. Torii. (1993), Heat Transfer Across the Solid Interface Governed by Its Microscopic Surface-Structure: Interface between Macro-and Micro-Mechanics, Journal of the Japan Society of Mechanical Engineers, Vol. 96, pp. 198-203.
- [4] M. Okada and K. Mastumoto. (1993), Progress in Heat Conduction and Contact Conductance Heat Transfer, Journal of Heat transfer Society of Japan, Vol. 32, pp. 25-36.
- [5] C.V. Madhusudana. (1996), Thermal Contact Conductance, Book.
- [6] T. Tomimura. Y. Takahashi. T. Do. K. Shigyo. and Y. Koito. (2014), Simple evaluation method for temperature drop at contact interface between rough surfaces under low contact pressure conditions, IOP Conference Series: Materials Science and Engineering, Vol. 61, 012040, 757-899X_61_1_012040.pdf
- [7] F. Tachibana. (1952), The Investigation of Thermal Contact Resistance, Journal of the Japan Society of Mechanical Engineers, Vol. 55, pp. 102-107.
- [8] K. Sanokawa. (1967), Heat Transfer between Metallic Surfaces in Contact : 4th Report, The Effect of Both the Shape of Surface Roughness and Waviness, and the Approximate Method of Calculating Thermal Contact Resistance, Transactions of the Japan Society of Mechanical Engineers, Vol. 33, pp. 1131-1137.
- [9] JSME Data Book: Heat Transfer (3rd Edition) (1983), p. 176. (In Japanese)

Mechanical behavior of compression molded glass microballoon/HDPE syntactic foams

Jayavardhana M L¹, Mrityunjay Doddamani²

1 Department of Mechanical Engineering, National Institute of Technology Karnataka, Surathkal, Mangalore 575025, India. email:gautham879@gmail.com

2 Department of Mechanical Engineering, National Institute of Technology Karnataka, Surathkal, Mangalore 575025, India.
email: mrdoddamani@nitk.edu.in

ABSTRACT: Mechanical behavior of glass microballoon (GMB) reinforced high density polyethylene (HDPE) matrix syntactic foams is investigated under tensile mode. GMB's are blended in HDPE using brabender and subsequently compression molded to form the syntactic foam sheets. GMBs with true particle density 200 kg/m³ are varied by 0, 20, 40 and 60 vol. % in HDPE matrix. With increase in microballoon content modulus is increases while strength decreases. Syntactic foams present lower fracture strain as compared to neat HDPE.

Keywords: GMB, HDPE, syntactic foam, tensile, compression molding.

1 INTRODUCTION

Hollow particles are light weight fillers when embedded with a matrix resin forms syntactic foam (SF). SF's are widely used in automotive, aerospace and marine applications owing to superior specific properties leading to weight saving potential [Sauvant-Moynot V. et al. (2006), Gupta. N and Woldesenbet E. (2003), Gupta N. et al. (2006), Woldesenbet. E and Peter S. (2007)]. Foams are classified as open cell and closed cell. Open cell foam has low compressive strength and modulus [Gupta N. et al. (2010), Gupta N. et al. (2008)]. Closed cell foam has better mechanical properties compared to their open cell counterparts. Syntactic foams are prepared by dispersing rigid hollow particles in the matrix material [Puterma M. et al. (1998)]. Structure of syntactic foam exhibits higher strength, lower density and moisture absorption compared to neat matrix [Gupta. N and Woldesenbet E. (2004)]. Usage of syntactic foams as core material in sandwich core applications ensures high rigidity and compressive strength of the sandwich structures at lower weights [Gupta N. et al. (2002)]. Mechanical properties of syntactic foam [Woldesenbet E and Peter S. (2007)],

Gladysz G. M and Chawla K. K. (2006), Choqueuse D and Davies P. (2008)] and their sandwich structures are available in recent past [Gupta N and Woldesenbet E. (2004), Choqueuse D and Davies P. (2008), Banhart J.(2001)].

Properties of these foams strongly depend on type of hollow filler used. Commercially available hollow fillers like glass, ceramic and phenolic fillers are used in fabricating most of the syntactic foams [Rutz B. H and Berg J. C. (2010), Shabde V. et al. (2006), Huang Y. J. (2010)]. Glass microballoon a versatile inorganic filler compared to other available filler are found to be promising with improved dimensional stability, increased impact strength, smoother surface finish, greater thermal insulation, easier machinability, faster cycle times and overall cost savings [Palumbo M. et al. (1996), Tres P. A. (2007), Belle B. V. (2002)]. Glass microballoon reinforced thermoset matrix material shows an improvement in mechanical and thermal properties [Rizzi E. et al. (2000), Wouterson E. M. et al. (2005), Kishore (2005), Maharsia R. et al. (2006), Tagliavia G. et al. (2012), Karthikeyan C. S. et al. (2001), H. S Kim and M. A Khamis (2001), Y. Hu et al. (2013)]. Filling GMB's in thermoplastics like HDPE results in saving of expensive polymer in addition to

weight saving and improvements in mechanical properties. High density polyethylene is a thermoplastic which is most commonly used in application of storage bins and house wares.

Thermoplastic matrix syntactic foams are promising in industrial applications of molded compounds. In the present work, GMB/HDPE syntactic foam composite is fabricated by Brabender and compression molding process. GMBs are blended with HDPE in 20, 40 and 60 by vol. %. Neat HDPE samples are also fabricated for comparison. All the samples are characterized for tensile behavior.

2 MATERIALS AND METHODS

2.1 Materials

HDPE having grade of 180M50 (Indian Oil Corporation Ltd., Mumbai, India) having a melt flow index of 20 g/10 min is used as a matrix material. Glass microballoon (SID-200Z) having a true particle density of 200 Kg/m³ supplied by Trelleborg, USA is used as filler. Matrix and fillers are used in as received condition.

2.2 Sample Preparation

GMB/HDPE syntactic foam sheets are fabricated by two processes brabender mixing and compression molding. Proportional ratio of GMB and HDPE are blended at 165°C temperature in brabender with twin screws rotating at 30 rpm. GMB/HDPE blend is then fed in to the compression molding machine having mold cavity of 150×150×3.2 mm. GMB/HDPE blend compressed at 190°C temperature and 100 bars pressure and later allowed to cool in the mold itself for 30 minutes. Three syntactic foams are fabricated with varying filler content of 20, 40 and 60.vol%. Neat resin samples are also casted with similar processing condition for comparison. The samples are trimmed from the prepared sheet with a dimension of 100×13×3.2 mm to carry out tensile test. Samples are coded according to convention HYYY-ZZ, where H denotes the HDPE matrix, YYY and ZZ are the density and volume fraction of microballoons.

2.3 Density Measurement

ASTM D792 - 13 standard is used for estimating densities of all the samples.

The densities of five specimens are measured and the average values and standard deviations are reported.

2.4 Tensile Test

As per ASTM D638-10 tensile test is conducted with a load cell of 2KN and a constant deformation rate of 5 mm/min using Tensometer (Kudale instruments private limited pune, india, MODEL PC2000). The acquired load and displacement data are used to calculate the stress and strain values, respectively. Average modulus and strength values of five specimens for each composite type are reported.

3 RESULTS AND DISCUSSION

3.1 Density

Experimental density and theoretical density are calculated for the GMB/HDPE sheets. Experimental densities are measured as per ASTM D792-13 standard and theoretical densities are calculated by rule of mixture. GMB/HDPE sheet has negligible matrix porosity as evident from micrograph of H200-60 (Fig. 1). Difference in experimental densities and theoretical density which quantifies the microballoon breakage during manufacturing is presented in

Table 1. From

Table 1 it is clearly observed that filler breakage increases with increasing GMB content. At higher filler loadings presence of matrix is minimal implying weight saving potential of the developed syntactic foams. H200-60 shows higher filler breakage. This might be due to increased particle to particle interaction at higher filler contents.

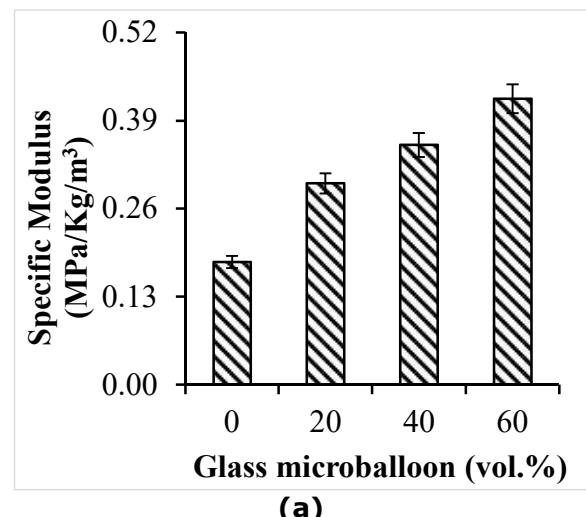
3.2 Tensile Behavior

Stress-strain response is presented in Fig. 2. Neat HDPE shows a linear elastic region followed by a plastic deformation leading to fracture at 12.39% strain (Fig. 2). Stress strain profile of GMB/HDPE syntactic foam is observed same as that of neat HDPE. Inclusion of glass microballoon to the matrix exhibits nominal decrease in fracture strain as observed in Table 2. GMB being brittle in nature decreases fracture strain of the composite system. Increasing filler content shows decrease in

fracture strain by 32.6, 55.44 and 81.19% compared to HDPE as noted from Fig. 2.

Tensile modulus, UTS, fracture strength and fracture strain of syntactic foams are listed in Table 2. Modulus shows an increasing trend with an increase in GMB content. Stiff GMB particle increases the stiffness of the composite. H200-60 foam with higher filler breakage shows tensile modulus 115.5% which is higher than neat HDPE. Several fractured fragments of GMB act as stress concentrators decreasing the load bearing capability of such foams. Micrograph of syntactic foam samples after the test is presented in Fig. 3. More intact particles are observed in H200-60 as compared to H200-20. From Fig. 3 it is clearly observed that more plastic deformation of HDPE is seen in H200-60 compared to H200-20. Similar failure features are previously observed in epoxy/glass hollow particle syntactic foam composites [Gupta. N and R. Nagorny (2006), Gupta N. et al. (2002)]. Fracture strength and strain are reduced with an increase in filler

content. Poor interfacial bonding and the lower particle survival are the reasons for such observations. Ultimate tensile strength is highest for neat HDPE compared to their syntactic foams. UTS of H200 decreases by 9.3, 35.71 and 62.02% respectively compared to HDPE for varying filler content (Fig. 4 Strength for HDPE and syntactic foams).



(a)

). Increasing filler content decreases ultimate strength owing to poor interfacial bonding between the constituents implying non effective load transfer between them. Surface modification of these constituents might improve strength.

Fig. 5 shows the Specific modulus and strength of HDPE and GMB/HDPE syntactic foams. Virgin HDPE shows lowest specific modulus 0.18 (MPa/Kg/m³) compared to GMB/HDPE sheets. Modulus is increased with an addition of filler content. Specific modulus increased by 66.66, 94.44 and 133.33% for varying filler content. Increase in filler content reduces the density, increases specific modulus indicating usage of these foams in potential weight saving applications. Specific strength of virgin HDPE shows maximum value 23.46 (MPa/Kg/m³) × 10⁻³ compared to H200 sheets. Addition of filler content lowers specific strength. Specific strength decreases in the range 5.5-57.67% compared to neat resin.

Table 1 shows GMB breakage is higher at higher filler loadings. Breakage of glass

leads to loss of porosity in the matrix resin affecting specific strength. Optimization of Brabender processing parameters to minimize filler failure might improve specific strength. Highest modulus and strength are observed for H200-60 and neat HDPE. Nevertheless, developed thermoplastic syntactic foam presents promising applications, if modulus is the design criteria.

4 CONCLUSIONS

The following conclusions are deduced from this study:

- Modulus increases with an increase in filler content.
- Strength is maximum for neat HDPE than compared to syntactic foams.
- Specific modulus shows developed GMB/HDPE thermoplastic syntactic

foam to be a promising material in weight sensitive applications.

ACKNOWLEDGMENTS

Authors acknowledge TERI Bangalore, Karnataka, India for providing Brabender facility for preparing the blends. Authors thank the ME department of NITK Surathkal for providing the support.

REFERENCES

- [1] Banhart J (2001), Manufacture, characterisation and application of cellular metals and metal foams, *Progress in Materials Science*, Vol.46, pp.559-632.
- [2] Belle, B V (2002), Advances in high-temperature syntactic foam technology for offshore systems, *Offshore Technology Conference*. Houston, USA' Paper 14120-MS.
- [3] Choqueuse D, and Davies P (2008), Ageing of composites in underwater applications in 'Ageing of composites' (eds.: Martin R.), Woodhead Publishing, Cambridge, pp.467-498.
- [4] Gladysz G M, and Chawla K K (2006), Syntactic and composite foams, *Proceedings of an engineering conferences international (ECI) conference Journal of Materials Science*, Vol.41, pp.3959-3960.
- [5] Gupta N, and Woldesenbet E (2003), Hygrothermal studies on syntactic foams and compressive strength determination , *Composite Structures*, Vol.61, pp.311-320.
- [6] Gupta N, and Woldesenbet E (2004), Microballoon wall thickness effects on properties of syntactic foams, *Journal of Cellular Plastics*, Vol. 40, pp. 461-482.
- [7] Gupta, N and R Nagorny (2006), Tensile properties of glass microballoon-epoxy resin syntactic foams, *Journal of Applied Polymer Science*, Vol.102(2), pp.1254-1261.
- [8] Gupta, N et al (2006), Characterization of mechanical and electrical properties of epoxyglass microballoon syntactic composites, *Ferroelectrics*, Vol.345, pp.1-12.
- [9] Gupta, N et al (2008), Characterization of vinyl ester-glass microballoon syntactic foams for marine applications, *Proceeding of 22nd Annual Technical Conference of American Society for Composites*. Seattle, USA' paper#072.
- [10] Gupta, N et al (2010), Comparison of tensile and compressive characteristics of vinyl ester/glass microballoon syntactic foam, *Composites Part B: Engineering*, Vol. 41(3), pp. 236-245.
- [11] Gupta,N et al (2002), Compressive fracture features of syntactic foams-microscopic examination, *Journal of Materials Science*, Vol.37(15), pp.3199-3209.
- [12] Gupta,N et al (2002), Compressive fracture features of syntactic foams-Microscopic examination, *Journal of Materials Science*, Vol.37, pp.3199-3209.
- [13] H S Kim and M A Khamis(2001), Fracture and Impact Behaviours of Hollow Micro-Sphere/Epoxy Resin Composites, *Composites Part A*, Vol.32(.9), pp.1311-1317.
- [14] Huang, Y J (2010), Enhancing specific strength and stiffness of phenolic microsphere syntactic foams through carbon fiber reinforcement, *Polymer Composites*, Vol. 31(2), pp.256-262.
- [15] Karthikeyan, C S et al (2001), Effect of Absorption in Aqueous and Hygrothermal Media on the Compressive Properties of Glass Fiber Reinforced Syntactic Foam, *Journal of Reinforced Plastics and Composites*, Vol. 20(11), pp.982 - 993.
- [16] Kishore (2005), Gradient syntactic foams: Tensile strength, modulus and fractographic features, *Materials Science and Engineering A*, Vol.412, pp.153-158.
- [17] Maharsia, R et al (2006), Investigation of flexural strength properties of rubber and nanoclay reinforced hybrid syntactic foams, *Materials Science and Engineering A*, Vol. 417(1-2), pp.249 - 258.
- [18] Palumbo,M et al (1996), On the compressive elasticity of epoxy resins filled with hollow glass microspheres, *Journal of Applied Polymer Science*, Vol. 60(1), pp.47.
- [19] Puterma, M et al (1998), Syntactic foams I. Preparation, structure and properties, *Journal of Cellular Plastics*, Vol.16, pp.223-229.
- [20] Rizzi, E et al (2000), Mechanical behavior of a syntactic foam: experiments and Modeling, *International Journal of Solids and Structures*, Vol. 37(40), pp.5773 - 5794.
- [21] Rutz B H, and Berg J C (2010), A review of the feasibility of lightening structural polymeric composites with voids without compromising mechanical properties, *Advance Colloid Interface Science*, Vol.160(1-2),pp.56-75.
- [22] Sauvant-Moynot, V et al (2006), Hydrolytic ageing of syntactic foams for thermal insulation in deep water, *Degradation mechanisms and water uptake model Journal of Materials Science*, Vol. 41, pp.4047-4054.
- [23] Shabde,V et al (2006), Experimental determination of the thermal conductivity of three-phase syntactic foams, *Journal of Material Science*, Vol. 41(13),pp.4061-4073.
- [24] Tagliavia, G et al (2012), Influence of moisture absorption on flexural properties of syntactic foam, *Composites Part B: Engineering*, Vol. 43(2), pp.115-123.
- [24] Tres, P A (2007), Hollow glass microspheres stronger spheres tackle injection molding, *Plastic Technology*, Vol. 53(5), pp.82-7.
- [25] Woldesenbet E, and Peter S (2007), Volume fraction effect on high strain rate properties of syntactic foam composites, *Journal of Materials Science*, Vol.10, pp. 3065-3074.
- [26] Wouterson, E M et al (2005), Specific properties and fracture toughness of syntactic foam: Effect of foam microstructures, *Composites Science and Technology*, Vol. 65(11-12), pp.1840 - 1850.
- [27] Y, Hu et al (2013), Behavior of high density polyethylene and its nanocomposites under static and dynamic compression loading, *Polymer Composites*, Vol. 34 (3), pp. 417-425.

Table 1 Density values of neat HDPE and their syntactic foams.

Foam type	GMB (vol. %)	Density(g/cm ³)		Microballoon Breakage (%)
		Theoretical	Experimental	
H	0	0.950	0.954±0.001	0.00
H350-20	20	0.800	0.916±0.004	12.71
H350-40	40	0.650	0.896±0.006	27.51
H350-60	60	0.500	0.886±0.007	43.57

Table 2 Average modulus and strength of HD PE and their syntactic foams.

Foam type	Modulus (MPa)	UTS (MPa)	Fracture strength (MPa)	Fracture strain (%)
H	173.03±3.46	22.40±0.45	22.30±0.45	12.39±0.25
H350-20	272.17±5.44	20.30±0.41	19.94±0.40	8.34±0.17
H350-40	317.70±6.34	14.40±0.29	14.43±0.29	5.52±0.11
H350-60	374.16±7.48	8.8±0.18	8.49±0.17	2.33±0.04

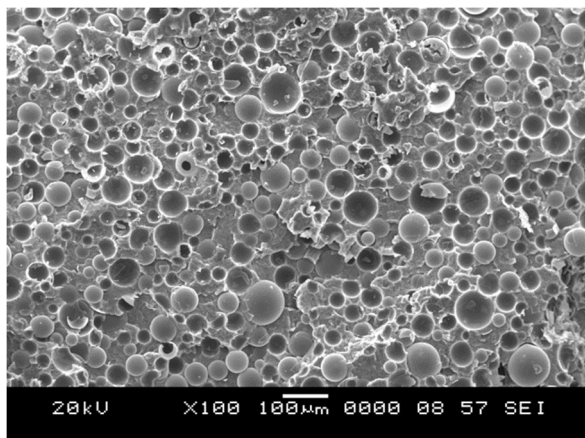
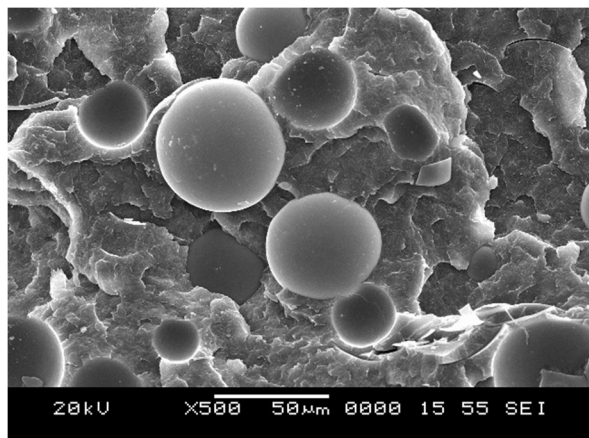
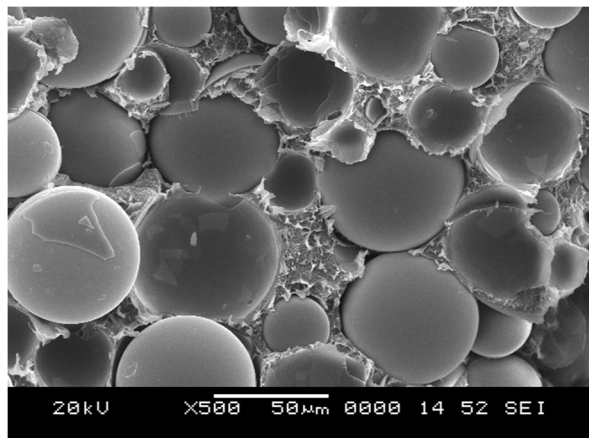


Fig. 1 SEM image of as cast freeze fractured H200-60 syntactic foam.



(a)



(b)

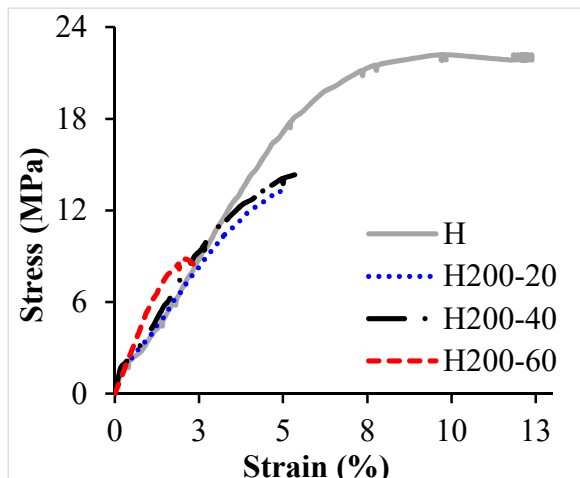


Fig. 2 Tensile stress strain curves for Neat HDPE, H200-20, H200-40 and H200-60 syntactic foams.

Fig. 3 SEM image of fractured surface of (a) H200-20 and (b) H200-60 syntactic foam.

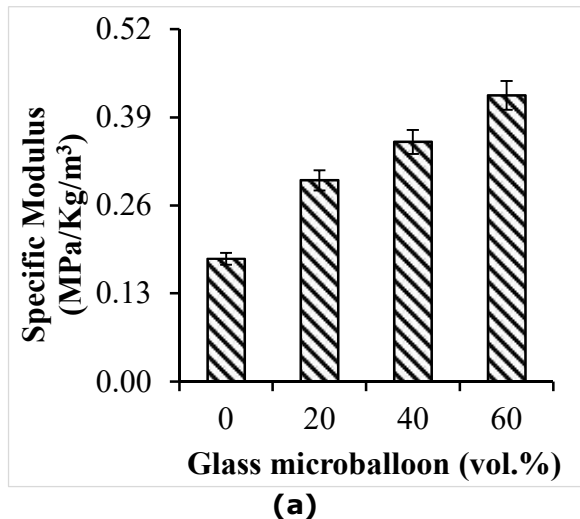
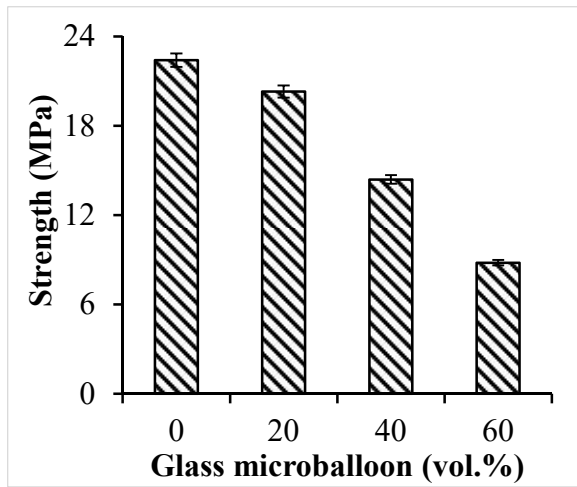


Fig. 4 Strength for HDPE and syntactic foams.

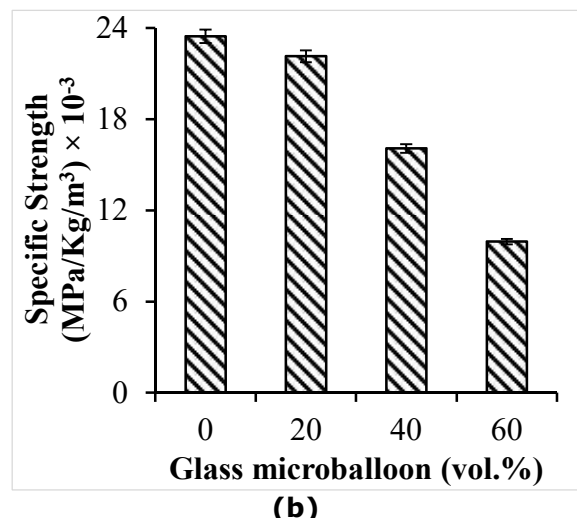


Fig. 5 (a) Specific modulus and (b) strength for HDPE and syntactic foams.

Investigation of heat transfer coefficient and Bubble dynamics of ethanol during subcooled flow boiling

Suhas B.G¹ and Sathyabhama.A²

1 Department of Mechanical Engineering, National Institute of Technology Karnataka, Surathkal, Mangalore 575025, India. email : suhas_bg@yahoo.co.in

2 Department of Mechanical Engineering, National Institute of Technology Karnataka, Surathkal, Mangalore 575025, India. email : bhamam722@gmail.com

ABSTRACT: In this paper, the subcooled flow boiling heat transfer coefficient of ethanol is determined by experiment in a conventional channel. The flow is visualized by using high speed camera to study the bubble dynamics. It is observed that an increase in heat flux and mass flux increases the subcooled flow boiling heat transfer coefficient of ethanol. Effect of heat flux is significant compared to mass flux. It is also observed that an increase in channel inlet temperature reduces the subcooled flow boiling heat transfer coefficient of ethanol. The bubble lifted off from the surface immediately after the departure without sliding. This is observed for all heat flux, mass flux and channel inlet temperatures. The results obtained are compared with the available literature correlations and they agree well with that of literature correlations.

Keywords: Bubble departure diameter, waiting period, growth period, flow visualization.

INTRODUCTION

The rising price of oil and environmental concern has motivated the automotive industries to develop hybrid electric vehicles (HEV). HEV can be powered by means of fuels and electric battery (Bruno et al, 2012). The rise in temperature of the batteries during operation is a serious problem because at higher temperature the chemical break down causes malfunctioning of the batteries (Anthony et al, 2013). The batteries can be cooled by air. But heat transfer coefficient of air is lower than that of liquid. For air circulation fan is required but it generates noise. So liquid can be chosen for cooling the batteries (Suhas and Sathyabhama, 2015). The liquid is passed through a cold plate which is placed above the battery cells. The cold plate acts as a conductive member. Heat dissipated from these cells is conducted through the cold plate and convected through the liquid (Hajmohammadi et al, 2013). When the battery is powered by means of diesel, the liquid can be used for fumigation to reduce the NO_x emission (Goldsworthy, 2013).

Usually ethanol is used for fumigation which can also be used for cooling the batteries. For proper designing of the cold plate, heat transfer coefficient of ethanol must be known. When ethanol passes through the cold plate, the latent heat is absorbed from the battery cells and undergoes subcooled flow boiling. So, the bubble dynamic study is important to understand the phenomena involved during subcooled boiling.

The present work consists of determining the heat transfer coefficient of ethanol in a horizontal rectangular channel. The various operating parameters are heat flux, mass flux and channel inlet temperature. Flow is visualised by using high speed camera. From the flow visualization, bubble departure diameter, bubble growth period and bubble waiting period are measured.

METHODOLOGY

Experimental test set up

Fig.1 shows the experimental test set up. It is a closed loop having rectangular aluminium block consisting of two rectangular channels of 10 mm (width) \times 10 mm (height) \times 150 mm (Length).

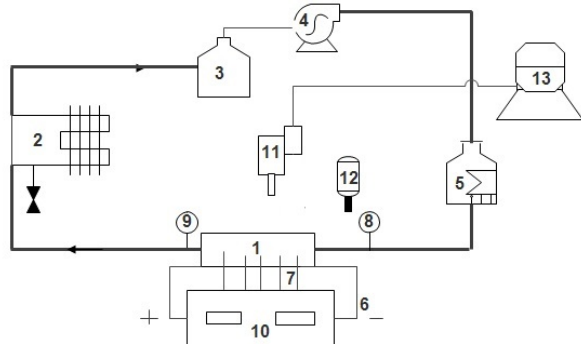


Fig.1 Schematic diagram of experimental setup.

- (1) Rectangular aluminium block consisting of two rectangular channels.
- (2) Condenser coil dipped in ice water bath.
- (3) Reservoir.
- (4) Pump having variable flow rate.
- (5) Preheater.
- (6) Cartridge heaters.
- (7) Thermocouples to measure wall temperature.
- (8) Channel inlet fluid temperature measuring thermocouple.
- (9) Thermocouples to measure channel inlet and outlet fluid temperatures.
- (10) Temperature indicator panel
- (11) High speed camera.
- (12) Light source.
- (13) Data Aquisition system for flow visualization.

Condenser coil dipped in ice water bath, reservoir, pump with variable flow rate and preheater. The aluminium block represents the cold plate which is used to place on battery cells of HEV.

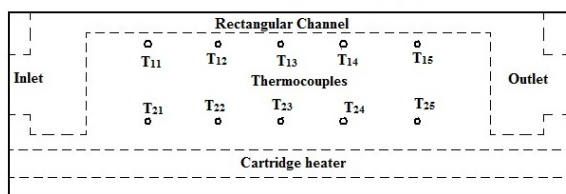


Fig.2 Arrangement of thermocouples in the Aluminium block

Fig. 2 shows the thermocouples arrangement in the cold plate to measure wall temperature and to calculate heat flux. The first set of five thermocouples ($T_{11}, T_{12}, T_{13}, T_{14}$ and T_{15}) are placed 2 mm below the channel in a row. The second set of five thermocouples ($T_{21}, T_{22}, T_{23}, T_{24}$ and T_{25}) are placed 20 mm below the first row of thermocouples. The distance between two thermocouple in a row is 25 mm. Two cylindrical cartridge heaters are placed 40

mm below the channels. The average of five heat fluxes and wall temperatures which are obtained from five different points in the channel are considered to calculate the heat transfer coefficient. It is observed that the heat flux value is higher at the inlet of the channel and decreases along the length of the channel. It is also observed that the wall temperature is lower at the entrance which marginally increases along the length of the channel.

Due to the possibility of solubility of air in water and ethanol, degassing is done for about thirty minutes before commencing the experiment. The liquid is preheated and pumped through the test set up. The heat is supplied to the channel to boil the liquid. The liquid after getting cooled in the condenser coil enters the reservoir.

Data Reduction

Fourier law of heat conduction is applied to calculate the heat flux from the measured values of temperature gradient and known value of thermal conductivity.

$$q'' = -k \frac{dT}{dx} \quad (1)$$

The heat flux is calculated from Equation (2) by substituting the values of thermal conductivity of aluminium, temperatures and the distance between the rows in Equation (1).

$$q'' = -k \frac{(T_{sr} - T_{fr})}{(x_{sr} - x_{fr})} \quad (2)$$

Where,

K=Thermal conductivity of aluminium cold block (kW/m²-K).

T =Temperature (K)

fr=First row

sr=Second row

X=Position (m)

For bottom wall of the channel, the heat flux is assumed to be same as the first row, because it is very near to the first rows of thermocouples (i.e. 2 mm). The wall temperature is calculated by Equation (3).

$$T_w = \frac{-q''}{k} (X_w - X_{fr}) + T_{fr} \quad (3)$$

Where,

W=wall

q''=Heat flux

The heat transfer coefficient (h) is calculated by Equation (4) from the calculated values of heat flux, calculated values of wall temperatures and measured

values of outlet temperature. The average of five readings of wall temperatures is calculated to determine the difference between the wall and outlet fluid temperature.

$$h = \frac{q^*}{(T_w - T_f)} \quad (4)$$

Where, f=Fluid.

The uncertainty of the measured and calculated parameters is calculated. Table 1 shows the uncertainties of measured and calculated parameters.

Table 1 Uncertainties of measured and calculated parameters

Parameters	Uncertainties
Thermocouple	$\pm 0.35^\circ\text{C}$ (RSS)/ $\pm 0.1^\circ\text{C}$ (resolution)
Preheater temperature	$\pm 0.1^\circ\text{C}$ (resolution)
Mass flow rate	$\pm 2.32\%$
Mass flux	$\pm 0.77\%$
Heat flux	$\pm 13.3\%$
Heat transfer coefficient	$\pm 9.11\%$
Bubble departure diameter	$\pm 13.02\%$

RESULTS AND DISCUSSIONS

Validation

Fig.3 shows the comparison of subcooled flow boiling heat transfer coefficient data of ethanol (h_{exp}) with those predicted using available literature correlations (h_{pred}). Gungour and Winterton (1986) correlation predicts the experimental data with mean absolute error (MAE) of 9.82 %. Kandlikar (1998) correlation predicts the experimental data with MAE of 12.46 %. Liu and Winterton (1991) correlation predicts the experimental data with MAE of 14.31 %. Chen correlation under predicts the experimental data with MAE of 19.37 %. The deviation is attributed to non uniform temperature distribution in cold plate, assumption of one dimensional temperature distribution to calculate the heat flux.

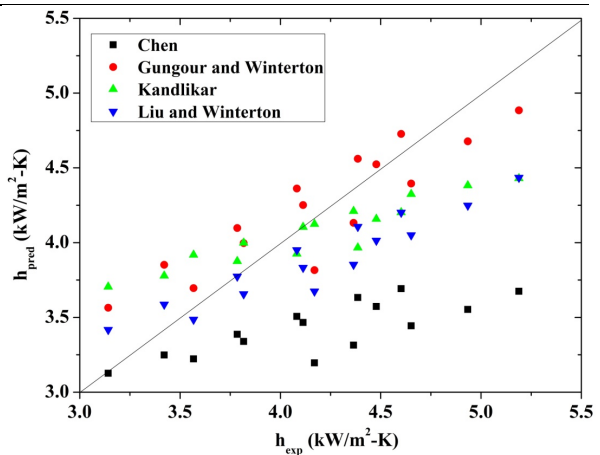


Fig.3: Comparision of subcooled flow boiling heat transfer coefficient values of ethanol with those predicted using correlations.

Boiling curve

The variation of heat transfer coefficient with wall superheat ($T_w - T_s$) for ethanol at inlet temperature=303 K is shown in Fig.4. The heat flux increases with increase in wall superheat for both single phase forced convection and subcooled boiling region. But the increase in heat flux is higher at subcooled boiling region. The boiling curves closely merge into a single curve for different values of mass fluxes. The increase in mass flux decreases the wall temperature in single phase forced convection region but the wall superheat does not vary significantly due to increase in mass flux at subcooled boiling regions. Decrease in wall temperature decreases the wall superheat. This shows that increase in mass flux has negligible influence on heat transfer in this region. During the onset of nucleate boiling (ONB), the bubble formation commences. The active nucleation sites occur due to micro layer evaporation in the corner of bottom wall of the channel. However, flow in the middle portion of the channel is subcooled. At higher heat flux, the buoyancy and inertial forces are significant than surface tension forces. The bubbles detach and depart from the corner and enter the subcooled region. With further increase in heat flux, the vapour generation commences, i.e, onset of vapour generation (OSV). This region is highly subcooled region. This results in the flow of surrounding fluid into the activation

sites. This causes vapour turbulence and agitation, which causes the heat flux contribution towards the subcooled boiling heat transfer and significant over the forced convective heat transfer.

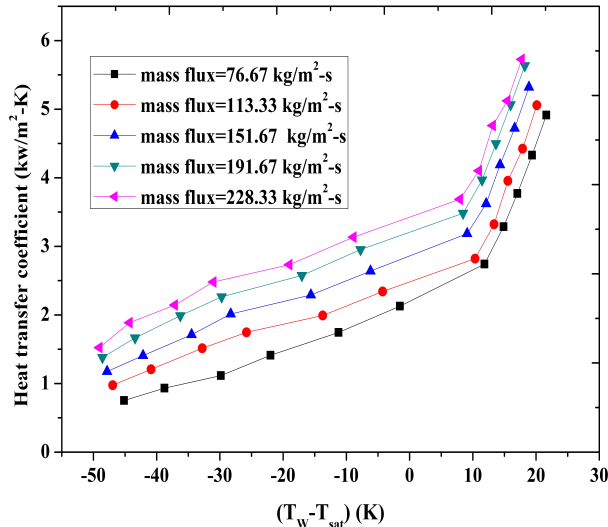


Fig.4: The variation of heat transfer coefficient with wall superheat for ethanol at inlet temperature=303 K.

As the mass flux increases at higher heat fluxes, the decrease in wall temperature is less due to decrease in subcooling of the fluid in the middle portion of the channel. The decrease in subcooling may be due to i) diffusion of the bubbles which departed from corners and ii) formation of new nucleation sites at the bottom wall of the channel. Similar trends are observed for various values of ethanol volume fractions and inlet temperatures.

Bubble departure diameter, bubble growth period and bubble waiting period

Fig.5 shows the photographic image of bubble growth of ethanol at heat flux of 90.4 kW/m^2 , mass flux = 115.33 $\text{kg}/\text{m}^2\cdot\text{s}$ and inlet temperature=303 K.



(a)



(b)



(c)



(d)

Fig.5: Bubble growth and waiting periods for Ethanol at heat flux=90.4 kW/m^2 , inlet temperature=303 K and mass flux of 115.33 $\text{kg}/\text{m}^2\cdot\text{s}$ (a) Bubble nucleation at 0 ms (b) Bubble in growth stage at 11.95 ms (c) Bubble departure at 23.9 ms (d) Next bubble nucleation at 22.3 ms after the departure.

In the images, some of the bubbles are larger in size. They are the coalesced bubbles and are not considered for measuring the bubble departure diameter. Larger and smaller bubbles can also be observed. Hence 20 to 30 bubbles are identified from 3 to 4 sites to measure the average bubble departure diameter. It can be observed that the bubble departure diameter decreases with increase in heat flux, mass flux and decrease in channel inlet temperature. But the influence of heat flux is observed to be more significant than mass flux. Because at higher heat flux and mass flux sufficient amount of energy will be acquired by the fluid and overcomes intermolecular force of the molecules causing change in phase of liquid locally. This causes bubbles to depart from the surface and thus reduces the bubble growth period.

The early bubble departure decreases the bubble growth period and bubble departure diameter size and thus increases the heat transfer coefficient. After the departure of the bubble, the molar latent heat of vaporization increases and more heat is available to break the intermolecular force of liquid in the same site and decreases the waiting period and heat transfer coefficient. Therefore the bubble growth period (t_g) increases with increase in waiting period (t_w) as shown in Fig.5.

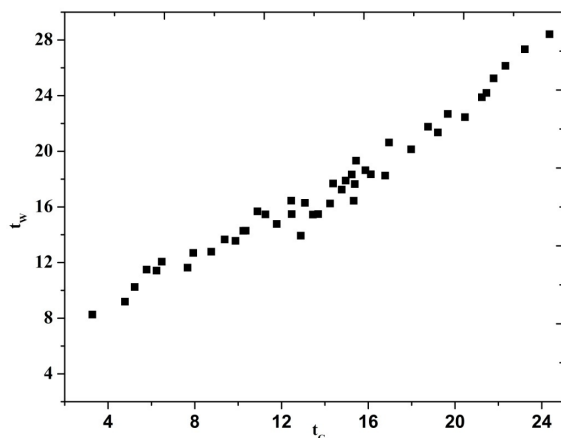


Fig.5: Variation of waiting period of bubbles with growth period of bubbles for Ethanol.

Force Balance approach

During subcooled flow boiling the forced convection is dominated by evaporation and agitation. Hence during subcooled flow boiling higher heat transfer coefficient has lower Jakob number.

Klausner et al. (1993) and Khelile Sefien et al (2012) conducted studies on force balance approach. They concluded that during flow, the influence of various forces acting on a bubble caused bubble departure and bubble lift-off. The forces acting on the bubble in the parallel and normal directions to flow are:

$$\sum F_x = F_{sx} + F_{qs} + F_{du} \sin\theta \quad (5)$$

$$\sum F_y = F_{sy} + F_{sl} + F_b + F_h + F_{cp} + F_{du} \cos\theta \quad (6)$$

Where,

F_b Buoyancy force (N).

F_{cp} Contact pressure force for the bubble (N).

F_{du} Unsteady drag force on the bubble (N)

F_h Force due to the hydrodynamic pressure (N).

F_{qs} Quasi steady-drag in the flow direction (N).

F_s Surface tension force (N).

F_{sl} , Shear lift force (N).

F_x Force parallel to flow direction (N).

F_y Force normal to flow direction (N).

θ Contact angle.

At Jakob number lower than 20, the difference between ($F_y - F_x$) is negative and at Jakob number above 20 the difference between ($F_y - F_x$) is positive. When the difference is positive it is observed that bubble departed and lifted off from the heated surface of channel wall but did not slid. This phenomenon is observed for ethanol as ethanol is having higher Jakob number.

The bubble caused the change in the flow field which resulted in the variation of quasi-steady drag force (F_{qd}) and surface tension force acting on it. These forces are balanced by unsteady growth rate (F_{dg}). Due to the initial immobility and the very small growth rate of the bubble in subcooled liquid, change in F_{qs} is not much significant. The breaking of the force balance in flow direction is caused by the sudden variation of the surface tension force between the wall and the liquid interface. The bubble contact diameter and the contact angles change due to the evaporation in the triple-phase line region at the bubble root during bubble growth. Tomio Okawa et al. (2015) found that the force balance in flow direction is broken by the disturbance from the main flow which alters the contact diameter and the contact angles, leading to the change of the surface tension force. This is achieved at higher mass flux and therefore the bubble departs earlier at higher mass flux.

6th International Engineering Symposium - IES 2017

March 1-3, 2017, Kumamoto University, Japan

CONCLUSIONS

The subcooled flow boiling heat transfer coefficient of ethanol is determined by experiment in a conventional channel. The flow is visualized by using high speed camera for studying the bubble dynamics. Following are the conclusions arrived from the present experimental work:

- It can be observed that an increase in heat flux and mass flux increases the subcooled flow boiling heat transfer coefficient of ethanol.
- The results obtained agreed well with that of literature correlations.
- An increase in heat flux is significant when compared with that of mass flux.
- It is also observed that an increase in channel inlet temperature reduces the subcooled flow boiling heat transfer coefficient of ethanol.
- The bubble lifted off from the surface immediately after the departure without sliding.

REFERENCES

- [1] Anthony J, Li YK. (2011), Design optimization of electric vehicle battery cooling plates for thermal performance. *J Power Sources*; vol.196: pp-10359–10368.
- [2] Bruno G, Iain S, Jin L. (2012) Current status of hybrid battery and fuel cell electric vehicles: from electrochemistry to market prospects. *Electrochim Acta* ; vol 84:pp-235–249.
- [3] Gungor, K. E., and Winterton, R. H. S., (1986), "A General Correlation for Flow Boiling in Tubes and Annuli," *International Journal of Heat and Mass Transfer*, 29(3),351-358.
- [4] Goldsworthy L., (2013) Fumigation of a heavy duty common rail marine diesel engine with ethanol-water mixtures. *Experimental Thermal Fluid Science*, vol. 47,pp-48–59.
- [5] Hajimohammadi.M.R, Salimpour M.R, Saber.M and Campo.A.,(2013) Detailed analysis for the cooling performance enhancement of a heat source under a thick plate, *Energy Conversion and Management*, vol.76: pp-691-700.
- [6] Kandlikar, S.G (1998), Heat Transfer Characteristics in Partial Boiling, Fully Developed Boiling, and Significant Void Flow Regions of Subcooled Flow Boiling, *J. Heat Transfer* 120(2), 395-401.
- [7] Khellil Sefiane, Yuan Wang and Souad Harmand.,(2012) Flow boiling in high-aspect ratio mini- and micro-channels with FC-72 and ethanol: *Experimental Thermal and Fluid Science* vol.36, pp-93–106.
- [8] Klausner, J.F., Mei, R., Bernhard, D.M., Zeng, L.Z., (1993), Vapor bubble departure in forced convection boiling. *Int. J. Heat Mass Transfer*, vol. 36 pp-651–662.
- [9] Ling Zou., (2010), Experimental study on subcooled flow boiling on heating surfaces with different thermal conductivities. Doctoral thesis, University of Illinois at Urbana-Champaign.
- [10] Liu, Z., & Winterton, R. (1991) A general correlation for saturated and subcooled flow boiling in tubes and annuli, based on a nucleate pool boiling equation. *International Journal of Heat and Mass Transfer*, 34(11), 2759–2766.
- [11] Suhas BG and Sathyabhamma.A (2015), Numerical Analyses of Single-Phase Pressure Drop and Forced Convective Heat Transfer Coefficient of Water-Ethanol Mixture: An Application in Cooling of HEV Battery Module, *Heat transfer Asian Research*, WileyPublications,45(7),680–690.doi: 10.1002/htj.21183.

Wear behavior of AM80 magnesium alloy processed by equal channel angular pressing

Gopi K R¹ and H Sivananda Nayaka²

1 Department of Mechanical Engineering, National Institute of Technology Karnataka, Surathkal, Mangalore 575025, India. e-mail: nitkgopi@gmail.com

2 Department of Mechanical Engineering, National Institute of Technology Karnataka, Surathkal, Mangalore 575025, India. e-mail: hsn_mech@nitk.ac.in

ABSTRACT: Equal channel angular pressing (ECAP) is considered to be an attractive technique, being capable of producing ultrafine-grained bulk materials and having potentials for scale-up and mass production. AM80 magnesium alloy was processed by ECAP using route B_c at 275 °C up to 4 passes. After ECAP, wear test have been conducted using pin-on-disk wear test machine. Microstructural analysis after ECAP and worn surfaces of the specimens after wear test were observed by scanning electron microscope (SEM). The effect of varying load (30 and 40N) and the number of ECAP passes on the wear mass loss have been discussed with reference to microstructure with different ECAP passes and wear mechanism. In the present work, investigation of wear behavior of AM80 magnesium alloy processed by ECAP was carried out and it was found that, as the number of ECAP passes increases the wear resistance increases with the reduction in grain size.

Keywords: ECAP, Grain refinement, AM80 alloy, Wear

INTRODUCTION

Severe plastic deformation (SPD) is one of the great techniques for creating bulk ultrafine grained material. By this method high strains are induced into the material which results in grain refinement. Some of the SPD techniques are Equal-Channel Angular Pressing (ECAP), High-Pressure Torsion (HPT), Accumulative Roll-Bonding (ARB), Multi-Directional Forging (MDF), Cyclic Extrusion and Compression (CEC), Repetitive Corrugation and Straightening (RCS), Twist Extrusion (TE) [Valiev R Z. et Al. (2006)]. ECAP is considered to be one of the effective tool for achieving grain refinement in the material [Valiev R Z and Langdon T G (2006)]. ECAP is a process in which high strains are induced into the material without any significant change in dimension of the specimen after processing [Valiev R Z. et Al. (2006), Yang Q, and Ghosh A K (2006)].

Magnesium and magnesium alloys are widely used in industrial applications like automobile and aerospace because of their

better properties like low density, high specific strength and also good machinability [Zhang T. et al. (2011)]. Since it is used in industrial application it will undergo material losses due to friction in movable parts. It is important to study the wear behavior of magnesium alloys and also less work has been reported on wear properties of ECAP processed magnesium alloy.

Wear test carried out on ECAP processed AZ31 magnesium alloy and explained that with increase in ECAP passes decrease in volume loss and depth of wear was observed [Xu J. et al. (2013)]. ES processed AZ31B magnesium alloy was subjected to wear test and the results showed improvement in wear resistance due to grain refinement [Hu H J. et al. (2015)]. ECAP processed AZ80 magnesium alloy showed better wear resistance with higher ECAP passes and wear rate was dependent on sliding speed [Fouad Y. et al. (2011)]. With the above literature it was found that limited work have been

6th International Engineering Symposium - IES 2017

March 1-3, 2017, Kumamoto University, Japan

conducted on wear properties of ECAP processed magnesium alloy and less work has been reported on AM series magnesium alloy. It possesses better damping and impact absorption properties and it is used in the manufacture of seat frames, brake pedals and brackets in automotive industries [Watanabe K. et al. (2010)]. In this work, wear behaviour of ECAP processed AM80 magnesium alloy was investigated and the results are related to microstructure and hardness of the material.

MATERIAL AND METHODS

Cast magnesium alloy AM80 (Mg-8.22Al-0.39Mn) was received in the form of ingots of dimension 240 mm×100 mm×24 mm. Cast ingots were machined to prepare the samples of dimension 15.8 mm in diameter and 95 mm in length for ECAP process. Hot die steel was used for ECAP die fabrication and the die has two channels of radius 8 mm on each plate and the channels intersected at channel die angle (ϕ) of 110° and outer radius (ψ) of 20° as shown in Fig. 1(a). ϕ and ψ values lead to a strain of ~0.8 for every pass during the ECAP process [Furuno K. et al. (2004)] and sample after ECAP process is shown in Fig. 1(b).

The machined samples were subjected to homogenization treatment at a temperature of 400 °C for a period of 24 hours in a furnace, so that the constituents are uniformly distributed in the matrix.

Homogenized samples were processed by ECAP at a temperature of 275 °C using route B_c at a cross head speed of 1 mm/s. Initially ECAP die was heated to 275 °C using resistance coils and is monitored till the die reaches the required temperature. Homogenized samples were placed in the channel of the die and allowed to heat for 15 min to reach the required temperature same as die temperature prior to pressing. Pressing was carried out using universal testing machine (UTM) and molybdenum disulfide (MoS₂) was used as a lubricant to avoid frictional losses. ECAP was carried out up to 4 passes using route B_c.

Homogenized and ECAP processed samples were prepared for microstructural analysis. Samples were prepared by slicing in a direction perpendicular to the direction of

pressing. Initially samples were subjected to mechanical polishing by SiC papers followed by cloth polishing using diamond paste. Polished samples were etched using picral and dried with blower. Microstructural analysis was conducted using scanning electron microscopy (SEM, JEOL JSM-6380LA) and grain size was analyzed by linear intercept method. Vickers microhardness test was conducted using omni-tech microhardness tester by applying a load of 25 g for 15 s. Indentations were taken on middle region of the sectioned samples at equal intervals. Wear test specimens were prepared by taking the central region of the homogenized and ECAP processed samples and the dimensions of wear test samples were prepared as per ASTM G99-05. Wear sample dimensions are 6 mm in diameter and 28 mm in length.

Wear tests were conducted using pin-on-disc wear test machine and the test was carried out on hard and polished steel disk of HRC 65 hardness. Samples were grinded with SiC papers of 2000 grit size. Samples were subjected to 30N and 40N load with sliding distance of 5000 m at a sliding speed of 3 m/s with track diameter of 110 mm. Initial and final weight of the samples were measured and the test was repeated for 3 times with the prescribed parameters. Worn surfaces of homogenized and ECAP processed samples were analyzed using SEM to study the wear mechanism.

RESULTS AND DISCUSSION

Microstructure and Hardness

SEM microstructural images of homogenized and ECAP processed samples are as shown in Fig. 2. Homogenized sample is having a grain size of ~100 µm as shown in Fig. 2(a). During initial ECAP passes larger grains were divided into smaller grains as observed in Fig. 2(b) for ECAP 2 pass sample. From microstructure Fig. 2(b), it can be observed that variation in grain size can be seen with larger and smaller grains which look like bimodal structure and grain refinement is more during initial stages due to higher dislocation rate. As the ECAP passes increases grain size gets refined further

6th International Engineering Symposium - IES 2017

March 1-3, 2017, Kumamoto University, Japan

and equiaxed microstructure was observed may be because of static recrystallization during initial heating before ECAP or dynamic recrystallization during ECAP process. Grain size of ECAP processed 4 pass sample was measured to be $\sim 3 \mu\text{m}$. Vickers microhardness test was conducted on homogenized and ECAP processed samples as the results are as shown in Fig. 3. As the number of ECAP passes increases the hardness increased compared to homogenized condition and also homogeneity of hardness increased as the ECAP passes increases as shown in Fig. 3. Hardness increased due to strain hardening and after ECAP 2 pass the hardness has decreased may be due to nucleation of new grains which hinders strain hardening.

Wear Analysis

Homogenized and ECAP processed samples were subjected to wear test under 30 N and 40 N load with sliding distance 5000 m. Wear mass loss verses number of ECAP passes can be observed from Fig. 4. Wear mass loss decreases with increase in ECAP passes compared to homogenized condition. This shows that ECAP processed samples exhibit higher wear resistance. Increase in load increases the wear mass loss for 40 N as shown in Fig. 4. Wear mass loss is less for ECAP 2 pass sample compared to other ECAP processed samples but compared to homogenized condition ECAP processed samples processes higher wear resistance. This variation in wear mass loss is related to microhardness values shown in Fig. 3 and is explained by Archard equation [Archard J (1953)]. Due to refined microstructure increase in hardness of ECAP processed samples was observed and also wear mass loss reduced for the ECAP processed samples compared to homogenized condition.

Worn surfaces of homogenized and ECAP processed samples under 30 N and 40N load are shown in Fig. 5 and Fig. 6. Worn surfaces consist of delamination, wear debris, ploughing in the sliding direction which showed plastic deformation as shown in Fig. 5 and Fig. 6. ECAP processed samples showed smooth surfaces compared to homogenized condition

because of increased microhardness which avoids the development of delamination and wear debris [Xu J. et al. (2013)]. Worn surfaces showed delamination, wear debris, plastic deformation and also microploughing along sliding direction and the wear mechanism may be identified as abrasive wear.

CONCLUSIONS

- ECAP processed AM80 Magnesium alloy grain size was reduced to an average of $3 \mu\text{m}$.
- ECAP processed samples showed reduced wear mass loss compared to homogenized condition.
- Worn surfaces showed delamination, microploughing, plastic deformation and wear debris and the wear mechanism was found to be abrasive wear.

REFERENCES

- [1] Archard, J (1953), Contact and rubbing of flat surfaces, *J. Appl. Phys.*, Vol. 24, No. 8, pp. 981-988.
- [2] Fouad, Y et al (2011), Wear Mitigation in Magnesium Alloy AZ80 Processed by Equal Channel Angular Pressing, In *International Journal of Engineering Research in Africa*, Vol. 6, pp. 1-11, Trans Tech Publications.
- [3] Furuno, K et al (2004), Microstructural development in equal-channel angular pressing using a 60 die, *Acta Materialia*, Vol. 52, No. 9, pp. 2497-2507.
- [4] Hu, H J et al (2015), Dry sliding wear behavior of ES-processed AZ31B magnesium alloy, *Russ. J. Non-Ferrous Met.*, Vol. 56, No. 4, pp. 392-398.
- [5] Valiev, R Z et al (2006), Producing Bulk Ultrafine-Grained Materials by Severe Plastic Deformation, *JOM*, Vol. 58, No. 4, pp. 33-39.
- [6] Valiev R Z, and Langdon T G (2006), Principles of Equal-Channel Angular Pressing as a Processing Tool for Grain Refinement, *Progr. Mater. Sci.*, Vol. 51, No. 7, pp. 881-981.
- [7] Watanabe, K et al (2010), Effect of Casting Method and Al Contents on Microstructure in AM-Type Magnesium Alloys, *Mater. Sci. Forum*, Vol. 654, pp. 663-666.
- [8] Xu, J et al (2013), Dry sliding wear of an AZ31 magnesium alloy processed by equal-channel angular pressing, *J. Mater. Sci.*, Vol. 48, No. 11, pp. 4117-4127.
- [9] Yang Q, and Ghosh A K (2006), Deformation Behavior of Ultrafine-Grain (UFG) AZ31B Mg Alloy at Room Temperature, *Acta Mater.*, Vol. 54, No. 19, pp. 5159-5170.
- [10] Zhang, T et al (2011), Effect of extrusion ratio on mechanical and corrosion properties of AZ31B alloys prepared by a solid recycling process, *Materials and Design*, Vol. 32, No. 5, pp. 2742-2748.

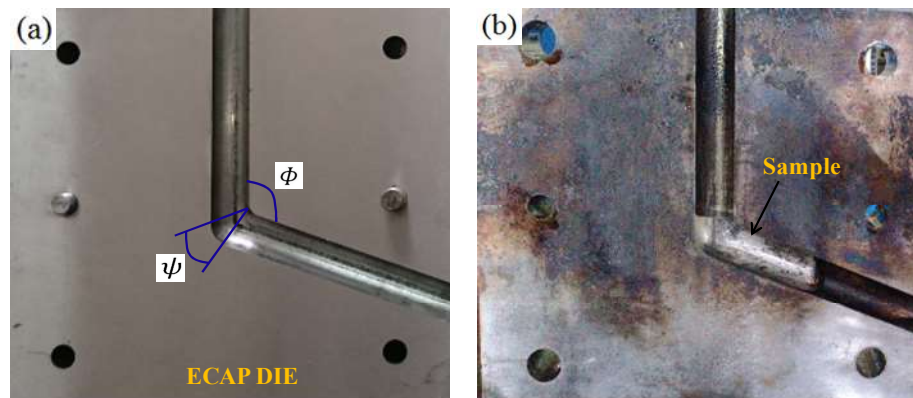


Fig. 1 (a) ECAP die (b) Sample after ECAP process

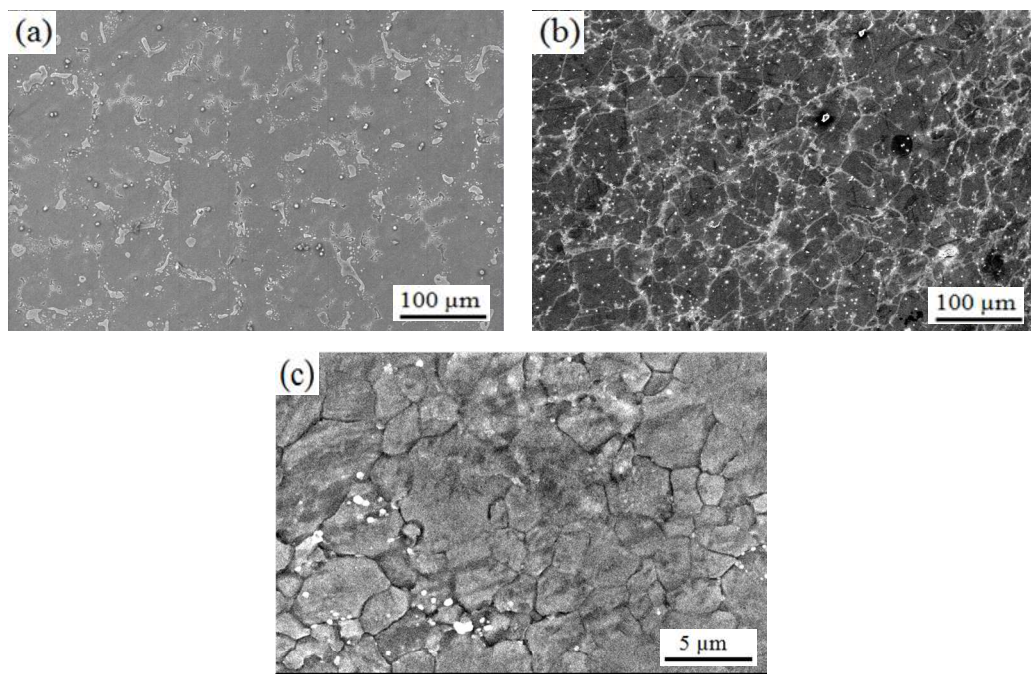


Fig. 2 Microstructure of (a) Homogenized (b) ECAP 2 pass and (c) ECAP 4 pass samples

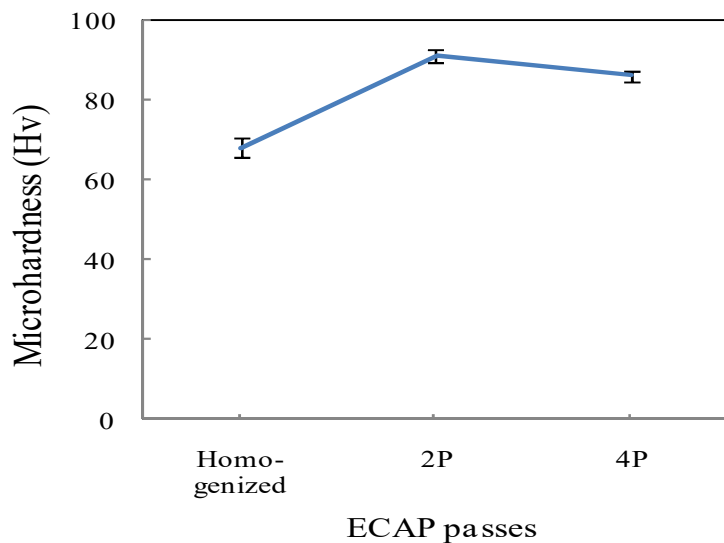


Fig. 3 Microhardness of Homogenized and ECAP processed samples

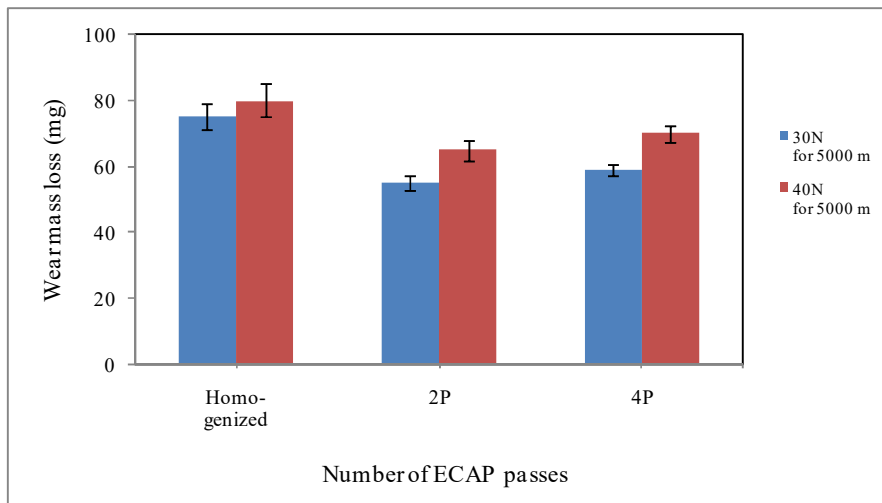


Fig. 4 Wear mass loss verses number of ECAP passes

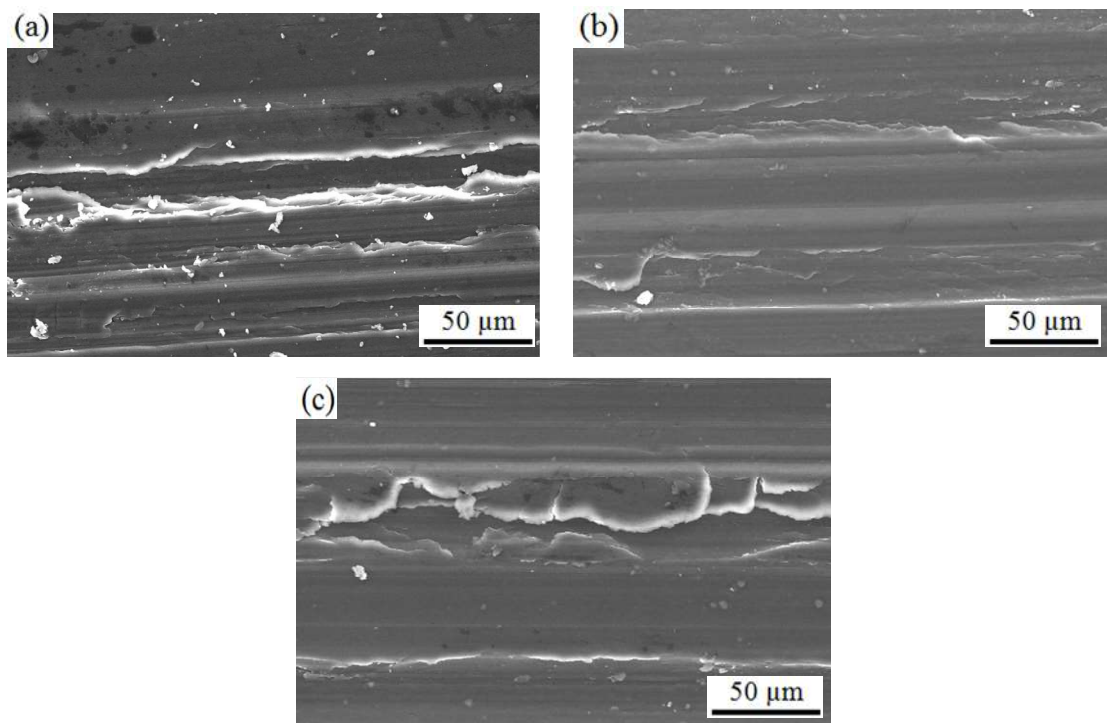


Fig. 5 Worn surface morphology of (a) Homogenized, (b) ECAP 2 pass and (c) ECAP 4 pass samples under 30 N load

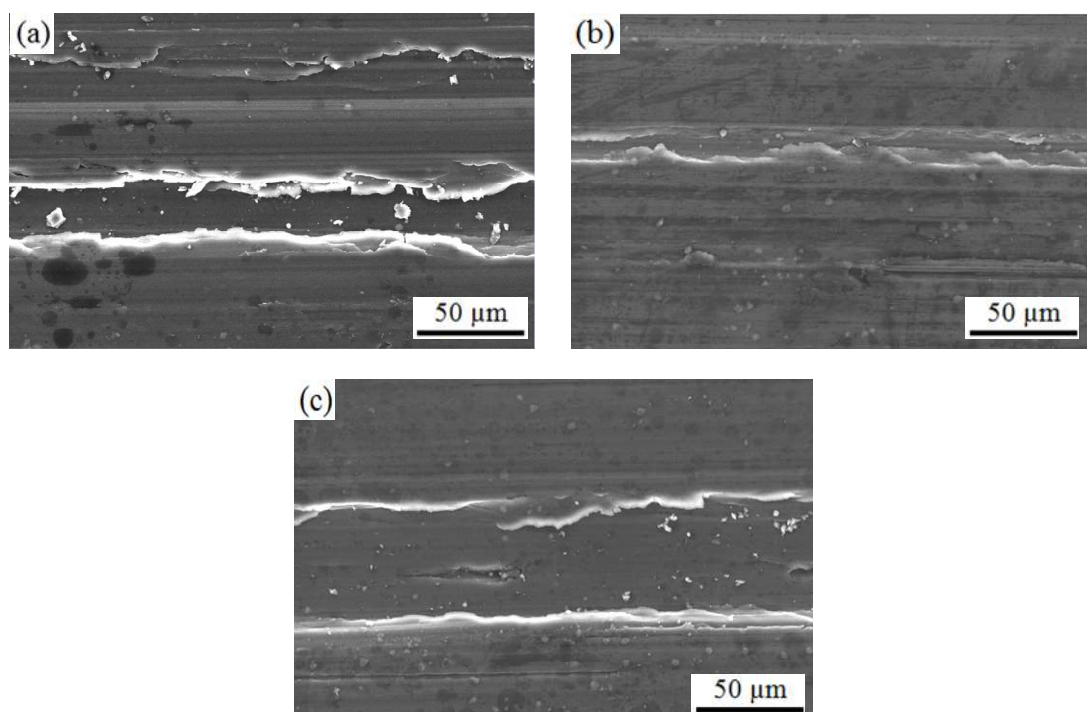


Fig. 6 Worn surface morphology of (a) Homogenized, (b) ECAP 2 pass and (c) ECAP 4 pass samples under 40 N load

EFFECT OF ELECTRO-THERMAL PARAMETERS ON LESION FORMATION DURING RADIOFREQUENCY ABLATION IN DIFFERENT TUMOR TISSUES

Charanakumar E.¹, Kamini Kaushal² and Ajay Kumar Yadav³

- 1 Department of Mechanical Engineering, National Institute of Technology Karnataka, Surathkal-575025, Karnataka, India.
E-mail : charan.yash@gmail.com
- 2 Department of Molecular biology and human genetics, Manipal University, Manipal-576104, Karnataka, India. Email: kaminikaushal10@gmail.com
- 3 Department of Mechanical Engineering, National Institute of Technology Karnataka, Surathkal -575025, Karnataka, India. E-mail : ajaykyadav@nitk.edu.in
-

ABSTRACT: Thermal therapies such as hyperthermia, radiofrequency ablation (RFA), cryoablation, etc. have shown great potential and have increasing clinical acceptance in the treatment of solid tumors. Radiofrequency ablation is being used for treatment of certain tumors like liver, kidney, prostate, lung, breast and pancreas tumor by generating heat using radiowaves to kill cancer cells. The objective of this work is to study the temperature distribution, heat transfer rate, lesion formation in the different types of tumors and surrounding tissues. In present studies, four different types of tumor tissues i.e., lung, liver, kidney and breast are considered. The effects of electrical conductivity, thermal conductivity, blood perfusion rate, size and location of tumors on ablation volume are studied. Input parameters such as applied voltage and exposure time are also varied for different tissues embedded with tumors. The induced thermal damage is computed by using the first-order Arrhenius rate equation. Study is carried out numerically by considering the various tissue models embedded with tumors of various sizes at different locations by using single needle monopolar electrodes. Computational model uses anatomically precise multilevel geometrical model of human tissues with known thermo physical and electrical properties. Three dimensional bioheat transfer equation is solved to get temperature profile and heat transfer rate in the computational domain. Results show that as the size of the tumor increases, temperature near the electrode increases due to the requirement of larger exposure time to form a complete necrosis of tumor. The effects of thermo electric properties i.e., electrical and thermal conductivity of tumor and tissue on lesion formation are presented. These results may be useful to provide practical and fast guidelines to clinical practitioners. This computational model is validated with published experimental data and found in good agreement.

Keywords: Radiofrequency ablation, lesion formation, tumor, bioheat transfer, temperature, computational model.

INTRODUCTION

Cancer is a major cause of death in human life. It is collection of related diseases involving abnormal growth of body cells which proliferate in an uncontrolled way

and potential to spread into surrounding tissues. As cells become more and more abnormal, survivability of old or damaged cells increase, and unwanted cells get generated. These cells get divided and form new cells and grow further at abnormal rate which lead to form tumors. The masses of tissue formed by the

6th International Engineering Symposium - IES 2017

March 1-3, 2017, Kumamoto University, Japan

abnormal cells are called solid tumors. Solid tumors are treated by potential and clinically accepted therapies such as hyperthermia, thermal ablation techniques, Cryoablation etc. (Kumar et al., 2016). In thermal therapies, the heat is used for the treatment depending on the treatment type where heat can flow in and out of the body. In cryoablation, the temperature is decreased to -50°C and heat flows out of the system (Jamil and Ng, 2015; Stauffer, 2005). In hyperthermia and heat ablation therapies temperature is maintained above 42°C and 50°C respectively (Berjano, 2006). Now a days, minimally invasive thermal ablation techniques have become common with advancement in modern imaging techniques (Singh and Repaka, 2015). Out of all the thermal ablative techniques, radiofrequency ablation is the widely applied treatment method for solid tumors like Liver, Lung, Kidney, prostate, bone, breast etc. (Zhang et al., 2016; Singh et al., 2016). RFA is a thermal strategy which utilizes the radiowaves generated at the low radiofrequency of 360 to 500kHz range to destroy the tumor tissue in a minimally invasive image guided procedure by increasing its temperature and causing irreversible cellular damage (Ulucakll, 2009).

The RFA of tumors are carried out by using RF system comprising of RF generator to generate high frequency alternating current, RF applicator that consists of an electrode and insulated shaft, and reference electrode to establish an electric circuit. In case of monopolar electrode, ground pads are usually placed on the patients back or thigh as a reference electrode. During ablation, the RF electrode is inserted percutaneously to the target tissue to be heated through image guidance like ultrasound imaging, computer tomography or MR imaging (Zhang et al., 2016). After electrode is positioned, the high frequency alternating current is passed through this electrode into the target tissue. The established electric fields between the electrode tip and the grounding pad cause the conduction of current from electrode to tissue. The oscillating electric and

magnetic fields at radio frequency cause the ions within tissue to agitate due to change in direction of current which results in resistive or frictional heating of tissue (Goldberg, 2001). Because of high impedance value of biological tissues, the resistive heating is dominant within the few millimeters of tissue surrounding the electrode. But actual heating of tumor is due to thermal conduction of heat. The rise in local temperature over a period of time causes irreversible damage to the cells. Generally, the coagulation begins at 43-45°C, but the desired damage ($w>1$) can be obtained at high temperature ($>50^\circ\text{C}$) (Singh et al., 2016). The increase in temperature around 100-105°C leads to charring of tissue and sudden increase of impedance (Alba et al., 2011). The main aim of the RFA of tumor is complete necrosis of the tumor tissue without re-occurrence. The complete heating of tumor volume depends on multiple factors viz. thermo-physical properties of tumor and surrounding tissue, blood perfusion rate, geometric parameters of the tumor (size, shape and location of tumor) and electrodes (electrode size, type and relative position of electrode with respect to tumor), applied voltage and exposure time (Schutt and Haemmerich, 2008; Jamil and Ng, 2013; Ng and Jamil, 2014; Zorbas and Samaras, 2014; Zhang et al., 2014).

In Present work numerical study has been carried out by considering the four different types of tissues embedded with various size of tumors and at different locations by using single needle monopolar electrode with constant voltage source. The objective of this work is to study a)The temperature distribution and lesion formation in different types of tissues like liver, kidney, lung and breast. b)The effect of tumor size and location of tumor on lesion formation and c)effect of electrical conductivity, thermal conductivity of tissue and tumor and perfusion rate on lesion formation during the RFA .

6th International Engineering Symposium - IES 2017

March 1-3, 2017, Kumamoto University, Japan

MATERIALS AND METHODS

Problem definition

The computational domain consists of three dimensional cubical model with 120mm side in which different diameter spherical tumors are embedded as shown in Fig.1 (Zorbas and Samras, 2014). The three dimensional cubic model represents the different body tissues i.e liver, kidney, lung and breast (gland, muscle and fat). In this study, three different sizes 15mm, 25mm and 35mm are considered as the diameter of spherical tumor. A 2mm diameter internal cooling single needle monopolar electrode with 10-30mm active length is modelled and inserted into the center of the tumor tissue. The breast tissue was modeled as gland, muscle and fat tissues separately. The material properties used for different tissues, tumor, electrode and blood are presented in the Table 1 (Zorbas and samras, 2014; Singh et al., 2016; Singh and Repaka, 2016). The Electrical and Thermo physical properties for different tissues are chosen at 460kHz. The values of density, thermal conductivity and specific heat have been assumed to be same for both tissue and tumor. The thermal conductivity and electrical conductivity are assumed to be constant.

Mathematical Modeling

RFA represents a coupled electro thermal problem. In the mathematical modeling of RFA two processes need to be considered i.e.

1. Heat transfer in biological tissue.
2. Spatial heat generation by the electric current at high frequency.

To evaluate heat transfer within the tissue, the modified version of pennes bioheat equation (Pennes, 1998) was used.

$$\rho c \frac{\partial T}{\partial t} = \nabla(k \cdot \nabla T) - \rho_b c_b \omega_b (T - T_b) + Q_m + Q_s \quad (1)$$

Where ρ , c , k are the density, specific heat and thermal conductivity of tissues respectively, w_b , ρ_b , c_b are the blood perfusion rate, density of blood and specific heat of blood respectively, Q_m is

the heat generated by metabolic activity, which is negligible due to its small magnitude, Q_s is the spatial heat generated by the electrode, T_b is the core blood temperature (i.e. 37°C), T is the unknown tissue temperature.

Since, the wavelength of the electromagnetic field is several orders of magnitude larger than the size of the active electrode in the frequency range of 350-500kHz, hence a quasi-static approximation has been assumed to solve the electro-magnetic problem. The electric field distribution within the tissue due to applied voltage on RF electrode can be computed by using the generalized Laplace equation

$$\nabla \cdot (\sigma \nabla V) = 0 \quad (2)$$

Where σ is the electrical conductivity and V is the applied voltage.

Electrical field intensity (E) and current density (J) generated within the tissue can be computed from

$$\begin{aligned} E &= \nabla V \\ J &= \sigma E \end{aligned} \quad (3)$$

The spatial heat generated by the electrode is

$$Q_s = J \cdot E = \sigma \cdot E^2 \quad (4)$$

To estimate the tissue damage (damage integral), a first order Arrhenius equation (Henriques, 1947) has been used. The tissue damage depends on both temperature and time.

$$\Omega(t) = \int_0^t A e^{\frac{E_a}{RT}} dt \quad (5)$$

Where T is the Temperature, t is the ablation time, A is the frequency factor, E_a is the Activation energy and R is the universal gas constant (8.314 J/mol K). A and E_a are the kinetic parameters whose values depend on the tissue type and are presented in the Table 2. A damage integral of $w=1.0$ (corresponds to 63 % probability of cell death) has been assumed to be the point at which tissue undergoes irreversible damage of constituting proteins and cell organelles (Henriques, 1947).

Boundary and Initial conditions

Initial temperature and voltage of an entire tissue domain have been set to 37°C (core body temperature) and zero

6th International Engineering Symposium - IES 2017

March 1-3, 2017, Kumamoto University, Japan

respectively. The outer periphery of the tissue was set to zero electrical potential (grounded). Electrical insulated condition has been set for the insulated trocar part. The RF electrode potential has been set to a constant source i.e V0. The 'heat-sink' effect due to cooling effect of the chilled solution circulating inside the RF electrode was approximated by convective boundary conditions at the chilled fluid-electrode interface with heat transfer coefficient $h=4416.3 \text{ W/m}^2/\text{K}$ and $T=10^\circ\text{C}$ (Zhang et al., 2014).

RESULTS AND DISCUSSION

The output of Radiofrequency ablation of the cancerous tumor tissue situated in the different body organs, depends on the electrical and thermo physical properties of the tumor and tissue, as well as geometrical parameters of the tumor. These properties vary with biological tissues. In this computational study, the temperature distribution and lesion size created during RFA of Liver, Lung and Kidney tissue with spherical tumors of diameter 15mm, 25mm and 35mm, at 35V constant voltage and 20 min time has been studied. The effect of tumor location on lesion creation has been studied by considering the tumor(25mm diameter) at different layers of breast i.e., glandular region, muscle and fat as per the American Joint Committee on Cancer guidelines (Compton et al.,2012). The effect of blood perfusion rate has been studied for tissues (Liver, Lung and Kidney) of 15mm diameter tumor. The different perfusion rates (0%, 25%, 50%, 75% and 100%) are used. The effect of electrical conductivity and thermal conductivity has been studied for liver tissue (15mm diameter tumor). The electrical and thermal conductivities of the tissue and tumor used for the study are given in the Table 4 and 5 respectively. The process has been carried out at constant voltage source with 20min ablation time.

Validation of Computational model

The computational model was validated by comparing with the results obtained during experimental study of RFA on bovine liver (Sethuraman et al.,2014) and FEM model

(Singh et al.,2016). For validation the following bovine liver properties are used such as electrical conductivity (σ)= 0.18 S/m , thermal conductivity (k)= 0.65 W/m-K , density(ρ)= 1060 kg/m^3 and specific heat (c)= 3600 J/kg-K . Fig.2 shows the comparison of the electrode tip temperature obtained after performing the RFA of bovine liver at 6W power and 15 min ablation time. A good agreement has been found between the results obtained in experimental and computational study.

Temperature distribution and Lesion formation in different tissues

The simulation results for the maximum temperature progress at a point in the tumor and ablation volume (measured at Isothermal temperature 50°C and damage integral (w)>1) for the Liver, Lung and Kidney with different diameters at 20 min ablation time are presented in Table 3. Fig.3(a, c and e) shows the temperature distribution in the tissue during the process from the electrode along y direction. The maximum temperature was attained in 35mm diameter size tumor of each tissue. Maximum temperature was obtained in the Lung tissue when compared to others. High temperature is concentrated near the electrode, it goes on decreasing as moved away from electrode. The Fig.3(b, d and f) shows the fraction of necrotic tissue formation at different points in the tumor with respect to time. The necrosis happens faster near the electrode and slower at a distance away from the electrode. High ablation volume is reported in larger tumor of 35 mm than 25 and 15 mm size tumors at constant voltage source of 35V. Highest ablation volume is reported in lung tissue and least in kidney. As size of the tumor increases, the ablation volume also increases but the complete ablation of tumor volume is achieved in smaller size tumor than the larger size tumor as reported in liver tissue. Values quoted within the parenthesis of Table 3 represents the volume obtained at temperature 105°C and time required to reach this temperature because in these cases maximum temperatures attained after reaching the study state have been higher than the charring temperature of tissue. The

temperature and ablation volume increases with increasing size of tumor because of high electrical and thermal conductivity of tumor. But the complete ablation of tumor volume decreases with increasing size of the tumor, so to achieve complete ablation of larger tumor either applied voltage or ablation time as to be increased and also we need to take care of charring of tissue in this case. The maximum attained temperature and ablation volume obtained for kidney is less because of high blood perfusion rate which causes the cooling effect.

Effect of Blood Perfusion rate

The Fig.4 shows the results for the effect of blood perfusion rates on lesion creation in liver, lung and kidney tissue with 15mm diameter at 40 V. The maximum and minimum ablation volume is reported in case of zero and 100% perfusion rates respectively. As the increase in blood perfusion rate, the cooling effect also increases which results sink effect. This in turn causes the decrease in lesion size formation. The lesion formation increases with decreasing blood perfusion rates. The maximum ablation volume created for the lung tissue compare to other tissues because of its lower perfusion rate than others. The minimum ablation volume created for the kidney compare to others in all the cases except 0% perfusion rate because of its high perfusion rate.

Effect of tumor location on lesion formation.

The effect of location of tumor within the different layers of breast tissue is studied by applying constant voltage source of 22V, 25V and 70V for the gland, muscle and fat layers respectively. The Table 3 shows the computational results for the breast. The Fig.5 shows the maximum temperature obtained at different tumor location. In this study the applied voltage and ablation time is varied for different tumor location based on the study (Singh and Repaka, 2016). The maximum temperature is obtained in gland and muscle region. Minimum temperature is obtained in fat region. The maximum ablation volume is obtained for the fat region and minimum ablation volume is

obtained for gland and muscle. These variations are because of the high electrical conductivity of gland and muscle tissue and low conductivity and low perfusion rate of fat.

Influence of electro-thermal properties of tissue and tumor on lesion formation

The results for the different electrical conductivity values for the tissue and tumor are presented in Table 4. The Fig.6 shows the fraction of necrotic tissue formation with time for the different values of electrical conductivity. The maximum temperature is obtained when the value of electrical conductivity of tumor is less than the tissue. The lesion formation is more when the value of electrical conductivity of tumor is more than the tissue (i.e. tumor-0.5 and tissue-0.143) and lesion is less when the electrical conductivity of tumor is less than the tissue (i.e. tumor-0.1168 and tumor-0.333). The formation of lesion increases with increasing electrical conductivity of tumor and decreases with increasing electrical conductivity of tissue. Table 5 shows the results obtained for the different thermal conductivity (k) values for the tumor and tissue. The maximum temperature and lesion size are obtained for the case 1 (k values 0.22 for tissue and 0.302 for the tumor). Low temperature and lesion size are obtained at case4 (k values 0.52 for tissue and 0.6 for the tumor). From these results, the ablation volume was found to be more for same k values of both tumor and tissue. If the k value of tumor is higher than the k value of tissue the ablation volume is more and vice versa as in the cases 1 (tissue-0.22, tumor-0.302) and 3 (tissue-0.564 and tumor-0.302).

CONCLUSIONS

The computational study is carried out by solving the three dimensional Pennes bioheat transfer equation. Each biological tissue and tumor possesses its own properties. Based on the study, geometrical properties of tumor, electro thermal properties of tumor and tissue affect the formation of lesion. The study concludes that

6th International Engineering Symposium - IES 2017

March 1-3, 2017, Kumamoto University, Japan

- The tumor size significantly affects on the complete necrosis of tumor.
- Complete ablation of larger tumor can be achieved either by varying supply voltage or by increasing ablation time or both.
- The blood perfusion rate is playing an important role in ablation of tumor volume.
- The electrical conductivity and thermal conductivity of both tissue and tumor affects the lesion formation during RFA.
- The outcome of the RFA treatment depends on tissue type.

REFERENCES

1. Alba,J et al.(2011), Theoretical and experimental study on RF tumor ablation with internally cooled electrodes: When does the roll-off occur?, 33rd Annual International IEEE EMBS Conference.
2. Bing Zhang, et al.(2014), Study of the relationship between the target tissue necrosis volume and the target tissue size in liver tumours using two-compartment finite element RFA modeling, Int. J. Hyperthermia, Vol 30(8),pp 593–602.
3. Berjano, E J (2006), Theoretical modeling for radiofrequency ablation: state-of-the art and challenges for the future, Biomed. Eng. Online 5.
4. Chu, K F and Dupuy, D E (2014), Thermal ablation of tumours: biological mechanisms and advances in therapy, Nature Reviews Cancer, Vol 14(3), pp 199–208.
5. Compton, C C et al. (2012), Part VII Breast. AJCC Cancer Staging Atlas: a companion to the seventh editions of the AJCC Cancer Staging Manual and Handbook, New York: Springer-Verlag, pp 419–440.
6. Dinesh Kumar, et al. (2016), A study on DPL model of heat transfer in bi layer tissues during MFH treatment, computers in Biology and medicine, Vol 75, pp 160-172.
7. Erol Ulucakli, M (2009), Heat Transfer and Tissue Damage In Radiofrequency Ablation Therapy, Proceedings of the ASME 2009 International Mechanical Engineering Congress & Exposition.
8. Erol Ulucakli, M and Christopher, S L (2013), Effect Of Perfusion Rate On The Radiofrequency Ablation Of Liver tumors, Proceedings of The ASME 2013 International Mechanical Engineering Congress and Exposition November 15-21,USA.
9. Fornage, B D et al. (2004), Small (r2-cm) breast cancer treated with US-guided radiofrequency ablation: feasibility study, Radiology, Vol 231, pp 215–224.
10. Francica, G and Marone, G(1999), Ultrasound guided percutaneous treatment of hepatocellular carcinoma by radiofrequency hyperthermia with a 'cooled-tip needle'. A preliminary clinical experience. European Journal of Ultrasound, Vol 9, pp 145–153.
11. Gillams, A and Lees, W (2005), Radiofrequency ablation of colorectal liver metastases, Abdom Imaging, Vol 30, pp 419–426.
12. Henriques, F C (1947), Studies of thermal injury: The predictability and significance of thermally induced rate processes leading to irreversible epidermal injury, Arch. Pathol, Vol 43, pp 489-502.
13. Jamil, M and Ng, E Y K (2013), To optimize the efficacy of bioheat transfer in capacitive hyperthermia: A physical perspective, Journal of Thermal Biology, Vol 38 (5), pp 272–279.
14. Jamil, M and Ng, E Y K (2015), Quantification of the effect of electrical and thermal parameters on radiofrequency ablation for concentric tumour model of different sizes, Journal of Thermal Biology, Vol 51,pp 23–32.
15. Nahum Goldberg, S (2001), Radiofrequency tumor ablation: principles and techniques, European Journal of Ultrasound, Vol 13,pp 129–147.
16. Ng, E Y K and Jamil, M (2014), Parametric sensitivity analysis of radiofrequency ablation with efficient experimental design, Int. J. Thermal Science, Vol 80, pp 41–47.
17. Pennes, H H (1998), Analysis of tissue and arterial blood temperatures in the resting human fore arm, Journal of Applied Physiology, Vol 85(1), pp 5-34.
18. Schutt, D J and Haemmerich, D (2008), Effects of variation in perfusion rates and of perfusion models in computational models of radio frequency tumor ablation, Medical Physics, Vol 35(8), pp 3462–3470.
19. Sethuraman, S et al.(2014), Integrated ultrasound thermometry and multiphysics modeling for liver RF ablation monitoring: Ex vivo studies, Proceedings of the IEEE Ultrasonics Symposium, Chicago, USA, pp 1650–1653.
20. Singh, S et al. (2016), Thermal analysis of induced damage to the healthy cell during RFA of breast tumor, Journal of Thermal Biology, Vol 58, pp 80–90.
21. Stauffer, P R (2005), Evolving technology for thermal therapy of cancer, Int. J. Hyperthermia, Vol 21,pp 731–744.
22. Sundeep Singh and Ramjee Repaka (2015), Preclinical modeling and simulation of hepatic Radiofrequency ablation, Excerpt from the proceedings of the COMSOL conference.
23. Sundeep Singh and Ramjee Repaka (2016), Temperature-controlled radiofrequency ablation of different tissues using two-compartment models, Int. J. Hyperthermia, Online, <http://dx.doi.org/10.1080/02656736.2016.1223890>.
24. Tungjitkusolmun, S et al.(2002), Three-dimensional finite-element analyses for radio-frequency hepatic tumor ablation.,

6th International Engineering Symposium - IES 2017

March 1-3, 2017, Kumamoto University, Japan

- | | |
|--|--|
| IEEE Transactions on Biomedical Eng., Vol 49, pp 3-9. | necrosis and mathematical modelling, Physica Medica, Vol 32, pp 961-971. |
| 25. Zhang, B et al.(2013), Radiofrequency ablation technique in the treatment of liver tumours: review and future issues, Journal of Medical Eng. and Technology, Vol 37,pp 150-159. | 27. Zorbas, G and Samaras, T (2014), Simulation of radiofrequency ablation in real human anatomy, Int. J. Hyperthermia, Vol 30,pp 570-578. |
| 26. Zhang, B et al. (2016), A review of radiofrequency ablation: Large target tissue | |

Table 1 Electrical and thermo physical properties of the different tissues, tumor and electrode.

Material	Electrical Properties	Thermo -Physical properties			
		Specific Heat capacity c (J/kg-K)	Thermal conductivity k (W/m-K)	Density ρ (kg/m ³)	Blood perfusion rate w_b (mL/min-kg)
Tissue/Electrode				Tissue	Tumor
Liver	0.143	3540	0.52	1079	902 111
Kidney	0.224	3763	0.53	1066	4161 924
Lung	0.122	3886	0.39	394	401 349
Breast Gland	0.563	2960	0.33	1041	28.82 305.48
Breast fat	0.0254	2348	0.21	911	13.17 349.07
Breast muscle	0.439	3421	0.49	1090	44.04 291.74
Electrode	10^8	840	18	6450	---
Trocars Base	10^{-5}	1045	0.026	70	---
Blood	---	3617	---	1050	---
Tumor	0.5	Same as corresponding tissue			---

Table 3 Results obtained during the computational study of RFA on different tissues with varying tumor diameter at constant voltage for the 20 min period of time.

Tumor		Applied voltage in V	Max. Temperature in (°C)	Time taken to reach max. Temperature	Ablation Volume in mm ³	
Type	Diameter (mm)				IT 50	Damage integral $W > 1$
Liver	15	35	72.9	397s	2386.75	2226.38
	25		104	415s	5425.30	1767.35
	35		121	540s(90s)	9289.18 (2412.76)	8581.35 (1098.2)
Lung	15	35	84.3	500s	11129.97	11250.95
	25		112	320s(110s)	12771.7 (5410.38)	8182.29 (1616.36)
	35		135	410s(25s)	17159.50 (5885.71)	10307 (288.73)
Kidney	15	25mm	74.9	135s	936.938	266.111
	25		99.7	240s	1697.61	1616.36
	35		112	135s(54s)	1988 (1108.53)	767.69 (33.51)
Breast Tissue						
Gland	25mm	22	108	240s	4445.75	50.97
Muscle		25	101	570s	5744.96	33.51
Fat		70	101	930s	151512.16	229877.7

6th International Engineering Symposium - IES 2017

March 1-3, 2017, Kumamoto University, Japan

Table 4 Maximum Temperature and lesion size for different electrical conductivity of tissue and tumor during RFA of 15mm Liver tumor at 40V constant source voltage and 20 min time.

Electrical Conductivity		Max.Temperature in °C	Lesion size in mm ³ (IT50)	Lesion size in mm ³ (w>1)
Tissue	Tumor			
0.143	0.5	86	3251.858	1767.375
0.333	0.1168	95.3	1810.132	326.158

Table 5 Maximum Temperature and lesion size for different thermal conductivity of tissue and tumor during RFA of 15mm Liver tumor at 40V constant source voltage and 20 min time.

Thermal Conductivity		Max. Temperature in °C	Lesion size in mm ³ (IT50)
Tissue	Tumor		
0.22	0.302	114	3682.41
0.302	0.302	111	3694.88
0.564	0.302	104	3230.37
0.52	0.6	82.2	3304.91

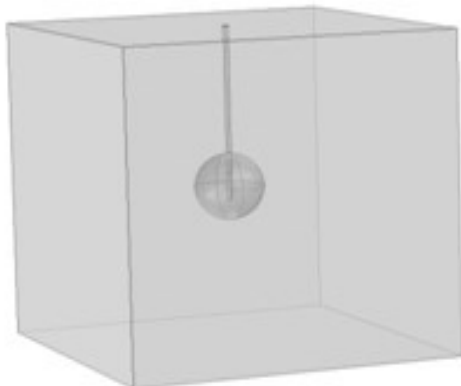


Fig.1 Three Dimensional Model representing a human tissue with spherical tumor and electrode embedded on it.

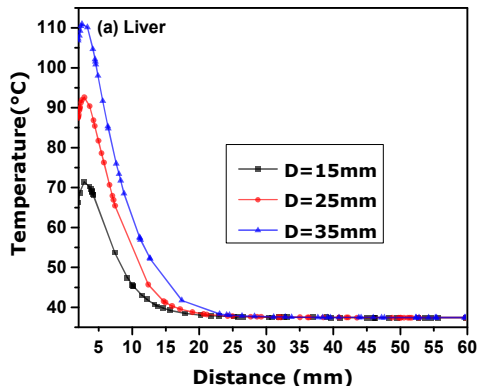


Table 2 Kinetic parameters of the different tissues and tumor.

Tissue	Kinetic parameters	
	Frequency factor A (1/s)	Activation Energy E _a (J/mol)
Liver	7.39x10 ³⁹	2.577x10 ⁵
Kidney	6.00x10 ³⁴	2.385x10 ⁵
Lung	7.39x10 ³⁹	2.577x10 ⁵
Breast	1.18x10 ⁴⁴	3.020x10 ⁵
Tumor	Same as corresponding tissue	

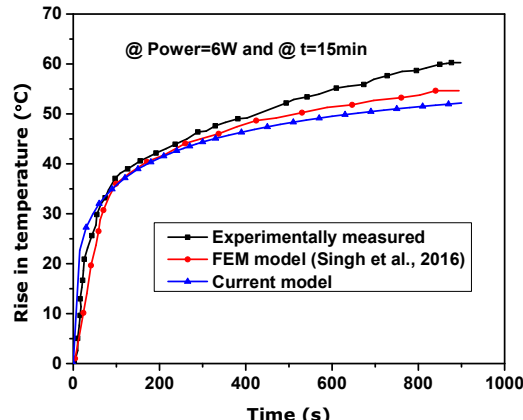
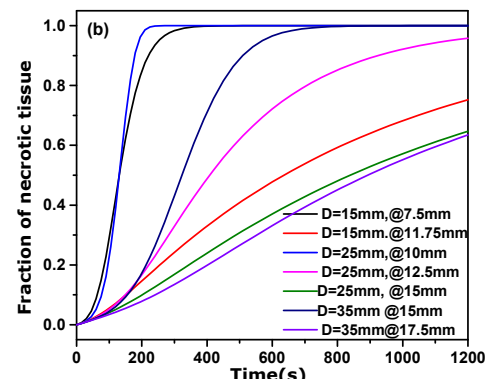


Fig.2 Comparison between experimentally and numerically (FEM model of singh et al. and current model) obtained temperature values at the tip of the electrode during RFA of bovine liver.



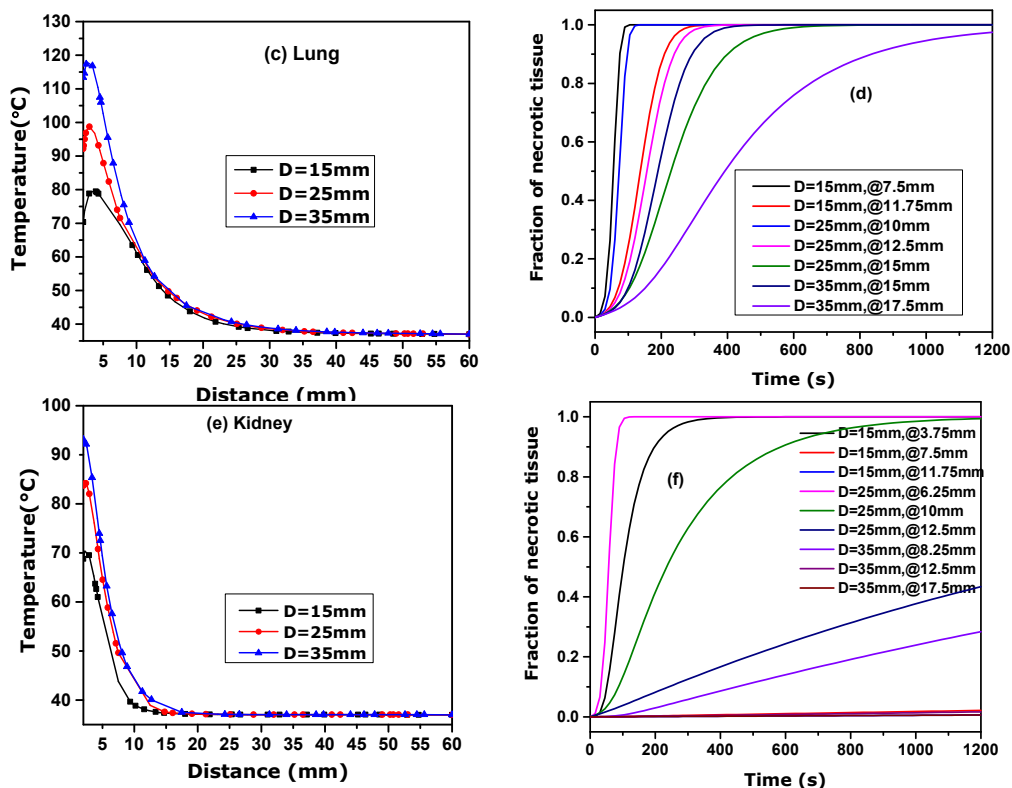


Fig.3 Temperature distribution along Y direction from the electrode in a) Liver, c) lung and e) Kidney, and Fraction of necrotic tissue with time in b)Liver, d)lung and f) Kidney.

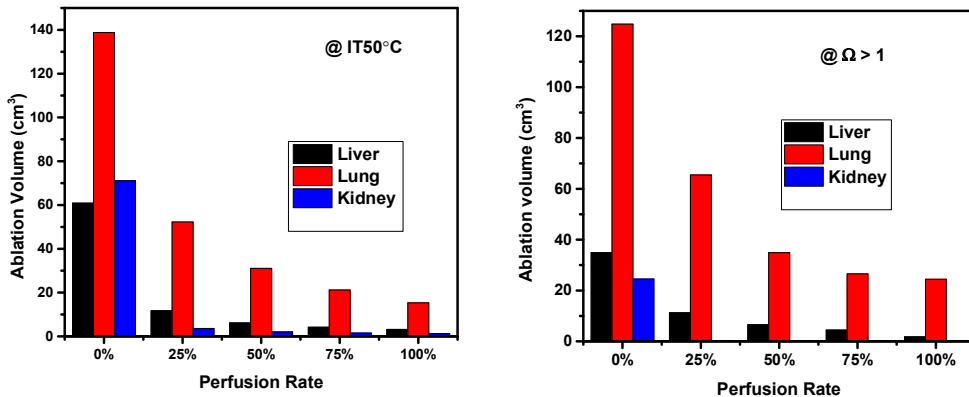


Fig.4 Ablation volume for different perfusion rates of liver,lung and kidney tissues.

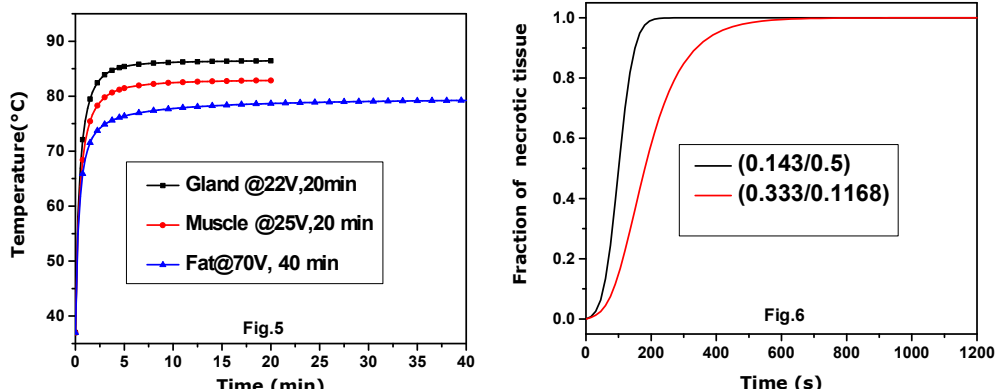


Fig.5 Variation of temperature with time for tumors located in different layers of breast and 6) Fraction of necrotic tissue with time for different values of electrical conductivity.

Semi Active Vibration Control of Partially Treated Magnetorheological Fluid Sandwich Composite Beams

Vipin Allien J¹, Hemantha Kumar² and Vijay Desai³

- 1 Department of Mechanical Engineering, National Institute of Technology Karnataka, Surathkal, Mangalore 575025, India. email: vipinallien@gmail.com
- 2 Department of Mechanical Engineering, National Institute of Technology Karnataka, Surathkal, Mangalore 575025, India. email: hemanta76@gmail.com
- 3 Department of Mechanical Engineering, National Institute of Technology Karnataka, Surathkal, Mangalore 575025, India. Email: vijayhdesai64@gmail.com
-

ABSTRACT: This paper presents semi-active vibration control of partially filled magnetorheological fluid (MRF) chopped strand mat glass fiber polymer matrix sandwich composite beam with varying magnetic field. The vibration controllability of MRF partially filled composite beam structure was investigated experimentally. The experimental investigation has been carried out in three samples of cantilever composite sandwich beams of different MRF core thickness. The structural behavior of the MRF can be varied by applying an external magnetic field. The vibration response control was observed in the form of variations in vibration amplitudes, natural frequency and loss factor. From the experimental results it was identified that the natural frequency increased with increase in MRF core layer thickness, the loss factor of the material is increased for increase in magnetic field and up to 90% vibration amplitude reduction can be obtained using MRF partially treated polymer matrix composite beam at 0.25 Tesla magnetic field.

Keywords: magnetorheological fluid, cantilever beam, vibration control

INTRODUCTION

Normally every structure has its own mechanical properties like strength, stiffness, natural frequencies, damping ratio etc. the ability to change the mechanical properties is possible in smart structures. MRF is a smart fluid, whose rheological properties such as viscosity, yield shear stress are reversible when subjected to magnetic field. The rheology properties of MRF depends on concentration and density of iron particles, particle size, shape, distribution, properties of the carrier fluid, additional additives, applied field, temperature and other factors (jolly, M.R., et al. 1999). The MRF is often mentioned as a Bingham plastic and behaves with linear viscoelastic properties within the pre-yield regions (Li, W.H., et al. 1999). MRF applications can

be categorized as controllable devices and adaptive structures. MRF based brakes, clutches, dampers and semi active prosthetic legs are some of MRF controllable devices.

MRF based adaptive structures mainly concern about the tunable properties subjected to external magnetic field. Rajamohan, V., et al. (2010) observed the vibration analysis of partially treated MRF multilayer aluminum beam and conducted experiments with four samples at different location MRF core and determined the natural frequency and loss factor at 0, 75, 175, 400 and 500 Gauss. Rajamohan, V., et al. (2010) has concluded that reduction in amplitude using controllable MR fluids has high significant effect on natural frequency and loss factor based on location and length of MRF core. Lara et al. (2010) studied the experimental vibration analysis of MR cantilever sandwich beams.

6th International Engineering Symposium - IES 2017

March 1-3, 2017, Kumamoto University, Japan

The stiffness and damping structural characteristics are controlled with vibration suppression capabilities of MRF as structural elements also found that at 0.11 Tesla damping ratio increase to 0.65% and at 0.23 Tesla damping ratio increased to 3.7%.

Many researchers investigated the vibration suppression capabilities of MRF in adaptive structures through experimentally. However, experimental investigation on adaptive structures made of partially treated MRF with composite face layers has not received much attention. Therefore, the aim of this study is to fabricate partially treated MRF composite sandwich beam structure and to calculate the tunable material properties such as natural frequencies, loss factor for varying magnetic field conditions.

SANDWICH BEAM DESIGN AND MANUFACTURE

The partially treated sandwich composite beam consist of 220mm length, 25mm width and of 5, 6.5 and 8 mm thickness were prepared. Chopped strand mat (CSM) glass fiber of 450 g/m² is reinforced with polyester resin and samples of 1.5, 2, 3.5 and 5 mm thickness polymer matrix composite samples were prepared by hand-layup process. Both top and bottom face plate are made of polymer matrix composite of 220mm length, 25mm width and 1.5mm thickness size. The middle core of fixed end and free end are made of polymer matrix composite of 75mm length and 25mm width, whereas thickness varied by 2, 3.5 and 5 mm for different sandwich beam. MRF is prepared by mixing 30 volume % carbonyl iron powder and 70 volume % silicone oil with 0.5 volume % grease. Silicone sealant is applied to cover the middle core gap with a very small gap is allowed to fill the MRF. MRF is filled inside the silicone sealant sandwich beam core and the voids in the core are removed and the small gap for filling MRF is sealed with silicone sealant. The Sandwich beam design considered for the study is shown in Fig. 1.

EXPERIMENTAL SETUP DETAILS

The prepared sandwich composite beam was clamped to a support. The

electromagnet (EMU-75 model) were used to generate the magnetic field over the beam. The electromagnet was connected to constant power supply. Different magnetic field intensity was realized by varying the horizontal pole position of the electromagnet with respect to the beam, which was measured near the beam surfaces using a Gauss meter. The measurements were performed in the absence of electromagnet (0 T) and seven different pole positions of the electromagnet leading to magnetic field intensities of 0.1, 0.125, 0.15, 0.175, 0.2, 0.225, 0.25 T at the beam surfaces. A single-axis accelerometer, was attached near to the fixed edge of the beam, to measure the acceleration response. An impact hammer were used to excite the beam. NI9234 DAQ data acquisition was used to collect the acceleration response from the accelerometer sensor and data was stored using LabVIEW software in the desktop. The experimental setup is shown in Fig. 2. The natural frequency of the partially treated MRF composite sandwich beam were identified from the peaks of frequency response function.

RESULTS AND DISCUSSION

Higher frequency vibration peaks were reduced effectively through the implementation of magnetic field. Fig. 3 (a) shows the amplitude to natural frequency curve of 2 mm MRF core beam. The natural frequency corresponding to the 1st three mode shapes were considered. Fig. 4 (a) shows the amplitude reduction in first mode of 2 mm MRF core based on applying magnetic field. At zero magnetic field 0.16988 (m/s²/N) amplitude was obtained and at 0.25 Tesla magnetic field the amplitude was reduced to 0.01935 (m/s²/N). Therefore 89% amplitude reduction was obtained.

Figure 3 (b) shows the amplitude to natural frequency curve corresponding to 1st three mode shapes of 3.5 mm MRF core beam. Fig. 4 (b) shows the first mode amplitude reduction based on applying magnetic field. At zero magnetic field 0.15419 (m/s²/N) amplitude was obtained and at 0.25 Tesla magnetic field the amplitude was reduced to 0.04721

6th International Engineering Symposium - IES 2017

March 1-3, 2017, Kumamoto University, Japan

(m/s²/N). Therefore 70% amplitude reduction was obtained.

Fig. 3 (c) shows the amplitude to natural frequency curve of 5 mm MRF core beam. The natural frequency corresponding to the 1st three mode shapes were considered. Figure 4 (c) shows the first mode amplitude reduction based on applying magnetic field. At zero magnetic field 0.04821 (m/s²/N) amplitude was obtained and at 0.25 Tesla magnetic field the amplitude was reduced to 0.00529 (m/s²/N). Therefore 90% amplitude reduction was obtained.

Fig. 5 (a), (b) and (c) shows the displacement to time curve of 2mm MRF core, 3.5mm MRF core and 5mm MRF core beam. From the figure it was observed that the displacement varied but time taken for excitation of beam was almost same while varying magnetic field.

Loss factor is the amount of energy dissipated for a complete cycle. Loss factor is directly related to damping ratio. It was calculated using half bandwidth equation (Carfagni, M., et. al 1998). Fig. 6 (a), (b) and (c) shows the loss factor dependence on magnetic field for first three modes of partially treated 70mm length MRF core of 2mm thickness, 3.5mm thickness and 5mm thickness. Considering 1st mode for 2mm MRF core at zero magnetic field 0.1139 loss factor and at 0.25 Tesla magnetic field 0.1951 loss factor was obtained. For 3.5mm MRF core at zero magnetic field 0.048458 loss factor and at 0.25 Tesla magnetic field 0.078731 loss factor was obtained. For 5mm MRF core at zero magnetic field 0.052704 loss factor and at 0.25 Tesla magnetic field 0.17352 loss factor was obtained. The results shows that loss factors increase with increase in the magnetic field. The loss factor is directly related to the loss modulus, which decreases in higher modes compared to those of the fundamental first mode.

The stiffness and damping structural characteristics are controlled with vibration suppression capabilities of MRF as structural elements. 2mm gap and 70mm length MRF beam have 10% vibration suppression at 0.1 Tesla and 89%

vibration suppression at 0.25 Tesla. 3.5mm gap and 70mm length MRF beam have 30% vibration suppression at 0.1 Tesla and 70% vibration suppression at 0.25 Tesla. 5mm gap and 70mm length MRF beam have 50% vibration suppression at 0.1 Tesla and 90% vibration suppression at 0.25 Tesla. Based on results 5mm gap and 70mm length MRF partially treated beam has better vibration suppression compared to 2mm and 3.5mm gap 70mm length MRF partially treated beams.

CONCLUSION

In this paper, the authors have described experimental investigations on the semi active damping of a MRF partially treated polymer matrix composite beam. In the first mode a slight variation in natural frequency was obtained for partially treated MRF sandwich composite beam with and without magnetic field. The natural frequency at higher modes is increased in partially treated MRF sandwich composite beam with increase in magnetic field. It was observed that loss factor and vibration amplitude suppression of partially treated MRF sandwich composite beam is improved to increase in magnetic field. The polymer matrix partially treated MRF sandwich composite beam has a very good vibration suppression and it is suitable for semi active vibration control.

REFERENCES

- [1] Rajamohan, V., et al (2010), Vibration analysis of a partially treated multi-layer beam with magnetorheological fluid, Journal of Sound and Vibration, Vol. 329, No. 17, pp. 3451-3469.
- [2] Lara-Prieto, V., et al (2009), Vibration characteristics of MR cantilever sandwich beams: experimental study, Smart Materials and structures, Vol. 19, No.1, pp. 015005.
- [3] Jolly, M. R., et al (1999), Properties and applications of commercial magnetorheological fluids, Journal of intelligent material systems and structures, Vol. 10, No.1, pp. 5-13.
- [4] Li, W. H., et al (1999), Viscoelastic properties of MR fluids. Smart Materials and Structures, Vol. 8, No. 4, pp. 460.
- [5] Carfagni, M., et al (1998), The loss factor as a measure of mechanical damping, In Proceedings-spie the international society for optical engineering, Vol. 1, pp. 580-284.

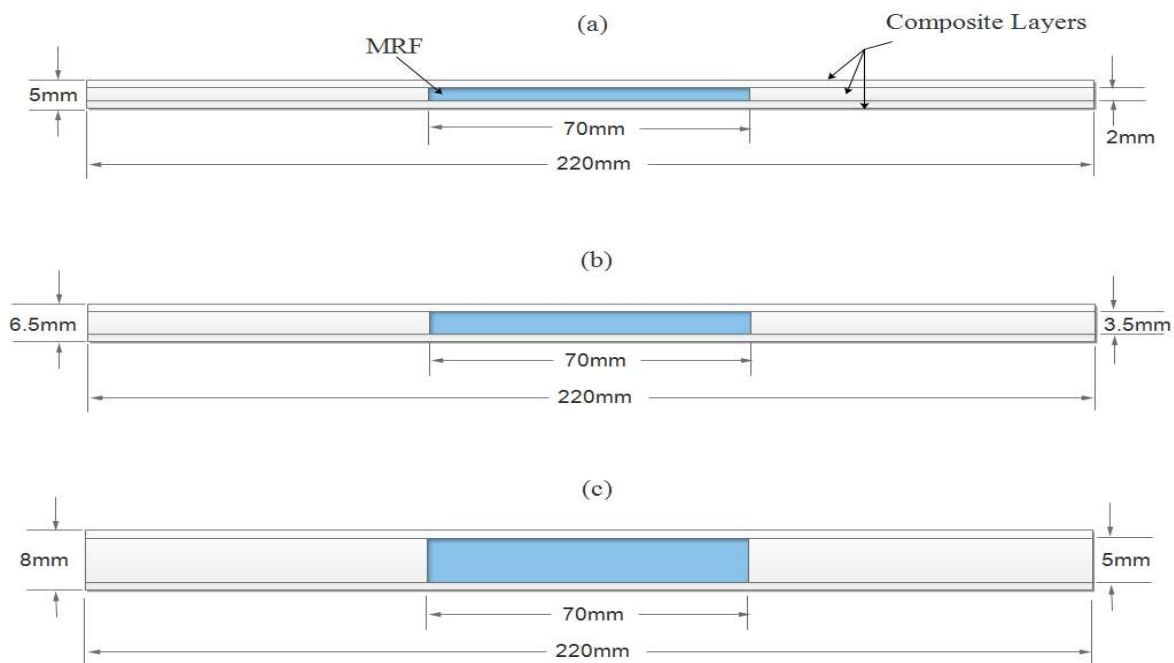


Fig. 1. Diagram of partially treated 70mm length MRF beam structure (a) 2mm thickness, (b) 3.5mm thickness and (c) 5mm thickness core.

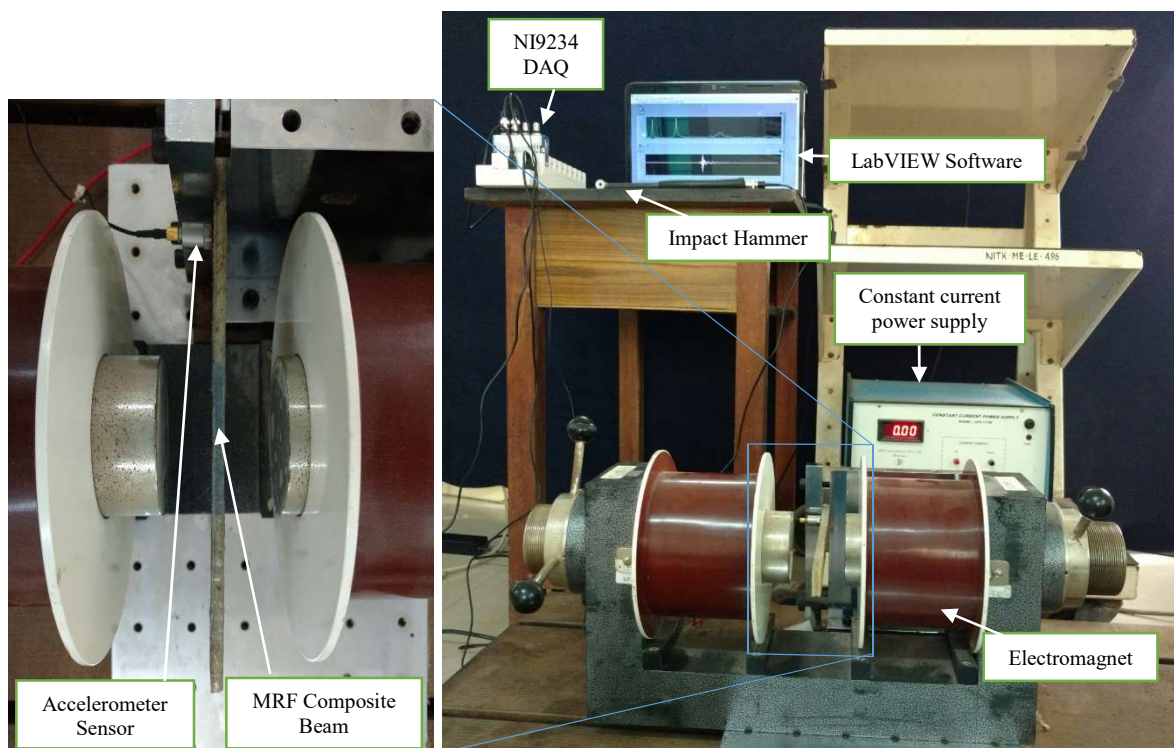


Fig. 2. Experimental setup

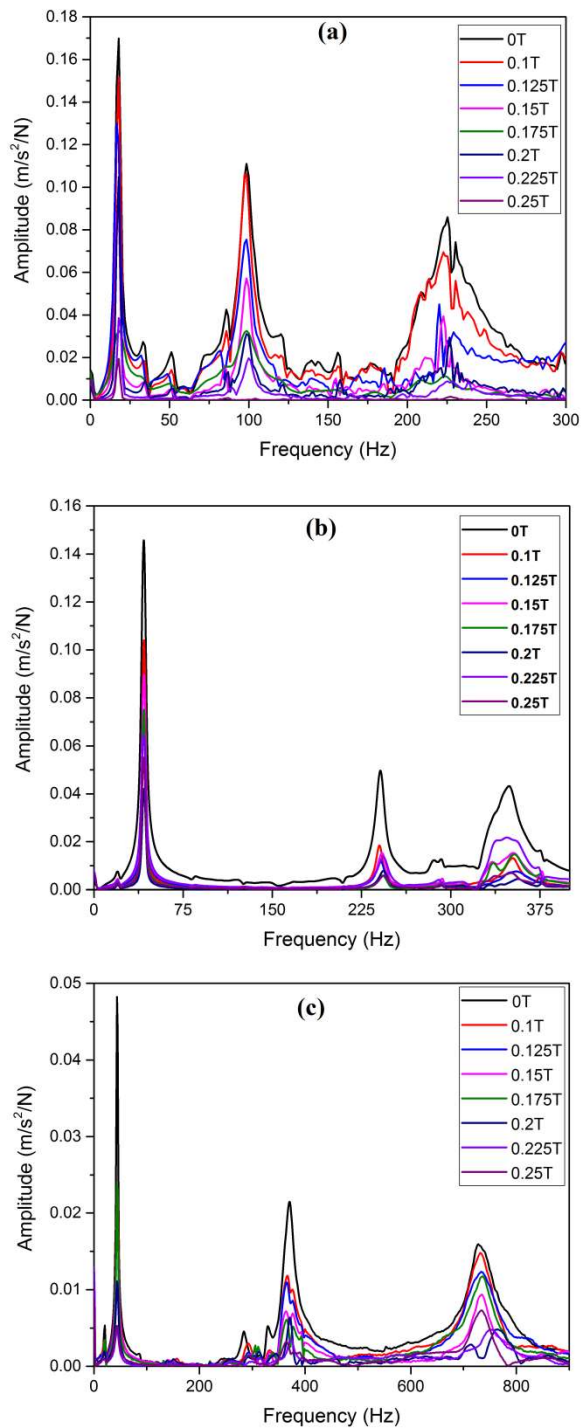


Fig. 3. Amplitude vs frequency curve for 1st three mode shape of partially treated 70mm length MRF beam of (a) 2mm thickness, (b) 3.5mm thickness and (c) 5mm thickness core.

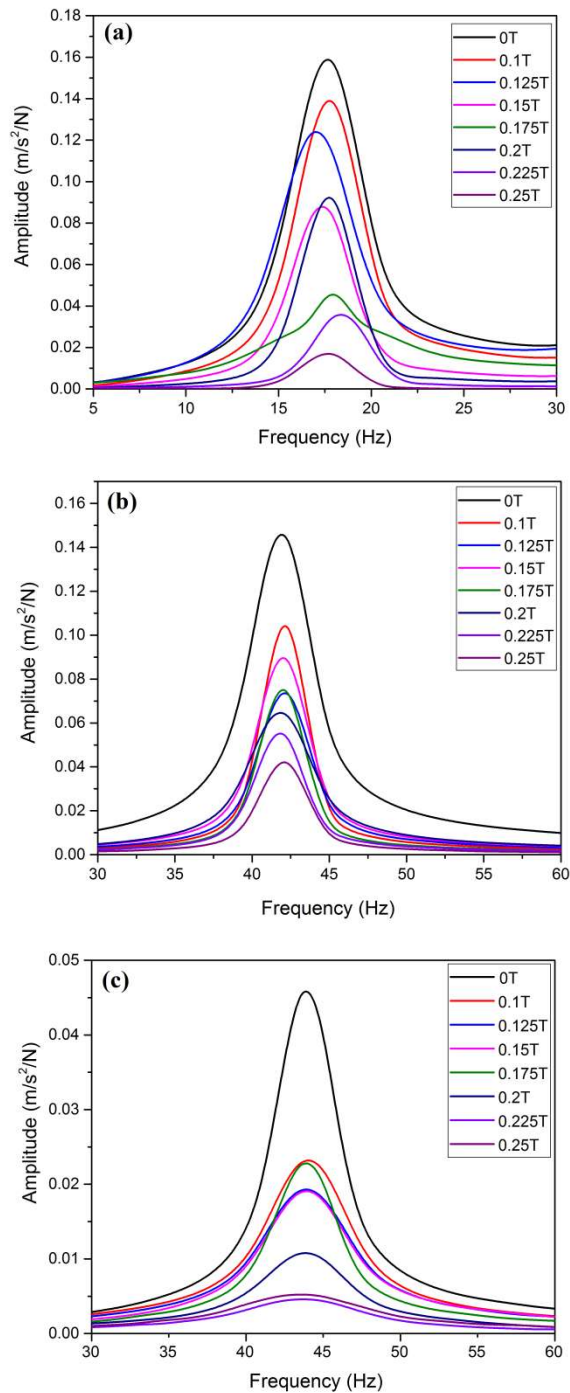


Fig. 4. Amplitude vs frequency curve for 1st mode shape of partially treated 70mm length MRF beam of (a) 2mm thickness, (b) 3.5mm thickness and (c) 5mm thickness core.

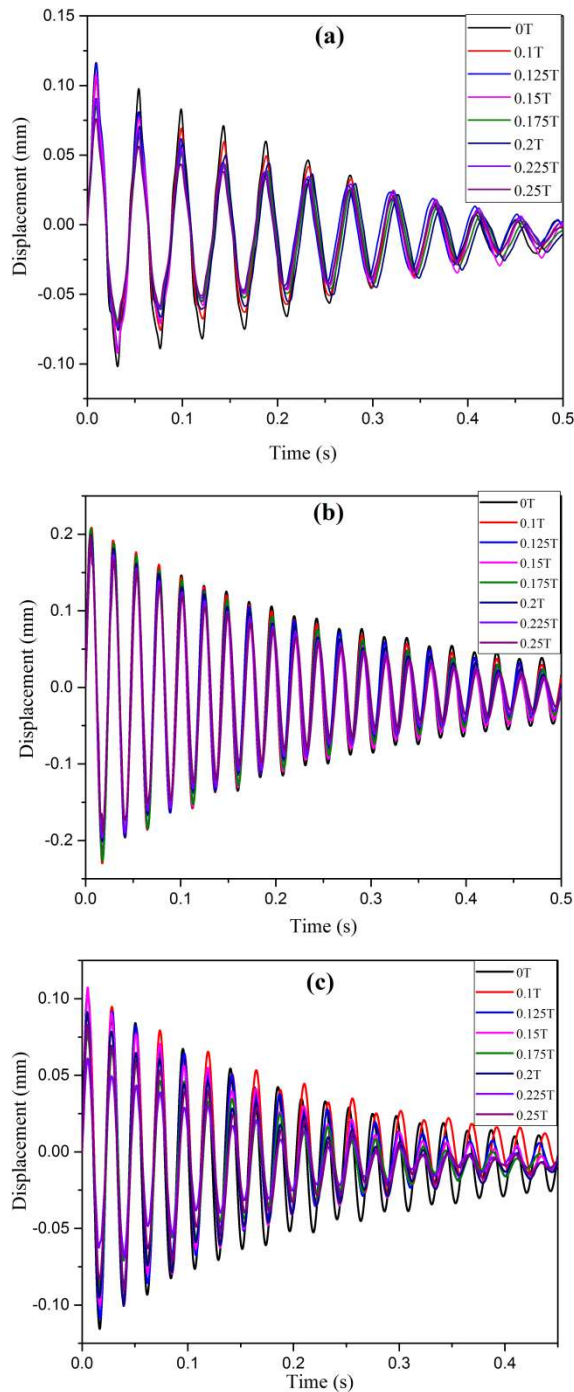


Fig. 5. Displacement vs time curve for partially treated 70mm length MRF beam of (a) 2mm thickness, (b) 3.5mm thickness and (c) 5mm thickness core.

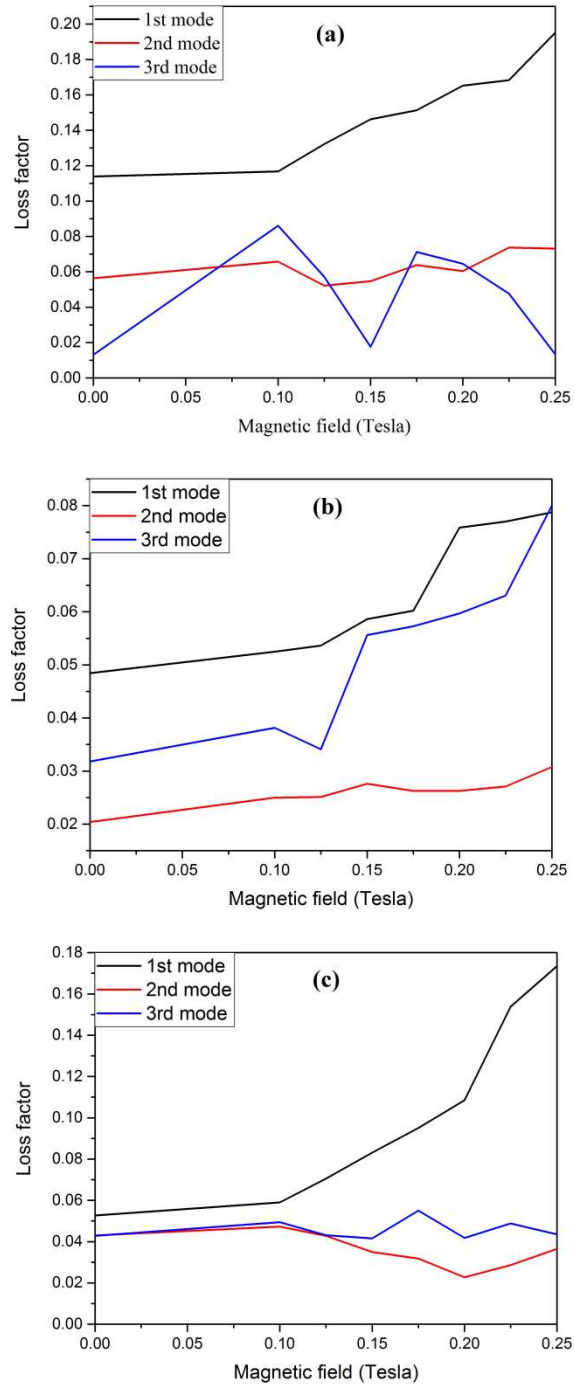


Fig. 6. Loss factor dependence on magnetic field for first three modes of partially treated 70mm length MRF beam (a) 2mm thickness, (b) 3.5mm thickness and (c) 5mm thickness core

6th International Engineering Symposium - IES 2017

March 1-3, 2017, Kumamoto University, Japan

**ELECTRICAL, ELECTRONICS,
COMPUTER ENGINEERING
&
RELATED FIELDS**

Wireless Monitoring of Water Resources in a Campus

N. Shekar V. Shet¹, Naveen Kumar Panguluri², Harsha M P³ and Abhishek MB⁴,

- 1 *Department of Electronics and Communication, National Institute of Technology Karnataka, Surathkal, Mangalore 575025, India.*
email: shekar_shet@yahoo.com
- 2 Thought focus, Tower 'B', 4th Floor, #12, Subramanya arcade, Bannerghatta road, Bangalore 560029, India.
email: naveen.panguluri@thoughtfocus.com
- 3 Thought focus, Tower 'B', 4th Floor, #12, Subramanya arcade, Bannerghatta road, Bangalore 560029, India.
email: harsha.mp@thoughtfocus.com
- 4 *Department of Electronics and Communication, National Institute of Technology Karnataka, Surathkal, Mangalore 575025, India.*
email: abhishek.mb@gmail.com
-

ABSTRACT: An attempt has been made to wirelessly monitor the distribution of water resources on a campus of an area approximately 330 acres. We are successful in collecting water distribution data from the three overhead tank locations and pressure values from the three other tanks, all on a daily basis. Web pages are created for the purpose and readings can be obtained anywhere, anytime. SMS can be sent and reply message is being obtained from the DTU (Data Transmission Units) placed at these locations. Our next project is to control the water flow by the use of wirelessly controlled solenoids. The attempt is to reduce the dependence on manpower for these daily tasks.

Keywords: Data transmission unit (DTU), ACE web, water monitoring and distribution.

INTRODUCTION

Pure potable water is one of the most important natural resources, which is the essence of life for any living organism. Human beings are ready to go to war to acquire hold of this natural resource. Conservation of this natural resource is of prime importance in today's world scenario, where potable water resources are depleting quite fast. Water has played a important role, not only in the history of countries, but in religion, mythology, and art. It affects every continent and approximately, 2.8 billion people, around the world. More than 1.2 billion people lack access to clean drinking water [1]. However, some observers have estimated that by 2025, more than half of the world's population will be facing water-based vulnerability. A report (UNESCO 2015)

suggests that by 2050, global water demand will exceed by 55%[2]. Therefore it becomes very important for us to conserve water by reducing wastage and proper utilization. Monitoring, distribution and controlling water supply through the pipeline are vital. It is a well-known fact that several lakhs of kilometers of water pipelines are already laid on the surface of the earth over the centuries. Even today most of the distribution is handled by human intervention while moving to specific locations and shutting OFF or turning ON valves. In this process, water is improperly managed and wastage is inevitable since man is prone to commit errors.

Methodology:

Our approach, is to use wireless technology to monitor the water level in

6th International Engineering Symposium - IES 2017

March 1-3, 2017, Kumamoto University, Japan

overhead tanks. We have also measured pressures at different inlet points of the three overhead tanks. Reed switch sensors are placed on common mechanical displacement water meters to measure the flow of water through inlet and outlet pipes. Once calibrated the difference in flow readings gives the amount of residual water in the tanks.

The Reed switches are wirelessly connected to an aggregator, which in turn records the readings of all the inlet and outlet meters. These readings are sent to ACE servers (ACE means " Affordable, Convenient and Efficient"). More about ACE is in appendix 1. The measured values are sent using a DTU (Data Transmission Unit) which have GSM SIM cards with unique cellular numbers. The DTU can be accessed via SMS to retrieve present readings, at each inlet and outlet. The measured pressure readings are also sent to the ACE web servers and are available for ready reference.

Appendix 1: [3]

ACE, is a hardware, communication, software and analytics technology platform developed by a team at "Thought Focus", Bangalore that helps easy data collection and analysis. ACE convolutes various networking technologies to collect data from the field and transmit to a central server. The last mile networking technology, which is used to monitor the measurement points can have traditional wired bus topology, Infrared, Optical Interfaces, low range RF, wireless LAN to push the data to the central server using the widely available long haul TCP/IP, GPRS, GSM networks. **Ubiquity, Agnostic, Affordability, Convenience, and Efficiency** is the primary characteristics of ACE. Its cloud presence allows centralized monitoring and analysis. Today the challenge for people willing to start measuring is where to save these measurements and how to access the historical measurements for meaningful analysis. Every hardware manufacturer tries providing software that works with its products only and ends up having multiple software's only to be disillusioned. ACE

solves that problem. It is capable of reading data from any device and brings all data to one common place.

Features of ACE:

- ACE is Thought Focus proprietary smart measurement framework that allows companies monitor their operations and assets, without boundaries of geography, location and time.
- Powerful web-based network management, data analytics platform that offers a range of features to deduce meaningful inferences from the data that is collected.
- Models Physical Sensor conforming to IEEE 802.15.4 Application Profiles. This makes it highly flexible to measure Utility Consumption (Water, Energy, and Fuel), Quality Measurement (Water, Air, and Milk), and Asset Location.
- Developed as Service Oriented Architecture using latest technology platforms, it allows data collection from ACE and NON-ACE networks.
- The range of sensor network technologies available that include Ghz and Sub-GHz RF networks, Optical Fiber Back Bones, Standard Industrial Bus Topology, GSM / GPRS.
- Works equally effective in Metropolitan networks (> 1000 sensors), Industrial Networks (>100 sensors), Private networks (<100 sensors).

System Overview Water Level Monitoring:

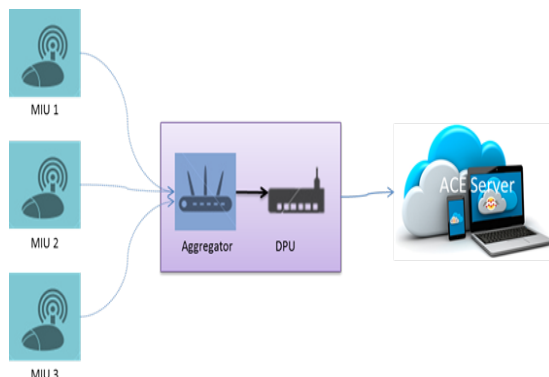


Fig.1 Block Diagram of Water levels monitoring.

System Overview Pressure Sensing

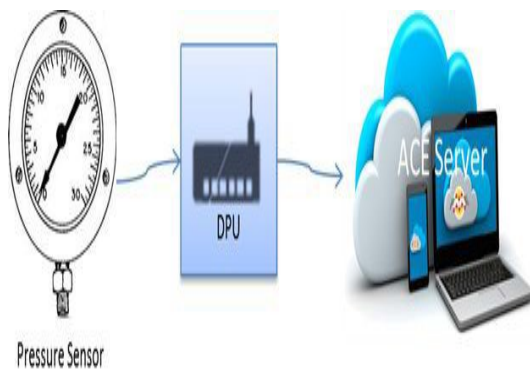


Fig.2 Block Diagram of pressure sensing.

The Fig[1,2] shows, the Reed switches along with RF modules connected to an aggregator, which in turn records the readings of all the inlet and outlet meters. These readings are sent to ACE servers which are capable of reading data from the aggregator and bring all data to the server and finally view in the ACE web.

A sample Structure of Pulse count query command by aggregator to RF modules:

COMMAND START BYTE	LENGTH	COMMAND TYPE	DESTINATION ADDRESS	READ / WRITE	CHECK SUM	END BYTE
0X2B (1Byte)	0X08 (1Byte)	0X01 (1Byte)	0X00000002 (4Bytes)	0X00 (1Byte)	0x62 (1Byte)	0X2C (1Byte)

Fig.3 Structure of Pulse count query.

Length (8) == Length (1) + Command Type (1) + Destination address (4) + Read/write (1) + Checksum (1)
Checksum = Sum of all bytes in command byte stream except check sum (1 byte addition).

A sample Response structure of Pulse count query command by RF modules to aggregator:

RESPONSE START BYTE	LENGTH	COMMAND TYPE	SOURCE ADDRESS	PULSE COUNT	CHECK SUM	END BYTE
0X2D (1 Byte)	0X0B (1 Byte)	0X01 (1 Byte)	0X00000002 (4 Bytes)	0X00000005 (4 Bytes)	0X6A (1 Byte)	0X2C (1 Byte)

Fig.4 Structure of Response Pulse counts query.

Length (11) == Length (1) + Command Type (1) + Destination address (4) + Pulse count (4) + Checksum (1)
Checksum = Sum of all bytes in command byte stream except check sum (1 byte addition).

A sample Structure of pulse count Reset command by aggregator to RF module:

COMMAND START BYTE	LENGTH	COMMAND TYPE	DESTINATION ADDRESS	READ / WRITE	CHECK SUM	ENDBYTE
0X2B (1Byte)	0X08 (1Byte)	0X02 (1Byte)	0X00000002 (4Bytes)	0X00 (1Byte)	0x63 (1Byte)	0X2C (1Byte)

Fig.5 Structure of Pulse count reset.

Length (8) == Length (1) + Command Type (1) + Destination address (4) + Read/write (1) + Checksum (1)
Checksum = Sum of all bytes in command byte stream except check sum (1 byte addition).

A sample Response structure of Pulse count reset command by RF module to Aggregator:

RESPONSE START BYTE	LENGTH	COMMAND TYPE	SOURCE ADDRESS	PULSE COUNT	CHECK SUM	END BYTE
0X2D (1 Byte)	0X0B (1 Byte)	0X02 (1 Byte)	0X00000002 (4 Bytes)	0X00000000 (4 Bytes)	0X68 (1 Byte)	0X2C (1 Byte)

Fig.6 Structure of Response Pulse count reset.

6th International Engineering Symposium - IES 2017

March 1-3, 2017, Kumamoto University, Japan

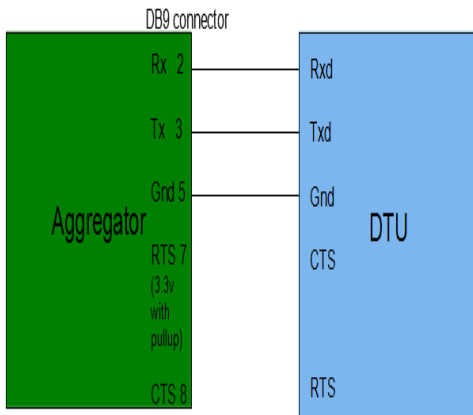
Length (11) == Length (1) + Command Type (1) + Destination address (4) + Pulse count (4) + Checksum (1)
 Checksum = Sum of all bytes in command byte stream except check sum(1 byte addition).

Table 1 Meter interface unit Address table.

Byte Stream Format from DTU to ACE Server (Split View)

3C|A100|03|00|0D0B07DC0F0505|00|07|37|1000000000002001|C02E|01|F020|0001|0002|000B|000C|0015|0018|001B|0000432100012340000456300003214000023130000ACFD000A4321xx3E

Interface diagram between aggregator and DTU.



UART configuration

Baud:9600 Bits:8 Parity:none Stop:1 Flow control:None

Fig.7 Interface diagram.

Pre-defined MIU Address table

MIU	Address
Inlet 1	0x00000001
Inlet 2	0x00000002
Inlet 3	0x00000003
Inlet 4	0x00000004
Inlet 5	0x00000005
Outlet 1	0x00000006
Outlet 2	0x00000007
Outlet 3	0x00000008
Outlet 4	0x00000009
Outlet 5	0x0000000A

Message header	Description	Length (bytes)	Type
3C	Start byte (constant)	1	int
A100	Message code (constant)	2	int
03	Status: 3 - Message with Retry counter and Time stamp	1	int
00	Retry counter	1	int
000B07DC0F0505	Time stamp in format DDMMYYYYHHMMSS (all in hex)	7	int
00	Indicates total number of responses that shall follow the current message stream	1	int
07	No of parameters in this message = 4+ Inlet 1 + Inlet 2 + Outlet 1 + Outlet 2 and so on ...	1	int
37	Total number of bytes following this (Sum of bytes from Device ID to Meter Alarm status value)	1	int
1000000000002001	Device ID	8	int
C02E	Device Type	2	int
01	Constant	1	int
F020	Constant	2	int
0001	Parameter code for Inlet 1	2	int
0002	Parameter code for Inlet 2	2	int
And so on...			
0003	Parameter code for Outlet 1	2	int
0004	Parameter code for Outlet 2	2	int
And so on...			
0005	Parameter code for Total Inlet	2	int
0007	Parameter code for Total Outlet	2	int
0008	Parameter code for Net Volume	2	int
0101	Parameter code for Meter Alarm value	2	int
00441C44	Inlet 1	4	float
00000E44	Inlet 2	4	float
And so on...			
0080EF00	Outlet 1	4	float
00088880	Outlet 2	4	float
And so on...			
00000036	Total Inlet	4	float
00003296	Total Outlet	4	float
0000FF69	Net Volume	4	float
00	Meter Alarm status value	1	int
BF	FCS (XOR ^ operation on all message heads excluding the Start and Stop Bytes)	1	int
3E	Stop byte	1	int

Fig.8 Byte Stream format.

Acknowledgement Byte stream format from ACE Server to DTU

Response Byte Format when

- Success: 3CA1000000A13E
- Failure: 3CA1000200A33E

Success: 3C|A100|00|00|A1|3E

Message header	Description	Length (bytes)
3C	Start byte (constant)	1
A100	Message code (constant)	2
0	Status, 0 - Success	1
0	Indicates total number of responses that shall follow the current message stream	1
A1	FCS (^ operation on all message heads excluding the Start and Stop Bytes)	1
3E	Stop byte	1

Fig.9 Acknowledgement Success Byte Stream Format.

Failure: 3C|A100|02|00|A3|3E

Message header	Description	Length (bytes)
3C	Start byte (constant)	1
A100	Message code (constant)	2
02	Status, >0 - Error	1
00	Indicates total number of responses that shall follow the current message stream	1
A3	FCS(^ operation on all message heads excluding the Start and Stop Bytes)	1
3E	Stop byte	1

Fig.10 Acknowledgement Failure Byte Stream Format.



Fig.12 Pipe installation

Conclusion:

The idea to wirelessly monitor the water flow and pressure values is successful. The next approach would be to wirelessly control the flow of water from a remote location without human intervention is to be realized.

- **Some Pictures of the installations:**



Fig.11 DTU unit



Fig.13 Water meter installation

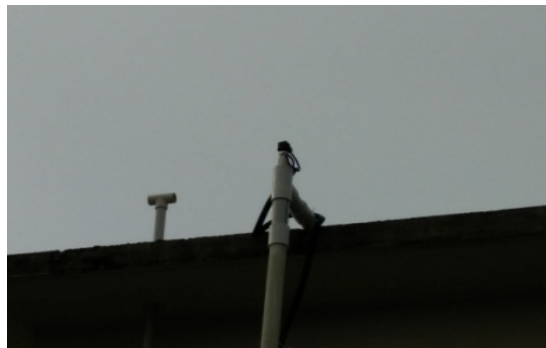


Fig.14 Pressure sensing installation

6th International Engineering Symposium - IES 2017

March 1-3, 2017, Kumamoto University, Japan

Result:

- Screenshots of the ACE web page:



National Institute of
Technology Karnataka

Home View Procurement CattleFeed Analytics Settings Devices Admin Dr. Shet

Live And Historical Data

NITK Storage Tank Monitoring

Select Parameters

Device Type: NITK-StorageTankMonitor
End Point: Storage Tank
 Show on Load

Parameters: Select All Inlet 1

Select Period
Start Date: 22/Jul/2015 End Date: 23/Jul/2015

Show Data

Summary **RawData** **Hour wise** **Day wise** **Week wise** **Month wise** **Year wise**

Raw Data for Period : 22/Jul/2015 [00:00]hrs to 24/Jul/2015 [00:00]hrs

Total No. of records : 53

Date (dd mm yyyy) (Ingress)	ConnectionName	Inlet 1 (Liters)	Inlet 2 (Liters)	Inlet 3 (Liters)	Inlet 4 (Liters)	Inlet 5 (Liters)	Outlet 1 (Liters)	Outlet 2 (Liters)	Outlet 3 (Liters)	Total Inlet (Liters)	Total Outlet (Liters)	Net Volume (Liters)
23/Jul/2015 00:18:45	Near PG Hostel	23579	428.6				91.9	185.7	198.9	23736.7	408.5	132
23/Jul/2015 09:18:47	Near PG Hostel	23579	428.1				91.8	184.9	198.2	23734.2	404.9	131.1
23/Jul/2015 08:18:48	Near PG Hostel	23579	423.5				91.4	181.9	197.1	23731.6	402.4	131
23/Jul/2015 07:18:50	Near PG Hostel	23579	421.8				90.8	182.0	196	23729.9	409.7	132
23/Jul/2015 06:38:50	English Medium school	16634.8	40.7	37943.9	8.7	51.3	14327.3	7.1		34638.4	13476.6	131.2
23/Jul/2015 06:18:52	Near PG Hostel	23579	421.2				92.5	181.3	195.4	23728.5	407	131.1
23/Jul/2015 05:38:53	English Medium School	16634.8	40.7	37939.4	8.7	51.3	14326.7	7.1		34633.9	13476	131.3
23/Jul/2015 05:18:54	Near PG Hostel	23579	419				90.2	181.9	195.1	23727.1	407.2	131.7
23/Jul/2015 04:38:55	English Medium	16634.8	40.7	37938.6	8.7	51.3	14326.5	7.1		34633.1	13475.8	130.8

Export **Export**

Acknowledgement:

We would like to thank "Centre of Excellence for Wireless Sensor Networks" and Department of Electronics and Communication, NITK, Surathkal Mangalore, India for their support and encouragement for the research presented in this paper. Further, the Authors wants to acknowledge the discussion, work and guidance given by Thought focus, Bangalore, especially Naveen Kumar Panguluri, and Ravi Kumar who was responsible for the installation of all devices.

Reference:

- [1]https://en.wikipedia.org/wiki/Water_scarcity
- [2]Water for a sustainable world, The United Nations World Water Development Report 2015.
- [3] NITK-Water Level and Pressure Monitoring System Quick Reference Guide Document version no 1.0,13, April 2015

Wirelessly monitoring of water usage in smart campus: A CPS perspective

Abhishek M B¹ and N.Shekhar V.Shet²

- ¹ Department of Electronics and Communication Engineering, National Institute of Technology Karnataka, Surathkal, Mangalore 575025, India. email: abhishek.mb@gmail.com.
- ² Department of Electronics and Communication Engineering, National Institute of Technology Karnataka, Surathkal, Mangalore 575025, India. email: shekar_shet@yahoo.com.
-

ABSTRACT: This paper presents a systematic approach of customizing the existing water pipeline infrastructure using wireless technology to explore the possibility to wirelessly monitor the water distribution through a storage tank and later bring out the aspects of Cyber Physical system (CPS). Our experiment was carried out at National Institute of Technology Karnataka (NITK), Surathkal, Mangalore, India to monitor the amount of water flow in storage tanks. A set up of RF transceiver modules interfaced with water meter has been installed to get the water inflow and outflow details for each pipe. With respect to sampling time in the monitoring unit, a set up of another RF transceiver interfaced with aggregator and Data transmission unit (DTU) will receive the water inflow and outflow details and will display in the web server. Presently, we are wirelessly monitoring 3 storage tanks acquiring inlet and outlet data from each storage tank in the campus. Our experiment aims to adapt ways and proposes to use CPS technology to overcome the improper handling and care of water supply infrastructure. Our effort is to study Water distribution CPS, starting with small scale experimental set up at NITK campus and then extending that understanding to large area. From our result it is noticed that the data analytics facilitates useful models which are absolutely essential to carry out large-scale simulation in order to improve the water utilization in an efficient way.

Keywords: Cyber Physical System, Water monitoring and distribution, RF transceivers module, Aggregator, Data transmission unit

INTRODUCTION

In the present scenario, water has become a scarce resource due to many reasons, including pollution and natural calamities. Preserving water and avoiding uneven usage of water is not just about utilizing enough water to meet the demands. Concerned efforts are needed to control the amount of water that is wasted in transit between the water source and end consumers. Even if small leak is left undetected in the pipe, it could result in loss of more than thousand litres of water. Hence, prior to determining the water

leakage in pipe, firstly we need to monitor the water distribution in pipe and then taking appropriate actions are major aspects in water management system. It is a well known fact that several thousands of kilometres of water pipe lines are already laid on the surface of the earth over the centuries. Even today, most of the distribution of water is handled by human intervention while moving to specific locations and shutting off or turning on valves. In this process, water is improperly managed and wastage is inevitable since man is prone to commit errors.

In this paper, we have made some alteration to the existing water pipeline infrastructure with the use of minimal wireless technology in order to monitor the usage of water in storage tanks. With the knowledge of these details, we can track the water distribution and amount of water being used by the consumer. We have made a set up of RF transceiver modules interfaced with the water meter to get water inflow and outflow details for each pipe. For the existing pipeline in the storage tank, we have installed water meter which is interfaced with RF transceiver modules in order to collect water flow details. With these details, we can make out the amount of water being collected from source and later being used by the consumers in each storage tanks. For every 15minutes all these details will be communicated with other RF transceiver modules which is interfaced with DTU and placed in the monitoring unit. All these details will be sent to a server with the help of DTU and displayed in ACE web. With the understanding of this inflow and outflow details, we can work out some novelty on data analytics in order to control the valves in the existing water infrastructures so that water can be tracked and utilized properly in each storage tanks.

Needless to say, with the increase in demand for water, monitoring, managing, distributing, controlling and preserving water supplies is becoming a great challenge. It is rather unreasonable and difficult to use wired connections to measure and control the water pressure and flow at several distant locations. Therefore, wireless sensors are extensively used to measure the pressure and flow of water in the existing pipelines in large areas/campuses. Further, the actuators which facilitate the control also involve wireless connectivity. The trend is to develop smart water management systems through the notion of Cyber Physical System.

CYBER PHYSICAL SYSTEM

Cyber physical system is going to be essentials to mankind in the future, since wired control is cumbersome, expensive,

labour intensive and difficult to maintain. Cyber physical system, Internet of things and IPV6 envisages addressing every grain of sand on the surface of this planet with a unique ID. The term cyber-physical systems (CPS) refers to a new generation of systems with integrated computational and physical capabilities that can interact with humans through many new modalities [1]. The ability to interact with and expand the capabilities of the physical world through computation, communication, and control is a key enabler for future technology developments [2]. CPS is not a standalone device, it is a network of interacting physical system with embedded devices. It is a coordination of physical and computational systems. The key technologies of water cyber physical systems with embedded sensors, processors and actuators that can sense and interact with the water environment includes wireless communications and networking, sensor technology, hydrodynamic modelling, data analysis and control [7].

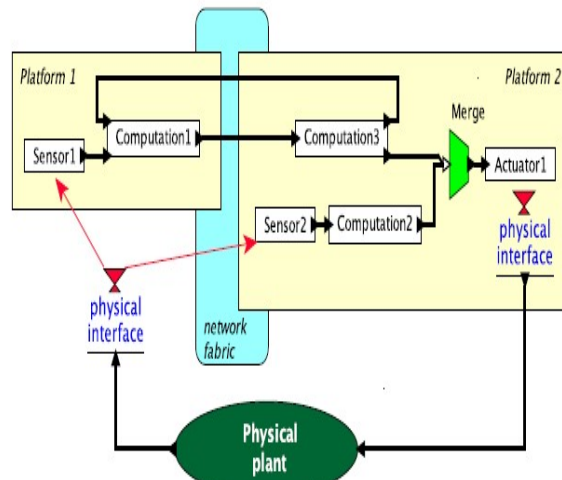


Fig.1 Example structure of Cyber physical system [3].

The example shown in Fig.1 is used to understand the simple working of CPS [3]. In Fig.1 CPS consists of 3 main parts.

- Physical plant- which consists of “physical” part of a CPS. It is a system which is not realised with computers or digital networks. It will be part of the system, which includes mechanical parts,

6th International Engineering Symposium - IES 2017

March 1-3, 2017, Kumamoto University, Japan

- biological or chemical processes, or human operators.
- Computational platforms- it consists of one or more computational blocks i.e., sensors, actuators, one or more computers, one or more operational systems.
- Network fabric – it provides the mechanisms for the computers to communicate.

The combination of the computational platforms and network fabric forms the “cyber” part of the CPS [3].

From the example shown in Fig.1 the working is as follows, the 2 networked platforms each with its own sensors and/or actuators [3]. The action taken by the actuators affect the data provided by the sensors through the physical plant. In Fig.1 platform2 controls the physical plant via actuators. It measures the processes in the physical plant using sensor2. The box labelled computation 2 implements a control law, which determines based on the sensor data what commands issued to the actuator. Such a loop is called a feed back control loop. Platform 1 makes additional measurements using Sensor1 and sends message to Platform2 via the network fabric. Computation 3 realizes an additional control law which is merged with that of computation2, possibly pre-empting it.

865-867 MHz RF module:

In this work we have used 865-867 MHz RF module which provides robust wireless communication for all conditions [4]. The main advantage is that it is suitable for adding wireless capability to any product with serial data interface. Other advantages include minimal power and provide reliability of data deliveries between devices.

The main features of this device are [4]:

- Supports point to point, point to multipoint and mesh topologies. (Here, star network is established).
- Supports 2 FSK, 2-GFSK.
- Configurable transmit power up to 10dBm.
- Maximum RF data rate is 500kbps.
- Data reliability, acknowledgement mode communication is used.

- Source/Destination addressing.
- Unicast and Broadcast communication.
- Analog to Digital conversion and Digital I/O line support.
- Power saving modes.

Table.1 Specification [4]

SL Num	Parameter	Details
1	Power	
i)	Supply Voltage	2.4 to 3.6 V.
ii)	Transmit Current	20mA@0dBm, 35mA@10dBm.
iii)	Idle/Receive Current	20mA.
iv)	Power-down Current	<10micro A.
2	General	
i)	Frequency	865-867MHz.
ii)	Nominal Transmit Power	10dBm.
iii)	RF Data Rate	2.4kbps to 500kbps(Max).
iv)	Receiver Sensitivity	-106dBm(at 9600 baud).
v)	Serial Data Rate	Up to 115200 baud.
vi)	Operating temperature	-40 to 85 ° C.
vii)	Antenna Connector options	MMCX.
viii)	On-board Antenna	Spring Antenna.
3	Network	
i)	Supported network topologies	Point to point, point to multipoint, mesh topologies.
ii)	Addressing options	PAN ID and addresses.
4	Mechanical	
i)	Dimension	36mm *26mm.
ii)	Interface connector	2 * 10 pin berg stick, 2.00 mm pitch.

PRELIMINARY STEPS TAKEN TO MONITOR THE TANK

TANK OVERVIEW

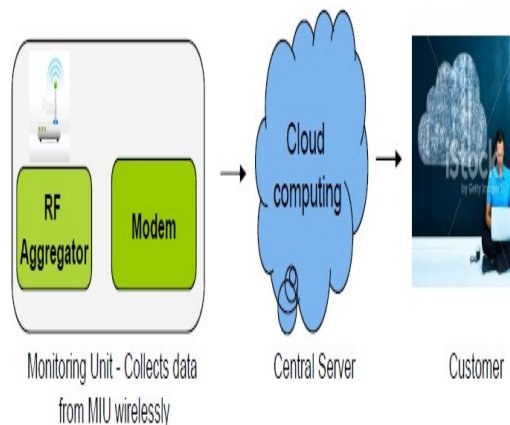


Fig.1 Monitoring Unit.

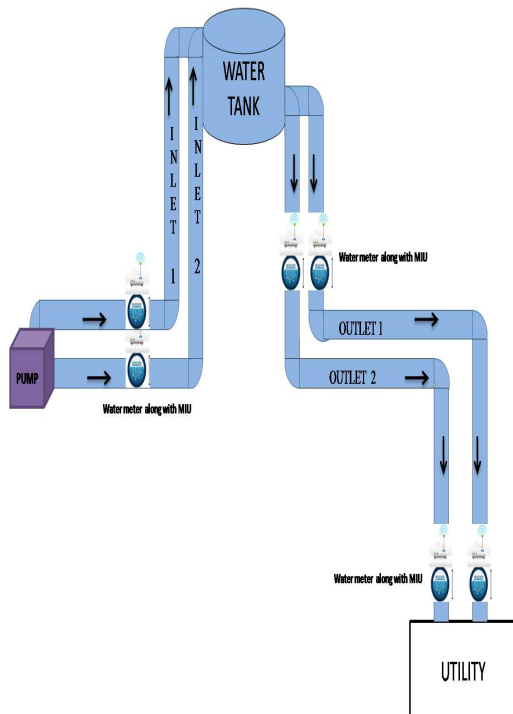


Fig.2 TANK OVERVIEW.

Each storage tank consists of water monitoring system as shown in Fig.1 shall include following components:

METER INTERFACE UNIT: MIU includes water meter, reed switch and RF module.

AGGREGATOR: To aggregate data from different MIUs and communicate with DTU.

DTU (Data transmission Unit): To process water flow related data and upload data to

server.

From Fig.2, we can observe the alteration we have made to the existing water pipeline infrastructure with the use of minimal wireless technology in order to monitor the usage of water in storage tanks. As shown in the Fig.2, we can notice that for every pipe we have installed MIU. In MIU, RF module is interfaced with reed switch. Whenever the needle in the water meter touches the magnet in the reed switch, reed switch discharges the RF pin. This discharge signal is counted as one. The number of discharge is stored into RF flash memory. From Monitoring Unit as shown in Fig.1, whenever DTU requires data from the RF modules, it will query it through aggregator. Aggregator sends the request data to all different RF modules with the help of RF transceivers and receives the data from different RF modules via wireless communication. When aggregator receives the data from different RF module and gives the received information to the DTU. DTU will process the received information and sends the received information to the cloud. In ACE web, we are able to view the information.

The pictorial representation of three Storage tanks that are installed in different places in NITK, Surathkal campus is shown below:

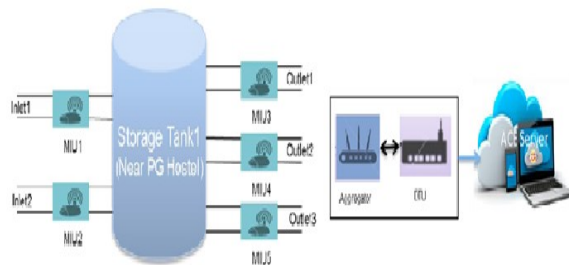


Fig.3(a) Storage tank one.

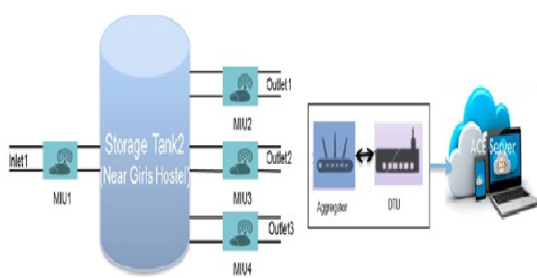


Fig.3(b) Storage tank two.

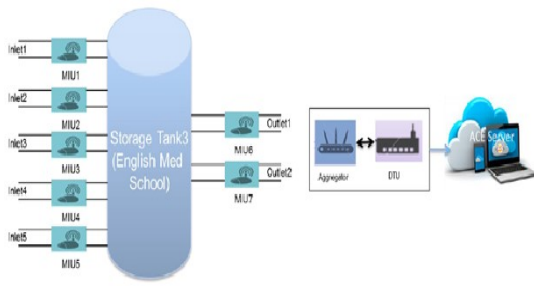


Fig.3(c) Storage tank three.

Fig.3 (a) shows the pictorial representation of storage tank one which consists of two inlets and three outlets. Similarly Fig.3 (b) and (c) shows the pictorial representation of storage tank two and storage tank three which consists of one inlet and three outlets, five inlets and two outlets respectively. Here each inlet and outlet pipe has RF module mounted on water meter. RF module is used to count the number of pulses with the help of water meter and stores the counted pulses into flash memory. Then aggregator communicates with all RF modules of respective tanks and receives the counted pulses and shares it with DTU. Finally, in ACE web, we are able to view the information.

Result

The communication between all the devices has been achieved successfully. Finally, we are able to display the amount of water flowing in individual storage tanks in the ace web. So now we can glimpse the undersupply water and when we are more often adequately using water. With these details, we can make a decision when water is needed and when water should be pumped. Further research is needed to resolve the water scarcity issue.

ACE web which is shown in Fig.4 (a and b) is a hardware, communication, software and analytics technology platform developed by a team at "Thought Focus" that helps easy data collection and analysis. ACE convolutes various networking technologies to collect data from the field and transmit to a central server. It is used to monitor the measurement points and can have

traditional wired bus topology, Infrared, Optical Interfaces, low range RF, wireless LAN to push the data to central server using the widely available long haul TCP/IP, GPRS, GSM networks. The main advantage of ACE web is that it is capable of reading data from any device and brings all data to one common place. Fig.4(a) shows the snapshot of resulting displaying in web server which shows full summary of inlet, outlet and total volume of water flows in each respective tank. Fig.4(b) shows the detailed flow of inlet, outlet in each respective tank for every 15minutes. Now the proposed frame work is ideal to monitor the water flowing in storage tanks and integrate into cyber physical system that can motivate the control based on historical real time flow information.

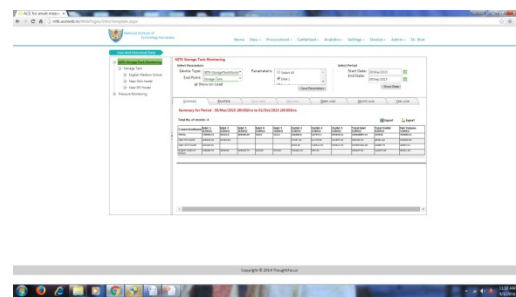


Fig.4 (a) displaying all tank details.



Fig.4 (b) displaying individual tank details.

CONCLUSIONS

In this work, we have addressed the customization of the existing water pipeline infrastructure with the use of wireless technology to monitor the water inflow and outflow details of each storage tank.

Taking off from this existing preliminary deployment in NITK campus and available data, we have the following strategies towards achieving useful research outcomes. It is now well established that the Data Analytics play a

6th International Engineering Symposium - IES 2017

March 1-3, 2017, Kumamoto University, Japan

significant role in any CPS. In fact, appropriate events detected in the data, in real-time fashion, facilitate alert and control mechanisms in our envisaged Water Management Solution.

ACKNOWLEDGEMENTS

We would like to thank "Centre of Excellence for Wireless Sensor Networks" and Department of Electronics and Communication, NITK, Surathkal Mangalore, India for their support and encouragement for the research presented in this paper. Further, the Authors would like to acknowledge the discussion, work and guidance given by Thought focus, Bangalore, especially Naveen Kumar Panguluri, and Ravi Kumar who were responsible for the installation of all devices.

REFERENCES

- [1] Clas Jacobson, et al (2014), Cyber Physical Systems, ERCIM.
- [2] Edward A.Lee et al (2015), The Past, Present and Future of Cyber Physical Systems: A focus on Models, sensors,2015
- [3] Lee, E. A. and S. A. Seshia, et al (2011) Introduction to embedded systems: A cyber-physical systems approach.
- [4] Tarang™ (2010), Tarang- Product Manual – Melange System Pvt Ltd, Website:www.melangesystems.com.
- [5] Sanaz Imen, Ni-Bin Chang, et al (2016), Developing a Cyber-Physical System for Smart and Sustainable Drinking Water Infrastructure Management, Proceedings of 2016 IEEE 13th International Conference on Networking, Sensing, and Control Mexico City, Mexico.
- [6] Xiuli Ma, Hongmei Xiao, Shuiyuan Xie, Qiong Li, Qiong Luo, Chunhua Tian, et al (2011), Continuous, Online Monitoring and Analysis in Large Water Distribution Networks, ICDE Conference, IEEE, pp-1332- 1335
- [7] Wang, Z., H. Song, D. W. Watkins, K. G. Ong, P. Xue, Q. Yang, and X. Shi et al (2015), Cyber physical systems for water sustainability: challenges and opportunities. Communications Magazine, IEEE, 53(5), 216–222.

Hierarchical Clustering Algorithm for Green IOT

Spoorthi P. Shetty¹

Udaya Kumar K.Shenoy²

1. Department of Master of Computer Applications, N.M.A.M Institute of Technology, Nitte, Karkala-574110, Karnataka, India. E-mail: sshetty.07@nitte.edu.in
 2. Department of Computer Science and Engineering, N.M.A.M Institute of Technology, Nitte, Karkala-574110, Karnataka, India. E-mail: ukshenoy@nitte.edu.in
-

ABSTRACT

Internet of things (IoT) is a developmental framework for the devices in the Internet, in which everyday objects have network connectivity, allowing them to send and receive data. In IoT, smart sensors communicate with each other where data are gathered and certain requests of users are satisfied through queried data. The development of energy efficient scheme for IoT becomes more complex since IoT network is usually of large scale. Because of this large scale network, most of the current protocols used in Wireless sensor networks (WSN) cannot be applied directly to IoT. This paper addresses this issue and proposes a deployment scheme to achieve green networked IoT. A hierarchical framework for a general IoT deployment is proposed in this paper. A model for green IoT is proposed based on this framework. i.e., a minimum energy consumption algorithm is proposed which involves a hierarchical clustering technique. The behaviour of the proposed algorithm is studied for varying number of nodes. The simulation results presented in the paper shows the number of dead nodes at different instances throughout the lifetime of the network. The results are compared with existing algorithm to establish the supremacy of the proposed algorithm.

Keywords: Internet of things, Wireless Sensor Networks, Clustering, Energy efficiency, network lifetime, simulation.

1. INTRODUCTION

Internet of Things(IoT) is a network terminology which is mainly used to communicate between the smart objects/things. IoT components can be mobile phones, sensors, RFID tags etc., which are connected to the internet using either wired or wireless network, i.e., IoT connects heterogeneous objects and enables communication between them. This communication can take place between two objects or between a object and a human being. So, this IoT can be predicted as future generation of sensor network.

In IoT communication, initially data will be sensed by sensing node, then the sensing node may send the

data in the form of query or continuously to sink. To do this communication, energy plays a vital role to maintain the network connectivity. Sensing nodes act as a backbone of IoT network, which should be provided with a function of sensing, wireless communication and with computational capability. But these nodes are equipped with low capacity battery [1]. Because of these limitation of sensing node, lifetime of network will get effected, i.e., after a certain period of communication, nodes may die and which in turn may shorten the lifetime of network too [6]. To achieve longer lifetime of IoT network, the lifetime of sensing node should be maintained for longer duration, hence energy efficiency

of sensing node leads to the energy efficiency of IoT network.

In WSN, a large number of research has taken place on energy efficiency [6,8], but IoT network faces more challenges than WSN as IoT network is very large compared to WSN and usually IoT network is a combination of heterogeneous device networks, hence green issue plays an important role in IoT. It is observed with WSN that hierarchical clustering protocols are more efficient for energy optimization. With IoT, as network is of large scale, energy consumption is also higher for transmission [6]. So, it is better to use hierarchical clustering algorithm for IoT.

This paper proposes a framework for IoT deployment. This framework can be scalable for large networks. A new clustering method - Energy Efficient Clustering Algorithm (EECA) is introduced and through simulation results it is shown that the proposed scheme works for large networks and hence it can be applicable to IoT deployment. The framework of EECA uses hierarchical structure, which can be used to deploy objects/things of IoT network. In this, communication is allowed between sensing node and cluster head but no intra communication between sensing nodes. By doing this, energy efficiency can be achieved and network lifetime can be extended. Many simulation experiments are conducted on IoT network and the results are compared with the LEACH protocol. The results show that the EECA algorithm is more preferable for green IoT.

The paper is organized as follows: Section 2 presents survey of related work, Section 3 is about System framework, Section 4 give details about Green IoT model and section 5 is about performance evaluation. Section 6 presents the experimental results and section 7 Concludes the paper.

2. RELATED WORK

The large scale WSN deployment can be divided into different schemes: exact, adhoc, hierarchy and hierarchy with adhoc [4,5]. Table 1 compares the existing hierarchical algorithms.

Why clustering?

Communication can be done in many ways. In sensor network power consumed for communication will be more than that of processing data. So, it is necessary to reduce the communication distance in order to reduce the power consumption of nodes. If data is sent directly from node to sink then the distance for communication will be more, in turn it also consumes more energy from the node. By reducing the distance between two transmitting nodes, the energy can be saved and this can be achieved by the clustering. Clustering is a process in which all the nodes are connected through some form of clusters. Each cluster will be headed by a node called as cluster head (CH).

Communication in Cluster

Initially each node captures the data, then it sends data to CH of its cluster. Then the CH sends the data to sink. By this, distance of single communication link can be reduced; hence energy efficiency can be obtained.

3. SYSTEM FRAMEWORK

Wireless sensor network is a rising research topic as most of the times data will be captured by small device called as sensor node. Many sensors are combined together to form a network. The main problem in these sensors is, these are embedded with a battery of limited power capacity. Hence it is necessary to save the energy to extend their life span. To achieve this energy efficiency many energy efficiency protocols are developed [7]. With this

growing trend, in IoT sensors take a major role in network. The same problem of energy efficiency continues in IoT network. Even though many energy efficiency algorithms are available for WSN, it does not perfectly suit IoT network as the network of IoT is large and heterogeneous. Therefore it is not sufficient to apply the same energy efficiency algorithm of WSN to IoT. In order to address this problem it is necessary to use different system framework for IoT.

The Figure 1 provides a system framework for IoT deployment. This framework includes three layers i.e., Sensing layer, Cluster Head (CH) layer and Cluster Co-ordinator layer (CCO). In sensing layer, all the sensing nodes are divided into clusters where each cluster will have CH. In any cluster sensing nodes are not allowed to communicate to each other, they will communicate either to CH or to sink whichever is nearest.

Once the CH receives the data, it sends it to nearest CCO or sink, whichever nearest to it. The CCO will send the received data to upper cluster co-ordinator (UCCO) and so on. It continues until data is received by sink.

In paper [2], it is mentioned that a node spends more energy on transmission of data than processing the data. As distance increases between the nodes, energy spent on transmission will be more. To overcome this problem, EECA algorithm uses inter clustering communication. In this framework, a general deployment scheme is proposed which has a facility to build scalable green IoT. To make this tiered framework as green IoT, the system framework should be formulated as below.

Let a and b be the two points in

Euclidean plane $d(a,b)$ i.e., d is the distance between a and b. Let n be the total number of sensing nodes in the sensing layer, m be the total number of relay nodes and CCO be the total number of cluster co-ordinator. The IoT network can be symbolised as $G(N,A)$ where N represents node set, A represents wireless link set. The communication of any 2 nodes can be described as:

- (i). To any $i \in n, j \in n$, i and j cannot communicate with each other.
- (ii). To any $i \in n, j \in m$, i can send data to j .
- (iii). To any $i \in m, j \in \text{CCO}$, i and j can communicate to each other.
- (iv). To any $i \in \text{CCO}, j \in \text{sink}$, i and j can communicate with each other.
- (v). To any $i \in \text{CH}, j \in \text{sink}$, i and j can communicate with each other.

With these notations and symbols following assumption can be made.

- (i) All nodes in the framework are at fixed place.
- (ii) All the nodes are given with same initial energy and have the same energy consumption parameter, transmission power, receiving power etc.
- (iii) Nodes of sensing layer can send data to sink in multi hop manner.
- (iv) Sensing nodes, CH and CCO are energy constrained nodes, but sink is not.

4. MODELING THE GREEN IOT

For the given hierarchical system framework, the goal of deploying green IoT helps to save power. This section starts with variable notations and definitions which are used in the rest of paper. Then it formulates the system constraint, later it address the IoT green deployment as an optimization problem. Finally an algorithm to solve such problem is proposed. The performance of algorithm is presented at the end.

Variable Definition

E_t - Energy consumption at a node for data transmission.

E_r - Receiving energy.

d_{pq} - Distance between node p and node q.

E_{elec} - Energy consumption of radio Electronics.

L - Length of data.

System Constraint

Sensing node can only communicate with Cluster Head of relay layer. Cluster head can send data to its Cluster Co-Ordinator (CCO). CCO can send data to it's upper CCO or sink whichever is nearer.

Energy Consumption Constraint

From the view of a system and as proved by Potty et al [2] that the energy required for communication will be more than the energy required for processing the data, the energy required for sending and receiving is taken with more care.

Energy Efficient Clustering Algorithm (EECA Algorithm)

1. Deploy n nodes in fixed area.
2. for each round <= rmax
3. Identify few CCO
4. Identify Cluster Head
5. Mapping of Cluster Head to its near CCO.
6. for each node
7. Select nearest CH from cluster
8. Data transfer
9. End for.
10. Maintenance phase-elimination of dead node
11. End of 2.
12. Display the remaining alive nodes.

Line 1 deploys nodes in a fixed area. Take the nodes as static. In line 2, out of n nodes few nodes are identified as cluster head and few nodes as cluster co-ordinators. After deploying all

different types of nodes start data transmission.

In data transmission, initially nodes send data to its Cluster Head (CH) or sink whichever is nearer. From CH it sends data to its near CCO or sink whichever is nearer. From its CCO then it sends data to its UCCO until it is sent to sink. At the end of each round it checks for all dead nodes. i.e., if the energy of any node reaches to zero, then that node will be considered as dead node. This process is performed in line 10.

5. PERFORMANCE EVALUATION

This Section validates the effectiveness of deployment scheme presented in this paper through numerical experiments. The 100 nodes are deployed in the area of $100 \times 100 \text{ m}^2$ as shown in Figure 2. Out of this 10 nodes (10% of n) are selected as CCO. In this nodes are randomly distributed. Sink node will be deployed at the centre. Initially energy=0.5J. For this set up various experiments are conducted and IoT energy consumption and network lifetime is evaluated.

5.1 Experimental Result

The experiments are conducted for many rounds and network lifetime is recorded.

Figure 3 shows the status of nodes after 1250, 1750 and 2000 rounds respectively. The number of dead nodes increases with each round. Experiments are also conducted for LEACH [3] algorithm (one of the energy efficient algorithm for WSN). The results of EECA algorithm and LEACH are compared and it is observed from Table 2 and Figure 4 that the EECA algorithm performs better for large network and energy efficiency can be obtained for the scalable network. Hence the EECA algorithm is more suitable for green IoT.

6. CONCLUSION

In this paper a framework for green IoT is proposed and then the EECA algorithm is implemented based on this framework. The Simulation results are presented and it shows that EECA algorithm gives better performance in terms of network lifetime as compared to existing algorithm.

REFERENCES

- [1] Akyildiz, I.F., Su, W., Sankarsubramanian, Y., Cayirci, E.(2002) : Wireless Sensor Networks: A Survey. Computer Networks 38, 393-422.
- [2] G. J. Pottie, W. J. Kaiser(2000), Wireless integrated network sensors, Communications of the ACM 43 (5) (2000) 51-58.
- [3] Heinzelman, Wendi Rabiner and Chandrakasan, Anantha and Balakrishnan, Hari (2000), "Energy-efficient communication protocol for wireless microsensor networks "System sciences, Proceedings of the 33rd annual Hawaii international conference on, IEEE.
- [4] Jun Huang,Yu Meng,Xuehong Gong,Yanbing Liu and Qiang Duan (2014)"A novel Deployment scheme for Green Internet of Things" IEEE Internet of things Journal vol 1,No 2.
- [5] Rudranath Mitra, Divya Nandy(2012):A survey on clustering techniques for wireless sensor network.: International Journal in Computer Science, Volume 2 Issue 4.
- [6] Seema Bandyopadhyay, Edward J. Coyle;Purdue University USA: An Energy Efficient Hierarchical clustering Algorithm for Wireless Sensor Networks.
- [7] Shalli Rani, Rajneesh Talwar, Jyoteesh Malhotra , Syed Hassan Ahmed, (2015) "A Novel Scheme for an Energy Efficient Internet of Things Based on Wireless Sensor Networks" Journal of Sensors.
- [8] Trang Tran Thi Thuy; Routing protocols in Internet of Things;

Table 1: compares the existing clustering algorithm

Characteristics	Exact	Adhoc	Hierarchical	Hierarchical with Adhoc
Node Deployment	Place in regularly distributed way.	Same as exact	Place in tired framework through some clustering algorithm.	Same like Hierarchy.
Nature of Communication	Each node captures data, disseminates it and acts as relay node.	Same as exact	In this sensor nodes are only permitted to communicate with relay/sink and no communication between the normal nodes.	Same as Hierarchical, but inter communication between the sensor nodes are allowed.
Advantage	Reliability and Serviceability is more.	Same as exact and extensible.	Network can be scalable.	Same as Hierarchical.
Disadvantage	Nodes around sink die faster, hence network lifetime becomes shorter.Hence not so suitable for IoT network.	Same as exact	No disadvantage like exact or adhoc.	Same as exact .

Table2: Compares the result of LEACH with IoT (EECA algorithm)

Sl.No.	Rounds	Dead Nodes	
		LEACH	EECA
1	750	0	0
2	1000	11	10
3	1250	70	20
4	1500	95	47
5	1750	100	73
6	2000	100	80
7	2250	100	87
8	2500	100	89
9	2750	100	90
10	3000	100	92

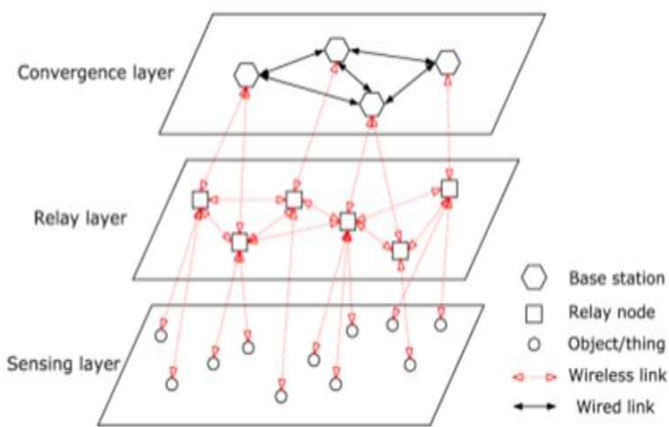


Figure 1: System Framework

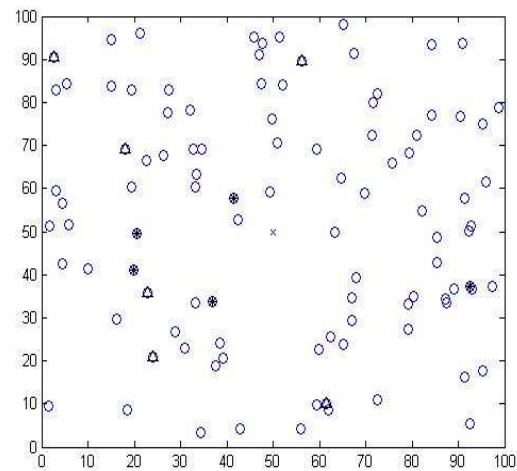


Figure 2: the deployment of nodes

(after 1250, 1750 and 2000 rounds)

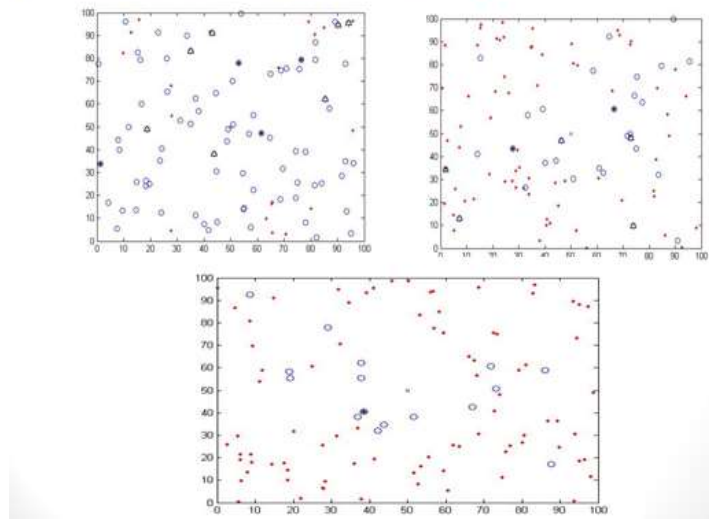


Figure3: Status of network after various rounds

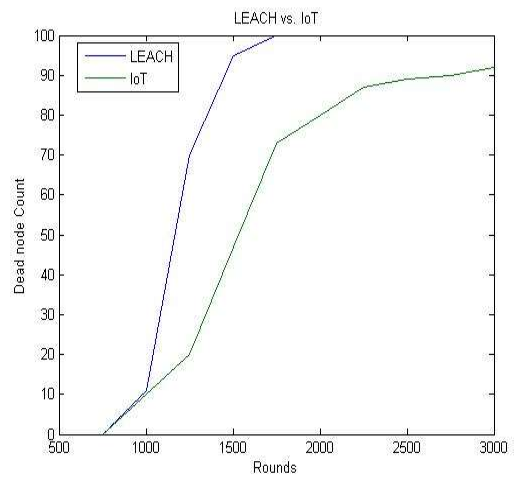


Figure 4:Comparision of LEACH and EECA

Heuristics for Strong Minimum Energy Topology Problem in wireless sensor networks

Pushparaj Shetty D

Department of Mathematical and Computational Sciences
National Institute of Technology Karnataka Surathkal
Mangalore 575025, India.
Email: prajshetty@gmail.com

Abstract:

Given a set of sensors, the strong minimum energy topology (SMET) problem is to assign transmit power to each sensor such that the resulting topology containing only bidirectional links is strongly connected. This problem is known to be NP-hard. Motivated by the current technology in wireless sensor networks (WSN) and out of theoretical interest, we consider several special cases of SMET problem. We establish the NP-completeness result for 3 special cases, namely K-Distinct-SMET, MST-restricted-SMET and Valley-free-SMET problems. We then present heuristics for the SMET problem. The proposed heuristics are based on the graph theory formulation of WSN. We propose two heuristics: namely Kruskal-incremental based heuristics and Local search based heuristics. The proposed heuristics are then compared with the existing heuristics like Prim-incremental heuristics and Valley-free heuristics. The performance comparison in terms of total range assignment for the nodes in these heuristics are presented in this paper.

Keywords: Wireless Sensor Network, Topology Control Problem, Transmission Power Assignment, Graph Theory, Minimum Spanning Tree, NP-hardness, heuristics

1. Introduction:

A wireless sensor network (WSN) consists of a collection of autonomous devices, each of which consists of a digital circuitry, radio transceiver, transmission amplifier and a small battery. The communication among these nodes is based on radio propagation. Since the battery of each sensor is of limited capacity and it is not possible to replace the battery always, energy conservation is a critical issue in order to increase the lifetime of a sensor network.

Each sensor node u has an Omnidirectional antenna, which can transmit signal within a certain specified range $r(u)$. Node u can directly communicate with other nodes located within its range. In general, communication is Multi-hop in nature, where intermediate nodes are

used to relay the transmission until destination is reached. A signal transmitted from source s with power P_s is attenuated by a factor

$P_f = P_s / \text{dist}(s, t)^\alpha$ where $\text{dist}(s, t)$ is the Euclidean distance between the nodes s and t and α is the *distance-power gradient*, which may vary from 2 to 5 depending on the various environmental factors. The message can be correctly decoded only when $P_f \geq \gamma$, where the constant $\gamma \geq 1$ is the transmission quality parameter.

Given a set of sensor nodes S , a range assignment for S is a function $f: S \rightarrow \mathbb{R}^+$. The cost of a range assignment f is the sum of overall power consumption, that is $\text{cost}(f) = \sum f(v)^\alpha$. Given a range assignment f for a set of sensors S , we

6th International Engineering Symposium - IES 2017

March 1-3, 2017, Kumamoto University, Japan

consider the undirected graph $G_f = (S, E_f)$, for range assignment f where the radio stations present in S represents the vertices and E_f represents the bidirectional edges.

Given a set of sensors S , and a connectivity constraint Π , the minimum range assignment problem, *Min-Range* (Π) is to assign transmission range f , to the nodes in S such that given connectivity constraint Π is satisfied and $\text{cost}(f)$ is minimum.

The connectivity constraint Π could be simple connected, strongly connected or biconnected (see [9]).

The symmetric connectivity is strong form of connectivity among all, as it contains only bidirectional links. The bidirectional/symmetric edges are preferred in wireless sensor networks, because the signal transmitted over a link are to be acknowledged. Bidirectional links also simplify routing protocols. The current MAC layer protocols such as IEEE 802.11 and S-MAC take into account only bidirectional links (see [3,6]). The bidirectional range assignment is studied by cheng et al. [6] and they named this problem as Strong Minimum Energy Topology (SMET)problem.

In this paper, we study the special cases of SMET problem namely 3-Distinct-Smet, Mst-restricted-Smet} and Valley-free-Smet problems. We establish NP-hardness of these special cases of SMET problem.

The rest of the paper is organized as follows. A summary of related work is presented in Section 2. In Section 3, we define SMET problem and the special cases of the SMET problem. In Section 4, we prove the NP-hardness of these problems. In Section 5, we study the heuristics for the SMET problem. Section 6 concludes the paper.

2. Previous and related work

A WSN is modeled as a complete weighted undirected graph $G=(V, E, c)$, where $c: E \rightarrow \mathbb{R}^+$ is the cost function.

Given a spanning sub graph H of G , the cost of H is defined as

$C(H) = \sum c(e)$ for $e \in E$. For a vertex $u \in V$, the power of u is the maximum cost of an edge in H , incident on u , i.e $P_{H(u)} = \max C(uv)$. The power of a graph is the sum of powers of its nodes.

We are interested in the minimum energy problem where the subgraph is a spanning tree. Minimum energy spanning problem is NP-hard for the sensors on a 2-dimensional plane (see [6]), it is APX-hard for sensor in 3-dimensional space [7].

The minimum energy symmetric connectivity problem is studied in [4] and[6]. Lloyd et al. [12] specified general topology control problem as a triple of the form $\langle M, P, O \rangle$, where $M \in \{\text{Dir, Undir}\}$ represents the graph model, P represents desired graph property and $O \in \{\text{MaxP, TotalP}\}$ (abbreviation for maximum power and total power) represents minimization objective. Prim-incremental heuristic for SMET problem was proposed by [6]. Valley-free heuristic for SMET problem was proposed by [2]. Panda and Shetty proposed a Kruskal-incremental based heuristic algorithm [14] and a local search based heuristic algorithm [15] for the SMET problem.

3. Special cases of Strong Minimum Energy Topology Problem

Definition 1(SMET):

Given a set of sensors in the plane, compute the transmit power of each sensor, such that there exists at least one bidirectional path between any pair of sensors and the sum of transmit powers of all the sensors is minimized.

Let $T = (V, E')$ be a spanning tree of a weighted graph $G = (V, E)$ having cost function w . Let $P_{T(v)} = \max \{w(uv) | uv \in E(G)\}$ and $P(T) = \sum P_{T(v)}$. The SMET problem now reduces to a problem of finding a spanning tree T of G such that $P(T)$ is minimum. Formally, we define SMET as follows:

6th International Engineering Symposium - IES 2017

March 1-3, 2017, Kumamoto University, Japan

Problem: SMET

Instance: (K_n, w, M) , where K_n is a complete graph with n nodes,
 $w: E(K_n) \rightarrow \mathbb{R}^+$ is the weight function,
and M is a positive real value.

Question: Does there exist a spanning tree T of K_n such that $P(T) \leq M$?

As status of SMET problem is known to be NP-hard [6] and also APX-hard for 3-dimensional space [7]. Motivated by the current technology in WSN and out of theoretical interest, we examine the computational complexity of the following special cases of the SMET problem.

(i) k -Distinct-Smet Problem: SMET problem with the restriction that the admissible range of a node is one of the k -distinct power threshold values. This special case is important as the currently available sensors in the market supports a discrete set of ranges.

(ii) Mst-Restricted-Smet Problem: SMET problem with the restriction that the feasible solution is an MST instead of just a spanning tree. This special case is important as any MST is a 2-approximate solution to the SMET problem.

(iii) Minimum energy valley-free spanning tree (MEVFST) problem:

SMET problem with the restriction that the feasible solution is a valley-free spanning tree instead of just a spanning tree. This special case is important as any valley-free MST is an optimal solution for the SMET problem.

4. NP-Hardness of special cases of SMET k -distinct SMET problem

In practice, it is usually impossible to assign arbitrary power levels to the transmitters of a radio network. Instead one can only choose from a constant number of predefined power levels corresponding to a constant number of ranges [5].

In this context, we study the k -Distinct-Smet problem which is formally defined below:

Problem: k -Distinct-Smet

Instance: (K_n, w, M) , where K_n is the complete graph with n nodes and $w: E(K_n) \rightarrow \{c_1, c_2, \dots, c_k\}$ is a weight function and M is a positive real value.

Question: Does there exist a spanning tree T of K_n such that $P(T) \leq M$?

We prove below that k -Distinct-Smet problem is NP-complete.

Theorem 1:

k -Distinct-Smet problem is NP-complete. The theorem is proved by reduction from X3CS (Exact cover by 3 sets) problem.

Proof: The proof is omitted due to space constraint.

Corollary 1: The 3 -Distinct-Smet problem is NP-complete.

MST-restricted SMET

When the power threshold values are picked from a discrete set, the corresponding communication graph has duplicate edge costs and this may result in multiple solutions for the MSTs. While the cost of these MSTs are same, the total energy may differ. In Mst-Restricted-Smet, the feasible set for SMET problem is the set of all MSTs. We know that MST gives a 2-approximation algorithm for SMET problem. Picking the minimum power MST from among all the MSTs is a challenging combinatorial problem. Below we show that Mst-Restricted-Smet is NP-hard. The Mst-Restricted-Smet problem is formally defined as below

Problem: Mst-Restricted-Smet

Instance: (K_n, w, M) , where K_n is the complete graph with n nodes and $w: E(K_n) \rightarrow \mathbb{R}^+$ is a weight function and M is a positive real value.

Question: Does there exist a minimum spanning tree T of K_n such that $P(T) \leq M$?

Theorem 2:

Mst-Restricted-Smet problem is NP-

6th International Engineering Symposium - IES 2017

March 1-3, 2017, Kumamoto University, Japan

complete

Proof: The proof is established by reduction from exact cover (XC) problem.

4.1 Valley-free spanning tree:

Aneja et al. [2] explained the concept of *valley-free* spanning trees and established a lower bound for the SMET problem using this concept. They provide a sufficient condition for the optimal solution of SMET. The main results and few terminologies used in [2] are explained below.

Consider a simple path v_0, v_1, \dots, v_p in $G(V, E)$ with cost sequence $c_{01}, c_{12}, \dots, c_{p-1,p}$. Define this path to be of type λ if minimum of the p numbers in this sequence is either c_{01} or $c_{p-1,p}$. A tree T of G is defined to be *valley-free* if for every two nodes $u, v \in V$, the unique path between u and v in this tree is of type λ . The following theorem provides a lower bound for the SMET problem.

Lemma 1: [2]

Consider a spanning tree $T(V, E)$ of G . Then T is valley-free if and only if its associated total power is given by $\sum c_{ij} + \max\{c_{ij}\}$ where $(i, j) \in E$.

Lemma 2: [2]

A valley-free MST is an optimal solution for SMET problem.

4.2 Minimum energy valley-free spanning tree (MEVFST)

We now study a special case of SMET problem, where the feasible set is the set of all *valley-free spanning trees*. We first show that the number of valley free spanning trees of a weighted K_n is always exponential in n .

Lemma 3:

The number of valley free spanning trees of any weighted K_n is at least $2^{n-2}+n-2$.

Proof:

Let $V(K_n) = \{1, 2, \dots, n\}$. Let $T = (V, E_i)$, where $E_i = \{ij, j \in V - \{i\}\}$. So, each T_i is a

star and a valley free spanning tree of K_n , $1 \leq i \leq n$. Let ij be an edge of K_n of maximum weight, let $X \subseteq V - \{i, j\}$. Let $T_x = (V, E_x)$, where $E_x = \{ix, x \in X\} \cup \{ij\} \cup \{jy | y \in (V - \{i, j\}) - X\}$.

T_x is a bi-star with bi-star centers i and j and is valley free as ij is the maximum weight edge in K_n . So, number of such valley free spanning trees is the number of non-empty proper subsets of an $n-2$ element set. This number is $2^{n-2}-2$. So, K_n has at least $2^{n-2}-2+n$ valley free spanning trees.

In view of the above result, the number of valley free spanning trees of any weighted K_n is always exponential in n . So, it would be interesting to find the minimum energy valley free spanning tree. However, we show that finding the minimum energy valley free spanning tree in a weighted K_n is NP-hard by showing the decision version of the above problem is NP-complete.

Problem: Minimum energy valley-free spanning tree (MEVFST) decision problem

Instance: A weighted K_n with weight function w and a real positive value M .

Question: Does K_n contain a *valley-free* spanning tree T such that $P(T) \leq M$?

Theorem 3: MEVFST decision problem is NP-complete.

Proof: The proof is established by reduction from vertex cover problem. We have the following result.

Theorem 4: Finding a MEVFST of a weighted complete graph is NP-hard.

5. Heuristics for SMET

Two important heuristics for SMET problem are found in the literature, namely MST based heuristic [11] and Prim-incremental heuristic [6].

Panda and Shetty proposed a Kruskal-incremental based heuristic algorithm [14]

6th International Engineering Symposium - IES 2017

March 1-3, 2017, Kumamoto University, Japan

and a local search based heuristic algorithm [15] for the SMET problem. Some details about these heuristics are presented here.

5.1 Kruskal-incremental power greedy heuristic

In the Kruskal-incremental power greedy heuristic, we select an edge xy such that the edge xy needs minimum incremental energy among all edges which are not selected so far subject to the condition that it does not form a cycle with the so far selected edges.

5.2 Local search based Algorithm

In this section, we present the local search based approximation algorithm for the SMET problem. Local search is an iterative heuristic used to solve many optimization problems. Typically, a local search heuristic starts with any feasible solution, and improves the quality of the solution iteratively. At each step, it considers only local operations to get a better feasible solution, if possible, in the neighborhood of the feasible solution obtained in the previous iteration. The algorithm stops in the r^{th} iteration if it fails to find a better solution in the neighborhood of the solution obtained in the $(r-1)^{\text{th}}$ iteration. The details about local search technique can be found in [13]. The algorithm performs local changes that improves the total energy. The local change includes swapping a tree edge with a non-tree edge.

Theorem 4 [15]

The k-Local Search Algorithm has a performance ratio of 2.

5.3 Experimental Results:

In this section, we compare the existing heuristics, namely, (i)MST-heuristic, (ii) Prim-incremental heuristic, (iii) Valley-free with (i) Kruskal-incremental power greedy heuristic and (ii) k-Local search heuristic with $k=1$. We assume n sensors are randomly distributed in a 1000 X 1000 square. The power function used

in the simulation study is $f(d)=t \cdot d^\alpha$, where α is a constant between 2 and 4. We take $\alpha=2$ in our simulation study, t is the threshold which is set to 1. For each n ranging from 10 to 100 in increments of 10, we run the heuristics 100 times with different seeds for random number generator. The average of the total powers is reported in Figure 1.

The Table 1 reports the total energy consumption for all the heuristics. This shows that the valley-free heuristic consumes 3.48 percent energy less than MST on average, whereas 1-Local search consumes 4.68 percent less than the MST on an average. We find that total energy decreases with the increase in number of nodes. This is because when the sensors are densely located, it requires less energy to reach the neighbor and in sparse networks the energy consumption is higher.

6. Conclusion

In this paper, we studied the special cases of SMET problem namely (i)3-Distinct-Smet, (ii)Mst-restricted-Smet and (iii)Valley-free-Smet problems. We established the NP-hardness of these special cases. We then study and compare the heuristics for the SMET problem. Through extensive simulation, we showed that our heuristics performs better than the existing heuristics.

References:

1. A. V. Aho, J. E. Hopcroft, J. D. Ullman, Data structures and algorithms, Addison-Wesley, 1983.
2. Y. P. Aneja, A. Bari, A. Jaekel, R. Chandrasekaran, K. P. K. Nair, Minimum energy strong bidirectional topology for ad hoc wireless sensor networks, in: IEEE Int. Conf. on Communications, 2009, ICC'09, IEEE, 2009, pp. 1–5.
3. D. Bil'o, G. Proietti, On the complexity of minimizing interference in ad-hoc and sensor networks, Theoretical Computer Science 402 (1) (2008) 43–55.
4. G. Calinescu, P.-J. Wan, Range assignment for high connectivity in

6th International Engineering Symposium - IES 2017

March 1-3, 2017, Kumamoto University, Japan

- wireless ad hoc net-works, in: Ad-Hoc, Mobile, and Wireless Networks, Springer, Lecture Notes in Computer Science 2865, 2003, pp. 235–246.
5. P. Carmi, M. J. Katz, Power assignment in radio networks with two power levels, *Algorithmica* 47 (2) (2007) 183–201.
6. X. Cheng, B. Narahari, R. Simha, M. X. Cheng, D. Liu, Strong minimum energy topology in wireless sensor networks: Np-completeness and heuristics, *IEEE Transactions on Mobile Computing* 2 (3) (2003) 248–256.
7. A. E. Clementi, P. Penna, R. Silvestri, Hardness results for the power range assignment problem in packet radio networks, in: Randomization, Approximation, and Combinatorial Optimization. Algorithms and Techniques, Springer, 1999, pp. 197–208.
8. A. E. Clementi, P. Penna, R. Silvestri, On the power assignment problem in radio networks, *Mobile Networks and Applications* 9 (2) (2004) 125–140.
9. B. Fuchs, On the hardness of range assignment problems, *Networks* 52 (4) (2008) 183–195.
10. M. R. Garey, D. S. Johnson, Computers and intractability, vol. 174, Freeman New York, 1979.
11. L. M. Kirousis, E. Kranakis, D. Krizanc, A. Pelc, Power consumption in packet radio networks, *Theoretical Computer Science* 243 (1) (2000) 289–305.
12. E. L. Lloyd, R. Liu, M. V. Marathe, R. Ramanathan, S. S. Ravi, Algorithmic aspects of topology control problems for ad hoc networks, *Mobile Networks and Applications* 10 (1-2) (2005) 19–34.
13. H.-i. Lu, R. Ravi, The power of local optimization: Approximation algorithms for maximum-leaf spanning tree, in: Proceedings, Thirtieth Annual Allerton Conference on Communication Control and Computing, 1996, pp. 533–542.
14. B. S. Panda, D. P. Shetty, an incremental power greedy heuristic for strong minimum energy topology in wireless sensor networks, in: Distributed Computing and Internet Technology, Springer, Lecture Notes in Computer Science Vol. 6536, 2011, pp. 187–196.
15. B. S. Panda, D. P. Shetty, A local search based approximation algorithm for strong minimum energy topology problem in wireless sensor networks, in: Distributed Computing and Internet Technology, Springer, Lecture Notes in Computer Science No. 7753, 2013, pp. 398–409.

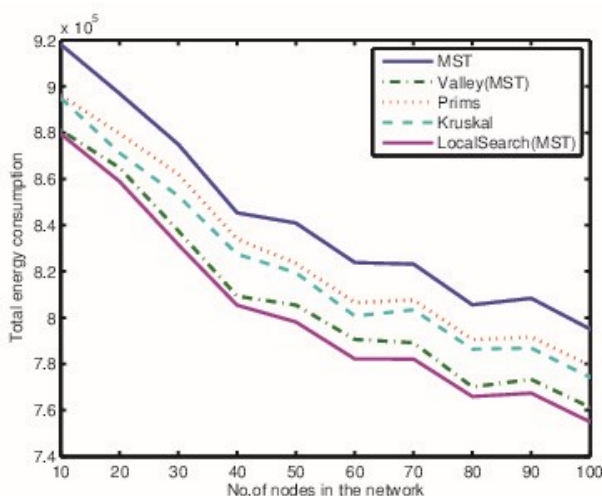


Figure 1: Total EnergyConsumption

6th International Engineering Symposium - IES 2017March 1-3, 2017, Kumamoto University, Japan

Table 1: Comparison of Total Energy

Nodes	MST	Prim-incr	Valley-free	Krus-incr	<u>LocalSearch</u>
10	918190	896209	881007	895056	879460
20	896949	879672	864862	871256	858914
30	874986	862112	837589	852658	831583
40	845371	834045	809327	827487	805419
50	840927	823525	805478	819464	798170
60	823853	806555	790591	800733	782171
70	823187	807685	789136	803403	782086
80	805569	790545	770070	786438	765918
90	808373	791634	773332	786917	767351
100	795075	779333	761235	774190	754943

Optimal Probabilistic Logical Key Hierarchy schema for secure group communication in Mobile Ad-hoc Networks

N. Hemanth Kumar ¹, Alwyn R. Pais ²

1. *Information Security Research Lab, Department of Computer Science Engineering, National Institute of Technology Karnataka, Surathkal, Mangalore 575025, India. e-mail: nhk.hemanth@gmail.com*
 2. *Department of Computer Science Engineering, National Institute of Technology Karnataka, Surathkal, Mangalore 575025, India. e-mail: alwyn.pais@gmail.com*
-

ABSTRACT: In recent years, many emerging Mobile ad hoc network (MANET) applications in field of disaster recovery and military battlefield situations are highly depend on secure group communication. But group key management faces many challenges because of unreliable media, limited energy resources, node mobility and node failures. In this paper, we have proposed a new schema Optimal Probabilistic Logical Key Hierarchy (OPLKH), where nodes are organized in a tree structure, based on their rekey probabilities. OPLKH reduces the rekey cost and energy consumption in the network and it is suitable for MANET where energy is a main concern. In simulation we have calculated the number of rekeys generated, energy consumption at key-server and energy consumption for key generation.

Keywords: Secure Group Communication; Key management; Rekey Cost; Energy Consumption.

INTRODUCTION

MANET is a self-configuring, infrastructure less, collection of mobile nodes connected through wireless links with dynamic topology. In MANET, nodes act as communication end-points as well as routers, enabling the multi-hop wireless communication. The mobile nodes have limited power resources and bandwidth. Network topology changes rapidly due to node mobility, physical obstacles on path and node failures. The main applications of MANETs are disaster recovery, military battlefield and rapid deployment applications.

MANET is potentially vulnerable to variety of attacks because of its open medium. So security is a major concern in MANET. Here, the security is mainly dependent on secure routing, key management and authentication technology, in which the key management for secure group

communication is to solve the most critical security problems of MANET. Generally cryptography techniques are used for secure communications in wired and wireless networks to achieve data confidentiality.

Harder E.J. et al. [24] addressed one of the major issues in key management approaches for secure group communication is maintaining the forward and backward secrecy. In other words, new joining members shouldn't know about the previous communication and also the old leaving members shouldn't know about the future communication after they left from the group. To provide forward and backward secrecy, key-server needs to change the group key for every join/leave of a member. It also encrypts the group key and sends it to every node individually.

6th International Engineering Symposium - IES 2017

March 1-3, Kumamoto University, Japan

In recent times, many methods are proposed for secure group communication in wired media and also in MANET. Many of the methods are based on LKH (Logical Key Hierarchy) schema only.

In this paper we are proposing a new rekeying method for MANET based on our earlier work [11]. In this method we organize the LKH tree with respect to rekeying probabilities of nodes. By implementing this method, we can reduce the rekey cost. Reduction in rekey cost leads to reduction in rekey messages, network overhead and energy consumption. So it will lead to a long survival of MANET as MANETS are energy concern networks.

RELATED WORK

In recent years, many key management approaches have been proposed for secure group communication. In that a few of them are described below.

In [7, 23] self-organized public-key management for MANET, to issue certificates, it allows users to generate their public-private key pairs without any centralized services. The CA (Certification Authority) functionality is completely distributed. All nodes in network have equal roles. They generate their own public-private key pairs and issue the certificates to their trusted nodes. Certificates are stored in every node rather than in centralized authorities.

A secure and efficient contributory cluster key agreement for MANET [2] is based on efficient local contributory cluster key management and gateway nodes. In this approach each node pairs up with its neighbor node, if available, to establish a new shared key. Otherwise the single node will behaves like an atomic sub cluster.

Jun Li et al. proposed a group key management scheme DVGKM in MANET [1], which is based on the secret sharing mechanism, in which each node holds a secret share and multiple nodes in a local neighborhood that can jointly update the group key.

Sencun Zhu et al. proposed GKMPAN [3], an efficient and scalable group

rekeying protocol for secure multicast in ad hoc networks. In this protocol each member distributes the group key to each member through a secure hop-by-hop transmission. Based on pre-deployed symmetric keys a probabilistic scheme is used for distribution of group key between members.

Jayanta Biswas et al. proposed a topology aware key management and distribution scheme [4] for MANET. They have used overlay approach for key distribution and their objective is to keep communication overhead low for key management and distribution.

Bing Wu et al. proposed a secure and efficient key management framework [5] (SEKM) for MANETs. SEKM builds PKI by applying a secret sharing scheme and a primary multicast server group. In SEKM, the server group creates a logical view of the certification authority (CA) and provides certificate update service for all nodes, including themselves.

K.Gomathi et al. proposed a cluster based key management scheme for MANET [15], in this approach, they divided the network into clusters. Each clusterhead will maintain the group key; it will update the group key whenever there is a membership change.

In Logical Key Hierarchy (LKH), a group manager distributes the new group key, encrypted with a separate (individual) key for each member. Wallner et al. [24] proposed the LKH schema. In LKH the key tree can be binary or k-ary and the basic LKH scheme was not designed specifically for ad hoc networks, Rhee et al. [23, 25, 12] suggested a LKH scheme for hierarchical ad hoc networks. As in [23] survey a number of refinements of the basic LKH schemes have been proposed OFT, OFC, ELK, LKH+, EBHT and LKH++. Among these schemes, only LKH++ is designed for wireless networks.

Selcuk A.A et al. [10] proposed Probabilistic Logical Key Hierarchy (PLKH) a refinement of basic LKH schema. PLKH scheme minimizes average rekey cost of LKH-based protocol by organizing the LKH

6th International Engineering Symposium - IES 2017

March 1-3, Kumamoto University, Japan

tree with respect to rekey likelihoods of members. Instead of maintaining uniform balanced tree, PLKH puts more dynamic members closer to the root and moves more stable members further down the tree. Here, the average rekey cost is reduced by decreasing the cost for more dynamic (i.e. more likely to rekey) members at the expense of increasing that cost for more stable members.

OPLKH Schema

We proposed OPLKH [11] schema which is the optimization for PLKH [10], which reduces rekey cost further. We organize the LKH tree with respect to members rekey probabilities as opposed to cumulative probability of PLKH. We concentrate on reducing number of rekeys that are caused due to member compromise or eviction.

Instead of placing members as leaf nodes as in PLKH, we provide new insert-operation which place the members either as leaf node or as internal node in LKH tree based on their probabilities. When a new member M joins the group, we place member M in a position such that all ancestors of M will have higher probability and all descendants of M will have lesser probability.

In OPLKH schema, we proposed a new insert method called MPUT that is used to insert new member in a position which preserves relative locations of existing members in the tree. It is similar to PUT operation of PLKH but creates a logical node.

When a member leaves the group his corresponding physical node is to be deleted from the tree. The physical node may be a leaf node or an internal node based on how it inserted and whether it has any dependent nodes at present. Our delete operation removes a physical node only if it is a leaf node; otherwise, we set its node type as replaceable and refresh affected keys. This replaceable node will be replaced whenever a node comes with suitable rekey probability. Our delete operation also removes unwanted logical and replaceable nodes present in affected

sub tree provided they do not have any dependent physical nodes.

From the development of the centralized key management, as in [17], the key-tree scheme is better and reduces the cost of re-keying from $O(n)$ to $O(\log n)$ (where n is the group size). We adopted OPLKH method to MANET and analyzed the rekey cost and energy consumption in MANET.

PROPOSED METHODOLOGY FOR THE MANET

In this method, we mainly focused on minimizing the rekey cost of LKH based protocols by organizing the nodes in tree based structure on the basis of rekey probabilities of the nodes.

We have implemented all the logical operations of OPLKH into MANET environment as explained in OPLKH [11]. In MANET, there is no key-server so we have chosen clusterhead as key-server. To select the clusterhead we have used weighted clustering algorithm (WCA) [6, 8, 14]. We have considered the rekey probability as one of the factor to be used in WC Algorithm since rekey probability causes re-clustering. The modified WCA algorithm as follows:

Clusterhead Selection Procedure

Step 1: Find all the neighbors (all the nodes within the transmission range) of each node u . This will give us the degree of node u say d_u , and H is the number of nodes that can be handled by Clusterhead.

Step 2: Compute the degree difference, $D_u = |d_u - H|$, for each node u .

Step 3: For each node, compute the sum of the distance S_u , with all its neighbors

Step 4: Calculate the running average speed for each node u . This gives the mobility of the node, u , and is denoted by M_u .

Step 5: Compute consumed battery power (T_u) for each node ' u '.

Step 6: Calculate the total weight for each node u , by using the equation given below

$$I_u = c_1 * D_u + c_2 * S_u + c_3 * M_u + c_4 * T_u, \quad (1)$$

6th International Engineering Symposium - IES 2017

March 1-3, Kumamoto University, Japan

Where, The coefficients c_1, c_2, c_3, c_4 are the constant weighting factors for the corresponding system.

Step 7: Compute the average of all nodes weights, A_I , and also compute the average of all nodes rekey probabilities, A_{rp} .

Step 8: Now for each node u , check

If (weight $I_u < A_I$ and also corresponding rekey probability, $rp_u < A_{rp}$) then

Calculate the new weight

$$N_{Iu} = I_u * 0.0001 + rp_u. \quad (2)$$

Step 9: After calculating the new weight for all nodes, select the node with minimum N_{Iu} as a clusterhead (Key-server).

To avoid re-clustering, initially we choose the best node as clusterhead from the available nodes using the modified WCA algorithm. The WCA algorithm uses physical parameters like energy, connectivity, location and mobility. Beside all these parameters, we also consider the rekey probability in our modified WCA algorithm as one the factor to avoid rekeying in early time. In some situations, when the key-server (clusterhead) node energy may deplete below the threshold then this cause key-server node to be change which leads to the re-clustering. In re-clustering process we again run the modified clusterhead selection algorithm and will select the best node as clusterhead among the available nodes and it will acts as a key-server. This process continues until the simulation ends. After the clusterhead selection process, the selected clusterhead acts as a key-server and responsible for key distribution in MANET.

To reduce the energy consumption in MANET, while using OPLKH schema for key management we are using group oriented rekeying which is better than key oriented and user oriented [9]. Because group oriented rekeying is good for server side and we can reduce the message transmission and receiving cost in the network and at server also. It is very important to minimize energy consumption at server because depletion of server energy will lead to change of key-server and ultimately which will increase the

rekey cost and other overheads like clusterhead selection, routing overhead and message transmission overhead.

- **Routing in MANET**

For routing in MANET, we have implemented both reactive routing protocol AODV [18, 19] and proactive routing protocol DSDV [16] and calculated the energy consumption at server.

- **Mobility Model**

For mobility as in survey [20], we have implemented Random Waypoint Model [21] in MANET environment development. According to Random Waypoint Model initially each mobile node randomly selects one location in the simulation field as destination. After reaching the destination, the node stops for a period of time, called pause time, again it will chooses another random location in simulation field and moves towards it. This procedure will repeats till the simulation ends.

- **Energy Consumption Model**

We have calculated the energy consumption for key generation [22] and for data transmission and receiving are [13]. The total energy consumption during the transmission of packet p is calculated as $E(p) = i*v*tp$ Joules, where i is a current in mili ampere, $i=280\text{mA}$ during transmission and $i=240\text{mA}$ during receiving, v the voltage chosen as 5V and the packet transmission time, tp , is calculated by $(\text{Packet-Size}/2*10^6)$ sec. Energy consumption for generation of AES-128 bit key is $7.83\mu\text{J}/\text{key}$.

SIMULATION RESULTS AND ANALYSIS

We simulated OPLKH schema using C language. We performed experiment on groups of 128, 256, 512, 768, 1024 nodes. For each experiment, we have generated the joining/leaving of members randomly, in addition, some members may leave because of power depletion and some members may leave/join based on link failure or availability respectively. For each leave/join operation we have recorded the number of rekeys generated, energy consumption at key-server and energy consumption for key generation.

6th International Engineering Symposium - IES 2017

March 1-3, Kumamoto University, Japan

In OPLKH schema, we have classified three scenarios namely static, semi-dynamic and dynamic based on number of nodes leaving and the rekey probabilities. But in MANET we added some more parameters to classify these scenarios. The additional parameters are node mobility, pause time and updating interval time. The additional parameters are listed in Table 1. During simulation for every updating interval time we have updated the node positions and routing tables.

Simulation Parameters

Table 1 Parameters used in Simulation

Simulation Parameters	Static	Semi-Dynamic	Dynamic
Mobility	0-5 m/s	0-10 m/s	0-20 m/s
Packet size	512 bytes	512 bytes	512 bytes
Mobility Model	Random Waypoint	Random Waypoint	Random Waypoint
Pause time	0-10 sec	0-5 sec	0 sec
Updating interval time	10 sec	5 sec	1 sec
No .of leaves	1/4 of Group size	1/2 of Group size	3/4 of Group size
Area (in sq. m)	1000 x 1000	1000 x 1000	1000 x 1000
Energy	0-1000 J	0-1000 J	0-1000 J

SIMULATION RESULTS

In our simulation, we have calculated the number of rekeys generated and energy consumption in static, semi-dynamic and dynamic scenarios for each group size of 128, 256, 512, 768 and 1024.

Fig.1 shows the Group size Vs Number of rekeys. In static group rekey operations i.e. number of join/leave operations are less as compare to semi-dynamic and

dynamic. In static scenario we considered 25% of nodes to leave from the group but due to energy depletion in nodes and link failures nearly 30 to 35% of nodes are leaving the group. In semi-dynamic we considered 50% of nodes to leave but nearly 60 to 65% nodes are leaving the group and in case of dynamic we considered 75% of nodes to leave from the group but nearly 80 to 90% of the nodes are leaving from the group.

Fig. 2 & 3 shows the Group size Vs Energy consumption at server. Energy consumption at server occurs because of key generation and key distribution. Fig. 2 shows the energy consumption at server using the AODV routing protocol and Fig. 3 shows the energy consumption at server using the DSDV routing protocol. As DSDV is a proactive routing protocol and computes routes to every node, it causes more energy depletion in the network whereas in case of AODV, which is a reactive routing protocol it computes the routes only when required so energy consumption is very less as compare to DSDV.

Fig. 4 shows the Group size Vs Energy consumption for key generation at server in all three scenarios for various group sizes of 128, 256, 512, 768 and 1024. As the number of rekey operations increases the energy consumption for key generation also increases.

CONCLUSION

In MANET, secure group communication is a challenging issue due to lack of fixed infrastructure or centralized administration and more power consumption. As the nodes have limited power resources in MANET, we have proposed OPLKH method which reduces the rekeying cost. Reduction in rekeying cost causes reduction in communication cost thereby decreasing the energy consumption, which leads to long survival of MANET.

6th International Engineering Symposium - IES 2017

March 1-3, Kumamoto University, Japan

REFERENCES

- [1] Jun Li, Guohua Cui, Xiaoqing Fu, Zhiyuan Liu, Li Su, "A Secure Group Key Management Scheme in Mobile Ad Hoc Networks", IEEE Computer Society Press, 2005.
- [2] Yuzhe Chen, Minghua Zhao, "An Efficient and Secure Group Key Agreement Using in the Group Communication of Mobile Ad-hoc Networks", IEEE Computer Society Press, 2006.
- [3] Sencun Zhu, Sanjeev Setia, Shouhuai Xu, Sushil Jajodia, "An Efficient Group Rekeying Scheme for Secure Multicast in Ad-Hoc Networks", in Proc. of the First Annual International Conference on Mobile and Ubiquitous Systems: Networking and Services, IEEE 2004.
- [4] Jayanta Biswas, S. K. Nandy, "Efficient Key Management and Distribution for MANET", in Proc. ICC IEEE, 2006
- [5] Bing Wu, Jie Wu, Eduardo B. Fernandez, Spyros Magliveras, "Secure and Efficient Key Management in Mobile Ad Hoc Networks", in Proc. of the 19th IEEE International Parallel and Distributed Processing Symposium (IPDPS'05), 2005.
- [6] Suchismita Chinara, Santanu Kumar Rath, "A Survey on One-Hop Clustering Algorithms in Mobile Ad Hoc Networks", in Proc. of Springer Science+Business Media, LLC 2009.
- [7] Srdjan Capkun, Levente Buttyán, Jean-Pierre Hubaux, "Self-Organized Public-Key Management for Mobile Ad Hoc Networks", IEEE Transactions on Mobile Computing, Vol.2, No.1, 2003.
- [8] Ratish Agarwal, Dr. Mahesh Motwani, "Survey of clustering algorithms for MANET", International Journal on Computer Science and Engineering, 2009.
- [9] Chung Kei Wong, Mohamed Gouda, and Simon S. Lam, "Secure Group Communications Using Key Graphs", in Proc. IEEE/ACM Transactions on Networking, Vol. 8, 2000.
- [10] Ali Aydin Selcuk, Deepinder Sidhu, "Probabilistic optimization techniques for multicast key management", in Proc Elsevier Science 2002.
- [11] Alwyn R. Pais, Shankar Joshi, "A new probabilistic rekeying method for secure multicast groups", in Proc. International Journal of Information Security- (2010) 9:275–286.
- [12] K.H. Rhee, Y.H. Park, and G. Tsudik, "A Group Key Management Architecture for Mobile Ad-hoc Wireless Networks," J.Inform. Sci. Eng., vol. 21, no. 2, Mar. 2005, pp. 415-28.
- [13] Dongkyun Kim, J.J Garcia-Luna-Aceves, Katia Obraczka, Juan-Carlos Cano and Pietro Manzoni, "Power-Aware Routing Based on The Energy Drain Rate for Mobile Ad Hoc Networks".
- [14] M. Chatterjee, S. K. Das, and D. Turgut, "An On-Demand Weighted Clustering Algorithm (WCA) for Ad hoc Networks", in Proc. of IEEE Globecom'00, 2000.
- [15] K.Gomathi, B.Parvathavarthini, "An Efficient Cluster based Key Management Scheme for MANET with Authentication", Trendz in Information Sciences & Computing (TISC), IEEE 2010.
- [16] Krishna Gorantala, "Routing Protocols in Mobile Ad-hoc Networks".
- [17] Sun, Bin, Yu, Bin, "A Hierarchical Key Management Scheme for MANET".
- [18] Fenglien Lee, "Routing in Mobile Ad Hoc Networks".
- [19] Ian D. Chakeres, Elizabeth M . Belding-Royer, "AODV Routing Protocol Implementation Design", in Proc. 24th International Conference on Distributed Computing Systems Workshops IEEE-2004.
- [20] Fan Bai and Ahmed Helmy, "A Survey of Mobility Models in Wireless Adhoc Networks".
- [21] Network Simulator 2.26 Sources Original Documentation, Website:<http://www-rp.lip6.fr/ns-doc/ns226-doc/html/classMobileNode.htm>.
- [22] Nachiketh R. Potlapally, Srivaths Ravi, Anand Raghunathan and Niraj K. Jha, "Analyzing the Energy Consumption of Security Protocols", in Proc. ISLPED'03, ACM 1-58113-682-X/03/0008.
- [23] Anne Marie Hegland et al., "Survey of key management in adhoc networks", in Proc. IEEE communications surveys-2006.
- [24] D. Wallner, E. Harder, and R. Agee, "Key Management for Multicast: Issues and Architectures," IETF RFC 2627, 1999.
- [25] K. H. Rhee, Y. H. Park, and G. Tsudik, "An Architecture for Key Management in Hierarchical Mobile Ad-hoc Networks," J.Commun. and Networks, vol. 6, no. 2, June 2004, pp. 156-62.

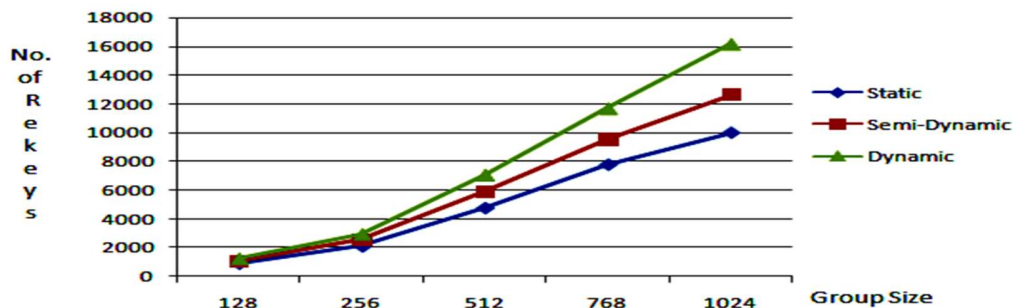


Fig.1 Group Size Vs No. of Rekeys

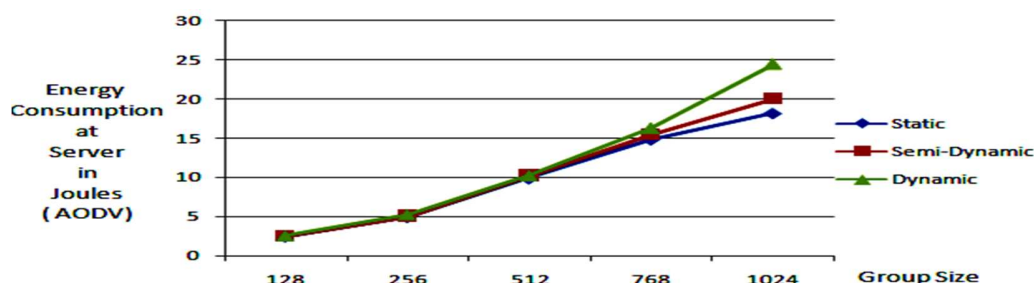


Fig.2 Group Size Vs Energy consumption at server in joules in case of AODV protocol

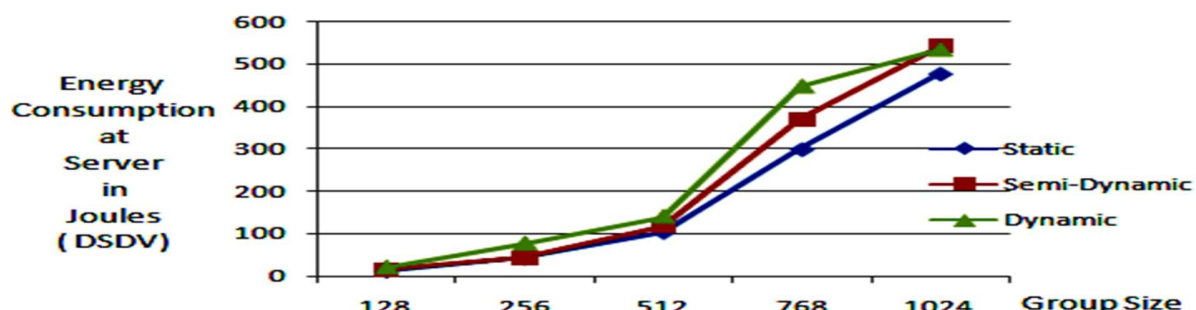


Fig.3 Group Size Vs Energy consumption at server in joules in case of DSDV protocol

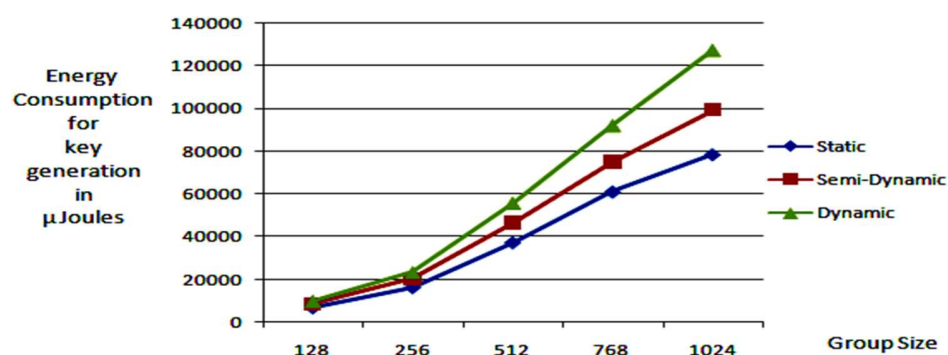


Fig.4 Group Size Vs Energy consumption for key generation μjoules

Performance Comparison of Region Consistency Activation Algorithm on Pixel wise Scene Labeling

Dinesh Naik ¹, Jaidhar C D ²

¹ Department of Information Technology, National Institute of Technology, Karnataka, Surathkal, Mangalore 575025, India. e-mail:din_nk@nitk.ac.in

² Department of Information Technology, National Institute of Technology, Karnataka, Surathkal, Mangalore 575025, India. e-mail:jaidharc@nitk.edu.in

ABSTRACT: A SegNet framework is combined with a novel strategy to improve global label consistency of scene labelling in image on pixel wise based approach is investigated to come with an improved image segmentation model. Label Distribution predictions extracted from the SegNet Network is investigated and used in the project for image labeling. An algorithm called Region Consistency Activation (RCA) to improve the global label consistency is implemented. The RCA is based on a novel transformation between Ultra metric Contour Map (UCM) and the Probability of Regions Consistency (PRC). These algorithms were rigorously tested on the CamVid dataset. Superior performances were achieved compared with the state- of- the-art methods on this dataset.

Keywords: Scene labelling, semantic segmentation, convolutional neural networks, deep learning

INTRODUCTION

Semantic Scene labelling (Yandong Li et al. 2015) (also called semantic segmentation) which is a vital step towards high level image understanding aims at labeling every pixel in an image with a specific object category. Scene labeling becomes a very challenging task in a computer vision problems. Accurately classifying every pixel in an image and ensuring global label consistency of the full image are the two key problems faced in a scene labeling system. We investigate the SegNet Encoder-Decoder Neural Network Architecture (Badrinarayanan et al. 2015) for image labeling in the first step. We then implemented an algorithm called Region Consistency Activation (RCA) (Yandong Li et al. 2015) to improve the global label consistency. It is based on a novel transformation from Ultrametric Contour Map(UCM) (P. Arbelaez et al. 2011) to Probability of Region Consistency (PRC) (Yandong Li et al. 2015). Fig.1 shows that learned features from ConvNets are powerful for scene labeling

and the proposed RCA effectively improves the global label consistency.

BACKGROUND

The most popular approach for scene labeling is the graph model which models the task of multi-class image labeling as a Markov random Fields (MRF) (P. H. O. Pinheiro and R. Collobert 2014) or Conditional Random Fields (CRF) (P. H. O. Pinheiro and R. Collobert 2014) problem. The rich hand-crafted features help in producing the unaries. Different from these works, deep learning (J. Donahue et al. 2014) provides a way to learn the features instead of designing or selecting handcrafted features. Recursive neural networks can also be used for scene labeling. Recurrent ConvNets (R. Achanta et al. 2012) can be used to learn the features of context patches around pixels. We use a model of multi scale ConvNets to learn hierarchical features for scene labeling. We base our work on superpixels (Y. Lecun et al. 1998) instead of pixels, which significantly reduce the size of both the training and testing sets. We also implement a novel algorithm called RCA to

improve the global label consistency. Instead of using learned features from specifically trained ConvNets, generic features extracted from large ConvNets (J. Donahue et al.2014) are used as they are very powerful for object recognition and detection.

SegNet

SegNet (Badrinarayanan et al. 2015) is a deep convolutional encoder-decoder architecture for image segmentation. It is a deep fully convolutional neural network architecture for semantic pixel-wise segmentation. This core trainable segmentation engine consists of an encoder network, a corresponding decoder network followed by a pixel-wise classification layer. The architecture of the encoder network is topologically identical to the 13 convolutional layers in the VGG16 network (J. Donahue et al.2014). The role of the decoder network is to map the low resolution encoder feature maps to full input resolution feature maps for pixel-wise classification. The novelty of SegNet lies is in the manner in which the decoder upsamples its lower resolution input feature map(s). Specifically, the decoder uses pooling indices computed in the max-pooling step of the corresponding encoder to perform non-linear upsampling. This eliminates the need for learning to upsample. The upsampled maps are sparse and are then convolved with trainable filters to produce dense feature maps. The design of SegNet was primarily motivated by road scene understanding applications. Hence, it is efficient both in terms of memory and computational time during inference. It is also significantly smaller in the number of trainable parameters than competing architectures and can be trained end-to-end using stochastic gradient descent without complex training protocols.

SegNet architecture is designed to be a core segmentation engine for pixel-wise semantic segmentation. It is primarily motivated by road scene understanding applications which require the ability to model appearance (road, building), shape (cars, pedestrians) and understand the

spatial-relationship (context) between different classes such as road and sidewalk. In typical road scenes, the majority of the pixels belong to large classes such as road, building and hence the network must produce smooth segmentations. The engine must also have the ability to delineate moving and other objects based on their shape despite their small size. Hence it is important to retain boundary information in the extracted image representation. From a computational perspective, it is necessary for the network to be efficient in terms of both memory and computation time during inference. It must also be able to train end-to-end in order to jointly optimize all the weights in the network using an efficient weight update technique such as stochastic gradient descent. Networks that are trained end-to-end or equivalently those that do not use multi-stage training or other supporting aids such as region proposals help establish benchmarks that are more easily repeatable. The design of SegNet arose from a need to match these criteria.

The encoder network in SegNet is topologically identical to the convolutional layers in VGG16 (J. Donahue et al.2014). The fully connected layers of VGG16 are removed which makes the SegNet encoder network significantly smaller and easier to train than many other recent architectures. The key component of SegNet (Badrinarayanan et al. 2015) is the decoder network which consists of a hierarchy of decoders one corresponding to each encoder. Of these, the appropriate decoders use the max-pooling (J. Donahue et al.2014) indices received from the corresponding encoder to perform non-linear up sampling of their input feature maps. This idea was inspired from an architecture designed for unsupervised feature learning. Reusing maxpooling indices in the decoding process has several practical advantages:

- It improves boundary delineation.
- It reduces the number of parameters enabling end-to -end training.
- This form of upsampling (J. Donahue et al.2014) can be incorporated

6th International Engineering Symposium - IES 2017

March 1-3, 2017, Kumamoto University, Japan

into any encoder-decoder architecture with only a little modification.

SegNet is different from scene understanding where the idea is to exploit co-occurrences of objects and other spatial context to perform robust segmentation. Some example test results produced on randomly sampled road scene images from Google are shown in Fig.2.

Contour Maps

Contour Maps (P. Arbelaez et al. 2011) are a low-level system for boundary extraction and segmentation of natural images and the evaluation of its performance. This problem arises in the framework of hierarchical classification, where the geometric structure of an image can be represented by an ultra metric contour map, the soft boundary image associated to a family of nested segmentations. We define generic ultra metric distances by integrating local contour cues along the regions boundaries and combining this information with region attributes.

Hierarchical organization (P. H. O. Pinheiro and R. Collobert 2014) is one of the main characteristics of human segmentation. A human subject segments a natural image by identifying physical objects and marking their boundaries up to a certain level of detail. If we suppose that different subjects segmenting a single image perceive the same objects then, up to variations in the exact localization of boundaries, the intersection of their segments determines the finest level of detail considered. Fig. 3 (Yandong Li et al. 2015) presents an example, with a natural image and composite human segmentations.

The segmentations are superimposed and the segments are represented by their mean color. Segmentation can be thought as a process of grouping visual information, where the details are grouped into objects, objects into classes of objects, etc. Thus, starting from the composite segmentation, the perceptual organization of the image can be represented by a tree of regions, ordered by inclusion. The root of the tree is the entire scene, the leaves are the finest

details and each region represents an object at a certain scale of observation.

Since the early days of computer vision, the hierarchical structure of visual perception has motivated clustering techniques to segmentation, where connected regions of the image domain are classified according to an inter-region dissimilarity measure. We consider the traditional bottom up approach, also called agglomerative clustering, where the regions of an initial partition are iteratively merged, and we characterize those dissimilarities that are equivalent to ultrametric distances.

The key point of hierarchical classification is the definition of a specific distance for a particular application. We design ultrametrics for contour extraction (P. Arbelaez et al. 2011) by integrating and combining local edge evidence along the regions boundaries and complementing this information with intra-region attributes.

METHODOLOGY

System Architecture

Figure 4. depicts a block diagram of the investigated framework for scene labeling. The model is based on two representations of the input image. The first one generates our pixel wise label distribution representation. We used the SegNet architecture to generate this representation. The second representation of the input image is the Ultra metric Contour Map (P. Arbelaez et al. 2011) of the image. Both of these representations are combined using the Region Consistency Activation (RCA) algorithm to get our final image labeling with improved label consistency.

Pixel-wise Label Distribution Representation

The objective of scene labeling is to transform a raw image X into a label space $L : L = f(X; \epsilon)$, where ϵ denotes the parameters of this transformation. The above process is decomposed into two steps. We transform X into a label probability distributions space $Y : Y = g(X ; (W; b))$ in the first step. W and b denote the trainable parameters of ConvNets. X is

represented by a series of pixels that need to be labeled by the (J. Donahue et al. 2014) CNN : $X = [x_1; x_2; \dots; x_n]$. These pixel representations are bounding boxes of different sizes centered on every pixel. For each representation x_i , we transform it into the label probability distribution space: $y_i = g(x_i; (W; b))$. The final label probability distribution is obtained by combining all the label probability distributions together: $Y = [y_1; y_2; \dots; y_n]$. The second step is to transform the label probability distributions into final labels: $L = h(Y; \psi)$. ψ denotes the hyperparameters of the threshold and a .

Trained ConvNets Features

An image X is represented by a series of pixels x_i in the framework. Each of the pixels is a candidate for training or testing with ConvNets (Yandong Li et al. 2015). We assume that the i^{th} layer of the ConvNets is H_i . H_0 is the input of the feature learning system. If the i^{th} layer is a convolution layer, it has trainable parameters W_i and b_i , where W_i is the shared weight vector of convolution kernels and b_i is the bias vector. The output of the convolution layer can be described as:

$$H_i = f(W_i H_{i-1} + b_i) \quad (1)$$

For a pooling layer H_i , the pooling process can be written as:

$$H_i = \text{pool}(H_{i-1}) \quad (2)$$

We assume Y denotes the output of ConvNets, which is the probability distribution of the different classes:

$$Y(i) = P(L = I^i | H_0; (W; b)) \quad (3)$$

Our target of training is to minimize the negative log likelihood of our ConvNets (Yandong Li et al. 2015). In order to avoid over fitting, we add an L2 regularization term to our final loss function:

$$E(W, b) = -\sum_{i=1}^{|Y|} \log Y(i) + \frac{\lambda}{2} W^T W \quad (4)$$

The hyper parameter λ , called weight decay, is used to control the effect of the regularization. In the training process, we minimize $E(W; b)$ by updating the trainable parameters of ConvNets using (M. D. Zeiler and R. Fergus 2014) stochastic gradient descent (SGD). Instead of a single column of ConvNet, heterogeneous multi-column ConvNets are employed. ConvNets of different structures are trained separately. In the test process, we fused all the predictions from ConvNets with a sliding window fusion process to achieve higher accuracy.

ConvNets Structure Used

The SegNet architecture was used for this project. It is deep convolutional encoder-decoder architecture for image segmentation. The SegNet ConvNet is an encoder-decoder network. The architecture of the encoder network is topologically identical to the 13 convolutional layers in the VGG16 network. The role of the decoder network is to map the low resolution encoder feature maps to full input resolution feature maps for pixel-wise classification. There is a decoder layer for every encoder layer. The final output from this CNN will be the label distributions of every pixel which will be used for the final RCA algorithm along with the UCM representation.

From UCM to PRC

UCM's contour detector combines multiple local cues into a globalization framework based on spectral clustering. A threshold is applied to the UCM and all the boundaries unless their probability is higher than that threshold are ignored. This produces a segmentation map of the image. We assume that regions have a stronger label consistency when they are in an over segmented map compared with the under segmented ones. Therefore, the relationship between the probability of region consistency (Yandong Li et al. 2015) (PRC) and the threshold applied to UCM is described using the following equation:

$$PRC = -\alpha \log(\text{threshold}) \quad (5)$$

6th International Engineering Symposium - IES 2017

March 1-3, 2017, Kumamoto University, Japan

The hyper parameter α describes the intensity of the inverse relationship between threshold and PRC.

Proposed Region Consistency Activation (RCA)

Two parameters, PRC and label probability distributions P of a region produced from UCM are required to activate label probability distributions of all the pixels in the image. The label distributions of a region R is the average of all the label distributions of the pixels in that region:

$$P = \frac{\sum_{i \in R} Y(i)}{\text{sum}(\sum_{i \in R} Y(i))} \quad (6)$$

Label distributions of each pixel are activated using the following equation:

$$Y(i,j) = Y(i,j) + PRC \times P \quad (7)$$

WORK DONE

Experiments

For the project we decided to use the CamVid dataset to benchmark the labeling scheme. This database consists of around 600 RGB images of road traffic. The SegNet architecture was built in Python using the Keras library that works on top of the Theano deep learning framework. This architecture was trained using the dataset mentioned before to output the label distributions of all pixels in the image. The data was split into the training and testing parts using a 70 - 30% split of the original data. This label distribution of the image is used in the RCA algorithm that is being implemented in the paper. The images are also hierarchically segmented using the Ultrametric Contour Map method. This segmentation was implemented using the skimage library in Python. This library has very convenient support to generate RAGs and to perform hierarchical merging of regions based on these graphs. The images were segmented using the following threshold values:

$$\text{threshold} = [0:05; 0:2; 0; 5; 0; 7; 0:9]$$

The experiment was repeated for all the above thresholds and results were noted. The above two representations of the image were further combined using the

Region Consistency Activation (RCA) algorithm which was also implemented in Python.

Results and Discussion

The accuracy of the pixel-wise labeling of the above experiments is as follows:

From the above table we can clearly see an improvement in the accuracy of the labeling when using the Region Consistency Activation algorithm , with the highest accuracy gain coming somewhere in the 0:4 - 0:6 range . Also using this dataset we saw a accuracy gains ranging from 1% to 3% using the RCA algorithm as opposed to without it. This clearly shows the importance of global pixel label consistency.

CONCLUSION

In this project we investigate the learned features from ConvNets and implemented an algorithm called Region Consistency Activation (RCA) for scene labeling. We concluded that general features are even more powerful compared with our trained ConvNets features. Experiments show that the RCA algorithm is an effective method to improve the global label consistency of a scene labeling system.

REFERENCES

- [1] Badrinarayanan et al. (2015),SegNet: A Deep Convolutional Encoder-Decoder Architecture for Image Segmentation, arXiv preprint arXiv:1511.00561.
- [2] J. Donahue et al. (2014),Decaf: A deep convolutional activation feature for generic visual recognition, in ICML.
- [3] M. D. Zeiler and R. Fergus (2014),Visualizing and understanding convolutional networks, in ECCV, pp.818–833.
- [4] P. Arbelaez et al. (2011),Contour detection and hierarchical image segmentation, IEEE TPAMI, 2011,vol. 33, no. 5.
- [5] P. H. O. Pinheiro and R. Collobert (2014),Recurrent convolutional neural networks for scene labeling, in ICML.
- [6] R. Achanta et al. (2012),Slic superpixels compared to state-of-the-art superpixel methods, IEEE TPAMI, vol. 34, pp.2274–2282.
- [7] Yandong Li et al. (2015),Outdoor Scene Labeling with Learned Features and Region Consistency Activation, published in Image Processing (ICIP), 2015 IEEE International Conference on 27-30 Sept. 2015. IEEE, 2015, pp 1374- 1378.

- [8] Y. Lecun et al. (1998), Gradient-based learning applied to document recognition, in Proceedings of the IEEE, pp. 2278–2324.

Table 1 Result

Thresholds	Without RCA	With RCA
0.05	80.3	82.6
0.2	80.3	81.4
0.5	80.3	83.9
0.7	80.3	81.3
0.9	80.3	82.5

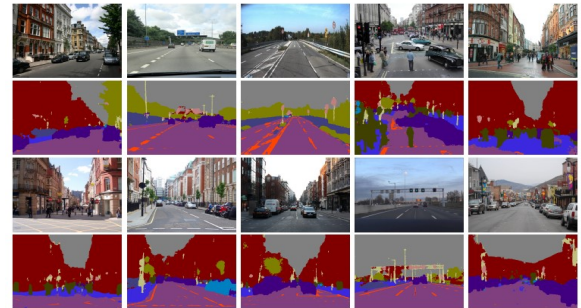


Fig. 2 SegNet predictions on urban and highway scene test samples from the wild.

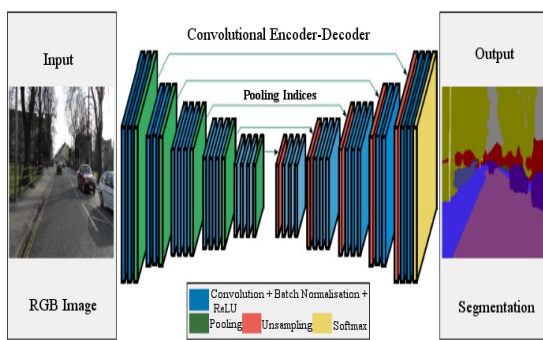


Fig.1 SegNet Framework.

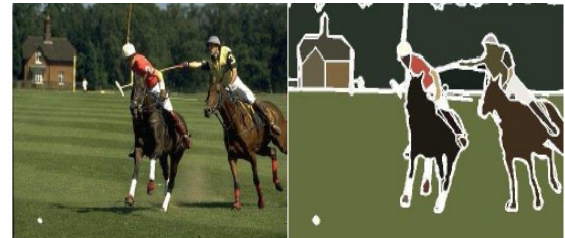


Fig. 3 Natural image and composite human segmentation.

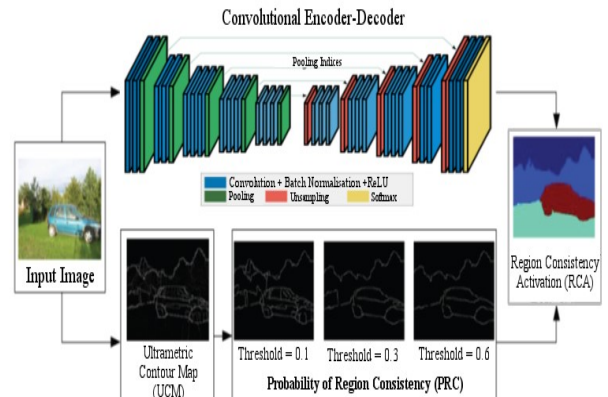


Fig. 4 Block diagram of our proposed scene labeling framework.

DESIGN OF FUZZY LOGIC SPEED CONTROLLER FOR BLDC MOTORS USING MATLAB/SIMULINK

Sukanya.M. Sundaram

*Department of Electrical and Electronics Engineering
National Institute of Technology Karnataka, Surathkal,
Mangalore- 575025, India.
Email: sukanyasundaram1@gmail.com*

ABSTRACT

BLDC motors are fast gaining popularity these days for various industrial purposes because of their high torque density, high efficiency and small size. Generally, BLDC motors are PID controlled. However, the major problem associated with the conventional PID controller is that the tuned gain parameters obtained for such BLDC servomotor drive control systems do not yield better transient and steady state responses under varied operating conditions such as parameter variations, load disturbances etc.

This presentation discusses a digital control strategy – fuzzy logic control for the improvement of performance of BLDC motors. A second order model approximation of a BLDC motor, working on a fuzzy logic based adaptive speed controller is thus implemented and validated through MATLAB/SIMULINK. The transient and steady state performance is investigated.

Predictive Data Analytics for Counterterrorism

Sahana Roy

*Department of Electronics and Communication Engineering, National Institute of Technology Karnataka, Surathkal, Mangalore 575025, India.
email:sahanaroy05@gmail.com*

ABSTRACT: Measures like increased surveillance and strict immigration laws have become obsolete in tackling lone-wolf style terrorism. This paper will propose the use of predictive data analysis involving natural language processing, graph databases and cognitive computing platforms to spot and understand behavioural patterns. This paper will also present a case study wherein the mentioned techniques will be suggested to tackle the ISIS problem, which is different from older terrorist organizations not only because of their hierarchical and organized line of command but also their lone-wolf style attacks.

Keywords: Lone-wolf attacks, Predictive Data Analysis, Racial Profiling, ISIS Case Study

INTRODUCTION

The need of the hour is for the government to find new ways to gather intelligence and accordingly analyse it to continue the fight against an ever evolving terrorism strategy. Private data has thus become a powerful resource for the government, thereby increasing the need for government intrusion on privacy. Many of the recent government programs which explore data-mining and data-analysis techniques for counterterrorism have caused a lot of public concern leading to legislative action. However, an intelligent and rational resolution to this debate is critical.

DATA MINING: A PRETEXT TO DATA ANALYSIS

Data mining is the process of extracting trends from huge datasets which were previously unknown using a variety of methods such as those from pattern recognition and machine learning. Data mining can be used to detect unusual patterns which maybe a result of terrorist activities and fraudulent behaviour [B. Thuraisingham (2003)].

Challenges

One of the main questions that needs to be answered before data mining can be applied for counterterrorism is whether false positives and false negatives can be completely eliminated. False positives can be disastrous for individuals while false negatives may mislead our ability to prevent and control terrorist activities. Another challenge is the building of real-time data mining models which require good training examples, which become difficult to procure in the unclassified setting of terrorist activities. The third challenge is of multimedia data mining because multimedia presents itself as an unstructured database. The existing tools can mine structured and relational databases so one way is to find structures in the unstructured data and then apply these tools on it. This leads us to graph and pattern mining [B. Thuraisingham (2003)]. Essentially one builds a graph structure based on the information he or she has. If multiple agencies are working on the problem, then each agency will have its own graph. The challenge is to be able to make inferences about missing nodes and links in the graph. Also the graph could be very large. The question is how one can reduce the graph to a more manageable size [Bill Schmarzo (2014)].

6th International Engineering Symposium - IES 2017

March 1-3, 2017, Kumamoto University, Japan

However, this doesn't solve the problem of web mining. In a way web mining encompasses data mining as one has to mine all the data on the web as well as mine the structure and usage patterns. By mining the usage patterns one could get patterns such as there are an unusual number of visits to a federal web site from Paris around 3am in the morning [B. Thuraisingham (2003)].

COUNTERTERRORISM: THE OBJECTIVE

Before discussing the application of data analytics to counterterrorism, we need to understand what counterterrorism is all about. Counterterrorism is a collection of techniques used to combat, prevent, and detect terrorism. The goal of this paper is to examine various data mining techniques to see how we can combat terrorism using these techniques.

Countering Non-Information Related Terrorism

Non-information related counterterrorism includes protecting from bombings, explosions, vandalism and other kinds of terrorist attacks not involved with computers. For example, hijacking an airplane and attacking buildings with airplanes is a case of non-information related terrorist activity. Firstly, a dataset of all the various scenarios and examples needs to be created i.e all kinds of terrorist attacks that have occurred in the past needs to be identified. Information about the suspects would also need to be gathered. This collected data then needs to be analysed to see whether any patterns emerge.

We also need to ensure there are physical safety measures. For example, we need surveillance cameras to see who is entering the building. These cameras should also capture perhaps the facial expressions of various people. The data gathered from the cameras should be analysed further for suspicious behaviour.

Countering Information Related Terrorism

Information related terrorism are basically malicious attacks and intrusions which can be due to viruses, spoofing, masquerading

and stealing data, say information assets. These attacks could be on databases and corruption of data that is to say, terrorism attacks can also include credit card frauds and identity thefts. Preventing malicious attacks is more challenging. We need to design systems in such a way that malicious attacks and intrusions are prevented. When an intruder attempts to attack the system, the system would figure this out and alert the security officer. There is research being carried out on secure systems design so that such intrusions are prevented [B. Thuraisingham (2003)].

Enforcing appropriate access control techniques is also a way to enforce security. For example, users may have certificates to access the information they need to carry out the jobs that they are assigned to do. The organization should give the users no more or no less privileges.

Countering Bio-terrorism and Chemical Attacks

First of all unlike say non information related terrorism where bombing and shootings are fairly explicit, bio-terrorism and even chemical attacks are not immediately obvious. Suppose a terrorist spreads the smallpox virus, it takes time, at least a few days before the symptoms surface and few more days before the diagnosis is made. By then it may be too late as millions of people may be infected in trains and planes and large gatherings and meetings. The challenge here is to prevent as well as detect such attacks as soon as possible. Chemical weapons may also be treated similarly. In the case of nuclear attacks, we need to determine what nuclear weapons have been used and then decide what actions to take.

HANDLING THREATS USING DATA MINING

Suppose, A is a real-time threat and B is a non-real time threat. Over time, a non-real time threat could become a real-time threat. Real-time threats have to be handled in real-time. When it comes to counter-measures for handling these threats, one needs to develop techniques

6th International Engineering Symposium - IES 2017

March 1-3, 2017, Kumamoto University, Japan

that meet timing constraints to handle real-time threats. In the case of non-real time threats, the data mining techniques could analyse the data and make predictions that certain threats could occur sometime later in the future [H. Chen (2003)].

Non-Real Time Threats

We need good data to carry out data mining and obtain useful results. We also need to reason with incomplete data. This means that the data mining tools have to make assumptions about the data belonging to other organizations [B. Thuraisingham (2003)].

The next step would be to collect information about various people, the more number of people, the better. Again to have complete information about people, we need to gather all kinds of information about them. This information could include information about their behaviour, where they have lived, their religion and ethnic origin, their relatives and associates, their travel records etc. From a technology point of view, we need complete data not only about individuals but also about various events and entities. After the collection of the data, it needs to be organised into structured and unstructured warehouses, so to speak, to run further analysis on it.

After that, we need to decide on the appropriate mining tool which will depend on what we want the outcome of the analysis to be.

The most difficult but important part is to understand whether the mining results are useful, in the sense, whether they yielded any false positives or false negatives. Therefore we need a human specialist to work alongside these tools to eliminate such redundant possibilities, until of course we are able to build intelligent mining tools.

The bottom line is that we have time to run all of the above steps in a non-real time threat, but a non-real time threat may become a real time threat.

Real Time Threats

The challenge with real time threats is that they may occur within a certain time and therefore require immediate response i.e

there are timing constraints associated with real time threats.

Essentially, data mining can be applied to data that has been collected over a certain amount of time as the goal is to make deductions and predict future trends after analysing the data. Here, the importance of data mining in real time arises. Hence, to make data mining effective, we need to use known patterns and past data to make predictions. Then again, to predict in real time, data mining tools need to be trained with past data but sometimes, the past data may not exist. For example, the 9/11 attacks came as a surprise to most of us because nothing of the sort had happened before. Thus, we need to use hypothetical data and simulated models. We need to work with counter-terrorism specialists and get as many examples as possible. Once we gather the examples and start training the neural networks and other data mining tools we need to understand the kind of models that we want to build. Data gathering is also a challenge for real-time data mining. In the case of non-real time data mining, we can collect data, clean data, format it, build warehouses and then carry out mining. All these tasks may not be possible for real-time data mining as there are time constraints.

ANALYSIS TECHNIQUES

Current tools are not capable of making the predictions and trends in real-time, although there are some real-time data mining tools emerging. There are a number of data mining outcomes and they include making associations, link analysis, forming clusters, regular classification and anomaly detection. The techniques that result in these outcomes are techniques based on neural networks, decisions trees, market basket analysis techniques, inductive logic programming, rough sets, link analysis based on the graph theory, and nearest neighbour techniques. The methods used for data mining are top down reasoning where we start with a hypothesis and then determine whether the hypothesis is true or bottom up reasoning where we start with examples and then come up with a hypothesis [B. Thuraisingham (2003)].

6th International Engineering Symposium - IES 2017

March 1-3, 2017, Kumamoto University, Japan

Association Technique

The goal is to find which items go together. For example, A is seen with B and B is friends with C and C and D travel a lot together and D has a criminal record. The question is what conclusions can we draw about A?

Link analysis is closely associated with making associations. While association-rule based techniques are essentially intelligent search techniques, link analysis uses graph theoretic methods for detecting patterns.

Clustering Technique

One could analyse the data and form various clusters. For example, people with origins from country X and who belong to a certain religion may be grouped into Cluster I. People with origins from country Y and who are less than 50 years old may form another Cluster II. These clusters are formed based on their travel patterns or eating patterns or buying patterns or behaviour patterns. While clustering divides the population not based on any pre-specified condition, classification divides the population based on some predefined condition.

Anomaly Detection

Another data mining outcome is anomaly detection. A good example here is learning to fly an airplane without wanting to learn to take-off or land. The general pattern is that people want to get a complete training course in flying. However there are now some individuals who want to learn flying but do not care about take-off or landing. This is an anomaly [B. Thuraisingham (2003)].

TACKLING THE ISLAMIC STATE (IS) PROBLEM: CASE STUDY

Assessing changes in modus operandi of IS and other religiously inspired terrorist groups provides a better understanding of the threat that these groups pose. It supports the development of likely future scenarios, based on which we can be better prepared for future attacks. It also stimulates the early exchange of information and intelligence between counterterrorism units.

Hence, one must first understand the nature of such groups and accordingly decide the objective with which data needs to be mined and hence further analyzed.

Nature of the Islamic State

The Islamic State has not only violated several moral boundaries by systematically and deliberately targeting civilians but also engages in guerrilla warfare, military attacks against other non-state actors, and insurgency against the Iraqi and Syrian armies [Nick Cumming-Bruce (2014)]. Concurrently, others of its members engage in "law enforcement" among the civilian populations under its control, and in service provision to these same populations.

These varied actions make the Islamic State a "hybrid terrorist organization" [Boaz Ganor (2012)] – that is, an organization that operates simultaneously in the (illegitimate) military-terrorist sphere and in the (pseudo-legitimate) civilian sphere.

As the heir of Al-Qaeda, IS is the new trend in modern terrorism, an inspiration to other terrorist networks and organizations, and individuals. Analysis of the evolution of modern terrorism reveals many instances in which an organization split up when some of its members left because they believed its leadership was too moderate i.e not militant enough. The dissident members then form a splinter organization, which is usually more violent and dangerous than its predecessor. Such splinter organizations tend to claim that they are "the real thing", unlike those in the mother organization, whom they claim have deviated from the path.

Target Recruits of the Islamic State: What Kind of Profiles to Look for While Mining Data

The IS has succeeded in using the Internet and social media to transmit a message of cruelty, which has won the hearts and minds of those youngsters who have come from around the world to join its ranks, or who have conducted lone wolf attacks of their own. Its message has inspired marginalized Muslim youth in Europe and the West, second- and third-generation immigrants (some of them with a criminal

6th International Engineering Symposium - IES 2017

March 1-3, 2017, Kumamoto University, Japan

past) who are disaffected, frustrated, seeking a sense of identity and belonging, full of hatred for the societies that have not adequately integrated them, and facing a bleak future with few prospects for development and self-actualization [Boaz Ganor (2011)]. When these problems are compounded by real personal and family distress, such young people become easy prey for IS's Internet propaganda, which seems to offer an outlet for their frustration and yearning for power and control. Thus, so-called "lone wolves" have been stirred by IS's instructional videos and other materials that it posts to the Internet with the express aim of their being used or imitated.

If the Islamist-religious dimension of the IS, the analysis is steered away from the root causes and thus an appropriate and consistent action against it cannot be found.

Geographical Significance of the Islamic State: Where Should Data be Mined From

At present, the Islamic State is focused on Syria and Iraq, and is developing an agenda that includes Libya and the Sinai Peninsula, but if it succeeds in stabilizing its rule in the areas under its control, we can expect it to expand further. Alternatively, if IS loses its territorial strongholds in Iraq and Syria, we can anticipate that it will not disappear, but rather will take on another form based in territories such as northern or central Africa, for example, or in Southeast Asia. This is what happened to Al-Qaeda, which changed following the loss of territory in Afghanistan, and especially following the killing of bin Laden.

Finding the Weak Point: How to Objectively Analyse the Collected Data

Beyond the difficulty of making additional military gains in Syria and Iraq, IS may still have to cope with an economic crisis. Thanks to its takeover of several oilfields and of gold and monetary reserves in the commercial banks of the cities it has conquered, the Islamic State has larger financial coffers than do other terrorist organizations. In addition, its policy of

kidnapping foreigners and demanding large ransoms for them has swelled its income. However, it may reasonably be assumed that without additional significant military victories, the Islamic State's financial resources will eventually dry up running [Boaz Ganor (2015)].

Taking Counterterrorism Further: Link Analysis and Developing on Predictive Data Analytics

Link analysis uses various graph theoretic techniques. It is essentially about analysing graphs. Note that link analysis is also used in web data mining, especially for web structure mining. With web structure mining the idea is to mine the links and extract the patterns and structures about the web [M. Berry and G. Linoff (1997)].

The challenge in link analysis is to reduce the graphs into manageable chunks. As in the case of market basket analysis, where one needs to carry out intelligent searching by pruning unwanted results, with link analysis one needs to reduce the graphs so that the analysis is manageable and not combinatorically explosive. Therefore results in graph reduction need to be applied for the graphs that are obtained by representing the various associations. The challenge here is to find the interesting associations and then determine how to reduce the graphs. Another challenge on using link analysis for counter-terrorism is reasoning with partial information.

Another challenge with link analysis as well with other data mining techniques is having good data. However for the domain that we are considering much of the data could be classified. If we are to truly get the benefits of the techniques we need to test with actual data.

CASE STUDY CONCLUSION

From the above study, we can reach the following conclusions:

- The IS is definitely planning more terrorist attacks, which will be primarily directed at soft targets, because of the impact it generates. Both the November Paris attacks and the October 2015 bombing of a Russian airliner suggest a shift in IS

6th International Engineering Symposium - IES 2017

March 1-3, 2017, Kumamoto University, Japan

strategy towards going global. In selecting their targets, local IS commanders are believed to enjoy tactical freedom to adapt their plans to specific local circumstances.

- The observed changes in modus operandi do not mean that other tactics are abandoned. Lone actor attacks by IS inspired or directed individuals still pose a serious threat.
- Since IS does not have an ally that could support it financially, and since it has no sea access, the organization may find itself in a financial crisis.
- Data mining needs to be done appropriately and from the right areas. Human intelligence is still required to build on possible links between datasets. Predictive data analytics needs to be applied such that future attacks are not only prevented but also the organization needs to be destabilized by attacking their financial resources.

ACKNOWLEDGEMENTS

The idea for this paper was motivated by Dr. Bhavani Thuraisingham's work on data mining for counterterrorism. I would also like to acknowledge Prof. Boaz Ganor, the Dean of Lauder School of Government and Diplomacy, for his work on the subject of the Islamic State, which has helped me immensely with my case study on the same.

REFERENCES

- [1] B. Thuraisingham, "Data mining, national security, privacy and civil liberties", SIGKDD Explorations, January 2003.
- [2] B. Thuraisingham (June 2003), "Data Mining for Counterterrorism"
- [3] B. Thuraisingham, CRC Press (June 2003) "Web Data Mining Technologies and Their Applications in Business Intelligence and Counter-terrorism"
- [4] B. Thuraisingham. Managing threats to web databases and cyber systems: Issues, solutions and challenges. In V. Kumar et al, editor, Cyber Security: Threats and Countermeasures. Kluwer.
- [5] Cumming-Bruce, Nick (October 2, 2014), "5,500 Iraqis Killed Since Islamic State Began Its Military Drive, U.N. Says" The New York Times; <http://www.nytimes.com/2014/10/03/world/middleeast/un-reports-at-least-26000-civilian-casualties-in-iraq-conflict-this-year.html>
- [6] DeRosa, Mary (March 2004), "Data Mining and Data Analysis for Counterterrorism", CSIS Report
- [7] F. Bolz et al. "The Counterterrorism Handbook: Tactics, Procedures, and Techniques", CRC Press, 2001
- [8] Ganor, Boaz (2015), "Four Questions on ISIS: A "Trend" Analysis of the Islamic State", Vol 9, No. 3
- [9] Ganor, Boaz (November 1, 2012), "The Hybrid Terrorist Organization and Incitement, The Jerusalem Center for Public Affairs"; and Azani, Eitan. "The Hybrid Terrorist Organization: Hezbollah as a Case Study." Studies in Conflict & Terrorism 36, no. 11 (2013): 899-916.
- [10] Ganor, Boaz, "An Intifada in Europe? A Comparative Analysis of Radicalization Processes Among Palestinians in the West Bank and Gaza versus Muslim Immigrants in Europe." Studies in Conflict & Terrorism Vol. 34, Issue 8, 2011.
- [11] H. Chen et al. (June 2003), "Proceedings of the 1st Conference on Security Informatics", Tucson, AZ
- [12] M. Berry and G. Linoff. Data Mining Techniques for Marketing, Sales, and Customer Support. John Wiley, New York, 1997.
- [13] Schmarzo, Bill (January 31, 2014), "How Can Graph Analytics Uncover Valuable Insights About Data?"
- [14] <http://www.kdnuggets.com>

Automation and Communication in Wildlife Monitoring & Management

Sukriti Singh

Department of Electrical and Electronics Engineering, National Institute of Technology Karnataka, Surathkal, Mangalore 575025, India. Email: sukritisingh1221@gmail.com

ABSTRACT: 'Wildlife monitoring and management' has become extremely significant in the present contrast of technological advancement and degrading environment. Recording and analysis of data through trail cameras in natural habitats and quadcopters is an important part of this process. The existing technology is limited in use to generic herd management & analysis, inefficient in extreme weather conditions and less data storage. This paper proposes an efficient model for the same based on automation (Programmable Logic Controllers) and communication (IoT and proximity wireless communication). The robust and PLCs will enable triggering of the cameras based on time-lapse and sensor-activation for capturing images, which will undergo species-specific classification. The advent of IoT allows immediate transmission of data reducing the risk from complete hardware destruction. Quadcopters can use this technology to predict species-specific habitat suitability based on further NDVI surveys and encroachments' forecast.

Keywords: *Wildlife monitoring, trail cameras, automation, IoT, species-specific*

INTRODUCTION

In a world of rapid technological growth and subsequent decline in bio-diversity, which consists majorly of a population of large vertebrates, it is becoming increasingly significant to monitor the intra-community interactions and analyse the functions of the ecosystem.

The conventional methods no longer meet the financial and logistical demands of the present state. The existent models of wildlife monitoring and management, comprising of trail cameras and quadcopters, come with numerous drawbacks like less storage and backup, generic herd monitoring, excessive manual cataloguing, necessity to synchronize internal clocks of systems for efficient identification, low battery lives, too many false positives (an image captured with no animal of interest in it) as well as false negatives (a failure to capture image when an animal of interest

is present), limited flexibility and hardly any options for future customization and data-retrieval and management issues, (Newey S, et al, 2015).

This paper proposes a model for wildlife monitoring and management by aiming at achieving the following:

- 1) Developing an end-to-end system by integrating independent technologies like sensor data aggregation and management with automated species identification, that can be easily moulded to suit the requirement.
- 2) Application of a customized IoT and remote networks' architecture to improve the quality of data acquisition, transfer and management.

In the sections that follow, the above expressed challenges are addressed with the design of a new wildlife monitoring

model that leverages recent advances in sparse coding, deep learning and Internet-of-Things (IoT), to automate image classification and analysis on a large scale. It is an end-to-end, distributed data acquisition and analytics model that implements an IoT architecture consisting of trail cameras, multiple tiers and a back-end public cloud.

ARCHITECTURE

The principal goal of the proposed model is to simplify and expedite the process of animal recognition using images from camera-traps deployed in the wild and quadcopters used to forecast habitat suitability. The multi-tier architecture of the model is represented in Figure 1.

The first tier, comprising of the trail cameras and the quadcopters, is the one with utmost importance since data is obtained basically at this level. Capturing of images based on time-lapse and motion-sensing has seen considerable advancement in the past too. However, classification of these images at the site of acquisition and automation using PLCs is a recent development and this model presents an algorithm for the same. Combination of dense scale-invariant feature transform (SIFT) with cell-structured local binary patterns (cLBP) extracts the local features to represent the animal of interest. Weighted sparse coding (for dictionary learning) and max-pooling is applied, thus enforcing both sparsity and locality, (Xiaoyuan Yu, 2013). Finally, linear support vector machine (SVM) algorithm is used for classification at, what is referred to as, the 'primary' level here.

The secondary classification happens at the second tier, to which the primarily classified images are sent via a proximity wireless connection, (Sajid Nazir, et al, 2016). The basis here is the OpenCv applications integrated with the Google TensorFlow system that requires a pre-trained model.

The training of the model for the TensorFlow algorithm, programming and updating the PLCs, changing settings of the trail-cameras and quadcopters based on requirements etc. is done at the third

tier. The fourth tier or the 'Public Cloud' is responsible for providing specific goals and suggesting modifications based on analysis. An IoT approach is pursued here to reduce the amount of manual work, time consumed and its advent in image classification avoids unnecessary data transfer.

This paper mainly focuses on the methodologies used at the first two levels. The other two tiers are also briefed in a section.

THE FIRST TIER

Camera trapping, both through trail cameras and quadcopters (the former being preferred), is a popular and promising approach to collect spatio-temporal data. Most of the even latest cameras use PIR sensors that are triggered by two means: first, motion-activated and second, a temperature difference (generally greater than approximately 5°C) between the background levels and the object in the detection zone of the sensor. However, these cameras come with major setbacks like generation of enormous number of images, false triggering due to non-animal activity and remote locations that make uploading data online unfeasible.

The proposed model aims at countering the mentioned setbacks by using Programmable Logic Controllers (PLCs), multiple modes, Sparse coding Spatial Pyramid Matching (ScSPM) technology and establishing wireless connectivity with a local reporting centre to which all the images are sent after first level of identification and classification near where the images are produced.

Programmable Logic Controllers enable proficient implementation of automatic identification of species in images. These robust controllers can be reprogrammed any number of times providing flexibility in survey goals and the large point-count provides broad scope for future customization. PLCs come in resourceful small sizes (commonly called 'brick' PLCs) and can be powered by solar power making it a non-invasive survey method. To reduce power consumption further, an

effective solution is programming the trail cameras to work in three modes- image capturing, sleep and test modes. The camera is normally in 'sleep' mode and periodically switches to 'test' mode to preset exposure settings so that when the camera is triggered, two images are captured in rapid succession, (Stenger Thomas A, 2008). The former is based on the stored settings and the latter is based on real-time settings, preventing the risk of false negatives that might result if the animal moved out of the sensor zone. Camera trapping is also enabled based on time-lapse.

Population characteristics are related to habitat use behaviour and habitat selection. Most of the surveys aim at monitoring a particular species and estimating their home-range size. Based on related work in this field that achieved an average accuracy of 82%, this model proposes use of improved, yet easy and simple to construct, Sparse coding Spatial Pyramid Matching (ScSPM) method for recognising species, (Xiaoyuan Yu, 2013). The initial procedure involves extracting local features using two kinds of local descriptors: SIFT and cLBP. Weighted sparse coding trains the dictionary for sparse representation of the same. An image or bounding box is converted to a single vector by max pooling Using SPM. Finally, the global features are classified to one species' category by applying pre-trained linear multi-class SVMs. Combination of dense scale-invariant feature transform (SIFT) with cell-structured local binary patterns (cLBP) extracts the local features to represent the animal of interest. Weighted sparse coding (for dictionary learning) and max-pooling is applied, thus enforcing both sparsity and locality. Finally, linear support vector machine (SVM) algorithm is used for classification of images.

Concatenation of SIFT and cLBP

A discriminant and invariant local feature extractor is required for the images containing noise and clutter. For moderate scaling and shifting change of edges and linear illuminance variation in image patch, dense scale-invariant feature transform (SIFT) also known as dense histogram of

oriented gradients, is a relevant measure. However, cell-structured local binary patterns (cLBP) are necessary for moderate non-linear illuminance variation. SIFT is competent at extracting silhouette of an animal, where as c-LBP is powerful in describing the skin texture. Concatenation of SIFT and cLBP is done only after extracting and coding them separately. This satisfies both the issues of discrimination and invariance, at both the pixel and the cell level. First, the gradients and LBP patterns are calculated on raw pixel patch and then, histograms are created for each of them.

Global feature extraction (Weighted sparse coding and max pooling)

The goal of dictionary learning is to describe the distribution of the inner space. A local image feature set X is obtained by random sampling in feature space. Dictionary learning is required to represent the incoming signal with minimum error, else X cannot be coded directly due to a huge number of signals.

Let X be in a D -dimensional features space, i.e. $X = [x_1, \dots, x_N] \in R^{D \times N}$. The dictionary, well known as a codebook that is precomputed in the training phase is $V = [v_1, \dots, v_K] \in R^{D \times K}$ with K atoms. To enforce sparsity and locality, the following is used: Min (V, U) such that $\|X - VU\|^{2+\lambda} \|WU\|^1 \|V^k\| \leq 1$, for all $1, 2, \dots, K$. Where $U = [u_1, \dots, u_N] \in R^{K \times N}$ is the matrix of sparse codes and W is a diagonal weighting matrix whose elements are computed as $W_{i,k} = \|X_i - V_k\|^2$, $k = 1, 2, \dots, K$, (Xiaoyuan Yu, 2013).

SPM models the spatial layout of the local image features at multiple scales. The pooled features from various locations and scales are combined to form a SPM representation of the image. In each pyramid, a max pooling function, beneficial for translational invariance, is applied on the absolute sparse codes:

$z_j = \max \{ |u_j^1|, |u_j^2|, \dots, |u_j^K| \}$, where z_j is the j^{th} element of z , u_j is the matrix element of the j^{th} row and i^{th} column of U , (Xiaoyuan Yu, 2013).

Finally, multiclass linear SVM is used to classify image of species. Similar ontologies may mislead the classification

process. Hence, biometric features like spots on the fur and shape of antlers can act as an alternative in recognition.

Owing to the rewritable characteristic of PLCs, the same PLC can be programmed for the identification of different species in different surveys, and thus increasing the simplicity of the system and making it economical.

The use of quadcopters to study wildlife habitats and encroachments is comparatively a recent phenomenon. The application of wireless communication can be used to full advantage in this case by capturing only the desired images and using the above algorithm (although not as complex) to identify green and non-green patches for comparison with NDVI surveys. This can prove extremely beneficial in acting upon the trends of encroachments & unbalanced ecosystems and also, predicting further trends in the same.

THE SECOND TIER

Once the primary classification has been done at the site of trail cameras itself and the images are obtained at the Local Reporting Centre at the second tier, further classification that is chosen to be called as 'secondary' takes place. Google TensorFlow is integrated with OpenCV applications for image recognition and analysis respectively, (Andy Rosales Elias, et al, 2016). This paper proposes training of the TensorFlow model by creating a tableau of 'fake' images of different orientations and illuminations. Some empty images (false positives) are transmitted from the camera using the IoT linkage. Labelled images of the animal(s) of interest are obtained through direct access to Google Images over the internet, preferably with white or transparent backgrounds. OpenCV is used to subtract the background automatically by replacing the required pixels with transparent pixels. Then, the animals' images are overlaid on the 'empty pictures' to produce numerous 'fake' images. The further filtering and classifying process is based on this deep-learning system and trained model through automatic comparison. Literature survey of similar approaches in the past reveals that the accuracy can be as high as 92%,

(Andy Rosales Elias, et al, 2016). The images after final classification are sent to the Central Data Centre via a long-distance microwave radio link or the internet depending on the distance and availability of commercial/government network coverages.

THE THIRD AND FOURTH TIERS

The third tier, that is the Central Data Centre, is used to change settings of the camera owing to the IoT linkage, (Sajid Nazir, et al, 2016). Settings imply the levels of sensitivity, user-based exposure settings, switching on or off of the flash, time lapse between two consecutive shots, changing the field of view by using the zooming options.

The Central Data Centre from where the data is made available to the Public cloud (or the fourth tier in this architecture) via a number of means, internet being the major one. The communication between the third and fourth tiers is two way. Based on the data collected and sent by the third tier as well as that made available by surveys regarding habitat trends, technological development, urban extension etc., the fourth tier involves itself in extensive analysis and evaluation. The predictions and the action plans that are decided upon determine how the existent model is modified. This information regarding modification is received by the third tier. After suitable (species-specific) programming is done and required changes are made in the TensorFlow models etc, the modifications are reflected in the first and second tier via an IoT linkage again.

CONCLUSION

In this paper, automatic wildlife monitoring was enabled by designing an end-to-end, IoT model for image classification, especially at a species-specific level. The multi-tier IoT system integrated with technologies like ScSPM and Google Tensorflow, connects motion-activated camera-traps to the public cloud through data centres at suitable discreet levels. Significant savings and resource conservation in network transfer and turn-around time can be made. Implementing

the proposed model will not only provide easy access to the advanced equipment used in remote locations, but also help in easier analysis of population and habitat of the species of interest. With the advent of latest technological advancements, these are steps to building a sustainable environment that is equally a home to all living species.

REFERENCES

- [1] Andy Rosales Elias, et al (2016), Where's The Bear? – Automating Wildlife Image Processing Using IoT and Edge Cloud Systems.
- [2] Newey S, et al (2015), Limitations of recreational camera traps for wildlife management
- and conservation research: A practitioner's perspective.
- [3] O'Connell A.F., Nichols J.D. and Karanth K.U., (2011), Camera traps in animal ecology: methods and analyses.
- [4] Paul Meek, Guy Ballard and Peter Fleming (2012), An introduction to camera trapping for wildlife surveys in Australia.
- [5] Sajid Nazir, Gorry Fairhurst and Fabio Verdicchio (2016), WiSE – a satellite-based system for remote monitoring.
- [6] Stenger Thomas A (2008), Wildlife-sensing digital camera with instant-on capability and picture management software
- [7] Xiaoyuan Yu, et al (2013), Automated identification of animal species in camera trap images

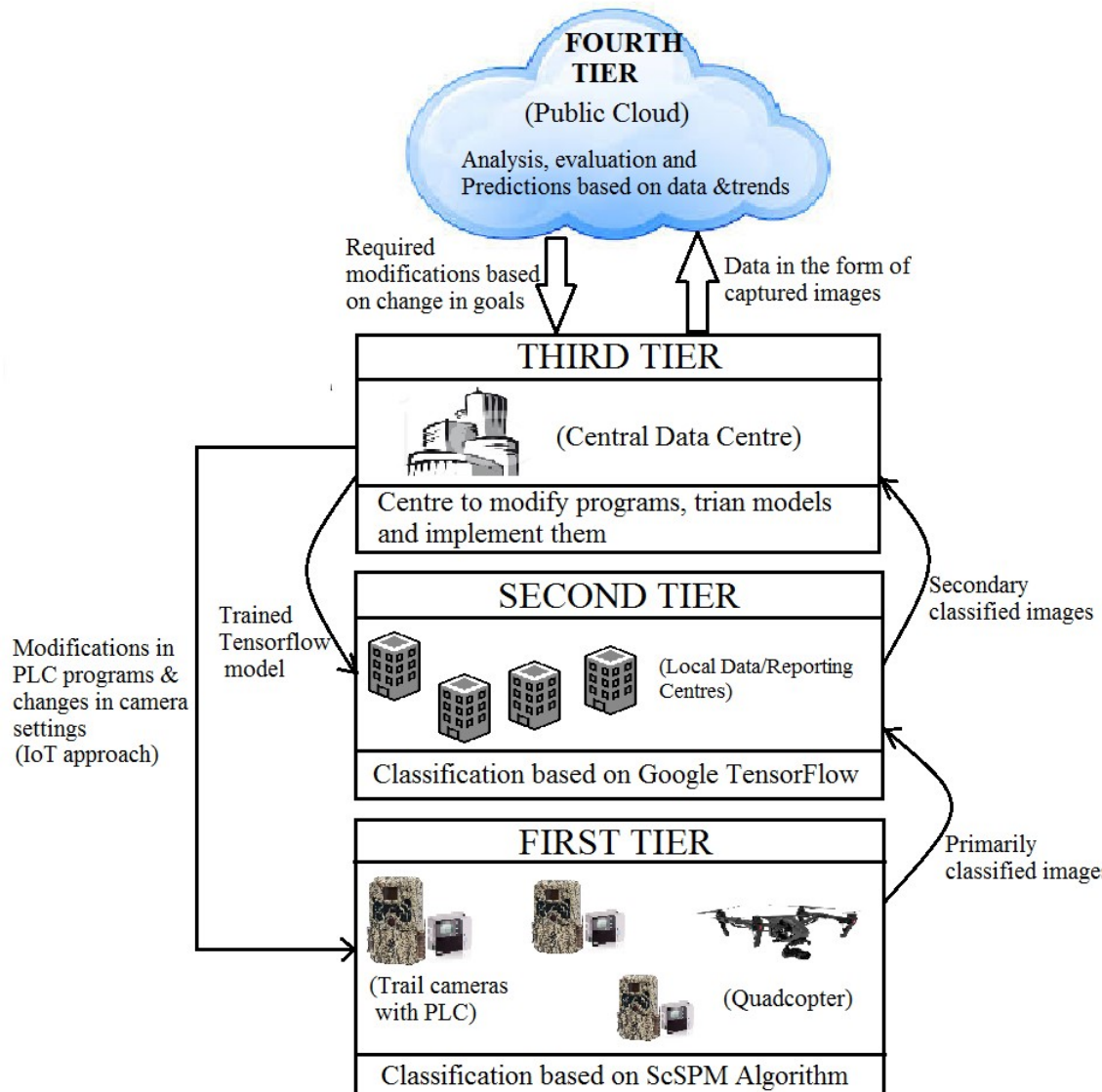


Fig.1 The architecture of the proposed model

Big Data Analytics in Transportation Economics: Opportunities and Challenges

Savita Bhat

*School of Management, National Institute of Technology Karnataka, Surathkal,
Mangalore 575025, India. email:savitapbhat@gmail.com*

ABSTRACT: Transportation economics deals with the application of economic concepts in varied areas of transportation like demand, costs, pricing and investments. Transportation economics has already become more quantitative in nature with the use of computer systems and econometric techniques. With the advent of big data technologies, that is, technologies with the capabilities of capturing, storing, sharing and analysing enormous amount of data, there is an impending need to understand the opportunities and challenges in using big data analytics in the context of transportation economics. Based on a review of literature, the present paper attempts to describe the potential applications of big data analytics in addressing some of the issues in transportation economics.

Keywords: *Transportation Economics, Big Data Analytics*

INTRODUCTION

The definitions of 'big data' concept have evolved rapidly (Gandomi and Haider, 2015). However, most of the studies proposing definitions of big data concur that big data is characterized by high-volume, high-velocity and high-variety of information that requires specific technologies for data capture, storage, distribution and analysis. High-volume implies that big data has very large size ranging from terabytes (10^{12}) to petabytes (10^{15}). High-velocity implies that the rate of creation of data is very high and hence, there is a need for real-time analysis of this data for decision making. High-variety implies that the data is generated by various sources and is available in various formats. Some of the formats are structured or semi-structured like those in databases, sensors and global positioning system (GPS) systems, while others are unstructured like the ones obtained from audio, video and social media.

More recently, other dimensions like veracity and value have also been associated with big data (Gandomi and Haider, 2015; Gupta and George, 2016). Veracity denotes the inherent unreliability

or uncertainty in some of the sources of data as they may be based on human judgement or subjective aspects. Such data are especially present in social media and the Internet in general. The dimension value indicates the possibility of appropriately analysing the big data to make relatively more accurate decisions.

The whole process of extracting useful insights from big data can be divided into two sub-processes, namely, data management and analytics. While data management deals with the techniques used for capturing, storing and retrieval of the big data, analytics deals with the sub-process of analysing and extracting insights from big data using specific techniques (Gandomi and Haider, 2015). Some of the widely used tools for big data analytics fall under the domain of predictive analytics, text analytics, audio analytics, video analytics, and social media analytics.

Big data analytics is being applied in various domains for better understanding of the systems. Transportation economics is a branch of economics that closely interacts with transportation engineering, planning, management, public administration and other related disciplines

6th International Engineering Symposium - IES 2017

March 1-3, 2017, Kumamoto University, Japan

to understand the economic problems of moving goods and people (Small and Verhoef, 2007; Button, 2010). Most of the economic analyses of transportation issues relate either to the micro level where focus is on economic aspects of decisions of individuals and firms or to the meso level where the focus is on transport industries (Button, 2010). Thus, transport economics broadly deals with topics like demand for transport, costs of transport, pricing of transport services, and investments on transport infrastructure (Small and Verhoef, 2007; Button, 2010).

With the widespread use of computer systems and econometric techniques, transport economics has become more quantitative in nature (Button, 2010). Researchers have utilized ordinary least square regression, multinomial logistic regression, panel regression models and other such econometric techniques to analyse issues related to transport economics. These techniques are data-driven and require collection of data on various aspects relevant for transportation. With the advent of big data technologies, there is tremendous scope for big data in solving problems related to transportation economics.

In 2015, the journal *Transportation Research Part C* came out with a special issue dedicated to application of big data analysis to specific problems in transportation. The attempt of the present study is to complement the research papers published in the special issue. Specifically, the present study attempts to explore the scope for using different big data analytics techniques (i.e. predictive analytics, text analytics, audio analytics, video analytics, and social media analytics) in solving some of the issues in transportation economics.

LITERATURE REVIEW

This section gives an overview of studies that have used big data in the context of issues in transportation economics are highlighted. The particular tools that these studies have used and the problems and challenges faced in using big data analytics are also indicated.

One of the important issues in transport economics is estimating the

demand for transport. However, demand for transport is considered to be derived demand (Cole, 2005) since it is based on the movement of goods and people for various other purposes. Thus, if there is an increased need for people to move from one place to another for work or leisure, one may notice increased demand for private and public transport like cars, buses, railways etc. Similarly, if there is an increased need for movement of finished goods or machinery from one place to another, one may notice increased demand for commercial vehicles like truck, train, ship or aircraft. Mismatch in demand and supply of transport (including transport infrastructure) can lead to transport related problems like congestion and low service quality (Rao and Rao, 2002).

According to Dong et al., (2015), real-time data on movement of vehicles and people can be collected through various devices that can be broadly classified into sensor-based technologies (like inductive loop detectors, microwave and laser based radar, magnetometers, and ultrasound detectors), video-based technologies (like traffic cameras and license plate recognition (LPR) systems), radio-frequency-based technologies (like radio frequency identification (RFID) and dedicated short range communications (DSRC)), and location-based technologies (like GPS devices, smart cards, and even call detail records from mobile phones). A raw GPS record may contain a large amount of profile information of the current vehicle state like identification, longitude, latitude, speed, timestamp, and even a flag marking whether the vehicle is occupied (Zhou et al., 2016). Similarly, microwave vehicle detection system (MVDS) can collect data continuously at short interval of time and may contain structured numeric data on different traffic parameters like spot speed, volume, occupancy and simple vehicle classification on each lane (Shi and Abdel-Aty, 2015).

These data have been utilized by researchers to deal with issues related to travel demand, especially in urban scenarios. For example, Shi and Abdel-Aty (2015) have used data generated by MVDS to identify congestion on urban

6th International Engineering Symposium - IES 2017

March 1-3, 2017, Kumamoto University, Japan

expressways in Central Florida. They adopted data mining (random forest) and Bayesian inference techniques for implementing real-time crash prediction models. In another study, Li et al. (2015) used Lasso Granger causality models to screen out most irrelevant data from Caltrans Performance Measurement System (PeMS) data to build parsimonious prediction models. PeMS contains data from sensors on the freeway system across all major metropolitan areas of the State of California. In the study, the authors do mention that their models did not consider nonlinear regression, which can be implemented via kernel trick. Still another study by Toole et al. (2015) used call detail records to estimate origin-destination matrices for traffic. The data collected for five metro regions from three different countries, namely, USA, Portugal and Brazil was analyzed to suggest a travel demand model. However, according to the authors, the algorithm used in their study was simple and did not include relatively high resolution GPS trajectory data of the drivers. Others like An et al. (2016) have also used GPS data to address specific problems related to travel demand like congestion.

Cui et al. (2016) attempted to use the GPS data from taxi services in Harbin, China to identify mismatch between travel demand and transport network services (Cui et al., 2016). However, two of the possibilities for further research as stated by the study were to include information on road conditions and to include GPS data from all types of vehicles.

Interestingly, a recent study by Chen et al. (2016) on human mobility attempts to stimulate future cross-discipline research between transportation researchers who have traditionally been working with small data like household travel surveys and the others (mainly computer scientists and physicists) who are using passively generated big data. According to the study, one of the challenges in modelling travel behaviour is to include in the model the factors that give rise to the observed travel behaviour (like socio-demographics and travel-mode choices).

In the context of supply chain and logistics, RFID and wireless sensor

networks (WSN) technologies are being used independently. According to Mejjaouli and Babiceanu (2015), use of an integrated RFID-sensor network system can help in better transportation of perishable goods.

Quadros et al. (2016) note that vehicular ad hoc networks (VANETs) can be used to improve and ease transportation problems. These networks can send simple, scalar data as well as text messages and multimedia content. However, since the transmission of the multimedia content is through flooding approach, often it can lead to interference of media from different vehicles in the same neighbourhood. This would ultimately reduce the quality of the transmitted audio-video data.

With regards to social media, a survey by Bao et al. (2015) explored the use of location-based social networks in creation of recommender system to facilitate people's travel. One of the challenges in creation of these recommendation systems is to understand the context of location of a user, his/her location history and location histories of others who may give recommendations on social network.

OPPORTUNITIES

Most of the studies that have addressed issues related to transport economics have focused mainly on one specific source of data like RFID or GPS or call detail records from mobile phones. These data are relatively structured and have been analyzed using predictive analytics techniques. Other formats of data like audio, video and social media have been used only to a limited extent. There is a scope for combining data obtained from different sources including multimedia and social media data along with structured data to make more informed decisions.

With social media becoming important source of unstructured data, there is a scope for using inter-disciplinary techniques where transportation researchers can collaborate with computer scientists and social scientists to give meaning to the large amount of unstructured content from social media.

6th International Engineering Symposium - IES 2017

March 1-3, 2017, Kumamoto University, Japan

CHALLENGES

As noted earlier big data may consist of voluminous data of different formats. Hence, the first challenge is to integrate the data of different formats and cleansing the data for the specific purpose of solving problems of transportation economics. The algorithms that are being used in practice are still relatively simple. Another challenge is with regards to the semantic interpretation of social media data. Each individual may have his/her own style of writing/commenting on social media. Finding the relevant information that can help in solving issues of transportation economics is a real challenge.

CONCLUSION

The following conclusions are deduced from this study:

- There is a scope for supplementing data from audio, video and social media with the structured and semi-structured data of devices like GPS and RFIDs for solving the issues in transportation economics.
- There is an impending need for collaboration between transportation researchers, computer scientists and social scientists for analyzing the big data for solving problems of transportation economics.

REFERENCES

- [1] An, S et al. (2016), Mining urban recurrent congestion evolution patterns from GPS-equipped vehicle mobility data, *Information Sciences*, Vol. 373, pp. 515-526.
- [2] Bao, J et al. (2015), Recommendations in location-based social networks: a survey, *Geoinformatica*, Vol. 19, No. 3, pp. 525-565.
- [3] Button, K (2010), *Transport Economics*, Edward Elgar, Cheltenham, UK.
- [4] Chen, C et al. (2016), The promises of big data and small data for travel behavior (aka human mobility) analysis, *Transportation Research Part C*, Vol. 68, pp. 285-299.
- [5] Cole, S (2005), *Applied Transport Economics: Policy, Management & Decision Making*, Third Edition, Kogan Page, London.
- [6] Cui, J X, et al. (2016), Identifying mismatch between urban travel demand and transport network service using GPS data: A case study in the fast growing Chinese city of Harbin, *Neurocomputing*, Vol. 181, pp. 4-18.
- [7] Dong, H et al. (2015), Traffic zone division based on big data from mobile phone base stations, *Transportation Research Part C*, Vol. 58, pp. 278-291.
- [8] Gandomi, A and Haider, M (2015), Beyond the hype: Big data concepts, methods, and analytics, *International Journal of Information Management*, Vol. 35, pp. 137-144.
- [9] Gupta, M and George, J F (2016), Toward the development of a big data analytics capability, Vol. 53, No. 8, pp. 1049-1064.
- [10] Li L et al. (2015), Robust causal dependence mining in big data network and its application to traffic flow predictions, *Transportation Research Part C*, Vol. 58, pp. 292-307.
- [11] Mejjaouli, S and Babiceanu, R F (2015), RFID-wireless sensor networks integration: decision models and optimization of logistics systems operations, *Journal of Manufacturing Systems*, Vol. 35, pp. 234-245.
- [12] Rao, A M and Rao K R (2012), Measuring urban traffic congestion-A review, *International Journal for Traffic and Transport Engineering*, Vol. 2, No. 4, pp. 286-305.
- [13] Shi Q and Abdel-Aty M (2015), Big data applications in real-time traffic operation and safety monitoring and improvement on urban expressways, *Transportation Research Part C*, Vol. 58, pp. 380-394.
- [14] Small, K A and Verhoef, E T (2007), *The Economics of Urban Transportation*, Routledge, London.
- [15] Toole, J L et al. (2015), The path most traveled: Travel demand estimation using big data resources, *Transportation Research Part C*, Vol. 58, pp. 162-177.
- [16] Quadros, C et al. (2016), QoE-driven dissemination of real-time videos over vehicular networks, *Computer Communications*, Vol. 91-92, pp. 133-147.
- [17] Zhou, Z et al. (2016), A method for real-time trajectory monitoring to improve taxi service using GPS big data, *Information & Management*, 53, pp. 964-977.

Face Classification using Convolution Neural Networks

Raghurama*, Gururaja Rao P#, Rajesh Poojary*, Gajendra S Patagara*, B. Neelima*

* NMAM Institute of Technology, Nitte, Udupi, Karnataka, India

#MulticoreWare India Pvt Ltd, Chennai, India

*raghuramraop@gmail.com; #gururajaop@gmail.com; *rajeshpoojary18@gmail.com;
*gajendra.st@gmail.com; *reddy_neelima@yahoo.com

Abstract - This paper proposes a new Convolution Neural Network (CNN) model for training and testing of face classification and compares its performance with existing popular image classification models.

There has been a buzz made by Artificial Neural Networks (ANNs) in the field of Machine Learning (ML) in recent years. One of the major problem domains that attracted many researchers towards these ANNs is, object classification using CNNs. Face classification is one of the classic applications of object classification. However, face classification is not as straightforward as it seems, because it has to deal with different variation of images such as face orientation, illuminating conditions, background cluttering, facial expression etc. to name a few. A Lot of intense computations are used in order to deal with these challenges. These intense computations involved in these CNN layers make it highly expensive job. Since, most of these computations are data parallel in nature, Graphics Processing Unit (GPU) becomes very important tool in high performance computing of these operations.

The proposed model is highly customized for face classification. The proposed work gives a new CNN model for face classification and compares its accuracy and performance with the existing popular classification models such as Alexnet, VGGnet and overfeat. Proposed model takes relatively much lesser time for training and testing while maintaining almost same accuracy.

Keywords — Face Classification, Artificial Neural Networks (ANNs), Convolution Neural Network (CNN), Machine Learning (ML), Graphics Processing Unit (GPU).

I. INTRODUCTION

Machine Learning (ML) is a science of providing computers the ability to learn without being explicitly programmed in order to perform specific tasks or operations. It deals with computer programs that can grow and change themselves when exposed to new data. Artificial Neural Networks (ANNs) is a subset of machine learning and is inspired by neurons and neural networks in the brain. Convolution Neural Network (CNN) or ConvNet, is a type of ANN and is inspired by the structure of visual system and thus deals with image applications. CNN can be used in dealing with problems like face detection, face classification, emotion detection, etc. The close connection and spatial formation

between layers of CNN makes it suitable for image processing and understanding the images.

A CNN has set of layers and each of these layers transform one volume of activations to another using differentiable function [1]. The major layers used in a typical CNN for object classification are convolution layers, pooling layers and fully connected layers, as discussed below:

- **Convolution layer:** This is the most important layer of CNN and has most of the intense computations of the network. It performs dot product of weights and small region of input volume and adds the bias to this result and gives output of the neurons that are connected to the corresponding local regions of the input image [1].

- **Pooling layer:** It is used to reduce the spatial size and the amount of parameters of the network. Typically it performs a down sampling operation along the spatial dimensions of the input volume resulting in reduced input volume for the next layer. Thus it helps in reducing the computation and also avoiding over fitting [1].
- **Fully connected layer:** It has full connection to all activations of previous layer and are used to compute the class scores and hence classification [1].

Another popular layer of CNN is ReLU, that applies activation function to every element of the input volume and mainly used for thresholding. It also helps in reducing the over fitting since it disables some of the neurons in the network depending on the output of previous layer and activation function.

The paper is organized as follows: Section II describes existing classification using CNN. Section III describes the reference model used for face classification to compare with the existing model performance. Section IV describes the input data set used. Section V details the proposed model for face classification. Section VI gives results and analysis and the paper concludes in section VII along with future directions of the work.

II. CLASSIFICATION USING CONVOLUTION NEURAL NETWORKS

This section gives the background details of the different classifications using convolution neural networks.

A. Object classification using CNN

Object classification is one of the fundamental challenges in the field of Computer Vision [2]. The technique of classifying objects detected in the image into different classes is known as object classification. Even though object classification has been the area of interest for many researchers for decades, the accuracy obtained was not up to the mark. Recent approaches for classification of objects using CNN improved the accuracy of classification by a large extent. Also CNN can deal with the low quality images for training and still come up

with good accuracy [3]. Thus, CNNs have become one of the major approaches in object classification.

B. Face classification using Convolution Neural Network

Face classification is one of the popular problems studied by the researchers. But the existing face classification algorithms can only deal with identification of near frontal faces. The CNN is inspired by the robustness of the human visual system in identifying different objects under different circumstances. Fortunately, CNNs can handle face images with various face orientations, different facial expressions and challenging backgrounds accurately and effectively. However, training a CNN involves multiple tasks such as pre-processing, segmentation, feature extraction, etc. for a good performance [4].

C. General classification algorithm of CNN

The general steps of object classification using CNN are as follows:

Step 1: The CNN or ConvNet model consisting of various layers like convolution layers, pooling layers and fully connected layers are initialized using either pre-trained checkpoints or random numbers. These layers will have weights and biases that get tuned during the training phase.

Step 2: The CNN is trained using a batch of labelled input images from the training data set. The weights and biases of the network update during backward propagation and thus the network learns. In the training phase a forward propagation followed by backward propagation is run, where the network evaluates its result using the labels in forward propagation and updates its weights and biases in the backward propagation based on the results of the forward propagation.

Step 3: Step 2 is repeated till all the images in the training data set is used.

Step 4: For each epoch (one round of training the neural network, using the forward-backward propagation algorithm with all the input images in training data set) validation, a forward propagation algorithm, is used to validate the accuracy of the network for that epoch.

Step 5: Step 2-4 are repeated till the network achieves desired or maximum accuracy.

Step 6: Once after training the ConvNet model, a forward propagation algorithm is used with entirely new set of test data to check the correctness or accuracy of the trained network.

This helps in identifying the actual accuracy of the model in practical applications. It also helps in identifying if over fitting is achieved by the model by any chance.

III. REFERENCE MODELS USED FOR FACE CLASSIFICATION

This section gives the brief idea of the popular imangenet classification models used as reference models in the proposed work. These ConvNet models are used for classification of millions of images over thousands of classes. Three of the most popular models from imangenet are used in proposed work, namely alexnet, vgg and overfeat.

A. Alex net

Alexnet consists of five convolution layers, three pooling layers and one fully connected layer. In fully connected layer, it has three non-linear rectification layers and logsoftmax loss layer for the score computation. It uses ReLU as activation function and dropout of 0.5 for regularization [5].

B. VGG Net

VGG net can have a stack of Convolution Layers followed by three fully connected layers. First two fully connected layers have 4096 channels each and the last fully connected layer consists of "n" channels where n is the number of classes that are to be classified. Activation function used in VGG net is ReLu. VGG net incorporates three non-linear rectification layers instead of a single layer, which makes the decision function more discriminative [6].

C. Overfeat

Overfeat uses multi-scale and sliding window concept efficiently inside the Convolution Neural Network. Similar to alexnet model, overfeat has five convolution layers, three pooling layers and one fully connected layer. Overfeat too has ReLU activation function and uses dropout for regularization [7]. The main difference between alexnet and overfeat is that they use different hyper parameters. For example they differ in sizes of layers, splitting and concatenation of activation maps and way of wiring up, etc [8].

IV. INPUT DATA SET

Data set used in proposed face classification experiment consists of images randomly chosen

from internet. Each of these coloured images either has a face or background so that they can be classified into either face or no-face. In order to check accuracy at different level, they are divided into three categories namely Training, Testing and Validation. All of these categories contain images from the classes face and no-face and sub-categorized accordingly.

All the images used in the dataset are resized to 256x256x3 (256x256 image size and 3 RGB colour channels) using bi-linear image scaling algorithm in order to achieve least data loading and adjusting time. Finally, each of these images is cropped randomly to 224x224x3 just before feeding them as input to the network.

V. PROPOSED MODEL FOR FACE CLASSIFICATION

This section explains the proposed model used in this paper. As mentioned previously, the proposed model is customized for face classification. After comparing with various reference models, it is found that for a two class classification like face classification that has only two classes such as face and no face can use less number of convolution layers. Further, same accuracy can be achieved by using relatively less deep ConvNet with tuned hyper parameters. Since convolution layer is the most expensive layer of the CNNs, by reducing the number of convolution layers used in the network with appropriate changes in hyper parameters, same accuracy can be achieved in relatively less time.

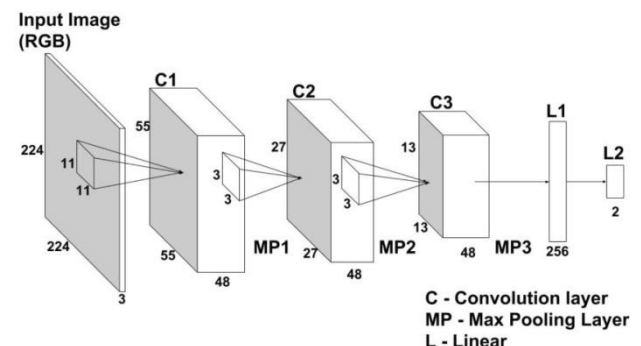


Fig. 1 An illustration of the architecture of the proposed model

Figure 1 shows the pictorial summary of the proposed model. It contains five learning layers, three convolution and two fully-connected. The complete convolve layer comprises of three spatial convolution layers, three maximum pooling layers

along with ReLU activation function. The proposed model uses ReLU since it runs faster on large data sets compared to traditional activation functions like tanh or sigmoid. ReLU also helps in reducing the chances of over fitting, since it disables neurons with negative inputs. Fully connected layer consists of non-linear layers, regularization layer and loss functions. There are two non-linear rectification layers in the proposed model which is used to improve the class scores. Also, dropout layer with probability of 0.5 is used for regularization that helps in avoiding over fitting of the model. At the end of the fully connected layer, logsoftmax loss function used. The output of the last fully-connected layer is fed to this logsoftmax layer and it produces the distribution of scores over the two class labels, face and no-face.

The first convolution layer filters 224x224x3 input image with 48 filters or kernels of size 11x11x3 with a stride of 4 pixels. The output of this layer is normalized and pooled using ReLU and max pooling and fed as input to next convolution layer. Second convolution layer filters this input using 48 filters of size 3x3x48 with a stride of 1 pixel. Again the output of this layer is regularized and pooled, and fed as input to succeeding convolution layer. The third convolution layer filters this input using 48 filters of size 3x3x48 with a stride of 1 pixel. Output of this layer is given as input to the fully-connected layer which contains two nonlinear layers with 256 and 2 neurons in order, along with other layers. Finally, the output of the fully-connected layer is given to a two-way logsoftmax which produces the scores over the two classes.

In the proposed experiment, a Learning Rate (LR, hyper parameter for the magnitude of change in the network during the backward propagation or rate of leaning of the network) of 0.01 to 0.0001 is used. Also, momentum (hyper parameter used to balance the oscillation in update) of 0.9 and weight decay (hyper parameter that decays the weights to zero if there is no update) of 0.0005 is used.

Torch-7 framework is used for all the layer implementations of the CNN model as their forward-backward algorithms can use GPUs for parallel computation.

VI. RESULTS AND ANALYSIS

This Section gives the details of experimental set-up along with the results and analysis of the results.

A. Experimental setup

All the experiments are done in the same system, having system configuration as follows: Ubuntu 16.04 Operating System, 4 GB RAM. The GPU used is Nvidia GeForce GTX Titan X with compute capability 5.2 and cuda 7.5. All our training, validation and testing are run on GPU. Torch 7 machine learning framework is used for the training and testing, as it has inbuilt functions that can run the computations of training and testing in GPUs using CUDA. Each model is trained for twelve epochs and corresponding train and test accuracy are calculated.

B. Results and analysis

After training all the models for twelve epochs, they achieve a training accuracy of 95% - 96% and testing accuracy of 88% - 90%. Table 1 shows the accuracy of various models after training for twelve epochs. Clearly, the proposed model achieves almost same accuracy of reference imangenet winners.

Table 1: Train, validation and test accuracy after twelve epochs of training for face classification

Model	Train Accuracy (%)	Validation Accuracy (%)	Test accuracy (%)
Alex net	96.79	96.28	90.04
Overfeat	96.36	94.89	90.90
VGG	96.06	95.49	88.21
Proposed Model	95.23	95.04	89.55

The biggest challenge of training any CNN is not meeting over fitting. Over fitting is a phenomenon where the model gets over tuned for the training dataset and thus resulting in very high training accuracy and low testing accuracy. Based on the accuracy values of all models from Table 1, it is clear that over fitting was not met in any of the models.

Figure 2 shows the gradual improvement in the accuracy of various models over the epochs during training phase. It is obtained by plotting epochs along X-axis and train accuracy for each epoch along Y-axis. Clearly, after 8-10 epochs the increase in the accuracy of the models is almost negligible. All of the models achieve 95% to 96% at the end of the training phase.

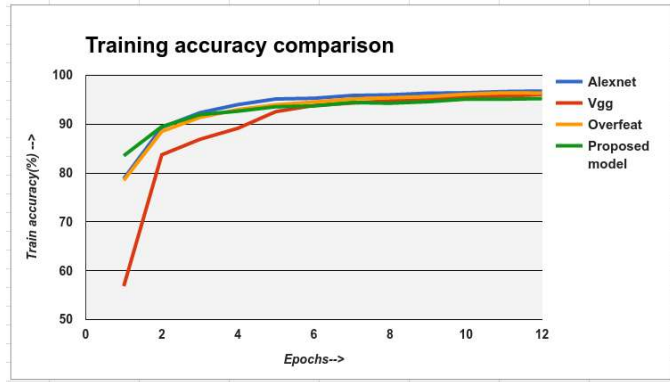


Fig. 2 Training accuracy achieved by the models for the first twelve epochs of training phase

The proposed model was mainly used to reduce the training and testing time while maintaining the accuracy similar to reference models. Figure 3 shows the average time taken for training, validation and testing phase per epoch by each model. Clearly the proposed model takes the least time while maintaining the accuracy almost same as standard reference models. Proposed model takes ~600s, ~200s & ~300s for the training, validation and testing phase respectively.

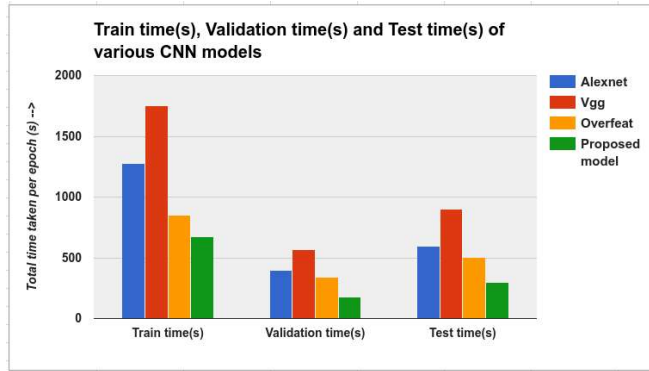


Fig. 3 : Total time taken for training, validation and testing per epoch by various models

The input image for the forward and backward propagation algorithm of all the models is of

size 224x224. The average time taken by each image for both forward and backward propagation is shown in Figure 4. Clearly, the proposed model takes the least time of all the models tested. VGG model takes the maximum time of ~15s for both forward and backward propagation, whereas proposed model takes ~5s and ~7s for forward and backward propagation respectively.

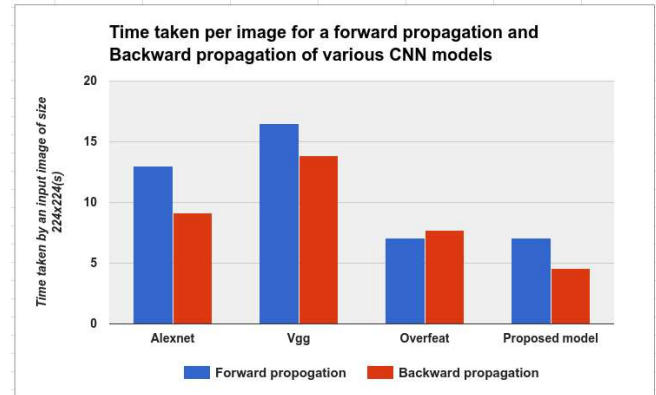


Fig. 4 Average time taken by an input image of size 224x224 for forward and backward propagation

Figure 5 shows the speedup of forward and backward propagation phase of proposed model per input image with respect to the reference models. The proposed model gives speedup of 1.84x, 2.33x and 1x during the training phase with respect to reference models alexnet, vgg and overfeat respectively. Similarly, it gives speedup of 2x, 3.03x and 1.7x in the testing phase with respect to reference models alexnet, vgg and overfeat respectively.

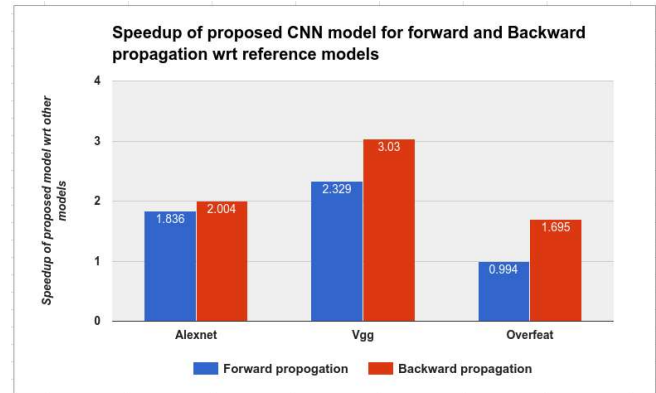


Fig. 5 Speedup of forward and backward propagation phases of proposed model against reference models

Thus, the results show that the proposed model achieves same accuracy while taking much lesser time for training and testing.

VII. CONCLUSIONS

In this paper, a simple CNN model for face classification is provided and its accuracy is compared with various CNN classification winner models. Also, the model is designed to achieve higher speedup compared to the existing standard classification models. All the models are tested for accuracy using same set of training, validation and testing data set in the same platform. In every model, coloured image of 256x256 is used as input to the application and cropped image of 224x224 is provided to the forward and backward propagation of the model. Torch 7 framework is used for the design and training of all the models.

The proposed model achieves accuracy of ~95% training accuracy and ~89% testing accuracy for face classification, which is almost same as accuracies of the existing imangenet winner models. Also, the proposed model gives 1x to 2.4x speedup in forward propagation and 1.7x to 3x in backward propagation with respect to reference models.

The following future works are planned for the proposed work.

- The proposed model can be tested and compared for the accuracy after training for 50 to 100 epochs. A better accuracy is expected by the models when trained for more epochs.
- The proposed model's hyper parameters can be tuned further to achieve better accuracy while maintaining less training and testing time.
- The proposed model can be modified to achieve multi-GPU usage and thus enhancing the speedup.
- The CNN layers used in the proposed model can be optimized further to achieve higher speed up and better accuracy.
- The proposed model can be tuned to detect multiple objects in single image.

ACKNOWLEDGEMENT

The basic classification code for various imangenet winning models is taken from Soumith's "Training and object classifier in torch-7 on multiple GPUs over imangenet" [9]. This application is used for training the classifier over imangenet data consisting of millions of data from thousands of classes, using multiple GPUs in torch-7 framework. This classification code is modified to support all the experiments described in the paper. Hence, we thank Soumith for the open source classification code. Further, we thank Nvidia for the GPU hardware donation under university relations program.

REFERENCES

- [1] <http://cs231n.github.io/convolutional-networks>, *CS231n: Convolution Neural Networks for Visual Recognition*, an online course on CNN by Stanford
- [2] Ross Girshik, Jeff Donahue, Trevor Darrell and Jitendra Malik, "Region-based Convolutional networks for Accurate Object Detection and Segmentation", IEEE Transactions on Pattern Analysis and Machine Intelligence, 38(1):142-58 Jan 2016
- [3] Hao Jiang and Shiquan Wang, "Object Detection and Counting with Low Quality Videos", Report 287 - 2016 of *CS231n: Convolution Neural Networks for Visual Recognition*, a course of stanford university
- [4] A.R.Syafeeza, M.Khalil-Hani, S.S.Liew, R.Bakhteri, "Convolutional Neural Network for Face Recognition with Pose and Illumination Variation", International Journal of Engineering and Technology, 6(1):44-57 Jan 2014
- [5] Alex Krizhevsky, Ilay Sutskever and Geoffrey E.Hinton, "ImageNet Classification with Deep Convolutional Neural Networks", Advances in Neural Information Processing Systems 25, proceedings from the conference "Neural Information Processing Systems 2012"
- [6] Karen Simonyan and Andrew Zisserman , "Very Deep Convolutional Network for Large-Scale Image Recognition", arXiv technical report 2014, arXiv:1409-1556
- [7] Pierre Sermanet, David Eigen, Xiang Zhang, Michel Mathieu, Rob Fergus and Yann LeCun, "Overfeat: Integrated Recognition, Localization and Detection Using Convolutional Network", arXiv technical report 2014, arXiv:1312-6229
- [8] Subrath Kumar Rath, Siddharth Swarup Rautaray, "A Survey on Face Detection and Recognition Techniques in Different Application Domain", International Journal of Modern Education and Computer Science, PP.34-44, Aug 2014, DOI: 10.5815/ijmecs.2014.08.05
- [9] <https://github.com/soumith/imagenet-multiGPU.torch>, opensource git repository on "Training and object classifier in torch-7 on multiple GPUs over imangenet" by Soumith Chintala

Gesture Based Home Automation Using Internet-of-Things

Srinivasan.C.K¹, Subhin Antony² and Sreekantha.D.K³

- 1 Department of Electronics and Communication Engineering, NMAM Institute of Technology, Nitte, Udupi, Karnataka, 574 110, India. e-mail: cksri260@gmail.com
 - 2 Department of Electronics and Communication Engineering, NMAM Institute of Technology, Nitte, Udupi, Karnataka, 574 110, India. E-mail:
 - 3 Department of Computer Science and Engineering, NMAM Institute of Technology, Nitte, Udupi, Karnataka, 574 110, India. Email:
-

ABSTRACT: Gesture based home automation system is gaining more importance now a days. Most of the electronic appliance focuses on the hand gesture recognition and the corresponding user interface. Our project consists of a Micro Electro Mechanical System (MEMS), an accelerometer which is mostly based on hand gesture recognition algorithm which is used to control the electronic appliances. The accelerometer is used to sense the acceleration of hand motion in the three perpendicular directions that is x, y, z and the signal is transmitted to a wireless protocol using Radio Frequency (RF). The RF signal transmission has a frequency of 2.25 GHz. The predefined gesture motion codes are stored in the microcontroller at the receiving end. Thus the hand gestures made by a person is recognised and compared with the templates stored in the receiver. If these are matched to the predefined templates, then accordingly the home appliances are controlled. This project serves the most possible solution to control the appliances for physically challenged people.

Keywords: Micro Electro Mechanical System (MEMS), Radio Frequency (RF)

INTRODUCTION

The use of hand gestures provides an attractive alternative way to interface devices for human-computer interaction. The aim behind the project is to be able to sense the movement of a user's hand and to recognize the gestures using a gesture recognition algorithm. Gestures can be recognized by using sensors, camera, accelerometer etc. Hand gesture -based gesture recognition performs matching in time domain. The detected and recognized hand gestures are used as the command signals for controlling devices, some user interfaces. Hand Gesture Based Remote or a glove is a device to replace all other remotes used in households and perform all their functions. Normally in homes, remotes are used for appliances like TV, CD player, Air Conditioner, DVD Player and Music System. But these remotes or gloves

can also used for turning the lights ON/OFF, Door Opener etc

A simple Micro Electro Mechanical System (MEMS), an accelerometer is utilized to get dynamic / static profile of movement of the user's hand. It gives the acceleration sensed by the device in each of the 3 axis. An Arduino UNO board is used for serial communication of this accelerometer data. Based on values from the accelerometer, hand movements are detected and classified into previously trained/predefined gestures.

In a smart environment, people usually hope to use the most natural and convenient ways to switch on the appliances or Button pressing, often used in the remote control panel, provides the most traditional means of giving commands to household appliances. Such kind of operation, however, is not natural and sometimes even inconvenient,

6th International Engineering Symposium - IES 2017

March 1-3, 2017, Kumamoto University, Japan

especially for elders or visually disabled people who are not able to distinguish the buttons on the device. In this regard, gesture-based interaction offers an alternative way in a smart environment. Most of previous work on gesture recognition has been based on computer vision techniques. However, the performance of such vision-based approaches depends strongly on the lighting condition and camera facing angles, which greatly restricts its applications in the smart environments. Suppose we are enjoying movies in our home theatre with all the lights on. If we intend to change the volume of TV with gesture, it turns out to be rather difficult to accurately recognize the gesture under poor lighting condition using a camera based system. In addition, it is also uncomfortable and inconvenient if we are always required to face the camera directly to complete a gesture.

Gesture recognition from accelerometer data is an emerging technique for gesture based interaction. With the rapid development of the MEMS (Micro Electro-Mechanical System) technology, people can wear/carry one or more accelerometer-equipped devices in daily life, for example, Apple iPhone, Android phones, Nintendo Wiimote. These wireless-enabled mobile/wearable devices provide new possibilities for interacting with a wide range of applications, such as home appliances, mixed reality, etc. The first step of accelerometer based gesture recognition system is to get the time series of a gesture motion. Now most accelerometers can capture three-axis acceleration data, i.e. 3D accelerometers, which convey more motion information than 2D accelerometers. They have been embedded into several commercial products such as iPhone and Wiimote.

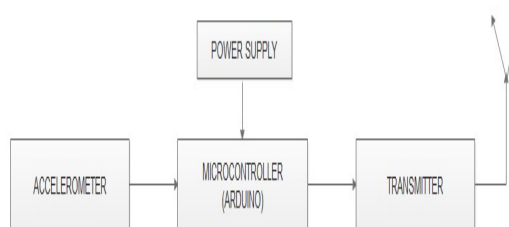
DESIGN OF THE SYSTEM AND WORKING

The accelerometer based home automation system is designed for physically challenged people. The system

comprises accelerometer, microcontroller, RF transmitter and receiver and the communication is through RF signals, the communication can also be done using a Bluetooth module. The accelerometer senses the hand gestures and signals are transmitted to receiver section through RF transmitter. RF receiver receives the transmitted signal compares with the already stored gestures, only when the similar hand gestures are identified, then the home appliances are controlled.

The Transmission section

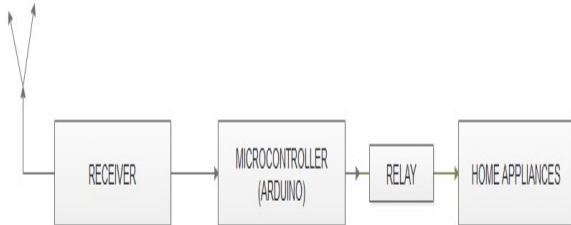
The hand gestures are sensed using the accelerometers placed in the gloves to be worn by the person. The sensed signals are given to the microcontroller that is powered by 5V. The signals from the microcontroller are given to the RF transmitter. The RF transmitter operates at a frequency of 434 MHz, transmits the signal to the RF receiver.



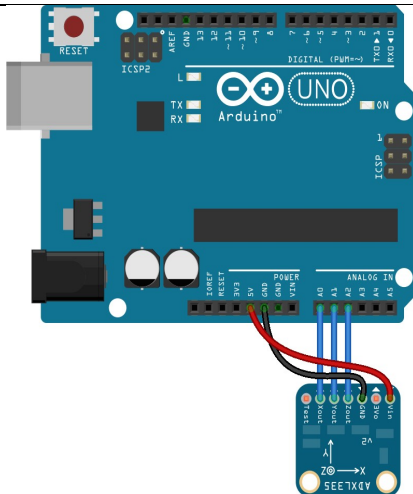
Block diagram of the transmitter.

The receiving section

The transmitted data is received by an RF receiver operating at the same frequency as that of the transmitter. The received signals are then given to the microcontroller that compares the received and stored hand gestures, and then the signals are given to the relay and thus accordingly the home appliances are controlled.



Block diagram of the receiving section.



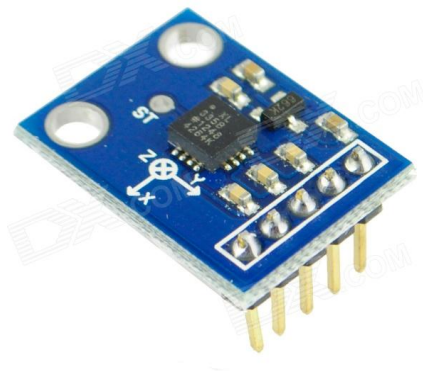
Accelerometer connect to the Microcontroller (Arduino)

WORKING:

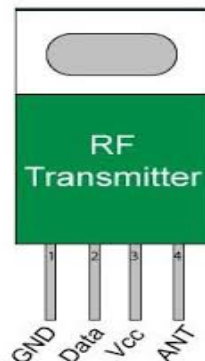
1) Accelerometer: The accelerometer shown in fig. is a micro-electromechanical system basically used to measure the static and dynamic force of acceleration. The accelerometer sensors are used for interaction with home appliance using recognized hand gestures. Gestures made are up, down, left, right. It basically operates in tri-axial mode.

2) RF Transmitter:

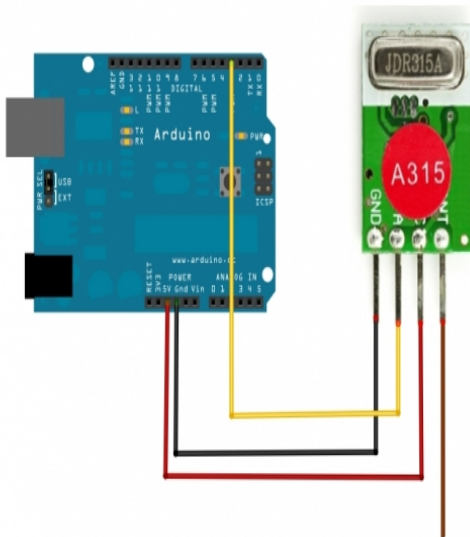
In fig. The RF transmitter shown operates at a frequency of 434 MHz. An RF transmitter receives serial data from controller and transmits it wirelessly through RF antenna. The transmission occurs at the rate of 1Kbps - 10Kbps.



Accelerometer ADXL 335



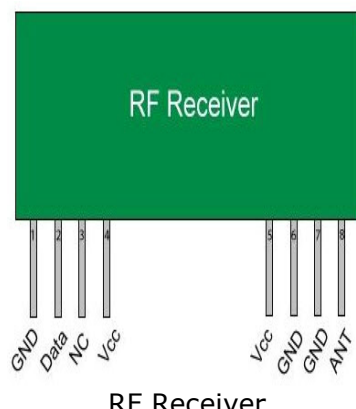
RF Transmitter



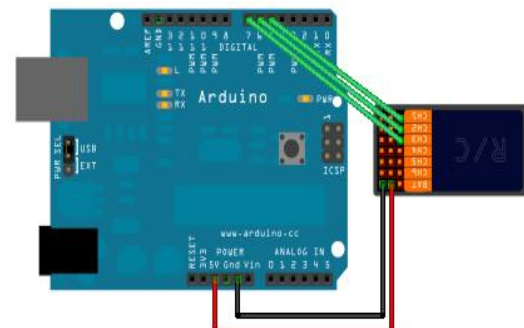
RF receiver connection to the Microcontroller (Arduino)

3) RF Receiver:

The wireless RF receiver in fig. receives the data with an operating frequency of 434MHz, same as that of the transmitter. The RF receiver works well with microcontroller to create a simple wireless data link. The received radio frequencies are sent to the microcontroller.



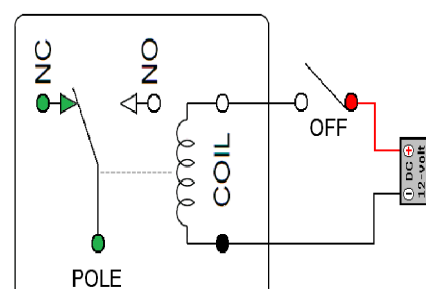
RF Receiver



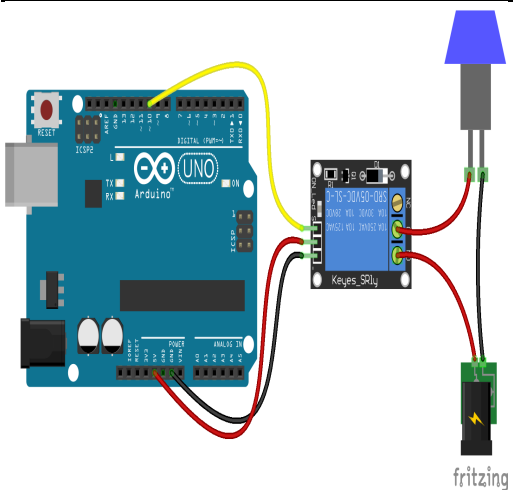
RF transmitter connection to the Microcontroller (Arduino)

4) Relay:

A relay is an electromechanical device that is triggered by an electrical current shown in fig. The current flowing in one circuit can switch ON and OFF a current in another circuit. Relays are employed in this device to switch ON and OFF the home appliances.

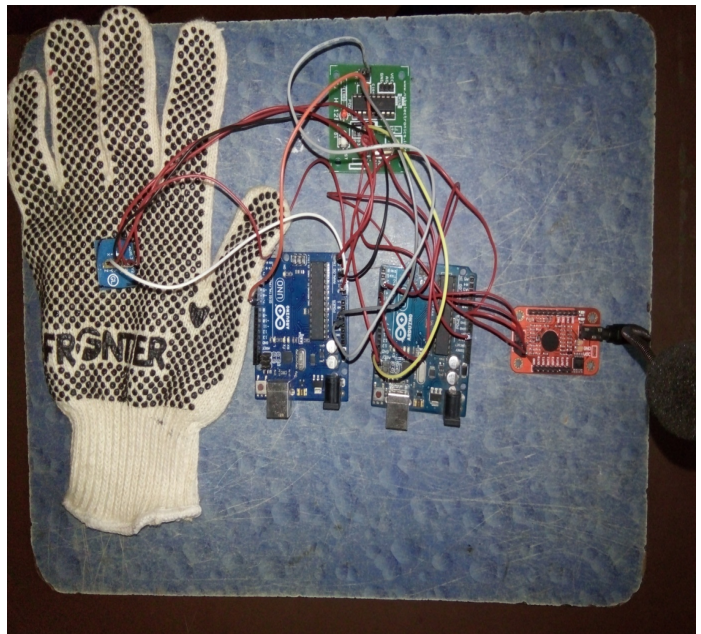


Relay



Relay connection to the Microcontroller.

cost. The device helps the aged persons too.



Advantages and Applications:

Advantages:

- It consumes low power.
- It is user friendly.
- Low cost.
- It requires small space.
- Device can be controlled more comfortably.

Applications:

- It can be used by patient suffering from Paralysis.
- It can be used to control various home appliances.
- It can be used in home theatre system where short distance communication is required.
- Suitable for physically challenged people to operate the devices within room.

CONCLUSIONS

The objective of this project is to develop such a system which will help physically impaired to control home appliances by hand gestures using accelerometer. This provides comfort and convenience for common as well, for physically impaired. The stored gesture in the receiver section is compared with the hand gestures. The stored template then matches with the received inputs. The project now done is used to control the opening and closing of the door. In future more home appliances can be controlled by incorporating those devices with newer versions of gestures, also implemented in every home at low

The above picture depicts the circuit for the sensor (accelerometer) based remotely controlled home automation, which mainly includes the vital components like microcontroller (Arduino) that encodes and decodes the signal sent through the accelerometer and relay that enhances switching ON and OFF of the electrical appliances.

REFERENCES

- [1] HAND GESTURE BASED HOME AUTOMATION FOR VISUALLY CHALLENGED, Smitha.M, T. Ayesha Rumana, Sutha.P
- [2] AUTOMATIC HAND GESTURE BASED REMOTE CONTROL FOR HOME APPLIANCES Mrs. Rupali Deshmukh1, Abhishek Bange2, Akshay Nerkar3, Sandip Mane4
- [3] Automatic Hand Gesture Based Remote Control for Home Appliances Apoorva Bharambe1 , Divya Chanekar2 , Divya Naik3 , Prof. A. B. Vitekar4
- [4] Gesture-controlled user interfaces, what have we done and what's next? Moniruzzaman Bhuiyan and Rich Picking
- [5]<http://a4academics.com/final-year-be-project/12-be-ece-electronics-and-communication-project/511-gesture-recognition-using-accelerometer>
- [6]<https://wiki.analog.com/university/contest/design/submissions/avengers>

Trust Aware Secure Service-Composition in Cloud Environment

Usha Divakarla¹ and K.Chandrasekaran²

- ¹ Department of Computer Science and Engineering, National Institute of Technology Karnataka, Surathkal, Mangalore 575025, India. email:ushachavali@gmail.com
² Department of Computer Science and Engineering, National Institute of Technology Karnataka, Surathkal, Mangalore 575025, India. email:kchnitk@gmail.com
-

ABSTRACT: Cloud Computing is the most important aspect in academics and industry. Generally business process are comprised and implemented in the distributed environment. Cloud based business processes are implemented as the composite service and these services are connected by different workflow patterns. On the other hand, trust was initially used in security or authentication process. From the past research it is known that trust can be successfully used in composition of web services. In the context of cloud computing, there are several research works that used trust for cloud service composition. Trust plays an important role in service selection. Selecting the trust worthy service for service configuration with various attributes like cost, time and other constraints is a tedious task. In this paper, Trust based Cloud service selection framework for service composition is proposed. The proposed model calculates a trust value which allows the user to select service provider based on the calculated trust values.

Keywords: Trust, service composition, cloud environment, dynamic trust, migration trust

INTRODUCTION

Cloud Computing (CC) has emerged as an important research area attracting much attention from the research and industry. Cloud Services are available across the world in a loosely coupled distributed environment. Consumer is able to select the services based on the Quality of Service and their requirements as represented by M.P.Papazoglou,P.Traverso,S.Dustdar,Leymann (2008). As cloud service is an online service and pay and use service, consumer needs trust worthy services from the provider. When there is a functionally similar set of services, consumer should have the choice to choose the best service based on the trust value of the service. But maintaining a trust worthy services is a challenge L.H. Vu, Hauswirth, M., Aberer, K (2005). Trust is the probability by which a

person expects that other person performs a required task perfectly. Trust management is a serious issue in CC environments. In business world, every process consists of numerous services and each service may need to invoke another service to form the composite service. To satisfy any specific requirement, a service may have to invoke other services forming composite Web services which needs trust dependencies between services and service provider D.A. Menasc'e (2004). Though the trust dependencies enhance service provision, they at some time equally increase computation complexity which makes trust based service selection more complex.

6th International Engineering Symposium - IES 2017

March 1-3, 2017, Kumamoto University, Japan

LITERATURE SURVEY

L. Li, Y. Wang, E. P. Lim.(2009), L. Li, Y. Wang, E. P. Lim.(2010) proposed service invocation graph and service invocation matrix for composite service representation. He proposed trust based service selection and discovery algorithm based on Monte Carlo method.

L. Li, Y. Wang, E. P. Lim.(2010) proposed trust based mediator framework which uses trust metrics like whitewashing, cold start and trust bootstrapping methods.

Z. Chen, L. Ge, H. Wang, X. Huang, J. Lin (2006) proposed trust model based on trust behavior which used trust gravitation method to analyze the trust relationship between pervasive entities.

Diana, B. Harun, R. Roland, Z. Michael and G. Kurt (2009) proposed multi objective based heuristic algorithm for the selection of services in service orchestrations. The OPTIM_HWeight algorithm is based on weight factors and the OPTIM_PRO algorithm is based on priority factors for performing the service selection.

R. Wang, Chi-Hung Chi, Jianming Deng (2009) proposed the fast heuristic algorithm for Service Selection where the utility function is described to reflect the QoS parameters of the service selection model. to solve the MMKP.

T. Yu, Y. Zhang, K. A. Lin (2007) proposed WS-HEU algorithm for web service selection for composite web service which is intended to find solutions for MMKP. But the search time taken by the algorithm is more.

Milanovic, N. and Malek, M (2004) proposed four necessary requirements for service composition namely connectivity, nonfunctional qualities, correctness, and scalability. But these service requirement qualities are not extendable.

Menasc'e, D. A (2004) studies show how qualities of service are aggregated in different service composition scenarios. The

approach requires knowing the invocation probabilities of the services. But this information is not always available due to the provider's non interest in revealing information and also due to non-trivial invocation probabilities.

Wu, G., Wei, J., Qiao, X., and Li, L, (2007) developed a model for consumer's assessment of a service's quality using Bayes network, where the root represents the capability of a service and a child represents the capability of quality of the service. This approach enables consumers to estimate the overall quality assessment.

Lin, W.-L., Lo, C.-C., Chao, K.-M., and Younas, M (2008) proposed to select services according to the consensus of group preference based on various qualities. Consumers express their preferences among the values of the qualities in fuzzy terms. Author used fuzzy logic to resolve the conflicts between the subjective interpretations of service qualities of each consumer. Then they aggregate different fuzzy views from both consumers and providers to reach a consensus of the preferred order of quality metrics.

Yue, K., Liu, W., and Li, W (2007) approach constructs web service Bayesian networks (WSBN) based on the invocations between the services. However, this approach fails to consider the dynamism of service composition because the relationships are fixed.

Liu, W (2005) views a service-oriented environment as an ecosystem and distinguishes three levels: (1) trust: atomic service (service selection), (2) composition: composite service (service composition), and (3) emergent behavior: network economy (organizational behaviors, consumer communities, business alliances, and trusted third parties). At the trust level, author suggests that an ideal trust representation be flexible and adaptive to diversified needs of agents and exchangeable so agents can help each other. Author adopts XML Topic Maps for knowledge representation.

Paradesi, S., Doshi, P., and Swaika, S (2009) built trust based framework for web service compositions. They adopted the trust representation from Wang, Y. and Singh, M. P (2010) and introduced operators for combining trust in different types of service compositions including sequence, concurrent, conditional, and loops.

Maximilien, E. M. and Singh, M. P (2004) developed a trust-aware approach to select services based on a well-defined ontology that provides a basis for describing consumers' requirements and providers' advertisements. The ontology enables consumers to define nonfunctional properties.

Wang, Y. and Singh, M. P (2010) developed a trust model for multi agent systems that formalizes how agents map evidence to trust and vice versa.

PROPOSED TRUST MODEL

Trust based Cloud Service Composition (TCSCF) is a framework used to select the services for service composition and it is shown in Figure 1. It selects trust worthy service for composition. Trust plays a vital role in this composite service selection model. Cloud provides on-demand service. Service consumers need the trust worthy service for interaction. This framework enables the user to select trustworthy services for composition. Trust is calculated of the candidate services for composite Service.

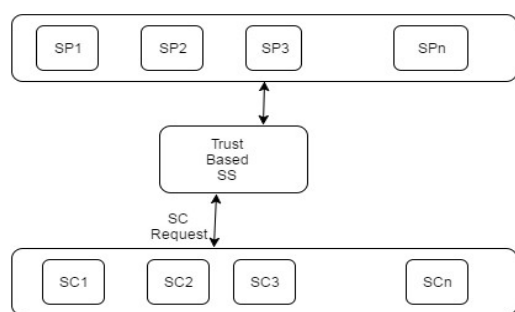


Figure-1. Trust based Cloud Service Composition

Trust value of the service is estimated in 2 methods such as dynamic trust and trust value for migration. Dynamic trust value is estimated by using the initial trust and the number of successful transactions made by the consumer on the services requested by him.

Dynamic Trust is calculated as:

The initial trust of the user is stored in a space called Effective Trust Storage. This initial trust is retrieved and the final dynamic trust is calculated which is based on the number of successful transactions performed by the consumer for a given service as below:

Initial Trust i_t is calculated as:

$$i_t = C_{it} * R_{it} \quad (1)$$

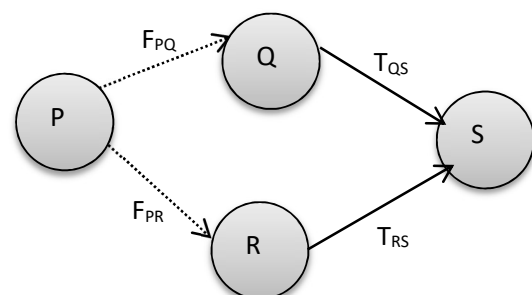
Where R_{it} is initial resource trust value
 C_{it} is initial consumer trust value.

Now based on the initial trust and number of successful transactions of the user, the dynamic trust is calculated as:

$$D_t = i_t + \sum_{i=0}^{i=n} t_i / \text{total No. of transactions} \quad (2)$$

Where t_i is No. of successful transactions and D_t must always be greater than the initial trust value as i_t is the initial trust required to perform any transaction. If D_t is greater, then the consumer can be allotted the requested new service.

Proof of Concept: Let us assume a multiple network as shown below. Here the node P can have trust on node S as T_{PS} in two paths P-Q-S or P-R-S.



6th International Engineering Symposium - IES 2017

March 1-3, 2017, Kumamoto University, Japan

Let $F_{PQ} = T\{P:Q, \text{ on feedback}\}$ and $F_{PR} = T\{P:R, \text{ on feedback}\}$. Using the maximal ratio combining theorem we get:

$$T\{P:S, \text{ Usage}\} = \omega_1 (F_{PQ} * T_{QS}) + \omega_2 (F_{PR} * T_{RS}) \quad (3)$$

$$\text{Where } \omega_1 = F_{PQ}/(F_{PQ} + F_{PR})$$

$$\omega_2 = F_{PR}/(F_{PQ} + F_{PR})$$

From (3) it is understood that if any feedback tends to zero the trust also tends to initial trust. Hence if the feedback trust of service is zero the trust value equals to the initial trust of the service.

Trust Value for Migration is calculated as:

The new trust value calculated for the customer on resources is stored in central table which can be retrieved by all Cloud Service providers (CSP).

When a customer wants to migrate to a different service provider the initial trust of the customer with the new CSP is calculated as :

$$M_t = (i_t + D_t)/0.5 \quad (4)$$

Where $0 < M_t$ for availability

$M_t < 0$ for non-availability is the ideal case meaning that the requested service is not available.

it is initial trust by (1)

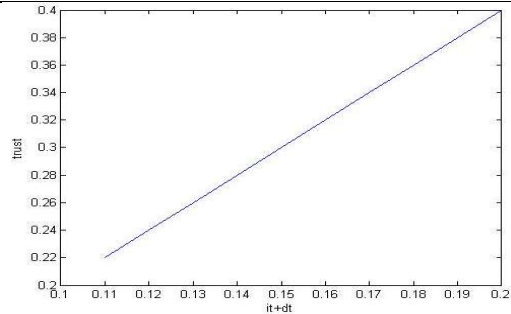
D_t is the dynamic trust by (2)

0.5 is the minimum trust required by any entity for a successful transaction on requested service.

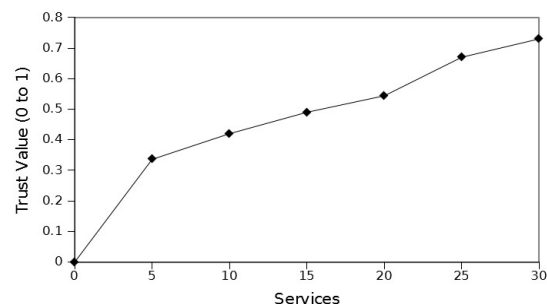
RESULTS AND ANALYSIS

We conducted our experiment with three cloud platforms namely: Aneka, Opennebula and Eucalyptus and virtualization software VMware.

From the figure below it is noted that as the dynamic trust increases the trust value of the service also increases. Assuming that the initial trust and dynamic trust value starts from 0.1 as it's the minimal trust required to request for any services, we see that trust values increase with every increase in initial and dynamic trust.



We created 12 VM's(Virtual Machine) altogether and formed a temporary multi cloud environment. Each VM could accommodate a minimum of 5 service requests with a minimum of 5 users operating at the same instance. We found that as the number of successful transactions increases the dynamic trust value increased which in turn also increased the migration trust value.



The above figure shows the increase in trust value as the number of requested services increase for successful transactions. Here 30 services were considered where the resources were utilized for successful completion of the transactions.

Our experiment concluded that if the resources are utilized for the successful completion of transaction then the trust on services provided by the service provider increases.

6th International Engineering Symposium - IES 2017

March 1-3, 2017, Kumamoto University, Japan

CONCLUSION

Services are the back-bone of any service provider. If the service provided is of utmost satisfaction the trust on the service provider increases. But the basic trust of services is of major concern as the data involved in the transaction is crucial. So a trust value for the services provided by the service provider increases the trust of the customer on the services.

Our experiments concluded that as the number of services with successful complete transactions increases the trust value of the specific service also increases.

Our future work involves evaluation of trust of the resources of the service providers without involving migration.

REFERENCES

- [1] Josang, R. Ismail, C. Boyd,(2007). A survey of trust and reputation systems for online service provision. *Decision Support Systems*, vol. 43, no. 2, pp.618-644.
- [2] Diana, B. Harun, R. Roland, Z. Michael and G. Kurt (2009).Heuristic Approaches for QoS based Service Selection. Springer LNCS, pp.441-455.
- [3] D.A. Menasc'e (2004), Composing web services: A QoS view. *IEEE Internet Computing*, vol.8, no. 6, pp.88-90.
- [4] L. Li, Y. Wang, E. P. Lim.(2009),Trust oriented Composite service selection and discovery. ICSOC Service Wave 2009, LNCS 5900, pp. 50-67.
- [5] L. Li, Y. Wang, E. P. Lim.(2010),Trust oriented Composite service selection with QoS constraints. *Journal of Universal Computer Science*, vol. 16, no. 13, pp. 1720-1744.
- [6] L.H. Vu, Hauswirth, M., Aberer, K (2005),QoS-based service selection and ranking with trust and reputation management. Springer LNCS, vol. 3760, pp. 466-483.
- [7] Lin, W.-L., Lo, C.-C., Chao, K.-M., and Younas, M (2008),Consumer-centric QoS-aware selection of web services. *Journal of Computer and System Sciences* 74, 2, 211-231.
- [8] Liu, W (2005),Trustworthy service selection and composition—reducing the entropy of service oriented web. In Proceedings of the 3rd IEEE International Conference on Industrial Informatics (INDIN). IEEE Computer Society, Los Alamitos, CA, USA, 104-109.
- [9] Maximilien, E. M. and Singh, M. P (2004),A framework and ontology for dynamic web services selection.IEEE Internet Computing 8, 5 (Sept.), 84-93.
- [10]Menasc'e, D. A (2004), Composing web services: A QoS view.IEEE Internet Computing 8, 6, 88-90.
- [11]Milanovic, N. and Malek, M (2004),Current solutions for web service composition. *IEEE Internet Computing* 8, 6, 51-59.
- [12]M.P.Papazoglou, P.Traverso, S.Dustdar,Leymann (2008), Service-Oriented Computing:a research roadmap. *International Journal of Cooperative Informations Systems*, vol.17, no.2, pp.223-255.
- [13]Paradesi, S., Doshi, P., and Swaika, S (2009), Integrating behavioral trust in web service compositions. In Proceedings of the 7th IEEE International Conference on Web Services (ICWS). IEEE Computer Society, Los Alamitos, CA, USA.
- [14]R. Wang, Chi-Hung Chi, Jianming Deng (2009),A fast heuristic algorithm for the composite web service selection. Springer LNCS, (2009), pp. 506-518.
- [15]T. Yu, Y. Zhang, K. A. Lin (2007), Efficient Algorithms for Web Service Selection with end-to-end QoS constraints. *ACM Transactions on the Web*, vol. 1, no. 1, (2007).
- [16]Wang, Y. and Singh, M. P (2010),Evidence-based trust: A mathematical model geared for multiagent systems. *ACM Transactions on Autonomous and Adaptive Systems (TAAS)* 5, 3 (Sept.).
- [17]Wu, G., Wei, J., Qiao, X., and Li, L, (2007),A Bayesian network based QoS assessment model for web services. In *IEEE International Conference on Services Computing*. IEEE Computer Society, Los Alamitos, CA, USA, 498-505.
- [18]Yue, K., Liu, W., and Li, W (2007),Towards web services composition based on the mining and reasoning of their causal relationships. In *Advances in Data and Web Management*. Lecture Notes in Computer Science 4505. Springer, Berlin, 777-784.
- [19]Z. Chen, L. Ge, H. Wang, X. Huang, J. Lin (2006), A trust based service evaluation and selection model in pervasive computing environment. *International symposium on pervasive computing and application*.
- [20]Z. M. Aljazzaf. (2011).Trust based Service Selection. Dissertation, University of Western Ontario.

6th International Engineering Symposium - IES 2017

March 1-3, 2017, Kumamoto University, Japan

**CHEMISTRY,
CHEMICAL ENGINEERING
&
RELATED FIELDS**

6th International Engineering Symposium - IES 2017

March 1-3, 2017, Kumamoto University, Japan



Aqueous Two-phase Extraction of anthocyanin from fruits of *Garcinia Indica*

Basavaraj Nainegali¹, Regupathi I² and Prasanna B. D³

¹ Department of Chemical Engineering, National Institute of Technology, Karnataka, India-575025 basubiotech@yahoo.com

² Department of Chemical Engineering, National Institute of Technology, Karnataka, India-575025. ponregu@gmail.com

³ Department of Chemical Engineering, National Institute of Technology, Karnataka, India-575025. Prsnbhat@gmail.com

ABSTRACT: Synthetic colorants and flavouring compounds are posing serious health concerns and hence natural pigments are in the spotlight due to their health benefits and consumer acceptance. Anthocyanin pigments are considered as an important additive in food and medicine due to their antioxidant and anti-microbial properties along with attractive colour. An aqueous two-phase system (ATPS) was used to purify anthocyanin present in *Garcinia indica* from accompanying sugars and proteins. Various PEG-salt and water miscible alcohol-salts ATPS were screened for the extraction of anthocyanin and 1-propanol - magnesium sulfate system was found to be superior. The binodal curve of the selected system was developed at 303.15 K and the effect of 1-propanol and magnesium sulphate concentrations, was studied on the partitioning coefficient and yield of anthocyanin. The maximum yield (98.51 %) of anthocyanins with a partitioning coefficient of 70.36 and reduction of 85.92 % sugars was achieved in the system which contains the composition of 30 % (w/w) of 1-propanol and 32 % (w/w) MgSO₄.

Keywords: anthocyanin, aqueous two-phase extraction, phase equilibrium

INTRODUCTION

The use of natural colorants with antioxidant and biological properties is gaining popularity because of proven long term toxicological effects of some synthetic additives. Natural pigments can be called as healthy pigments now days due to their positive impacts on health by preventing cardiovascular, inflammatory and neurological diseases (Silva et al. 2007). Anthocyanins are harmless pigments of the vascular plants, gaining importance due to their use as natural water-soluble colorants and easily incorporated in aqueous media (Pazmino-Duran et al. 2001). Anthocyanins extraction from natural sources like grape, berries (blue berry and mulberry), red cabbage, kokum fruits, purple sweet potatoes, jamun fruits, etc., are reported in the literature. Phytochemical studies have shown that, when compared with any other natural sources, the fruit rind of *Garcinia indica* (kokum) contains the highest concentration of anthocyanins (2.4 g/100 g of kokum fruit) (Nayak et al.

2010, Nayak, Srinivas et al. 2010). *Garcinia indica*, popularly known as kokum belongs to the family Guttiferae are distributed throughout the tropical Asian, African and Polynesian countries and mainly in tropical humid evergreen rainforests of the Western Ghats of south India, as well as in the north-eastern states of India (Chandran 1996). The presence of two different anthocyanins in *Garcinia indica* namely, cyanidin-3-glucoside and cyanidin-3-sambubioside in the ratio of 4:1 are reported (Nayak, Srinivas et al. 2010) among more than 500 different varieties of anthocyanins. The non-conventional liquid-liquid extraction, Aqueous two-phase extraction (ATPE) was extensively used for the separation and purification of biomolecules such as proteins (Asenjo and Andrews 2012), nucleic acids (Luechau et al. 2009), enzymes (Mehrnoosh et al. 2012), flavor compounds (Cardoso et al. 2013), antioxidants and antibiotics (Azevedo et al. 2009). Recently, aqueous two-phase extraction (ATPE) has been utilized to

6th International Engineering Symposium - IES 2017

March 1-3, 2017, Kumamoto University, Japan

separate anthocyanins because of its mild conditions and high capacity. ATPE based on polyethylene glycol (PEG)/magnesium sulphate system was reported as a most suitable system for the effective differential partitioning of anthocyanins from red cabbage and Jamun fruit (Chandrasekhar and Raghavarao et al. 2015a). Multistage ATPE was successfully used for removal of sugars and other contaminants (Chandrasekhar and Raghavarao et al. 2015b). Recently, hydrophilic alcohols/salt systems have been used as a novel ATPE system to purify natural compounds (Jiang et al. 2009). Short-chain alcohols (ethanol, methanol, 1-propanol and 2-propanol) could form stable and adjustable ATPE system with inorganic salts (e.g., phosphate and sulfate and citrates) (Khayati and Shahriari 2016, Wang et al. 2009) with very low surface tension (wang et al. 2011). Ethanol-ammonium sulphate system was identified as an economical ATPE system to extract and concentrate the anthocyanins from various sources like Mulberry (Wu X et al. 2011), purple sweet potatoes (Liu et al. 2013) and Blueberry fruits (Hua et al. 2013). Multistage and scale up extractions with Ethanol-NaH₂PO₄ also worked well for extraction and preliminary purification of anthocyanins from grape juice by removing the majority of sugars(Wu Y et al. 2014).

The ATPS consist of PEG, Ethanol and Propanol with different salts was investigated for partitioning of anthocyanins from *garcina indica*. The effect of 1-propanol and magnesium sulfate concentrations was studied on the partitioning coefficient, recovery of anthocyanins and removal of impurities like sugars.

MATERIALS AND METHODS

MATERIALS

Analytical grade polyethylene glycols of molecular weight PEG 6000, Standard anthocyanin- Kuromarin chloride (cyanidin-3-O-glucoside) and Standard protein BSA were purchased from Sigma Chem. Co. USA. Hydrochloric acid, sulphuric acid, phenol, sodium hydroxide, glucose and different salts like, ammonium sulfate, magnesium sulfate, mangenous

sulfate, sodium citrate and sodium sulfate salts (> 99%) and HPLC-grade solvents like, 1-propanol, 2-propanol, and ethanol were purchased from Merck, Mumbai, India. Double distilled water was used throughout the experiment. Fresh kokum (*Garcinia indica*) fruits were procured from the local market near Mangalore, India.

METHODS

The crude extract is prepared by mixing the acidified water (0.1% hydrochloric acid at 1:2 ratio) with washed, cut into four equal pieces (rinds) of 1 kg fresh kokum fruits and grinded after the removal of seeds. The extract was stored at 4° C for further use after filtered twice using muslin cloth and centrifuged to remove fine particles.

Predetermined weighed quantities of polymer, immiscible alcohols, salts and water, selected from phase diagrams reported in the literature (Chandrasekhar and Raghavarao 2015b, Khayati and Shahriari 2016) were added to the crude extract of anthocyanins, making the total weight of the system 100% on w/w basis at 30°C (303.15 K). The contents were mixed thoroughly using a vertex mixer, allowed for about an hour to equilibrate and phase separation. After clear separation, the top and bottom phases were collected, noted the volumes, weight and subjected to analysis of anthocyanins as well as sugars.

Cloud point titration method was used to determine the binodal curve at 303.15 K for 1-Propanol and magnesium sulfate system.

To study the effect of phase component concentration on the partition coefficient of anthocyanin and sugars (K_a and K_s), required amount of MgSO₄ and 1-Propanol were added with 1 g of crude extract in 15 ml centrifuge tubes and de-ionized water was added to make up the system for a total weight of 10g. After equilibration, the anthocyanin and sugar concentrations in both the phases were determined. Total monomeric anthocyanin content of the samples was determined according to the pH differential method (Flueki and Francis, 1986). The pH of the extract of anthocyanins was adjusted and measured using a pH meter (digital pH meter Eutech

6th International Engineering Symposium - IES 2017

March 1-3, 2017, Kumamoto University, Japan

Instruments, Singapore). Concentration of anthocyanins content as cyanidin-3-glucoside equivalents was calculated using the following equation (Giusti and Wrolstad 2001) (Eq. (1)):

$$\text{Anthocyanin concentration (mg/l)} = \frac{A \times MW \times Df \times 10^3}{\epsilon \times L} \quad (1)$$

Where A is the total absorbance $(A_{\lambda_{max}} - A_{700})_{\text{pH-1.0}} - (A_{\lambda_{max}} - A_{700})_{\text{pH-4.5}}$

Molecular weight of anthocyanins (MW) and their extinction coefficient (ϵ) are 449.2 g/mol and 26900 L/cm mol, respectively. Df is the dilution factor and L is the path length (1 cm).

Similarly, the total sugars present in the samples were determined through Dubois method (Dubois et al. 1956) Glucose was used as a standard for the determination of sugars. The absorbance of the sample was recorded at 490 nm using UV spectrophotometer. The partition coefficient (K_a and K_s) of the anthocyanins and sugars, yield of anthocyanins (Y_a , % w/w) in the top phase and yield of sugars (Y_s , % w/w) in salt-rich (bottom) phase were calculated using the eq. (2), (3) and (4), respectively (Chandrasekhar and Raghavarao 2015a, 2015b, Wu X et al. 2011).

$$K_a \text{ and } K_s = \frac{C_T}{C_B} \quad (2)$$

$$Y_{TA} = \frac{C_T V_T}{C_T V_T + C_B V_B} * 100 \quad (3)$$

$$Y_{BS} = \frac{C_B V_B}{C_B V_B + C_T V_T} * 100 \quad (4)$$

Where, C_T and C_B represent the equilibrium concentrations of anthocyanins or sugars in the top and bottom phase, respectively. V_T and V_B represent the volume of top and bottom phase, respectively.

RESULTS AND DISCUSSION

Initially, the crude extract rich with anthocyanins was prepared by employing three different extraction methods namely, aqueous extraction, 0.1 % HCl treatment and incubating with propanol. In all the techniques the solid-liquid ratio was maintained at 1:2 (Chandrasekhar and Raghavarao, 2015b). The anthocyanins content was higher in propanol extract (151 mg/L) than the acidic water extract (143 mg/L) and aqueous extract (130

mg/L). The propanol extract was further used for the partitioning studies.

SELECTION OF SUITABLE ATPS

The partitioning of target biomolecule in ATPE depends on size, charge, and hydrophobicity of target biomolecule and system properties like concentration of phase forming components (salt and polymer/alcohols), pH and phase volume ratio. Polymer-salt systems are preferred over polymer-polymer ATP systems because of high cost and handling problems due to high viscosity of the polymers (Ozlem et al. 2011). Short chain alcohol-salt systems are also preferred because of low cost, high water content, low surface tension, faster phase separation, easily recyclable and more suitable for hydrophilic compounds (Wu X et al. 2011). Hence, eight different ATPSs consist of different phase forming salts (magnesium sulfate, sodium sulfate, ammonium sulfate, sodium citrate, and manganese sulfate) along with PEG 6000; 1-Propanol and Ethanol were considered for the selective partitioning of *garcina indica* anthocyanins by leaving the other impurities as shown in Fig 1. The different compositions of the phase forming components of the systems were considered based on the binodal curve of the respective systems. In all the selected systems the anthocyanins found to selectively partition in the top phase (PEG or alcohol rich phase) by leaving the impurities in the salt rich bottom phase. The PEG6000-MgSO₄ and PEG6000 - (NH₄)₂SO₄ systems provided a partition coefficient of 15.70 and 6.43 with a yield of 90 and 70 %, respectively. Both the system exhibits a native pH between 4 and 5. These systems are also worked well for anthocyanins from red cabbage and jamun fruits as reported earlier by Chandrasekhar and Raghavarao (2015a, b). The Ethanol-(NH₄)₂SO₄ system was considered for the partitioning since this system was used extensively for the recovery of anthocyanins from Purple sweet potatoes (Liu 2013), Mulberry (*Morus atropurpurea Roxb.*), (Wu X 2011) and Blueberry (*Vaccinium uliginosum Linn*) (Hua 2013). Around a yield of 83% *garcina indica* anthocyanin was noticed with this system.

Further the phase forming ability of the ATPS consisting of 1-Propanol with different salts like, MgSO₄/ (NH₄)₂SO₄/ MnSO₄/Na₃C₆H₅O₇/Na₂SO₃ were examined and the anthocyanin partitioning was carried out in all the mentioned system. The 1-Propanol-MgSO₄ system showed a very high partitioning of anthocyanin in the top phase with a partition coefficient of 25.57 and yield of 93.58 % w/w (Fig. 1). However, the (NH₄)₂SO₄ and MnSO₄ salts also provide a significant yield and partitioning coefficient but lesser than 1-Propanol-MgSO₄ system. The sodium salts namely, Na₃C₆H₅O₇ and Na₂SO₃ failed to provide a significant yield due to the degradation of anthocyanins. It was observed that the partitioning and yield of the *garcina indica* anthocyanin was majorly depends on the native pH of the ATPS.

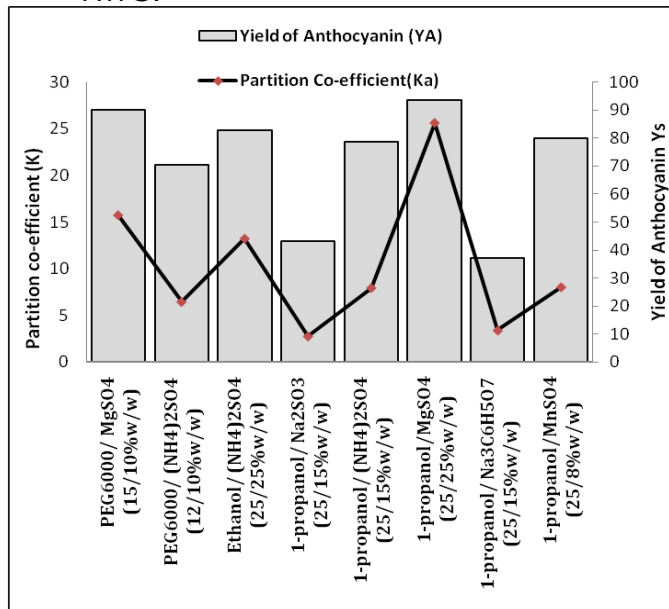


Figure 1: Effect of different ATPE systems on partitioning of Anthocyanin and yield. K_a represents partition co-efficient of anthocyanin and Y_a represents yield of anthocyanin.

The ATPS formed with 1-propanol - MgSO₄/ (NH₄)₂SO₄/ MnSO₄/ Na₃C₆H₅O₇/ Na₂SO₃ has the pH of 3.9, 5.2, 5.9, 8.8 and 9.5, respectively. As the pH moves from acidity to basicity the yield was found to decrease, since the anthocyanin molecules are stable at acidic pH than basic pH. Hence, the maximum yield was obtained for 1-propanol/MgSO₄ system which offers the pH of 3.9. The

propanol/MgSO₄ system was selected for further studies since it showed a good yield of *garcina indica* anthocyanin. In general, most of the anthocyanin from other sources has a better stability below the pH value of 4. However it was observed that the *garcina indica* anthocyanins able to withstand up to the pH value of 6 with 1-propanol as one of the phase forming component.

DIFFERENTIAL PARTITIONING OF ANTHOCYANINS AND SUGARS

With the aim of partitioning the anthocyanins in any one of the phases of ATPS by leaving the other impurities like total sugars and proteins in the other phase, the experiments were conducted to improve the partitioning coefficient and yield of anthocyanins by varying the system conditions of 1-propanol/MgSO₄ system. The effects of 1-propanol and MgSO₄ concentration on the partitioning of anthocyanins were analysed by selecting the appropriate concentration from the phase diagram developed (Fig. 2).

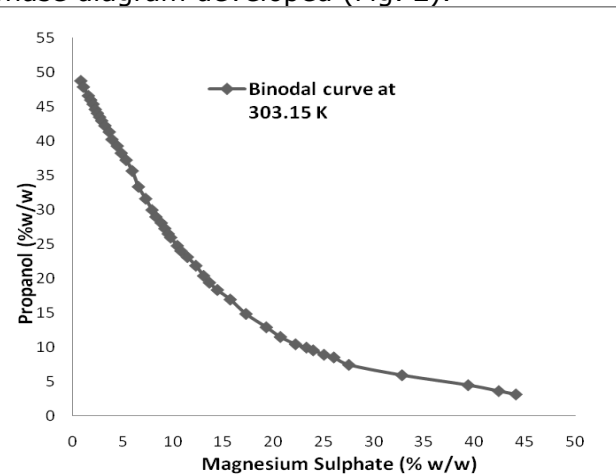


Figure 2: Binodal curve for 1-propanol and MgSO₄ system at 303.15° K.

The effect of salt concentration was studied at different 1-propanol concentration. From the Fig 3, it was observed that the partitioning coefficient of anthocyanins increases with increasing salt concentration, which indicates that the anthocyanins present in the salt phase was expelled to the top phase due to the salting out phenomena of the system. The MgSO₄ salt molecules prefer to surround by the same molecules than the other molecules, hence the anthocyanins are

shifted from salt rich bottom phase to alcohol rich top phase. The maximum partitioning was achieved between 30-32 % (w/w) $MgSO_4$ concentrations irrespective of 1-propanol concentration (Fig 3). Higher anthocyanins partitioning coefficient (K_a) between 66.27 to 70.36 is observed for the system contains 30 % (w/w) 1-propanol and 30-32 % (w/w) $MgSO_4$ with the maximum yield of 98.60 % by removing 85.92 % sugars.

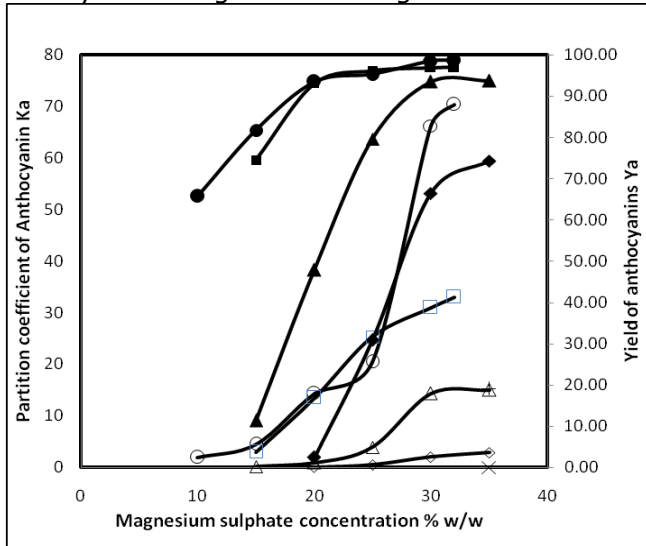


Figure 3: Effect of 1- propanol and magnesium sulfate concentration on partitioning co-efficient (K_a) and % yield of anthocyanins. K_a at different 1-Propanol concentration represented as (w/w) 30% (○), 25% (□), 20% (△), 15% (◊), 10% (×) and % yield as 30% (●), 25% (■), 20% (▲), 15% (◆), 10% (+).

Even though the anthocyanin molecules are preferred to partition in top phase, the associated proteins and sugars are partitioned in the bottom phase due to the ionic effect of the salt rich bottom phase. Lower the partitioning coefficient of the sugar is better for the removal of sugar from the top phase where anthocyanin molecules are partitioned. It was observed that the partitioning coefficient of sugar decreased with increasing concentration of $MgSO_4$ (Fig. 3). Since the native pH of the system is in acidic range (3.9 pH), the proteins and the associated sugar molecules become more hydrophilic than the anthocyanin molecules and they prefer to stay in the salt rich phase. Salt concentration more than 15 % w/w is

required to get higher yield of sugars in bottom phase. Maximum sugar partitioning ($K_s = 0.08$) towards bottom phase (92.10 % yield) is observed with 25% w/w 1-propanol and 30-32 % w/w $MgSO_4$ system (Fig. 4). However the partitioning coefficient was found to decrease at higher salt concentration above 32 % due to the salting out effect and the non-availability of the free volume of solvent to dissolve them. The trend observed in the present work is similar to the anthocyanin partitioning in Ethanol/ $(NH_4)_2SO_4$ ATPS reported by Hua (2013).

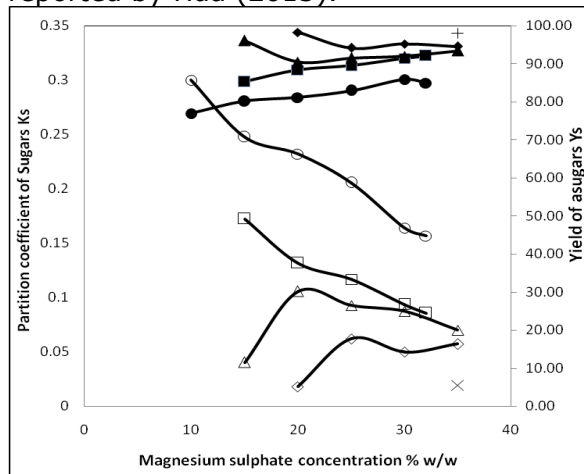


Figure 4: Effect of 1- propanol and magnesium sulfate concentration on partitioning co-efficient (K_s) and % yield of sugars in bottom phase. K_s at different 1-Propanol concentration represented as (w/w) 30% (○), 25% (□), 20% (△), 15% (◊), 10% (×) and % yield as 30% (●), 25% (■), 20% (▲), 15% (◆), 10% (+).

Similarly, the experiments were conducted by varying the 1-propanol concentration at a constant salt concentration of 32 % (w/w) to study the effect of 1-propanol concentration on the partitioning of anthocyanins in 1-propanol/ $MgSO_4$ system. The anthocyanins partitioning coefficient was found to increase along with corresponding decrease in the partitioning coefficient of sugars, as the concentration of 1-propanol increases. The impurities like sugars and proteins have higher interaction with the salt rich phase due to the higher hydrophilicity and hence the anthocyanins molecules are transferred to the alcohol phase. As the concentration of alcohol increases, the free volume

6th International Engineering Symposium - IES 2017

March 1-3, 2017, Kumamoto University, Japan

available for the dissolution of anthocyanin in the system also increases. The combined effect of hydrophobic force and the free volume of the system favour the partitioning of anthocyanin in to the top phase and proteins associated with the sugars to the bottom phase. The maximum partitioning of anthocyanin (K_a of 70.36) with lower partitioning of sugar (K_s of 0.156) and was achieved at 30% (w/w) of 1-propanol Fig 3 and 4).

CONCLUSION

An aqueous two-phase system composed of hydrophilic alcohol and an inorganic salt i.e 1-propanol and magnesium sulfate, is found to be suitable for the extraction of anthocyanins from *Garcinia indica* fruit rinds. The concentration of 30 % (w/w) 1-propanol and 30-32% (w/w) $MgSO_4$ system resulted the maximum yield of 98.60 % anthocyanin with partition coefficient 70.36. Maximum sugar removal (92.10 % yield) towards the bottom phase was achieved with 30% (w/w) 1-propanol and 30-32 % (w/w) $MgSO_4$ system. This ATPS can be a suitable system for the extraction and preliminary purification of sensitive natural pigments. After appropriate optimization of the other system and operating variables, it can be considered for the industrial scale purification of anthocyanins.

REFERENCES

- Asenjo, J A and Andrews, B A (2012), Aqueous two-phase systems for protein separation: phase separation and applications, *Journal of Chromatography A*, Vol 1238, pp. 1-10.
- Azevedo, et al. (2009). Chromatography - free recovery of biopharmaceuticals through aqueous two-phase processing, *Trends in biotechnology*, Vol. 27, No. 4, pp. 240-247.
- Cardoso, L C et al. (2013), High pressure extraction of antioxidants from *Solanum stenotomum* peel, *Molecules*, Vol. 18, No. 3, pp. 3137-3151.
- Chandran, M D S (1996), Nature watch: The Kokum tree, *Resonance*, No. 1, pp. 86-89.
- Chandrasekhar, J and Raghavarao KSMS (2015a), Process integration for purification and concentration of red cabbage (*Brassica oleracea* L.) anthocyanins, *Separation and Purification Technology*, Vol. 141, pp. 10-16.
- Chandrasekhar, J and Raghavarao, K S M S (2015b), Separation and Concentration of Anthocyanins from Jamun: An Integrated Process, *Chemical Engineering Communications*, Vol. 202 No. 10, pp. 1368-1379.
- Dubois, M et al (1956, Colorimetric method for the determination of sugars and related substances, *Anal. Chem*, Vol. 28, pp. 350-356.
- Flueki, T and Francis, F J (1986), Quantitative methods for anthocyanins 2. Determination of total anthocyanin and degradation index for cranberry juice, *J. Food Sci*, Vol. 33, pp. 78-83.
- Giusti, M M and Wrolstad, R E (2001), Characterization and measurement of anthocyanins by UV-visible spectroscopy, *Current protocols in food analytical chemistry*.
- Hua, Z et al (2013), Extraction and purification of anthocyanins from the fruit residues of *Vaccinium uliginosum* Linn, *Journal of Chromatography and Separation Techniques*
- Jiang, B et al (2009), Aqueous two-phase extraction of 2,3-butanediol from fermentation broths using an ethanol-phosphate system, *Process Biochemistry*, Vol. 44, No. 1, pp. 112-117.
- Khayati, G and Shahriari, M (2016), Measurement and Correlation of Phase Diagram Data of Hydrophilic Alcohols (1-Propanol/2-Propanol)+ Salts ($Na_2SO_4/(NH_4)_2SO_4/NH_4NO_3$)+ Water Systems, *Chemical and Biochemical Engineering Quarterly*, Vol. 3, No.1, pp. 73-80.
- Liu, X (2013), Optimisation of aqueous two-phase extraction of anthocyanins from purple sweet potatoes by response surface methodology, *Food chemistry*, Vol. 141, No.3, pp. 3034-3041.
- Luechau F et al (2009), Primary capture of high molecular weight nucleic acids using aqueous two-phase systems, *Sep. Purif. Technol*, Vol. No. 66, pp. 202-207
- Mehrnoosh A et al (2012), Optimization of Serine Protease Purification from Mango (*Mangifera Indica* cv. Chokanan) Peel in Polyethylene Glycol/Dextran Aqueous Two Phase System, *Int J Mol Sci*, Vol. 13, pp. 3636-3649.
- Nayak, et al (2010), Bioactive constituents present in *Garcinia indica* Choisy and its potential food applications: A review, *International Journal of Food Properties*, Vol. 13, pp. 441-453.
- Nayak, C. A., Srinivas, P., et al (2010), Characterization of anthocyanin from *Garcinia indica* choisy *Food Chemistry*, Vol. 118, pp. 719-724.
- Ozlem, A et al (2011), Aqueous two-phase extraction of lactic acid: Optimization by response surface methodology, *Separation Science and Technology*, Vol. 46, pp. 1164-1171.
- Pazmino-Duran, A. E., et al (2001), Anthocyanins from oxalis triangularis as potential food colorants, *Food Chemistry*, Vol. 75, No.2, pp. 211-216.
- Silva, E et al (2007), Optimisation of the adsorption of polyphenols from *Inga edulis* leaves on macroporous resins using an experimental design methodology, *Separation and Purification Technology*, Vol. 53, pp.274-280.
- Wang, Y et al (2009), Phase diagrams of ammonium sulfate+ ethanol/1-propanol/2-propanol+ water aqueous two-phase systems at 298.15 K and correlation, *Journal of Chemical & Engineering Data*, Vol. 55, No. 2, pp. 876-881.
- Wang, Y et al (2011), Application of water-miscible alcohol-based aqueous two-phase systems for extraction of dyes, *Separation Science and technology*, Vol. 46, No.8, pp. 1283-1288.
- Wu, X., et al (2011), Aqueous two-phase extraction, identification and antioxidant activity of anthocyanins from mulberry (*Morus atropurpurea Roxb.*), *Food Chemistry*, Vol. 129, No. 2, pp. 443-453.
- Wu, Y et al (2014), Extraction and preliminary purification of anthocyanins from grape juice in aqueous two-phase system, *Separation and Purification Technology*, Vol. 124, pp.170-178.

Simulation and Control of Continuous Crystallization Process

Yashas Mohankumar¹, Sai Dinesh B² and C. Sankar Rao³

¹ Department of Chemical Engineering, National Institute of Technology Karnataka, Surathkal, Mangalore 575025, India. mail:yashas1354@gmail.com

² Department of Chemical Engineering, National Institute of Technology Karnataka, Surathkal, Mangalore 575025, India. mail:saidineshbille123@gmail.com

³ Department of Chemical Engineering, National Institute of Technology Karnataka, Surathkal, Mangalore 575025, India. mail:csankarrao@gmail.com

ABSTRACT: The work deals with the dynamic and control study of continuous crystallization process. The objective of the present work is to design a controller for the stabilization of the third moment of the crystal size distribution and the crystallizer temperature. The stirring rate and the coolant flow rate are the manipulated variables for controlling crystal size distribution and temperature respectively. Firstly, a mathematical model of continuous crystallization process is developed by the first principle model. The population balance model is solved by the method of moment. These mathematical models are solved in SIMULINK and a study has been carried out on the effect of operating parameters on the crystal size distribution. A linear model is obtained from the nonlinear equations and designed the controller by the relay based method and IMC based method using the local linearized model and implemented on the actual nonlinear model. The closed loop servo and regulator responses are obtained. By observing the control performance of both controllers, the controller designed based on the IMC based method gives better closed loop performance in terms of time integral errors such Integral Square Error (ISE), Integral Absolute Error (IAE) and Integral Time weighted Absolute Error (ITAE).

Keywords: continuous crystallization, non-linear model, simulation, controllers

INTRODUCTION

Crystallization is a solid-liquid separation technique process in which mass transfer of a solute from the liquid solution to a pure solid crystalline phase. This process is used at some stage in all process industries as a method of production, purification or recovery of solid materials. This process not only used to control purity but also used to produce crystals of a desired size distribution, shape. It is practiced on all scales from the isolation of milligrams of synthesized substance in research laboratory to isolation of products on million-ton scale in industry. Crystallization of the solution is an important process in industry because variety of materials that are marketed in

the crystalline form. An important example for this chemical separation technique is the production of sucrose from sugar beet, where the sucrose is crystallized out from an aqueous solution.

Continuous crystallization has long been a standard method for the crystallization of bulk commodity chemicals and large volume speciality chemicals, but it has only recently become a focus in the pharmaceutical and fine chemical industries.

Continuous crystallization is a highly non-linear process mainly because it involves two nonlinear distinct kinetic steps: nucleation and growth. The formation of a new crystalline entity from the solution starts through a process called nucleation process. Nucleation process is defined as

6th International Engineering Symposium - IES 2017

March 1-3, 2017, Kumamoto University, Japan

the series of atomic or molecular processes by which the atoms or molecules of a reactant phase rearrange into a cluster of the product phase large enough as to have the ability to grow irreversibly to a macroscopically larger size. Nucleation can be homogeneous and heterogeneous. Homogeneous nucleus occurs in the absence of foreign particles or crystals in the solution. Whereas heterogeneous occurs in the presence of foreign particles in the solution. Both types of nucleation are collectively known as primary nucleation. Secondary nucleation takes place when the nucleation is induced by the presence of crystals of the same substance. In addition, there are interactions between kinetic, fluid dynamics, and crystal size distribution. All those factors might lead to an unstable operation (J. N'yvt and J. W. Mullin (1970)) that affects the quality of the final product. A nonlinear feedback controller is developed by using geometric control theory to be applied to a non-isothermal crystallizer. Operating conditions are analysed based on the combined effects of secondary nucleation and cooling temperature Pedro Alberto Quintana-Hernández et al (2012).

For control of a system which is represented by a non-linear model, two approaches are usually taken. First approach is to linearize the model and use linear control design techniques. Small signal approximation around the operating condition, exact linearization using different geometric theory (Daoutidis and Kravaris, 1991; Kravaris and Soroush, 1990) and variable transformation (Kokotovic, 1985) are among the various techniques employed for linearization of non-linear models. Second approach involves non-linear control design techniques. Non-linear model based control design and more specifically non-linear model predictive control (NMPC), and the differential geometric approach, are common techniques for this purpose S. Rohani et al (1999).

This paper discusses control of continuous crystallization using two methods. First, the non-linear equations controlling kinetics and growth are linearized around

their mid-point and control parameters are determined for PI controller. Second, the control parameters for PI and PID gains are determined by using Ziegler-Nichols (ZN) and Tyreus-Luyben methods. The controllers thus obtained are used in a feedback system for temperature and crystal growth and their performances are tested. The responses are plotted against time for both the control settings, (PI and PID).

POPULATION BALANCE MODEL

Mathematical Modelling

Randolph and Larson (1971) presented a general crystallization model developed under the following assumptions: continuous operation, perfect mixing, infinitesimal new generated particle size, and constant volume.

The following population balance describes the evolution of $n(L)$ as function of time and crystal size:

$$\frac{\partial n}{\partial t} + \frac{\partial(nG)}{\partial L} = -\sum_k \frac{q_k n_k}{V} + B\delta(L - L_0) \quad (I)$$

in which n is the population density, G is the crystal growth rate, L is the internal coordinate (characteristic crystal length), B is the nucleation rate density, and $\delta(L - L_0)$ is the Dirac delta function acting at $L = L_0$. The boundary and initial conditions for (I) are given as follows:

$$\text{BC: } n(0, t) = 0 \quad n(\infty, t) = 0 \quad t \geq 0,$$

$$\text{IC: } n(L, 0) = f(L) \quad 0 \leq L \leq \infty$$

Salcedo-Estrada (2000) reported growth and nucleation equations (II) for ammonium sulfate-water system. The equations involved k_g , k_b , g , h , o and p that were evaluated from experimental data. Both equations are reported as a function of supersaturation and agitation rate.

$$G = k_g \Delta c^g N_r^h \quad (II)$$

$$B = k_b \Delta c^b M_T^o N_r^p$$

The non-linear equations used for system identification are:

$$\frac{d\mu_o}{dt} = \frac{\mu_o^e}{\tau} - \frac{\mu_o}{\tau} + G \quad (1)$$

6th International Engineering Symposium - IES 2017

March 1-3, 2017, Kumamoto University, Japan

$$\frac{d\mu_1}{dt} = \frac{\mu_1^e}{\tau} - \frac{\mu_1}{\tau} + G\mu_o \quad (2)$$

$$\frac{d\mu_2}{dt} = \frac{\mu_2^e}{\tau} - \frac{\mu_2}{\tau} + G2\mu_1 \quad (3)$$

$$\frac{d\mu_3}{dt} = \frac{\mu_3^e}{\tau} - \frac{\mu_3}{\tau} + G3\mu_2 \quad (4)$$

$$\frac{d\mu_4}{dt} = \frac{\mu_4^e}{\tau} - \frac{\mu_4}{\tau} + G4\mu_3 \quad (5)$$

$$\frac{d\mu_5}{dt} = \frac{\mu_5^e}{\tau} - \frac{\mu_5}{\tau} + G5\mu_4 \quad (6)$$

$$\frac{dC_1}{dt} = \frac{(sC)_e - C + C\mu_3^e - 3\tau kG\mu_2(\rho_c - C)}{\tau(1 - \mu_3)} \quad (7)$$

$$\rho V C_p \frac{dT}{dt} = \rho q C_p (T_{in} - T) - \Delta H_c 3\rho_c k_v V k_g \Delta c^g N_r^h \mu_2 - UA(T - T_j) \quad (8)$$

$$\rho_j V_j C_{pj} \frac{dT_j}{dt} = \rho_j q_j C_{pj} (T_{j,in} - T_j) - UA(T - T_j) - U_o A_o (T_j - T_\infty) \quad (9)$$

Δc is evaluated as $(C - C_{sat})/C_{sat}$, N_r is the agitation rate and M_T is the total crystal mass per volume.

Lugo-Martinez (2005) reported a polynomial function for the upper metastable zone limit, C_{mz} , for the ammonium sulfate-water system as function of temperature. The lower limit (saturation concentration, C_s) was evaluated using the polynomial reported by Perry et al. (1997). Both (10) and (11) are valid in the range from 20 to 50°C

$$c_{mz} = 1.3179 \times 10^{-7} T^3 + 2.6136 \times 10^{-6} T^2 + 2.6280 \times 10^{-3} T + 0.70758, \quad (10)$$

$$c_s = 4.0 \times 10^{-5} T^2 + 2.0 \times 10^{-4} T + 0.73 \quad (11)$$

The nonlinear model equations are simulated using SIMULINK and analysed the dynamic behaviour. The obtained responses are shown in Fig 1, 2 and 3. Fig. 1 shows that mean crystal size distribution and percentage of CV and phase diagram are shown in Fig. 2 and 3 respectively. The dotted line represents the metastable zone limit and solid line indicates the solubility curve. The mean crystal size and coefficient of variation can be calculated using the following relationships of the moments in order to obtain the complete Crystal size distribution:

$$L_{43} = \frac{\mu_4}{\mu_3} \quad (10)$$

$$CV = \sqrt{\frac{\mu_5}{\mu_3} - \left(\frac{\mu_4}{\mu_3} \right)^2} \times \frac{\mu_3}{\mu_4} \quad (11)$$

The crystal size distribution is calculated using the above equations

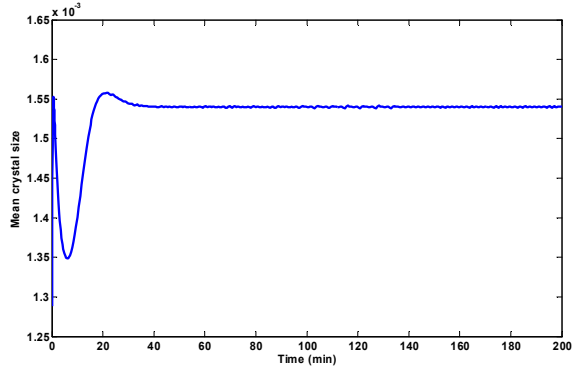


Fig.1 Mean crystal size distribution

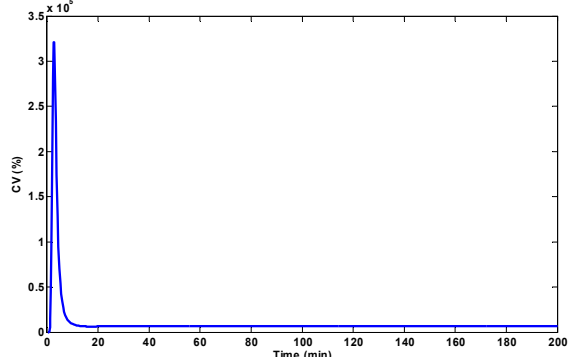


Fig.2 Percentage of CV

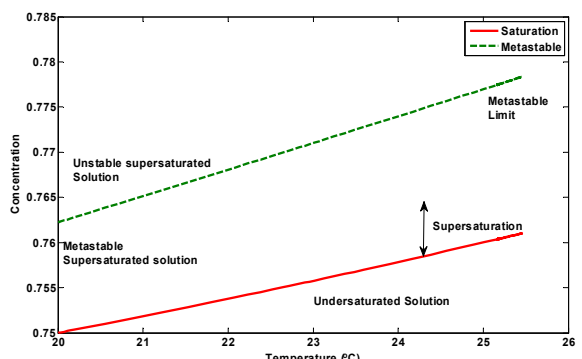


Fig. 3 Phase Diagram

Linearization

The above non-linear model equations (equation 1-9) of continuous crystallization are linearized around equilibrium points. The obtained transfer function model can be written as:

6th International Engineering Symposium - IES 2017

March 1-3, 2017, Kumamoto University, Japan

$$\frac{T(s)}{q_j(s)} = G_1(s) = \frac{1.44 \times 10^{-3}}{(0.6056s + 1)(1.7193s + 1)}$$

$$\frac{\mu_3(s)}{N_r(s)} = G_2(s) = \frac{0.0121(s + 0.399)}{(2.6s + 1)^2}$$

CONTROLLER DESIGN

Relay based method

The PID parameters are obtained by relay auto tuning method and IMC-based PID tuning method. The relay auto-tuning technique is very effective in determining the ultimate gain and ultimate frequency of the system. Instead of bringing the system to the verge of instability, the critical point is obtained by use of a stable limit cycle. The continuous cycling of the controlled variable is generated from a relay feedback experiment and the important process information, ultimate gain (K_u) and ultimate frequency (ω_u) is extracted directly from the experiment [Yu, 1984]. Relay tuning is based on theory that, when the output lags behind the input by n radians, the closed-loop system may oscillate with a period P_u [Astrom and Hagglund, 1984]. The relay feedback test for the given system is implemented in the Matlab-SIMULINK to obtain the model parameters K_u and ω_u . The values of 'h', 'a' and P_u are obtained from the graphs generated in the SMULINK. Where 'h' is the magnitude of the relay and a is the amplitude of the limit cycle.

The ultimate gain of the system is given by as:

$$K_u = \frac{4h}{\pi a} -$$

The parameters of the controller obtained by usage of Z-N tuning rules are given Table 1. The parameters are shown in Table 1 for both temperature and μ_3 . The responses are plotted against time for the designed control settings.

method, process transfer function (P) is split in to two parts. First part consists of the invertible part (contains poles and negative zeros of the process). Second part is noninvertible part which contains positive zeros and time delay term of the process. The IMC controller (Q) is selected as the inverse of the invertible part multiplied by an IMC filter. The order of the denominator of the filter is selected so as to make the IMC controller proper (the order of numerator is less than or equal to the denominator). The filter is required in IMC system to make the controller realizable and to make the closed loop system robust. In particular, in the absence of modelling errors, the filter determines the speed of response and in presence of modelling errors, the problem of robustness is addressed by adjusting the filter time constant.

From the IMC controller, PID controller settings are obtained using $GC=Q/(1-PQ)$. Some of the investigators used Maclaurin series expansion and others used an approximation to time delay term to derive PID controller settings.

Table 1 PID settings for μ_3 and temperature controller

	Third Moment (μ_3)		Temperature	
	Relay	IMC	Relay	IMC
K_c	784.91	1.2917	784.91	1661
T_I	3.15	2.7126	3.64	2.3251
T_D	0.7878	0.0047	0.91	0.4479

The controllers are designed by the above illustrated two methods. The obtained settings are enlisted in Table 1. These two set of PID settings are implemented on the actual non-linear system. The servo and regulatory responses are obtained and the error analysis is being carried out. 10% change is given as perturbation to the steady state value as a step input.

IMC Method

Internal model control is a well-established method for stable systems. In this

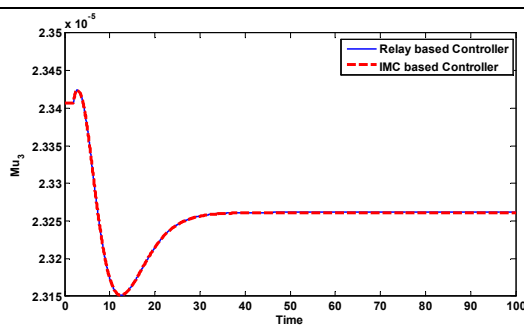


Fig.4 Closed loop servo response for μ_3 of nonlinear Crystallization system using PID controller settings designed by relay tuning method and IMC based method.

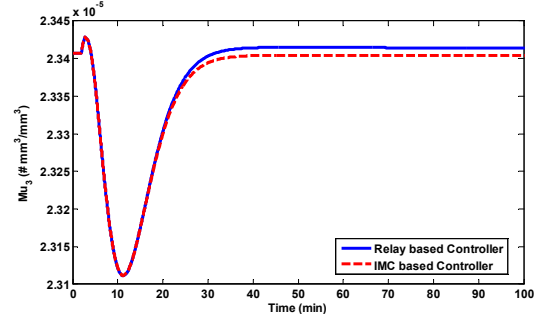


Fig.6 Regulatory response for μ_3 of a continuous crystallizer for a step change in load variable

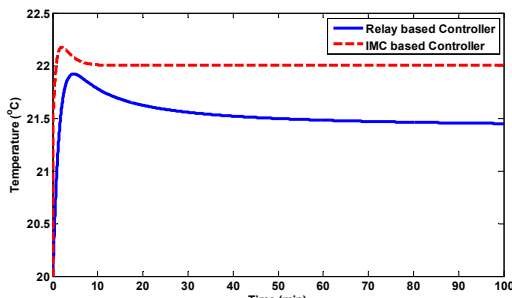


Fig.5 Closed loop servo response for T of nonlinear Crystallization system using PID controller settings designed by relay tuning method and IMC based method.

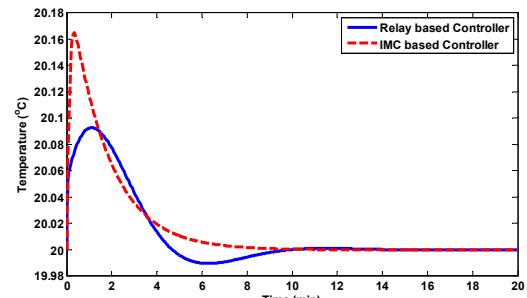


Fig.7 Regulatory response for temperature of a continuous crystallizer for a step change in load variable

Table 2 Closed loop performance

Methods		Servo Problem			Regulatory Problem		
		ISE	IAE	ITAE	ISE	IAE	ITAE
Relay	μ_3	6.214×10^{-10}	0.0002493	0.01245	7.542×10^{-13}	4.373×10^{-6}	0.0001198
	T	610.9	246.7	1.25×10^{-10}	7.557×10^{-13}	3.958×10^{-6}	7.648×10^{-6}
IMC	μ_3	6.216×10^{-10}	0.0002493	0.01245	6.216×10^{-10}	0.0002493	0.01245
	T	0.1808	0.8834	2.67	0.03064	0.3308	0.594

The servo control problem for both third moment and temperature is evaluated by giving a step input to the set point value. Fig. 4 and Fig. 5 show the closed-loop dynamic responses obtained when two set of controller parameters are implemented on the nonlinear crystallizer system. It can be seen from Fig. 4 that for both controllers, the system reaches the set point values. There is no appreciable difference is found. But in case of temperature control, there is a mismatch

between the responses. The time integral analysis has been carried for the evaluation of the closed loop responses and enlisted in Table 2. For servo problem, the time integral errors such as ISE, IAE and ITAE for the third moment are obtained very less values from both the controller settings but for the temperature, ISE, IAE and ITAE values are large when relay based controller settings are implemented. Similarly, regulatory response for the third moment and

6th International Engineering Symposium - IES 2017

March 1-3, 2017, Kumamoto University, Japan

temperature is evaluated by introducing 10% step input in load variable. The obtained results are shown in Fig 6 and Fig. 7. The controller designed based IMC method produces small errors than that of the controller designed by relay tuning. From the above analysis, it is evident that PID controller designed based on IMC method has the best performance for both third moment and temperature control in terms of time integral errors.

CONCLUSIONS

A population balance model has been presented which takes into account of crystal growth and nucleation kinetics which are highly nonlinear in nature. The population balance model has been solved using method of moments. A dynamic behaviour of the continuous crystallization has been carried out. The nonlinear equations are linearized around the operating points. Using the transfer function models, controllers are designed. Different tuning methods such as relay based method and IMC based methods are used to control the third moment and temperature of the crystallizer. A comparison of the closed loop responses reveals that controller designed by the IMC method gives better performance than that of the relay based method. From the closed loop responses, it is found that the controller designed by IMC method gives good results than that of the relay based method.

REFERENCES

- [1] Astrom K. J. and T. Hägglund (1984a), 'Automatic tuning of simple regulators', in *Proceedings of IFAC 9th World Congress*, Budapest, pp. 1867-72
- [2] Astrom K.J. and T. Hägglund (1984b), 'Automatic tuning of simple regulators with specification on phase and amplitude margins', *Automatica*, 20, 645-51
- [3] Astrom K.J. and T. Hägglund (1984c), 'A frequency domain method for automatic tuning of simple feedback loops', in *Proceedings of the 23rd IEEE conference on decision and control*, Las Vegas, pp.299-304
- [4] Daoutidis, P., & Kravaris, C. (1991). Inversion and zero dynamics in non-linear multivariable control. *A.I.Ch.E. J.*, 37(4), 527–538.
- [5] D. Ramkrishna, Population Balances: Theory and Applications to Particulate Systems in Engineering, Academic, San Diego, Calif, USA, 2000.
- [6] D. Randolph and M. A. Larson, Theory of Particulate Processes, Analysis and Techniques of Continuous Crystallization, Academic Press, New York, NY, USA, 1971.
- [7] J. N'yvlt and J. W. Mullin, "The periodic behaviour of continuous crystallizers," *Chemical Engineering Science*, vol. 25, no. 1, pp. 131–147, 1970.
- [8] J.R.Lugo-Martinez, "Estudio para la determinacion de la zona de saturacion metaestable a traves del analisis del proceso de nucleacion para el sulfato de amonio," Chemical Engineering Department, Instituto Tecnologico de Celaya, Guanajuato, Mexico, 2005.
- [9] Kokotovic, P. V. Recent trends in feedback control design. *Automatica*, 21(3), 225–236.
- [10] Kravaris, C., & Soroush, M. (1990). Synthesis of multi-variable nonlinear controller by input/output linearization. *A.I.Ch.E. J.*, 36(2), 249–264.
- [11] K. R. Sundaresan, C. Chandra Prasad, P. R. Krishnaswamy, "Evaluating Parameters from Process Transients", *Ind. Eng. Chem. Process Des. Dev.*, 1978, 17 (3), pp 237-241.
- [12] L. I. Salcedo-Estrada, "Control de cristalizadores batch," in Chemical Engineering Department, Instituto Tecnologico de Celaya, Guanajuato, Mexico, 2000.
- [13] Pedro Alberto Quintana-Hernández, Raúl O campo-Pérez, Salvador Tututi-Avila and Salvador Hernandez-Castro, "Nonlinear MIMO Control of a Continuous Cooling Crystallizer" Modelling and Simulation in Engineering Volume 2012, Article ID 912071, 11 pages doi:10.1155/2012/912071.
- [14] R. H. Perry, J. O. Maloney, and D. W. Green, Perry's Chemical Engineers' Handbook, McGraw-Hill, New York, NY, USA, 1997.
- [15] S. Rohani, M. Haeri, H.C. Wood, "Modelling and control of a continuous crystallization process Part 2. Model predictive control", *Computers and Chemical Engineering* 23 (1999) 279–286.
- [16] Yu, C.C, "Auto tuning of PID Controllers: A Relay Feedback Approach", 2nd Edition, Germany, Springer Science + Business Media, 2006.

Photoluminescence Quenching in Calcium Interacted Graphene Quantum Dots

Praveen Mishra ¹, Badekai Ramchandra Bhat ²

¹ Department of Chemistry, National Institute of Technology Karnataka, Surathkal, Mangalore 575025, India. email: praveenmishra25@hotmail.com

² Catalysis and Materials Laboratory, Department of Chemistry, National Institute of Technology Karnataka, Surathkal, Mangalore 575025, India. email: ram@nitk.edu.in

ABSTRACT: Graphene quantum dots (GQD) are few nanometre wide fragments of graphene with finite band gap which shows excellent photoluminescence (PL). This PL can be utilized for analytical estimation by PL turn off mechanism. We synthesised GQDs via modified hydrothermal (HT) route using Graphene oxide obtained by Tour's method as a precursor. GQD particles produced blue PL on excitation with UV wavelength. On further reaction of GQDs with Calcium (II) Phosphate significant decrease in the intensity of PL was observed. We also explore the plausible scenario leading to the quenching. Photoluminescence (PL) quenching is utilized in quantitative estimation of Ca(II) species in aqueous media. The method can be extended for the fast sensing of calcium in compounds.

Keywords: Graphene Quantum Dots, Photoluminescence, Quenching

INTRODUCTION

Graphene Quantum Dots (GQDs) are Zero-dimensional graphene as in the movement of exciton is confined to all three-spatial direction. Unlike graphene which is a zero-band gap material, GQD possess a finite band gap which when clubbed with exciton confinement leads to photoluminescence. The infinite Bohr radius of the GQDs also provide researchers with ability to tune its property by varying its size. These properties of GQDs makes it widely used for variety of purposes, including production of photovoltaic devices [1], organic light-emitting diodes [2], fuel cells [3] and drug delivery systems [4].

In recent years GQDs have found widespread applications as sensors [5]. The sensing ability of GQDs ranges from metal ions to toxic anions, from biomolecules to oxidants, and from toxins to explosives. The mode of sensing studied with GQDs ranges from electrochemical sensor, photoluminescent/fluorescent sensors, colorimetric sensors and hybrid sensors. GQDs have shown immense potential in electrochemical sensing of biomolecules,

like DNA [6], proteins [7], Amino acids [8], Uric Acid [9], Glucose [10] and even detection of virus [11] have been reported. This shows promising potential in Graphene Quantum Dots to be employed as a choicest material for bio sensing applications. Here we are studying how the PL of GQDs can be utilized in possible detection of Ca(II) ions.

MATERIALS AND METHOD

Graphite used for the study was procured from Sigma Aldrich. Sulphuric Acid, Nitric Acid, Phosphoric acid, Hydrogen peroxide, Hydrogen chloride and Sodium hydroxide used were from Finar and used without further purification.

In a typical synthesis, Graphene oxide was prepared using Improved Hummer's method [12]. Further, as prepared Graphene Oxide were put in a Teflon lined autoclave in alkaline medium and reaction was kept for 16 hours at 200°C which is in accordance to hydrothermal Synthesis reported by Pan *et.al.* [13] with modification. Aqueous GQDs thus synthesized were added with Calcium phosphate and stirred for 30 minutes.

For characterization, GQDs were studied under Bruker Alpha FTIR, Analytik Jena Specord UV Vis Spectrophotometer and Horiba Fluoromax Spectrofluorometer.

RESULT AND DISCUSSION

Graphene oxide as synthesized using Improved Hummer's method analysed using X-ray diffraction. Presence of the characteristic broad peak at 2θ of 7.5-15 degree corresponding to the (002) plane of graphene oxide (fig. 1) instead of usual sharp peak at 26 degree for graphite suggest synthesis of high purity graphene oxide.

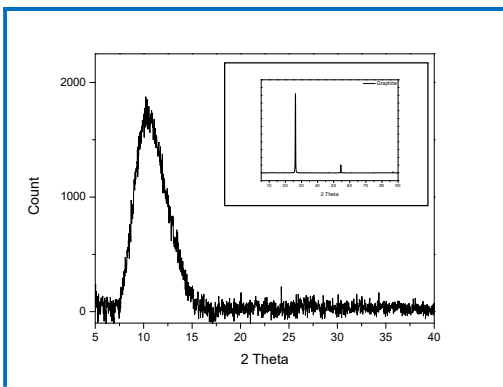


Figure 1: XRD spectrum of Graphene oxide (Inset: XRD Spectrum of Graphite)

Fig. 2(A) represents the IR spectra of Graphite, graphene oxide and GQDs as recorded from $4000-600\text{ cm}^{-1}$. The spectra reveal the presence of oxygen containing functional groups attached to the all carbon structure. In the present graph, there are no peaks for graphite, which confirms the absence of oxygenated functional groups from the starting material.

In graphene oxide, we observe characteristic peaks corresponding to the $-\text{OH}$ at $3200-3600\text{ cm}^{-1}$, C=O at $1670-1820\text{ cm}^{-1}$ and $-\text{COC}$ at $1000-1300\text{ cm}^{-1}$, which are the usual defects 2-dimensional sheet of graphene oxide. In GQDs, we observe only peaks corresponding to the $-\text{OH}$ at $3200-3600\text{ cm}^{-1}$, C=O ($1670-1820\text{ cm}^{-1}$) which are indicative of $-\text{COOH}$ terminating edges of GQDs. These $-\text{COOH}$ groups further play important role in binding with calcium ions. Fig. 2(B) shows the fingerprint region of IR for as prepared and Ca(II) interacted GQDs. It clearly shows the

presence of P-O bending and rocking vibrations at 610 cm^{-1} and 627 cm^{-1} [14], which are absent in as prepared GQD. This indicates the successful binding of GQDs to Ca(II) ion through phosphate.

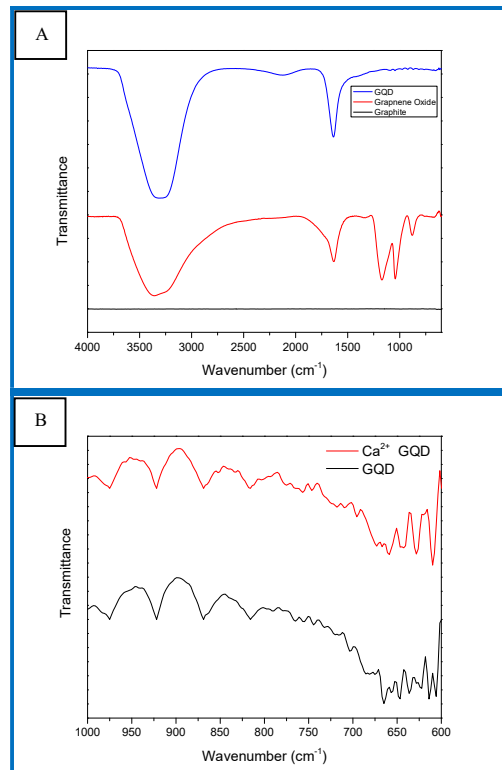


Figure 2: (A) FTIR spectra of Graphite, Graphene Oxide and GQDs, (B) Finger print region of GQD and $\text{Ca}^{(II)}$ interacted GQD

As discussed earlier, Luminescence is a very important property for quantum dots. GQDs prepared herewith showed typical blue luminescence. Fig. 3(A) shows the observed difference in intensity of luminescence of as prepared GQDs and Ca(II) interacted GQDs. Fig. 3(B), shows the PL spectra of as prepared GQDs (at 1.5 nm slit width) and Ca(II) interacted GQDs (at 2 nm slit width) and it is evident that luminescence of GQDs have drastically quenched due to interaction with Ca(II). The slit width was varied in order to achieve appreciable luminescence intensity in Ca(II) interacted GQDs. It is inferred that the long-range conjugation of GQDs around Ca(II) ions which relieves the excitonic barrier is responsible for the photoluminescence quenching in Ca(II) interacted GQDs.

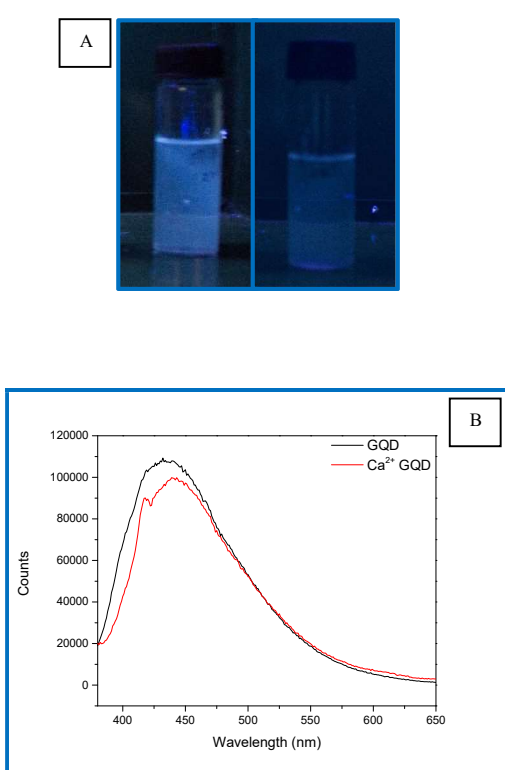


Figure 3: (A) GQD and Ca(II) interacted GQD under 365nm irradiation (left and right respectively), (B) PL spectra of GQD (1.5nm slit width) and Ca(II) interacted GQD (2nm slit width) at 365nm excitation

CONCLUSIONS

From the above study, we may arrive at following conclusions:

- GQDs are well synthesized via Hydrothermal cutting of GO sheets and this reduction in size leads to the excitonic entrapment within the GQDs structure leading to its semiconducting non-zero band gap and subsequent photoluminescence.
- Ca(II) interact with GQD core via phosphate linkage which is generally available salt of calcium in water bodies.
- The quenching of PL observed in Ca(II) interacted GQDs is due to long range conjugation around Ca(II) ions which relax excitonic barrier.
- This PL quenching may well be used in utilized in fast sensing of calcium.

ACKNOWLEDGEMENTS

The author, Mr. Praveen Mishra would like to acknowledge National Institute of Technology for extending the research fellowship.

REFERENCES

- [1] Hamilton, Irma P., et al. "Alignment of colloidal graphene quantum dots on polar surfaces." *Nano letters* 11.4 (2011): 1524-1529.
- [2] Tang, Libin, et al. "Deep ultraviolet photoluminescence of water-soluble self-passivated graphene quantum dots." *ACS nano* 6.6 (2012): 5102-5110.
- [3] Li, Yan, et al. "Nitrogen-doped graphene quantum dots with oxygen-rich functional groups." *Journal of the American Chemical Society* 134.1 (2011): 15-18. APA
- [4] Wang, Xiaojuan, et al. "Multifunctional graphene quantum dots for simultaneous targeted cellular imaging and drug delivery." *Colloids and Surfaces B: Biointerfaces* 122 (2014): 638-644.
- [5] Benítez-Martínez, S., and M. Valcárcel. "Graphene quantum dots in analytical science." *TrAC Trends in Analytical Chemistry* 72 (2015): 93-113.
- [6] Zhao, Jing, et al. "Graphene quantum dots-based platform for the fabrication of electrochemical biosensors." *Electrochemistry Communications* 13.1 (2011): 31-33.
- [7] Li, Li, et al. "Paper-based electrochemiluminescence immunodevice for carcinoembryonic antigen using nanoporous gold-chitosan hybrids and graphene quantum dots functionalized Au@ Pt." *Sensors and Actuators B: Chemical* 202 (2014): 314-322.
- [8] Zhang, Qi, et al. "Photoluminescent sensing for acidic amino acids based on the disruption of graphene quantum dots/europium ions aggregates." *Biosensors and Bioelectronics* 65 (2015): 204-210.
- [9] Mazloum-Ardakani, Mohammad, et al. "Fabrication of modified glassy carbon electrode using graphene quantum dot, gold nanoparticles and 4-((4-mercaptophenyl) imino) methyl benzene-1, 2-diol by self-assembly method and investigation of their electrocatalytic activities." *Journal of Electroanalytical Chemistry* 738 (2015): 113-122.
- [10] Razmi, Habib, and Rahim Mohammad-Rezaei. "Graphene quantum dots as a new substrate for immobilization and direct electrochemistry of glucose oxidase: application to sensitive glucose determination." *Biosensors and Bioelectronics* 41 (2013): 498-504.
- [11] Wang, Xindong, et al. "Electrochemical immunoassay with graphene quantum dots and apo ferritin-encapsulated Cu nanoparticles double-assisted signal amplification for detection of avian

6th International Engineering Symposium - IES 2017

March 1-3, 2017, Kumamoto University, Japan

leukosis virus subgroup J." Biosensors and Bioelectronics 47 (2013): 171-177.

[12] Marcano, Daniela C., et al. "Improved synthesis of graphene oxide." ACS nano 4.8 (2010): 4806-4814.

[13] Pan, Dengyu, et al. "Hydrothermal route for cutting graphene sheets into blue - luminescent graphene quantum dots." Advanced materials 22.6 (2010): 734-738.

[14] Bertoluzza, Alessandro, et al. "Hydrogen bonds in calcium acid phosphates by infrared and Raman spectra." Journal of molecular structure 127.1-2 (1985): 35-45.

Optimization of lipase mediated enrichment of n-3 PUFA glycerides in Indian Sardine oil

Charanyaa Sampath¹, Prasanna D Belur² and Regupathi I³

¹ Department of Chemical Engineering, National Institute of Technology, Karnataka, Mangalore 575025, India. e-mail: charansampath.2853@gmail.com

² Department of Chemical Engineering, National Institute of Technology Karnataka, Surathkal, Mangalore 575025, India. email: prsnbhat@gmail.com

³ Department of Chemical Engineering, National Institute of Technology Karnataka, Surathkal, Mangalore 575025, India. email: ponregu@gmail.com

ABSTRACT: Indian Sardine oil is a rich source of n-3 polyunsaturated fatty acids (n-3 PUFA) such as eicosapentaenoic acid (EPA) and docosahexaenoic acid (DHA), which exists in the form of glycerides. The current work aims to optimize a process to enhance n-3 PUFA esters in the refined sardine oil by optimizing the enzymatic hydrolysis of glycerides having saturated fatty acid esters, using *Pseudomonas cepacia* lipase (PCL). Degree of hydrolysis (DOH) of PCL dissolved in solvent (polypropylene glycol) in the presence of surfactants like tween 80 and SDS was observed to be the highest at 40°C, 6 mg/mL enzyme load, surfactant to enzyme ratio of 2:1 (v/v), oil to water ratio of 1:1 (w/w), hydrolyzed for 15 minutes. After hydrolysis, oil was deacidified using a two-step methanolic extraction. Upon analysis of oil by using Gas Chromatography with FID, an increase in n-3 PUFA content from 17.91% (w/w) to 39.32% (w/w) was evidenced. RP-HPLC equipped with ELSD showed that most of the fatty acids exist in the form of monoglycerides.

Keywords: Docosahexaenoic acid, ELSD, Eicosapentaenoic acid, Indian Sardine oil, hydrolysis, *Pseudomonas cepacia* lipase.

INTRODUCTION

The beneficial effects of n-3 polyunsaturated fatty acids (n-3 PUFA) in the prevention and treatment of coronary, neuromuscular, immunological disorders and allergic conditions are well documented(Nettleton and Katz, 2005). Oil extracted from several pelagic fishes are found to be the rich source of n-3 PUFA. In order to meet the increasing demands of PUFA concentrates, industries have employed various techniques which lead to the production of PUFA concentrates in the form of free fatty acids which is nutritionally unfavourable and acts as the precursors for the initiation of oxidation in the oil (Wanasundara and Shahidi, 1998). These techniques are known to involve extremes of pH and temperature which may destroy the natural n-3 PUFA by oxidation, *cis-trans* isomerization and

double bond migrations (Halldorsson et al.,2004). Use of lipases for hydrolysis has been a reliable technique to concentrate important n-3 PUFA like eicosapentaenoic acid (EPA) and docosahexaenoic acid (DHA) due to the mildness it offers during the course of reaction in terms of temperature, pH and pressure which most certainly prevents the n-3 PUFA from destruction. Also, few lipases exhibit strong preferences for EPA and DHA. Much has been published on hydrolysis by using lipases to concentrate EPA and DHA in the fish oil. (Wanasundara and Shahidi,1998; Halldorsson et al.,2004). Nevertheless, not many literatures are available on hydrolysis of Indian Sardine oil using *Pseudomonas cepacia* (PCL). In the current study, n-3 PUFA enriched glycerols from Indian Sardine oil via hydrolysis using PCL was attempted.

6th International Engineering Symposium - IES 2017

March 1-3, 2017, Kumamoto University, Japan

Further, HPLC was performed to find out the form of concentrates in the oil.

MATERIALS AND METHODS

Materials and solvents

Crude fish oil acquired from Mukka Fish Oil Industries (Mangaluru, India) was centrifuged and stored at 4°C in the dark. Orthophosphoric acid (OPA), methanol, activated charcoal, iso propanol, acetonitrile, n-hexane, ethanol, diethyl ether, sodium hydroxide, hydrochloric acid, boron trifluoride in methanol (10%). *Pseudomonas cepacia* lipase (PCL) and glyceride standard for HPLC was purchased from Sigma Aldrich, India. All the reagents (analytical grade) and solvents (chromatographic grade) were purchased from Merck, India and used without further purification.

Methods

Refining of Crude fish oil, obtained from Mukka Fish Oil Industries (Mangaluru, India) was taken for the study. Different quantities of PCL (2mg, 4mg, 6mg, 8mg, 10mg) were dissolved in 1 mL of various solvents (hydrophobic and hydrophilic), followed by the addition of various surfactants (non-ionic, anionic and cationic) to the enzyme solution. Various parameters like dilution of surfactants (2%, 4%, 6%, 8%, 10%) and quantity of surfactants in enzyme solution (2:1, 4:1, 6:1, 8:1, 10:1) (v/v) were optimized.

Effect of mixed surfactants

This experiment was performed according to Kawase et al. (1985).

Lipase-catalysed hydrolysis of sardine oil.

The reaction system containing 1 g of fish oil and 1 g of water (1:1 w/w) were placed in the conical flask under constant stirring at 300 rpm after which lipase preparations were added to these homogenized substrates to start hydrolysis reaction. The degree of hydrolysis was studied by subjecting the system to the variations in the parameters like temperature (30°C, 40°C, 50°C, 60°C), oil-water ratio (1:1, 1:2, 1:3, 1:4, 1:5), concentration (2mg/mL, 4mg/mL, 6mg/mL, 8mg/mL, 10mg/mL) of lipase and time of hydrolysis (15 minutes, 30 minutes, 45 minutes and 60 minutes).

Analysis

The degree of hydrolysis (DOH) was determined by measuring the acid value of both hydrolyzed and unhydrolyzed oil as well as the saponification value of the unhydrolyzed oil. The hydrolysis was performed under the optimized reaction conditions of PCL for 15 minutes and the reaction was stopped by adding 10 ml of ethanol. The hydrolyzed oil was subjected to methanol extraction in the ratio (1:1 w/w) oil to methanol, to eliminate the FFA released during the process. The solvent extracted oil (hydrolyzed) was studied for its fatty acid composition through GC which was compared with the fatty acid composition of the refined oil measured before hydrolysis. Hydrolysis was done under vacuum conditions in order to prevent oxidation of oil. The acid value of oil was calculated according to the official method of American Oil Chemist's Society (AOCS) (2009) methodologies, (Cd3d-63).

Determination of fatty acid composition in oil.

After the solvent was evaporated and dried, the residue was esterified with boron trifluoride methanol agent and analyzed by gas chromatography using the guidelines from Ichihara and Fukubayashi (2010).

Determination of the form of glycerides in the hydrolysed oil

To analyze the contents of TG, DG, MG after the hydrolysis reactions, the reaction products were analysed by HPLC on RPC18 column in accordance with Aoki T et al. (2004).

RESULTS AND DISCUSSIONS

The competence of lipase for the fatty acid selectivity such as EPA and DHA has allowed the separation of these fatty acids from the remaining fatty acids in fish oils, resulting in the increased yields of n-3 PUFA rich concentrates and hence, in the present study, the DOH was studied under various conditions with the aim of obtaining elevated amounts of EPA and DHA in the hydrolysed oil with the minimum production of unwanted impurities that may develop during hydrolysis. The hydrolysis was performed with the refined sardine oil with the composition as mentioned in Table 1.

6th International Engineering Symposium - IES 2017

March 1-3, 2017, Kumamoto University, Japan

Modification of lipases

PCL was treated with a concoction of solvents and surfactants with the purpose of increasing the DOH of the enzyme in the oil.

Effect of solvents on PCL.

From Fig.1 it is clear, when PCL was treated with 1 mL of various solvents there was an increase in DOH in the presence of polypropylene glycol (PPG) as compared to the other solvents. The reason for the increased hydrolysis by PCL dissolved in PPG is probably because of the neutral pH of this solvent in which PCL remains active due to the presence of residues of amino acids at the active site of PCL which result in maximum binding of the substrate. Studies by Iyer and Ananthanarayan (2008), explained that the addition of polyols like PPG to the enzyme strengthens the hydrophobic interactions among the non-polar amino acid residues which lead to protein rigidification and resistance to thermal deactivation. Pencreach (1997) reported that PCL is optimally active at pH 7.0 (neutral) which is in concurrence with the present study.

Effect of PCL concentration on DOH

It was noticeable that the DOH at 4mg/mL was recorded to be the highest (10.1%) after which the trend slowed down with the increase in enzyme concentration (Fig.2). It could be reasoned out that beyond 4mg/mL, the oil-lipase solution interface generated under these conditions gets saturated with lipase and there is a formation of monolayer at the interface and accumulated intermediates (Pongket et al.,2015). Therefore, further studies were carried out using a 4 mg/mL of PCL.

Protective effect of surfactant mixture

In order to protect the lipase from a huge decrease in the hydrolysis ability, the effects of mixture of non-ionic surfactants and anionic surfactants were studied. When the oil was treated with PCL, in presence of tween 80 and SDS, the DOH was 10.93% and 10.1% respectively. It is evident that DOH in oil by tween 80 is higher than SDS which could be because of the slight inactivation of lipase by SDS. When tween 80 was added first and SDS after ten minutes to PCL solution, the DOH was found to have increased to 11.04%. This increase in the hydrolysis efficiency

proves not only the combined positive effect of the surfactants on the activity of PCL, but also the protective effect of tween 80 as opposed to SDS. Non-ionic surfactants in general are considered as mild detergents and they do not extensively interact with the protein structure.(Salameh and Wiegel.,2010). Hence a mixture of tween 80 and SDS were used for the further studies.

Effect of dilution of surfactants

It's evident from Fig.3 that at 8% of mixed surfactants (4% tween 80 and 4% SDS) with PCL showed a maximum DOH of 10.36% respectively. Beyond 8% of mixed surfactants, a drastic reduction in DOH was observed which is due to the increased concentration of tween 80 and SDS in the system causing the partial or complete unfolding of the tertiary structure of the protein due to the additional hydrophobic interactions. (Otzen.,2002). Mogensen et al. (2005) contends the deactivation of lipase in the presence of nonionic and zwitterionic surfactants at high concentrations.

Effect of surfactant to enzyme ratio (v/v)

It is seen that 2:1 (v/v) of mixed surfactants to PCL, promoted the highest DOH in the oil (Fig.4). Beyond this ratio, the DOH tends to decrease, which is attributed to the inhibitory effects of surfactants by impairing the lipase adsorption at liquid- water interfaces. (Delorme et al.,2011).

Effect of temperature

Trials to determine the maximum DOH for PCL were done at a temperature range of 30°C to 60°C, and it was perceived that PCL showed a maximum DOH of 10.9% at 40°C. However, a rapid decrease in the DOH was observed at the rest of the temperatures (Fig.5). This is due to the denaturation of the enzyme structure at these temperatures. The reaction rate of PCL increased from 25°C to 45°C, and remained constant at 50°C and decreased at higher temperatures (Pencreach et al.,1997).

Effect of amount of water for hydrolysis on DOH.

Since lipases are known to cleave the ester bonds of triglycerides with the utilization of

6th International Engineering Symposium - IES 2017

March 1-3, Kumamoto University, Japan

water molecules, it becomes essential to study the amount of water required for hydrolysis. From the Fig.6 it was apparent that the DOH was highest at the oil to water ratio of 1:1 (w/w). The ratios above 1:1 (w/w) showed lesser activities because higher quantity of water leads to a thicker water layer around PCL which increases the flexibility of the lipases, causing denaturation. (Sharma et al.,2014).

Effect of time on DOH of PCL

Figure. 7 shows the time course of hydrolysis of PCL. PCL were shown to give maximum DOH at 15 minutes. It is clear from the trend in figure that initially with increase in time the product formation was increased up to 15 min. A further increase in time up to 1 hour did not lead to any improvement in the product formation. This may be due to the attainment of equilibrium for PCL in terms of the conversion rates (Halldorsson et al.,2004). The maximum was achieved in a shorter reaction time with high EPA and DHA content, maybe because of the lower amounts of fatty acids in the oil to be removed (Table 1).

Enhancement of n-3 PUFA in oil.

After hydrolysis with PCL there was an increase in the EPA (26.26%) and DHA(13.06%) from EPA (11.81%) and DHA (6.1%) in the refined oil. It was observed that PCL resulted in the concentration of EPA almost in the same rate as DHA. These results concur with the observations made by Halldorsson et al.,2004 in concentration of EPA and DHA in sardine oil.

Analysis of the hydrolyzed oil by HPLC

Having studied the EPA and DHA content in the hydrolysed and unhydrolyzed oil, we were also interested in testing these oil samples to have an idea of the form of fatty acid glycerides. Figure.8 reveals the differences among the hydrolyzed oil, unhydrolyzed refined oil and the HPLC standards. Interestingly, it was observed that the hydrolyzed oil contained pronounced quantities of monoglycerides with the drastic reduction in the diglycerides and the triglyceride forms of fatty acids.

It can be derived from the GC and HPLC results that the DOH exhibited by PCL in sardine oil having C16:0 as the most

predominant fatty acid proved to be a good substrate for hydrolysis. The high DOH of PCL can be explained because of the non-specificity of the enzyme to a particular fatty acid and secondly, the anatomy of the fatty acid binding sites. PCL is known to have a crevice-funnel shaped substrate binding sites which accommodates bulky substrates and results in the hydrolysis of triglycerides in sardine oil (Kapoor and Gupta, 2012). The efficiency of the hydrolysis can be visualised in the HPLC chromatograms where the reduction in the concentrations of triglycerides and diglycerides to the respective monoglycerides were evident.

CONCLUSIONS

The following conclusions are deduced from this study:

- There was a dramatic increase in the n-3 PUFA content (2.19 times) in hydrolysed oil compared to the unhydrolysed oil.
- DOH carried out by PCL is significantly influenced by a combination of solvents and surfactants
- Hydrolysis of the oil for 15 minutes led to significant increase in the n-3 PUFA concentrate for the use in nutraceuticals.

ACKNOWLEDGEMENTS

Authors would like to thank SERB,MOFPI, Govt. of India for financial support (SERB/MOFPI/0016/2012).

REFERENCES

- [1] AOCS. (2009), Official Methods and Recommended Practices of the American Oil Chemists' Society, Sampling and analysis of fats and oils.
- [2]Aoki,T.,Otake,I.,Gotoh,N.,Noguchi,N.,Wada,S.(2004), Quantification Method For Triglyceride Molecular Species in Fish Oil with High Performance Liquid Chromatography- Ultraviolet Detector, Journal of Oleo Science. Vol 53. No.6,pp. 285-294.
- [3]Delorme,V.,Dhouib,R.,Canaan,S.,Fotiadu,F.,Carrier e,F.,Cavalier,J.F.(2011), Effects of Surfactants on Lipase Structure, Activity, and Inhibition, Pharmaceutical Research, Vol.28,No.8,pp.1831-1842.
- [4]Halldorsson,A.,Kristinsson,B.,Haraldsson,G.(2004), Lipase selectivity toward fatty acids commonly found in fish oil, European Journal of Lipid Science and Technology.Vol, 106, No.2,pp. 79-87.
- [5] Ichihara K., Fukubayashi Y.(2010), Preparation of fatty acid methyl esters for gas-liquid chromatography, Journal of Lipid Research Vol.51, No.3,pp. 635-640.
- [6] Iyer P.V., Ananthanarayan,L. (2008), Enzyme stability and stabilization- aqueous and non-aqueous environment, Process Biochemistry, Vol.43,No.10,pp. 1019-1032.

6th International Engineering Symposium - IES 2017

March 1-3, 2017, Kumamoto University, Japan

- [7] Kapoor,M.,Gupta.M.N(2012), Lipase promiscuity and its biochemical applications, Process Biochemistry, Vol. 47, No.4, pp.555–569.
- [8] Kawase,T.,Hashimoto,T., Fujii,F., Minagawa, M.(1985), Studies on the Effects of Surfactants on Lipase Activity, Oil chemistry. Vol.34, No.7, 530-538.
- [9] Mogensen JE, Sehgal P, Otzen DE.(2005). Activation, inhibition, and destabilization of *Thermomyces lanuginosus* lipase by detergents, Biochemistry, Vol.44, No.5, 1719-1730.
- [10] Nettleton, J. A.,Katz, R. (2005), n-3 long-chain polyunsaturated fatty acids in type 2 diabetes: a review, Journal of the American Dietetic Association, Vol. 105, No.3,pp. 428-440.
- [11] Otzen D.(2002), Protein unfolding in detergents: effect of micelle structure, ionic strength, pH, and temperature, Biophysical Journal, Vol.83, No.4,pp.2219-2230.
- [12] Pencreach,G., Leullier,M., Baratti.J.C.(1997), Properties of Free and Immobilized Lipase From *Pseudomonas cepacia*, Biotechnology and Bioengineering,Vol.56, No.2,pp.181-189.
- [13] Pongketa,U.,Piyatheerawong,W.,Thapphasaraphong,S., Kittikun.A.H.(2015), Enzymatic preparation of linoleic acid from sunflower oil: an experimental design approach,Biotechnology and Biotechnological Equipment, Vol.25, No.5,pp.926-934.
- [14] Salameh,M.A.,Wiegel.J.(2010), Effects of Detergents on Activity, Thermostability and Aggregation of Two Alkalithermophilic Lipases from *Thermosyntropha lipolytica*, The Open biochemistry Journal, Vol.4,pp.22-28.
- [15] Sharma,A., Satyendra P., Chaurasia.,Dalai A.K.(2014), Non - Selective Hydrolysis of Tuna Fish Oil For Producing Free Fatty Acids Containing Docosahexaenoic Acid,The Canadian Journal of Chemical Engineering,Vol.92, No.2,pp.344-354.
- [16] Wanasinghe, U. N., & Shahidi, F. (1998), Lipase-assisted concentration of n 3 polyunsaturated fatty acids in acylglycerols from marine oils, Journal of American Oil Chemist's Society, Vol. 75, No. 8,pp. 945-951.

Table 1 Composition of refined Indian Sardine oil

Parameters	Values
Free fatty acid (% oleic acid)	0.56%
Phospholipid (ppm)	5.66
Iron (ppm)	BDL*
Copper (ppm)	0.1
Mercury (ppm)	BDL*
Fatty acids (% w/w)	
C _{14:0}	26.18
C _{16:0}	46.87
C _{18:1}	5.06
C _{18:2}	5.76
C _{20:5} (EPA)	11.81
C _{22:6} (DHA)	6.1

* BDL-Below detection limit

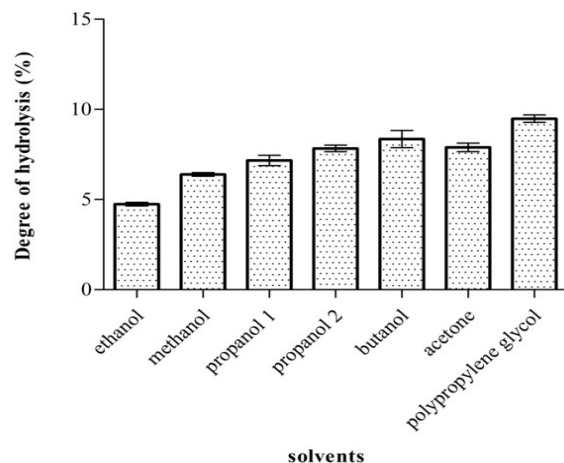


Fig. 1 Effect of solvents on PCL and its DOH in Sardine oil

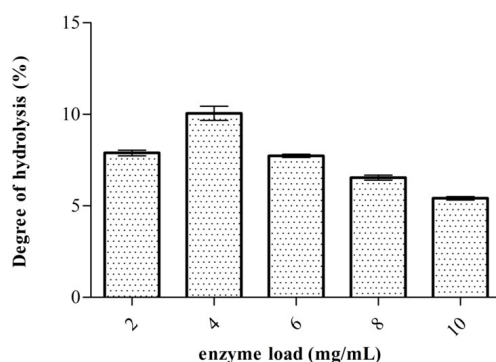


Fig. 2 Effect of PCL load on DOH

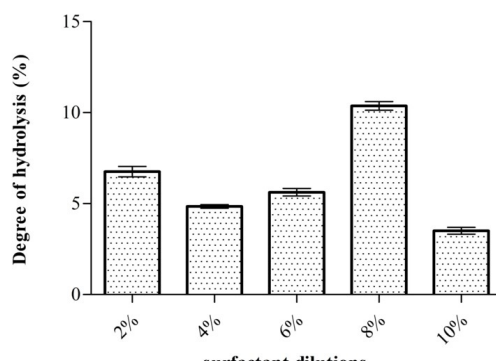


Fig. 3 Effect of dilutions of mixed surfactants on PCL and its DOH

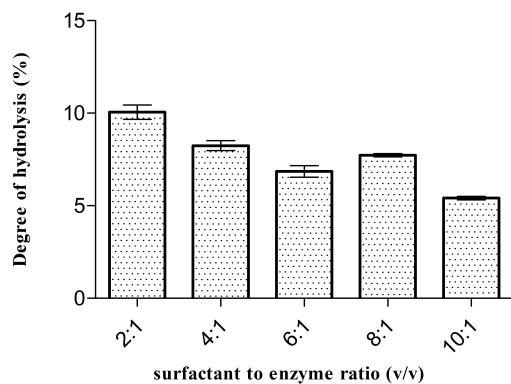


Fig. 4 Effect of quantity of surfactants to PCL (v/v) and its DOH

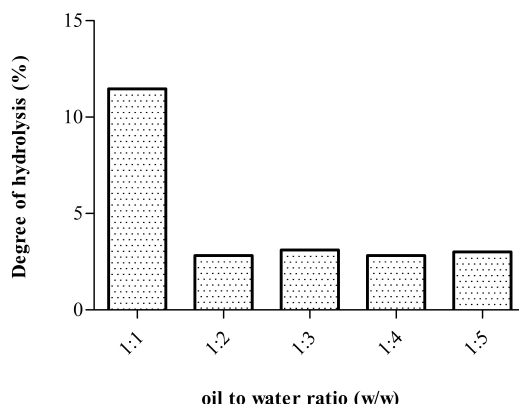


Fig. 6 Effect of quantity of water on DOH

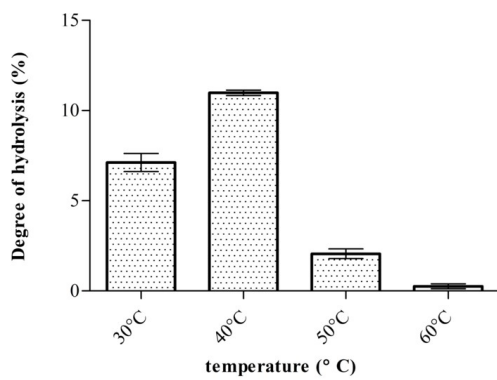


Fig. 5 Effect of temperature on DOH

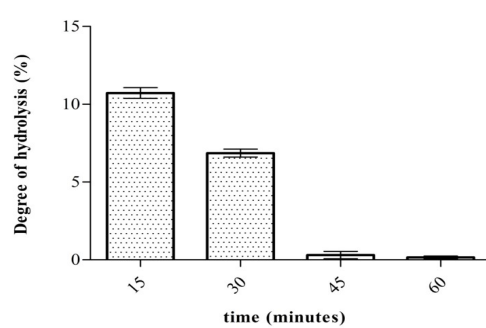


Fig. 7 Effect of time on DOH

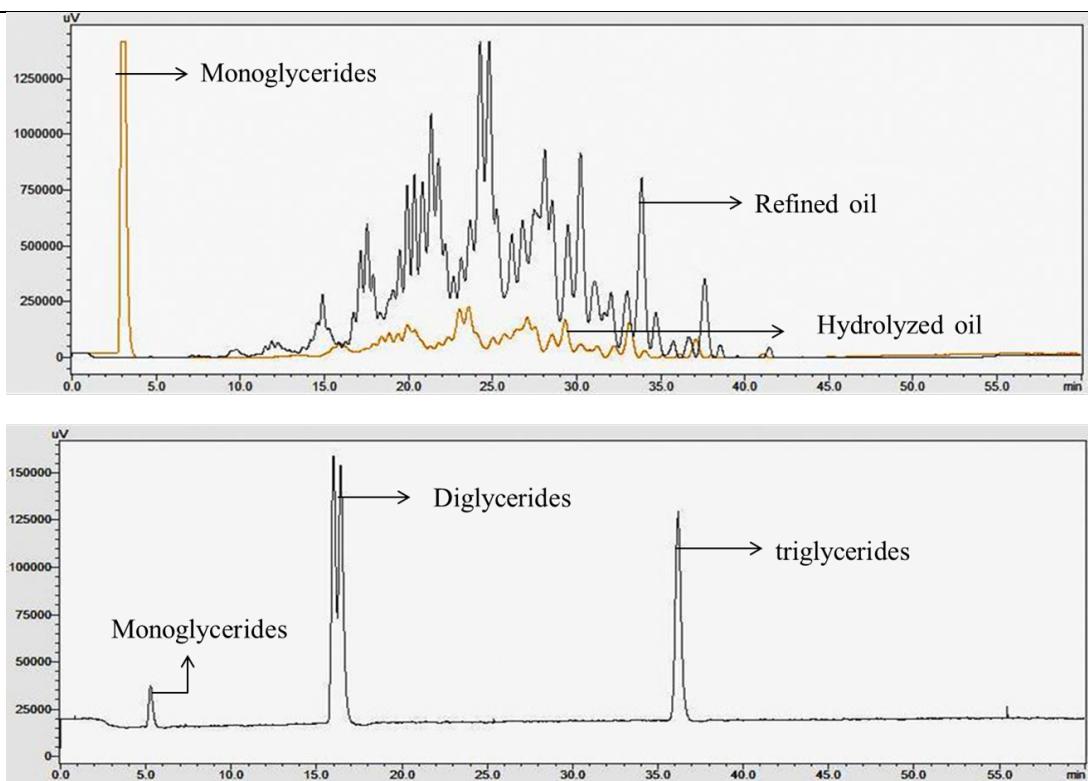


Fig.8 HPLC chromatograms of oil before and after hydrolysis and HPLC glyceride standards.

Ultrasound assisted synthesis of γ -MPS modified HNTs-Polystyrene Nanocomposites by Miniemulsion Polymerization

Kezia Buruga ¹ and Jagannathan. T. K ²

¹ Department of Chemical Engineering, National Institute of Technology Karnataka, Surathkal, Mangalore 575025, India. email:kezia.nitk@gmail.com

² Department of Chemical Engineering, National Institute of Technology Karnataka, Surathkal, Mangalore 575025, India. email:jagantk@gmail.com

ABSTRACT: Halloysite nanotubes (HNTs) were modified by γ -methacryloxypropyl trimethoxysilane (MPS) to improve its interaction with polymers and was subsequently used for the synthesis of HNT-polystyrene nanocomposites by miniemulsion polymerization carried out with the aid of ultrasound. The exfoliation of HNTs into the polymer matrix was confirmed by the presence of characteristic peaks of HNT in the Fourier transform and infrared spectroscopic analysis. The decrease in intensity of significant peaks in X-ray diffraction analysis also confirmed the same. Scanning electron microscopy analysis revealed relatively fine distributed morphologies also, there was reduction in aggregation of HNTs as a result of modification. Differential scanning calorimetry analysis showed significant improvement in glass transition temperature (T_g) of the nanocomposites. Zeta potential analysis confirmed the particles were in nanoscale and possess good stability in emulsion. Modification of HNTs together with miniemulsion polymerization assisted by ultrasound proves to be a promising technique to accomplish better dispersion of particles in polymer matrix and to obtain nanocomposites with unique and enhanced properties.

Keywords: Halloysite Nanotubes (HNTs), Ultrasonication, Miniemulsion polymerization, Morphology, Thermal stability.

INTRODUCTION

In recent years polymer nanocomposites reinforced with inorganic nanoscale materials such as metal nanoparticles, carbon nanotubes and layered silicate clays have attracted tremendous interest in both industrial and academic researchers. These nanomaterials have size less than 100 nm in at least one dimension, and therefore, they have high aspect ratio and extremely large surface area, incorporation of these materials into the polymer matrix improves various polymer properties due to better interaction between filler and polymer. Also, these materials combine the properties of organic and inorganic materials together which results in overall property enhancement, these unique and

fascinating properties extends their usage in various commercial sectors.

Halloysite nanotubes (HNT) belongs to class of aluminosilicate clay with hollow nanotubular structure with inner and outer diameter varying between 10-30 nm and 30-80 nm respectively and length varying between 1-3 μ m. Recently, these materials have been reported to be used as nanofillers in polymers such as natural rubber, nitrile rubber and polypropylene, the incorporation of HNTs in a polymer greatly improved the mechanical, thermal stability and flame retardancy of the nanocomposites significantly Du et al. (2006). End properties of nanocomposites greatly rely on filler properties, preparation techniques and polymer chemistry Zhao et al. (2008). Uniform dispersion of nanofillers, and its interaction

6th International Engineering Symposium - IES 2017

March 1-3, 2017, Kumamoto University, Japan

with the polymer matrices plays a very crucial role in determining the overall properties of nanocomposites, one way to achieve this is to modify the surface of filler with small organic molecules or polymers, which in-turn improves the physical and chemical properties of nanosurfaces, Bansal et al. (2006). Surface chemistry plays an important role in the overall performance of nanoparticles, better understanding of the surface chemistry of filler and its modification helps to improve their performance and to develop new applications. Also, the presence of covalent bonds between the nanofillers and polymer matrices could considerably improve thermomechanical properties of the resulting polymer nanocomposites. HNTs have a different structure on their outer and inner lumen surfaces. HNTs' inner lumen surface consists of Al-OH octahedral sheet, and outer surface consists of Si-O-Si groups. Therefore the inner surface of HNTs is chemically active, and the outer surface is regarded as nonreactive. However, some hydroxyl groups (Al-OH or Si-OH) existing on external surfaces within the edges and defects provide active sites for chemical reactions. Hence, in the present work we have modified the surface of HNTs by chemical functionalisation using silane treatment.

Nanocomposites synthesis techniques also plays a major role in overall property enhancement. Nanocomposites can be synthesised using various methods, Noh and Lee (1999) followed emulsion polymerization, Xie et al. (2003) carried out suspension polymerization, Bottcher and Hallensleben (2002) followed living free radical polymerization. But among these various techniques, emulsion more specifically miniemulsion polymerization has emerged as a convenient alternative technique as it is capable of synthesizing nanoparticles dispersed in continuous phase for encapsulation purposes. Conventionally mini-emulsions are aqueous dispersions of mini droplets with a size less than 500 nm. They are fabricated at high shears in a system containing oil, water and surfactant. A highly water-insoluble compound such as hexadecane or cetyl alcohol is used as co-surfactant to

suppress Ostwald ripening of the droplets Landfester et al. (1999). This aids in obtaining particles in the desired size range. Additionally, ultrasonic cavitations can produce high temperature and high pressure and a rigorous environment for chemical reaction to occur Li et al. (1999). Under these rigorous conditions, free radicals are produced due to decomposition of surfactant, monomer and water or rupture of polymer chains to initiate the polymerization of monomer Borthakur, L J et al. (2010). In this present work we reported modification of HNT with γ -MPS and reinforced these into polystyrene by miniemulsion polymerization. The effect of the HNT modification on the thermal stabilities of the resulting nanocomposites is also discussed. HNT modification is being reported in literature, also, synthesis of polymer-HNT nanocomposites by miniemulsion polymerisation is also reported kezia et al (2017). But the use of these modified HNTs in polystyrene by miniemulsion polymerisation and the effect of surface modification on increasing interaction between polymer and filler and improvement in properties has not been investigated hence we have reported it in this paper.

EXPERIMENTATION

Materials

Halloysite nanotubes, styrene and γ -methacryloxypropyl trimethoxysilane (MPS) have been procured from sigma Aldrich, Span-60 and sodium dodecyl benzene sulfonate (SDBS) were used as surfactant and were received form CDH and Rolex respectively. Hexadecane was provided by Sigma Aldrich. The initiator 2,2-azo-isobutyronitrile (AIBN) was procured from Kemphasol. Deionised water was used for carrying out all the experiments and inert atmosphere was maintained using nitrogen for all the reactions.

Modification of HNT using γ -methacryloxypropyl trimethoxysilane

For modification of HNT, 40 ml ethanol was poured into 100 ml beaker, 4 ml γ -MPS was added to it and was sonicated for 10 min at 50% amplitude and pulse time of

6th International Engineering Symposium - IES 2017

March 1-3, Kumamoto University, Japan

3s on and 2 s off. 10 g of HNT was added to this and sonicated again for 30 min, the suspension was then magnetically stirred for 30 min and centrifuged for 20 min at 10000 RPM. Supernatant was separated and the precipitated was dried in oven at 40 °C overnight and named as MPS-HNT.

Synthesis of HNT-Polystyrene nanocomposites by miniemulsion polymerisation

Mini-emulsion polymerization was carried out in a jacketed vessel with provisions for water circulation, N₂ inlet and temperature sensor. For experimentation 10 ml styrene, 0.5 g MPS-HNT and 50 ml water was magnetically stirred for 30 min and sonicated for 30 min and cooled to 0°C. 0.1 g SDBS, 0.1g Span-60, 0.1 ml hexadecane were sonicated for 30 min and added to previously prepared suspension and sonicated for 30 min. N₂ gas was purged for 15 min, heated to 70 °C and then 0.14g AIBN was added and allowed to polymerize for 7 h. Polymerization was inhibited by addition of 1 % hydroquinone solution. The milky solution was filtered and precipitate was dried in oven at 40° C overnight and characterized. The same experiment was carried out with γ-MPS modified HNT and without modification to study effect of modification of HNT on properties of nanocomposites.

CHARACTERISATION

X-ray diffraction (XRD) analysis was done in order to understand the detailed structure of nanocomposites, it was performed using Joel diffractometer with Cu-Kα ($\lambda=1.542 \text{ \AA}$) radiation. SEM analysis was carried out by JEOL-JSM-6360LV model to investigate morphology of the specimen. FT-IR analysis was done on BRUKER spectrometer using ATR mode of operation in spectral range of 4000–450 cm⁻¹. Zeta size and potential measurements were carried out on Horiba particle size analyzer. DSC was carried out on Perkin-Elmer Pyrus in the range between 0–300°C at heating rate of 10 °C min⁻¹ under nitrogen flow.

RESULTS AND DISCUSSIONS

Studies on structure of modified HNTs and synthesised nanocomposites

Fig.1 shows the diffraction patterns of HNT, γ-MPS and nanocomposites synthesised using HNT and γ-MPS modified HNT. It can be seen that there is slight increase in the d-spacing on modification of with γ-MPS, which indicates that there was slight intercalation of MPS into the interlayer of HNT, as most of the interlayer inner-surface Al-OH groups of HNT were unavailable for modification as they were blocked by the strong hydrogen bonds between layers. However surface hydroxyl groups of HNT was functionalised with MPS increased its dispersion by reducing the aggregates. A significant peak in MPS-HNT appeared at 2θ value of 11.89 indicating d-spacing of 7.44 Å, whereas this peak in the composite is shifted to a lower 2θ value as compared to that MPS-HNT. This reduction of 2θ and increase in the d-spacing of the HNTs is due to intercalation of the HNTs with the polymer. Further, it can be observed that nanocomposites synthesised on using MPS modified HNT showed a drastic decrease in sharp peaks and intensity on comparing with those synthesised without clay modification which indicates complete exfoliation of clay into the polymer matrix thus suggesting improved properties and clearly confirms the formation of nanocomposites. This clearly explains the role of HNTs modification on formation of nanocomposites. The presence of broad peak indicated the amorphous nature of polymer. Also, ultrasound energy further exfoliates HNTs into the polymer matrix. The intense energy produced during sonication aids in forming completely exfoliated structure.

Studies on morphology of modified HNTs

The SEM image of the untreated HNT Fig. 2a shows tubular nanostructure of the nanotubes. Whereas, on modification with MPS, the SEM micrographs revealed relatively fine distributed morphologies also, there was reduction in aggregation of HNTs as a result of modification (Fig. 2b). Intramolecular forces within the particles resulted in aggregation of particles whereas treatment γ-MPS i.e Fig. 2b caused decrease in agglomerates of HNTs, as the surface of HNTs was made

6th International Engineering Symposium - IES 2017

March 1-3, 2017, Kumamoto University, Japan

hydrophobic due absorption of silanes onto the surface of HNTs with their surface hydroxyl groups via chemical bonds.

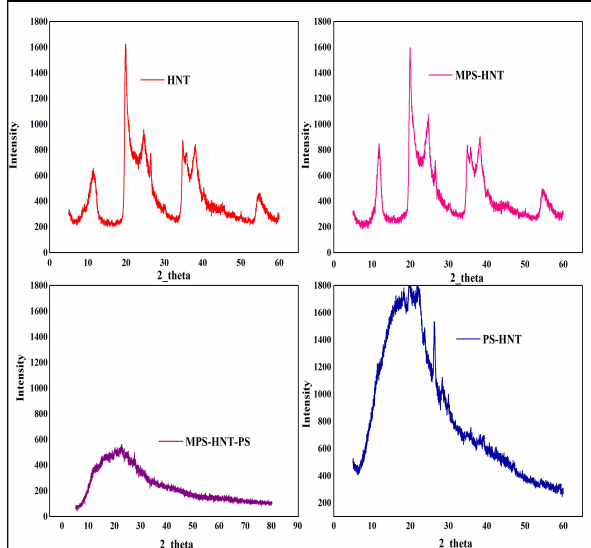


Fig.1 XRD image HNT, γ -MPS-HNT, MPS-HNT-PS and PS-HNT

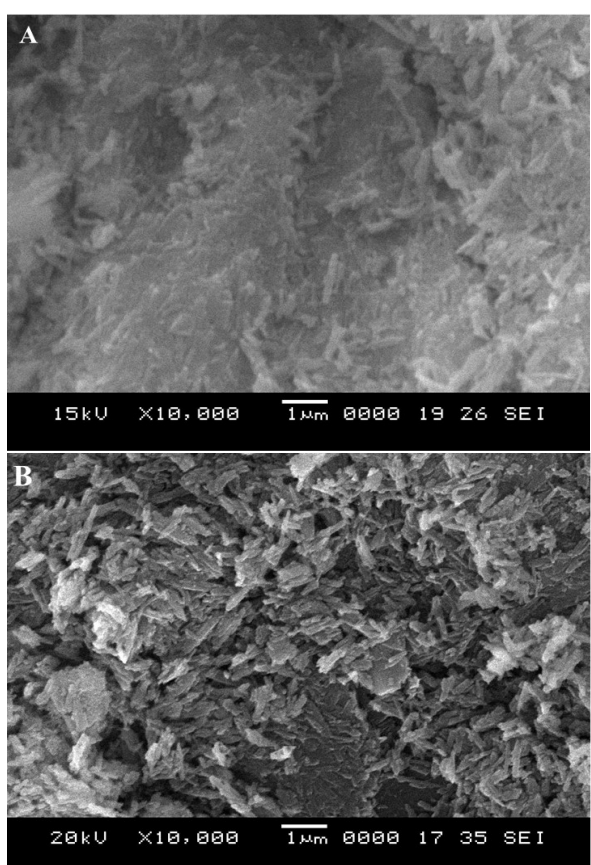


Fig.2 SEM micrographs A) HNT B) γ -MPS-HNT

Studies on functional groups of modified HNTs and synthesised nanocomposites

The surface modification of HNT was done using functional organic silanes (Fig. 3). γ -MPS displayed new FTIR bands at 1476.96 which is assigned to the scissoring of $(\text{CH}_2)_3$, wavenumbers at 1726.1 and 2959.96 cm^{-1} can be assigned C-O and C-H stretching vibration respectively. Also, in comparison with the FT-IR analysis of untreated HNT, the peak at 1726.1 cm^{-1} attributes to stretching vibration of C=O bond of MPS in the FT-IR spectrum of MPS-HNT this confirms the successful modification of HNT with silane γ -MPS. Further the presence of significant peaks of MPS-HNT in MPS-HNT-PS nanocomposite confirms the presence of MPS-HNT in the polymer matrix.

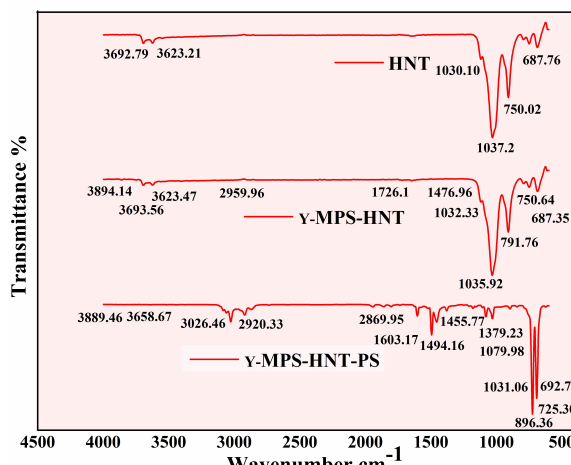


Fig.3 Fourier transform and infrared

Zeta Potential results

Zeta potential value indicates the stability and homogeneity of polymer nanocomposite latex. It can be observed from table.1 that the zeta potential value of the neat PS was -120.5 mV whereas on addition of HNTs the zeta potential values increased to -98.4 mV as HNTs have charged surfaces and can aid in stabilizing the emulsion, further on addition of MPS-HNT the stability increased to -73.5 mV. It can be observed that the zeta potential values of PS-MPS-HNT nanocomposite is well below that of virgin PS which indicates increase in latex stability. The reason for increase in latex stability is due to self-arrangement of the MPS-HNT and within the polymer particles which inturn influences the surface tension of latex and stabilizes the latex. From table.1 it can

also be observed that there was decrease in the particle size of nanocomposites on modification of HNT and use of ultrasound, because surface modification combined with ultrasound together aided in reduction of particle aggregates.

Table. 1 Zeta potential and particle size of PS, HNT-PS and MPS-HNT-PS

Sample	Zeta Particle size	Zeta potential
PS	150	116.5
HNT-PS	110	-98.4
MPS-HNT-PS	78	-73.5

Studies on thermal properties of modified HNTs and synthesised nanocomposites

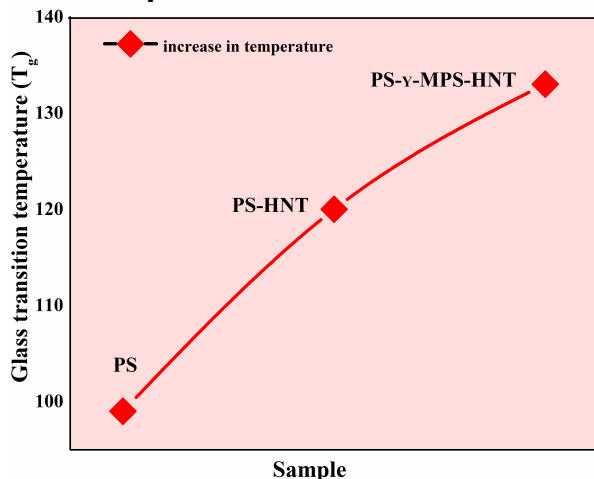


Fig. 4 DSC plot of polystyrene (PS), polystyrene-HNT (PS-HNT) and PS-y-MPS-HNT (PS-y-MPS-HNT)

DSC analysis was done to investigate thermal properties of nanocomposites. It can be seen from fig. 4 that there was increase in T_g on inclusion of HNT into polymer matrix. T_g of virgin PS, PS-HNT were estimated to be 99 °C and 119 °C respectively, whereas T_g of PS-MPS-HNT was 134 °C. PS-MPS-HNT nanocomposites showed higher T_g than that of pure PS and PS-HNT, the T_g is evidently improved. Functionalization improves intercalation of polymer chains between the layers due to incorporation of appropriate organic links between the polymer matrix and the nanofiller. Also, there is reduction in surface energy of silane treated clay which facilitates macromolecule access between

the layers of clays which restricts the movement of intercalated polymer chains between the sheets of the HNT, which prevents the segmental motions of the polymer chains. Another reason for increase in T_g is uniform distribution of HNTs on modification with MPS which creates tortuous path for heat to pass through it thus enhancing thermal properties.

CONCLUSIONS

In this work the surface of HNT was propitiously modified by γ -methacryloxypropyl trimethoxysilane. After modification these modified filler was reinforced into polystyrene matrix by miniemulsion polymerisation technique which was assisted by ultrasound. FT-IR results clearly showed the presence of characteristic HNT peaks in the polymer which confirms its presence in polymer. XRD results showed that there was no prominent shift in the basal spacing specifying that very little amount of MPS was intercalated into the interlayers of HNT, but the surface of HNT was modified. The presence of broad peak of synthesised nanocomposites displayed amorphous nature of synthesised nanocomposite. SEM analysis showed reduction in aggregates as a result of surface modification and sonication. Zeta size and zeta potential analysis showed that the particles was in nanoscale and possessed good stability. DSC analysis showed improvement in thermal stability as a result of modification. Thus modification of HNTs together with miniemulsion polymerization assisted by ultrasound proves to be a promising technique to accomplish better dispersion of particles in polymer matrix and to obtain nanocomposites with unique and enhanced properties.

REFERENCES

- [1] Bansal, A et al. (2006), Controlling the Thermomechanical Properties of Polymer Nanocomposites by Tailoring the Polymer-Particle Interface, *Journal of Polymer Science: Polymer Physics*, Vol. 44, pp 2944-2950.
- [2] Borthakur, L J et al. (2010), Development of core-shell nanocomposite of poly (styrene-co-methyl acrylate) and bentonite clay by ultrasonic assisted

6th International Engineering Symposium - IES 2017

March 1-3, 2017, Kumamoto University, Japan

mini-emulsion polymerization, Materials Chemistry and Physics, vol. 124, pp 1182–1187.

[3] Bottcher, H and Hallensleben, M L (2002), Organic/inorganic hybrids by 'living'/controlled ATRP grafting from layered silicates, Material Chemistry, vol.12, pp 1351-1354.

[4] Du, M L et al. (2006), Thermal stability and flame retardant effects of halloysite nanotubes on poly(propylene), European Polymer Journal, Vol.42, pp 1362-1369.

[5] Kezia, B and Jaganathan, T K (2017), Sonochemical synthesis of poly(styrene-co-methylmethacrylate)-HNT nanocomposites by miniemulsion polymerisation, Materials, Energy and Environment Engineering Springer book publication, pp 59-69.

[6] Landfester, K et al (1999), Formulation and stability mechanisms of polymerizable miniemulsions, Macromolecules, vol. 32, 5222-5228.

[7] Li, C Y et al. (1999), Preliminary study on the degradation kinetics of agarose and carrageenans by ultrasound, Food Hydrocolloids, vol.13, pp 477-481.

[8] Noh, M W and Lee, D C (1999), Synthesis and characterization of PS-clay nanocomposites by emulsion polymerization, Polymer Bulletin, Vol. 42, pp 619-626.

[9] Xie, W et al. (2003), A study of the effect of surfactants on the properties of polystyrene-montmorillonite nanocomposites, Polymer Engineering Science, vol. 43 pp 214-222.

[10] Zhao, M and Liu, P (2008), Halloysite nanotubes/polystyrene nanocomposites via in situ bulk polymerization. Journal of Thermal Analysis and Calorimetry, Vol. 94, No.1, pp. 103-107.

Screening of Reverse micellar system for the extraction of Bovine Lactoferrin

Swapnali S. Pawar¹, Regupathi I² and Prasanna B. D³

1 Department of Chemical engineering, National Institute of Technology Karnataka, Mangalore- 575025, India. Email: swapnali1706@gmail.com

2 Department of Chemical engineering, National Institute of Technology Karnataka, Mangalore- 575025, India. Email: regupathi@yahoo.com

3 Department of Chemical engineering, National Institute of Technology Karnataka, Mangalore- 575025, India. Email: prsnbhat@gmail.com

ABSTRACT: Lactoferrin (LF) is a multifunctional and an iron-binding protein ($Mw \sim 77-80$ kDa) present in animal milk. It is an important additive used in milk based infant formula, cosmetics, health supplements, oral care products due to its unique biological attributes. Present global demand of LF is estimated to be around 2, 62,000 kg/year. Reverse micellar extraction, a selective extraction, can be an alternate for chromatography and simulated moving bed (SMB) technology as it overcomes all the difficulties like high process cost and scale-up. Present work focuses on the selection of suitable reverse micellar system by considering anionic (Bis (2-ethylhexyl) sulphosuccinate sodium salt), cationic (Cetyltrimethylammonium bromide) and non-ionic (Triton X 100) surfactants with organic solvents for the extraction of LF from the aqueous solution. All the RMSs were characterized (critical micelle concentration, water content, and micelle size) and their extraction efficiency were analysed. Cetyltrimethylammonium bromide with n-heptanol RMS was found to offer 100% yield. The identified RMS may be further considered for the commercial extraction of LF from complex biological sources.

Keywords: Lactoferrin, Reverse Micellar Extraction, Surfactants.

Introduction:

Lactoferrin (LF) is a multifunctional protein majorly available in animal sources (Ammons and Copie, 2013). It shows antiviral, antimicrobial, antibacterial activity. LF has high influence on iron distribution on organisms. Apart from these important functions LF also helps to inhibit tumour growth (Adlerova et al., 2008). It is the second most generous whey protein (Rai et al., 2014). The demand of LF is observed to be increased yearly and it is expected to reach 2,62,000 kg in 2017. According to market survey huge global shortage of LF has been reported (Carvalho et al., 2016). Inverse proportion of demand and supply of the LF has been observed but countable reports are available for LF extraction from whey (Chen et al., 2007). Currently extraction of lactoferrin with ion exchange chromatography (Ye et al., 2000), Magnetic affinity absorbents, (Chen et al.,

2007) at batch scale is reported. However, the Conventional downstream process reported in the literature like chromatography, precipitation techniques used for the separation and purification of LF are difficult to scale up. Hence the present research focused on the development of simplified LF extraction and purification process.

Liquid- liquid extraction with biomolecule compatible solvents has the potential to extract the component like LF with higher purity and opened a new window to scale up the process in an economical way (Madhusudhan and Raghav Rao, 2013). Reverse micellar based extraction system is an interesting option to extract a specific protein selectively from a complex mixture like whey, since the separation is based on electrostatic interaction and size differences of the target molecules, (Mazzola et al., 2008). Reverse micellar extraction of proteins like soy protein

(Chen et al., 2014), BSA (Xiao et al., 2013), lectin (He et al., 2015), bromelain (Wan et al., 2016) from their respective biological crude mixtures has been reported.

Since the selective extraction of a specific protein is based on the type of surfactant and organic solvent associated with the reverse micelle system, different reverse micellar systems (RMSs) which are formed by anionic (AOT), cationic (CTAB) and non-ionic (Triton X 100) surfactants with organic solvents are examined for the extraction of LF from the aqueous solution. The physicochemical characteristics like Critical Micelle Concentration (CMC), water content (W_0) and size of all the RMSs were measured. The LF extraction efficiency of the RMSs was also studied to ascertain the suitability of the selected systems.

MATERIALS AND METHOD:

Materials: The surfactants CTAB (cetyltrimethylammonium bromide - cationic), AOT (anionic) and Triton X100 (non-ionic) having 99% purity were procured from Sigma Aldrich, India and used for experiments without further purification. Bovine lactoferrin (LF) were purchased from Sigma Aldrich, India. Bovine serum albumin was purchased from Hi media, India. Organic solvents of analytical grade namely Isooctane, n-Decanol, toluene, n-heptanol were procured from Loba. Folin-Ciocalteu reagent (FCR) is purchased from Merck, India.

Characterization of RMSs: Based on physicochemical properties of surfactants and organic solvents (Table 1), six different reverse micellar systems were selected. Triton X 100/ Isooctane, AOT/ Isooctane, AOT/ n-decanol, CTAB/ Toluene, CTAB/ Isooctane, CTAB/ n-heptanol were chosen for the LF partitioning study. CMC of different reverse micellar systems was found by estimating the physical properties like refractive index (Digital Refractometer, RX-500, ATAGO Co. Ltd. Japan) and density (Digital density meter, DDM 2911, Rudolph, USA)

of the surfactant/ solvent mixture using properties. Water content (W_0) of all selected micellar system at CMC was measured using Karl Fischer Titrator (899 coulometer, Metrohm, Switzerland). The reverse micelle size (Eq. 1) was calculated using the water content and reported in the Table 2.

$$R_m = 0.175W_0 \quad (1)$$

Reverse micellar extraction of Lactoferrin (LF): All the six RMSs are considered for the extraction of LF. Initially equal amount of organic phase (containing surfactant concentration above CMC) were mixed thoroughly with aqueous phase (containing LF concentration 0.1mg/ml) using magnetic stirrer at 800 rpm and room temperature for 20 min. Then the mixture was subjected to centrifugation at 474g and 20 min (Remi C-24 plus, India) for phase separation. The organic phase was carefully separated. Protein concentration after LF concentration in each phase was measured using Folin-Lowry's assay. The absorbance was measured at a wavelength of 660 nm using the spectrophotometer (UV3000+, Labindia). Extraction efficiency was calculated by using following equation,

$$\text{LF Extraction efficiency (\%)} = \left(\frac{\text{LF conc. in organic phase}}{\text{LF conc. in feed phase}} \right) \times 100 \quad (2)$$

The effect of surfactant concentration (5-100 mM), pH (2-9), and addition of electrolyte salts (NaCl and KCl - 0.1 to 1 M) were also studied for the higher extraction efficiency of LF.

RESULT AND DISCUSSION:

Reverse micellar Characterisation: The Physical and chemical properties of the surfactants and organic solvents plays important role in reverse micelle formation. Topological surface area, rotatable bond count and number of hydrocarbon chain present in surfactant and solvents mainly responsible for the RM

formation and also for the W_0 (Tang et al., 2014). The physical and chemical properties of all the selected surfactants and solvents are listed in Table 1. The CMC, size of the micelle and W_0 were measured for all the six selected systems and reported in Table 2.

Table 1: Physical and chemical characteristics of phase forming components

System component s	Topolo gical surface Area (A°)	Hydro - carbo n chain	Rotatable Bond count
TX100	29.5	1	6
AOT	54	2	18
CTAB	0	1	15
Isooctane	18.5	1	2
n-decanol	20.2	1	8
n-Heptanol	20.2	1	5
Toluene	0	0	0

The systems in which the surfactant and solvents are showing topological surface charge (TX100/Isooctane, AOT/Isooctane, AOT/n-decanol), the formation of reverse micelle is best understood with taking in consideration the sum of the average of total surface area of solvent and surfactant, presence of hydrocarbon chain around central molecule, rotatable carbon atoms in solute and surfactants (Moulik and Ray, 1994). Taking all physical and chemical properties in account a relation between CMC value and W_0 of all reverse micellar systems has been found and these parameters are proportional to the sum of averages of Rotatable carbon atom and average charge on participants in group, is lower (28) in TX100/Isooctane system for CMC value 0.3mM and corresponding less W_0 (4.35). In case of AOT/Isooctane the total rotatable bond count and average charge on the system found to be increased to 46.25, as result CMC and W_0 found to be increased to 1mM and 5.66 respectively. Similar result has been observed in AOT /n-decanol system with a little fall in CMC (0.8mM) which supports the above conclusion. Whereas in systems

(CTAB/Isooctane-CMC 2mM, CTAB/ n-heptanol- CMC 1mM and CTAB/Toluene-CMC 2mM) where the solvent and surfactant both are charged or any one of them shows zero topological surface charges, the availability of side chain hydrocarbon in components along with sum of the average of total surface charge of solvent and surfactant plays major role (Tadros, 2005).

Table 2 Physical Characteristics of RMSs

RMSs	CM C (m M)	W_0		RM size	
		With hou t LF (mol ratio)	With LF (mol ratio)	With out LF (nM)	With LF (nM)
AOT/Isooo ctane	1	5.6 6	-	0.99	-
CTAB/ Isooctan e	2	7.8 7	13.4	1.37	2.34
TX100/ isoctane	0.3	4.3 5	9.88	0.76	1.72
AOT/ n- decanol	0.8	6.4 8	-	1.13	-
CTAB/ Toluene	2	8.9 5	-	1.56	-
CTAB/n- Heptanol	1	9.6 4	15.9 1	1.68	2.78

The side chain hydrocarbons interact with each other in different symmetry and are responsible for steric repulsion between surfactant and solvent molecules leading to formation of equilibrium for retention of water with in it. As in these cases the CMC value is high if the system doesn't have any net charge them, the RM formation is solely performed by presence of side chain and the steric repulsion between surfactant and solvent molecule.

Reverse micellar extraction of LF: Out of the six RMSs (Table 2) studied for the extraction of LF, only three RMSs (TX100/isoctane, CTAB/Isooctane and CTAB/n-Heptanol) were found to provide a favourable LF extraction (Fig. 1). There was no LF extraction observed with

AOT/Isooctane, AOT/ n-decanol and CTAB/ Toluene due to weak electrostatic interaction between surfactant and solute molecule (He et al., 2015). LF precipitation at the interphase between the aqueous and organic phase was observed for AOT/Isooctane, AOT/ n-decanol systems. Further the extraction was found less due to the organogel formation in the presence of excess water in organic phase of CTAB/ Toluene system(Vaidya et al.,2011). Hence these three systems were discontinued for the further LF extraction studies.

The surfactants CTAB and TX100 contain only one lipophilic chain, therefore not able to form reverse micelles in organic media without addition of second surface active agent, called as co-surfactant. In case of CTAB/n-heptanol, n-heptanol is used as organic phase which also acts as co-solvent and aid the spontaneous formation of more number of reverse micelle to capture more amount of LF (Street,1994). However, the lesser extraction efficiency was found in case of TX 100/Isooctane and CTAB/Isooctane due to the longer chain alkane (Isooctane) which is more hydrophilic than lipophilic in nature used as organic phase.

aqueous phase was varied from 2-10 for all three RMSs (Fig.2). Better interaction between positively charged head group of CTAB and negative charge on protein resulted in 5% -CTAB/Isooctane (pH-9.6) and 45% in case of CTAB/n-Heptanol (pH-10) as a result of capture of lactoferrin into reverse micelles (Li et al.,2007). Only 3% of LF transfer has been observed in TX100/Isooctane (pH-7).

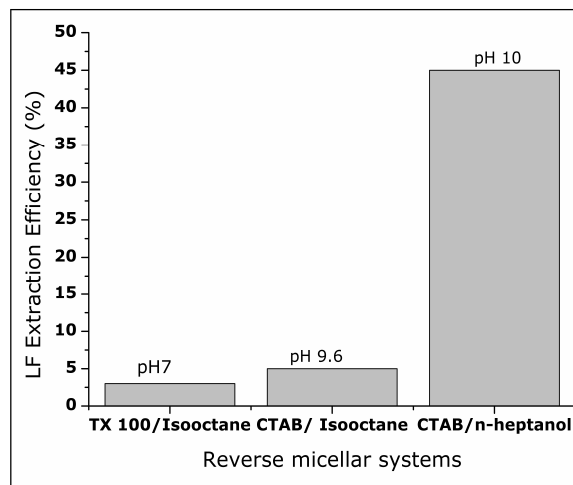


Fig.2 Effect of pH on LF extraction efficiency on TX100/Isooctane, CTAB/Isooctane and CTAB/n-heptanol

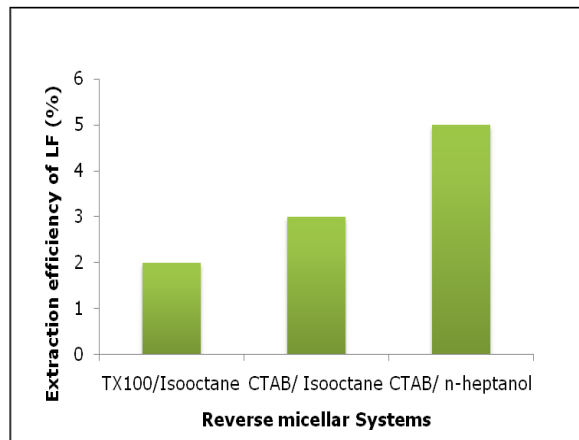


Fig.1 LF extraction efficiency of different RMSs (Without altering variables)

Effect of pH: Lactoferrin is a basic protein having pI of 9.4. Below pI, LF posses positive charge and above pI it carries negative charge (Steijns et al. 2011). To improve extraction efficiency pH of the

Effect of Ionic strength: Further salt concentration (KCl and NaCl- 0.1to 1.3M) was varied in the aqueous phase to achieve better extraction efficiency. Addition of electrolytes to the aqueous phase of TX100/ Isooctane RMSs could not help to improve LF extraction efficiency. 0.8M NaCl concentration in CTAB / Isooctane found to increase protein transfer efficiency to 7% whereas 1M of NaCl and 0.9M of KCl concentration in case of CTAB / n-heptanol (Table 3) resulted in increased protein transfer efficiency 98% and 100% respectively. Addition of ions to the aqueous phase helps to stabilise the micellar structure and also enhances the electrostatic interaction between polar head group of surfactant molecule and solute and results in better protein partitioning according to Lakshmi et al. (2011).

Table 3 Effect of Salt concentration on LF extraction efficiency of TX100/Isooctane, CTAB/Isooctane and CTAB/n-heptanol

Reverse Micellar Systems	NaCl		KCl	
	Conc. (M)	LF extra ction Effici ency %	Conc. (M)	LF extra ction Effici ency %
TX100/ Isooctane	-	-	-	-
CTAB/Isoo ctane	0.8	7	-	-
CTAB/n- heptanol	1	98	0.9	100

W_0 of micellar systems after extraction of the lactoferrin has been measured (Table 2) and notable increase in W_0 has been observed after LF transfer to the organic phase in all reverse micellar systems. Comparatively W_0 of non-ionic reverse micellar systems has observed to be low than ionic reverse micellar with isoctane and n-heptanol. Due to the lack of presence of strong interaction forces; partitioning of LF to organic phase is low which also resulted in less W_0 during LF Extraction in case of TX100/Isooctane, (Nagarajan,2002).

CONCLUSIONS

A suitable reverse micellar system, CTAB/n-heptanol, for the extraction of LF was screened by incorporating three types of surfactants in six different RMSs. Physicochemical properties of all the components used in the RMSs were studied. Physicochemical properties possible reveres micellar systems were also measured to ascertain the relation between the properties and LF extraction efficiency. CTAB/n-heptanol RMSs was found to be a favourable system at a pH of 7 and adding 1M of NaCl or 0.9M of KCl as a electrolytes for LF extraction. Hence, it can be further used to extract LF from complex biological materials.

REFERENCES

- [1] Adlerova, L et al (2008), Lactoferrin: a review, Veterinarni Medicina, Vol. 53, No.9, pp. 457-468.
- [2] Alsaed, A K et al (2013), Characterization, concentration and utilization of sweet and acid whey. Pakistan Journal of Nutrition, Vol.12, No.2, pp. 172.
- [3] Ammons M C, and Copie V (2013), Mini-review: lactoferrin: a bioinspired, anti-biofilm therapeutic, Biofouling, Vol.29, No.4, pp. 443-455.
- [4] Carvalho, B M A et al (2016), Steric mass action model for lactoferrin adsorption in cryogel with immobilized copper ions, Brazilian Journal of Chemical Engineering, Vol.33, No.1, pp. 215-223.
- [5] Chen, J. Et al (2014), The forward and backward transport processes in the AOT/hexane reversed micellar extraction of soybean protein, Journal of food science and technology, Vol. 51, No.10, pp. 2851-2856.
- [6] Chen, L et al (2007), Isolation of lactoferrin from acid whey by magnetic affinity separation, Separation and Purification Technology, Vol. 56, No.2, pp. 168-174.
- [7] Gunnarsson, G et al (1980), Surfactant association into micelles: An electrostatic approach, The Journal of Physical Chemistry, Vol. 84, No.23, pp. 3114-3121.
- [8] He, S et al (2015), Reverse micellar extraction of lectin from black turtle bean (*Phaseolus vulgaris*): Optimisation of extraction conditions by response surface methodology, Food chemistry, Vol. 166, pp. 93-100.
- [9] Krishna S H et al (2002), Reverse Micellar Extraction for Downstream Processing of Proteins/Enzymes, In History and trends in bioprocessing and biotransformation., Vol. 75, pp. 119-183.
- [10] Lai, W C & Lai, P H (2013), New Phases Found in Reverse Micelle Systems with High Concentrations of AOT, The Journal of Physical Chemistry B, Vol.117, No.32, pp. 9568-9575.
- [11] Lang, J et al (1991), Quaternary water in oil microemulsions. 1. Effect of alcohol chain length and concentration on droplet size and exchange of material between droplets, The Journal of Physical Chemistry, Vol. 95, No.23, pp. 9533-9541.
- [12] Lakshmi, M C, & Raghavarao, K S M S (2010), Downstream processing of soy hull peroxidase employing reverse micellar extraction, Biotechnoogy and Bioprocess Engineering, Vol. 15 No.6, pp. 937-945.

6th International Engineering Symposium - IES 2017

March 1-3, 2017, Kumamoto University, Japan

- [13] Madhusudhan, M C, & Raghavarao, K S M S (2013), Aqueous Two-Phase Extraction for the Recovery of Beet Pigments and Enzymes, Red Beet Biotechnology, pp. 393-408, Springer US.
- [14] Mazzola, P G et al (2008), Liquid-liquid extraction of biomolecules: an overview and update of the main techniques, Journal of chemical technology and biotechnology, Vol.83,No.(2),pp. 143-157.
- [15] Nagarajan, R (2002), Molecular packing parameter and surfactant self-assembly: the neglected role of the surfactant tail, Langmuir, Vol.18, No. 1, pp.31-38.
- [16] Rai, D et al (2014), Longitudinal changes in lactoferrin concentrations in human milk: a global systematic review, Critical reviews in food science and nutrition, Vol.54, No.12, pp.1539-1547.
- [17] Steijns, J M and Van Hooijdonk, A C M (2000), Occurrence, structure, biochemical properties and technological characteristics of lactoferrin, British Journal of Nutrition, Vol. 84, No.S1,pp. 11-17
- [18] Street, G. (Ed.). (1994). Highly selective separations in biotechnology, No. 577.15 HIG, Blackie Academic & Professional.
- [19] Tang, X et al (2014), Molecular Dynamics simulations of structure–property relationships of tween 80 surfactants in water and at interfaces, The Journal of Physical Chemistry B, Vol.118, No.45,pp. 12907-12918.
- [20] Tadros, T. F. (2005), Physical chemistry of surfactant solutions, Colloids in Agrochemicals, Volume 5, pp.19-40.
- [21] Vaidya, A A et al (2001), Design and evaluation of new ligands for lysozyme recovery by affinity thermo precipitation, Chemical Engineering Sciences, Vol.56, No.19,pp. 5681-5692
- [22] Wan, J et al, Reverse micellar extraction of bromelain from pineapple peel—Effect of surfactant structure, Food Chemistry, Vol. 197, pp. 450-456.
- [23] Xiao, J et al (2013), Reverse micellar extraction of bovine serum albumin—A comparison between the effects of gemini surfactant and its corresponding monomeric surfactant, Food chemistry, Vol. 136, No.2,pp. 1063-1069
- [24] Ye, X et al (2000), Isolation of lactoperoxidase, lactoferrin, α -lactalbumin, β -lactoglobulin B and β -lactoglobulin A from bovine rennet whey using ion exchange chromatography, The international journal of biochemistry & cell biology, Vol. 32, No.11,pp. 1143-1150.

6th International Engineering Symposium - IES 2017

March 1-3, 2017, Kumamoto University, Japan

